Mechanistic Studies on Histone Demethylases and Related Enzymes

A thesis submitted to the Board of the Faculty of Physical Sciences of the University of Oxford in partial fulfilment of the requirements for the degree of Doctor of Philosophy

Richard James Hopkinson

Pembroke College

Trinity Term 2011

Mechanistic Studies on Histone Demethylases and Related Enzymes

Richard James Hopkinson, Pembroke College **Trinity Term 2011**

Abstract

Histone lysyl demethylases (2OG demethylases) are a family of nuclear proteins that catalyse the demethyation of N^{ϵ}-methylated lysines on histone tails. 2OG demethylases belong to the 2-oxoglutarate and Fe(II) dependent dioxygenase superfamily, which utilise molecular oxygen to oxidise a wide variety of cellular substrates. The methylation states of histone lysines play crucial roles in regulating gene transcription, and consequently, the 2OG demethylases have been identified as important regulators of chromatin. Therefore, the understanding of the mechanisms and cellular activities of the demethylases is of considerable interest in the context of chromatin biology, and also for medicinal chemistry.

Work in this thesis has focused upon investigating the mechanisms and reactivities of 2OG demethylases *in vitro*. NMR spectroscopy techniques were used to monitor demethylation catalysed by the 2OG demethylase JMJD2E, which resulted in the acquisition of kinetic parameters. Also, the use of a ^{13}C-labelled substrate during NMR analysis enabled the first direct detection of enzymatically-produced formaldehyde. Studies with methylated lysine analogues using mass spectrometry and NMR methods revealed that many 2OG demethylases are capable of oxidising multiple substrates. One such substrate, N^{ϵ}-methylisopropyllysine, was found to be hydroxylated by JMJD2E, providing strong evidence that 2OG demethylase-catalysed lysyl demethylation proceeds via hydroxylation. Studies with the lysine analogues prompted investigations with methylated arginine peptides; unexpectedly, three 2OG demethylases were observed to demethylate methylated arginines in both histone peptide variants and at known methylarginine sites in histone peptides. These findings indicate that 2OG demethyases may have diversified functions in cells, and are capable of accepting substrates besides methylated lysines. Investigations with point-substituted variants of the 2OG demethylase JMJD2A revealed new insights into the role of lysine-241 during catalysis. Specifically, the proposed role of lysine-241 in oxygen binding was discredited, with evidence suggesting that lysine-241 is likely to be involved in binding the substrate in the active site. Mass spectrometry experiments with the 2OG demethylase FBXL11 identified hydrolysis of histone peptides during incubation with the protein. Further analyses using mass spectrometry revealed that a metalloprotease was the likely catalyst for histone cleavage, indicating that optimised expression and purification of FBXL11 is required for quantitative assays. Studies with deuterated methyllysine substrates revealed a small kinetic isotope effect during 2OG demethylase-catalysed demethylation, indicating that the hydroxylation step during catalysis is partially rate determining. Finally, work was concentrated on investigating the potential metabolism of formaldehyde released during histone demethylation. NMR studies were conducted monitoring the non-enzymatic reaction of glutathione and formaldehyde; these revealed two novel adduct species that may be formed in cellular environments. The function and mechanism of a putative formaldehyde activating enzyme (GFA) was then investigated. These studies showed a limited effect of GFA upon formaldehyde reactivity, suggesting that GFA is not involved in formaldehyde metabolism.

In summary, this work has revealed many new insights into both the substrate specificities and catalytic mechanisms of 2OG demethylases and has provided extensive studies probing potential formaldehyde metabolism. These investigations should form the basis of many new research areas on 2OG demethylases and related enzymes.

Table of Contents

Acknowledgements

Firstly, I should like to thank Prof. Chris Schofield for providing fantastic supervision during my D. Phil. studies and for allowing me the freedom to pursue a variety of interesting research projects. I have thoroughly enjoyed all aspects of my research within his group and shall be eternally grateful for all the help and advice that he has given me.

Work in this thesis would not have been possible without contributions from many collaborators. In particular, I am indebted to the many co-workers who kindly donated demethylase enzymes (Dr. Nathan Rose, Dr. Akane Kawamura, Dr. Olly King, Dr. Lars Hillringhaus, Dr. Stan Ng, Louise Walport, Tristan Smart and Owen Chang). My thanks also go to those who have collaborated on specific aspects of this work (Dr. Nathan Rose, Dr. Refaat Hamed, Dr. Wei Ge, Dr. Elena Sánchez-Fernández, Dr. Holger Kramer, Dr. Adam Hardy, Louise Walport, Luc Henry, David Ivison and Pippa Barlow). Individual contributions are acknowledged in the text where appropriate.

More generally, I should like to thank those workers who have instructed and assisted me during my time as a research student. Thanks go to Dr. Tim Claridge, Dr. Barbara Odell and Ivan Leung for answering my countless questions about NMR; Dr. James McCullagh, Dr. Holger Kramer, Dr. Frank Sobott, Dr. Tom Brown Jr., Marina Demetriades, Lingzhi Gong and Colin Sparrow for help with mass spectrometry; David Ivison and Luc Henry for advice during protein expression and purification; Dr. Nathan Rose, Dr. Akane Kawamura, Dr. Olly King, Dr. Lars Hillringhaus and Dr. Emily Flashman for help with enzyme assays; Dr. Jasmin Mecinovic and Anna Rydzik for synthetic discussions; Dr. Mike McDonough and Dr. Rashed Chowdhury for help with interpreting crystallographic data; Luc Henry and Ivan Leung for discussions on enzyme kinetics; and finally Dr. Adam Hardy and Wendy Sobey for advice with enzymology, as well as for maintaining the lab. In addition, I should like to acknowledge all other members of the CJS group past and present for the help and

advice they have given me, and for providing a relaxed and enjoyable environment in which to work. In no particular order, thanks go to Dr. Delphine Fischer, Dr. Steven Inglis, Dr. Esther Woon, Dr. Tobias Gruber, Dr. Maggie Ho, Dr. Aman Iqbal, Dr. Alex Wolf, Dr. Celia Webby, Dr. Mukram Mackeen, Dr. Ed Batchelar, Dr. Christoph Loenarz, Dr. Dante Rotili, Dr. Ian Clifton, Andrea Szöllössi, Rubén Gómez-Castellanos, Rok Sekirnik, Hanna Tarhonskaya, Monica Mantri, Eleanor Bagg, Nikita Loik, Inga Pfeffer and many others.

Finally, my most heartfelt thanks must go to my parents for their continued support throughout my education and research career. This thesis is testament to their love and encouragement. Also, I should like to thank my brother and best friend Matthew for his company and undying support during my time in Oxford.

Abbreviations

^{13}C-HCHO	^{13}C-labelled formaldehyde
$^{18}O_2$	^{18}O-labelled dioxygen
2,4-PDCA	pyridine-2,4-dicarboxylic acid
2OG	2-oxoglutarate
2TY	2-tryptone/yeast extract
ABH	AlkB homologue
AcH	acetaldehyde
ADH	aldehyde dehydrogenase
AlkB	Alkylation Repair Protein B
BSA	Bovine Serum Albumin
CD	circular dichroism
CENP-V	human Centromere Protein V
CHCA	α-cyano-4-hydroxycinnamic acid
COSY	correlation spectroscopy
Da	Dalton (mass unit)
dAFN	50 mM ammonium formate, 500 mM sodium chloride in D_2O
DCDO	deuterated formaldehyde
DMSO-d6	deuterated dimethylsulfoxide
DNA	deoxyribonucleic acid
E. coli	*Escherichia coli*
Et	ethyl
EXSY	exchange spectroscopy
FAD	flavin adenine dinucleotide
FBXL	Fbox, Leucine-rich repeat Protein
FDH	Formaldehyde Dehydrogenase
FIH	Factor Inhibiting Hypoxia Inducible Factor

Fmoc	Fluorenylmethyloxycarbonyl
FPLC	Fast Protein Liquid Chromatography
FTO	Fat and Obesity-Associated protein
GBBH	γ-Butyrobetaine Hydroxylase
GFA	Glutathione-Dependent Formaldehyde-Activating Enzyme
GSH	glutathione
GC	γ-glutamylcysteine
HDAC	Histone Deacetylase
HEPES	4-(2-hydroxyethyl)-1-piperazineethanesulfonic acid
HIF	Hypoxia-Inducible Factor
HMBC	heteronuclear multiple-bond correlation spectroscopy
HMG	*S*-hydroxymethylglutathione
HOBt	1-hydroxybenzotriazole
HP1	Heterochromatin Protein 1
HPLC	High Performance Liquid Chromatography
HSQC	heteronuclear single-quantum correlation spectroscopy
IPTG	isopropyl β-D-thiogalactopyranoside
JARID	Jumonji, AT rich interactive domain
JmjC	Jumonji-C
JMJD	Jumonji-C Domain containing protein
Ket2	N^{ϵ}-diethyllysine
Kfor	N^{ϵ}-formyllysine
Kipr	N^{ϵ}-isopropyllysine
Kme	N^{ϵ}-monomethyllysine
Kme2	N^{ϵ}-dimethyllysine
Kme3	N^{ϵ}-trimethyllysine
Kmeet	N^{ϵ}-methylethyllysine
Kmeipr	N^{ϵ}-methylisopropyllysine
LC-MS	Liquid Chromatography-Mass Spectrometry

LSD	Lysine Specific Demethylase
MALDI	Matrix-Assisted Laser Desorption/Ionisation
Me	methyl
MG	methylglyoxal
NAD	nicotinamide adenine dinucleotide
NMR	Nuclear Magnetic Resonance
NOESY	Nuclear Overhauser Effect Spectroscopy
NOG	*N*-oxalylglycine
Oet2	N^{ϵ}-diethylornithine
Ome2	N^{ϵ}-dimethylornithine
P3H	Collagen Prolyl-3-Hydroxylase
P4H	Collagen Prolyl-4-Hydroxylase
PADI4	Protein Arginine Deiminase 4
PAHX	Phytanoyl-CoA 2-Hydroxylase
PHD	Plant Homeodomain
PHD1-3	Prolyl Hydroxylase 1-3
PHF	PHD finger protein
ppm	parts per million
PTM	Post Translational Modification
Rme	N^{ω}-monomethylarginine
Rme2a	asymmetric N^{ω}-dimethylarginine
Rme2s	symmetric N^{ω}-dimethylarginine
RNA	ribonucleic acid
SDS-PAGE	Sodium Dodecylsulfate Polyacrylamide Gel Electrophoresis
SPPS	Solid Phase Peptide Synthesis
SUMO	Small Ubiquitin-Like Modifier
TauD	Taurine Dioxygenase
TFA	trifluoroacetic acid
TLC	Thin Layer Chromatography

TMLH	Trimethyllysine Hydroxylase
TOF	Time-of-Flight
TOCSY	Total Correlation Spectroscopy
Tris	tris(hydroxymethyl)aminomethane
UTX	Ubiquitously Transcribed Tetracopeptide repeat, X chromosome
UTY	Ubiquitously Transcribed Tetracopeptide repeat, Y chromosome
UV	Ultraviolet
Vis	Visible

Chapter 1

Introduction

1.1 2-Oxoglutarate and Iron(II) Dependent Oxygenases

The 2-oxoglutarate (2OG) and ferrous iron dependent dioxygenases (referred to hereafter as 2OG oxygenases) are a superfamily of non-heme enzymes that catalyse a wide variety of biologically important reactions.[1-5] 2OG oxygenases are present in most organisms, with over 60 members of the enzyme family having been identified in the human proteome.[5] Known reactions catalysed by human 2OG oxygenases are currently restricted to hydroxylation and demethylation; however, in plant and bacterial systems, a number of other oxidative processes including halogenation,[6, 7] epimerisation,[8, 9] desaturation,[9, 10] ring expansion[11] and ring closure[10] have been identified. Consequently, 2OG oxygenases possess one of the most diverse reactivity profiles of any enzyme family, a fact that alludes to their involvement in a wide range of biochemical pathways.

1.1.1 Mechanism of Oxidation

Despite their functional variety, members of the 2OG oxygenase family possess remarkably conserved catalytic machinery. Oxidation of a substrate molecule invariably occurs after oxidation of a redox active Fe(II) ion, which is bound within the enzyme active site by interactions with two or three protein residues (usually two histidines and one aspartic acid/glutamic acid).[12, 13] The iron binding site is positioned within a conserved double-stranded β-helix fold (commonly referred to as a β-barrel or jellyroll motif, Figure 1.1), which facilitates binding of all substrates and co-factors simultaneously. In some cases, the oxidised iron species has been identified as an Fe(IV)-oxo complex using UV-Vis, Mössbauer, EPR and Raman spectroscopies.[14] Oxidation of the catalytic iron is coupled to the conversion of 2OG to succinate, which

proceeds with concomitant reduction of molecular oxygen. Therefore, 2OG oxygenase activity in cells is dependent on the availability of both oxygen and 2OG, allowing 2OG oxygenases to play roles in both oxygen sensing and Krebs cycle regulation.[15, 16] Interestingly, some members of the 2OG oxygenase family appear to be more active in the presence of ascorbate.[3, 17-21] However, the manner in which ascorbate stimulates these enzymes is not conclusively understood.

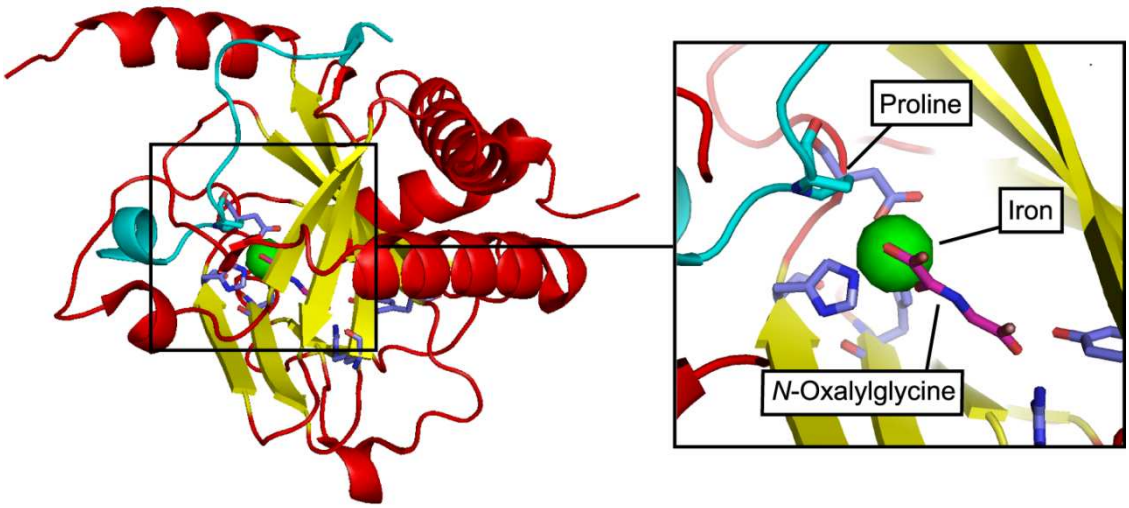

Figure 1.1 Views from a crystal structure of human hypoxia-inducible factor prolyl hydroxylase (PHD2) with bound substrate (Blue) (PDB ID 3HQU).[22] The double-stranded β-barrel is highlighted in yellow. The catalytic iron is bound in an octahedral geometry to two histidines and one aspartic acid residue in the active site. Binding at two of the remaining coordination sites by the 2OG analogue *N*-oxalylglycine is also shown (Pink). The last remaining site is proposed to accept molecular oxygen during catalysis.

A consensus mechanism for the 2OG oxygenases is outlined in Scheme 1.1.[23] In this Scheme, formation of the Fe(IV)-oxo intermediate is followed by oxidation (presumed radical) of a C-H bond on the substrate, resulting in the formation of a carbon radical and a Fe(III)-OH complex. A rebound mechanism between the two high-energy species then results in the formation of the hydroxylated product, with the catalytic iron returning to its +2 oxidation state. As this mechanism suggests that formation of the Fe(IV) intermediate is conserved throughout the 2OG oxygenase family, it is proposed that substrate binding is the predominant factor in determining reactivity. However, observed fluctuations in both oxygen binding and the rates of Fe(IV)-oxo intermediate

formation for different oxygenases have recently challenged this hypothesis, implying that the precise mechanisms of Fe(IV) formation may vary from enzyme to enzyme.[24]

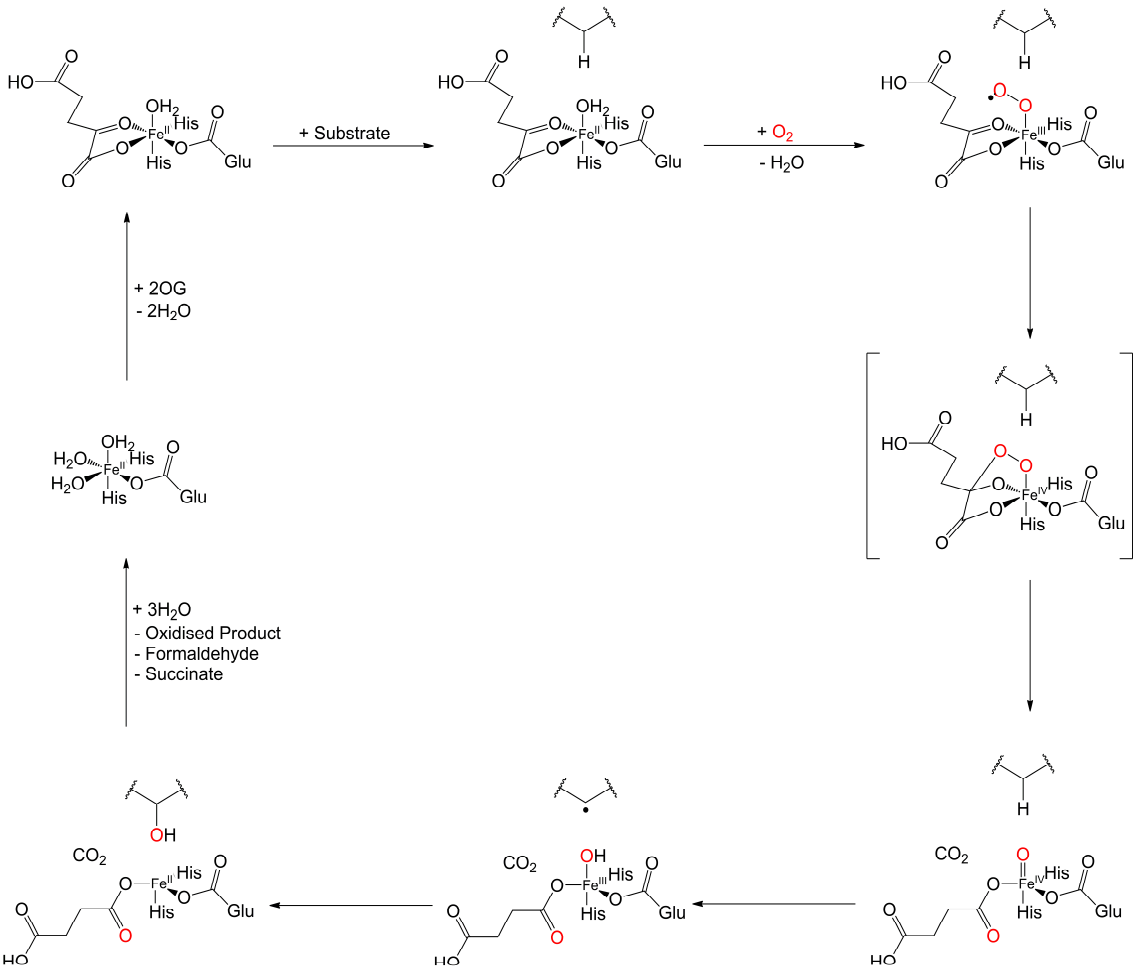

Scheme 1.1 Consensus mechanism for 2OG oxygenase catalysed oxidation, modified from Hoffart *et al.*[25]

1.1.2 Functions of Human 2OG Oxygenases

a) Modification of Collagen Structure

Collagen is the most abundant protein in humans and is a main component of connective tissue.[26] Functional analysis of collagen prolyl-4-hydroxylase (P4H), the first reported human 2OG oxygenase, revealed that prolyl hydroxylation at the *trans* position catalysed by this enzyme resulted in stabilisation of collagen structure.[27, 28] Interestingly, it was also discovered that prolyl hydroxylation at the 3-position by the 2OG oxygenase prolyl-3-hydroxylase (P3H), which occurs

after prolyl 4-hydroxylation on a neighbouring proline, destabilises the collagen triple helix,[28] suggesting that interplay between different oxygenase catalysed pathways can affect the overall stability of collagen structure. Oxygenase catalysed hydroxylation of collagen lysyl residues at the 5-position has also been identified as a regulator of collagen structure, possibly by facilitating subsequent glycosylation of the collagen protein.[29-31]

b) Oxygen Sensing

The hypoxia-inducible factor (HIF) prolyl hydroxylases (PHD1-3) catalyse *trans*-hydroxylation at the 4-position in an analogous manner to that observed for collagen prolyl-4-hydroxylase. However, PHD-catalysed prolyl hydroxylation on the HIF-α subunit (three isoforms of HIF-α have been identified, although the isoform HIF-1α is the most extensively studied) recruits the von Hippel-Lindau tumour suppressor protein, resulting in proteasomal degradation of HIF-α via the E3-ligase-mediated ubiquitylation pathway.[32-36] Under hypoxic conditions, the lack of available oxygen results in down-regulation of prolyl hydroxylation, stabilising the HIF-α subunit. HIF-α is then able to migrate to the cell nucleus and dimerise with HIF-β, signalling transcription of many target genes.[37] Another mechanism of oxygen-dependent transcriptional regulation involves asparaginyl hydroxylation of HIF-α by the 2OG oxygenase factor inhibiting HIF (or FIH).[38] In this case, hydroxylation of an asparagine residue blocks binding of the co-activator p300/CBP, inhibiting transcriptional activation.[39, 40] In addition to HIF-α, FIH has also been reported to catalyse asparaginyl hydroxylation on ankyrin repeat proteins.[41] It has been suggested that ankyrin hydroxylation may stabilise tertiary structure,[42] although the precise effects this modification may have on protein function has not been conclusively resolved.

c) L-Carnitine Biosynthesis

L-Carnitine, an important transport molecule facilitating fatty acid metabolism, is acquired by humans as a dietary supplement and also via biosynthesis.[43] The first step in carnitine biosynthesis in humans involves the β-hydroxylation of N^{ϵ}-trimethyllysine, which is catalysed by the 2OG oxygenase trimethyllysine hydroxylase (TMLH).[44] After subsequent fragmentation and oxidation catalysed by an aldolase and a dehydrogenase respectively, the last step in the biosynthesis again involves 2OG oxygenase catalysed hydroxylation. This step is catalysed by γ-butyrobetaine hydroxylase (GBBH or BBOX),[45] which is structurally related to TMLH.[46]

d) Phytanoyl-CoA Metabolism

Metabolism of phytanoyl-CoA, a derivative of the chlorophyll metabolite phytanic acid, is facilitated in peroxisomes via initial hydroxylation at the α-carbon.[47] This reaction, which is catalysed by the 2OG oxygenase phytanoyl-CoA 2-hydroxylase (PAHX) allows partial cleavage of the aliphatic chain, enabling further metabolism via conventional β-oxidation. Mutations in PAHX have been reported to ablate its hydroxylation activity, leading to an accumulation of phytanic acid in cell tissue (a condition referred to as adult Refsum's disease).

e) Lysyl Hydroxylation on RNA Splicing Proteins

In addition to the reported δ-lysyl hydroxylation in collagen proteins, the 2OG oxygenase JMJD6 has been observed to hydroxylate lysine residues in proteins involved in RNA splicing.[48-50] Initial investigations on JMJD6 identified this protein as an arginine demethylase, acting on histone substrates; however, these findings have been difficult to reproduce in other laboratories.[51] Recent studies characterising the lysyl hydroxylase activity of JMJD6 have indicated that

hydroxylation produces 5-hydroxylysine with (*S*)-stereochemistry at the δ-position,[52] which is the opposite of the stereochemistry observed in collagen.

f) DNA/RNA Modification

In *E.coli*, DNA is demethylated by the 2OG oxygenase AlkB, which catalyses the removal of methyl groups from *N*-methylated bases in single-stranded DNA.[53, 54] Demethylation is proposed to occur via hydroxylation on the methyl group, resulting in fragmentation of an unstable hemiaminal intermediate to form demethylated DNA and HCHO as products.[4, 55] AlkB has also been found to demethylate a variety of alkylated DNA and RNA substrates, thus rescuing these strands from their toxic alkylated states.[56-58] Despite its broad substrate specificity, however, it appears that the modified bases 1-methyladenine and 3-methylcytosine are the most readily dealkylated.

In humans, 8 AlkB homologues (ABH 1-8) have been identified to date; however, only two of these enzymes (ABH2 and ABH3) have been shown to possess demethylase activities.[59] More recently, ABH8 has been shown to hydroxylate 5-methoxycarbonylmethyluridine on tRNA, suggesting a diversified reactivity profile for the ABH subfamily.[60] In addition to the ABH enzymes, another 2OG oxygenase has also been reported to demethylate DNA. Fat mass- and obesity-associated enzyme (FTO) demethylates 3-methylthymine and 3-methyluracil, and is linked to genetic regulation of obesity.[61-63] Also, the TET family of 2OG oxygenases have recently been reported to hydroxylate the methyl group of 5-methylcytosine, potentially indicating a regulatory role for this novel DNA modification.[64-66]

g) Histone Demethylation

Finally, 2OG oxygenases are well known as lysyl demethylases on histone tails.[67-78] Histones are small basic globular proteins that interact with DNA in cell nuclei and are thought to both package DNA and regulate its transcription

by means of the 'histone code' (see below). The *N*-terminal tails of histones contain a number of lysine residues, which are reported to be methylated on their side chain amines by a number of methyltransferase enzymes.[79] Demethylation of these methyl marks is facilitated by lysyl demethylases, and is proposed to form HCHO as a side product.[74] Further details on histone modifications and on the histone demethylases are described in the next section.

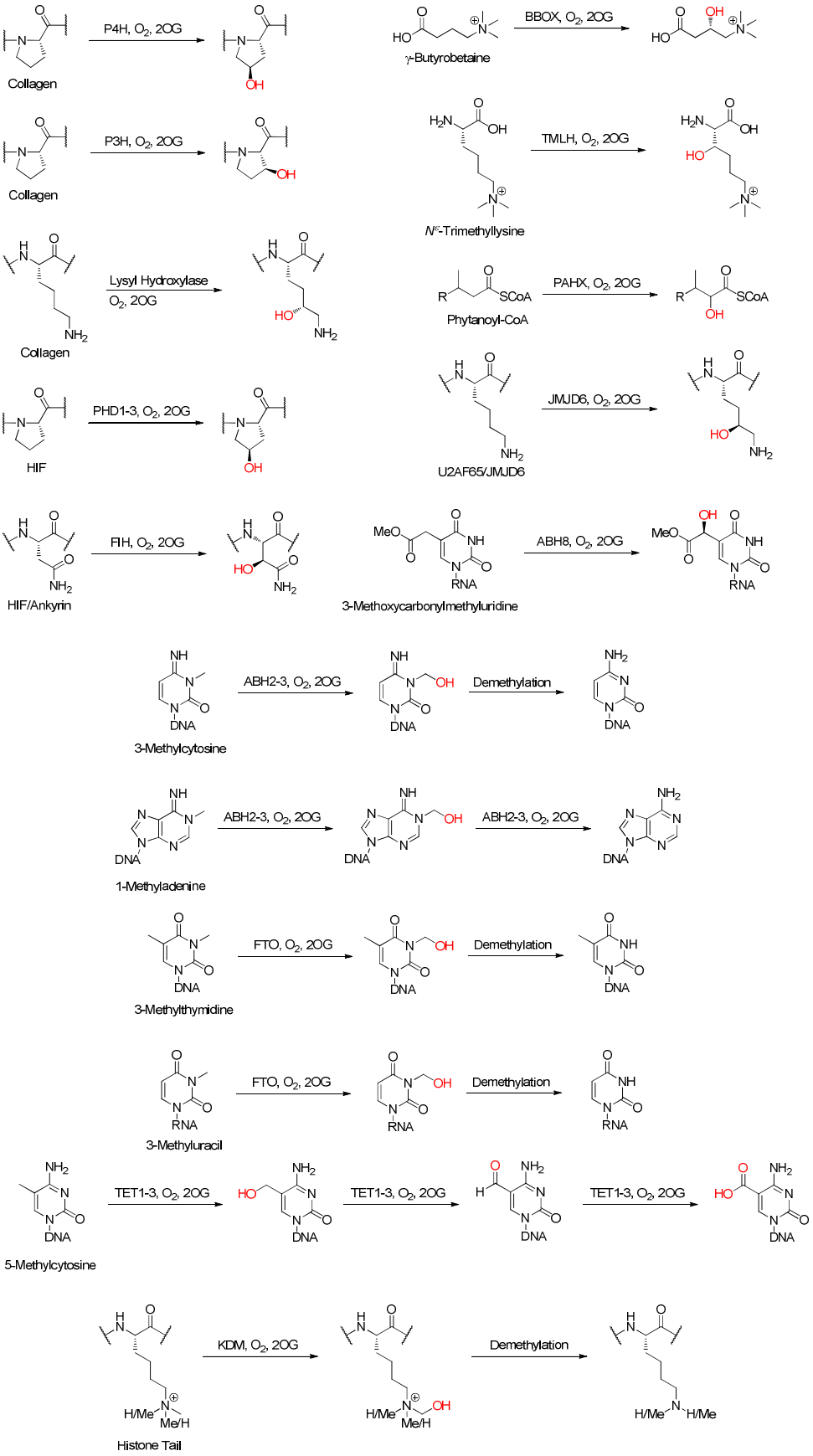

Scheme 1.2 Reactions catalysed by human 2OG oxygenases.

1.2 Epigenetics

1.2.1 Definition

In 1942, the biologist Conrad Waddington first coined the term 'epigenetics' to describe 'the branch of biology which studies the causal interactions between genes and their products'.[80] Subsequent advances in our understanding of genetic mechanisms have allowed this initial definition to be revised multiple times, and consequently, differing interpretive meanings of 'epigenetics' are present in the literature.[81, 82] Recently, the definition of epigenetics has been narrowed and is currently generally accepted as 'the study of heritable phenotypes resulting from changes in a chromosome without alterations in the DNA sequence'.[83] Chromosomal changes (such as variations in histone isoforms, DNA methylation and histone tail modifications) are therefore proposed to play vital roles in regulating gene expression, implying that, contrary to the central dogma of molecular biology,[84] the reading of genetic material is moderated by the activities of a number of chromatin modifying proteins.

1.2.2 Chromatin Structure

It has been proposed that epigenetic regulation of gene expression is facilitated by dynamic changes in chromatin structure. In cell nuclei, DNA is packaged with histone proteins to form nucleosomes. Each nucleosome contains 8 histones (4 pairs of histones H2A, H2B, H3 and H4 in animals), around which on average 146 base pairs of DNA is wrapped (Figure 1.2).[85] Multiple nucleosomes present on one gene result in the formation of higher order chromatin structures, which are proposed to be at least partially regulated by the histone H1.[86] In a simplified model, chromatin can exist in two distinct forms. Heterochromatin is formed when nucleosomes are packed in a condensed manner, impeding access to gene promoters. Conversely, euchromatin exists in a more open geometry, facilitating gene transcription by allowing activating proteins to bind to DNA.

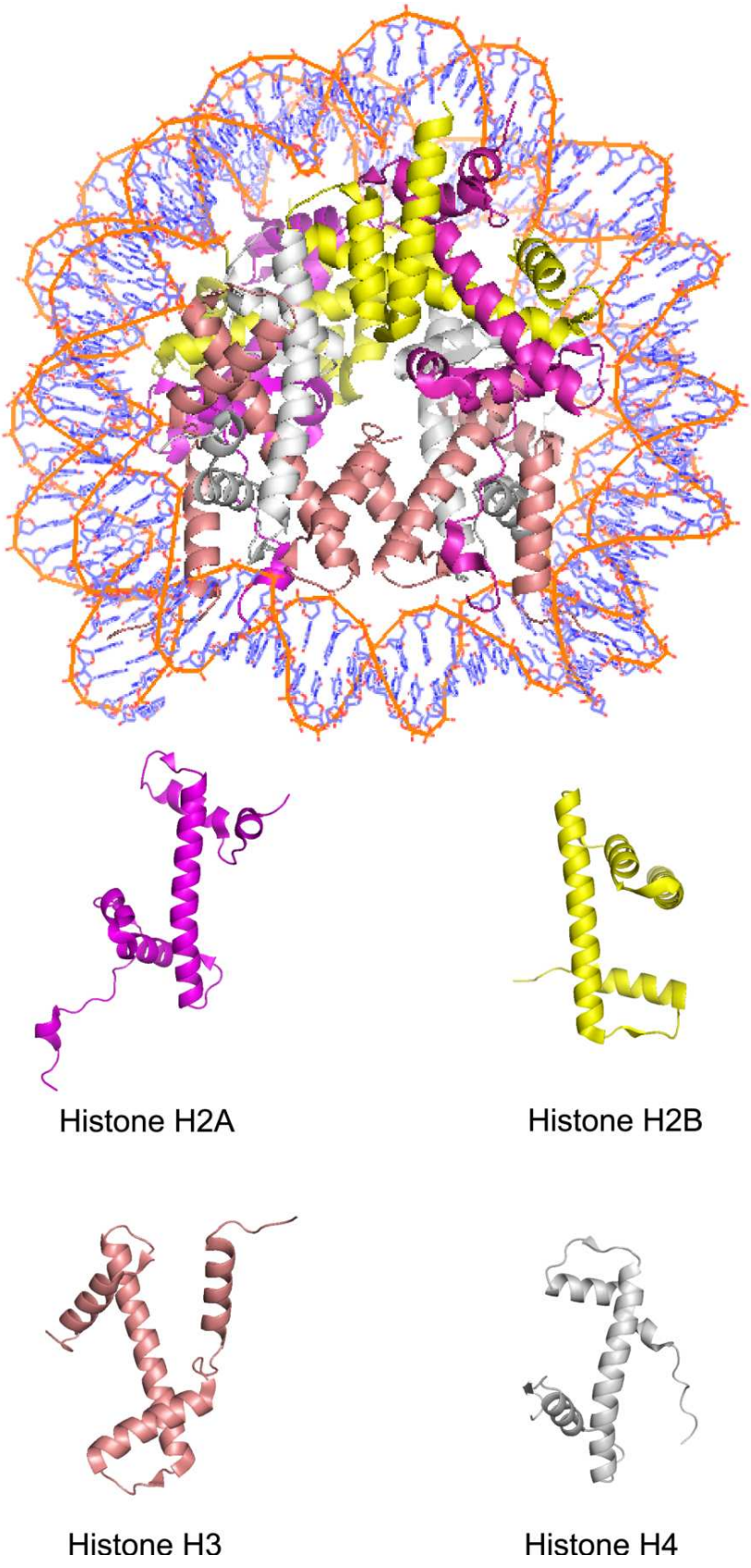

Figure 1.2 View from a crystal structure of the nucleosome (PDB ID 1KX3).[85] The structures of the four core histones (extracted from the nucleosome structure) are shown underneath.

All of the nucleosomal histones possess α-helical core regions, around which DNA binds. However, the *N*-terminal regions of the histones are disordered, and are known to interact with a variety of chromatin-associating enzymes. Also, these regions possess multiple sites amenable to post-translational modifications (PTMs).

It is the presence of PTMs on histone tails that forms the basis of the 'histone code' hypothesis of epigenetic regulation. In this model, modifications at particular residues induce conversion between transcriptionally repressive and active chromatin states, either through affecting nucleosomal structure directly (such as by destabilising the DNA-histone interactions through charge neutralisation), or through recruiting proteins capable of modifying chromatin structure.[87] Also, the fact that certain histone PTMs can recruit transcription factors and regulatory complexes indicates that gene expression can be controlled by PTM induced recruitment of transcription machinery.[88] Experimental evidence has suggested that PTMs at particular sites can be considered nominally 'activating' or 'repressive' with respect to their effects on gene expression. However, it should also be noted that cross-talk between different PTMs on the same gene likely plays some role in regulating transcription.

1.2.3 Histone PTMs

Known histone PTMs are summarised in Figure 1.3.

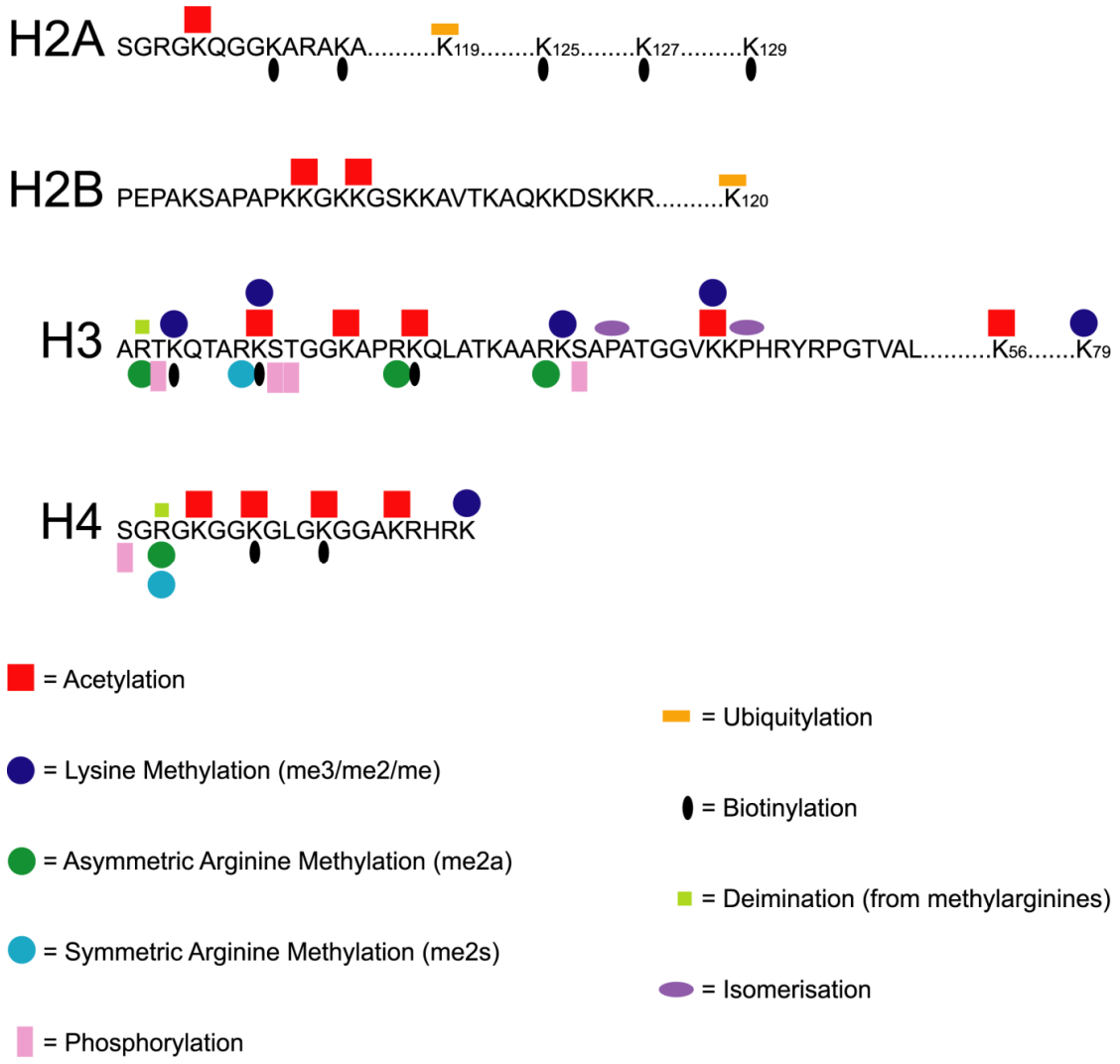

Figure 1.3 Schematic diagram displaying known post-translational modifications on the core histones. The precise positions of histone SUMOylation are currently undefined.

N^{ε}-Acetylation on lysyl residues is regulated through interplay between histone acetyltransferases (HATs) and histone deacetylases (HDACs). Acetylated lysines are generally associated with euchromatin, which may be due in part to their ability to reduce the net charge of the histone tails.[89, 90] Also, binding of acetyllysines to protein domains specific for this mark facilitates recruitment of enzymes associated with both gene transcription and chromatin remodelling.[87, 88]

Phosphorylation of serine and threonine residues has also been linked with transcriptional activation. This modification has the effect of neutralising the positively charged histone tails (akin to acetylation), potentially weakening the interactions

between the histones and DNA. Also, studies on H3S10 phosphorylation have indicated that this mark antagonises the formation of heterochromatin by repelling interactions between chromatin remodelling proteins and trimethylated H3K9.[91] This suggests that transcriptional activation induced by other phosphorylation sites may also be due to specific interactions with chromatin binding proteins.

Ubiquitylation occurs within the core regions of histones H2A and H2B and occurs via the E1/E2/E3 ubiquitylation pathway.[92] Ubiquitylation on H2A appears to be induced during gene silencing[93] and has been shown to be upregulated at DNA lesions, implying a role for this mark during DNA repair.[94] Conversely, ubiquitylation on H2B promotes gene transcription by inducing methylation at H3K4;[95] however, removal of ubiquitin by deubiquitinases is required for transcriptional elongation.[96] Interestingly, H2A ubiquitylation appears to inhibit H3K4 timethylation, indicating that the two ubiquitin marks have orthogonal functions during gene transcription.[97] In addition to ubiquitylation, SUMOylation has been identified on histone H4 in mammalians cells,[98] and on all core histones in yeast.[99] Although investigations into the roles of histone SUMOylation are ongoing, there is some evidence to suggest that this modification induces transcriptional repression, particularly in the case of H4 SUMOylation, which co-immunoprecipitates with HDAC1.[98, 99]

Histone biotinylation has been identified at sites on histones H2A, H3 and H4 and is catalysed by both biotinidase and holocarboxylase synthetase.[100-103] It is proposed that removal of biotin from histones may be enzyme-catalysed (possibly by biotinidase),[104, 105] although full characterisation of histone debiotinylases has so far not been reported. Analyses on global histone biotinylation levels appear to suggest that this mark is enriched in heterochromatin and also during cell proliferation.[100, 106] However, the effects of biotinylation on transcriptional regulation are currently speculative due to the lack of sufficient biochemical data for specific sites. Finally, there is some evidence that biotinylation at H4K12 may be downregulated after UV-induced DNA damage, although it is currently unknown whether loss of biotin at this position signals for DNA repair or apoptosis.[106, 107]

Deimination of arginine and N^{ω}-monomethylarginine residues (forming citrulline) is facilitated by the nuclear protein PADI4.[108, 109] This transformation blocks methylation by the arginine methyltransferases, antagonising the regulatory roles of arginine methylation. For example, methylation at H3R2 is known to block binding of H3K4me3 binding domain proteins, negating transcriptional activation.[110] Therefore, in this role, PADI4-mediated deimination allows binding at methylated H3K4, activating transcription. Conversely, PADI4 is reported to associate with the histone deacetylase HDAC1, signalling for transcriptional repression by promoting removal of activating histone acetyl marks.[111]

cis-trans Isomerisation (at P30 and P38 on histone H3) represents the only non-covalent histone modification reported to date. In yeast, isomerisation is catalysed by the isomerase Fpr4, a process which is targeted to the H3 prolines through interactions between a nucleolin-like domain on the protein and the H3 and H4 tails.[112] There is some evidence from *in vitro* and *in vivo* activity assays that isomerisation of P38 (from the *trans* to the *cis* conformation) ablates methylation at H3K36 by the lysyl methyltransferase Set2. Therefore, it is proposed that isomerisation at P38 acts as a repressive mark by antagonising the recruitment of activator proteins associated with H3K36 methylation. It is also reported that Fpr4 activity is downregulated by trimethylation at H3K36, which is presumed to occur after a breakdown in nucleosome structure during active transcription (thus removing the structural constraints imposed upon Set2 binding by P38). These findings suggest cross-talk between the activating H3K36 methylation mark and P38 isomerisation.

Methylation has been reported on side chain nitrogens of both histone arginines and lysines. Arginine methylation, which occurs on the ω-nitrogens, is catalysed by a number of arginine specific methyltransferases (PRMTs). Some members of the PRMT family (PRMT1-4, 6, 8) methylate on one of the two ω-nitrogens of the guanidinium group, producing asymmetric dimethylarginine.[113-119] The other PRMTs characterised to date (PRMT5, 7) transfer one methyl group onto each ω-nitrogen, producing symmetric dimethylarginine.[118, 120] To date, asymmetric dimethylarginine marks have been

identified at three sites on histone H3 and at one site on histone H4 (at H3R2, H3R17, H3R26 and H4R3 respectively) and symmetric dimethylarginine marks have been identified at one site on H3 and one site on H4 (at H3R8 and H4R3 respectively).[121] There is also some evidence that arginines on H2A are methylated.[122] The functions of methylated arginine marks appear to depend on both the positions of the modifications and on whether the residues are symmetrically or asymmetrically methylated. For example, asymmetric dimethylarginine at H3R2 is associated with heterochromatin and is thought to antagonise trimethylated H3K4 induced transcriptional activation by blocking its interactions with effector proteins and also by inhibiting Set1 methylation.[123, 124] Conversely, asymmetric dimethylated H4R3 activates transcription of β-globin by promoting H3 acetylation.[125] However, PRMT5 mediated formation of symmetric dimethylated H4R3 results in increased binding of DNMT3A to chromatin, upregulating DNA methylation and transcriptional repression.[126] Although monomethylated arginine marks on histone tails have been shown to be converted to citrulline by PADI4,[108, 109] to date no arginine demethylase has been identified. As stated above, the 2OG oxygenase JMJD6 was originally thought to demethylate histone arginines;[51] however, subsequent experimentation has questioned this assignment.

Methylation on the N^{ϵ}-amine of histone lysines has been reported at multiple sites (five on H3 and one on H4) and is catalysed by histone lysyl methyltransferases via a proposed S_N2-type mechanism (using *S*-adenosylmethionine).[127] The epigenetic functions of lysine methylation depend upon the position of methylation and also upon the methylation state. For example, trimethylation at H3K4 is located primarily in the promoter regions of active genes and is thought to induce transcription by recruiting chromatin modifying enzymes.[128-131] Conversely, trimethylation at H3K9 induces the formation of heterochromatin by recruiting HP1 (heterochromatin protein 1), thus repressing gene transcription. Furthermore, dimethylation at H3K4 appears to be involved in controlling centromere assembly during cell division,[132]. Lysine methylation was long considered to be irreversible, until the discovery of the first lysyl demethylase in 2004.[133] These enzymes fall into two classes, as described below.

1.3 Histone Lysyl Demethylases

1.3.1 Flavin Dependent Demethylases

The first demethylase to be discovered was LSD1 (or 'lysine specific demethylase 1').[133] LSD1 catalyses the demethylation of H4K4me2/me and H3K9me2/me (when associated with the androgen receptor)[134] via a flavin adenine dinucleotide (FAD) dependent oxidation mechanism (Scheme 1.3). More recently, the closely related LSD2 was identified, which catalyses the removal of H3K4me2/me methyl marks via a similar flavin dependent pathway.[135]

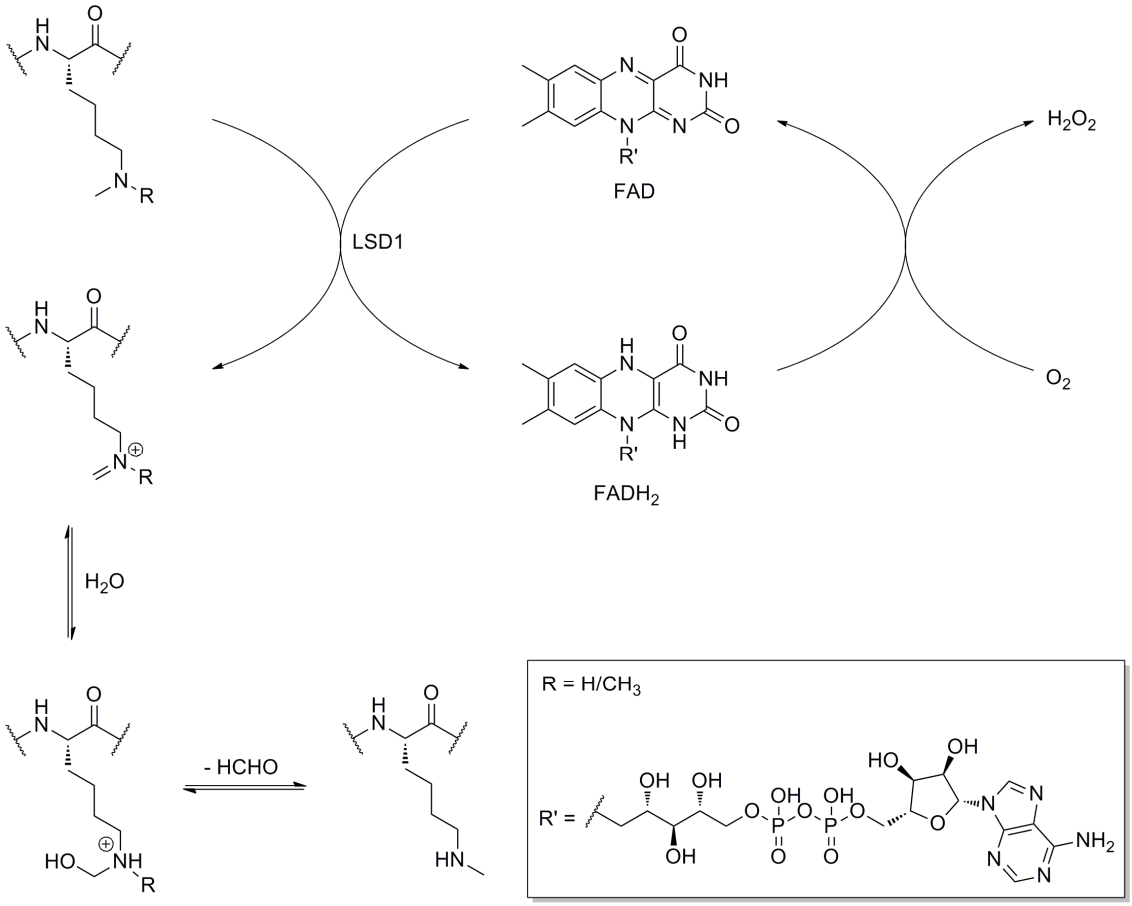

Scheme 1.3 Schematic diagram showing the mechanism of LSD1 catalysed lysyl demethylation.

LSD1, as part of the Co-REST complex, facilitates gene inactivation by removing activating methyl marks on H3K4.[133, 136] It is proposed that association within the Co-REST complex protects LSD1 from proteosomal degradation and also improves its

affinity for the K4 substrate. Additionally, LSD1 associates with the 2OG dependent demethylase JMJD2C and with the androgen receptor, resulting in gene activation by demethylating at H3K9.[72] In addition to histone substrates, LSD1 is known to demethylate other proteins in cell nuclei. Lysines 370 and 372 on the tumour suppressor protein p53 are demethylated by LSD1, which results in diminished binding between the protein and its binding partner p53BP1. The loss of this interaction restricts subsequent binding of the complex to DNA, negating p53 induced transcriptional regulation at specific genes. Also, LSD1 is reported to demethylate the DNA methyltransferase DNMT1, which is proposed to improve protein stability.[137] LSD1 depletion results in decreased global DNA methylation levels, implying that LSD1 plays a role in regulating DNMT1 function.

1.3.2 2OG Dependent Demethylases

The 2OG dependent demethylases (hereafter referred to as 2OG demethylases) represent the second class of histone demethylases and are capable of demethylating trimethylated, dimethylated and monomethylated lysine residues at multiple sites (Table 1.1).

Table 1.1 Table showing known human 2OG demethylases and their methylation specificities *in vivo*.

Demethylase	Substrate(s)
FBXL10	H3K36me2/me
FBXL11	H3K36me2/me
PHF2	H3K9me2/me
PHF8	H3K9me2/me, H4K20me
JMJD1A	H3K9me2/me
JMJD1B	H3K9me2/me
JMJD2A	H3K9me3/me2, H3K36me3/me2
JMJD2B	H3K9me3/me2, H3K36me3/me2
JMJD2C	H3K9me3/me2, H3K36me3/me2
JMJD2D	H3K9me3/me2
JMJD2E (pseudogene)	H3K9me3/me2
JARID1A	H3K4me3/me2
JARID1B	H3K4me3/me2
JARID1C	H3K4me3/me2
JARID1D	H3K4me3/me2
JMJD3	H3K27me3/me2
UTX	H3K27me3/me2
KIAA1718	H3K27me2/me

The mechanism of demethylation is thought to proceed via hydroxylation on the N^{ϵ}-methyl groups, resulting in demethylation after fragmentation of the produced hemiaminal intermediate (Scheme 1.4). Therefore, it is possible for 2OG dependent demethylases to demethylate trimethylated lysines, unlike the LSDs (which require formation of an imine).

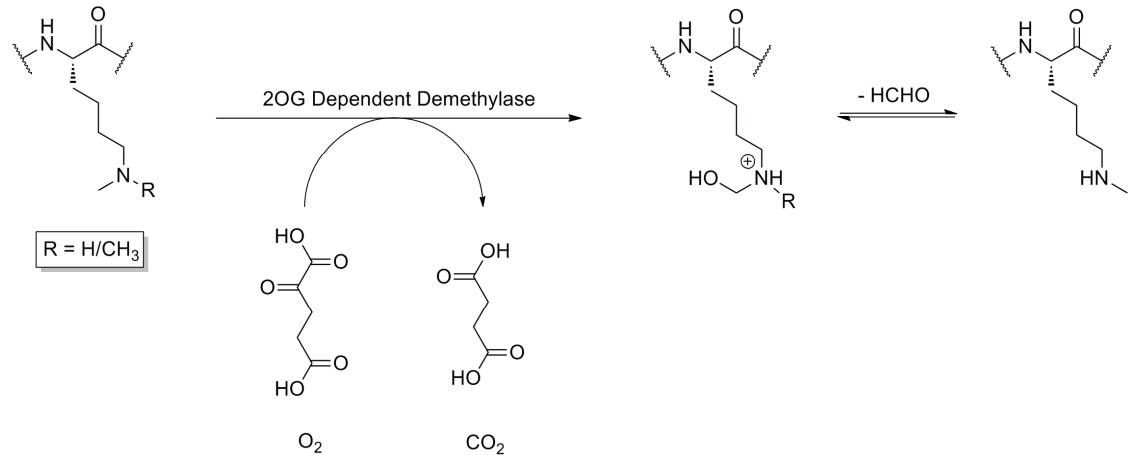

Scheme 1.4 Proposed mechanism for 2OG demethylase catalysed lysyl demethylation.

All of the 2OG dependent demethylases possess a Jumonji-C (JmjC) catalytic domain, which contains the jelly-roll motif present within all 2OG oxygenases. However, subtle variations within the JmjC domains of different demethylases are thought to induce specificities for particular methylation states.[138, 139] In addition to the JmjC domain, many of the demethylases possess other domains within their structures (Table 1.2). Many of these domains are involved in binding DNA or other histone PTMs, thus regulating enzyme function.

Table 1.2 Table showing known non-catalytic domains in human 2OG demethylases and their proposed functions.

Domain	Demethylases in which the Domain is Present	Function
JmjN	JMJD2A-F, JARID1A-D	Unknown (required for catalytic activity)
PHD	FBXL10-11, JMJD2A-C, JARID1A-D, PHF2, PHF8, KIAA1718	Lysine/Methyllysine Binding
Tudor	JMJD2A-C	Methyllysine Binding
Fbox	FBXL10-11	Protein-Protein Interactions (with Skp1)
BRIGHT/ARID	JARID1A-D	DNA Binding
CXXC	FBXL10-11	DNA Binding
Leucine-rich Repeat	FBXL10-11	Protein-Protein Interactions
C5HC2 Zinc Finger	JARID1A-D	Unknown
Tetratricopeptide Repeat	JMJD3, UTX	Protein-Protein Interactions

A number of crystal structures of the 2OG dependent oxygenases (truncated catalytic domains) have been resolved, including structures of JMJD2A and PHF8 complexed with methylated histone peptides (PDB IDs 2OQ6, 2OX0, 2OS2, 2OT7 and 3KV4 respectively).[139, 140] These structures reveal that the methylated lysyl residue is able to bind close to the catalytic iron centre by filling a large cleft in the active site. Binding of the lysine within this cleft appears to be stabilised by interactions between the protein and the peptide backbone, as well by the presence of a hydrophobic pocket close to the iron (stabilising the lysyl methylammonium group). Substrate selectivity may be due in part to the flexibility of binding within the cleft; binding of trimethyllysine ensures that one methyl group is positioned close to the iron, facilitating hydroxylation at this

position. However, for the dimethylated and monomethylated lysines, some orientations of the methylammonium group result in the methyl group pointing away from the iron, impeding hydroxylation. The structure of PHF8 reveals that this enzyme possesses a slightly more compact active site than JMJD2A, particularly around the iron centre.[140] Therefore, it is possible that the lack of observable trimethyllysine demethylation may be due to steric clashes between PHF8 and this substrate.

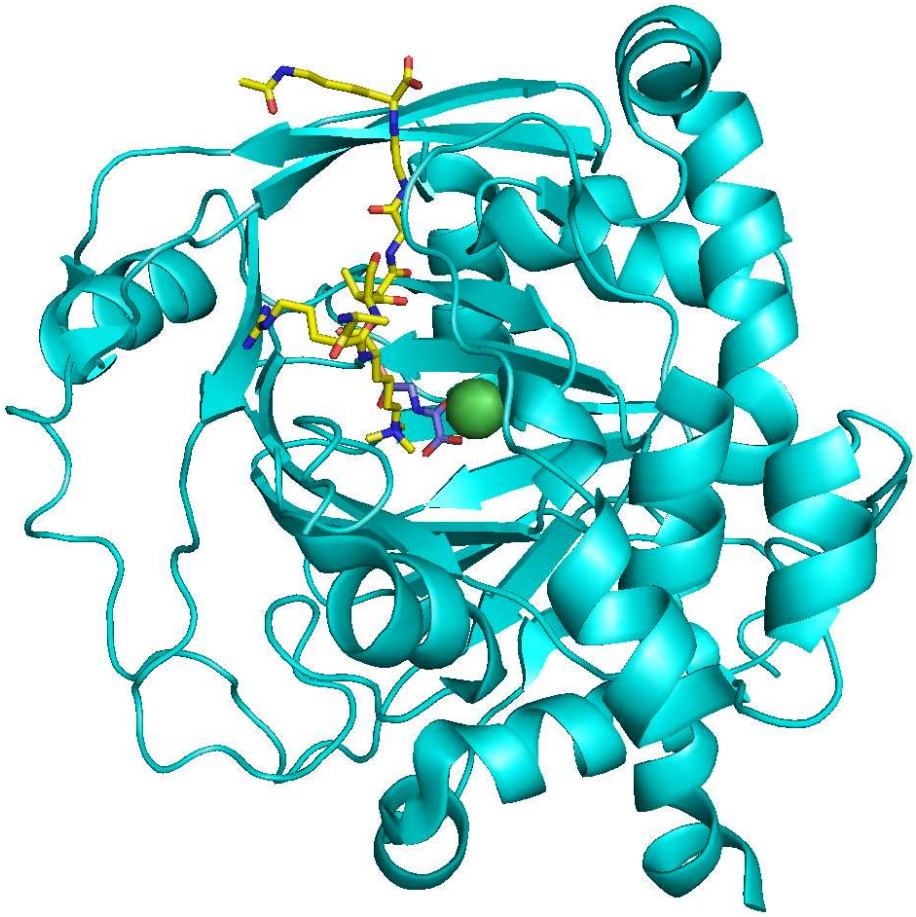

Figure 1.4 View of a crystal structure of JMJD2A with bound histone peptide, trimethylated at lysine-9 (PDB ID 2OQ6).[139]

1.4 Formaldehyde in Biology

Formaldehyde (HCHO), the simplest aldehyde, is present in the intercellular medium and very likely in all cells. Although uptake of HCHO may occur through exposure to environmental sources (HCHO is widely used in industry and can be found in many

household items),[141-144] it is proposed that a significant proportion of intracellular HCHO is produced via metabolic processes, including demethylation of histones.[74, 133, 145-148] Above threshold levels, HCHO is reported to be cytotoxic[149] and has been linked to both nasal and oesophageal cancers in workers exposed to high HCHO levels.[150, 151] Such effects on cell viability are proposed to be induced by the formation of HCHO derived cross-links between DNA and proteins; however, experimental evidence confirming the toxicity of such species is currently lacking.[143, 152, 153]

1.4.1 HCHO Metabolism/Detoxification

In humans, HCHO is thought to be metabolised by at least two separate pathways. One pathway utilises the ubiquitous tripeptide glutathione (GSH) as a co-factor (Scheme 1.5).[154, 155]

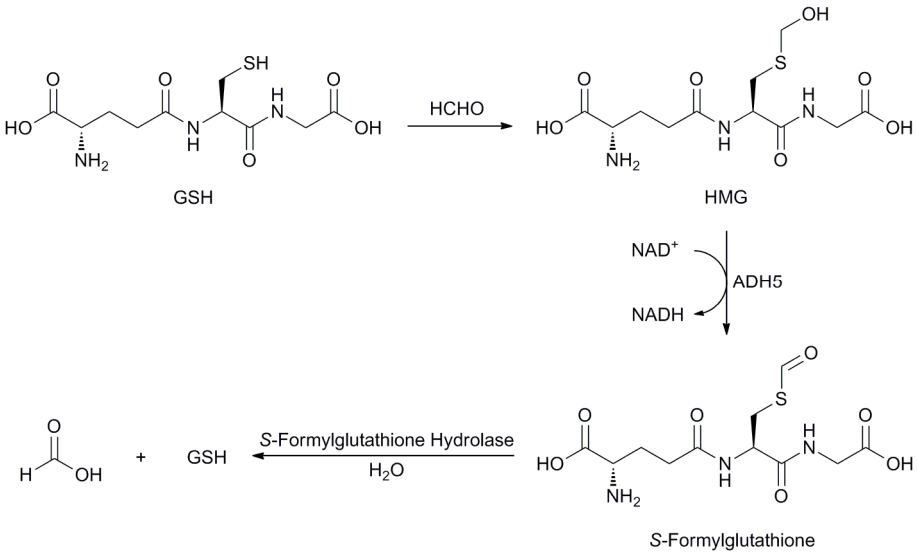

Scheme 1.5 Proposed GSH-mediated HCHO metabolic/detoxification pathway.

The first step in this pathway is the formation of the hemithioacetal adduct *S*-hydroxymethylglutathione (HMG). This species is then oxidised by the class III alcohol dehydrogenase ADH5, forming the thioester *S*-formylglutathione. Further metabolism by *S*-formylglutathione hydrolase produces formate, returning GSH in its reduced form. The reaction of GSH and HCHO to form HMG was long thought to be spontaneous in cells. However, recent studies on *Paracoccus denitrificans* have indicated that this step

may be enzyme-catalysed.[156] Glutathione-dependent formaldehyde-activating enzyme (or GFA) was identified from cell extracts grown under methylotrophic conditions by measuring the exchange rate between GSH and HMG at equilibrium, using proton exchange NMR (EXSY) spectroscopy (exchanges rate were observed to increase upon addition of cell extracts containing GFA, and also upon addition of the recombinant protein). Although the reported data imply a role for GFA in HCHO metabolism, it was noted that the protein is not present in many organisms that contain homologues of ADH5 and *S*-formylglutathione hydrolase. Therefore, the requirement for GFA to catalyse HMG formation may be restricted to particular species. Recently, a human variant of GFA, named centromere protein-V (or CENP-V), has been identified and shown to be essential for chromatin organisation during mitosis.[157] The biochemical function of this protein, however, has not been elucidated.

A crystal structure of GFA reveals a unique catalytic domain, which binds a zinc ion in a trigonal coordination (Figure 1.5a).[158] However, co-crystallisation of GFA with GSH resulted in the ejection of zinc at this site and the formation of a disulfide bond between the protein and GSH (Figure 1.5b). These observations enabled a mechanism for GFA-catalysed HMG formation to be formulated (Figure 1.5c).

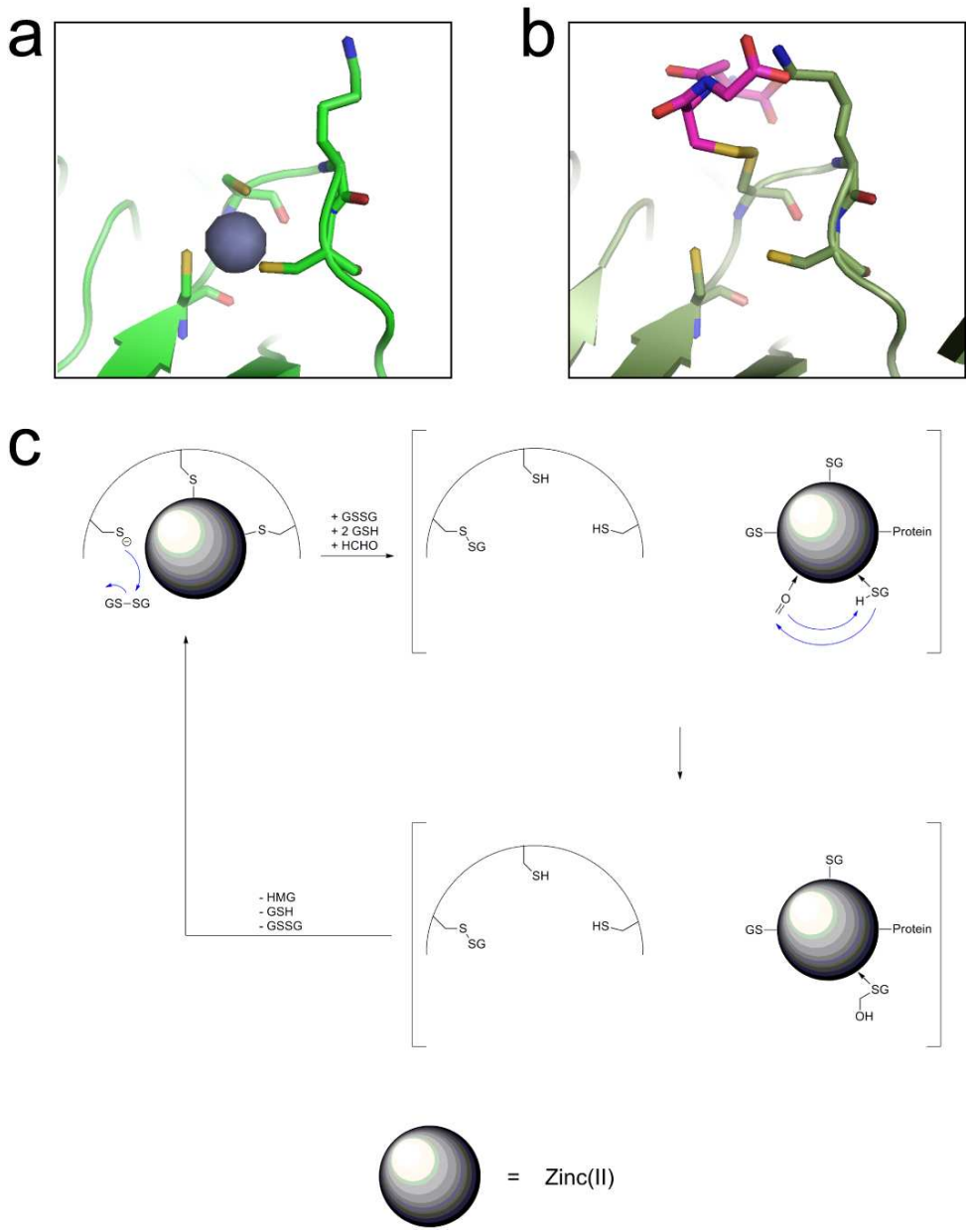

Figure 1.5 (a) View from a crystal structure of GFA without GSH binding (PDB ID 1X6M).[158] Zinc (purple) is bound in a trigonal geometry by three cysteinyl residues on the protein. (b) View from a crystal structure of GFA with GSH binding (PDB ID 1XA8).[158] GSH (pink) is observed to bind covalently to C55. Zinc is not observed at this site. (c) Proposed mechanism of GFA-catalysed HMG formation, based on the crystal structure data. Zinc ejection occurs after formation of the disulfide bond between GSH and GFA. The zinc then migrates to an undetermined site on the protein, where HMG formation is catalysed. HMG then leaves the protein, and the zinc returns to its original site after reduction of the protein-GSH disulfide bond. Scheme modified from Neculai *et al*.[158]

In addition to the GSH-mediated metabolic pathway, HCHO has also been hypothesised to be a methyl source in the formation of 5,10-methylenetetrahydrofolic acid.[159, 160] This intermediate is then able to transfer the methyl group to homocysteine, resulting in the production of *S*-adenosylmethionine (SAM) after further reaction.[161] Therefore, HCHO can act as the methyl source for histone methyltransferases (which transfer the *S*-methyl group of SAM to histone lysines and arginines), indicating cross-talk between histone methylation and demethylation.

1.5 Aims

The broad aims of the research described in this thesis focus on;

1. Evaluation of 2OG demethylase-catalysed histone lysyl demethylation using NMR spectroscopy, focusing upon the detection of HCHO released during catalysis.
2. Investigations of the mechanism of 2OG demethylase-catalysed demethylation using substrate lysine analogues.
3. Reviewing the propensity of 2OG demethylases to demethylate methylated arginine substrates.
4. Investigations of the role of lysine-241 in the 2OG demethylase JMJD2A.
5. Investigations of histone peptide fragmentation during *in vitro* demethylation assays.
6. Investigations of demethylation kinetics using deuterated lysine substrates.
7. Analysis of the non-enzymatic reactions of GSH and HCHO using NMR spectroscopy.
8. Investigations with the HCHO-activating enzyme GFA from *Paracoccus denitrificans*.

Chapter 2

Monitoring Histone Demethylation by NMR: Detection of Enzymatically Produced Formaldehyde

2.1 Introduction

The mechanism of 2OG dependent lysyl demethylation utilises/produces a variety of substrates, co-factors and products. Previous studies using mass spectrometry, radioactivity and fluorescence based techniques have enabled some kinetic analyses of the demethylation reaction;[13, 162-164] however, these experimental methods have been unable to give substantial insights into aspects of the reaction mechanism due to their inability to identify the multiple products of the reaction simultaneously. The current assay techniques have also not demonstrated the *in vitro* release of HCHO as a direct product of lysyl demethylation - this is proposed to be a crucial aspect of the oxidative demethylation mechanism catalysed by the 2OG demethylases (the formaldehyde dehydrogenase (FDH) coupled assay mentioned above relies on the production of HCHO during the reaction; however, it has not been possible to prove that the HCHO is produced from direct oxidation of the lysyl N^{ϵ}-methyl groups using this assay).

Work in this Chapter uses NMR spectroscopy to monitor JMJD2E-catalysed demethylation. In contrast to previous assay methods, this technique has the potential to allow evaluation of multiple substrates and products simultaneously, and therefore, should provide a more comprehensive analysis of the demethylation reaction. Also, NMR can facilitate monitoring of demethylation directly, without the need for coupling the formation of products to other enzymatic processes, thus complicating the analysis. Primarily, work focused upon confirming HCHO as a product of methyl group oxidation, and also upon attempts to detect the proposed hemiaminal intermediate.

All NMR work was carried out in collaboration with Dr. Nathan R. Rose and Dr. Refaat B. Hamed.

2.2 Results

2.2.1 Monitoring JMJD2E-catalysed Demethylation by ^{1}H NMR

Time course and kinetic experiments in this section were carried out by Dr Nathan R. Rose and Dr. Refaat B. Hamed.

Initial experiments focused upon monitoring JMJD2E-catalysed demethylation of a histone peptide fragment, N^{ϵ}-trimethylated at lysine 9 (sequence ARKme3STGGK, synthesised via solid phase peptide synthesis). This peptide was selected for NMR work due to its known activity in both MALDI mass spectrometry and FDH assays,[65, 165] and also due to its relatively short length, which it was proposed could help to minimise overlap of signals in the ^{1}H NMR spectrum. Prior screening of potential buffers identified ammonium formate (50 mM, 500 mM NaCl in D_2O, named hereafter as dAFN) as a suitable buffer based on the relatively high activity of JMJD2E in dAFN buffered samples, and also on its downfield ^{1}H resonance at δ_H 8.42 ppm. Before analysis of the demethylation reaction was undertaken, a sample of the peptide in dAFN (pD 7.5) was analysed by NMR in order to identify specific signals of interest. The ^{1}H NMR spectrum (together with assignments for each ^{1}H signal) is shown in Figure 2.1.

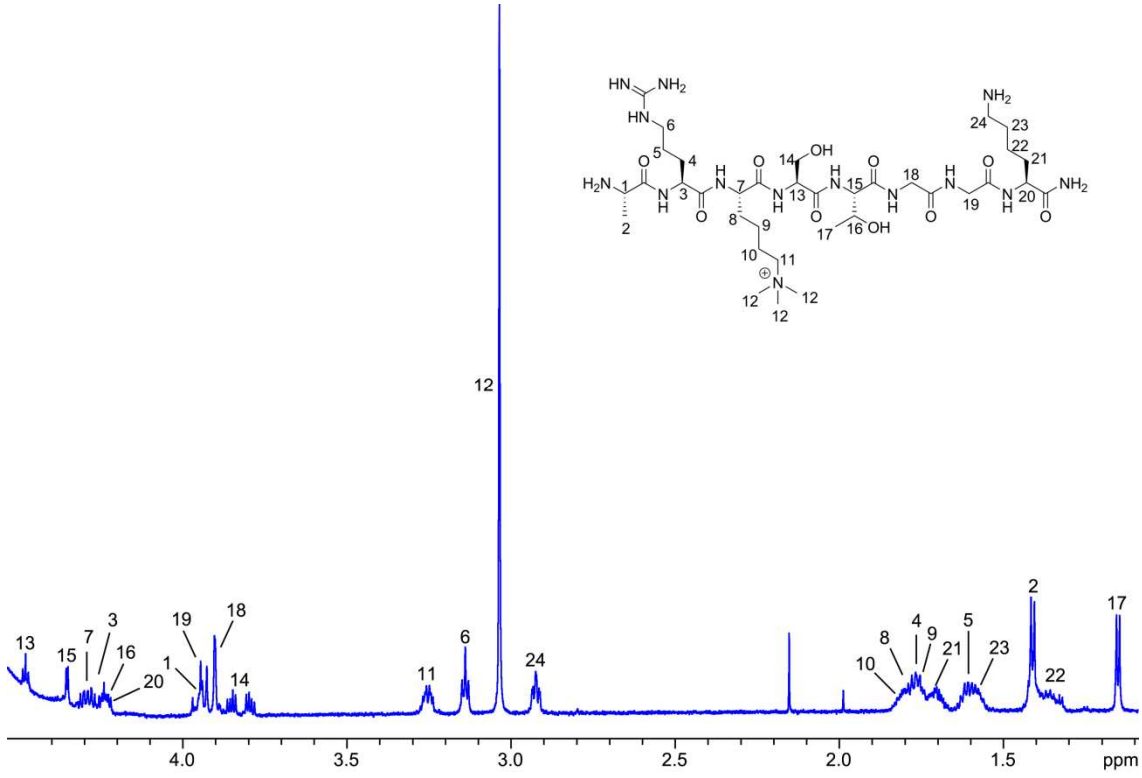

Figure 2.1 ^{1}H NMR spectrum (700 MHz) of the histone peptide ARKme3STGGK in dAFN buffer. ^{1}H Assignments are highlighted.

Analysis of the spectrum revealed a singlet resonance at δ_H 3.04 ppm, which was assigned to the N^{ε}-methyl protons at lysine 9 (i.e. the protons attached to three carbons at position 12, Figure 2.1). It was proposed, therefore, that JMJD2E-catalysed demethylation may be analysed by monitoring the intensity of this signal over time, and also by observing the emergence of new singlet resonances corresponding to the dimethylated and monomethylated peptide products respectively. In order to facilitate identification of the monomethylated and dimethylated signals in the reaction mixture, and also to confirm that their chemical shifts are suitably removed from the trimethylated substrate, ^{1}H NMR spectra were attained for samples of both the dimethylated and monomethylated peptide in dAFN (Figure 2.2).

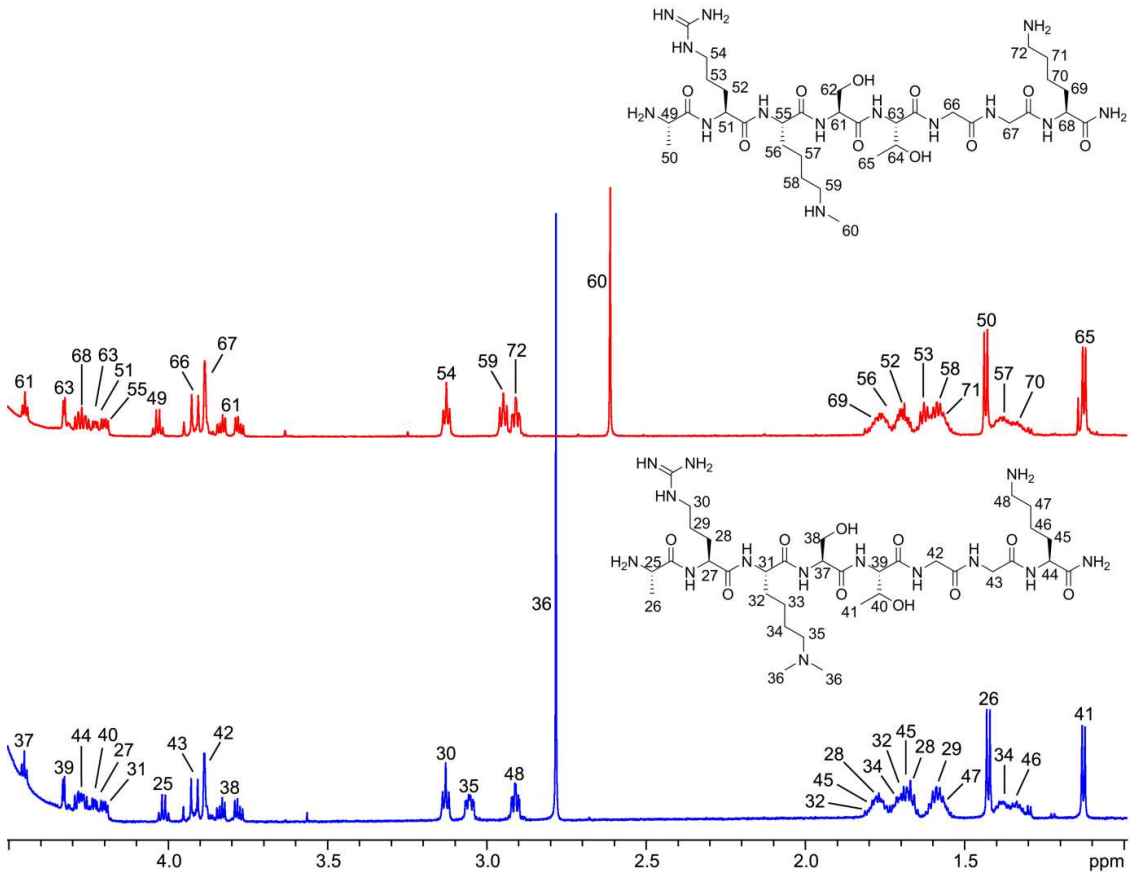

Figure 2.2 ^{1}H NMR spectra (700 MHz) of the histone peptides ARKme2STGGK (Below) and ARKmeSTGGK (Above) in dAFN buffer. ^{1}H Assignments are highlighted. *Characterisation of the dimethylated peptide was conducted by Philippa S. Barlow*.

Comparison of the spectra indicated that the N^{ϵ}-methyl group resonances for the dimethylated and monomethylated peptides possess lower chemical shifts relative to the trimethylated peptide, suggesting that the extent of JMJD2E-catalysed demethylation may be evaluated by monitoring the relative intensities of these signals over time. Although most of the other signals in the ^{1}H NMR spectra possessed similar chemical shifts to the corresponding resonances in the trimethylated sample, it was also noted that the signals assigned to the ε-lysyl methyl protons at lysine 9 (labelled 35 and 59 in Figure 2.2) shift depending upon the methylation state of the ε-amine. It was postulated, however, that analysis of these signals during demethylation might be hampered by overlap with other resonances in the samples and also by their low relative intensities. The degree of overlap of the peptide signals with those of 2OG and ascorbate was ascertained by acquiring ^{1}H NMR spectra for both species in dAFN. No overlap was

observed between resonances from these species and the peptide N^{ϵ}-methyl group signals, suggesting that analysis of the latter peaks during demethylation should be viable (Figure 2.3).

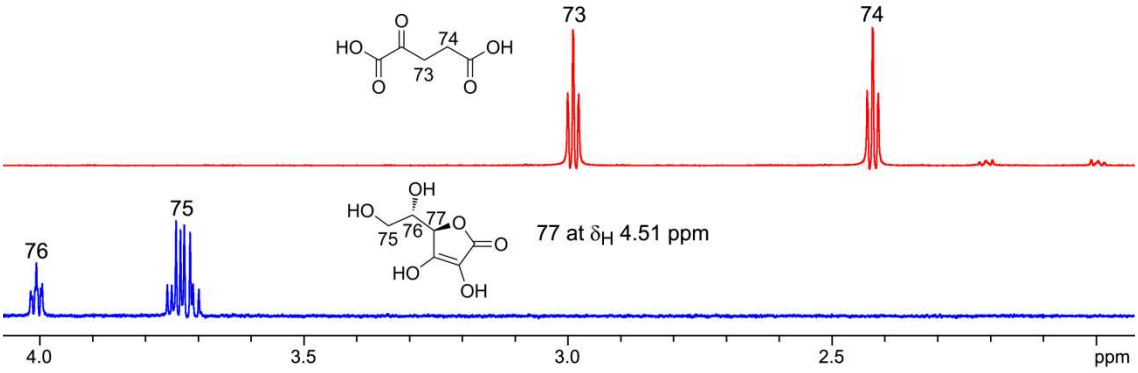

Figure 2.3 ^{1}H NMR spectra (700 MHz) of 2OG (Top) and ascorbate respectively (Bottom) in dAFN buffer.

Time course data for JMJD2E-catalysed demethylation was acquired by preparing a sample containing trimethylated peptide, enzyme, 2OG, sodium ascorbate and ferrous iron (as described in Table 2.1) and analysing the subsequent reaction by ^{1}H NMR using a 700 MHz NMR spectrometer. In order to reduce the time delay between mixing and NMR analysis, the sample was pipetted into a 2 mm NMR tube and transferred to the spectrometer immediately after preparation. The ^{1}H spectra over the first hour of reaction are shown in Figure 2.4.

Table 2.1 Composition of the demethylation assay mixture.

Reagent	Final Assay Concentration
JMJD2E	10 μM
Sodium L-Ascorbate	1 mM
Ammonium Ferrous Sulphate	100 μM
ARKme3STGGK	1 mM
2OG Disodium Salt	5 mM

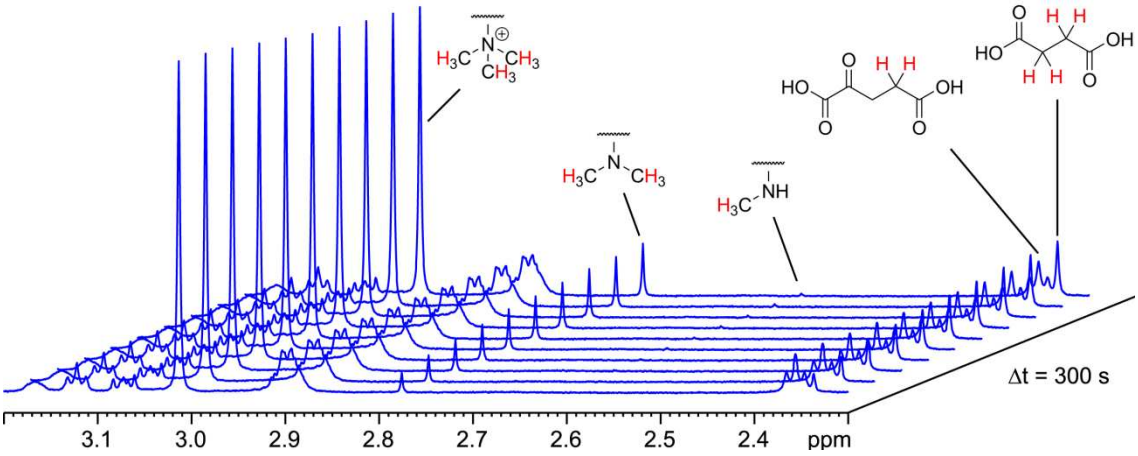

Figure 2.4 ^{1}H NMR spectra (700 MHz) of a time course monitoring JMJD2E-catalysed demethylation of the histone peptide ARKme3STGGK in dAFN buffer. Signals for the N^{ϵ}-methyl groups, as well as for 2OG and succinate, are highlighted.

Demethylation of the substrate N^{ϵ}-methyl groups was detected in the sample by observing the loss of intensity of the trimethylated signal and also by the formation of a signal at δ_H 2.78 ppm, corresponding to the dimethylated product. Trace amounts of the monomethylated peptide was present in the sample (as evidenced by the emergence of a singlet resonance at δ_H 2.61 ppm), indicating that some of the dimethylated peptide had been further demethylated to the monomethyl form. Production of unmethylated peptide was not observed, although it is possible that the ^{1}H-resonances corresponding to this species overlap with other signals in the ^{1}H NMR spectra. Peptide demethylation appeared to correlate with loss of the 2OG signals and the formation of a singlet resonance at δ_H 2.35 ppm, which was assigned to the aliphatic protons of succinate by analogy to a reference sample. Integration of the demethylated product peptide resonances and the succinate resonance revealed that the overall turnover of 2OG was greater than the total extent of peptide demethylation, suggesting that 2OG oxidation does not always lead to demethylation of the peptide. Kinetic parameters for the demethylation of the substrate peptide were then determined by plotting the initial rates (v) of demethylation at varying peptide concentration (Figure 2.5 left) and then calculating K_M and V_{max} using the Michaelis-Menten equation (Equation 2.1). Kinetic data were also attained for the dimethylated peptide (Figure 2.4 right) in order to compare the values with those of the trimethylated substrate.

$$v = \frac{V_{max}[\mathrm{S}]}{\mathrm{K_M} + [\mathrm{S}]}$$

Equation 2.1 Michaelis-Menten equation. v = initial rate of reaction. V_{max} = maximal velocity. K_M = Michaelis-Menten Constant. [S] = substrate concentration.

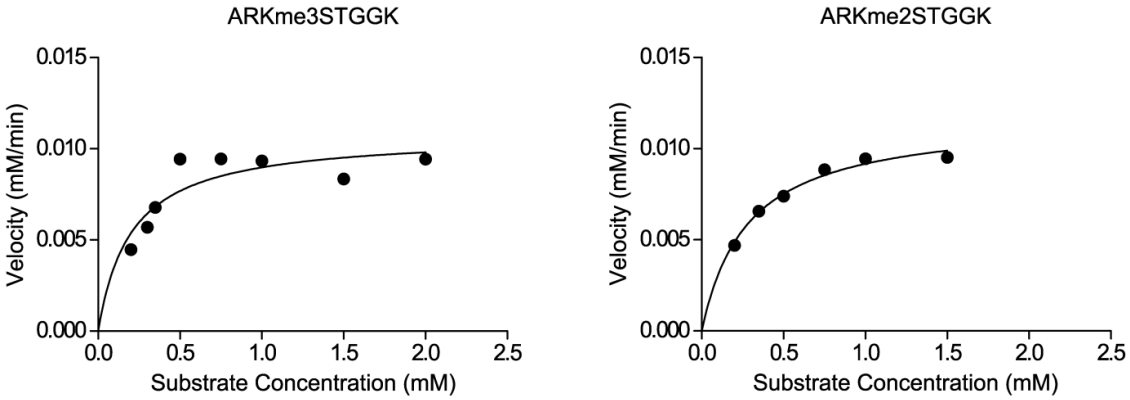

Figure 2.5 Dose-response curves for JMJD2E catalysed demethylation of ARKme3STGGK (Left) and ARKme2STGGK (Right), as determined by ^{1}H NMR.

The K_M value for the trimethylated peptide (188 ± 69 μM) was lower than that of the dimethylated peptide (281 ± 36 μM). However, the respective values for V_{max} (0.161 ± 0.017 μM s^{-1} and 0.197 ± 0.007 μM s^{-1} for the trimethylated and dimethylated peptides respectively) and k_{cat} (0.016 ± 0.002 s^{-1} and 0.019 ± 0.001 s^{-1} for the trimethylated and dimethylated peptides respectively) were more similar. These preliminary kinetic observations suggest that demethylation of both peptides might be subject to the same rate determining step, implying that the greater reactivity of the trimethylated peptide may be due to a stronger interaction with the protein. The kinetic data attained using NMR corroborated the trends in reactivity observed using the FDH assay (*Dr. Nathan R. Rose*, Table 2.2). However, both K_M and k_{cat} values were found to be smaller under the NMR conditions. This loss of activity may be due to variations in sample preparation, such as limited oxygen availability in the NMR tube, and a less efficient buffer system.

Table 2.2 Kinetic parameters attained using NMR and FDH techniques. *Values from the FDH assay were acquired by Dr. Nathan R. Rose*.

Substrate	K_M by NMR (μM)	K_M by FDH (μM)	k_{cat} by NMR (s^{-1})	k_{cat} by FDH (s^{-1})
ARKme3STGGK	188 ± 69	21.6 ± 1.3	0.016 ± 0.002	0.063 ± 0.000
ARKme2STGGK	281 ± 36	28.5 ± 3.9	0.019 ± 0.001	0.065 ± 0.002

The NMR assay was also used to investigate the dependence of the demethylation reaction on ascorbate. Ascorbate is known to stimulate or, in some cases, be near essential for the activity of some 2OG oxygenases;[3, 17-21] however, the exact role that ascorbate plays in catalysis is unknown. Ascorbate dependence upon enzyme activity appears to vary for 2OG family members, suggesting that the roles ascorbate may play during catalysis might not be necessary for the function of some oxygenases. Assay data acquired using MALDI has previously shown that ascorbate is not required for JMJD2E-catalysed demethylation; however, the rate of demethylation in the absence of ascorbate has been shown to be moderately impaired. Therefore, the dependence of ascorbate on JMJD2E activity was analysed using the NMR assay in order to test the findings from the MALDI experiments, and also to investigate whether ascorbate has an effect on the degree of uncoupled 2OG turnover. Samples containing the trimethylated or dimethylated peptides were prepared without ascorbate, and the initial rates of both demethylation and succinate formation were compared to the corresponding values from samples containing ascorbate (Figure 2.6).

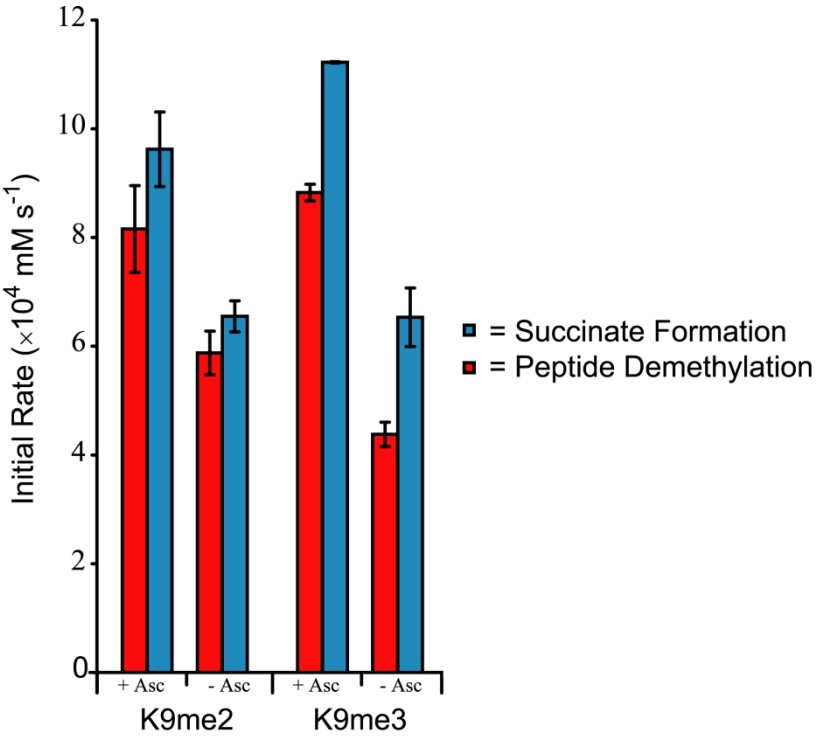

Figure 2.6 Initial rates of peptide demethylation (Red) and total succinate formation (Blue) in the presence and absence of ascorbate. Error bars are displayed as standard deviations.

In the absence of ascorbate, the initial rates of both peptide demethylation (for both trimethylated and dimethylated peptide) and succinate formation were observed to decrease relative to samples containing ascorbate. This observation suggests that ascorbate is able to increase the overall activity of the enzyme under the tested *in vitro* conditions. The data also suggest, at least in the samples containing trimethylated peptide, that ascorbate is able to increase the rates of demethylation and succinate formation to the same extent. Assuming that release of the demethylated peptide and succinate products is not rate determining (and this may not be a valid assumption), it could therefore be envisaged that any improvement of enzymatic activity by ascorbate may be due to acceleration of a process or processes either prior to or during formation of the catalytic Fe(IV). One hypothesis that may at least partially explain these observations is that ascorbate may increase activity by maintaining the presence of Fe(II) in the enzyme active site, either by reducing any residual Fe(III) in solution or by reducing any Fe(III) produced during catalysis. Work with the 2OG oxygenase TauD

has suggested that ascorbate may be involved in processes leading to self hydroxylation, thus indicating another potential regulatory mechanism.[166]

2.2.2 Indirect HCHO Detection by NMR

Having concluded that histone demethylation can be analysed using NMR, subsequent experiments focused upon detecting the release of HCHO during the reaction. Radioactivity studies in cell lysates, using tritiated methyllysine-containing histones,[74] and also the previously described FDH assay,[13] have strongly suggested that HCHO is produced during demethylation. However, the process by which HCHO is released during the reaction (and more specifically whether the carbon atom of HCHO derives from a lysyl methyl group) has not been conclusively evaluated. The presence of HCHO was not detected in the ^{1}H NMR spectra described in Section 2.2.1 presumably due, at least partially, to overlap of the hydrated HCHO signal (at δ_H 4.73 ppm based on a reference sample in D_2O, Section 8.2.1) with that of residual water. Also, HCHO in solution is known to oligomerise and also to react with nucleophiles, prohibiting its detection in ^{1}H NMR spectra (see Chapter 8). Consequently, initial NMR experiments were carried out using the HCHO trapping agents dimedone and glutathione in order to sequester any HCHO produced and allow its detection indirectly. These experiments are described below.

a) Trapping with Dimedone

Dimedone, a cyclic 1,3 diketone, is able to react with HCHO to form two stable adduct species (boxed, Scheme 2.1). Dimedone has been used extensively as a trapping agent for HCHO;[167] it was therefore postulated that addition of dimedone to the demethylation assay mixtures would result in the formation of the known adducts, which could then be detected using ^{1}H NMR spectroscopy.

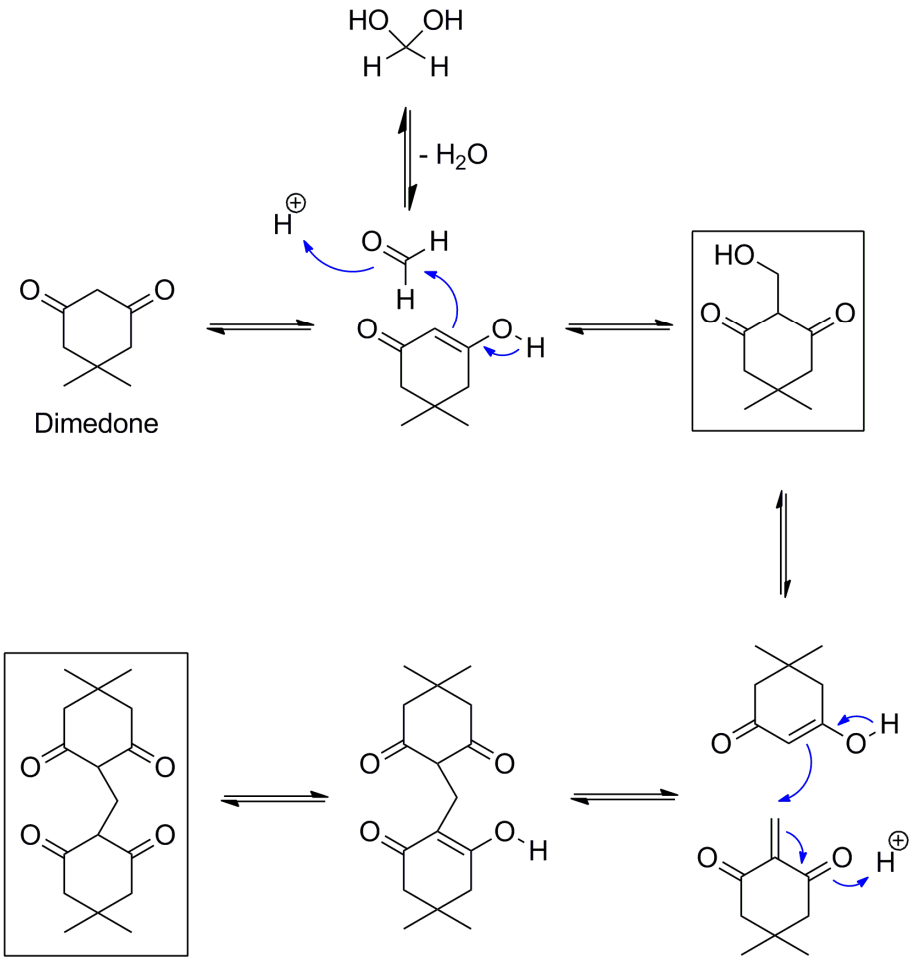

Scheme 2.1 Proposed scheme for the reaction of dimedone with HCHO. 'Stable' adducts are boxed.

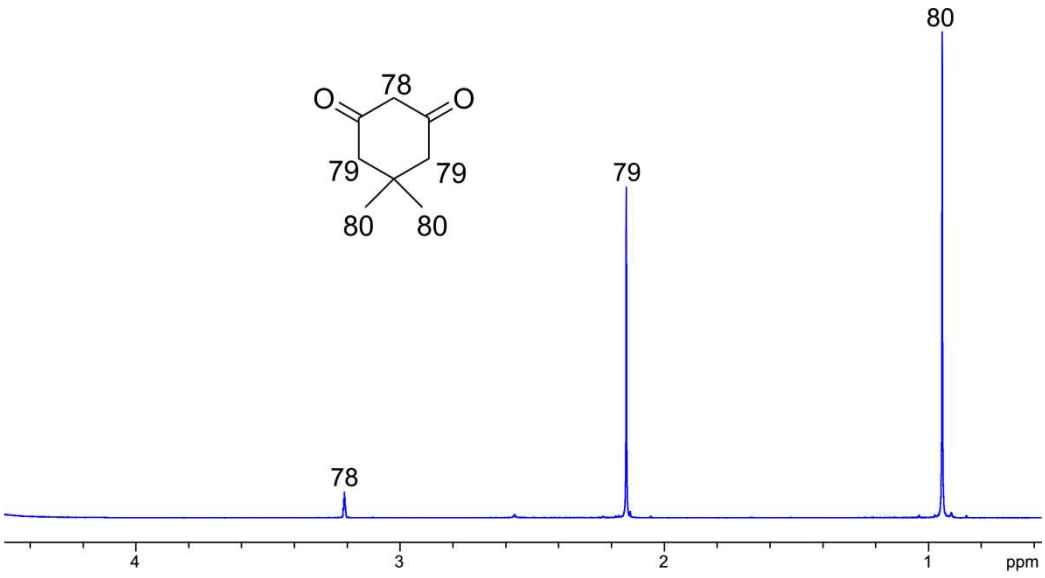

Figure 2.7 ^{1}H NMR spectrum (700 MHz) of dimedone in D_2O. The signal at δ_H 3.21 ppm under-integrates due to partial proton-deuterium exchange with D_2O.

Initially, dimedone was reacted with a reference sample of HCHO in order to identify resonances corresponding to the dimedone-HCHO adducts. Analysis of the spectra resulted in the detection of resonances corresponding to all three proton environments in the two adducts (Figure 2.8), suggesting that adduct production could be analysed by monitoring the loss of any of the dimedone resonances shown in Figure 2.7. However, it was expected that analysis of the terminal methyl groups (labelled 80 in dimedone) would be the most revealing in the demethylation samples, as this signal has the greatest intensity and is likely to be far removed from other resonances in the ^{1}H spectrum. The time course data of the reaction with HCHO identified two new signals at δ_H 0.92 ppm and δ_H 0.89 ppm close to the dimedone resonance at δ_H 0.94 ppm, which were assigned to the methyl groups of the dimeric and monomeric dimedone-HCHO adducts respectively (Figure 2.8). Therefore, it was proposed that adduct formation in the enzymatic sample could be detected by monitoring the growth of these signals.

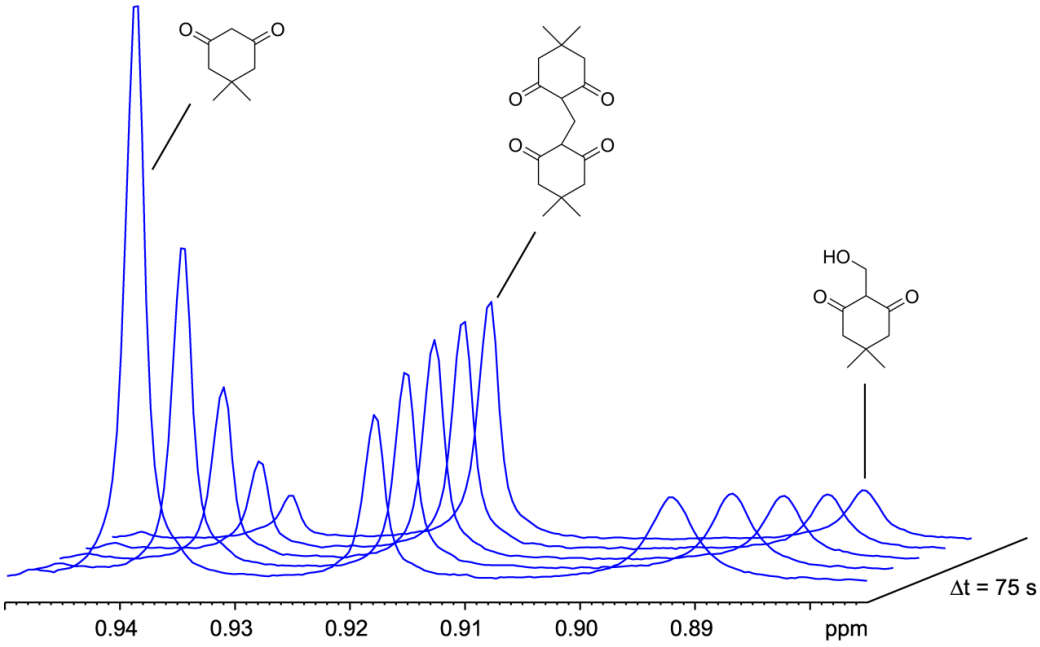

Figure 2.8 ^{1}H NMR spectra (700 MHz) monitoring a time course of dimedone and HCHO in dAFN buffer. Signals corresponding to the methyl groups of dimedone and the adducts are highlighted.

The JMJD2E demethylation assay was then prepared with added dimedone (1 mM final concentration) and monitored directly by ^{1}H NMR. Signals at δ_H 0.92 ppm and δ_H 0.89 ppm were detected in the first ^{1}H spectrum after mixing (~ 300 s) and were both observed to increase in intensity over the reaction period (Figure 2.9). It was therefore concluded that the previously identified dimedone-HCHO adducts had been formed in the sample, thus confirming the enzymatic formation of HCHO during demethylation.

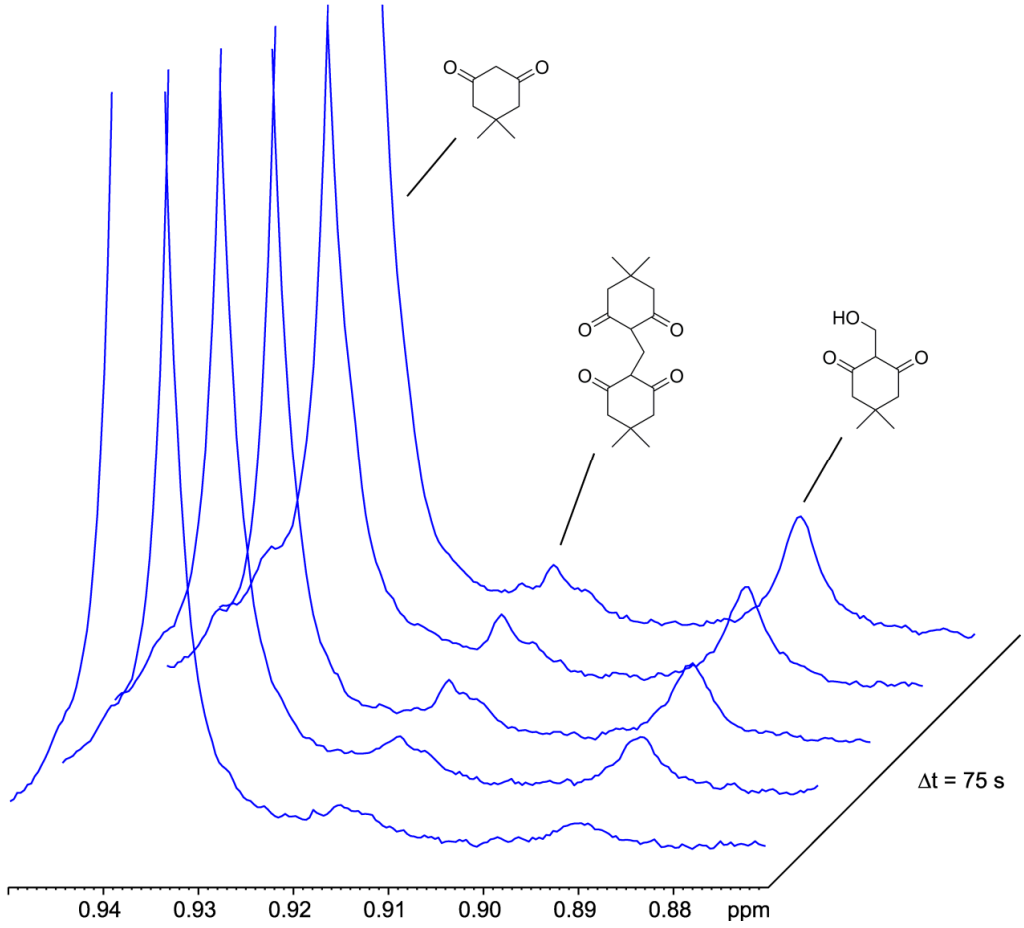

Figure 2.9 ^{1}H NMR spectra (700 MHz) monitoring JMJD2E-catalysed demethylation of ARKme3STGGK with added dimedone in dAFN buffer. Signals corresponding to the methyl groups of dimedone and the adducts are highlighted.

b) Trapping with Glutathione

HCHO detection was also attempted using the endogenous thiol glutathione (GSH). GSH is known to react with HCHO in cells via its sulfhydryl group,

forming the hemithioacetal *S*-hydroxymethylglutathione (HMG).[168] This species is then oxidised by aldehyde dehydrogenase 5 (in humans), facilitating HCHO detoxification (for detailed analysis of the GSH HCHO reaction, see Chapter 8).[154, 155] As well as reacting with free HCHO in solution, it was postulated that GSH may also help to fragment the intermediate hemiaminal produced during demethylation either in or near to the active site, and therefore may form adducts with the oxidised peptide. GSH was added to samples containing either the tri- or dimethylated peptides and the subsequent reactions were then monitored by ^{1}H NMR. In both samples, neither HMG nor any peptide-GSH adducts could be detected. This may be due partially to the low levels of HCHO in the samples and also to overlap of the adduct signals with other resonances. Therefore, it was postulated that HCHO detection using GSH may require labelling, either on GSH itself or on the produced HCHO (see Section 2.2.5a).

2.2.3 Direct HCHO Detection by NMR

Although HCHO was shown to be produced during demethylation, experiments with trapping agents dimedone and GSH did not give conclusive evidence that the HCHO was produced directly via oxidation of the N^{ϵ}-methyl groups. Therefore, the dimethylated peptide, ^{13}C-labelled on its methyl groups, was synthesised in order to correlate the loss of the methyllysine signals with the production of HCHO unambiguously. The synthesis of the labelled peptide and subsequent experimentation is described below.

a) Synthesis of Fmoc-Lys($^{13}CH_3$)$_2$-OH

Before synthesis of the ^{13}C-labelled peptide via solid phase peptide synthesis could be attempted, sufficient amounts of the monomeric ^{13}C-labelled N^{ϵ}-dimethyllysine were required. It was also necessary that this methylated lysine be protected on the α-amine using an Fmoc group in order to allow peptide synthesis via comparable methodology to that used for the previously described non-labelled peptides (see below). (*S*)-2-(9H-Fluoren-9-

ylmethoxycarbonylamino)-6-(^{13}C-dimethylamino)hexanoic acid (hereafter referred to as Fmoc-Lys($^{13}CH_3$)$_2$-OH) was prepared in two steps from the commercially available (*S*)-2-(9H-fluoren-9-ylmethoxycarbonylamino)-6-tert-butoxycarbonylaminohexanoic acid (Fmoc-Lys(Boc)-OH, Scheme 2.2).

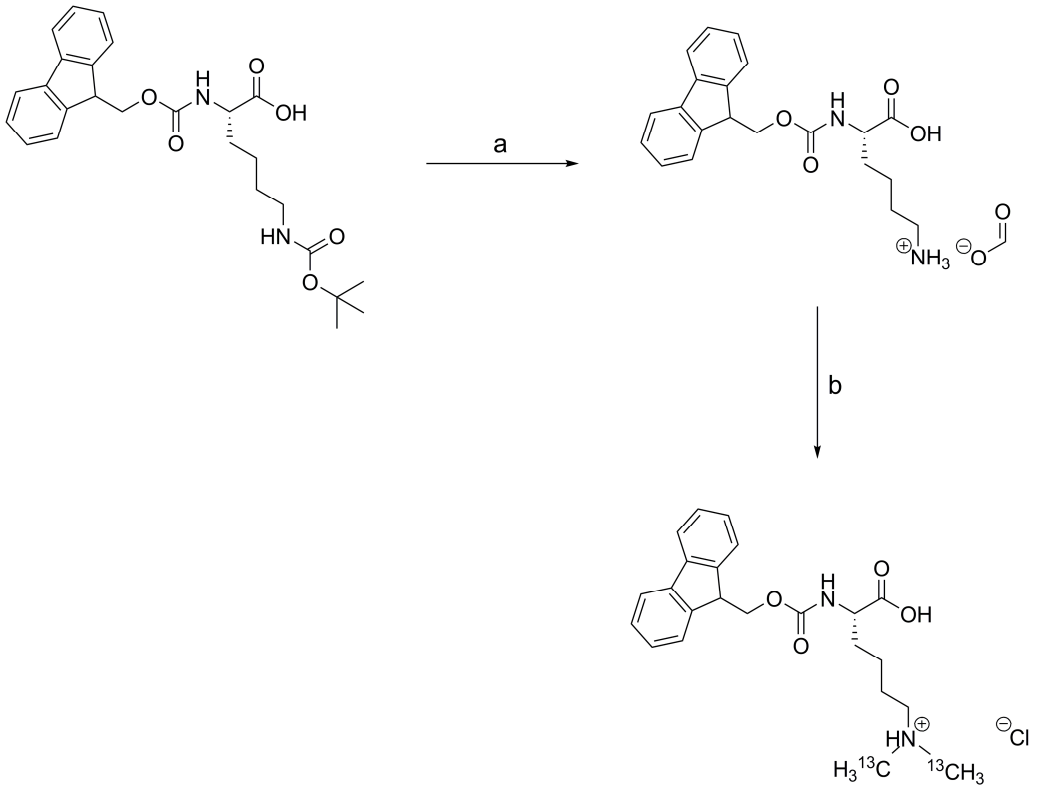

Scheme 2.2 Reaction scheme for the synthesis of Fmoc-Lys($^{13}CH_3$)$_2$-OH. a) HCOOH, b) 6 eq. ^{13}C-HCHO, 2.1 eq. $NaBH_3CN$, MeOH.

The first step in the synthesis required the removal of N^{ε}-Boc group, which was achieved by treatment of the starting material with neat formic acid at room temperature. Removal of the formic acid *in vacuo*, followed by trituration in diethyl ether, resulted in isolation of the deprotected material as the formate salt. This product was then used directly in the second step, which was optimised from a literature procudure.[169] After dissolving the lysine in methanol at 0°C, a portion of 20 % wt. ^{13}C-HCHO solution (6 equivalents) in water was added, followed by 2.1 equivalents of sodium cyanoborohydride dissolved in methanol. The reaction was then left stirring at room temperature for two hours. After reaction completion (which was assessed by both TLC and mass spectrometry

analyses), the solution was neutralised with glacial acetic acid and the solvent removed *in vacuo*. The crude solid was then redissolved in dry acetone and filtered to remove the precipitate. Removal of the acetone *in vacuo* provided the methylated product as a white solid. ^{1}H NMR analysis of the product suggested that the Fmoc protected dimethylated lysine was over 80 % pure, which was deemed suitable for use in peptide synthesis.

b) Solid-Phase Peptide Synthesis – Description

Synthesis of the ^{13}C-labelled peptide (and indeed all other peptides mentioned in this thesis unless otherwise stated) was achieved via standard Fmoc-mediated solid phase peptide synthesis (SPPS) using a CS336X peptide synthesiser (CS Bio, USA). A schematic representation of SPPS protocol is shown in Scheme 2.3.

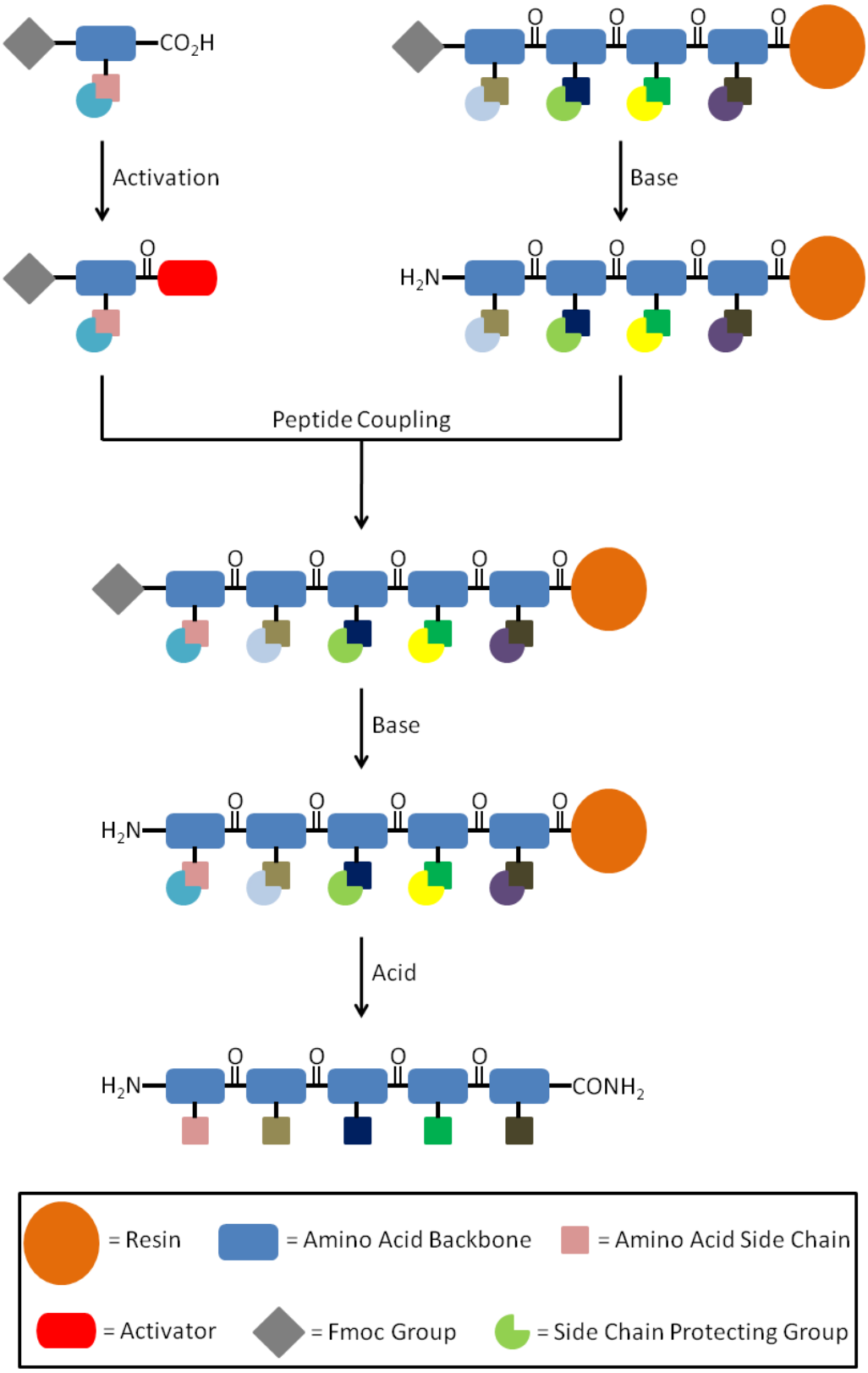

Scheme 2.3 Schematic representation of Fmoc-mediated solid phase peptide synthesis. The amino acid side chain protecting groups and the resin are acid labile.

The standard procedure for SPPS utilised in this work relies upon systematic addition of amino acids to a polystyrene resin, which is connected to the first amino acid (i.e. the *C*-terminal amino acid) by an organic linker. Connecting the peptide to an insoluble solid support facilitates the synthesis by allowing removal of the many soluble reagents required in the individual synthetic steps by filtration. After the last amino acid (the *N*-terminal amino acid) is attached and the N^{α}-Fmoc group is removed, the completed peptide can be cleaved from the resin and linker by treatment with acid (usually TFA). Selectivity of the coupling reaction is ensured by limiting the nucleophilic centres able to react with the activated amino acid. This is achieved by protecting all the nucleophilic side chains of the amino acids already incorporated into the peptide, as well as protecting the activated amino acid side chain and its N^{α}-amino group. Side chains are protected with acid labile protecting groups into ensure orthogonality with N^{α}-Fmoc protection and also to facilitate their collective cleavage during acid-catalysed removal of the resin. After an amino acid is attached to the growing peptide, the remaining reagents and side products from the coupling reaction are washed away, and the peptide is then reactivated for the next coupling by removal of the N^{α}-amino group. This cycle is repeated until the last amino acid has been attached. For synthesis of a peptide via this method to be successful, it is important to ensure that the coupling of each amino acid is high yielding. Therefore, it is common to use a large excess of activated amino acid relative to the peptide during each coupling step.

Activation of the amino acid and its subsequent coupling to the peptide can be achieved using various coupling agents. Care must be taken when selecting a coupling method, however, in order to ensure that the reaction proceeds in a high yielding manner whilst minimising peptide racemisation. Peptide synthesis described in this thesis used diisopropylcarbodiimide (DIC) and the nucleophilic catalyst hydroxybenzotriazole (HOBt) to facilitate coupling, which resulted in

overall good yields for peptide formation. The coupling mechanism using this procedure is shown in Scheme 2.4.

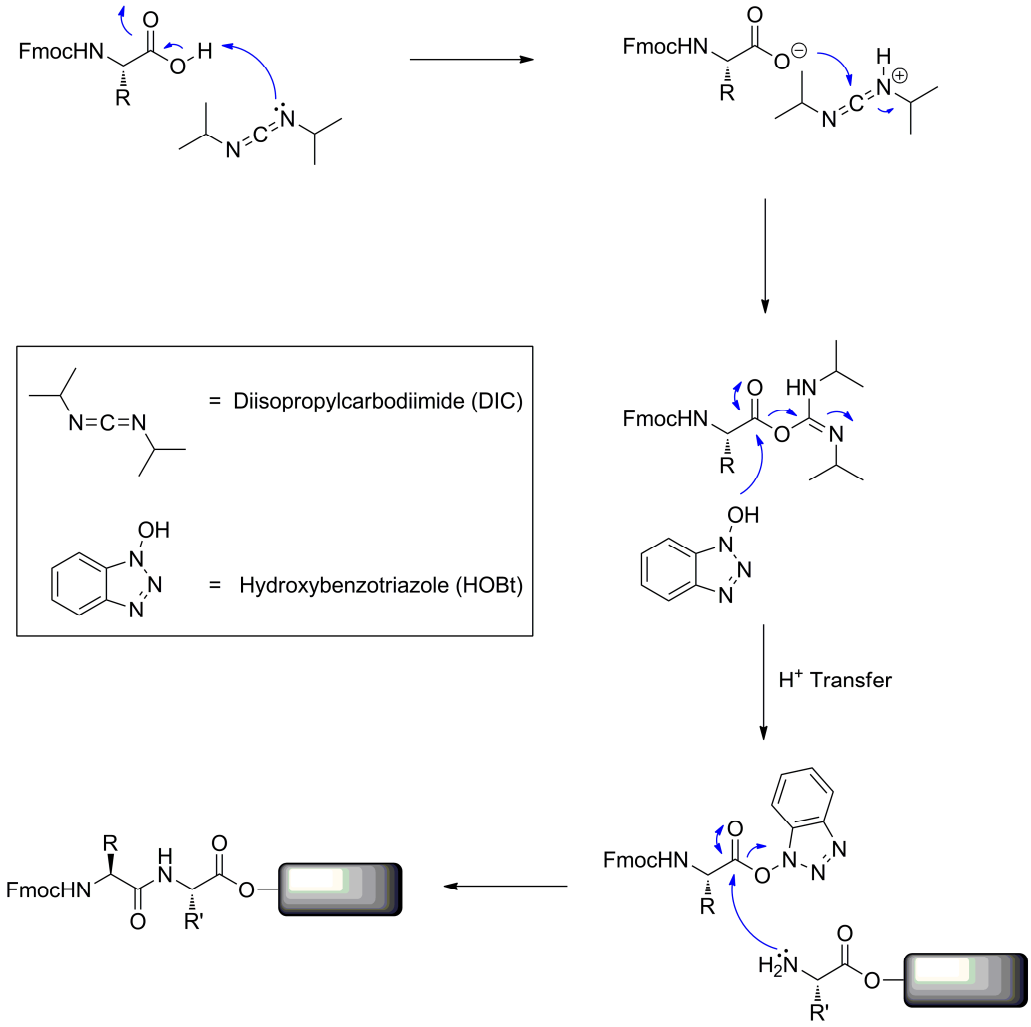

Scheme 2.4 Mechanism of peptide coupling using DIC and HOBt. Acylation of DIC results in the formation of an *O*-acylurea intermediate. This species is then reacted with HOBt to form the active ester and *N,N'*-diisopropylurea. Peptide bond formation is facilitated by nucleophilic attack of the active ester by the peptidic amine, reforming HOBt.

c) Synthesis and Characterisation of ARK($^{13}CH_3$)$_2$STGGK

After SPPS of the ^{13}C-labelled peptide (using the ^{13}C-labelled dimethyllysine), the crude product was purified by preparative LC-MS in order to produce a sample suitably purified for NMR analyses. MALDI analysis of the purified sample indicated that the peptide was greater than 95 % pure, which was

deemed sufficiently pure for NMR experiments. In order to confirm the sequence of the synthesised peptide, and also to ensure that the ^{13}C-labelled methyl groups had been incorporated into the structure, the ^{1}H NMR spectrum of the sample was collected in dAFN and compared to the previously characterised ^{1}H spectrum of the unlabelled dimethylated peptide (Figure 2.10). The ^{1}H spectrum matched closely to that of the unlabelled peptide with the exception of the N^{ε}-methyl group signal, which was observed to be split ($^{1}J_{CH}$ = 143 Hz), presumably due to a one bond ^{1}H-^{13}C coupling.

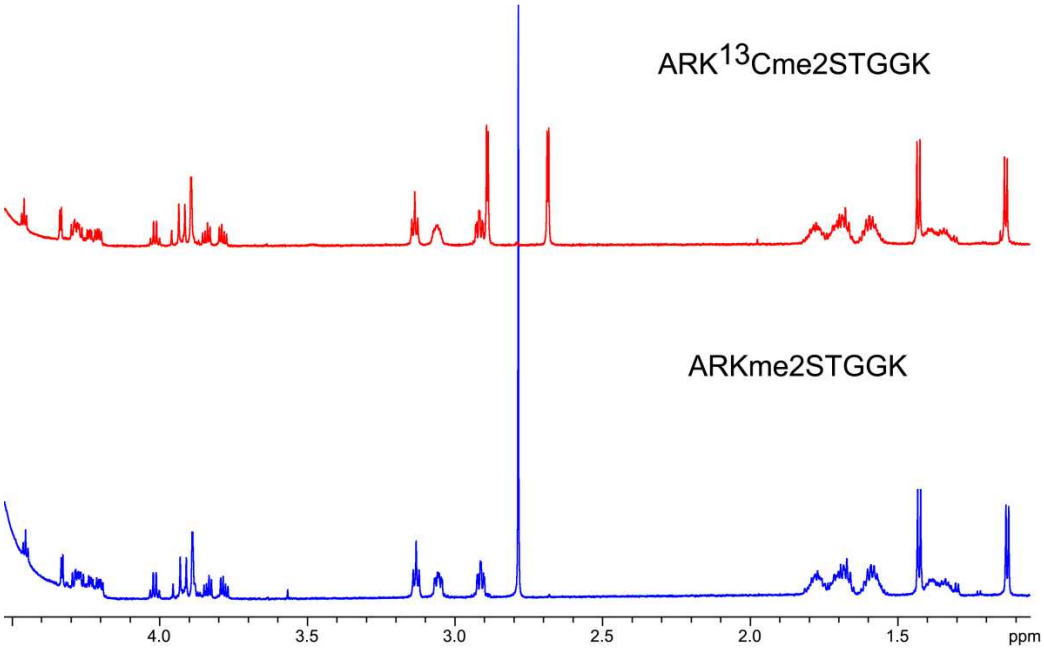

Figure 2.10 ^{1}H NMR spectra (700 MHz) of ARKme2STGGK (Bottom) and ARK^{13}Cme2STGGK (Top) in dAFN buffer.

Before NMR experiments using the labelled peptide were attempted, the peptide was first tested as a substrate of JMJD2E by MALDI mass spectrometry. The peptide, dissolved in 50 mM HEPES buffer pH 7.5 (100 µM final concentration), was incubated with JMJD2E (2 µM), 2OG (50 µM), ascorbate 100 µM) and ferrous iron (10 µM), and the subsequent reaction was analysed after one hour. Peaks corresponding to both the starting material and the monomethylated peptide (i.e. a peak with a mass 15 Da lower than that of the

substrate peptide) were observed in the mass spectrum after one hour, confirming the labelled peptide as a substrate of JMJD2E (Figure 2.11).

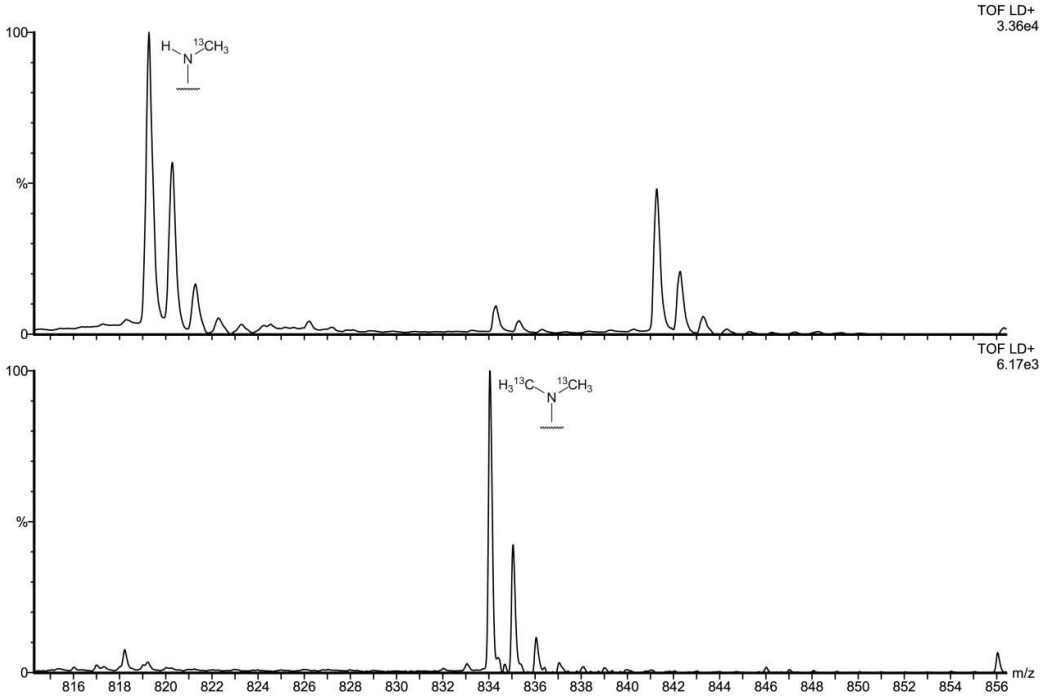

Figure 2.11 MALDI mass spectra of ARK[13]Cme2STGGK with JMJD2E, 2OG, ascorbate and ferrous iron after one hour at 37 °C (Top), and a control experiment without JMJD2E (Bottom). The peak at 841 m/z corresponds to the sodium adduct of the monomethylated product.

d) Detection of ^{13}C-labelled HCHO

Having prepared the ^{13}C-labelled substrate peptide, NMR time course experiments (as described in Section 2.2.1) were carried out in order to probe for the formation of ^{13}C-HCHO during demethylation. It was proposed that analysis of the time course experiments may be conducted using a 1D coupled ^{13}C-heteronuclear single-quantum correlation spectroscopy (HSQC) method, which allows for sole observation of proton resonances attached to a ^{13}C-labelled carbon by limiting the number of transients during data acquisition. This experiment was expected to accentuate signals from the N^{ϵ}-methyl groups and ^{13}C-HCHO over all unlabelled resonances, enabling their detection. It was hoped that ^{1}H NMR may also allow detection of ^{13}C-HCHO due to the presence

of a large one bond ^{1}H-^{13}C *J*-coupling in its ^{1}H spectrum, potentially shifting at least one of the two peaks away from the residual water resonance. Consequently, the demethylation reaction was monitored by both 1D HSQC and ^{1}H NMR.

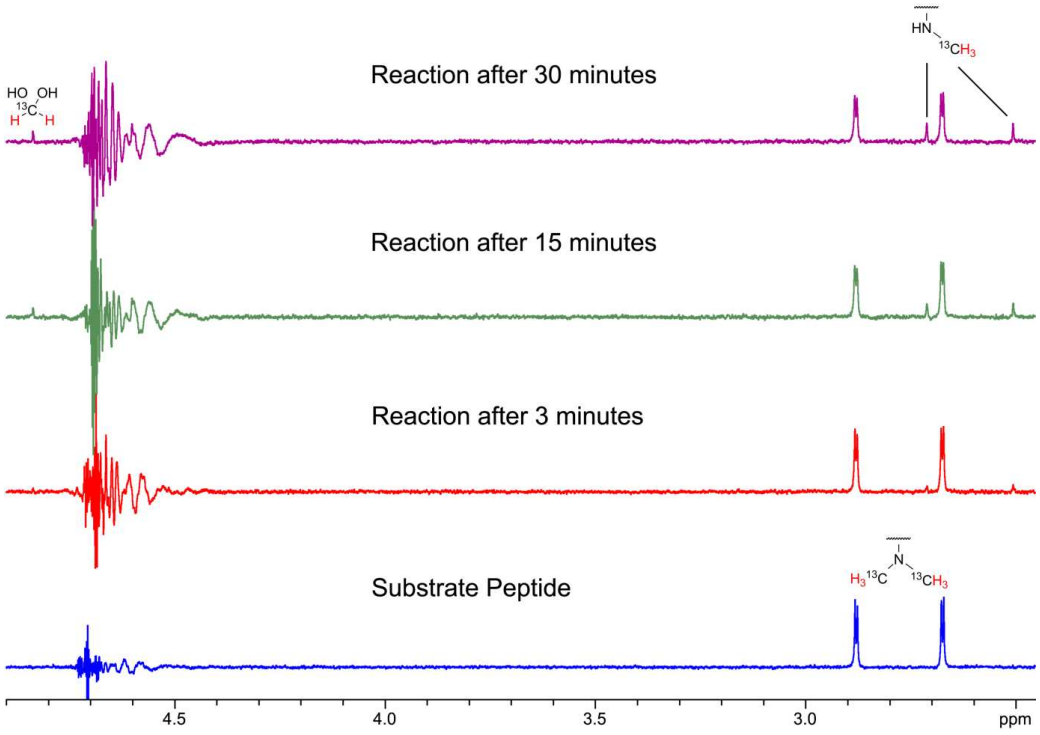

Figure 2.12 1D HSQC spectra (700 MHz) of a time course monitoring JMJD2E-catalysed demethylation of ARK^{13}Cme2STGGK at 25 °C in dAFN buffer.

The 1D HSQC analysis of JMJD2E-catalysed demethylation over the first 30 minutes of reaction (at 25 °C) is shown in Figure 2.12. Demethylation of the substrate peptide was implied by the emergence of a doublet resonance at δ_H 2.61 ppm ($^{1}J_{CH}$ = 143 Hz), which was assigned to the ^{13}C-labelled N^{ϵ}-methyl groups of the monomethylated peptide. In addition to this signal, another resonance was observed during the reaction downfield of the methyl group signals at δ_H 4.84 ppm. Analysis of the sample by 2D HSQC revealed that the carbon atom attached to the protons at this resonance possessed a ^{13}C chemical shift at δ_C 81.7 ppm (Figure 2.13), which correlated to the expected carbon shift of hydrated HCHO (as shown in Section 8.2.1). Therefore, this resonance was postulated to represent ^{13}C-HCHO released during demethylation.

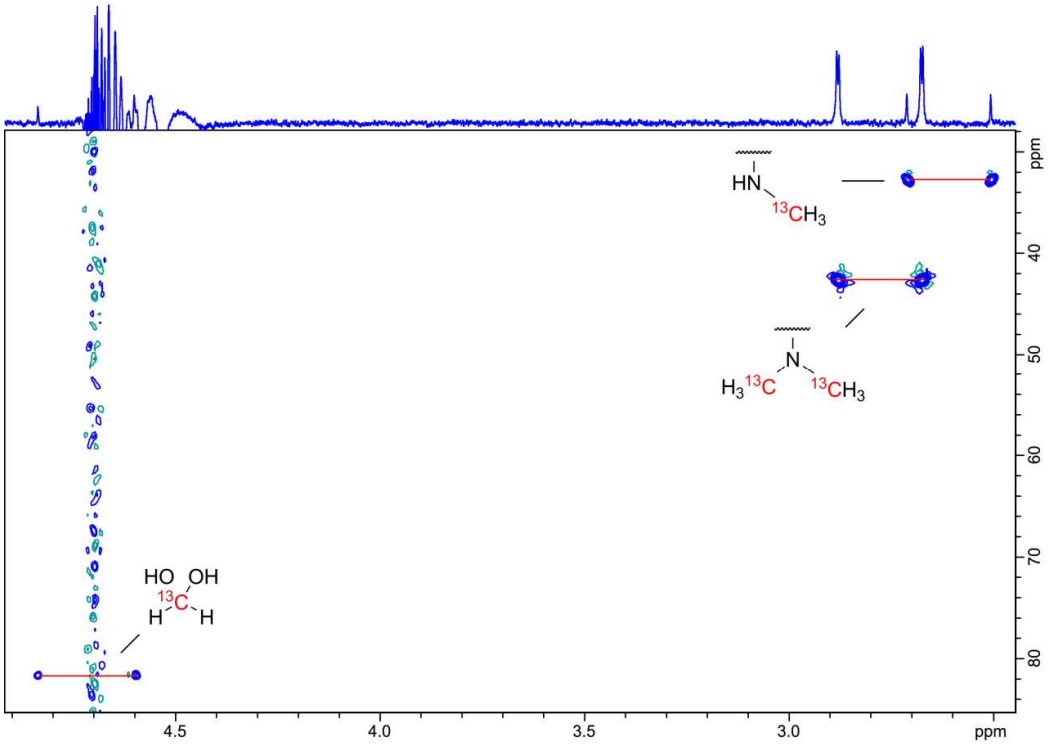

Figure 2.13 2D HSQC spectrum (700 MHz) of JMJD2E-catalysed demethylation of ARK^{13}Cme2STGGK after 30 minutes in dAFN buffer.

The 2D HSQC spectrum also suggested that the observed signal at δ_H 4.84 ppm was part of a doublet resonance (as expected for ^{13}C-HCHO); however, the other part of this signal was not detectable in the 1D HSQC spectrum due to overlap with the signal arising from the residual solvent. Therefore, the sample was cooled to 4 °C in the hope that the solvent resonance would shift relative to the other signals in the spectrum (Figure 2.14). The resultant spectrum revealed the other ^{13}C-HCHO signal at δ_H 4.60 ppm.

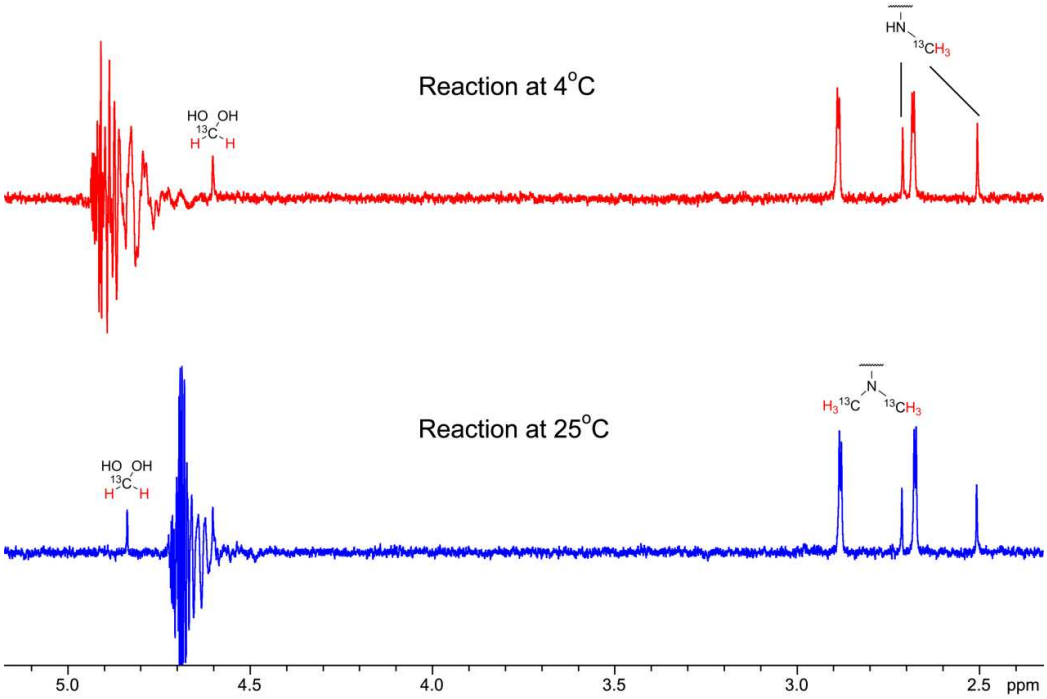

Figure 2.14 1D HSQC spectra (700 MHz) of JMJD2E-catalysed demethylation of ARK^{13}Cme2STGGK at 25 °C (Bottom) and 4 °C (Top) in dAFN buffer.

Finally, the presence of ^{13}C-HCHO was confirmed by the addition of authentic ^{13}C-HCHO to the sample, which resulted in accentuation of the ^{1}H resonance, as observed by 1D HSQC (Figure 2.15).

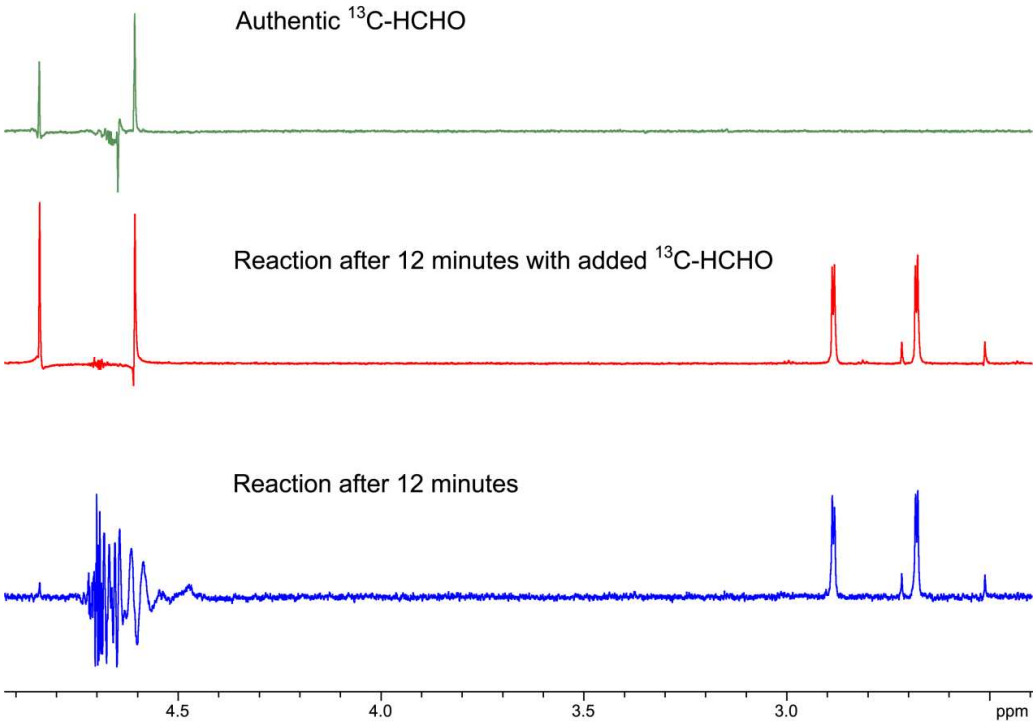

Figure 2.15 1D HSQC spectra (700 MHz) of JMJD2E-catalysed demethylation of ARK^{13}Cme2STGGK with added ^{13}C-HCHO in dAFN buffer.

Having conclusively detected ^{13}C-HCHO during demethylation by 1D HSQC, attempts were then made to analyse HCHO formation by ^{1}H NMR. The demethylation reaction was repeated at 25 °C and ^{1}H NMR spectra were attained over initial time points of the reaction, which revealed formation of ^{13}C-HCHO in the sample by the emergence of a ^{1}H-resonance at δ_H 4.84 ppm (Figure 2.16, bottom). The corresponding peak at δ_H 4.60 ppm was observed in the ^{1}H NMR at 4 °C (Figure 2.17, top), thus confirming the production of ^{13}C-labelled HCHO.

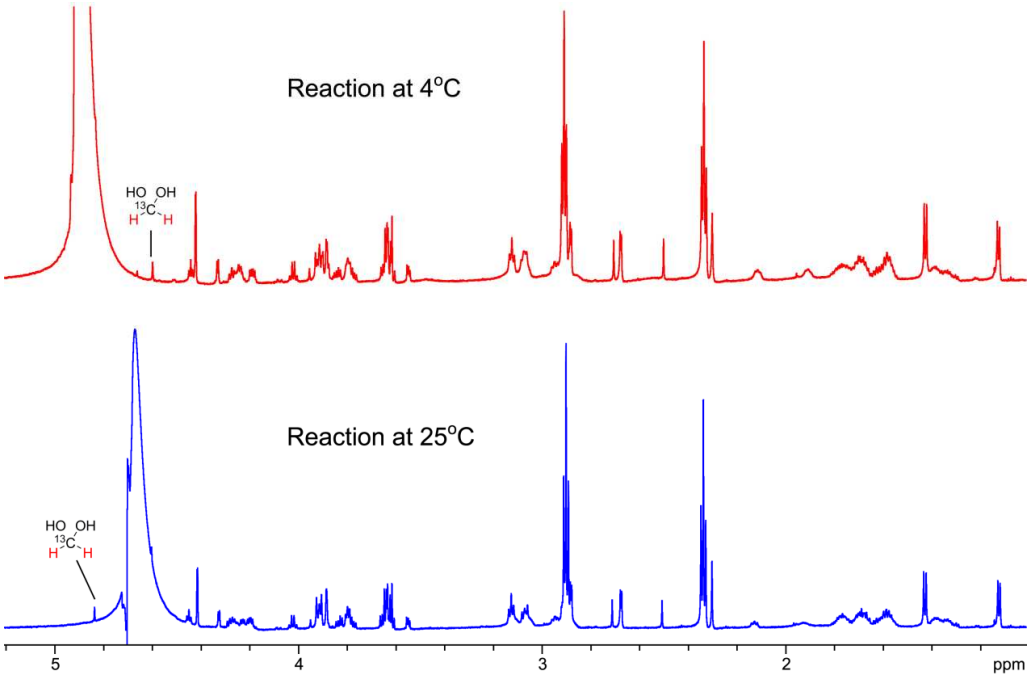

Figure 2.16 ^{1}H NMR spectra (700 MHz) of JMJD2E-catalysed demethylation of ARK^{13}Cme2STGGK at 25 °C (Bottom) and 4 °C (Top) in dAFN buffer. Signals corresponding to ^{13}C-HCHO are highlighted.

Overall, the NMR analyses of the JMJD2E-catalysed demethylation of a ^{13}C-labelled peptide enabled the detection of enzymatically produced HCHO. The source of the carbon atom present in the released HCHO was confirmed as the N^{ε}-methyl groups at lysine-9, thus confirming that HCHO is formed via direct oxidation of the methyl C-H bonds. This work has provided conclusive evidence that HCHO is produced during demethylation, and is believed to be the first documented example of using NMR to detect enzymatically produced HCHO.

2.2.4 Hemiaminal Detection

Having confirmed the formation of HCHO, attention was focused towards the attempted detection of the proposed hemiaminal intermediate during catalysis (Scheme 1.4). Analysis of the 1D HSQC spectra described in Section 2.2.4 did not reveal any ^{13}C-labelled signals apart from those assigned to the peptide methyl groups and HCHO, suggesting that the hemiaminal may be too unstable to be detectable by NMR directly. However, detection of free ^{13}C-HCHO using the 1D HSQC methodology implied that addition of GSH to the mixture may result in the formation of the ^{13}C-labelled

hemithioaminal intermediate HMG, allowing detection by NMR. Analysis with unlabelled peptide did not allow detection of any GSH adducts (Section 2.2.3b); however, it was proposed that using the labelled peptide may amplify the N^{ϵ}-methyl group derived signals in the intermediate, facilitating their detection by 1D HSQC. GSH was added to the demethylation assay sample and monitored directly by 1D HSQC. The 1D HSQC spectra acquired after a 45 minute reaction (at 25 °C and 4 °C) are shown in Figure 2.17.

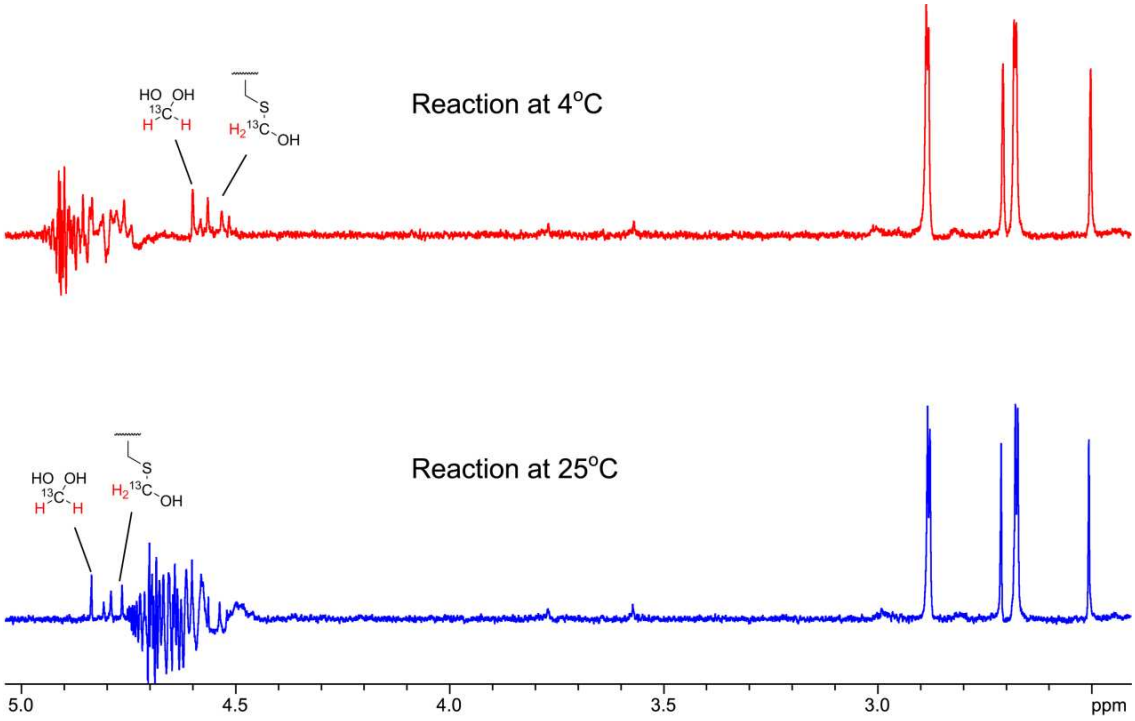

Figure 2.17 1D HSQC spectra (700 MHz) of JMJD2E-catalysed demethylation of ARK^{13}Cme2STGGK at 25 °C (Bottom) and 4 °C (Top) in dAFN buffer. Signals corresponding to ^{13}C-HCHO and ^{13}C-HMG are highlighted.

Interestingly, using the ^{13}C-labelled peptide in the reaction facilitated the detection of ^{13}C-labelled HMG as manifested by the observation of a doublet of a doublet of a doublet (ddd) ^{1}H resonance at δ_H 4.67 ppm by 1D HSQC (Figure 2.17). Although this species was not observed in the previous experiments (Section 2.2.3b), the results with the labelled peptide suggest that the HMG was likely present in these earlier samples, but was not detectable due to overlap of its characteristic ^{1}H-signals. However, the 1D HSQC spectra did not indicate the presence of any signal derived from the potential

GSH-peptide adduct, implying that this species is not formed during demethylation (the small signals at δ_H 2.80 ppm, δ_H 2.99 ppm, δ_H 3.58 ppm and δ_H 3.77 ppm in Figure 2.17 were assigned to the ^{13}C satellite resonances of the α-glycinyl protons of GSH and the α-keto CH_2 of 2OG respectively). Overall, this work did not indicate formation of the hemiaminal intermediate, implying that this species is either not produced, remains enzyme bound, or is too unstable to be detected by NMR techniques.

2.3 Conclusions and Future Work

Work in this Chapter details the first reported use of NMR to monitor the reactions of 2OG dependent histone demethylases. In particular, NMR experiments with JMJD2E allowed the determination of not only kinetic parameters for demethylation, but also of initial demethylation and succinate formation rates in the presence and absence of ascorbate. The direct detection of enzymatically produced HCHO was not possible using a non-labelled substrate; however, addition of the HCHO 'scavenger' dimedone to the reaction mixture enabled the detection of HCHO indirectly. Analysis of the reaction using a synthesised ^{13}C-labelled histone peptide enabled detection of ^{13}C-HCHO, which was observed to react with the cellular thiol GSH, forming the biologically relevant adduct HMG. Overall, these studies have shown NMR to be a useful tool for monitoring enzymatic reactions, especially those which produce multiple products. However, it should be noted that the technique possesses a number of limitations. Firstly, the fact that only one sample can be monitored in the NMR spectrometer at a time, and the fact that each experiment requires a relatively large sample volume suggests that, at least as presently configured, NMR is not a suitable method for multiple analyses, e.g. potential inhibitor screening. Also, the NMR experiments employed have been unable to confirm the existence of any oxidised intermediate species formed during the demethylation reaction. Assuming that demethylation of the lysyl residue must proceed via oxidation on an N^{ϵ}-methyl C-H bond, it seems likely that any intermediate species produced during the reaction is too unstable to be detected by NMR techniques. Therefore, future experimentation probing

the formation of intermediates during demethylation would in all probability require new methodologies, possibly using substrate analogues (see Chapter 3).

Chapter 3

Probing the Reactions of 2OG Demethylases with Lysine Analogues

3.1 Introduction

The work described in Chapter 2 illustrated that demethylation of peptidic N^{ε}-methylated lysine by JMJD2E (and by implication all other members of the 2OG demethylase family) results in the formation of HCHO. However, these experiments could not conclusively determine the nature of the intermediate species produced during demethylase-catalysed oxidation, and therefore, some aspects of the mechanism by which HCHO is produced could not be determined. These observations imply that the intermediate(s), such as the proposed hemiaminal intermediate (Scheme 3.1), may be too short-lived to be detectable by the previously described methods. Therefore, it was proposed that new approaches may be required in order to further elucidate the mechanism of oxidation, and in particular to demonstrate that it proceeds via a hydroxylation step.

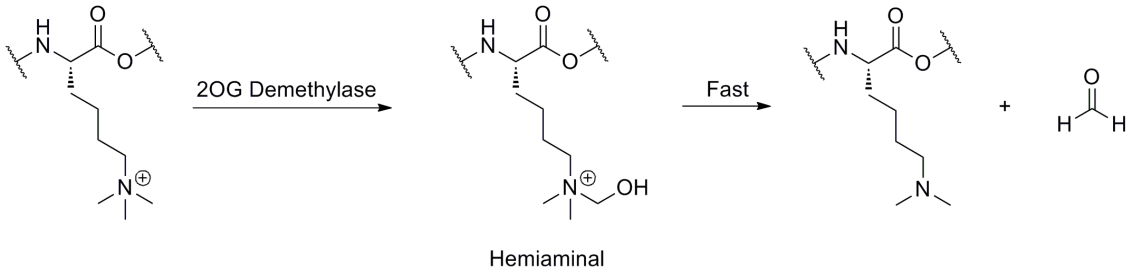

Scheme 3.1 Scheme showing the proposed formation and fragmentation of the hemiaminal intermediate during 2OG demethylase catalysed lysyl demethylation. The hemiaminal intermediate is too short-lived to be detected directly.

This Chapter describes work using methylated lysine analogues as potential substrates of histone demethylases. It was hoped that these substrates may enable the detection of novel oxidative reactions with the demethylase enzymes, and would therefore provide new information on many aspects of the demethylation mechanism. In particular, it was proposed that analysis of any novel products produced during catalysis may give evidence for the occurrence of hydroxylation during methyllysine demethylation. In addition to revealing new insights into the reactivity of the lysyl demethylases, it was also hoped that the lysine analogues may probe the active site space available for substrate binding, and therefore, may help in the development of novel substrate-competitive inhibitors.

MALDI analyses with PHF8 were carried out in collaboration with Louise Walport.

3.2 Results

3.2.1 Design of Lysine Analogues

In order for the lysine analogues to be useful for investigations with histone demethylases, a number of factors had to be considered. Firstly, it was important to ensure that the analogues be suitably similar to the methylated lysine residues in order to ensure a good chance of binding in the active site. This would include leaving the α-amido and carbonyl groups of the lysine residue intact, not only to allow incorporation into a peptide, but also to retain any hydrogen-bonding interactions between the peptidic backbone and the enzyme.[139, 140, 170] It was also deemed necessary for the analogues to possess oxidisable bonds (preferentially alkyl C-H bonds) positioned close to the ferrous iron during catalysis. In order to probe for evidence of the proposed hemiaminal intermediate, it was also deemed prudent to produce analogues with a potentially oxidisable bond in an analogous position to the N^{ε}-methylated lysine methyl group (i.e. a bond attached to a side chain carbon atom ~ 6 atoms away from the α-carbon). This would hopefully facilitate oxidation of this bond in a similar fashion to the natural substrate, allowing observation of the hemiaminal intermediate or analogous product. It was also intended that the synthesis of the analogues (as N^{α}-Fmoc protected

amino acids), as well as their incorporation into peptides, should be suitably efficient to ensure that peptide screening is viable.

Taking these factors into consideration, the following lysine structures shown in Figure 3.1 were targeted.

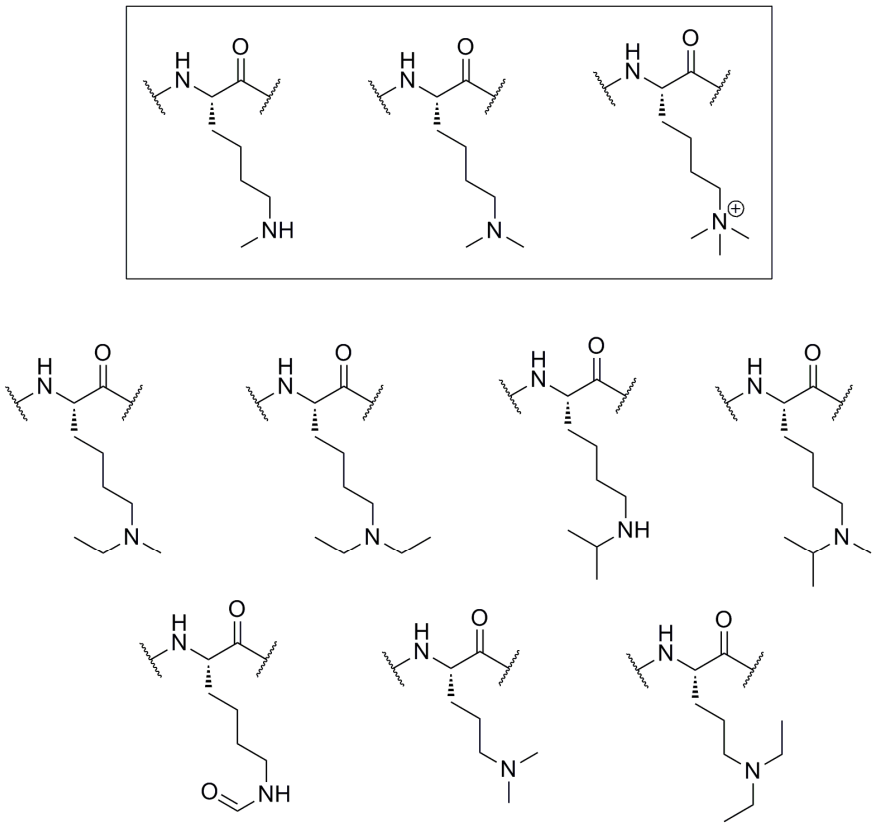

Figure 3.1 Structures of the proposed lysine analogues. The structure of the natural methylated lysine substrates are boxed.

All of the analogues selected for investigation with the demethylases possessed alkyl groups connected to a side-chain amino group. It was therefore hoped that these analogues would be suitably similar to the methylated lysine substrates to allow their binding in the enzyme active sites. Additionally, all of the analogues except for N^{δ}-dimethylornithine possess C-H bonds in analogous positions to the N^{ε}-methyl group C-H bonds of methylated lysines. It was therefore postulated that these bonds may be oxidised by the demethylases, resulting in the formation of new products and providing evidence for the formation of a hemiaminal during lysyl demethylation. A number of

the analogues were also targeted in order to allow comparisons with the natural methyllysine substrates. For example, comparing the demethylation of dimethyllysine with any reactions of methylethyllysine and diethyllysine analogues may give insights into the relative binding affinities of each species, and may also reveal the enzyme specificities for methyl versus ethyl groups on the lysine residue.[140] Comparing the reactions of dimethyllysine, methylethyllysine and methylisopropyllysine analogues may also give information on the preference of substitution around the oxidised C-H bond. Analysing the reactions of the ornithine derived analogues should reveal whether the ε-amine is required for oxidation.

It was anticipated that all of the analogues proposed could be produced from the corresponding N^{α}-Fmoc protected lysine or ornithine in a maximum of two steps (Scheme 3.2). This was expected to allow efficient synthesis of sufficiently large amounts of the amino acids, and therefore, it was hoped that peptide formation should be enhanced by allowing more of the monomeric analogues to be used for each synthesis.

3.2.2 Synthesis of Lysine Analogues

The synthetic procedures used for each lysine analogue are defined in Scheme 3.2.

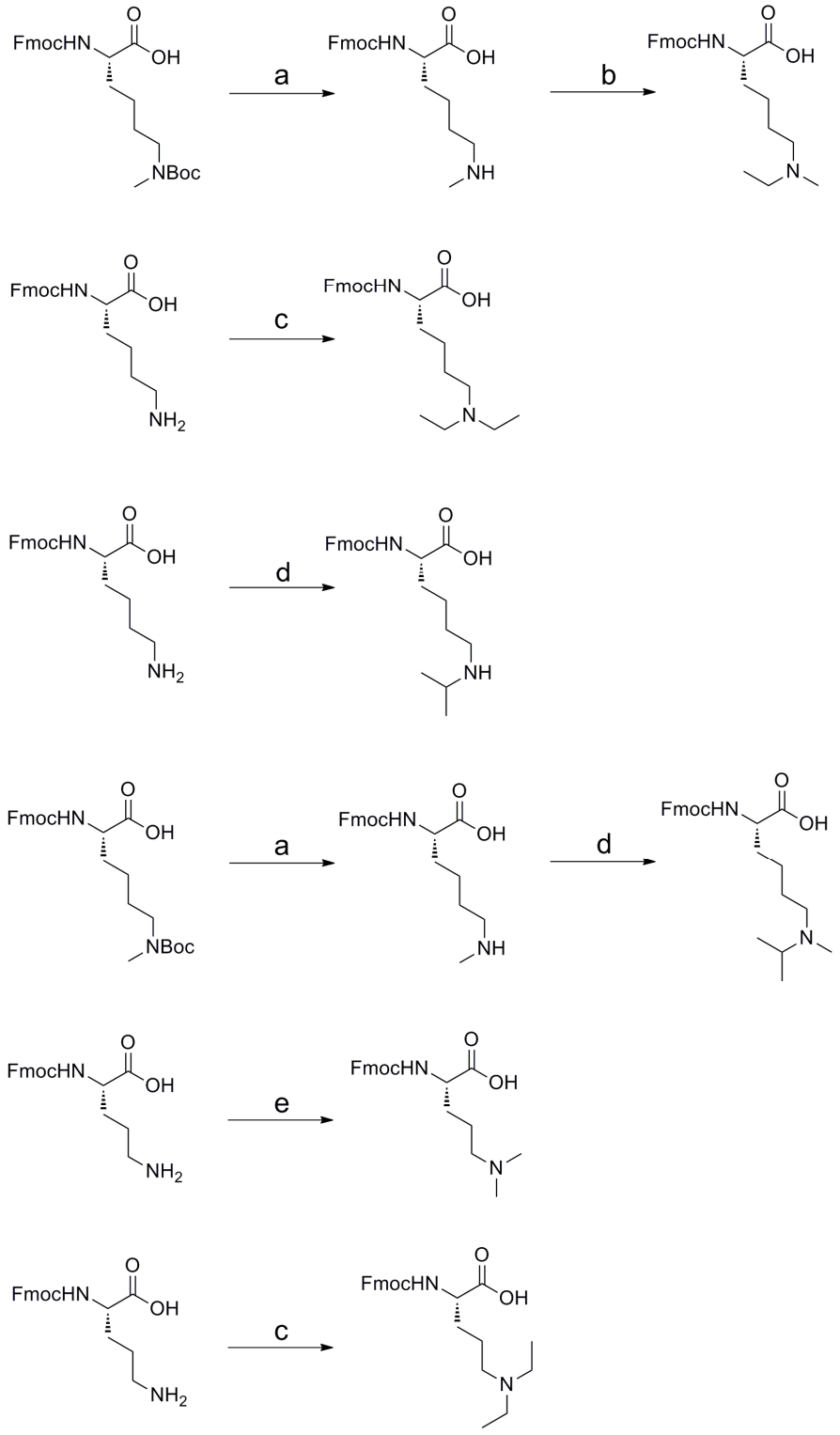

Scheme 3.2 Synthetic procedures for preparation of the N^{α}-Fmoc protected lysine analogues. a) TFA, triisopropylsilane; b) AcH (5 eq.), $NaBH_3CN$ (1.1 eq.), EtOH; c) AcH (5 eq.), $NaBH_3CN$ (2.1 eq.), EtOH; d) acetone (1.5 eq.), $NaBH_3CN$ (1.1 eq.), EtOH; e) HCHO (6 eq.), $NaBH_3CN$ (2.1 eq.), MeOH.

The alkylation steps used in the syntheses involved the reduction of imine intermediates, produced *in situ* from the side-chain amine and an aldehyde/ketone. These steps generally proceeded in good yields, resulting in the production of the alkylated products in large amounts. The most challenging aspect of the syntheses, however, was found to be purification of the products. Although in all cases, the product in crude form was found to be suitably pure for direct use in peptide synthesis (as assessed by ^{1}H NMR), purification was attempted on the analogues in order to facilitate their characterisation. Purification of the analogues was impeded by a number of factors. Firstly, extraction of the analogues into organic solvents was impeded by their polarity (a number of the species were found to be soluble in water). This polarity also hampered purification by silica-gel liquid chromatography, which resulted in the products sticking to the polar column. Attempts at purification by HPLC were unsuccessful, presumably due in part to the hydrophobicity of the Fmoc groups. Purification was finally achieved by trituration with diethyl ether. This allowed removal of the organic impurities in the crude mixtures, and produced the desired products in over 80 % purity as white solids. Descriptions of the synthetic procedures used, as well as characterisation of the analogues, are described in Chapter 10.

3.2.3 Incorporation of Lysine Analogues into Substrate Peptides

In order to give the lysine analogues a good chance of reacting with the 2OG demethylases, it was important to incorporate the analogues into suitable substrate peptides, i.e. by substituting the methylated lysine for the analogues in the histone peptide fragments. The selected peptides are shown in Table 3.1.

Table 3.1 Peptides with incorporated lysine analogues.

Peptides	Enzymes to be tested
ARTKme3QTARKmeetSTGGKA	JMJD2E, JMJD2A, PHF8
ARTKme3QTARKet2STGGKA	JMJD2E, JMJD2A, PHF8
ARTKme3QTARKiprSTGGKA	JMJD2E, JMJD2A, PHF8
ARTKme3QTARKmeiprSTGGKA	JMJD2E, JMJD2A, PHF8
ARTKme3QTARKforSTGGKA	JMJD2E, JMJD2A, PHF8
ARTKme3QTAROme2STGGKA	JMJD2E, JMJD2A, PHF8
ARTKme3QTAROet2STGGKA	JMJD2E, JMJD2A, PHF8
PATGGVKmeetKPHRY	JMJD2A, FBXL11
PATGGVKet2KPHRY	JMJD2A, FBXL11
PATGGVKiprKPHRY	JMJD2A, FBXL11
PATGGVKmeiprKPHRY	JMJD2A, FBXL11
PATGGVKforKPHRY	JMJD2A, FBXL11
PATGGVOme2KPHRY	JMJD2A, FBXL11
PATGGVOet2KPHRY	JMJD2A, FBXL11

For investigations with H3K9 substituted analogues, 15-mer peptides trimethylated at position 4 (corresponding to lysine-4 in histone H3) were selected (the 15-mer peptides of the sequence ARTKmexQTARKmexSTGGKA are known to be better substrates for JMJD2E, JMJD2A and PHF8 than the previously described 8-mer peptides, sequence ARKmexSTGGK, Dr. Nathan Rose, personal communication). Demethylation activity of PHF8 (at H3K9) has been shown to be significantly increased in the presence of trimethylated H3K4,[140, 171] and therefore, it was proposed that peptides incorporating this modification would likely have a greater chance of reacting with this enzyme. Previous experiments with the analogous dimethyllysine peptides have shown that trimethylation at position 4 does not affect demethylation at position 9 by JMJD2E and JMJD2A, allowing these doubly modified peptides to be tested as substrates for these enzymes as well. For studies with K36 selective demethylases (JMJD2A and FBXL11), the analogues were incorporated into a standard 12-mer peptide (in place of H3K36).

3.2.4 Analyses of the Reactions of Analogue Peptides with Demethylases

Having synthesised and purified the lysine analogue containing peptides, each peptide was incubated with the corresponding 2OG demethylases highlighted in Table 3.1 and the samples were analysed for evidence of reaction. Initial analyses were carried out using MALDI mass spectrometry, which allowed the detection of any oxidised products

in the samples by displaying new peaks in the mass spectra. In some cases, identified products from the reaction were then subjected to further analysis by MALDI and NMR in order to give insights into their formation and to identify any small molecule species released. Analysis of each lysine analogue is described below.

a) N^{ε}-Methylethyllysine

The MALDI mass spectrum of the reaction of JMJD2E with the peptide ARTKme3QTARKmeetSTGGKA is shown in Figure 3.2

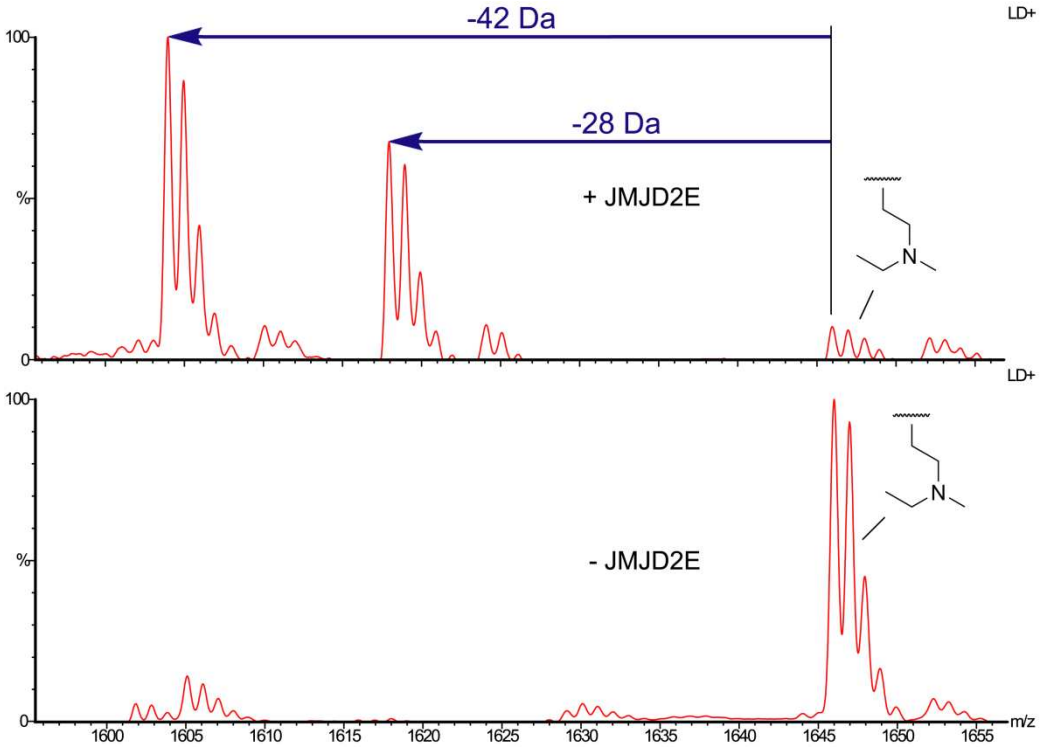

Figure 3.2 MALDI mass spectrum of a sample containing JMJD2E (2 µM), ARTKme3QTARKmeetSTGGKA (10 µM), 2OG (50 µM), ascorbate (100 µM) and ferrous iron (10 µM) after one hour at 37 °C. The control experiment without enzyme is shown below.

After one hour, significant new peaks were detected in the MALDI mass spectrum. The intensity of these new peaks (at 1604 m/z and 1618 m/z respectively) was significantly greater than that of the starting material, which suggested that reaction had occurred on the methylethyllysine peptide. The masses of the new peaks appeared to correspond to the substrate peptide with a

loss of the N^{ϵ}-ethyl group (at 1618 m/z, loss of 28 Da) and a loss of both the N^{ϵ}-ethyl group and N^{ϵ}-methyl group (at 1604 m/z, loss of 42 Da) respectively. These observations imply that JMJD2E can catalyse both demethylation and 'deethylation', presumably by oxidative mechanisms.

In order to investigate whether a monoethyllysine peptide intermediate could be observed, the reaction was repeated and monitored over the first 30 minutes by MALDI mass spectrometry (Figures 3.3 and 3.4). In addition to facilitating detection of monoethyllysine peptide, this experiment was intended to allow the concentrations of each species in the mixture to be quantified over time, which, it was hoped, would reveal whether some of the peptides present were substrates for subsequent reactions.

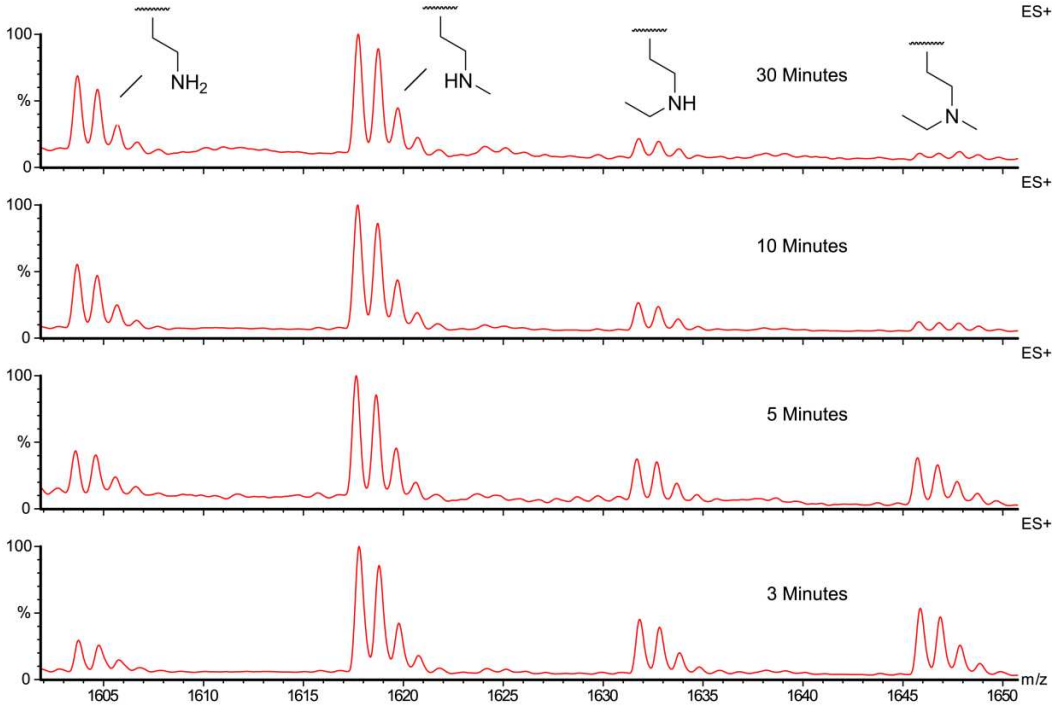

Figure 3.3 MALDI mass spectra of a sample containing JMJD2E (2 µM), ARTKme3QTARKmeetSTGGKA (10 µM), 2OG (50 µM), ascorbate (100 µM) and ferrous iron (10 µM) over time at 25 °C.

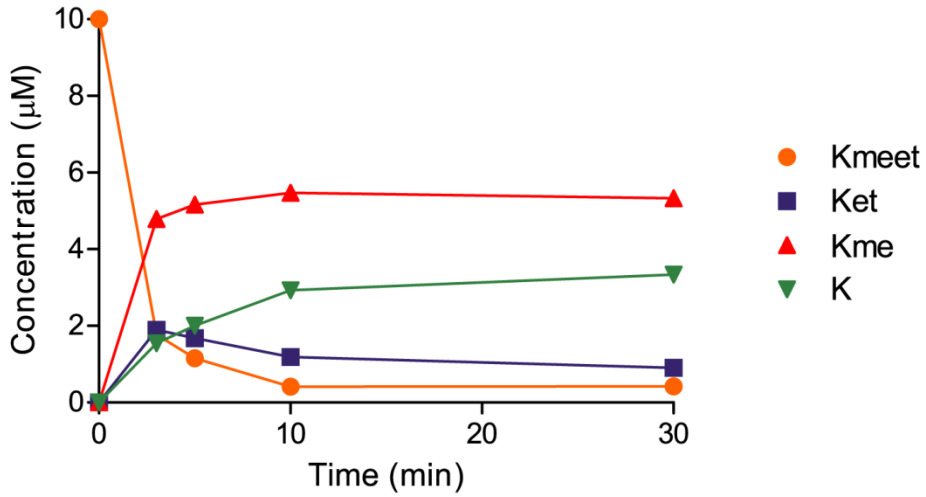

Figure 3.4 Concentrations of peptidic species derived from ARTKme3QTARKmeetSTGGKA, during the reaction with JMJD2E.

Firstly, it was noted that after 10 minutes reaction, nearly all of the substrate methylethyllysine peptide had been reacted in the sample, either to the monomethyl peptide, unalkylated peptide or to a species identified by its mass peak at 1632 m/z. The latter indicates that monoethyllysine peptide is formed, presumably via demethylation of the substrate peptide. This species was most prevalent in the sample after 3 minutes reaction (2 μM), however its concentration was much lower than that of the monomethyllysine peptide over all time points. The apparent preference for deethylation over demethylation may indicate that the bulkier ethyl group is preferentially orientated close to catalytic iron in the enzyme active site. After 3 minutes, the amount of monoethyllysine peptide in the sample appeared to diminish, which coupled to the observed increase in the peak intensity at 1604 m/z. This observation indicated that the monoethyllysine peptide can be further demethylated to the free lysyl form. In addition to deethylation of monoethyllysine, it is possible that the free lysyl peptide may also be formed via demethylation of the monomethyllysine peptide; however, the rate of demethylation of this species appeared to be lower than the deethylation of monoethyllysine peptide, despite the higher monomethyllysine peptide concentration. These observations imply that the deethylation rates of both methylethyllysine and monoethyllysine

peptides by JMJD2E are faster than the demethylation rates of the corresponding methylethyllysine and monomethyllysine peptides respectively.

In order to compare the dealkylation rates of methylethyllysine and dimethyllysine peptides, the MALDI experiment was repeated in the presence of dimethyllysine peptide (10 μM, sequence ARKme3QTARKme2STGGK). This peptide was deliberately selected so that peaks for the monomethylated and unmethylated peptides deriving from methylethyllysine and dimethyllysine peptide could be distinguished from one another. Analysis by MALDI over initial time points revealed that loss of the dimethyl peptide was comparable to, albeit slightly faster than, the loss of the methylethylpeptide, indicating that reactions on the two modified lysines occur with similar rates (Figure 3.5).

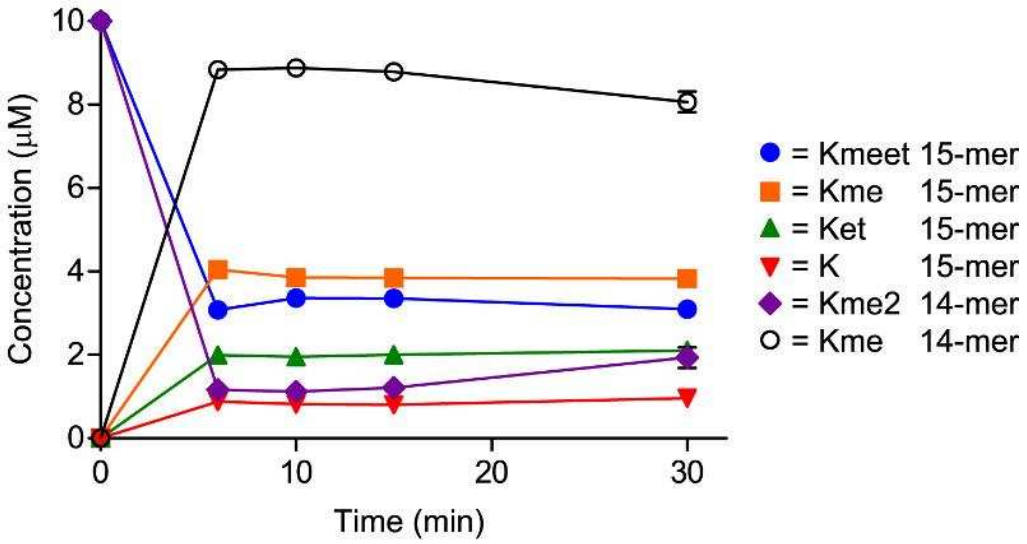

Figure 3.5 Concentrations of peptidic species derived from the incubation of JMJD2E with ARTKme3QTARKmeetSTGGKA and ARTKme3QTARKme2STGGK.

Having identified demethylation and deethylation of methylethyllysine at H3K9, experiments using ^{1}H NMR were then conducted in order to further investigate products formed during the reaction. In particular, it was hoped that these experiments would help to identify the side product(s) produced during deethylation in order to offer insight into the reaction mechanism of this process. The methylethyllysine peptide was incubated with JMJD2E (10 μM),

2OG (5 mM), ascorbate (1 mM) and ferrous iron (10 μM) in dAFN buffer, as described in Chapter 2. The reaction was then monitored by ^{1}H NMR over 30 minutes at 25 °C (Figure 3.6).

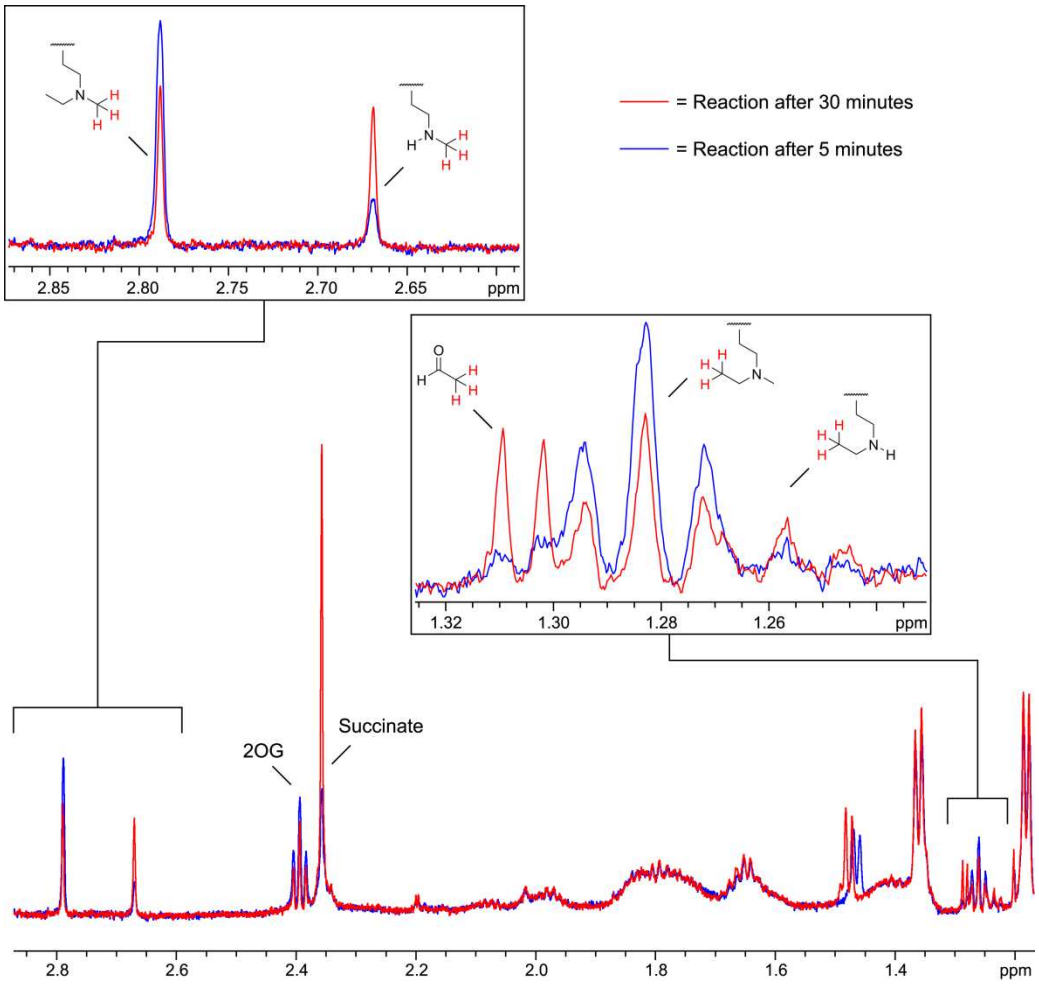

Figure 3.6 ^{1}H NMR spectra (700 MHz) of the reaction of ARTKme3QTARKmeetSTGGKA with JMJD2E after 5 minutes (Blue) and 30 minutes (Red) respectively in dAFN buffer.

In addition to the formation of succinate, it was evident that reaction of the peptide had occurred by observation of new peaks in the ^{1}H NMR spectra. By analysis of their respective chemical shifts, multiplicities and relative intensities over time, it was possible to assign each of the new signals to products of the reaction. Firstly, it was noted that the singlet resonance at δ_H 2.79 ppm, which was assigned to the N^{ϵ}-methyl group protons at lysine-9 on the substrate peptide, decreased in intensity over the reaction period. This loss in intensity appeared to correlate with the emergence of a new singlet resonance at δ_H 2.67 ppm,

suggesting that this new signal corresponds to protons attached to one of the proposed dealkylated peptide products. The fact that this signal possessed a similar chemical shift to that observed for the N^{ϵ}-methyl groups of ARKmeSTGGK (Figure 2.2), and also that no *J*-coupling between these protons and other protons in the structure was detected, allowed this resonance to be assigned to the N^{ϵ}-methyl group protons at lysine-9 on the peptide ARTKme3QTARKmeSTGGKA. It was also possible to detect the formation of the monoethyllysine containing peptide by the emergence of a triplet resonance at δ_H 1.26 ppm. The intensity of this signal over the reaction period, however, was much lower than that of the aforementioned resonance at δ_H 2.67 ppm, suggesting that the monoethyllysine species was present at much lower concentration in the sample (consistent with the MALDI experiments). The emergence of this signal appeared to correlate with the loss in intensity of the substrate terminal N^{ϵ}-ethyl group resonance (at δ_H 1.28 ppm), supporting assignment of this signal to the monoethyl product.

Having confirmed the formation of monomethyllysine and monoethyllysine containing peptides in the NMR sample, attention was turned towards the detection of other potential products. It was proposed that demethylation of the substrate peptide would likely result in the formation of HCHO, which could be detected *in situ* by the addition of dimedone to the reaction mixture (see Chapter 2). The likely product of deethylation was postulated to be acetaldehyde (AcH), although it was also noted that other mechanistic pathways may be possible in the sample, resulting in formation of other species (Scheme 3.3).

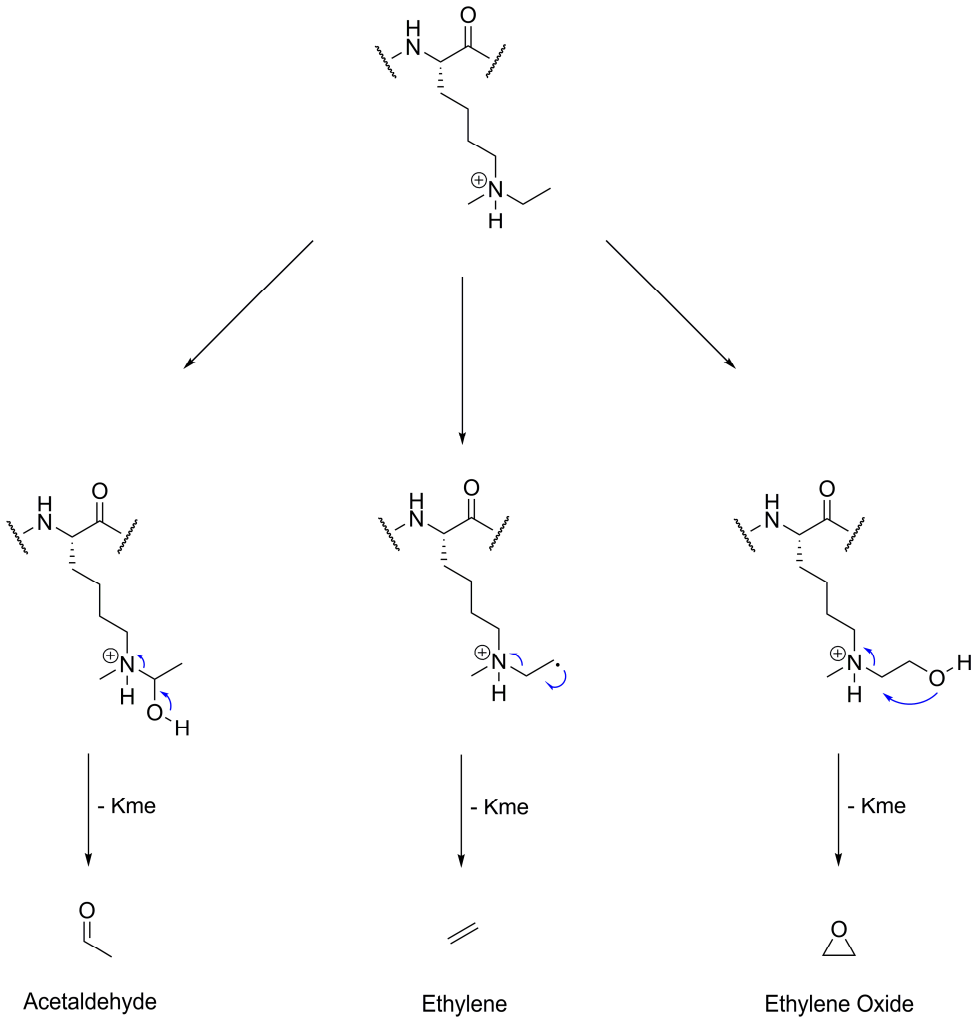

Scheme 3.3 Possible reaction pathways for the deethylation of methylethyllsine. Potential small molecule products are shown.

Firstly, the production of HCHO in the sample was investigated by adding dimedone (1 mM final concentration) to the NMR mixture. Analysis of the spectra revealed formation of a signal at δ_H 0.89 ppm, which appeared to increase in intensity over time. This signal was assigned to the hydroxymethyldimedone adduct by analogy to the spectra in Section 2.2.3a, implying that HCHO is produced (Figure 3.7).

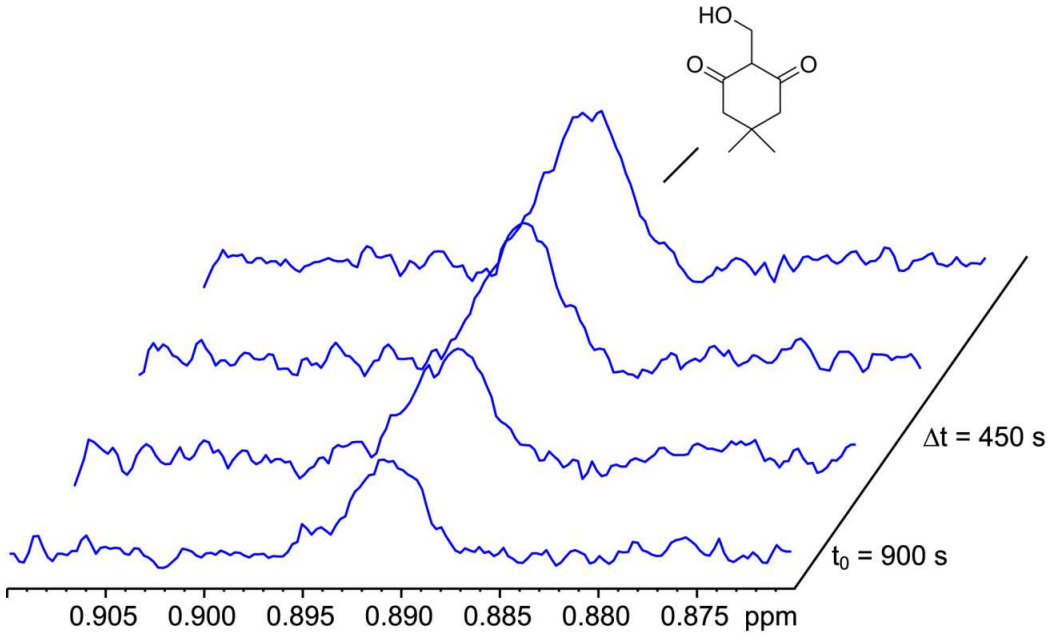

Figure 3.7 ^{1}H NMR spectra (700 MHz) of the reaction of ARTKme3QTARKmeetSTGGKA with JMJD2E with added dimedone in dAFN buffer. The signal at δ_H 0.89 ppm increased in intensity over time.

The formation of AcH as a product of deethylation was demonstrated by ^{1}H NMR analysis. In addition to the new signals described above, the NMR spectra revealed two new doublet resonances at δ_H 1.28 ppm and δ_H 2.19 ppm respectively. The intensities of the two signals increased in a near linear fashion over the 30 minute analysis period, which suggested that their production was coupled to dealkylation. Although accurate quantification of the sample concentrations was hampered by the low levels of products, it appeared that the production of the new signals correlated to the observed formation of the monomethyllysine peptide. This observation suggested that the new peaks corresponded to protons attached to the small molecule product of deethylation. Addition of authentic AcH to the reaction mixture allowed the assignment of the two signals to the methyl protons of AcH, in the aldehyde and hydrate forms respectively (Figure 3.8).

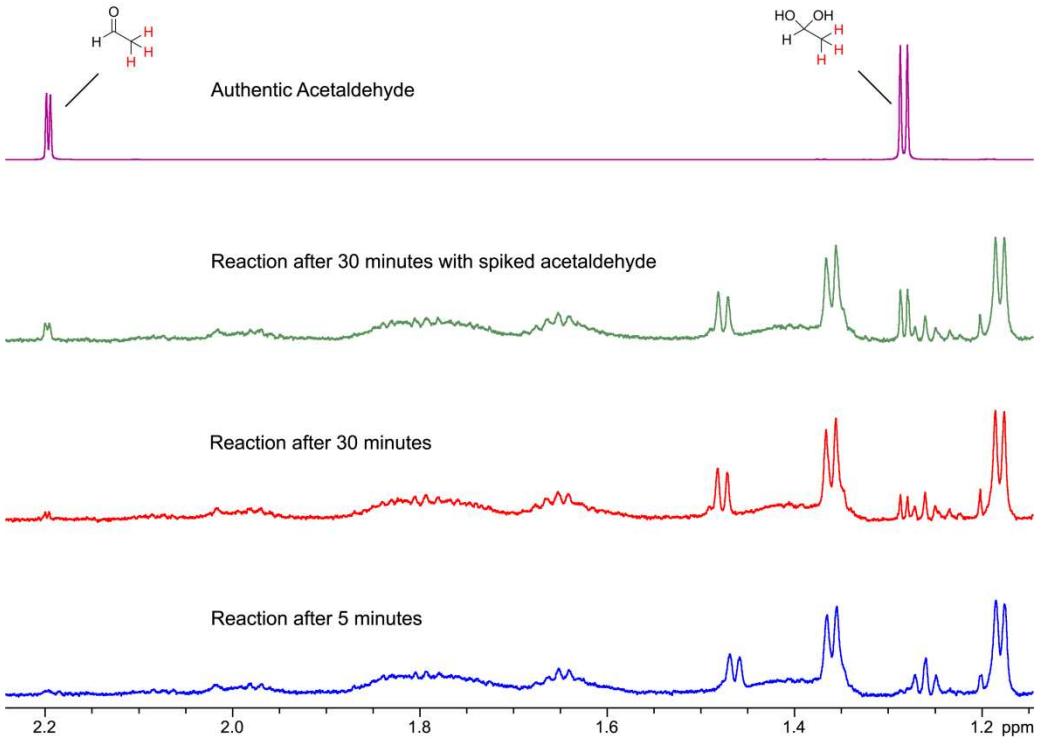

Figure 3.8 ^{1}H NMR spectra (700 MHz) showing production of AcH during deethylation of ARTKme3QTARKmeetSTGGKA by JMJD2E in dAFN buffer. The spectrum of authentic AcH is shown above.

Having identified JMJD2E-catalysed demethylation and deethylation of the methylethyllysine containing peptide at lysine-9, the same peptide was reacted with JMJD2A and analysed by MALDI mass spectrometry to order to determine whether similar reactivity could be detected. Interestingly, analysis of the reaction after one hour at 37 °C did not reveal any reaction of the substrate peptide. Although it is tempting to equate the lack of observable reaction in the sample with a variation in substrate specificity between the two JMJD2 enzymes, it was also noted that the batch of JMJD2A used in this study was significantly less active than the corresponding sample of JMJD2E. After one hour at 37 °C, JMJD2E was able to catalyse the complete demethylation of the peptide ARTKQTARKme3STGGKA by MALDI analysis. However, the batch of JMJD2A was only capable of demethylating the trimethylated peptide to predominantly the dimethyl form, indicating that the demethylation reaction was significantly slower with this enzyme. Analysis of all the reaction mixtures

containing JMJD2A and the lysine analogue peptides described in Table 3.1 did not reveal any reaction products identifiable by MALDI analysis. This implied that the relatively low activity of the JMJD2A sample was responsible for the lack of reaction, at least in some cases.

Therefore, the methylethyllysine peptide was reacted with the non-JMJD2 2OG demethylase PHF8 in order to identify any observable reaction. The MALDI spectrum after one hour at 37 °C is shown in Figure 3.9.

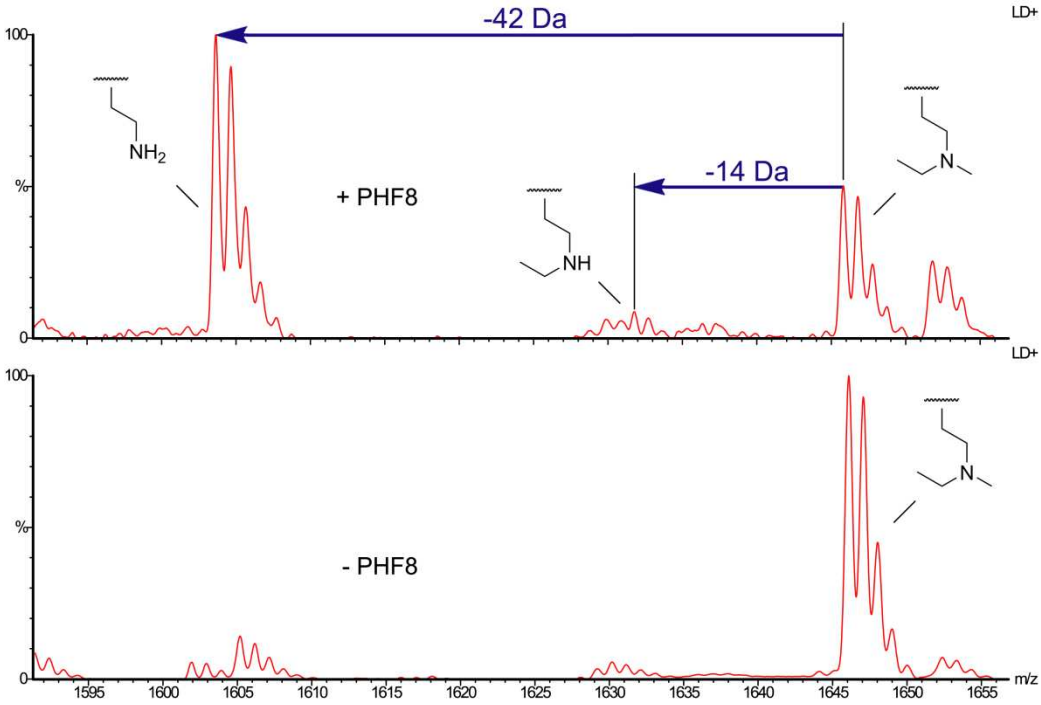

Figure 3.9 MALDI mass spectrum of a sample containing PHF8 (2 µM), ARTKme3QTARKmeetSTGGKA (10 µM), 2OG (50 µM), ascorbate (100 µM) and ferrous iron (10 µM) after one hour at 37 °C. The control experiment without enzyme is shown below.

Analysis of the MALDI spectra revealed the formation of a species with a mass of 1604 m/z, which was assigned to the unalkylated peptide at K9 by analogy with the data with JMJD2E. Interestingly, there was no evidence for the monomethyllysine peptide in the sample, although there did appear to be a small amount of the monethyllysine peptide present, as indicated by a peak at 1632 m/z. In order to investigate the time dependence of each peptides' concentration,

and also to determine whether any other peptides were formed during the incubation period, MALDI experiments were carried out monitoring over a 30 minutes reaction (Figure 3.10).

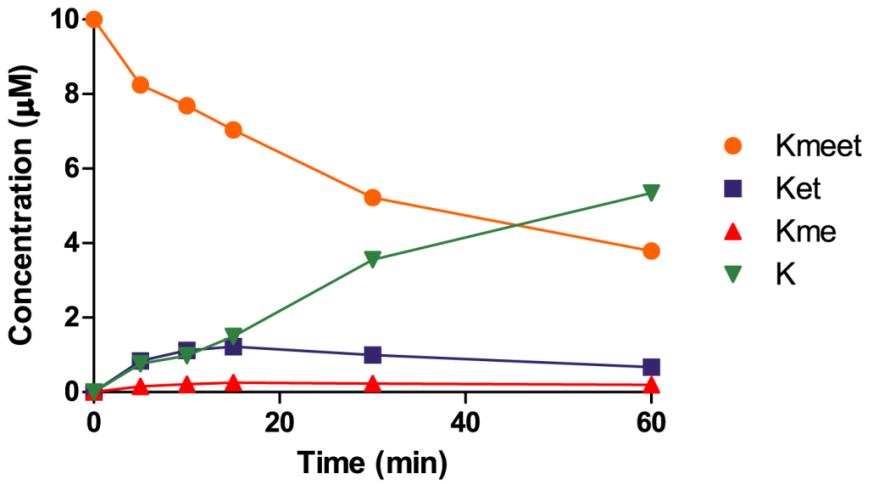

Figure 3.10 Concentrations of peptidic species derived from ARTKme3QTARKmeetSTGGKA, during the reaction with PHF8.

The monomethyllysine peptide was not observed at a significant concentration at any point during the 30 minute period, suggesting that this species was either not produced as an intermediate during dealkylation, or that its demethylation rate in the sample was very fast relative to its formation. Monomethyllysine is known to be a good substrate for PHF8; however, time course analysis on the reaction of dimethyllysine peptide (sequence ARTKme3QTARKme2STGGK) with PHF8 by MALDI has indicated that monomethyllysine can be observed at low levels.[164] Although these findings may therefore suggest that methylethyllysine cannot bind in an orientation facilitating deethylation, it was also noted that the lack of observable monomethyllysine in the methylethyllysine sample may be due to a slower rate of methylethyllysine deethylation relative to the rate of monomethyllysine demethylation. Time course experiments in the presence of a 14-mer dimethyllysine peptide (sequence ARTKme3QTARKme2STGGK) did not reveal significant concentrations of monomethyllysine peptide derived from methylethyllysine

peptide (Figure 3.11), although monomethyllysine peptide derived frm the 14-mer dimethyllysine peptide is observed. As the addition of the extra alanine on the *C*-terminal is not expected to significantly affect the rate of demethylation of monomethyllysine peptides, it was therefore concluded that deethylation of methylethyllysine is not catalysed by PHF8. However, analysis of the MALDI spectra did indicate that deethylation of the intermediate monoethyllysine (produced via demethylation of the methylethyllysine peptide) is catalysed by PHF8, resulting in formation of 15-mer unalkylated lysine peptide.

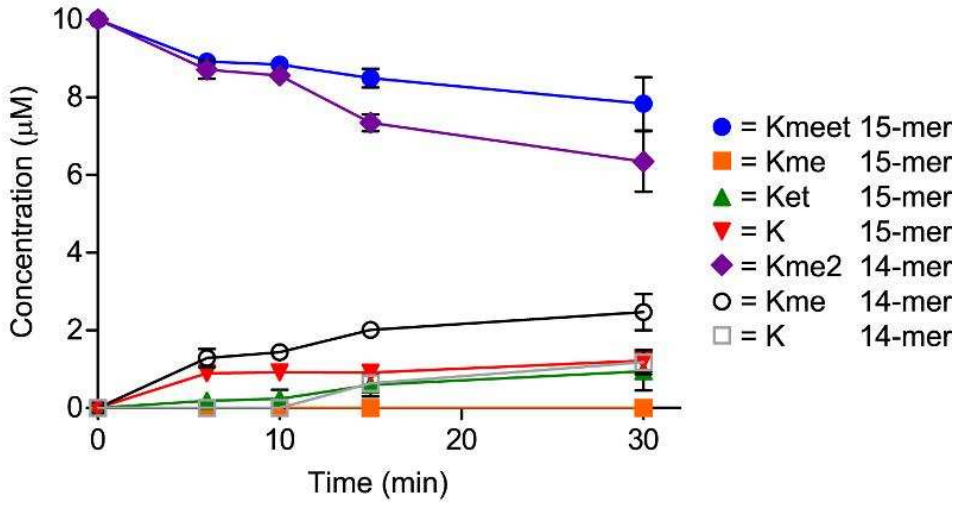

Figure 3.11 Concentrations of peptidic species derived from ARTKme3QTARKmeetSTGGKA and ARTKme3QTARKme2STGGK, during the reaction with PHF8.

The methylethyllysine peptide PATGGVKmeetKPHRY was then tested for reaction with FBXL11. The peptide was incubated with FBXL11 (1 μM), 2OG (50 μM), ascorbate (1 mM) and ferrous iron (10 μM), and the reaction was monitored after one hour at 37 °C using MALDI mass spectrometry. Analysis of the sample revealed formation of both the monoethyllysine and unalkylated lysine products, suggesting that both demethylation and deethylation had occurred in the sample (Figure 3.12). Reaction on the substrate peptide, however, appeared to be significantly less proficient with respect to demethylation of the corresponding dimethyllysine peptide.

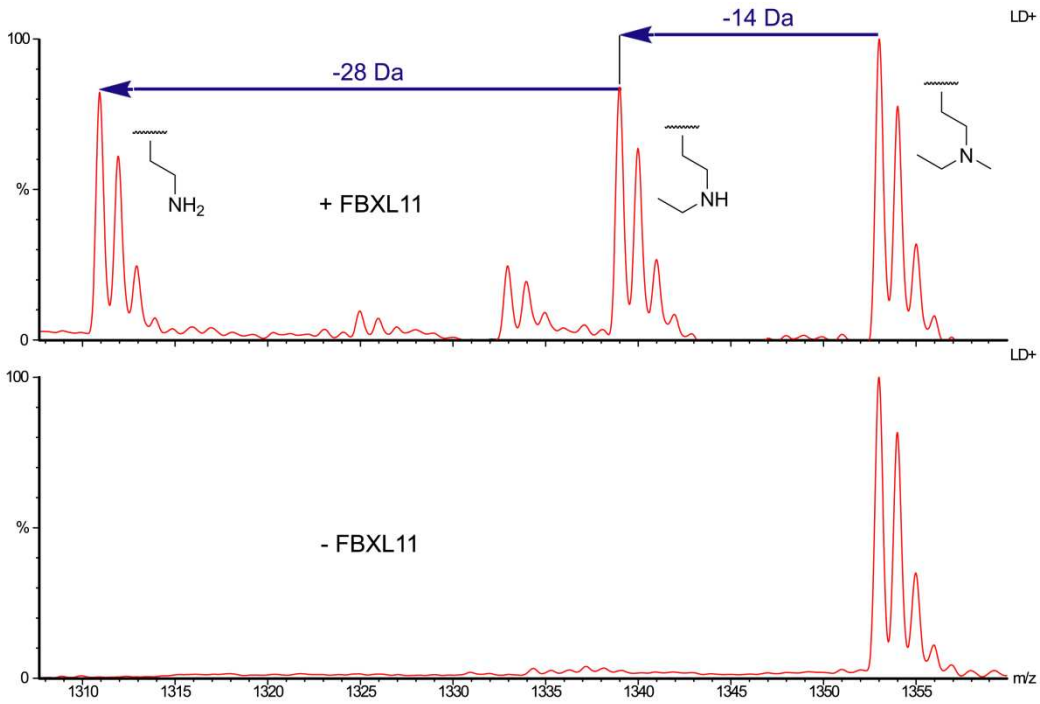

Figure 3.12 MALDI mass spectrum of a sample containing FBXL11 (1 µM), PATGGVKmeetKPHRY (10 µM), 2OG (50 µM), ascorbate (100 µM) and ferrous iron (10 µM) after one hour at 37 °C. The control experiment without enzyme is shown below.

Analysis of the FBXL11 reaction over a 30 minute period revealed only very small concentrations of monomethyllysine peptide (Figure 3.13). Over the reaction period, it appeared that the predominant reaction on the substrate peptide was demethylation, forming the monoethyllysine peptide. These results suggest that, unlike in the reactions with JMJD2E, deethylation of methylethyllysine is not the fastest reaction (if in fact the reaction occurs at all), indicating a potential difference in the preferred methylethyllysine binding modes within the two enzymes.

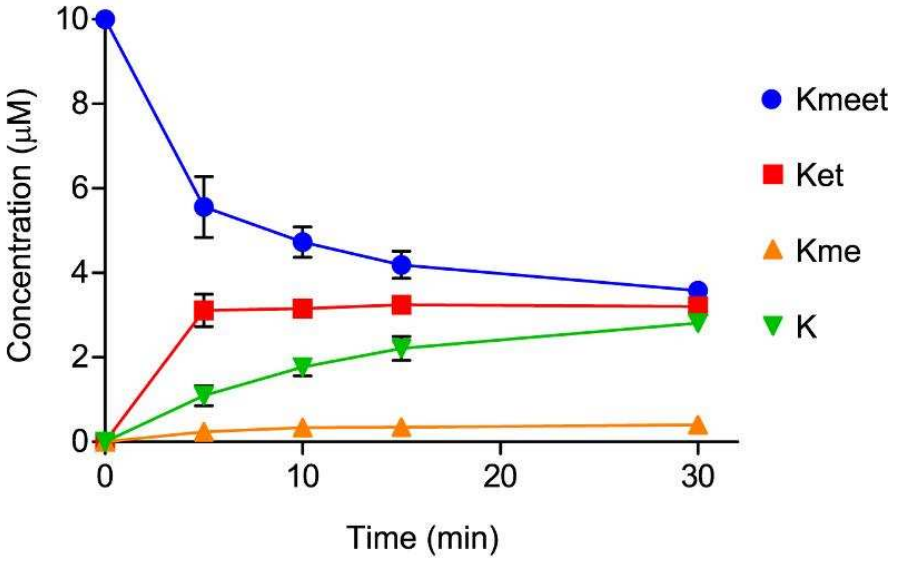

Figure 3.13 Concentrations of peptidic species derived from PATGGVKmeetKPHRY, during the reaction with FBXL11.

Despite the relatively poor reactivity observed in the MALDI sample for FBXL11 compared to the experiments with JMJD2E and PHF8, analysis of the reaction using ^{1}H NMR was attempted in the hope of confirming the demethylation reaction and also to test for production of HCHO. The ^{1}H NMR spectrum of the reaction (prepared in an analogous fashion to that described with JMJD2E) did indicate demethylation of the substrate peptide by revealing losses in intensity of both the triplet resonance at δ_H 1.24 ppm and the singlet resonance at δ_H 2.77 ppm (corresponding to the N^{ϵ}-methyl protons and the terminal N^{ϵ}-ethyl protons of methylethyllysine respectively, Figure 3.14). It was also possible to detect the emergence of a new triplet resonance at δ_H 1.22 ppm, which was assigned to the terminal N^{ϵ}-ethyl protons of the monoethylated product. However, the low turnover observed in the sample inhibited observation of the produced HCHO using added dimedone.

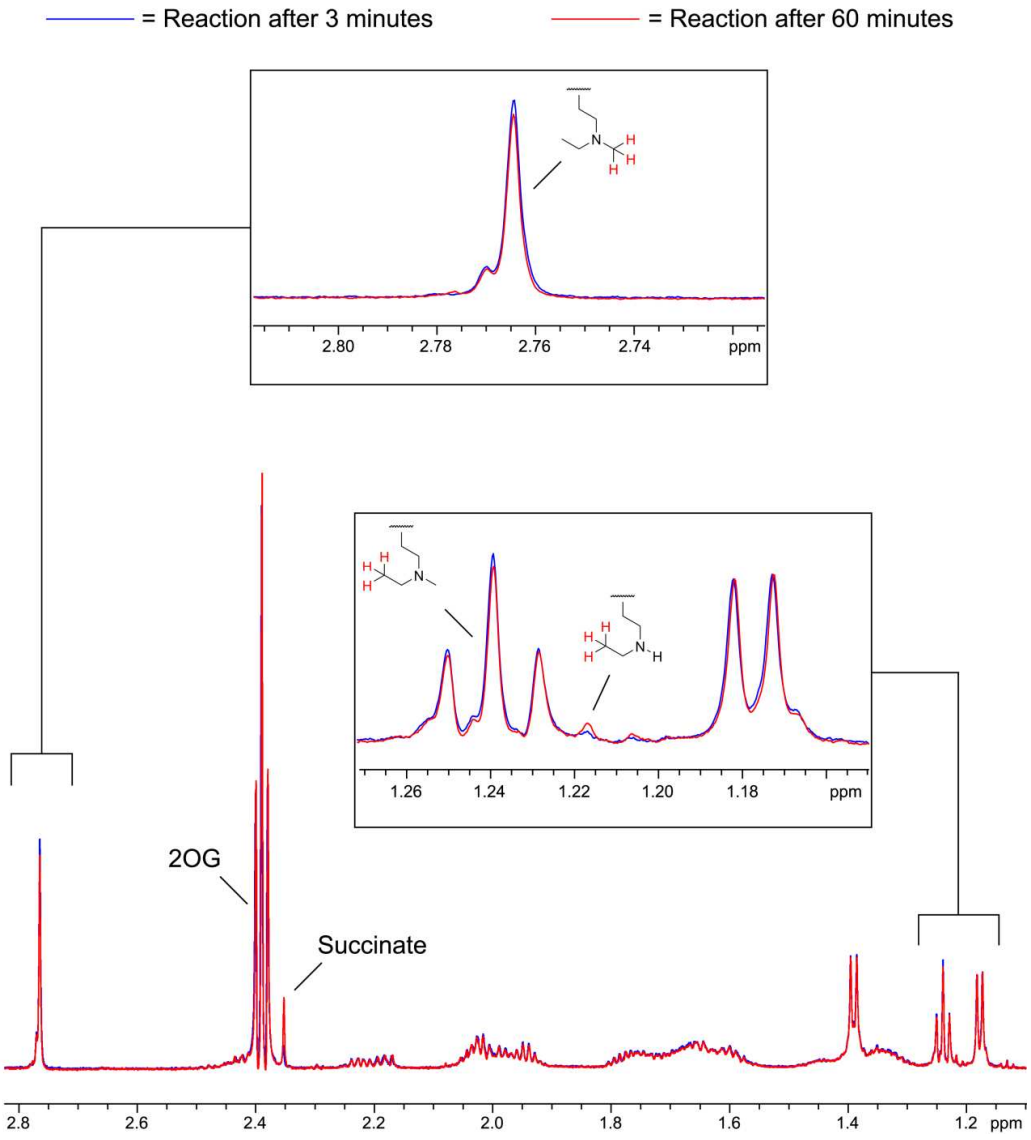

Figure 3.14 ^{1}H NMR spectra (700 MHz) of the reaction of PATGGVKmeetKPHRY with FBXL11 after three minutes (Blue) and 60 minutes (Red) respectively in dAFN buffer.

Overall, the experiments with methylethyllysine containing peptides revealed that the demethylases JMJD2E, PHF8 and FBXL11 are able to catalyse dealkylation of the modified lysine. It was also apparent that, in addition to demethylation, these enzymes can catalyse deethylation, either from the methylethyllysine peptide (by JMJD2E and possibly PHF8 and FBXL11) or from the monoethyllysine intermediate. The side product produced during deethylation by JMJD2E was identified as AcH using ^{1}H NMR, suggesting that the mechanism of deethylation resembles that of demethylation.

b) N^{ε}-Diethyllysine

Having identified deethylation as a reaction catalysed by the demethylases, experiments were carried out on the diethyllysine peptides. Interestingly, no reactions on the two diethyllysine containing peptides were observed in the MALDI mass spectra, suggesting that this substrate could not bind productively in the enzyme active sites to allow oxidation. Given that reaction on the N^{ε}-ethyl group was detected in the methylethyllysine samples for the tested demethylases (except JMJD2A), it would appear that the extra steric bulk of the diethyl moiety results in a loss of reactivity. Although these findings appear to corroborate the lack of clearly observed deethylation of methylethyllysine by FBXL11 (and also the possible lack of deethylation by PHF8), it is somewhat surprising that the diethyllysine peptide is not a substrate of JMJD2E. Both deethylation and demethylation of methylethyllysine peptide are catalysed by JMJD2E, indicating that the ethyl group can be accommodated both close to the iron (for deethylation) and away from the iron (for demethylation) in the active site. However, it would appear that the ε-amine of the modified lysine must be orientated in different positions when adopting these two conformations in order to explain the apparent lack of reactivity with the diethyllysine peptide.

c) N^{ε}-Isopropyllysine

The experiments with methylethyllysine peptides indicate that deethylation is possible on the intermediate monoethyllysine peptide. Therefore, it was proposed that an analogous reaction may occur on the structurally related isopropyllysine residue. Firstly, a sample containing the isopropyllysine peptide ARTKme3QTARKiprSTGGKA (10 μM), JMJD2E (2 μM), 2OG (50 μM), ascorbate (100 μM) and ferrous iron (10 μM) was prepared, and the mixture was analysed after one hour at 37 °C using MALDI mass spectrometry. The mass spectrum is shown in Figure 3.15.

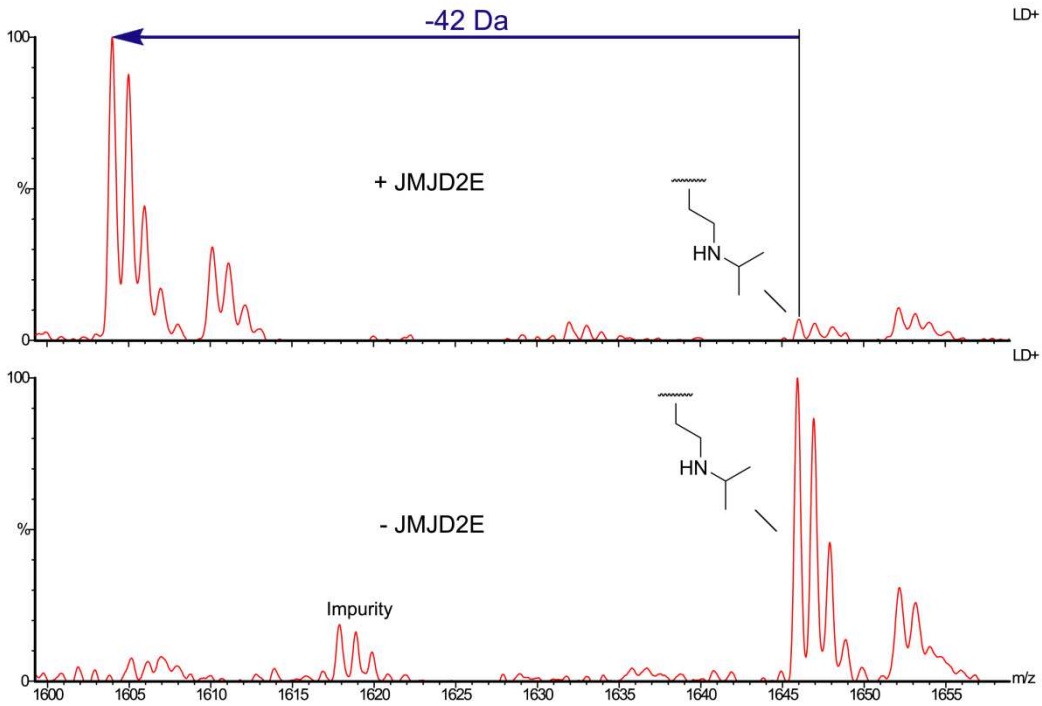

Figure 3.15 MALDI mass spectrum of a sample containing JMJD2E (2 µM), ARTKme3QTARKiprSTGGKA (10 µM), 2OG (50 µM), ascorbate (100 µM) and ferrous iron (10 µM) after one hour at 37 °C. A control experiment without enzyme is shown below.

Analysis of the spectrum revealed the formation of a species with a mass of 1604 m/z, which is 42 Da lower than the substrate mass. This species was assigned to the unalkylated lysine peptide at K9 by analogy with the data with the methylethyllysine peptide, and therefore, it was proposed that 'deisopropylation' had occurred in the sample. This hypothesis was corroborated by MALDI time-course experiments (Figure 3.16), in which formation of the species at 1604 m/z coincided with the dissipation of the peak at 1646 m/z. However, a species with a mass 16 Da higher than the substrate was also present in the sample at low levels, suggesting that JMJD2E catalyses partial hydroxylation of the isopropyllysine peptide.

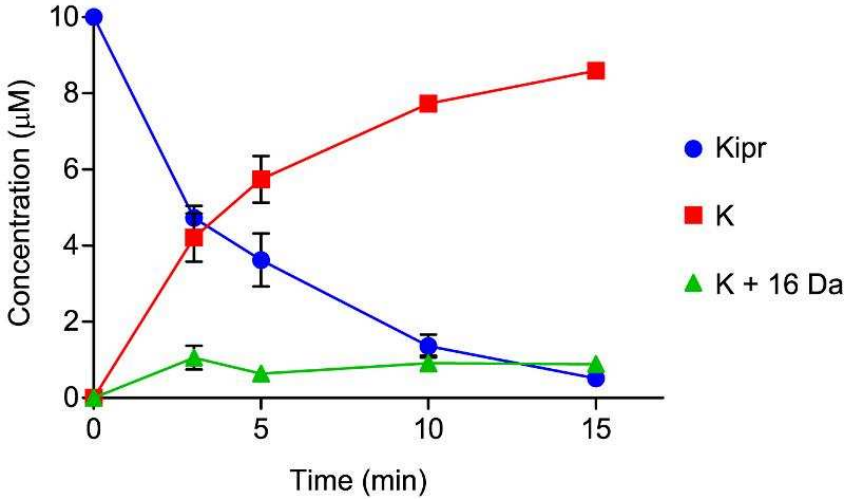

Figure 3.16 Concentrations of ARTKme3QTARKiprSTGGKA and ARTKme3QTARKSTGGKA, during the reaction with JMJD2E.

Analysis of a sample containing a 1:1 mixture of isopropyllysine and monomethyllysine peptide (sequences ARTKme3QTARKiprSTGGKA and ARTKme3QTARKmeSTGGK respectively) using MALDI indicated that deisopropylation was significantly more efficient with respect to demethylation (Figure 3.17). This observation implies that replacing the methyl group on the ε-amine for a bulkier isopropyl group results in more efficient reaction, presumably due to improved binding of the substrate.

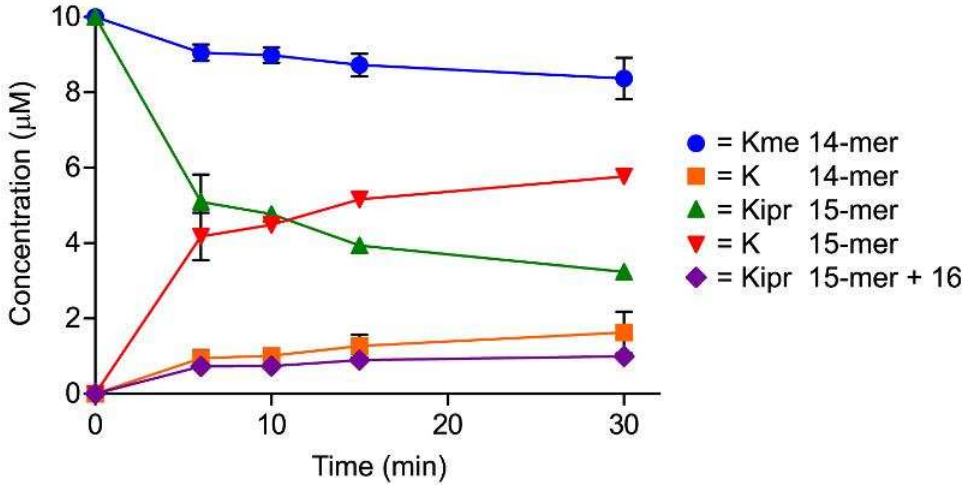

Figure 3.17 Concentrations of peptidic species derived from ARTKme3QTARKiprSTGGKA and ARTKme3QTARKmeSTGGK, during the reaction with JMJD2E.

Having identified deisopropylation, ^{1}H NMR experiments were used to identify any small molecule(s) formed during the reaction. The substrate peptide was incubated with JMJD2E under the conditions optimised for NMR (see above) and the sample was monitored by ^{1}H NMR in order to identify peaks corresponding to the small molecule product(s) (Figure 3.18).

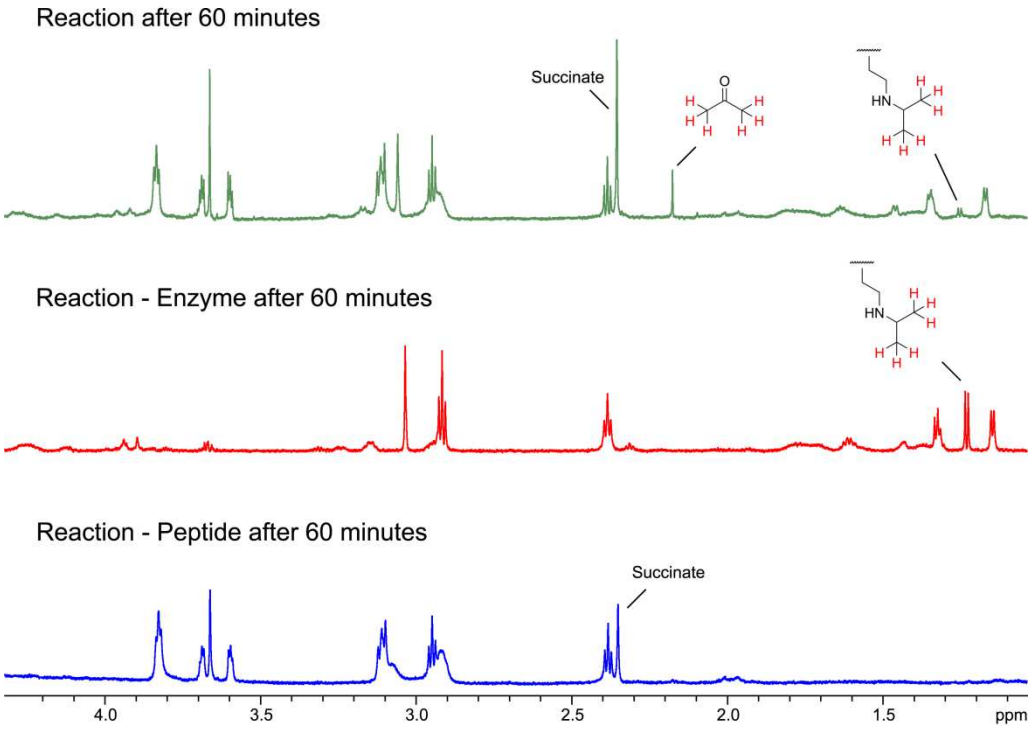

Figure 3.18 ^{1}H NMR spectra (700 MHz) of the reaction of ARTKme3QTARKiprSTGGKA with JMJD2E after 60 minutes (Top) in dAFN buffer. The control experiments without enzyme and without peptide are shown below.

Deisopropylation of isopropyllysine peptide was indicated by the loss of intensity of the doublet ^{1}H-resonance at δ_H 1.24 ppm, which corresponds to the terminal isopropyl protons of the substrate peptide. It was also possible to detect a new singlet resonance in the NMR spectrum (at δ_H 2.17 ppm), which was not present in the control experiments without enzyme and without peptide. This peak was assigned to the protons of acetone by chemical shift analysis, suggesting that acetone is a product of deisopropylation. This assignment was corroborated by the addition of authentic acetone to the reaction mixture, which increased the intensity of the signal in the NMR spectrum (Figure 3.19).

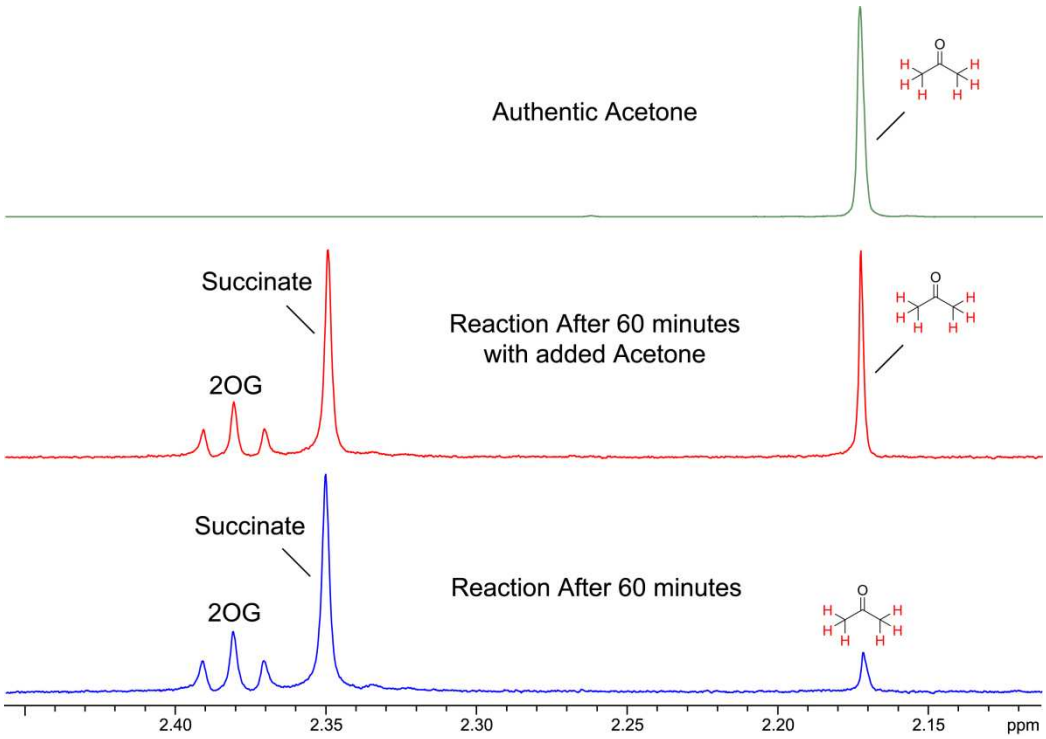

Figure 3.19 ^{1}H NMR spectra (700 MHz) identifying acetone as a product of deisopropylation. Below = reaction after 60 minutes in dAFN buffer, Middle = reaction after 60 minutes in dAFN buffer with added acetone, Top = authentic acetone in dAFN buffer.

Although the NMR experiments indicated the formation of acetone during JMJD2E-catalysed deisopropylation, it was noted that the concentration of acetone in the sample appeared to be smaller than the observed decrease in concentration of the substrate peptide. This observation implied that either some of the acetone formed during the reaction was sequestered by other species in the reaction mixture, or that deisopropylation had occurred in the sample without the concomitant formation of acetone. As mentioned above, it is possible that oxidation on the isopropyl group at positions other than at the carbon adjacent to the ε-amine may result in species other than acetone being released during dealkylation. However, analysis of the ^{1}H NMR spectra did not indicate significant concentrations of other products (although this may be due in part to signal overlap).

The observation of reaction on the isopropyllysine containing peptide when incubated with JMJD2E, and also the observation that monoethyllysine can be

deethylated by PHF8, suggested that isopropyllysine may be a substrate for PHF8. Therefore, the peptide was incubated with PHF8, 2OG, ascorbate and iron (as described above) and the reaction was monitored using MALDI mass spectrometry after one hour at 37 °C (Figure 3.20).

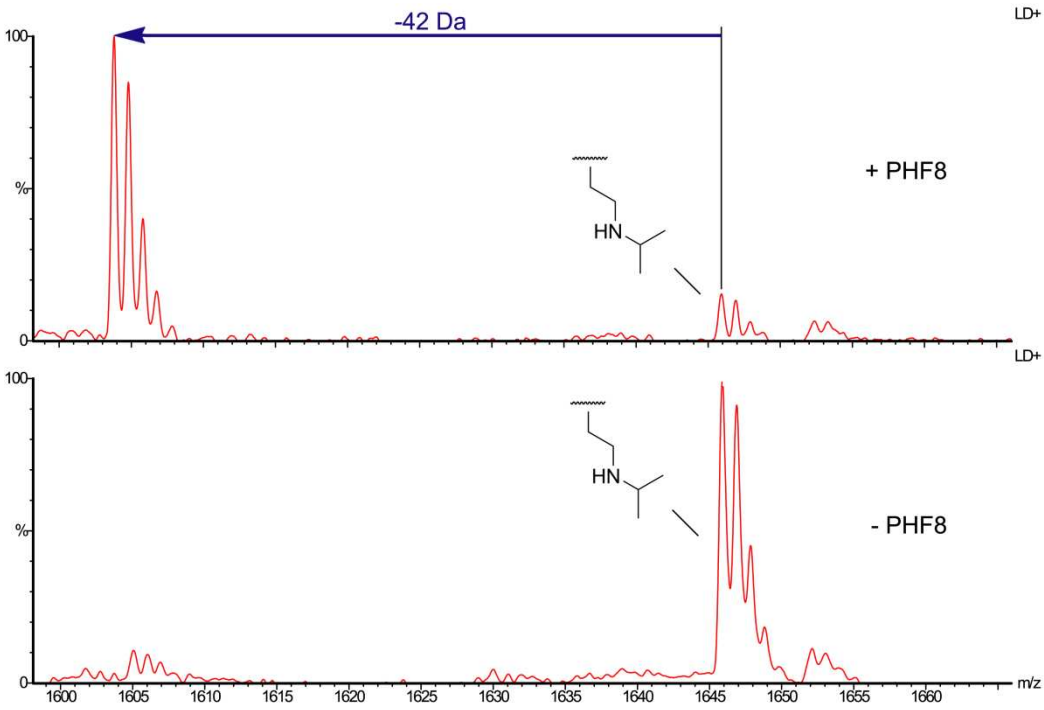

Figure 3.20 MALDI mass spectrum of a sample containing PHF8 (2 µM), ARTKme3QTARKiprSTGGKA (10 µM), 2OG (50 µM), ascorbate (100 µM) and ferrous iron (10 µM) after one hour at 37 °C. The control experiment without enzyme is shown below.

The MALDI mass spectrum of the reaction after one hour revealed formation of the non-alkylated peptide, implying that deisopropylation of the substrate is catalysed by PHF8, presumably via an analogous mechanism to that of JMJD2E. No other peptidic products were detected in the sample by MALDI analysis, indicating that the deisopropylation reaction was predominant. Monitoring the reaction over the first 30 minutes of reaction did not allow identification of any intermediate species during the deisopropylation reaction (Figure 3.21).

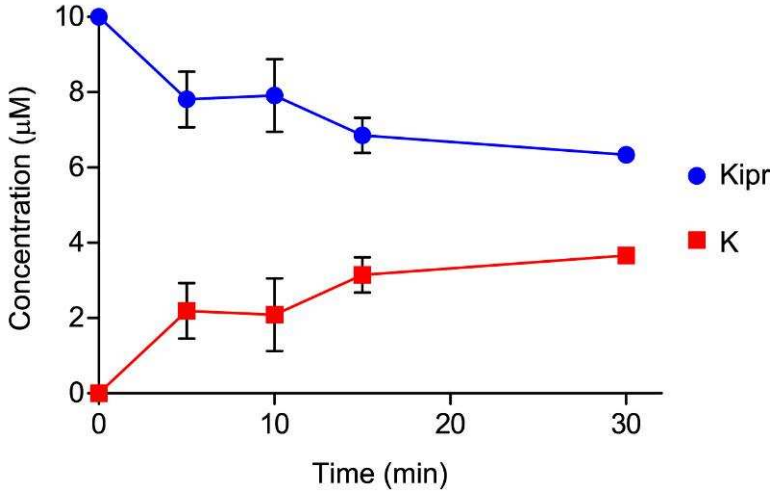

Figure 3.21 Concentrations of peptidic species derived from ARTKme3QTARKiprSTGGKA, during the reaction with PHF8.

In contrast to the reactions of the isopropyllysine peptide with JMJD2E, competition with the monomethyllysine peptide (sequence ARTKme3QTARKmeSTGGK) revealed that demethylation of the corresponding methylated lysine (at position 9) is preferred to deisopropylation (in fact no deisopropylation of the peptide was detected in the experiment, Figure 3.23). This observation implies that binding of the isopropyl group close to the catalytic iron is disfavoured relative to binding of a methyl group in the same orientation.

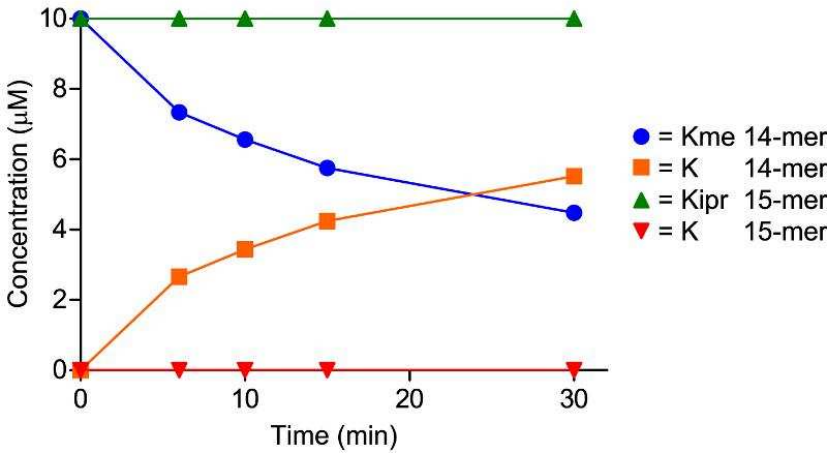

Figure 3.22 Concentrations of peptidic species derived from ARTKme3QTARKiprSTGGKA and ARTKme3QTARKmeSTGGK, during the reaction with PHF8.

Finally, the reaction of isopropyllysine peptide with FBXL11 was investigated. The mutated K36 peptide (sequence PATGGVKiprKPHRY) was incubated with FBXL11, 2OG, ascorbate and ferrous iron and the reaction was monitored after one hour at 37 °C. No reaction was observed in the sample by MALDI analysis.

Overall, the experiments with isopropyllysine peptides reveal that JMJD2E and PHF8 are capable of removing the isopropyl group, producing the deisopropylated peptide product. Acetone was also identified as a side product using ^{1}H NMR, at least in the case of JMJD2E catalysis, although it is possible that deisopropylation may occur without concomitant release of acetone. Finally, no reaction was observed with FBXL11, implying that the isopropyllysine residue is not accepted as a substrate for this enzyme, at least with the tested batches.

d) N^{ε}-Methylisopropyllysine

The observed deisopropylation of isopropyllysine peptide by JMJD2E and PHF8 suggested that an isopropyl group can be accommodated in their active sites. However, it was proposed that upon binding of the isopropyllysine peptide, the preferred position of the ε-amine may be different to that adopted during methyllysine demethylation. This shift in binding geometry may be necessary to allow binding of the bulky isopropyl group, and could result in a loss of available space for other alkyl groups attached to the amine to bind. Therefore, it was hoped that the reactions of methylisopropyllysine peptides with the demethylases may indicate whether binding of both the methyl group and the isopropyl group can be facilitated to allow reaction on the isopropyl group, and therefore, may give insight into the preferred binding modes of each species. Firstly, MALDI analysis was conducted after one hour on a sample containing the K9meipr peptide (sequence ARTKme3QTARKmeiprSTGGKA),

JMJD2E, 2OG, ascorbate and ferrous iron. The resultant MALDI spectrum is shown in Figure 3.23.

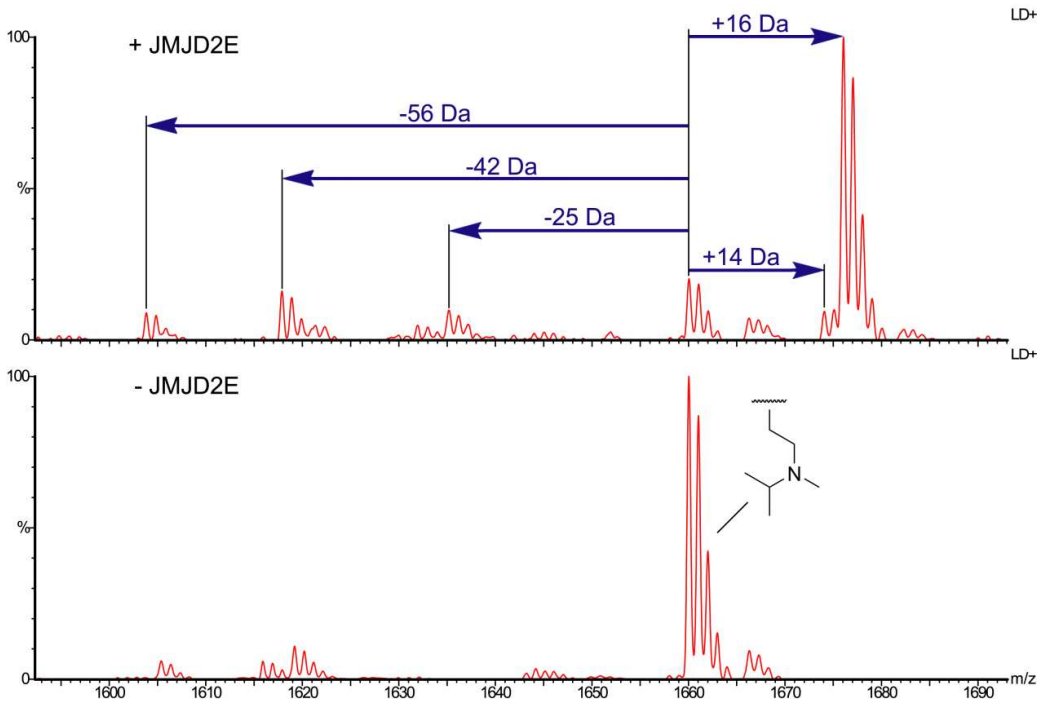

Figure 3.23 MALDI mass spectrum of a sample containing JMJD2E (2 µM), ARTKme3QTARKmeiprSTGGKA (10 µM), 2OG (50 µM), ascorbate (100 µM) and ferrous iron (10 µM) after one hour at 37 °C. The control experiment without enzyme is shown below.

Analysis of the mass spectrum indicated that a number of peptidic species had been formed during the reaction period. Unexpectedly, one peak, at mass 1676 m/z, appeared to be predominant over all others in the sample. This peak was assigned to the hydroxylated substrate peptide, implying that oxidation of the substrate peptide had not resulted in dealkylation during the reaction. This is an important result because it provides strong evidence that 2OG demethylase catalysis proceeds via hydroxylation.

Hydroxylation of the substrate peptide was also supported by MALDI experiments using ^{18}O-labelled molecular oxygen. It was proposed (by analogy with the hydroxylation mechanisms of 2OG dependent prolyl and asparaginyl hydroxylases) that JMJD2E-catalysed hydroxylation would result in the

incorporation of one oxygen atom from molecular oxygen into the peptide C-H bond. Therefore, performing the reaction under an $^{18}O_2$ atmosphere was expected to result in a shift in the product peak from 1676 m/z to 1678 m/z, allowing observation using MALDI mass spectrometry. The MALDI experiment was prepared in deoxygenated buffer and sealed under vacuum. $^{18}O_2$ was then injected into the sample and the reaction was left concealed for one hour at 37 °C. Analysis by MALDI mass spectrometry revealed a peak at 1678 m/z (molecular ion) indicating a +18 Da mass shift (Figure 3.24).

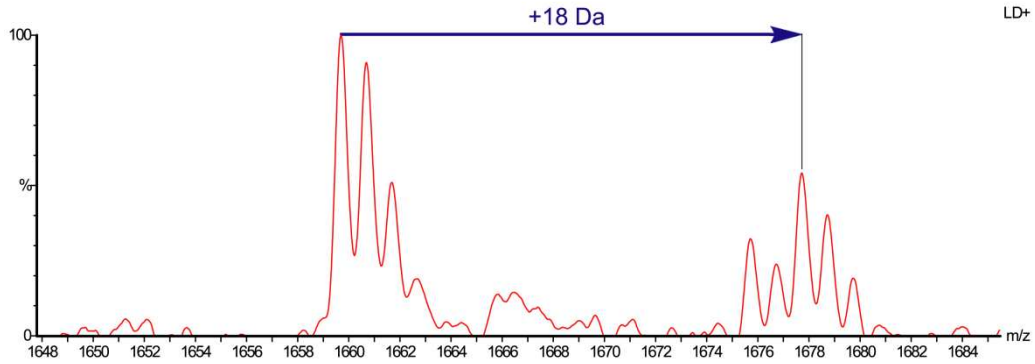

Figure 3.24 MALDI mass spectrum of a sample containing JMJD2E (2 µM), ARTKme3QTARKmeiprSTGGKA (10 µM), 2OG (50 µM), ascorbate (100 µM) and ferrous iron (10 µM) under an atmosphere of $^{18}O_2$, after one hour at 37 °C.

The other new species in the MALDI mass spectrum were observed at significantly lower concentrations than the hydroxylated product. It was proposed that these were unlikely to be intermediates in the formation of the hydroxylated product due to their low intensities and masses. The two peaks at 1604 m/z and 1618 m/z likely correspond to the unalkylated and monomethylated lysine-9 peptides respectively. These assignments suggest that the substrate peptide may undergo both demethylation and deisopropylation reactions as well as hydroxylation. It was also noted that these dealkylation processes may occur on the hydroxylated product (demethylation of monomethyllysine product of deisopropylation was observed during reactions with methylethyllysine). The mass of the fourth product in the sample (1674

m/z) appeared to be 14 Da higher than that of the starting material. Although this mass shift could indicate methylation of the substrate peptide, it is difficult to envisage an oxidative reaction catalysed by JMJD2E which could facilitate such a modification. Therefore, it was hypothesised that the mass increase may be due to double hydroxylation at the same position on the peptide, which could subsequently form a carbonyl group with concomitant loss of water. Analysis of the sample reacted under an $^{18}O_2$ atmosphere did reveal the presence of a species at 1676 m/z, which may correlate to the ^{18}O-labelled carbonyl product. However, it is probable that any incorporation of ^{18}O as a carbonyl would be removed via exchange with the unlabelled water solvent, and therefore it is more likely that this peak represents unlabelled hydroxylated product (which could be formed from trace $^{16}O_2$ in the sample).

The species with a mass of 1635 m/z appears to indicate that the substrate had suffered a mass loss of 25 Da during oxidation by JMJD2E. This mass shift does not appear to correspond to loss of any alkyl, amino or hydroxyl group, and therefore, it was proposed that this species is formed via hydroxylation of the impurity at mass 1619 m/z (Figure 3.24).

In order to identify any previously unobserved products, and also to detect variation in product concentrations, the MALDI experiment was repeated and monitored over the first 30 minutes of reaction. At all time points, the major species in the mixture was the hydroxylated product, indicating that the hydroxylation reaction was predominant in the reaction (Figure 3.25). The monomethylated and unalkylated peptides, as well as the product with a +14 Da mass shift, were only present in trace amounts throughout the analysis period.

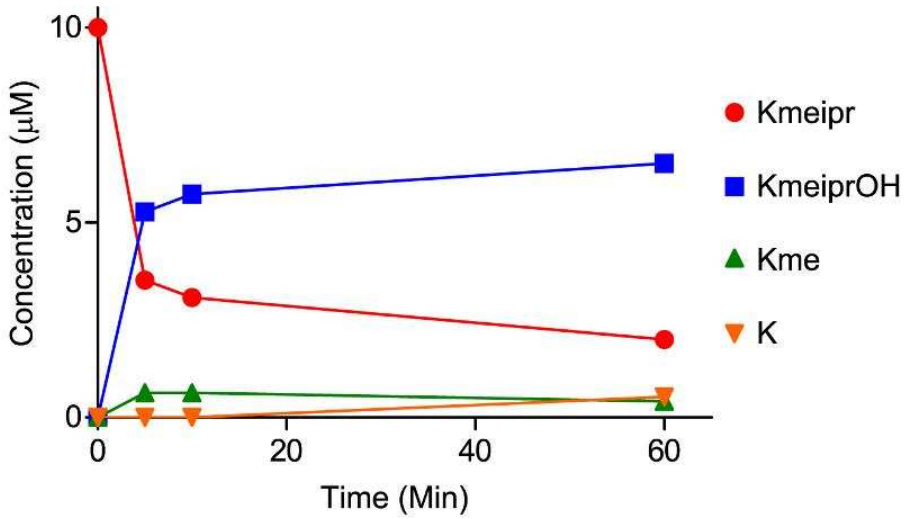

Figure 3.25 Concentrations of peptidic species derived from ARTKme3QTARKmeiprSTGGKA, during the reaction with JMJD2E.

Although hydroxylation of the methylisopropyllysine peptide appeared to be relatively proficient in the reaction mixture, competition experiments with dimethyllysine peptide (sequence ARTKme3QTARKme2STGGK) revealed that demethylation (of dimethyllysine) was favoured. After 3 minutes reaction, the dimethyllysine peptide had been fully demethylated. However, only roughly 10 % of the methylisopropyllysine peptide had been hydroxylated over the same period (Figure 3.26).

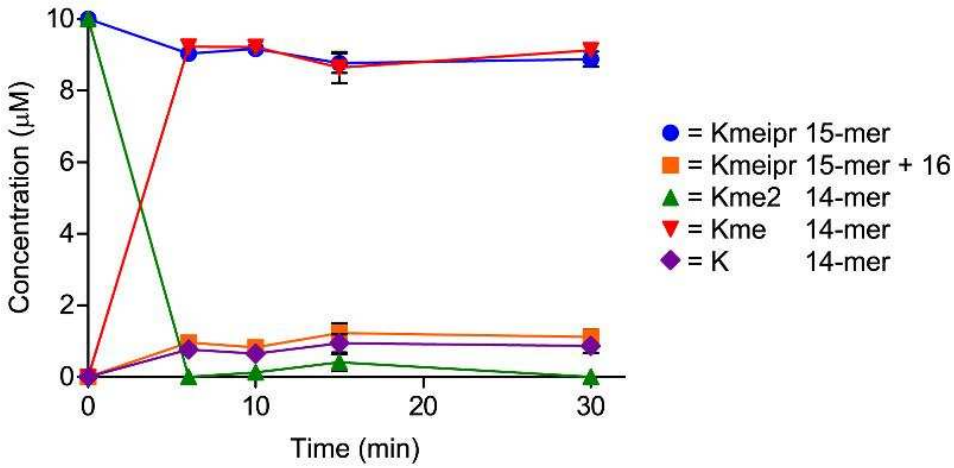

Figure 3.26 Concentrations of peptidic species derived from ARTKme3QTARKmeiprSTGGKA and ARTKme3QTARKme2STGGK, during the reaction with JMJD2E.

Having confirmed hydroxylation on the substrate peptide, attention was then focused toward identifying the position of hydroxylation on the methylisopropyllysine residue. These experiments were carried out using NMR spectroscopy, which, it was proposed, would allow the hydroxylated product to be characterised by revealing correlations between the protons attached the hydroxylated carbon with those attached to neighbouring carbons. A reaction sample was prepared containing the substrate peptide, JMJD2E, 2OG, ascorbate and iron (in dAFN buffer, as described above) and the reaction was monitored until reaction completion. The ^{1}H NMR spectra after 5 minutes and 3 hours reaction are shown in Figure 3.27.

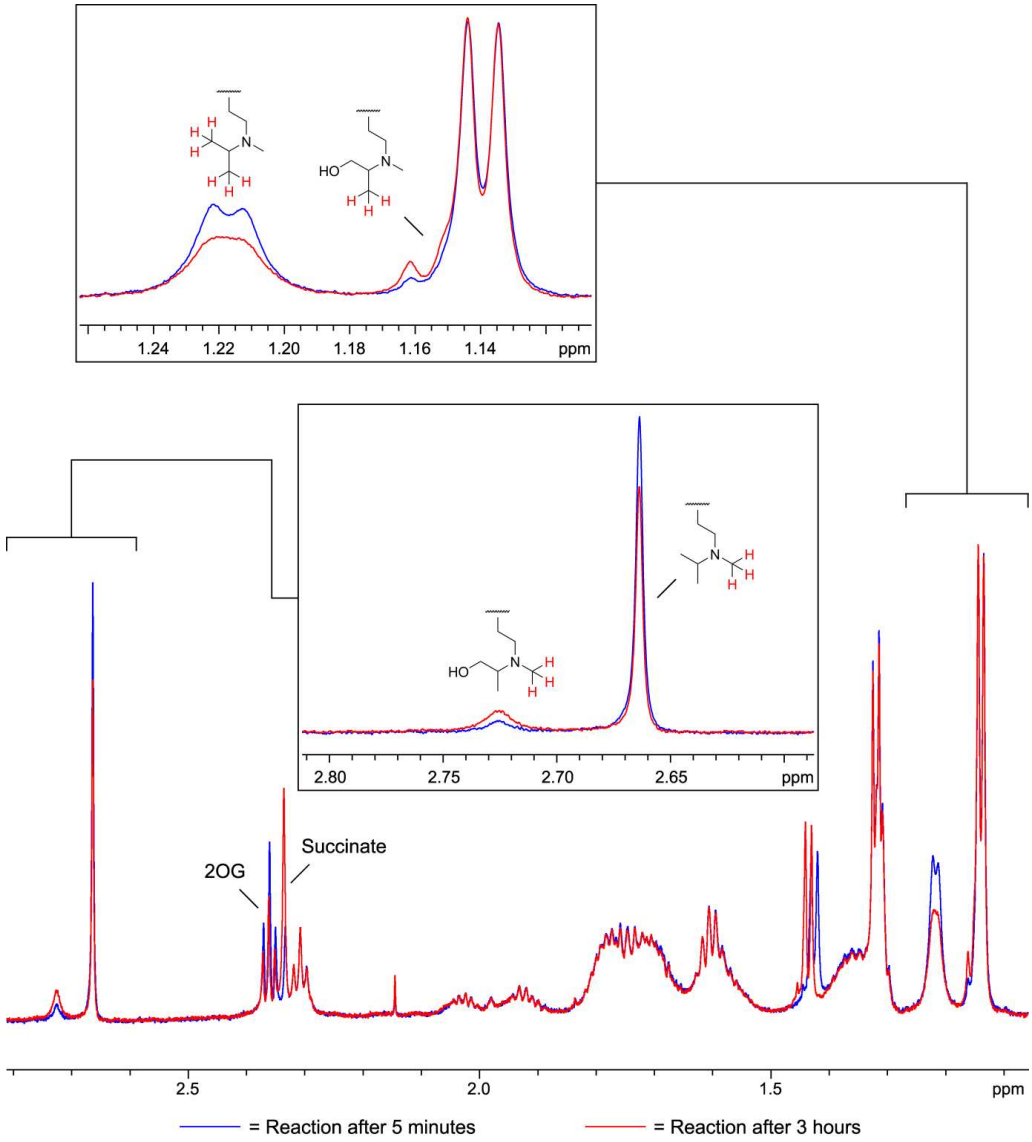

Figure 3.27 ^{1}H NMR spectra (700 MHz) of the reaction of ARTKme3QTARKmeiprSTGGKA with JMJD2E after five minutes (Blue) and three hours (Red) respectively in dAFN buffer.

Reaction on the substrate peptide was implied by the emergence of new peaks in the ^{1}H NMR spectra. These signals appeared to increase in intensity during the reaction period, which correlated with the observed decrease in intensity of the signals at δ_H 1.22 ppm and δ_H 2.66 ppm (which were assigned to the terminal isopropyl protons and the methyl protons on the methylisopropyllysine residue respectively). In particular, it was observed that the emergence of the new singlet resonance at δ_H 2.73 ppm appeared to correlate with the decrease in intensity of the singlet resonance at δ_H 2.66 ppm. This observation, coupled with

chemical shift and multiplicity analyses, implied that this new signal corresponded to the N^{ε}-methyl group on the hydroxylated methylisopropyllysine. In addition to this assigned resonance, it was possible to identify a new signal partially underneath the large doublet resonance at δ_H 1.14 ppm (at δ_H 1.15 ppm). This signal could not be conclusively integrated due to signal overlap; however, the fact that the corresponding chemical shift was observed to be close to that of the substrate terminal isopropyl protons, enabled the resonance to be tentatively assigned to the terminal alkyl methyl group protons on the hydroxylated product.

Having provisionally assigned the resonance at δ_H 1.15 ppm to the terminal methyl protons on the product isopropyl group, it was hoped that any hydroxylation on this group could be inferred from through-bond NMR correlations between the protons at this resonance and protons on neighbouring carbons. Firstly, a 2D COSY experiment was conducted on the reaction mixture in order to identify correlations between the signal at δ_H 1.15 ppm and adjacent protons. One correlation was observed, which was provisionally assigned to the 3-bond correlation between the terminal methyl protons of the isopropyl group and the proton attached to the tertiary isopropyl carbon (at δ_H 3.50 ppm, see Figure 3.28). The shift of this proton appeared to be coincident with that of the analogous proton on the substrate peptide, which was observed to correlate to the substrate resonance at δ_H 1.22 ppm. However, a TOCSY spectrum of the reaction mixture (which indicates correlations between protons separated by multiple carbons) revealed that the protons at δ_H 1.15 ppm possessed correlations to protons at δ_H 3.62 ppm and δ_H 3.74 ppm respectively. No TOCSY correlations were observed for the equivalent resonance of the substrate (at δ_H 1.22 ppm), and therefore, it was proposed that the structure of the isopropyl group had been altered during reaction with JMJD2E. Assuming no rearrangement of the isopropyl group, it was possible to deduce that hydroxylation had occurred on one of the terminal isopropyl methyl groups,

based on the observed TOCSY correlations (Figure 3.28). Unfortunately, analysis by 2D HSQC did not reveal the ^{13}C chemical shifts for the carbons attached to the protons at δ_H 1.15 ppm, δ_H 3.62 ppm and δ_H 3.74 ppm (presumably due to the small sample size), inhibiting conclusive assignment of the hydroxylated product. Nevertheless, the combind MS and NMR analyses, coupled to the observed stability of the product, all support the proposed assignment.

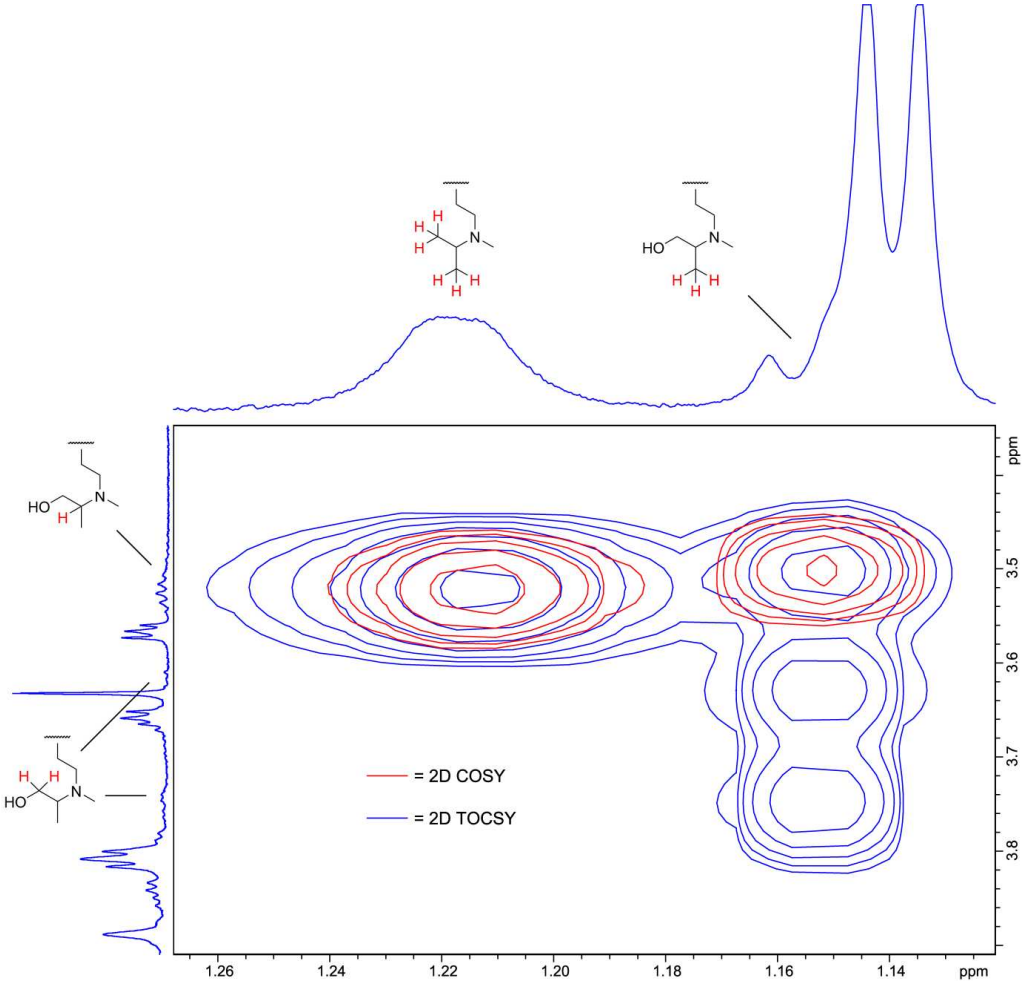

Figure 3.28 2D COSY (Red) and 2D TOCSY (Blue) NMR spectra (700 MHz) of the reaction of ARTKme3QTARKmeiprSTGGKA with JMJD2E.

Although the predominant reaction in the sample appeared to be hydroxylation, the emergence of a small singlet resonance at δ_H 2.14 ppm (which was assigned as acetone by analogy with the experiments containing isopropyllysine) implied that deisopropylation had also occurred. The amount of acetone released during

the reaction appeared to be very small, which corroborated the difference in reactivity observed by MALDI analysis. Although it was postulated that removal of the isopropyl-derived group may occur after hydroxylation, no evidence was accrued for the production of α-hydroxyacetone (however, the possibility of α-hydroxyacetone formation cannot be entirely eliminated).

Having identified JMJD2E-catalysed hydroxylation on methylisopropyllysine, experiments were then carried out in order to monitor reactions with PHF8. Interestingly, MALDI analysis revealed no reaction on the peptide after incubation with PHF8, implying that methylisopropyllysine is not a substrate for PHF8. This finding is intriguing beacause the isopropyllysine peptide was observed to be deisopropylated by PHF8. Therefore, it is apparent that the active conformation adopted by isopropyllysine in the active site is not adopted by methylisopropyllysine, presumably due to the increased steric bulk induced by the ε-amino methyl group. It would also appear that the preferred conformation adopted by the methylisopropyllysine residue in the active site of JMJD2E (which likely results in hydroxylation) cannot be adopted by this species in PHF8. This may indicate that either JMJD2E can allow bulky groups to bind closer to the catalytic iron than in PHF8, or that PHF8 cannot accept the larger lysine analogues in any conformation.

Finally, the K36 methylisopropyllysine peptide was incubated with FBXL11, 2OG, ascorbate and ferrous iron in order to detect any reaction. The MALDI mass spectrum of the sample after one hour at 37 °C is shown in Figure 3.29.

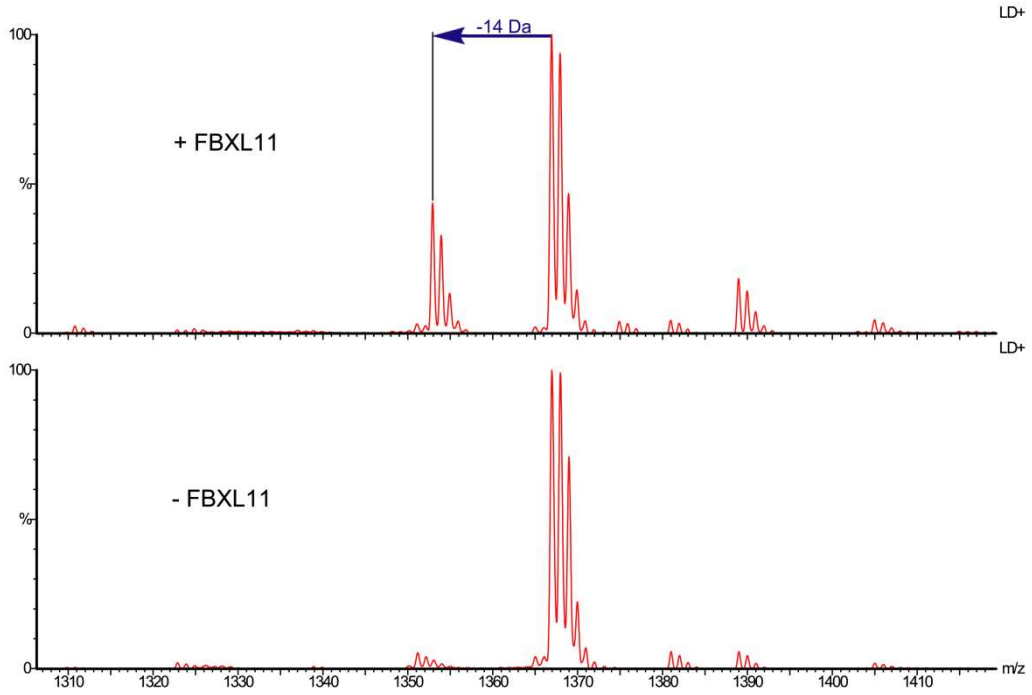

Figure 3.29 MALDI mass spectrum of a sample containing FBXL11 (1 µM), PATGGVKmeiprKPHRY (10 µM), 2OG (50 µM), ascorbate (100 µM) and ferrous iron (10 µM) after one hour at 37 °C. The control experiment without enzyme is shown below.

Analysis of the spectrum did not reveal any of the reactions observed with JMJD2E. However, a peak 14 Da lower than that of the substrate peptide indicated that demethylation, presumably on the N^{ε}-methyl group, had occurred. However, the rate of demethylation was found to be significantly slower than demethylation of the corresponding dimethyllysine peptide (sequence PATGGVKme2KPHRY, Figure 3.30). Although the demethylation reaction can be expected to follow the standard demethylation mechanism facilitated by the lysyl demethylases, the relatively low rate of reaction with FBXL11 inhibited the detection of HCHO by ^{1}H NMR analysis.

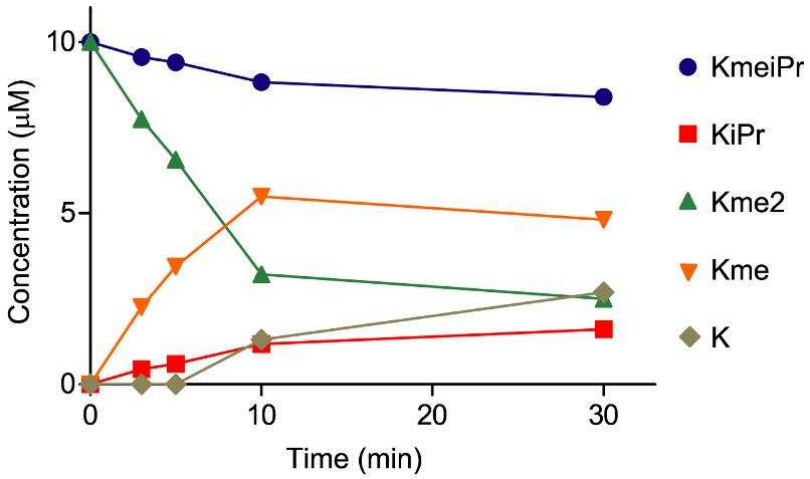

Figure 3.30 Concentrations of peptidic species derived from PATGGVKmeiprKPHRY and PATGGVKme2KPHRY, during the reaction with FBXL11.

Overall, the experiments with methylisopropyllysine have revealed that multiple reactions can be catalysed by the demethylases on this substrate, including not only oxidation adjacent to the ε-amine, but also hydroxylation on the terminal isopropyl group. These findings represent the first reported evidence of demethylase-catalysed hydroxylation, and therefore strongly imply that demethylation of natural substrates occurs via a hydroxylation mechanism. Also, in the case of JMJD2E, it appears that the ARTKme3QTARKmeiprSTGGKA peptide can be oxidised at different positions on the isopropyl group, indicating that multiple binding modes may be adopted.

e) N^{ϵ}-Formyllysine

No reactions were observed in the MALDI assays with N^{ϵ}-formyllysine containing peptides, indicating that this analogue is not accepted as a substrate by the demethylases tested. For this residue, it would appear unlikely that the lack of observable reaction is due to steric clashes between the proteins and the modified lysyl side chain, as the structure of this species resembles that of the proposed hemiaminal intermediate produced during demethylase-catalysed oxidation of methyllysines. Therefore, any loss of peptide binding would likely

be due to charge or stereoelectronic factors. Another potential explanation for the lack of reactivity is that the formyl C-H bond (or indeed any other oxidisable bond) may not be positioned sufficiently close to the catalytic iron. In this case, oxidation would likely be impaired, although it is probable that uncoupled 2OG turnover may be enriched as a consequence.

f) N^{δ}-Dimethylornithine

No reaction was observed in the MALDI sample containing N^{ϵ}-dimethylornithine and JMJD2E, suggesting that this species is not accepted as a substrate for this enzyme. However, analysis of the samples containing PHF8 and FBXL11 respectively did reveal evidence of demethylation (Figure 3.31 and Figure 3.32). In both cases, however, demethylation of the dimethylornithine substrate peptides was less efficient than demethylation of the corresponding dimethyllysine peptides.

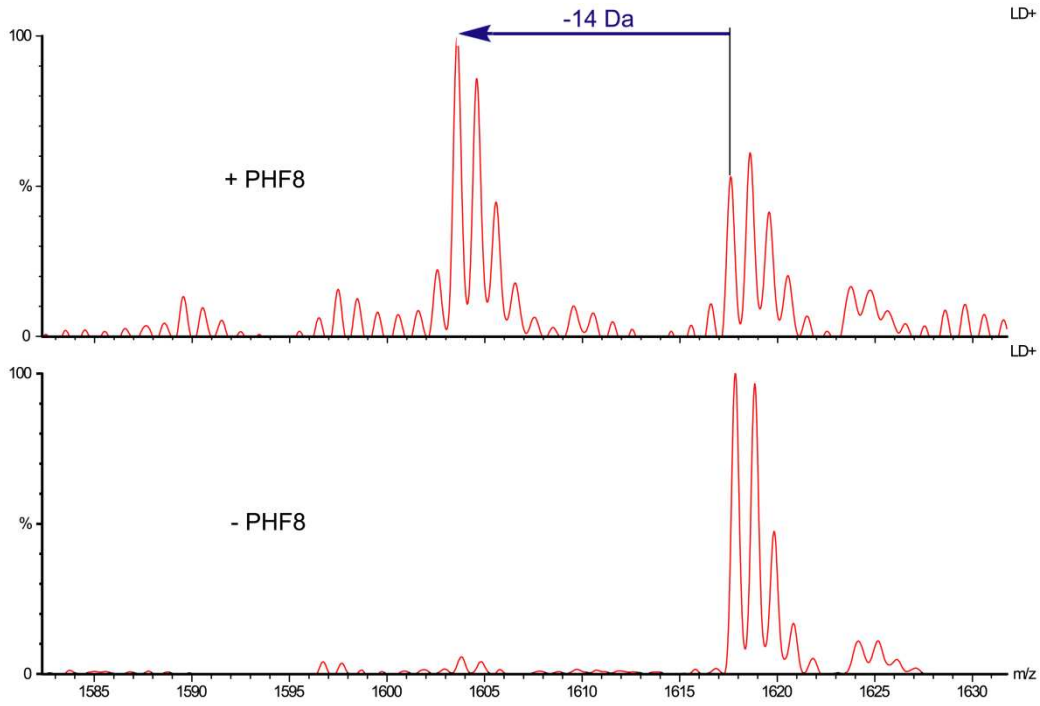

Figure 3.31 MALDI mass spectrum of a sample containing PHF8 (2 µM), ARTKme3QTAROme2STGGKA (10 µM), 2OG (50 µM), ascorbate (100 µM) and ferrous iron (10 µM) after one hour at 37 °C. The control experiment without enzyme is shown below.

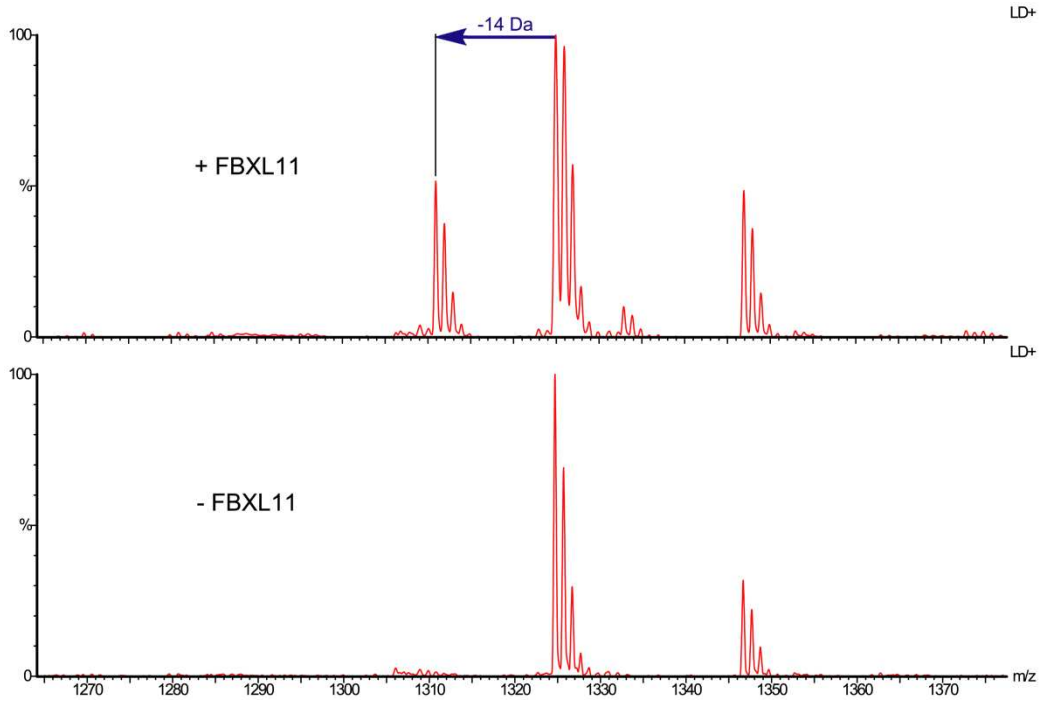

Figure 3.32 MALDI mass spectrum of a sample containing FBXL11 (1 µM), PATGGVOme2KPHRY (10 µM), 2OG (50 µM), ascorbate (100 µM) and ferrous iron (10 µM) after one hour at 37 °C. The control experiment without enzyme is shown below.

g) N^{δ}-Diethylornithine

A sample containing the peptide ARTKme3QTAROet2STGGKA and JMJD2E (with 2OG, ferrous iron and ascorbate) revealed the formation of a species with a mass of 1662 m/z, which was tentatively assigned to a hydroxylated product from JMJD2E catalysis (Figure 3.33). Based upon the observations for the other lysine analogue peptides, it seems likely that hydroxylation by JMJD2E is likely to occur on the terminal CH_3 group of the N^{ε}-ethyl groups of the modified ornithine. However, characterisation of the position of hydroxylation is impeded by the low turnover observed in the MALDI experiments.

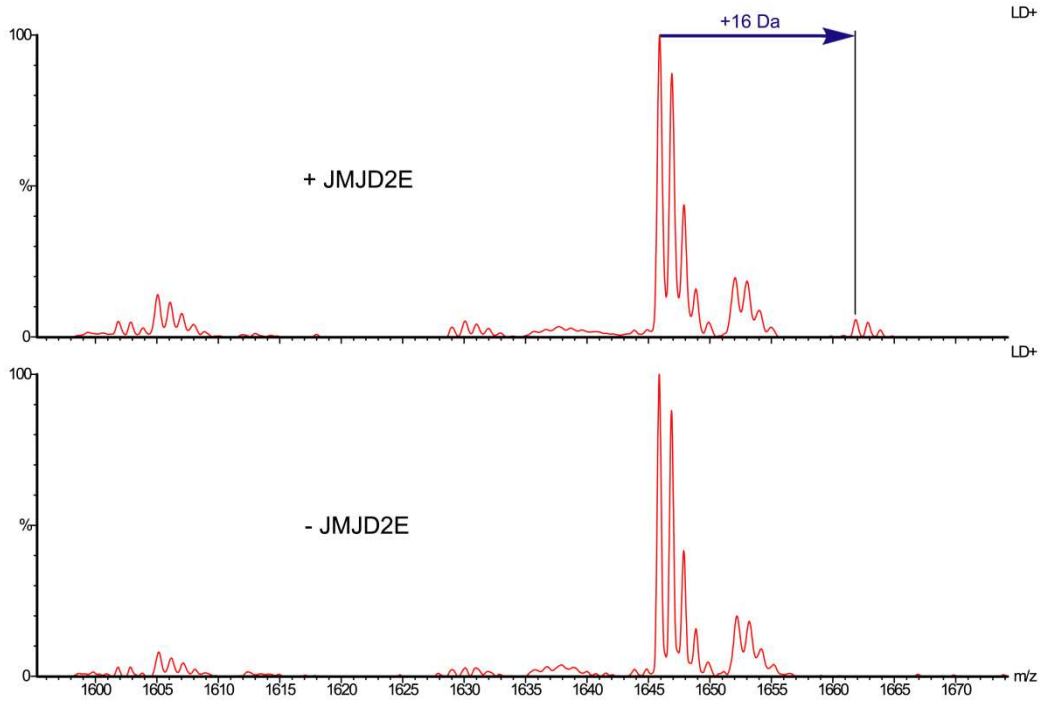

Figure 3.33 MALDI mass spectrum of a sample containing JMJD2E (2 μM), ARTKme3QTAROet2STGGKA (10 μM), 2OG (50 μM), ascorbate (100 μM) and ferrous iron (10 μM) after one hour at 37 °C. The control experiment without enzyme is shown below.

3.3 Conclusions and Future Work

Overall, the experiments with lysine analogues have revealed many new reactions catalysed by the 2OG oxygenases JMJD2E, PHF8 and FBXL11, and have provided new insights into the substrate selectivities and reactivities of these enzymes. In particular, strong evidence for hydroxylation was acquired from experiments with N^{ε}-mehylisopropyllysine containing peptides, suggesting that 2OG demethylase-catalysed demethylation occurs via hydroxylation.

Although rationalisation of substrate selectivity is somewhat speculative without structural data, the apparent variation in reactivity observed for the different enzymes tested allows for many interesting points to be raised. Firstly, the broad scope of oxidative reactions observed, from hydroxylation to demethylation, deethylation and deisopropylation, suggests that the histone demethylases are capable of catalysing multiple reactions, presumably by accepting a large number of substrates into their

active sites. This implies that lysyl demethylation may not be the only reaction catalysed by these enzymes *in vivo*. Also, the fact that oxidation can occur at least two carbon atoms away from the side chain amine (as observed with N^{ε}-methylisopropyllysine and N^{δ}-diethylornithine) implies that the substrate specificity of these enzymes may not be due solely to a preference for substrates containing an amino methyl group adjacent to the oxidised centre. It should be noted at this stage that the structure of N^{ε}-methylisopropyllysine bears some resemblance to that of asymmetric N^{ω}-dimethylarginine, suggesting that lysyl demethylases may catalyse arginine demethylation in cells (see Chapter 4).

Regarding the differences in substrate specificity observed between 2OG demethylases, it is possible to propose potential contributing factors by analysing their available crystal structures.[139, 140, 170] Structures of all four enzymes in complex with either 2OG or the 2OG analogue *N*-oxalylglycine (NOG) are available within this laboratory (the structures of JMJD2A, PHF8 and FBXL11 are available for downloading from the RCSB protein data bank, PDB codes 2OQ7, 3K3O and 2YU1 respectively). It is also possible to analyse structures of JMJD2A and PHF8 in complex with their respective H3K9 substrate peptides (PDB codes 2OQ6 and 3KV4 respectively), which allow the position of methylated lysines in the active sites to be visualised. By assessing the molecular space available for the lysine analogues to fill, it is possible to make some general hypotheses explaining the observed selectivity profiles. Firstly, analyses of the structures of JMJD2A and JMJD2E reveal a large space around the catalytic iron (Figure 3.34). This implies that these enzymes may facilitate binding of a number of larger lysine analogues, potentially resulting in their oxidation. This hypothesis is endorsed by the observed hydroxylations of N^{ε}-methylisopropyllysine and N^{δ}-diethylornithine, and also by the observed deisopropylation of N^{ε}-isopropyllysine. The structure of JMJD2A with substrate peptide indicates that the methyllysine ammonium group is positioned slightly above the ferrous iron. Based on this geometry, it is difficult to envisage oxidation of a lysine analogue shorter than the natural substrate (assuming that binding of the substrate is relatively similar for all lysine analogues), as this species

would in all probability be too far away from the iron centre to allow reaction to occur. This may explain the lack of demethylation observed with N^{δ}-dimethylornithine peptide with JMJD2E (which is postulated to be structurally very similar to JMJD2A when substrate is bound). Conversely, the structure of PHF8 with substrate peptide indicates that the methylated lysine penetrates much deeper into the active site relative to the substrate with JMJD2A (Figure 3.34), implying that demethylation of shorter lysine analogues may be possible. Demethylation of N^{δ}-dimethylornithine is observed with PHF8, and also with FBXL11, which may imply that the binding of lysyl substrates within FBXL11 is similar to the binding geometry observed within PHF8.

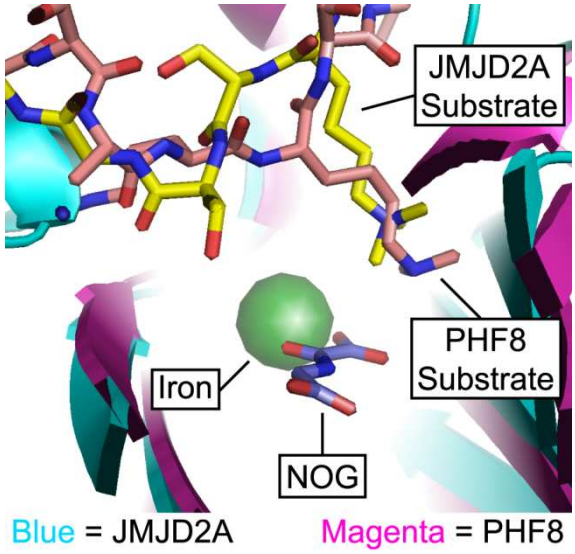

Figure 3.34 Views from crystal structures of JMJD2A (blue) and PHF8 (magenta) with bound substrates. The methylated lysine of the substrate penetrates further towards the catalytic iron in PHF8 (shown in pink).

In the case of JMJD2E, it is apparent that a large number of lysine analogues can be accommodated within the enzyme active site. Interestingly, oxidation occurs at different positions on the lysyl analogues depending upon their structure, suggesting that the proximity of a particular C-H bond to the catalytic iron is the defining factor for determining the position of oxidation. For example, JMJD2E is capable of removing both the methyl group and the ethyl group of N^{ε}-methylethyllysine peptide, implying not only that the longer ethyl group can be accommodated both near to and away from

the iron centre, but also that oxidation preferentially occurs next to the ε-amine. However, changing the ethyl group to an isopropyl group (N^{ϵ}-methylisopropyllysine) results in a loss of demethylation activity and changes the preferred position of oxidation on the isopropyl group to a terminal CH_3. This observation implies that the increased steric bulk of the isopropyl group relative to the ethyl group causes significant changes to the binding of the analogue, resulting in the isopropyl CH_3 group being positioned in the preferred orientation for oxidation. When JMJD2E is reacted with N^{ϵ}-isopropyllysine, however, it appears that the preferred binding mode for this analogue orientates the isopropyl CH group in the preferred oxidation position, resulting in deisopropylation. Presumably, this binding mode either cannot be adopted by N^{ϵ}-methylisopropyllysine or is less favoured relative to that resulting in CH_3 group hydroxylation. Overall, these findings suggest that subtle changes to analogue binding around the iron centre can result in different products being formed during oxidation. There is limited evidence, based on these analogues, that the position of oxidation is dependent upon the strength of the C-H bond (oxidation of the terminal CH_3 is preferred to oxidation of the CH in N^{ϵ}-methylisopropyllysine). However, more experimentation is required to confirm this.

Although broad substrate selectivity is observed for JMJD2E, this does not appear to be the case for both PHF8 and FBXL11. In the case of PHF8, both deethylation (of N^{ϵ}-ethyllysine) and deisopropylation (of N^{ϵ}-isopropyllysine) are observed, indicating that large alkyl groups can be accommodated close to the catalytic iron, at least when the side chain is monoalkylated. However, no reaction is observed with N^{ϵ}-methylisopropyllysine, nor is there observable deethylation of N^{ϵ}-methylethyllysine, indicating that double substitution on the side chain amine blocks binding of the peptide in an active conformation. These observations suggest that the substrate binding pocket is smaller than that of JMJD2A and JMJD2E, resulting in fewer lysine analogues being accepted as substrates. The active site of FBXL11 appears to be very similar to that of PHF8 by analysis of their crystal structures, suggesting that the restrictions on substrate binding observed for PHF8 may also apply for FBXL11. However, FBXL11 is able to

demethylate N^{ε}-methylisopropyllysine, suggesting not only that the selectivity profile varies significantly to that of PHF8 (and therefore implying that binding of substrates in their active sites is very different), but also that FBXL11 is able to accommodate large bulky alkyl groups away from the catalytic iron whilst orientating a methyl group in a catalytically active conformation. The fact that FBXL11 appears to preferentially catalyse demethylation of N^{ε}-methylethyllysine over deethylation suggests that groups larger than a methyl group are disfavoured close to the iron.

Although the investigations described in this Chapter go some way to revealing the reactivities and substrate specificites of the tested 2OG demethylases, it is noted that further studies may continue on these proteins using a second generation of lysine analogues. One analogue that would likely be of interest is N^{δ}-isopropylornithine; this species has a similar structure to dimethyllysine, and therefore, would likely be accepted as a substrate by the tested 2OG demethylases (Scheme 3.4). Also, the lack of an ε-amine in N^{δ}-isopropylornithine would likely allow any hydroxylated product to be stable. Initial attempts to incorporate N^{δ}-isopropylornithine into histone peptides during the course of this work were unsuccessful, possibly due to cyclisation or Fmoc deprotection during SPPS. However, optimisation of the synthetic conditions may allow production of the appropriate peptides. In addition to investigations with novel analogues, further studies may concentrate upon investigating the reactions of other 2OG demethylases, such as JMJD3 (for the reaction of JMJD3 with N^{ε}-methylisopropyllysine peptide, see Chapter 4), UTX, KIAA1718, JARID1A-D and JMJD1A-B. However, such studies may be impeded by the availability of active protein.

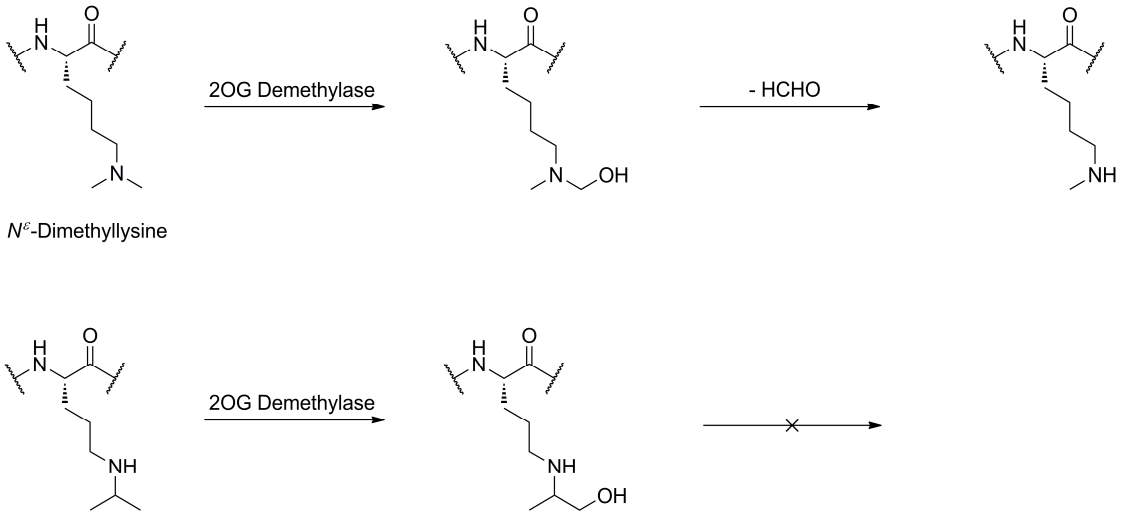

Scheme 3.4 Proposed reaction of N^{δ}-isopropylornithine with 2OG oxygenases. The demethylation scheme is shown above.

Chapter 4

Investigating Demethylation of Methylated Arginine by Histone Lysyl Demethylases

4.1 Introduction

N^{ω}-methylation of arginine residues is an important post-translational modification in histone proteins and has been linked to both the transcriptional activation and repression of target genes.[120, 124, 126, 172-176] As in the case of histone lysine methylation, it has been proposed that methylation of arginine may be regulated by interplay between arginine methyltransferases and demethylases. However, the notion that arginine methylation is dynamic is currently ambiguous due to the lack of identified arginine demethylases. Although a number of histone arginine methyltransferases have been identified,[113-118, 177-181] the only confirmed arginine demethylase identified to date is the deiminase PADI4, which has been shown to convert monomethylarginine to citrulline on histones.[182] This transformation, however, cannot be considered a true demethylation as the reaction does not reproduce the unmethylated arginine. Work by Chang *et al.* identified JMJD6 as a 2OG-dependent arginine demethylase acting on the histone arginines H3R2 and H4R3.[51] Subsequent investigations on this enzyme, however, have been unable to reproduce these results and more recently, JMJD6 has been revised as a lysine hydroxylase, suggesting that the function of this enzyme had been previously misassigned.[48]

As described in Chapter 3, studies on histone peptides incorporating lysine analogues have revealed that 2OG demethylases are capable of accepting many substrates other than the known methylated lysines. This observation implies that the 2OG demethylases may have other substrates in cells and may be able to regulate epigenetic mechanisms

by processes not involving lysine demethylation. The observation that JMJD2E is able to hydroxylate an N^{ε}-methylisopropyllysine containing peptide (Section 3.2.4d) suggests that this enzyme may be able to demethylate asymmetric N^{ω}-dimethylarginine due to their relatively similar structures (Scheme 4.1).

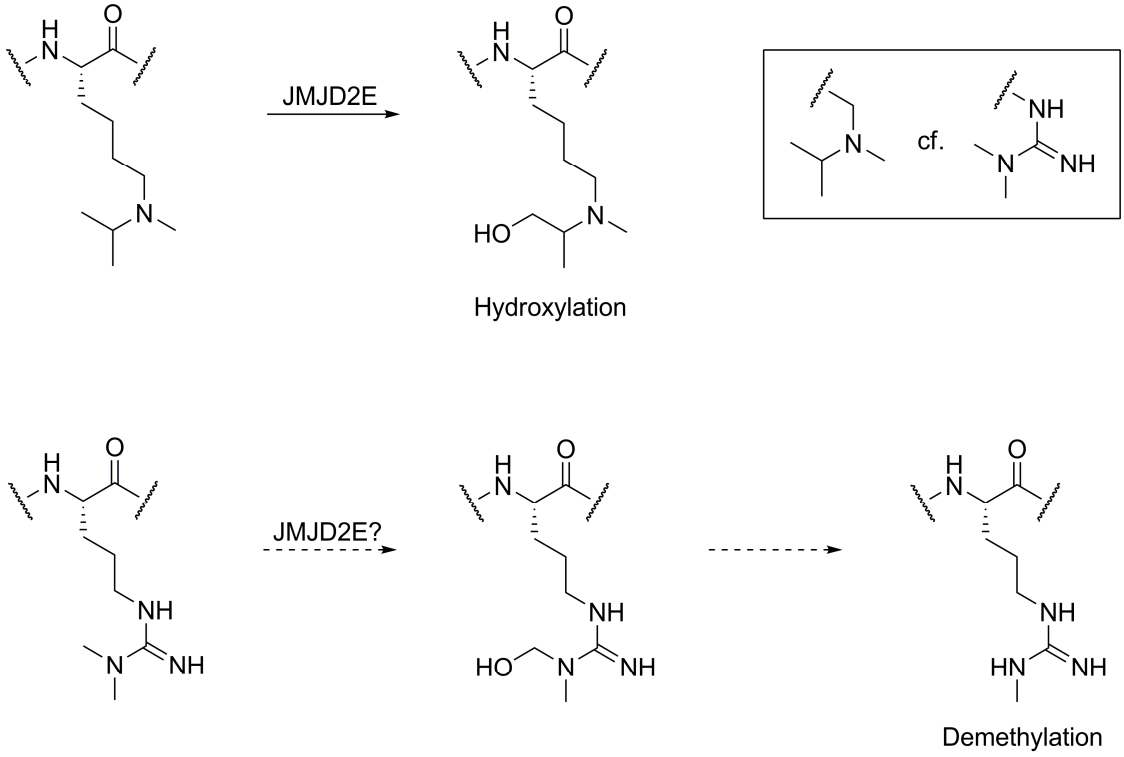

Scheme 4.1 Scheme showing comparison between hydroxylation of N^{ε}-methylisopropyllysine and demethylation of asymmetric N^{ω}-dimethylarginine.

Work in this Chapter investigates the potential for 2OG demethylases to demethylate methylated arginines. It was hoped that any demethylation activity observed with these enzymes may indicate that 2OG demethylases function as both lysine and arginine demethylases in cells, and consequently, that their biological roles may be more complex than previously envisaged. Also, any observable demethylation would represent the first evidence for *bona fide* enzyme-catalysed arginine demethylation, and could therefore be considered a breakthrough in the study of histone marks in cellular contexts.

Much of the histone peptide library screening, as well as all MALDI and FDH experiments with JMJD3, were carried out by Louise Walport. Other FDH assays were done in collaboration with Louise Walport. Peptides used in the screening studies were synthesised by Dr. Wei Ge.

4.2 Results

4.2.1 Initial Detection

Initial experiments focused upon analysing the reaction of an asymmetric dimethylarginine peptide with JMJD2E, which was considered the most likely enzyme to react with dimethylarginine due to its hydroxylation of the isosteric N^{ϵ}-methylisopropyllysine (see Chapter 3). In order to give the best chance of demethylation, it was proposed that asymmetric dimethylarginine should be incorporated into a histone peptide in place of lysine-9 (the known substrate for JMJD2E). It was hoped that substitution at this position would at least result in some binding of the peptide in the JMJD2E active site and may induce demethylation by forcing the arginine towards the catalytic iron. This hypothesis was endorsed by the previously described hydroxylation of N^{ϵ}-methylisopropyllysine, which was also substituted for lysine-9 in a histone peptide. An 8-mer peptide containing the desired mutation had already been prepared in the laboratory (sequence ARRme2aSTGGK, *provided by Dr. Wei Ge*), and therefore, this peptide was first tested for demethylation by incubating (at 10 μM final concentration) with JMJD2E (2 μM), 2OG (50 μM), ascorbate (100 μM) and ferrous iron (10 μM) and left for one hour at 37 °C. The sample was then analysed for demethylation using MALDI mass spectrometry (Figure 4.1).

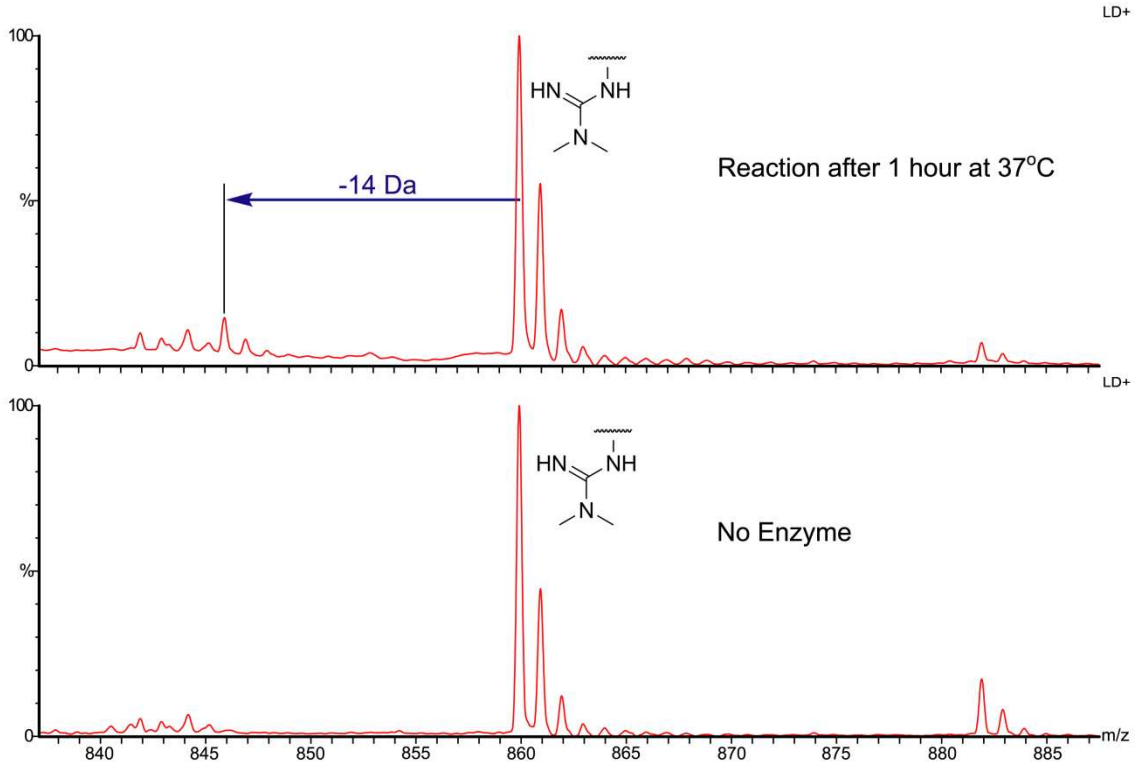

Figure 4.1 MALDI spectra showing the reaction of JMJD2E with the peptide ARRme2aSTGGK, 2OG, ascorbate and iron after one hour at 37 °C.

The MALDI mass spectrum after one hour revealed the presence of a peak at 845 m/z, which did not appear in the control experiment without enzyme. This peak correlated to the mass of the starting material minus 14 Da, implying that demethylation of the peptide had occurred in the sample. Despite this finding, less than 10 % of the starting material appeared to have been demethylated during the reaction period, suggesting that demethylation of the peptide was inefficient relative to demethylation of the corresponding lysyl peptide. Consequently, overlap of the peak with those of sample impurities impeded its conclusive assignment to the monomethylated arginine containing peptide. Therefore, the peptide was incubated with a higher concentration of JMJD2E (8 μM) in the hope that the demethylated peptide would become more prevalent in the sample, facilitating detection of the corresponding peak in the MALDI spectrum. Analysis of the sample by MALDI revealed that the demethylated peak represented nearly 30 % of the total peptide after one hour, allowing its unambiguous detection above the background noise (Figure 4.2).

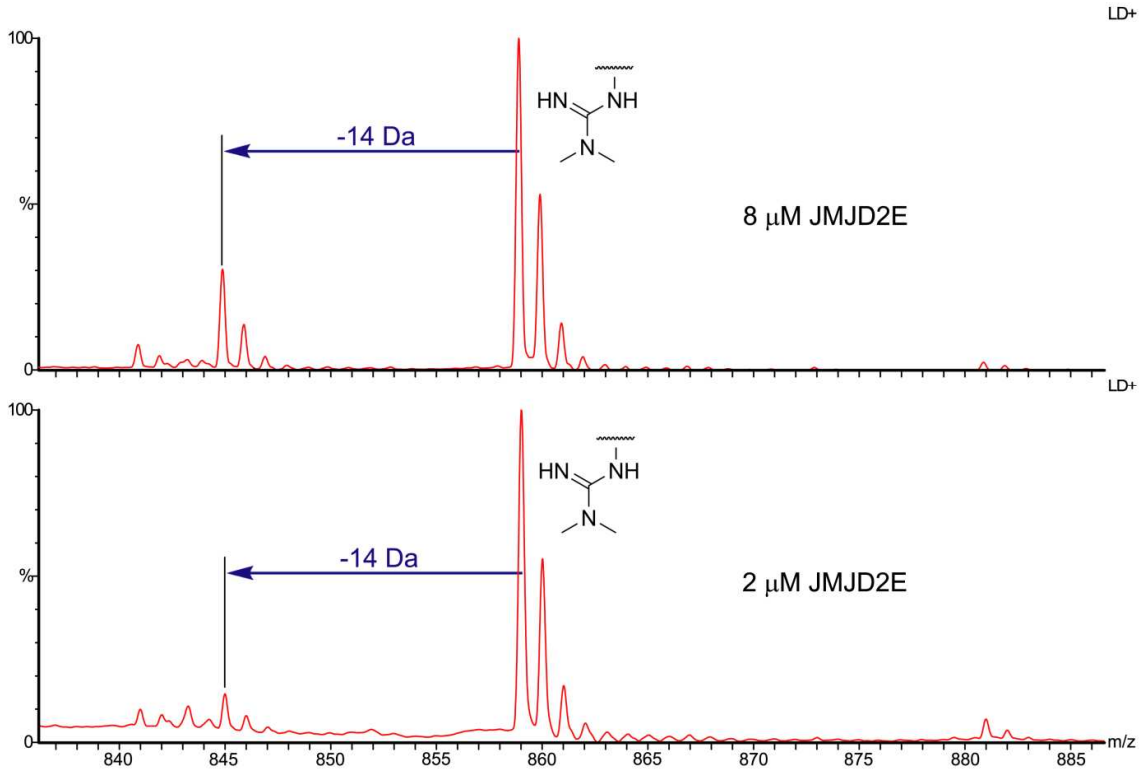

Figure 4.2 MALDI spectra showing the reaction of 2 μM (Bottom) and 8 μM (Top) JMJD2E with the peptide ARRme2aSTGGK, 2OG, ascorbate and iron after one hour at 37 °C.

4.2.2 Characterisation of Demethylation

Having detected potential arginine demethylation by JMJD2E, characterisation of the reaction was carried out in order to confirm the formation of demethylated peptide. These experiments were performed on the histone peptide ARTKQTARRme2aSTGGKA, which was selected in the hope that its increased length may facilitate more efficient demethylation. A MALDI spectrum of the peptide after synthesis (*by Dr. Wei Ge using a Multipep synthesiser*) revealed the product to be rather impure; however, incubation of the sample with JMJD2E resulted in clearly observable demethylation of the target peptide (Figure 4.3 bottom). It was also evident by MALDI analysis that JMJD2E was able to catalyse further demethylation of the monomethylarginine peptide, indicating that this monomethyl peptide was also a substrate for demethylation. FDH and NMR experiments were carried out using a pure sample of peptide, which was synthesised separately using a CS Bio peptide synthesiser (for description of solid phase peptide synthesis, see Chapter 2).

a) 2OG, Ascorbate and Iron Dependence

Although increasing the amount of JMJD2E in the MALDI analysed reactions appeared to increase the degree of peptide demethylation, it was noted that the improved activity observed may not be due to the increase in JMJD2E concentration. Although no arginine demethylases have been identified to date (implying that the presence of any demethylase active impurities would be unlikely), it could not be ruled out that impurities in the protein sample may be the actual catalysts of the reaction, and therefore improved demethylation may be the result of an increase in the concentration of the impurities in the enzyme sample rather than of an increase in JMJD2E (see Chapter 6). Consequently, experiments omitting the catalytically essential 2OG were conducted in order to confirm that demethylation is the result of 2OG-catalysed oxidation, and therefore likely to result from JMJD2E catalysis. The MALDI spectrum after one hour at 37 °C showed no peak at 1603 m/z (corresponding to the demethylated peptide), suggesting that the reaction is dependent upon 2OG (Figure 4.3). The demethylation reaction was also shown to be impaired upon the removal of iron from the sample, which further endorsed the hypothesis that demethylation is catalysed by JMJD2E (Figure 4.3). The demethylation rate also appeared to be moderately dependent on the concentration of ascorbate, as evidence by the slightly diminished demethylation activity in the sample omitting ascorbate.

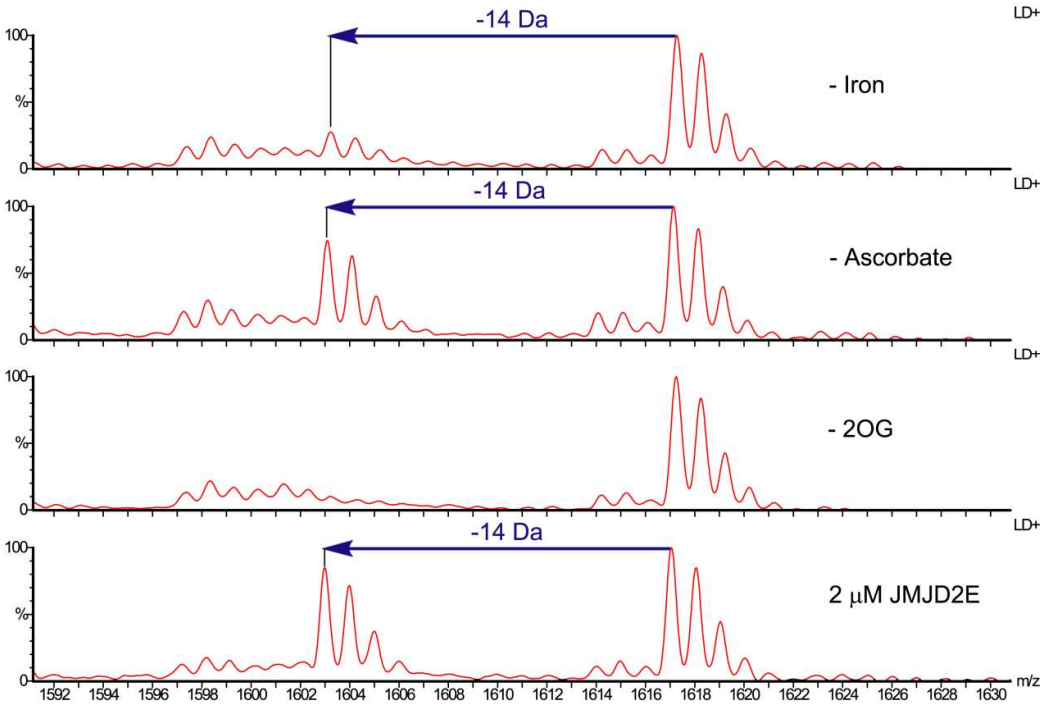

Figure 4.3 MALDI spectra showing JMJD2E-catalysed demethylation of ARTKQTARRme2aSTGGKA in the absence of iron, ascorbate and 2OG respectively.

b) HCHO Detection

Detection of HCHO produced during the demethylation reaction was attempted using the NMR and FDH assay techniques. However, analysis by both methods did not allow observation of demethylation, presumably due to the relatively low enzyme activity under the sample conditions (as observed for the lysine peptides by NMR relative to the MALDI analyses, Chapter 2). This observation suggests that demethylation of arginine in this peptide sequence is significantly less efficient relative to demethylation of the analogous lysyl peptide.

4.2.3 Comparison with Lysyl Demethylation

Both MALDI and NMR experiments characterising the demethylation reaction have suggested that arginine demethylation by JMJD2E is significantly less efficient than the equivalent lysyl demethylation. In order to corroborate these observations, a peptide mixture containing 1:1 equivalents of asymmetric dimethylarginine containing peptide and monomethyllysine containing peptide (sequence ARTKQTARKmeSTGGKA) was

incubated with JMJD2E (2 μM) and the rates of demethylation for each peptide were analysed and compared using MALDI mass spectrometry. As expected, the experiment revealed that demethylation of the monomethyllysine peptide is more efficient than the equivalent reaction on the asymmetric dimethylarginine peptide (Figure 4.4). It can also be assumed, therefore, that demethylation of the dimethylarginine peptide is less efficient than demethylation of the equivalent trimethylated and dimethylated lysyl peptide, given that these species are known to be better substrates than the monomethyllysine peptide (Chapter 2, Dr. Nathan R. Rose, personal communication).

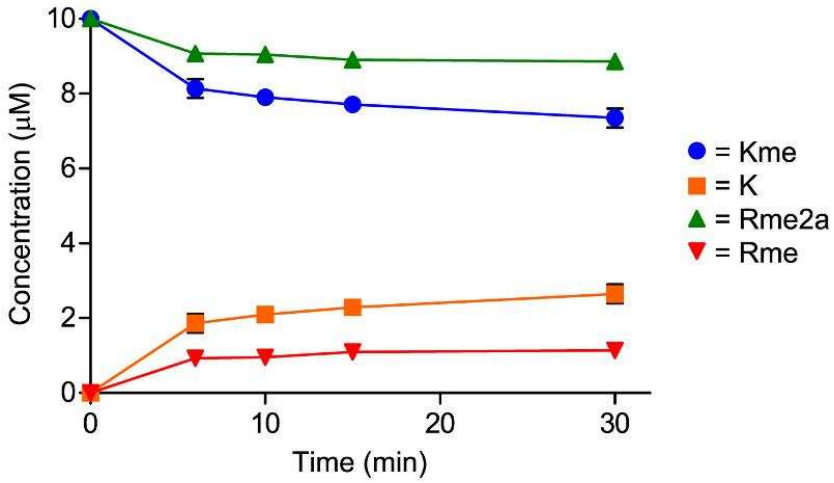

Figure 4.4 Concentrations of peptidic species derived from ARTK3QTARKmeSTGGKA and ARTKQTARRme2aSTGGKA, during the reaction with JMJD2E.

4.2.4 Demethylation State Selectivity

Having confirmed that demethylation of asymmetric dimethylarginine peptide is catalysed by JMJD2E, further experiments were carried out in order to investigate whether this enzyme was capable of demethylating symmetric dimethylarginine. Symmetric dimethylarginine possesses one methyl group on each of the N^{ω}-nitrogens of the guanidino group, and therefore the structure of this residue differs significantly from that of its asymmetric homologue (Figure 4.5). It was therefore postulated that demethylation of the two dimethylarginine tautomers may not necessarily be facilitated by the same enzyme; as such an enzyme would have to be able to bind both species. However, as JMJD2E has been shown to catalyse oxidation on a variety of lysine

analogues (although diethyllysine, the analogue most structurally similar to symmetric dimethylarginine, does not react), it was proposed that binding of both dimethylarginines may be possible.

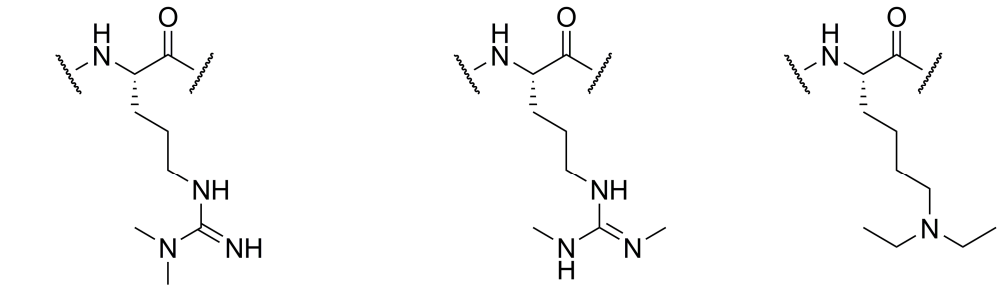

Figure 4.5 Structures of asymmetric dimethylarginine, symmetric dimethylarginine and diethyllysine.

In order to test for demethylation activity, the symmetric dimethylarginine containing peptide ARTKQTARRme2sSTGGKA was prepared using a peptide synthesiser and was incubated (10 µM) with JMJD2E (2 µM), 2OG (50 µM), ascorbate (100 µM) and ferrous iron (10 µM) at 37 °C. Interestingly, MALDI analysis of the sample revealed evidence of demethylation (Figure 4.6, bottom).

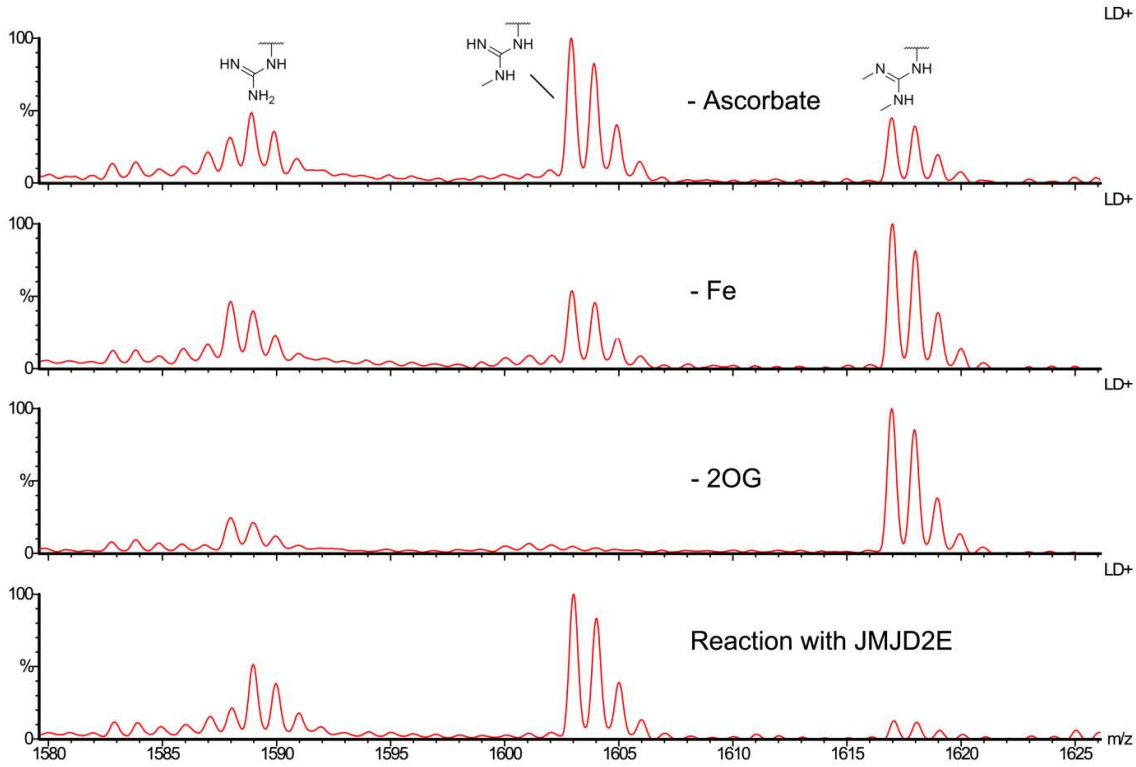

Figure 4.6 MALDI spectra showing JMJD2E-catalysed demethylation of ARTKQTARRme2sSTGGKA in the absence of iron, ascorbate and 2OG respectively, after one hour at 37 °C.

In addition to the emergence of a peak at 1603 m/z, corresponding to the monomethylarginine peptide, a peak at 1589 m/z also appeared to increase in intensity during the incubation period (one hour). It was proposed that this peak corresponds to the unmethylated arginine, suggesting that demethylation of the monomethylarginine product had occurred in the sample (as observed for samples containing the asymmetric dimethylarginine peptide). Although direct comparison of the asymmetric and symmetric dimethylarginine peptide demethylation rates by MALDI was impeded by their identical masses, competition experiments were carried out using the asymmetric dimethylarginine peptide and a symmetric dimethylarginine peptide trimethylated at K4 (sequence ARTKme3QTARRme2sSTGGKA, *synthesised by Dr. Wei Ge*, see Section 4.2.7). An approximately 1:1 mixture of the symmetric and asymmetric dimethylarginine peptides (the relative impurity of the symmetric dimethylarginine peptide sample hindered accurate determination of concentration) was prepared and the

mixture was reacted (as above) and monitored over a period of 30 minutes. Interestingly, analysis of the spectra revealed that the symmetric dimethylarginine peptide was marginally more active in the sample (no demethylation of the asymmetric dimethylarginine peptide could be observed, although it is possible that the demethylated products of the reaction may be obscured by sample impurities, Figure 4.7). This finding suggests that symmetric dimethylarginine may be an intrinsically better substrate for JMJD2E than the asymmetric analogue (at least for the sample tested); however, more experimentation is required to confirm this.

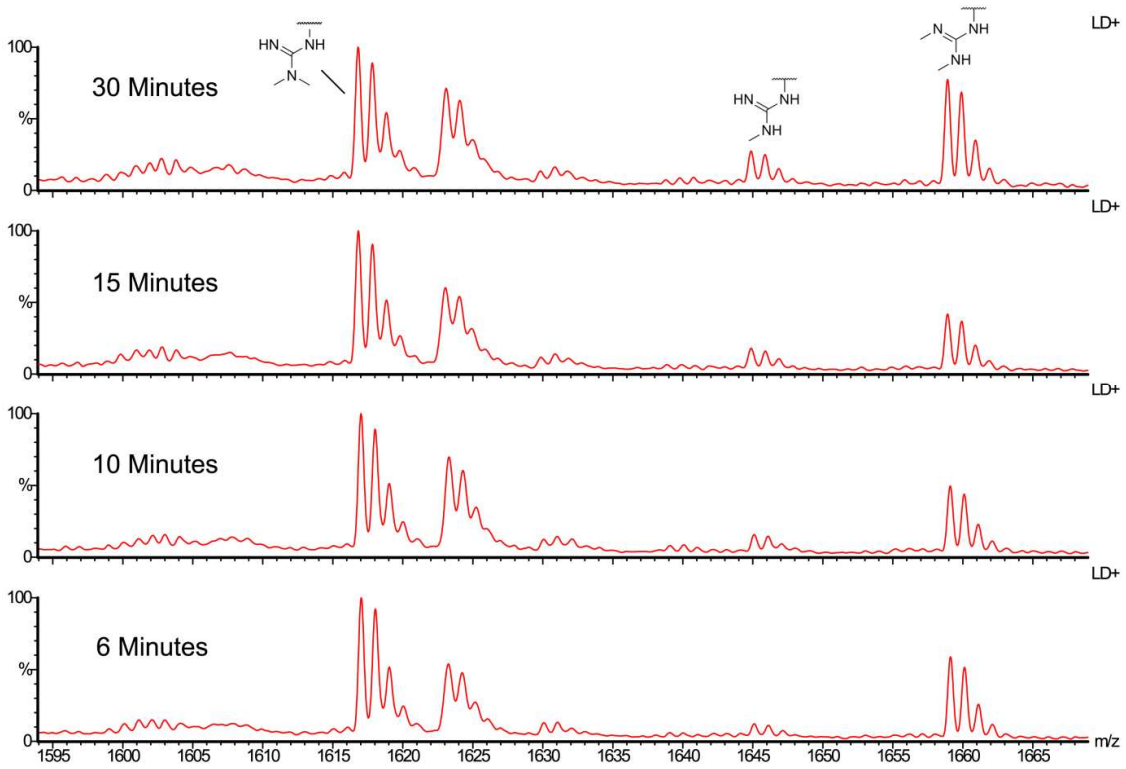

Figure 4.7 MALDI spectra showing JMJD2E-catalysed demethylation of ARTKQTARRme2aSTGGKA and ARTKme3QTARRme2sSTGGKA over time at 25 °C.

4.2.5 Screening of Histone Peptides

MALDI experiments were then undertaken in order to investigate whether JMJD2E is able to catalyse demethylation on known histone arginine marks. A histone peptide library containing methylated arginines (*acquired from Dr. Wei Ge*) was prepared, and each of the peptides was incubated with JMJD2E, 2OG, ascorbate and ferrous iron and

the reactions were monitored after one hour at 37 °C. A summary of the reactions is shown in Table 4.1.

Table 4.1 Table showing histone peptides tested for arginine demethylation with JMJD2E. Observed demethylation is indicated.

Peptide Sequence	Histone Mark	-14 Da?	-28 Da?
ARRme2aSTGGK	H3K9 mutant	Yes	No
ARTKQTARRme2aSTGGKA	H3K9 mutant	Yes	Yes
ARTKQTARRme2sSTGGKA	H3K9 mutant	Yes	Yes
ARTKQTARRmeSTGGKA	H3K9 mutant	Yes	N/A
ARTKme3QTARRme2aSTGGKA	H3K4 H3K9 mutant	Yes	Yes
ARTKme3QTARRme2sSTGGKA	H3K4 H3K9 mutant	Yes	Yes
ARTKme3QTARRmeSTGGKA	H3K4 H3K9 mutant	Yes	N/A
ARme2aTKQTARKSTGGKAPRK	H3R2	Yes	Yes
ARme2sTKQTARKSTGGKAPRK	H3R2	Yes	Yes
ARme2aTKme3QTARKSTG	H3R2 K4me3	Yes	Yes
ARme2sTKme3QTARKSTG	H3R2 K4me3	Yes	Yes
ARTKQTARme2aKSTGGKAPRK	H3R8	Yes	Yes
ARTKQTARme2sKSTGGKAPRK	H3R8	Yes	No
ARTKQTARmeKSTGGKAPRK	H3R8	Yes	N/A
TKQTARme2aKacSTGGK	H3R8 H3K9	No	No
STGGKAPRme2aKQLATKAARK	H3R17	No	No
STGGKAPRme2sKQLATKAARK	H3R17	No	No
STGGKAPRmeKQLATKAARK	H3R17	No	No
TGGKAPRme2aKacQLATK	H3R17	No	No
TGGKacAPRme2aKQLATK	H3K14 H3R17	No	No
TGGKAPRme2aKacQLATK	H3R17 H3K18	No	No
TGGKAPRme2sKacQLATK	H3R17 H3K18	No	No
QLATKAARme2aKSAPATGGV	H3R26	No	No
QLATKAARme2sKSAPATGGVK	H3R26	No	No
QLATKAARme2aKSAPATGGV	H3R26	No	No
SGRme2aGKGGKGLGKGGAK	H4R3	Yes	No
SGRme2sGKGGKGLGKGGAK	H4R3	No	No
SGRme2aGKQGGKARAKTR	H2AR3	No	No

In addition to the observed demethylation of the H3K9R mutant peptides, it was apparent that demethylation on peptides with methylated H3R2, H3R8 and H4R3 histone marks is catalysed by JMJD2E. These findings suggest that *in vivo* demethylation of known histone arginines could be catalysed by JMJD2E, indicating not only that this enzyme may possess other cellular substrates (assuming that JMJD2E is expressed in cells), but also that epigenetic regulation may be facilitated by arginine

demethylation catalysed by histone 'lysyl' demethylases. This is the first evidence that 2OG demethylases may act on non-lysyl cellular substrates and also indicate that biologically relevant arginine demethylation may be catalysed by members of the 2OG oxygenase family. Although comparison of the peptides' demethylation activities was difficult due to the relative impurity of many of the samples, it was possible to provisionally rank the substrates according to their reactivity. These experiments indicated that the H3R2 peptide containing asymmetric dimethylarginine (H3R2me2a) was the best substrate for JMJD2E.

In order to investigate whether the H3R2me2a peptide is a better substrate than the K9R mutant peptide, direct competition experiments were carried out. A pure sample of H3R2me2a peptide was synthesised (sequence ARme2aTKQTARKSTGGKA) and a 1:1 mixture of this peptide with the equivalent K9R peptide (sequence ARTKQTARRme2aSTGGKA) was prepared. This mixture was then incubated with JMJD2E, 2OG, ascorbate and iron (as described above) and the reaction was monitored over 30 minutes using MALDI mass spectrometry. The sample revealed that demethylation of the modified R2 peptide was more efficient than the corresponding R9 peptide (Figure 4.8). However, after 30 minutes, only roughly 50 % of the R2 peptide had been demethylated, indicating that demethylation at R2 is still significantly less efficient with respect to lysyl demethylation of trimethylated K9 peptide (which is fully demethylated after 30 minutes under the same conditions).

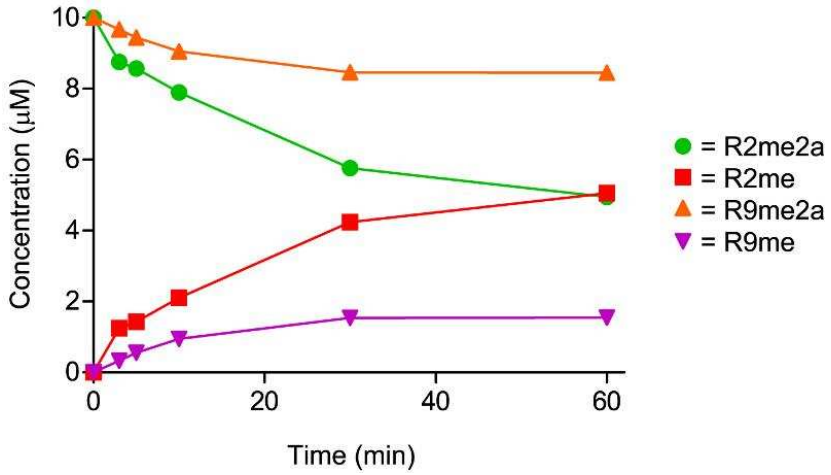

Figure 4.8 Concentrations of ARme2aTKQTARKSTGGKA, ARmeTKQTARKSTGGKA, ARTKQTARRme2aSTGGKA, and ARTKQTARRmeSTGGKA over time, when incubated with JMJD2E, 2OG, ascorbate, and iron.

Analysis of a sample containing the trimethylated R2K mutant peptide (sequence AKme3TKQTARKSTGGKA) did not result in observed demethylation after one hour at 37 °C (*carried out by Louise Walport*). These observations imply that demethylation of methylated lysines and arginines may be less efficient when either substrate is substituted for the other in a peptide. This may indicate that the preferred binding orientations of methylated lysines and methylated arginines are facilitated by interactions between the protein and specific surrounding peptide residues, and therefore, different amino acid sequences may be important in determining whether demethylation of arginine or lysine is preferred. Although arginine demethylation of the histone peptides appears to be less efficient with respect to lysyl demethylation at K9 (at least with respect to the trimethylated peptide), it appears that JMJD2E is able to accept more methylated arginine substrates than lysine substrates (JMJD2E is known only to demethylate methylated K9 peptides). This may suggest that JMJD2E is amenable to accepting methylated arginine substrates with varying amino acid residues close to the methylated arginine, implying that these residues may not be important for determining substrate specificity in a cellular environment (i.e. with full length protein and substrate). It is also possible that demethylation of either methylated lysines or arginines is promoted by the presence of other post translational modifications in the

peptides, as observed during PHF8-catalysed demethylation at K9 in the presence of trimethylated K4.[140, 171]

Given that the H3R2 peptide is a better substrate than the corresponding H3K9R mutant peptide, ^{1}H NMR experiments with the R2 peptide were carried out in the hope that demethylation might be observed. The NMR sample was prepared as described in Chapter 2, except that in this case, JMJD2E was added at 20 μM final concentration in the hope that increased enzyme would increase the degree of demethylation in the sample. After 30 minutes reaction, a singlet resonance at δ_H 2.35 ppm, corresponding to succinate, was observed, indicating 2OG turnover (Figure 4.9). However, detection of demethylation (as evidenced by a decrease in intensity of the singlet resonance at δ_H 2.98 ppm) was hampered by signal overlap. Despite this, it was possible to detect the emergence of a small singlet resonance at δ_H 2.78 ppm, which may correspond to the methyl protons of monomethylarginine in the product peptide. The low concentration of this species, however, impeded characterisation, and therefore, doping experiments with an authentic sample of monomethylated peptide would likely be required to confirm the assignment.

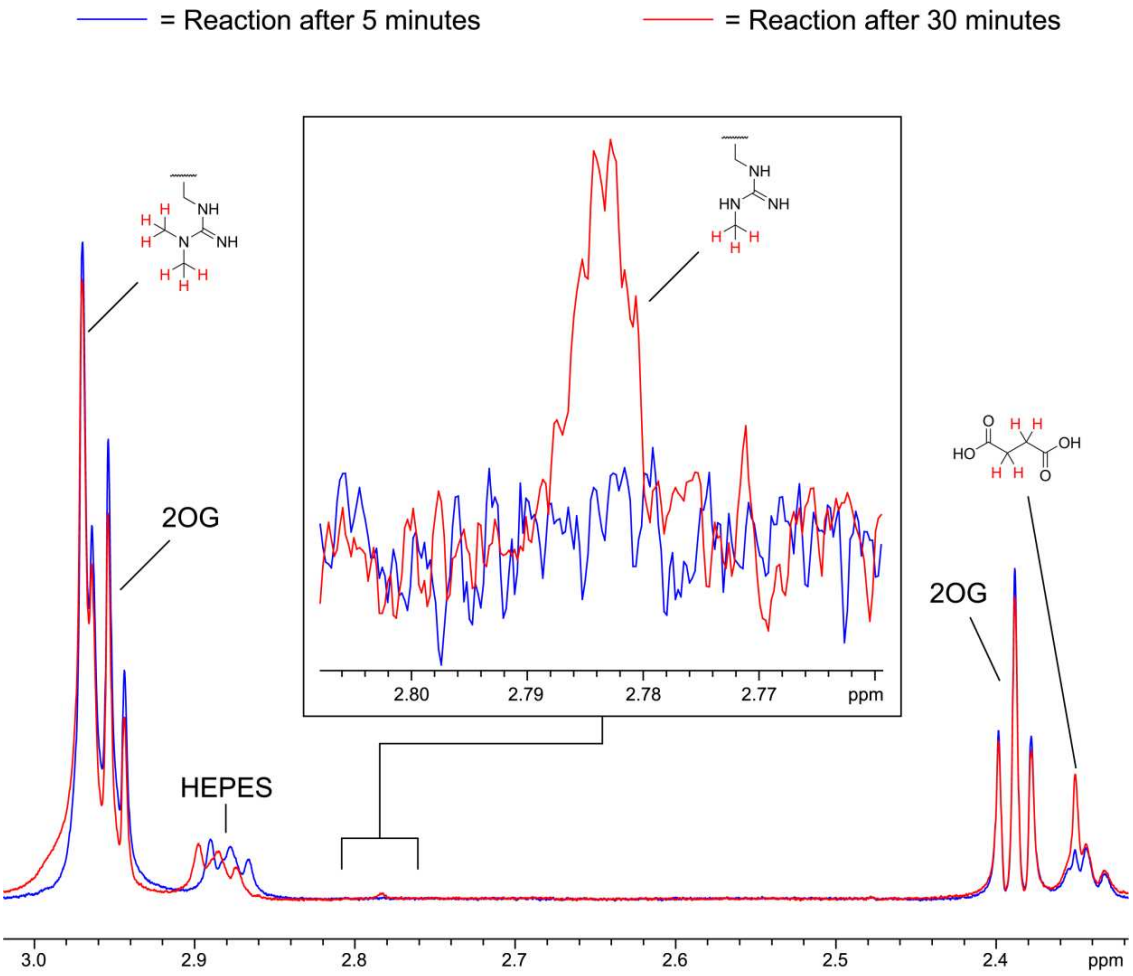

Figure 4.9 ^{1}H NMR spectra (700 MHz) of a sample containing ARme2aTKQTARKSTGGKA (1 mM), JMJD2E (20 µM), 2OG (5 mM), ascorbate (1 mM) and ferrous iron (100 µM) after 5 minutes and 30 minutes respectively in dAFN buffer.

Finally, the increased demethylation observed with the R2 peptide allowed for analysis of the reaction using the FDH assay. A sample containing the R2 peptide, 2OG, ascorbate, iron, FDH and NADH (for concentrations, see Chapter 10) was prepared, and the degree of demethylation over time was monitored by recording an increase in fluorescence intensity at 460 nm. Analysis of the sample facilitated the indirect observation of arginine demethylation and also indicated that HCHO was produced as a product of demethylation (as observed for lysyl demethylation, Chapter 2). Monitoring the reaction at variable peptide concentration allowed for the initial rates of peptide demethylation to be attained, resulting in the determination of kinetic parameters (Figure 4.10).

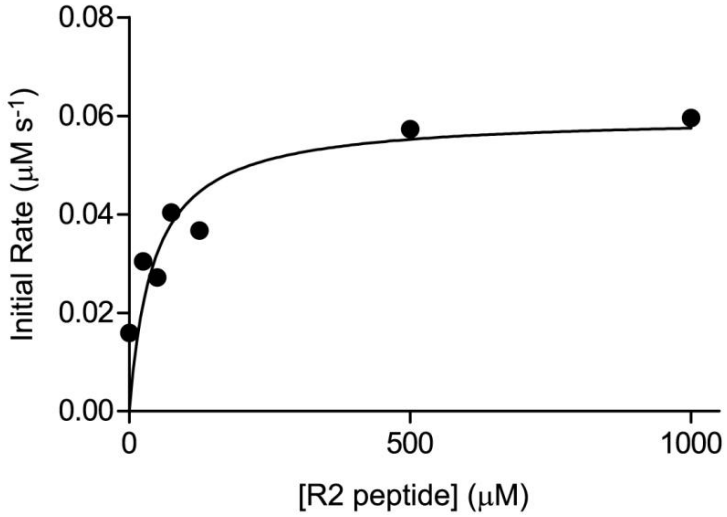

Figure 4.10 Dose-response curves for JMJD2E catalysed demethylation of ARme2aTKQTARKSTGGKA.

The K_M value attained for the R2 peptide (43.3 ± 12.2 μM) was higher than the calculated K_M values for the analogous trimethylated K9 peptide using the FDH assay (17.4 ± 2.5 μM). However, the K_M values for the R2 peptide and the analogous dimethylated K9 peptide (32.2 ± 7.4 μM) were the same within experimental error. The similarity in the K_M values attained for the asymmetric dimethylated R2 peptide and the dimethylated K9 peptide suggest that these peptides have a similar binding affinity for the enzyme. Despite this apparent similarity in binding affinity, analysis of the k_{cat} values for the two peptides (0.03 ± 0.002 s^{-1} and 0.07 ± 0.004 s^{-1} for the dimethylated R2 and dimethylated K9 peptides respectively) suggested that demethylation of the dimethylated R2 peptide is slower than the dimethylated K9 peptide. These findings may indicate that the demethylation pathways for the two substrates possess different rate determining steps (or at least some steps in the overall rate equation are slowed in the case of the dimethylated R2 peptide).

4.2.6 Screening of other JMJD2 Demethylases

Although demethylation of methylated arginines was observed with JMJD2E, this enzyme is proposed not to be expressed in cells. Therefore, screening of the histone peptide library was carried out with the JMJD2E homologues JMJD2A and JMJD2D,

which are known to be expressed in cell nuclei and may therefore indicate biologically relevant arginine demethylation. JMJD2D is expected to display a very similar substrate specificity profile to JMJD2E (at least with the constructs available), as the residues that formulate the substrate binding pocket are highly conserved. The catalytic domain of JMJD2A is also very similar to that of JMJD2E, however it is possible that the variations in the substrate methyllysine binding pocket (S288 and T289 in JMJD2A, which are substituted for A288 and I289 in JMJD2E) may induce different arginine binding propensities. Also, it was hoped that the data attained with JMJD2A (as the truncated catalytic domain) would allow the arginine demethylation activities of JMJD2B and JMJD2C to be predicted, as the catalytic domains of these enzymes are highly conserved.

Analysis of the reactions of the histone peptides and JMJD2D did not reveal any demethylation after one hour at 37 °C. Although these findings are somewhat surprising given the structural similarity between JMJD2D and JMJD2E, it was noted that the batch of JMJD2D available in the laboratory was significantly less active than the corresponding samples of JMJD2E. A sample containing JMJD2D (at 10 μM final concentration) and the standard trimethylated K9 peptide (sequence ARKme3STGGK) only revealed roughly 30 % demethylation to the dimethylated peptide after one hour at 37 °C. However, samples containing this peptide are known to be completely demethylated to the monomethylated peptide after 10 minutes with JMJD2E. It is acknowledged, therefore, that the lack of observed arginine demethylation with the peptide library may be due to the inherently low enzyme activity rather than to any specificity of JMJD2D for lysine substrates.

The JMJD2A construct used in this study was also found to be less active than JMJD2E with respect to lysyl demethylation. However, incubation of JMJD2A with the arginine peptides did indicate that the enzyme was capable of catalysing arginine demethylation, albeit at very low levels (Table 4.2).

Table 4.2 Table showing histone peptides tested for arginine demethylation with JMJD2A. Observed demethylation is indicated.

Peptide Sequence	-14 Da?	-28 Da?
ARTKQTARRme2aSTGGKA	No	No
ARTKQTARRme2sSTGGKA	No	No
ARTKme3QTARRme2aSTGGKA	Yes	No
ARTKme3QTARRme2sSTGGKA	Yes	No
ARme2aTKQTARKSTGGKAPRK	Yes	No
ARme2sTKQTARKSTGGKAPRK	No	No
ARme2aTKme3QTARKSTG	Yes	No
ARme2sTKme3QTARKSTG	No	No
ARTKQTARme2aKSTGGKAPRK	No	No
ARTKQTARme2sKSTGGKAPRK	No	No
ARTKQTARmeKSTGGKAPRK	No	N/A
TKQTARme2aKacSTGGK	No	No
STGGKAPRme2aKQLATKAARK	No	No
STGGKAPRme2sKQLATKAARK	No	No
STGGKAPRmeKQLATKAARK	No	No
TGGKAPRme2aKacQLATK	No	No
TGGKacAPRme2aKQLATK	No	No
TGGKAPRme2aKacQLATK	No	No
TGGKAPRme2sKacQLATK	No	No
QLATKAARme2aKSAPATGGV	No	No
QLATKAARme2sKSAPATGGVK	No	No
QLATKAARme2aKSAPATGGV	No	No
SGRme2aGKGGKGLGKGGAK	Yes	No
SGRme2sGKGGKGLGKGGAK	No	No
SGRme2aGKQGGKARAKTR	No	No

4.2.7 Screening of other 2OG Dependent Oxygenases

The peptide library was then used to investigate whether other 2OG demethylases can catalyse arginine demethylation. A number of available lysyl demethylases were selected for screening with the histone library in the hope that these enzymes may allow reaction with the methylated argninines. Also, screening was carried out on the 2OG oxygenase ABH5, which to date has no known substrate. In addition to screening the enzymes against the histone library, the known lysyl substrate peptides for each enzyme (excluding ABH5) were synthesised with methylated arginine residues substituted for the reactive lysine. It was hoped that these peptides may give a high probability of arginine demethylation due to their known binding affinities; however analysis of the reactions with JMJD2E suggest that lysine to arginine substitution may not necessarily

produce efficient demethylation. The enzymes selected for screening, as well as the sequences of their mutated substrate peptide are shown in Table 4.3.

Table 4.3 Table showing the screened 2OG oxygenases and the synthesised mutated substrate peptides.

Enzyme	Mutated Substrate Peptides
PHF8	ARTKme3QTARRme2aSTGGKA
	ARTKme3QTARRme2sSTGGKA
	ARTKme3QTARRmeSTGGKA
FBXL11	PATGGVRme2aKPHRY
	PATGGVRme2sKPHRY
	PATGGVRmeKPHRY
KIAA1718	KQLATKAARRme2aSAPAT
	KQLATKAARRme2sSAPAT
	KQLATKAARRmeSAPAT
JMJD1A	ARTKQTARRme2aSTGGKA
	ARTKQTARRme2sSTGGKA
	ARTKQTARRmeSTGGKA
JMJD3	Same as for KIAA1718
UTX	Same as for KIAA1718
ABH5	N/A

Analysis of the MALDI spectra for each of the 2OG oxygenases with the histone peptide library indicated that the majority of the enzymes did not catalyse arginine demethylation on the peptides. The only observed demethylation during the screen was the demethylation of the asymmetric dimethylarginine containing K27R peptide and the monomethylarginine containing K27R peptide with JMJD3 (Table 4.4 and Figure 4.11). No demethylation of known histone arginine marks was observed, nor was there any apparent hydroxylation (it was postulated that FBXL11 may facilitate hydroxylation of asymmetric dimethylarginine by analogy to its demethylation of N^{ϵ}-methylisopropyllysine, Scheme 4.2) or formation of citrulline. These results implied that the enzymes tested (with the exception of JMJD3) were most likely not reacting with the methylated arginine peptides.

Table 4.4 Table showing the demethylation by the screened 2OG.

Enzyme	Reported Substrate(s)	Evidence of Arginine Demethylation
PHF8	H3K9me2/me1	No
FBXL11	H3K36me2/me1	No
KIAA1718	H3K27me2/me1	No
JMJD1A	H3K9me2/me1	No
JMJD3	H3K27me3/me2/me1	Yes
UTX	H3K27me3/me2/me1	No
ABH5	Unknown	No

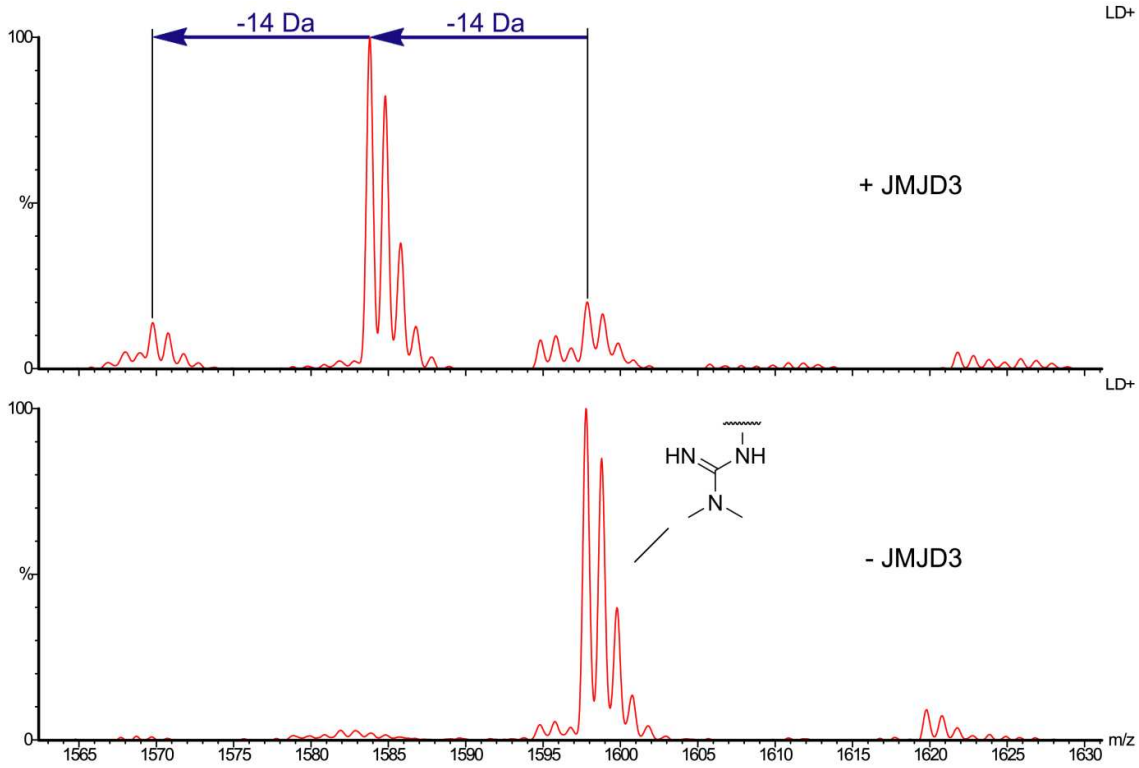

Figure 4.11 MALDI mass spectra of a sample containing JMJD3 (2 µM), KQLATKAARRme2aSAPAT (10 µM), 2OG (50 µM), ascorbate (100 µM) and ferrous iron (10 µM) after one hour at 37 °C. A control experiment without enzyme is shown below.

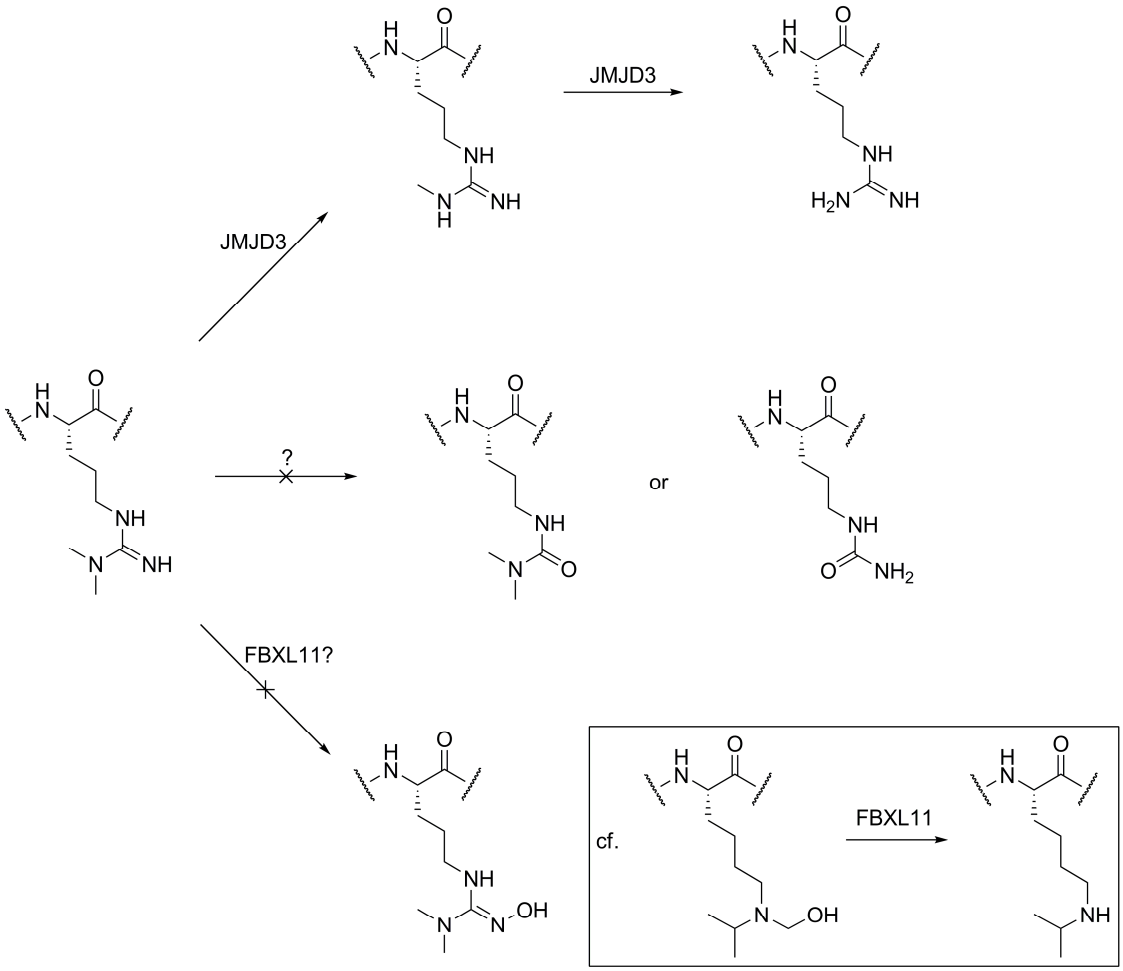

Scheme 4.2 Scheme showing the demethylation of asymmetric dimethylarginine and monomethyarginine by JMJD3. Hydroxylation or citrulline formation does not appear to occur.

Based on the MALDI experiments, it appeared that demethylation of H3K27R asymmetric dimethylarginine peptide by JMJD3 was more efficient than the observed demethylation of H3R2 asymmetric dimethylarginine peptide by JMJD2E (at least under the MALDI reaction conditions). Therefore, it was proposed that both NMR and FDH analyses on the reaction may allow the demethylation product to be characterised and kinetic parameters to be attained. Firstly, the demethylation reaction was monitored using ^{1}H NMR as described in Section 4.2.5. JMJD3 (10 μM final concentration) was incubated with a purified batch of the K27R peptide (1 mM), 2OG (5 mM), ascorbate (1 mM) and ferrous iron (10 μM), and the reaction was monitored over the first 30 minutes of reaction. In addition to the formation of succinate, analysis of the sample revealed the time dependent formation of a singlet resonance at δ_H 2.78 ppm (Figure 4.12),

coupled to a decrease in intensity of the singlet resonance at δ_H 2.98 ppm. It was therefore proposed that the new resonance corresponds to the methyl group protons on the monomethylated arginine peptide. However, further characterisation is required to confirm the NMR assignment.

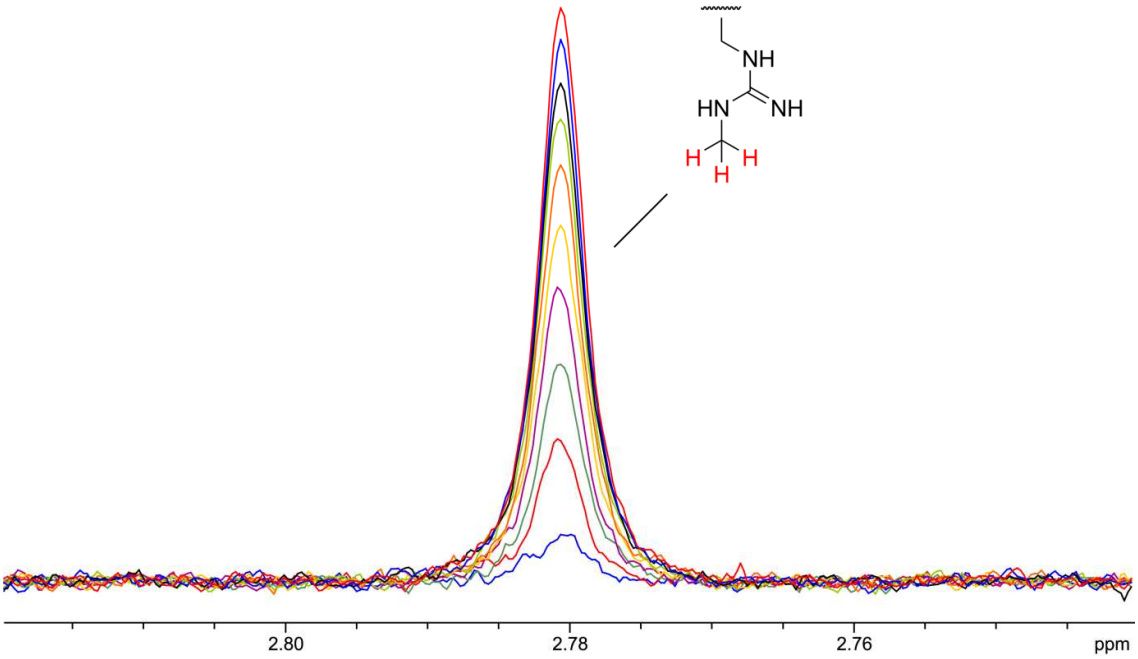

Figure 4.12 ^{1}H NMR spectra (700 MHz) of the reaction of KQLATKAARRme2aSAPAT, JMJD3, 2OG, ascorbate and ferrous iron in dAFN buffer. The singlet resonance at δ_H 2.78 ppm is observed to increase in intensity over time (Δt = 89 s).

As the demethylation reaction with JMJD3 appeared to produce substantial demethylated peptide by NMR, it was proposed that the detection of HCHO produced may be possible using this technique. Therefore, dimedone (1 mM final concentration) was added to the reaction mixture after 30 minutes in the hope that the characteristic dimedone-HCHO adduct(s) may be detected in the ^{1}H NMR spectrum. Analysis by ^{1}H NMR revealed the emergence of a signal at δ_H 0.895 ppm, which was assigned to the hydroxymethyldimedone adduct by analogy to the experiments described in Section 2.2.3 (Figure 4.13).

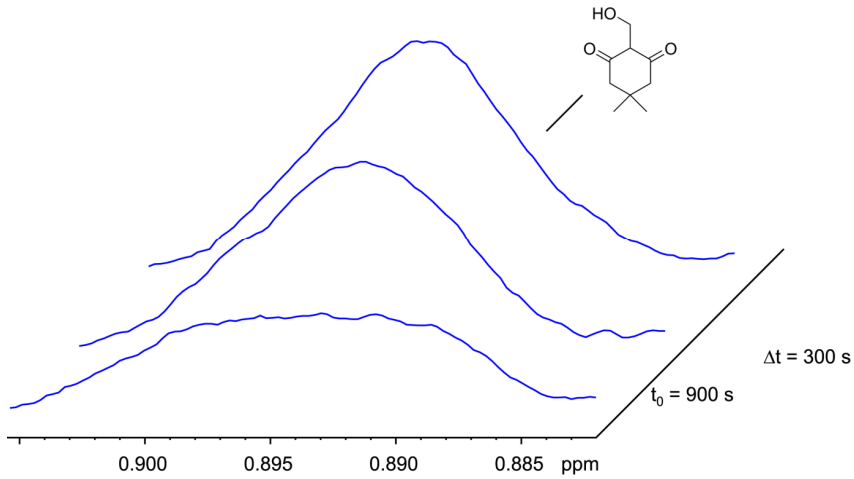

Figure 4.13 ^{1}H NMR spectra (700 MHz) of the reaction of KQLATKAARRme2aSAPAT, JMJD3, 2OG, ascorbate and ferrous iron in dAFN buffer, after addition of dimedone. The singlet resonance at δ_H 0.895 ppm is observed to increase in intensity over time.

The production of HCHO during the demethylation reaction was further implied by the observation of increased fluorescence intensity (at 460 nm) during analysis of the reaction by FDH. As with the experiments detailing the reaction of the asymmetric diemethylated R2 peptide with JMJD2E, it was possible to calculate kinetic parameters by monitoring the reaction of JMJD3 with the asymmetric dimethylated K27R peptide (at variable concentration) over initial time points (K_M = 68.36 ± 9.35 µM, V_{max} = 0.160 ± 0.006 µM s^{-1} and k_{cat} = 0.080 ± 0.003 s^{-1} respectively, Figure 4.14).

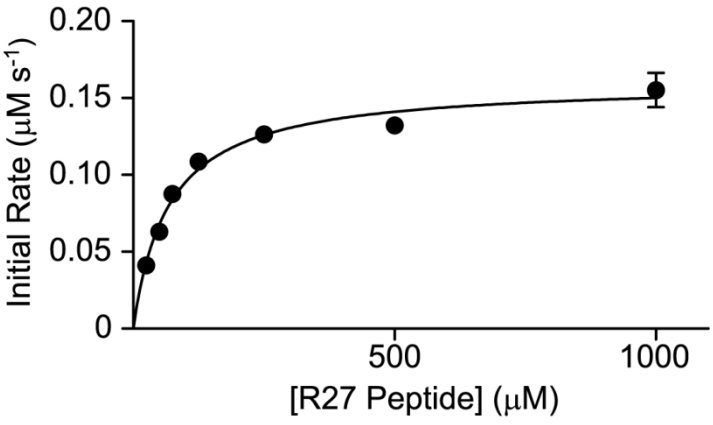

Figure 4.14 Dose-response curve for the reaction of KQLATKAARRme2aSAPAT with JMJD3.

As JMJD3 has been shown to demethylate asymmetric dimethylarginine, it was proposed that this enzyme may facilitate the hydroxylation of N^{ϵ}-methylisopropyllysine

in an analogous manner to that observed for JMJD2E. Such hydroxylation would give further credence to the hypothesis that these two species bind in similar conformations in the active site, and should also imply that demethylation occurs via initial hydroxylation. The mutated K27 peptide containing the modified lysine residue (sequence KQLATKAARKmeiprSAPAT) was synthesised and purified as described in Chapter 3, and the peptide was subsequently incubated with JMJD3 (2 μM), 2OG (50 μM), ascorbate (100 μM) and ferrous iron (10 μM). The reaction mixture was then analysed after one hour at 37 °C using MALDI mass spectrometry (Figure 4.15).

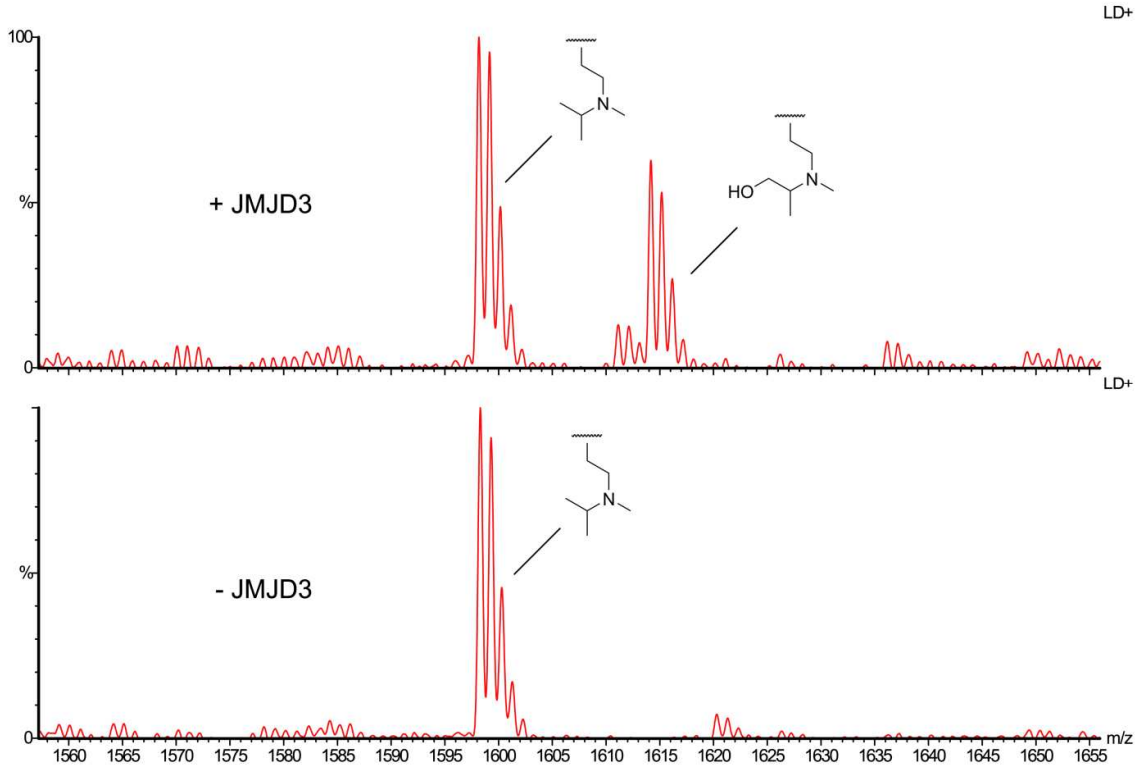

Figure 4.15 MALDI mass spectrum of a sample containing JMJD3 (2 μM), KQLATKAARKmeiprSAPAT (10 μM), 2OG (50 μM), ascorbate (100 μM) and ferrous iron (10 μM) after one hour at 37 °C. Hydroxylation of the substrate peptide can be clearly observed.

The MALDI mass spectrum indicated that a new species at mass 1615 m/z had been formed in the sample, which was assigned to the hydroxylated peptide. Therefore, it was apparent that JMJD3 is able to hydroxylate N^{ε}-methylisopropyllysine, presumably at the same position as that observed with JMJD2E. This observation therefore indicates that both JMJD2E and JMJD3 can accept methylated arginine and N^{ε}-

methylisopropyllysine in their active sites and can facilitate oxidation at the analogous positions on the substrates.

4.3 Conclusions and Future Work

Work in this Chapter describes the detection of arginine demethylation by three histone lysine demethylases (JMJD2A, JMJD2E and JMJD3). These findings provide the first conclusive evidence that demethylation of arginine can be achieved enzymatically (arginine demethylation by JMJD6 has been proved to be non-reproducible in this laboratory and elsewhere),[48, 51] and also imply that lysine and arginine demethylation may be performed by the same enzymes. MALDI experiments with JMJD2A and JMJD2E have suggested that these enzymes are able to demethylate known methylarginine marks on histone H3 and H4, indicating that, under certain conditions, the JMJD2 subfamily may facilitate histone arginine demethylation in cells. Time course and NMR experiments have also implied that demethylation of asymmetric dimethylarginine at H3R2 is more efficient than demethylation of the mutated K9R analogue. This finding, as well as the observed lack of demethylation of the R2Kme3 mutant peptide (sequence AKme3TKQTARKSTGGKA), may suggest that subtle differences in the preferred binding modes of methylarginine and methyllysine marks invoke variable demethylation propensities. Although demethylation of known histone marks was only observed for the JMJD2 enzymes, the most active demethylase with respect to arginine demethylation was JMJD3. This may indicate that JMJD3 (and potentially the JMJD2s) may facilitate arginine demethylation on non-histone substrates. More generally, this work suggests that arginine methylation (at least on histones) is likely to be dynamic and may rely on the reactivity of some lysyl demethylases.

The preliminary detection of 2OG demethylase-catalysed arginine demethylation has the potential to illuminate many new areas of epigenetic research. Of the many questions that this work raises, one of the most prominent must be whether 2OG demethylases are able to catalyse both lysyl and argininyl demethylation on histones in

cells. It should be noted at this stage that the asymmetric dimethylarginine mark at H3R2 is proposed to signal for transcriptional repression.[124] It is therefore intriguing that the JMJD2 enzymes, which remove the transcriptionally repressive H3K9 methyl mark, may also facilitate removal of H3R2 methylation.[13, 69, 75] It is also possible that targeting of specific lysine or arginine marks may be facilitated by interactions other histone binding domains. For example, the structures of JMJD2A-C possess multiple methylated lysine binding domains (two PHD domains and two tudor domains respectively), which may recognise specific marks on the histone tails.[183] These interactions may then orientate the catalytic domain of the demethylase toward a specific methylated arginine or lysine residue. This type of targeting pathway has already been proposed for the demethylase PHF8, which demethylates dimethylated H3K9 upon binding of trimethylated H3K4 by a PHD domain.[140, 171]

Future areas of investigation in this field rely on the conclusive characterisation of cellular arginine substrates for the lysyl demethylases. This work would require utilisation of cellular assays (such as fluorimetry and immunoprecipitation techniques) to identify biologically relevant substrates. Further experiments may then focus on determining the scope of arginine demethylation in cells, in the hope that this process may be essential for cellular homeostasis. For *in vitro* characterisation, it would be necessary to increase the intrinsic activity of the 'arginine demethylases' in order to acquire binding information and kinetic parameters. This may be facilitated by identifying better substrates for these enzymes.

Chapter 5

Probing the Role of Lysine-241 during JMJD2A-Catalysed Demethylation

5.1 Introduction

X-ray crystallographic studies on the JMJD2 subfamily of histone demethylases have revealed the presence of a structurally conserved lysyl residue.[67] This residue (labelled as K241 in JMJD2A, and named as such hereafter) is located in a potentially important position in the active site, close to not only the iron centre, but also to the methylated lysine substrate and molecular oxygen binding sites. It has therefore been hypothesised that K241 may play a role in one or more catalytically important processes during the demethylation reaction. Although present in all members of the JMJD2 subfamily, K241 does not appear to be conserved in other 2OG-dependent histone demethylases, suggesting that any catalytically important process involving this residue may be unique to the JMJD2 enzymes.

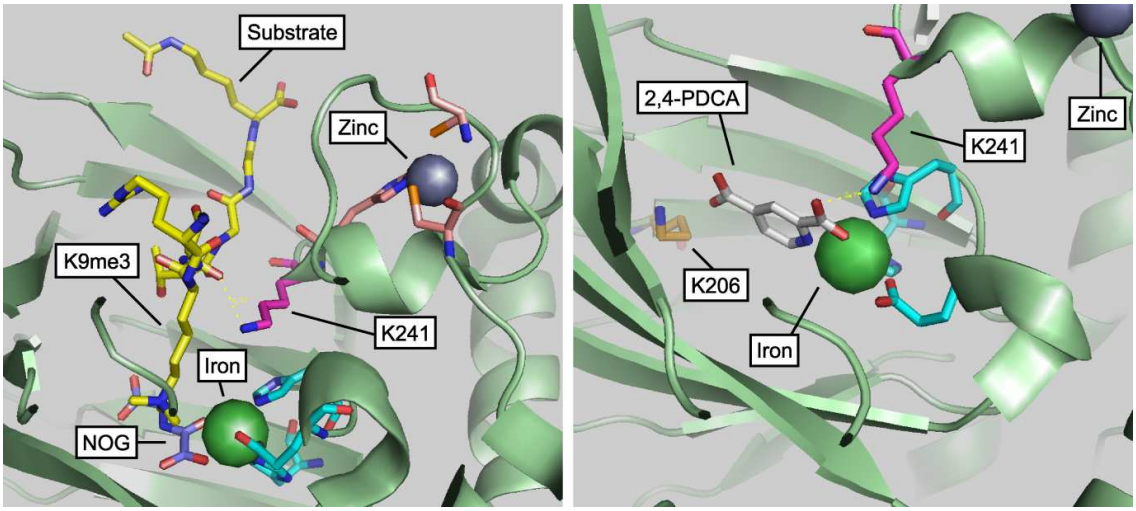

Figure 5.1 (Left) View from the crystal structure of JMJD2A complexed to *N*-oxalylglycine (NOG) and histone substrate. (Right) View from the crystal structure of JMJD2A complexed to 2,4-pyridine dicarboxylic acid (2,4-PDCA). K241 is highlighted pink in both structures.

5.1.1 Background

One potential role of K241 during demethylation has been inferred from X-ray crystallography data on JMJD2A. Work by Chen *et al*. identified a v-shaped region of electron density in the crystal structure of JMJD2A complexed with a histone peptide close to the iron centre in the active site.[67] This region was hypothesised to represent two discrete binding modes of oxygen, and therefore it was suggested that oxygen may be actively transported into the active site during demethylation. It was also noted that K241, which is positioned close to this region of electron density, has the potential to form hydrogen bonds to oxygen in both proposed binding modes, and therefore it was hypothesised that this residue may facilitate the transport of oxygen towards the iron centre. In order to investigate this hypothesis, the K241A and K241L variants of JMJD2A were produced and tested for demethylation activity. MALDI analyses revealed that both variants were inactive with respect to demethylation, consistent with a potential role of K241 in oxygen binding. Although these findings suggest that K241 is important for demethylation activity, a number of questions remain unanswered regarding its role during catalysis. Firstly, although a potential role in oxygen transport is supported by the observation of electron density close to the N^{ε}-group of K241, the

assignment of this density region to molecular oxygen may be considered somewhat ambiguous given the relatively low atomic resolution of the protein crystal structure (1.99 Å). Therefore, it is difficult to correlate the loss of activity in the K241 mutants solely to a loss in oxygen transport based only on the structural evidence. It can be envisaged that such a loss of activity may be due to a number of other factors besides oxygen transport as K241 is located in close proximity to the catalytic centre. For example, the N^{ε}-group of K241 is suitably close to the histone binding pocket to possess a hydrogen bond with the substrate, and therefore, K241 may be involved in either allowing suitably strong substrate binding, or in orientating the substrate into the catalytically active conformation. It should also be noted that K241 is positioned close to the structural zinc binding site, implying a potential role in stabilising protein structure.

5.1.2 Objectives

Work in this Chapter describes efforts to further investigate the role of K241 in JMJD2A-catalysed demethylation by analysing the structures and activities of wild-type JMJD2A and also of two novel K241-depleted mutants. It is hoped that these analyses will give new insights into the role of this residue during demethylation and also help to either confirm or disprove the hypothesised oxygen transport mechanism.

Cloning of the JMJD2A mutants was carried out by Dr. Nathan R. Rose. Expression and purification of the mutant proteins was done in collaboration with David Ivison. Protein mass spectra were acquired by Dr. Adam Hardy.

5.2 Results

5.2.1 Design of K241 Mutants

As K241 has been shown to be positioned close to the structural zinc and active site, it is proposed that mutation of K241 has the ability to affect both the structure and the catalytic mechanism of the protein. Therefore, it was important to select mutations at this position which would allow concise investigation of each of the potential effects of

K241 removal. Although previous work had utilised K241A and K241L substitutions, it was felt that substituting the lysine to more structurally similar residues would allow a more informative evaluation of the roles of K241 during catalysis. Therefore, two variants were chosen as shown in Figure 5.2.

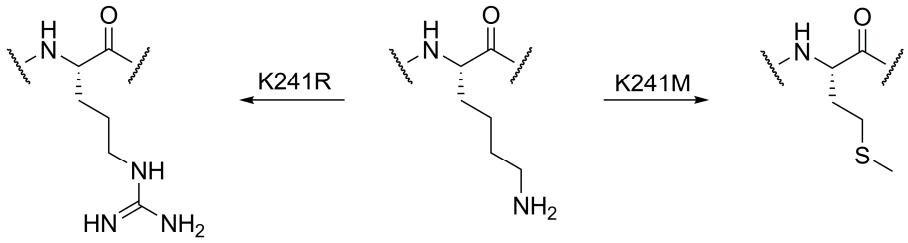

Figure 5.2 Mutations of K241 to arginine (left) and methionine (right).

Firstly, the residues chosen for substitution at K241 (arginine and methionine respectively) have similar side chain lengths to lysine. It was hoped, therefore, that any potential deviations in protein tertiary structure upon removal of such a long alkyl chain would be minimised. The substitution of lysine with arginine, in contrast to the mutations previously investigated, has the propensity to maintain hydrogen bonding/electrostatic interactions, and therefore may be still possess the ability to orientate the substrate and oxygen when bound in the active site. It should also be noted that the arginine side chain is slightly longer than lysine, which may result in steric clashes with the bound substrate. It is also possible that this increased length may facilitate an interaction with D191, blocking binding of the substrate. In contrast to arginine, the substitution of lysine with methionine removes the potential of hydrogen bonding, either to the histone substrate or to molecular oxygen. Therefore, this variant might give insight into the importance of both potential interactions during demethylation. Also, the methionine side chain is slightly smaller than that of lysine, implying that any steric clashes with the substrate might be avoided.

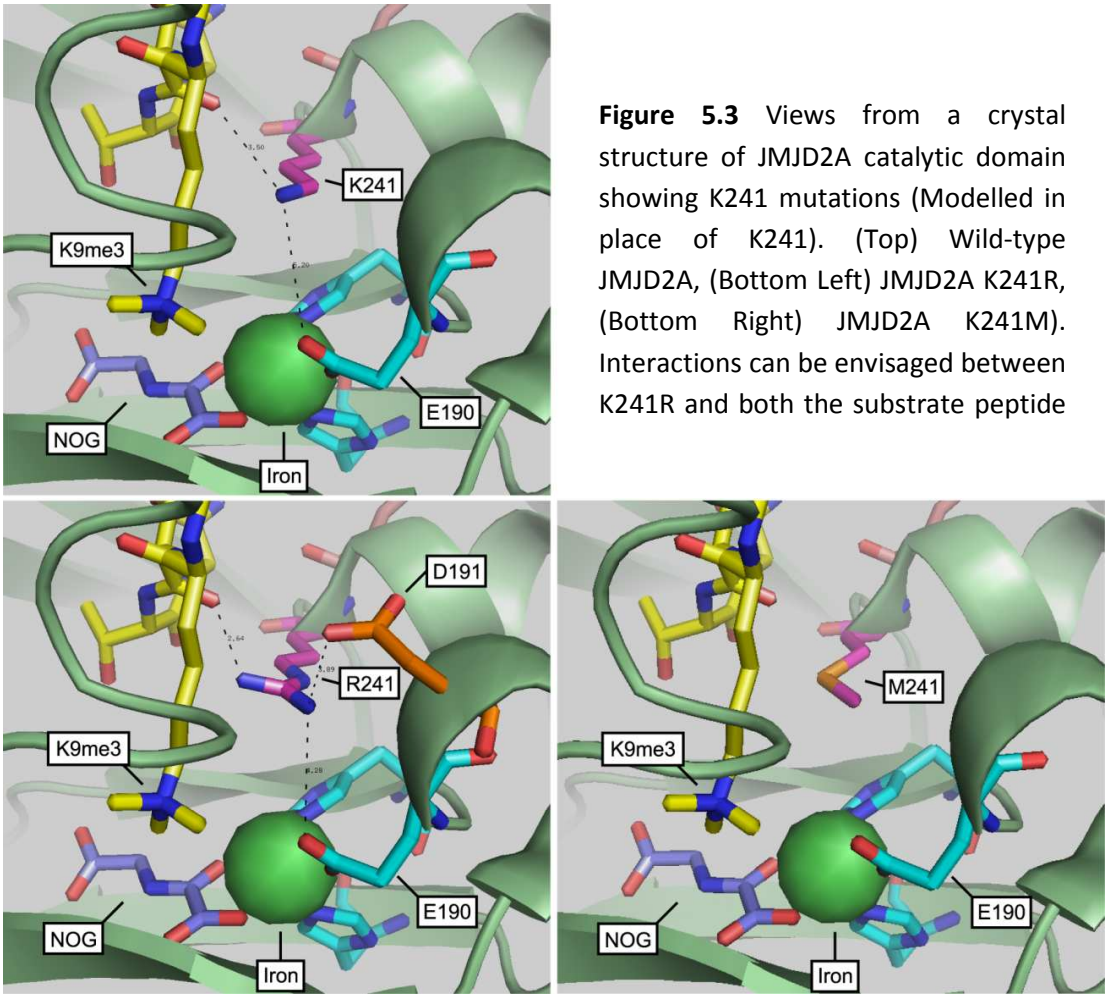

Figure 5.3 Views from a crystal structure of JMJD2A catalytic domain showing K241 mutations (Modelled in place of K241). (Top) Wild-type JMJD2A, (Bottom Left) JMJD2A K241R, (Bottom Right) JMJD2A K241M). Interactions can be envisaged between K241R and both the substrate peptide

5.2.2 Mutagenesis, Expression and Purification of Mutants

Point substitutions at K241 were achieved using the Quick-Change® (Stratagene) protocol (*Dr. Nathan R. Rose*). The mutated plasmid DNA was then transformed into *E. coli* BL21 (DE3) competent cells by heat-shock treatment and expressed in 2TY media in a manner analogous to that used for wild-type JMJD2A. Starter cultures were grown at 37 °C overnight and were then used to inoculate larger flasks of 2TY media. After reaching an OD_{600} of 0.6, protein expression was induced in the larger flasks by the addition of isopropyl-β-D-thiogalactopyranoside (IPTG, 0.5 mM). The flasks were then incubated overnight at 15°C before the cells were harvested by centrifugation. After storage overnight at -80°C, the cells were lysed by sonication and the expressed proteins were purified via affinity chromatography, which resulted in the acquisition of the proteins in high purity (greater than 90 % by SDS-PAGE analysis, Figure 5.4).

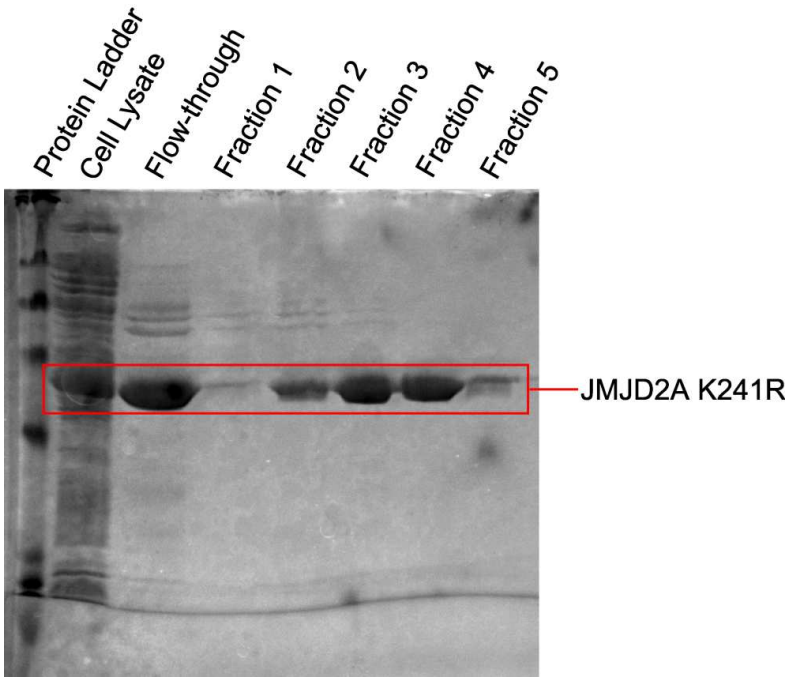

Figure 5.4 SDS-PAGE gel indicating purification of JMJD2A K241R via affinity chromatography.

In order to assess the purity of the acquired variants, and also to confirm that the mutations had been incorporated into the proteins, mass spectra of the variant proteins were obtained under denaturing conditions using a LCT mass spectrometer. Each spectrum appeared to contain one protein in large excess affirming the purity of samples. The masses of these major proteins correlated to the expected masses of the variants (Figure 5.5).

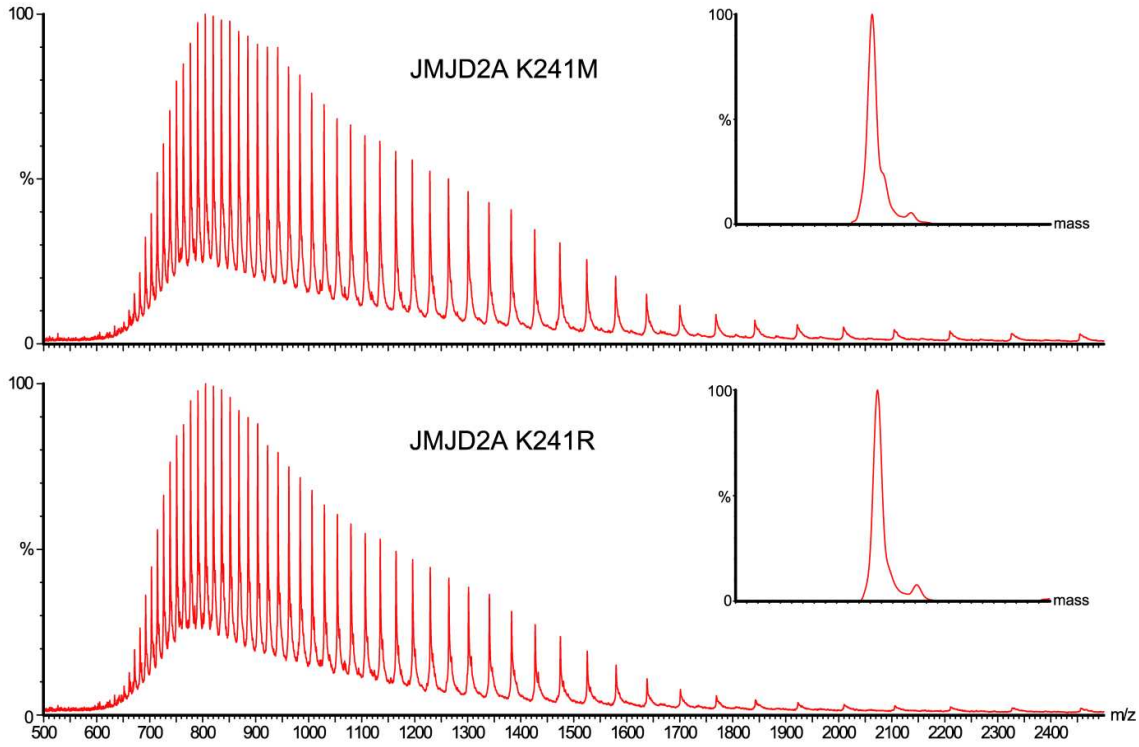

Figure 5.5 Denaturing MS spectra of JMJD2A K241M (above) and JMJD2A K241R (below).

5.2.3 Probing Structural Integrity

It was envisaged that changes in protein structure upon substitution of K241 may be a cause of inactivation, and therefore studies analysing the structure of the two variants were undertaken in order to evaluate any structural deviation. Analysis was carried out using circular dichroism and zinc ejection techniques, as described below.

a) Circular Dichroism

Circular dichroism (CD) analysis allows evaluation of both secondary (the far-UV region, 200-220 nm) and tertiary (the near-UV region, 250-300 nm) structure elements, and consequently, it was envisaged that comparing the CD spectra of the variant proteins with wild-type JMJD2A would give valuable information regarding the structural integrity upon removing K241. Spectra of the substituted and wild-type proteins were obtained under identical conditions

using a CD spectrophotometer and were then superimposed in order to identify any differences in the structures of the proteins (Figure 5.6).

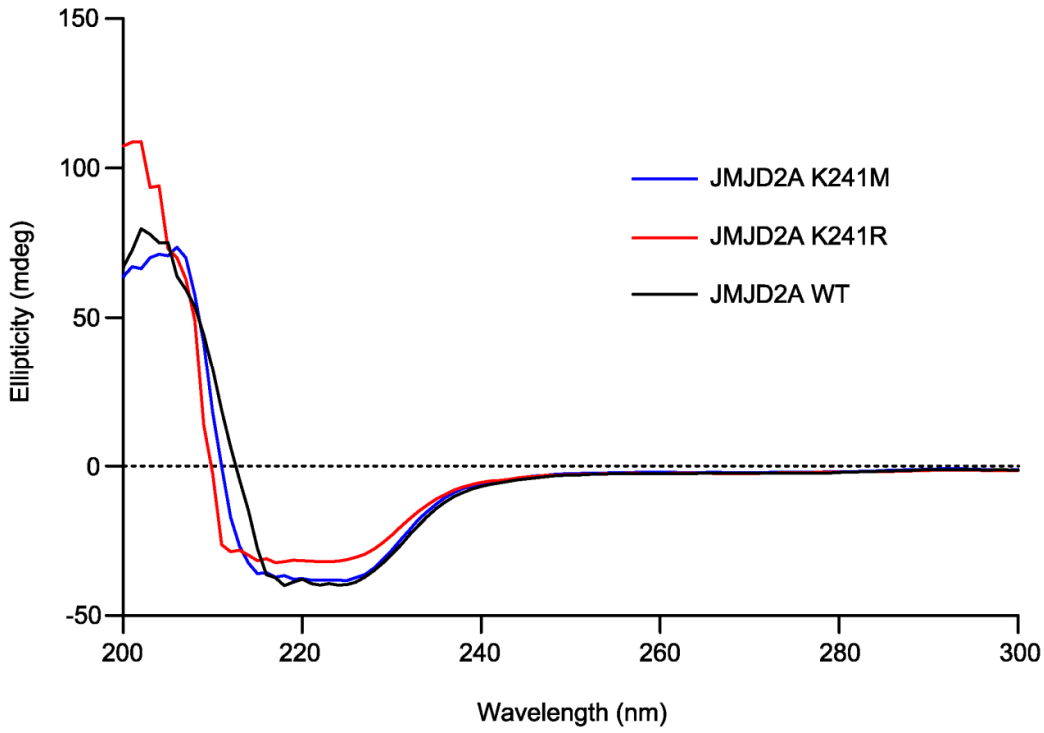

Figure 5.6 CD spectra of JMJD2A K241M (blue), JMJD2A K241R (red) and wild-type JMJD2A (black).

Firstly, it was apparent that both variants likely possess folded structures due to the presence of non-zero ellipticity in their CD spectra. Non-folded protein would be expected to show a constant ellipticity of zero in the CD spectrum due to the loss of regular secondary and tertiary structure. However, the spectra over the far-UV region suggest that the variants possess slightly different secondary structure relative to each other, although in the case of the K241M mutant, the spectrum matched closely to the corresponding region of the wild-type spectrum. In this preliminary study, the far-UV spectrum of the K241R mutant differed from both the mutant and wild-type spectra; however, this variation may be at least partially due to the relatively high noise in this region of the spectrum. As K241 is not thought to possess bonding interactions with other residues within the JMJD2A catalytic domain, it can be envisaged that altering

this residue to methionine, which is smaller than lysine and unable to facilitate hydrogen bonding, does not significantly affect secondary structure. Conversely, substituting lysine with the larger arginine may alter the structure by inducing new bonding interactions with active site residues, such as D191 (Figure 5.3). The near-UV regions of the CD spectra, which can give information on the tertiary structure of proteins, were identical in the two variants and the wild-type. This may suggest that any deviations in the secondary structure of the K241R mutant do not significantly affect the overall fold of the protein, although, given that the signals in this region are very low, the data are inconclusive in this regard.

b) Zinc Ejection

The integrity of zinc binding in the JMJD2A mutants was also investigated by evaluating the degree of zinc ejection by the known zinc ejector compound Ebselen. This compound has been shown to remove zinc from the active site of JMJD2A, thus rendering the enzyme inactive to histone demethylation (Scheme 5.1).[184] Therefore, the enzymes were treated with Ebselen and the subsequent reactions were monitored using a fluorimetry based zinc ejection assay in order to ascertain whether the mutants are able to bind zinc, and also whether any bound zinc is susceptible to Ebselen-induced ejection,.[184] Removal of zinc from the enzyme was monitored by measuring the fluorescence of the zinc chelator FluoZin-3^{TM} (FZ-3) after addition of Ebselen. The relative stability of zinc binding was then evaluated by comparing the data with the wild-type control.

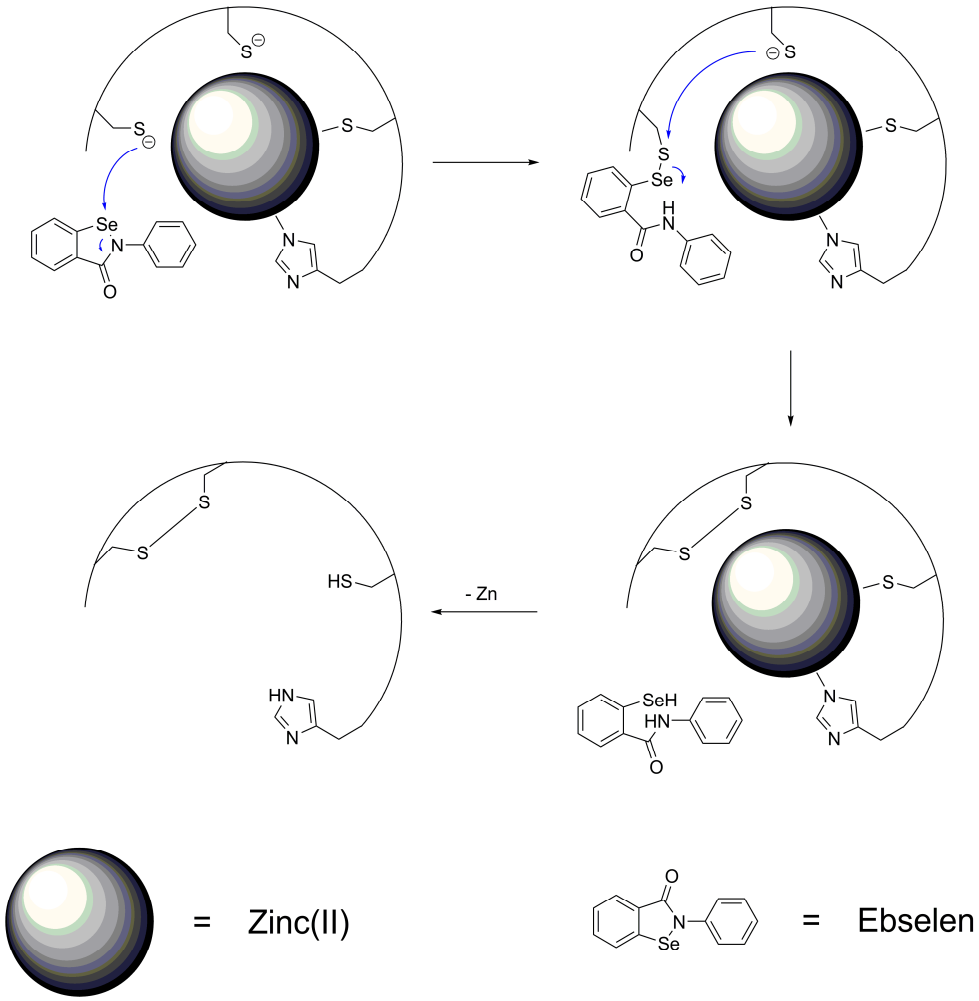

Scheme 5.1 Potential mechanism of zinc ejection by Ebselen.

The ejection reactions revealed a significant increase in emmitance intensity for the K241R and K241M variants, indicating that both possess zinc ions in their structures (Figure 5.7). After one hour, the largest emitance intensities were observed for the K241 variants. Given that larger emitance signals correlate to the efficient release of zinc (therefore resulting in the increased formation of the FluoZin-3^{TM} zinc complex), it can thus be suggested that the variants, although being able to bind zinc, may possess somewhat compromised zinc binding sites relative to the wild-type protein. However, further studies are required to verify this proposal. Although it is apparent that removal of the lysine at position 241 has a detrimental effect on zinc site integrity (at least when mutated to arginine and methionine), the mechanisms by which the binding of zinc is compromised

are difficult to establish. It is possible that interactions of the substituted side chains result in small conformational changes of the zinc site ligands, thus resulting in weaker binding. Also, K241 may be involved in inhibiting zinc removal by providing a hydrophilic environment close to zinc site, repelling potential zinc ejectors. Although both explanations are plausible at this stage, more experimentation is needed to confirm the role K241 plays in maintaining the zinc site.

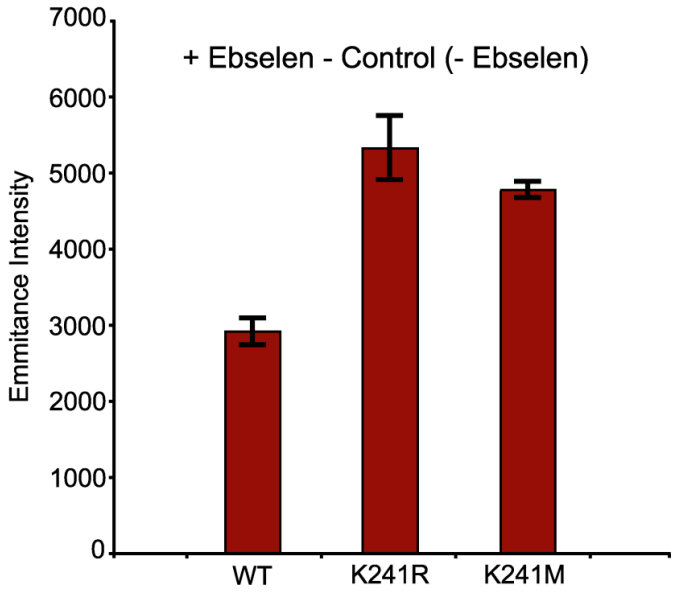

Figure 5.7 Emmitance intensities at 520 nm of samples of wild-type JMJD2A, JMJD2A K241R and JMJD2A K241M with ebselen and FluoZin-3^{TM} after one hour. The intensities from the control sample (ie. Enzyme and FluoZin-3^{TM}) are subtracted.

5.2.4 Activity Studies

a) Succinate Formation

Although previous work on K241A and K241L variants reported a loss of demethylation activity, no experiments probing variant-catalysed succinate formation were described. Assuming K241 is involved in recruiting molecular oxygen into the active site, formation of succinate via oxygen dependent 2OG oxidation would likely be inhibited upon removal of K241, as it could be assumed (at least in the case of the K241A, K241L and K241M mutants) that

oxygen would not be able to reach the iron centre. Therefore, investigating this reaction was expected to offer valuable insights into the role of K241 in a potential oxygen transport mechanism. Succinate formation was analysed in two samples containing the variant proteins (one per sample), 2OG, ferrous iron and sodium ascorbate in deuterated ammonium formate buffer. After mixing, the samples were transferred to 2 mm NMR tubes and monitored using ^{1}H NMR. The ^{1}H NMR spectra of the mutant samples over the first hour of reaction exhibited a singlet resonance at δ_H 2.37 ppm, which was assigned to the CH_2 protons of succinate. It was therefore concluded that both K241 mutants were able to catalyse the oxidation of 2OG to succinate, presumably via an analogous mechanism to the wild-type protein.

In order to ascertain the relative activities of the proteins with respect to succinate formation, the intensities of the succinate signals were plotted as a function of time for each variant and compared against analogous time-course data with the wild-type protein (Figure 5.8). The resulting data appeared to suggest that the variant proteins were slightly more active than the wild-type, perhaps indicating that K241 has a role in regulating catalytic activity.

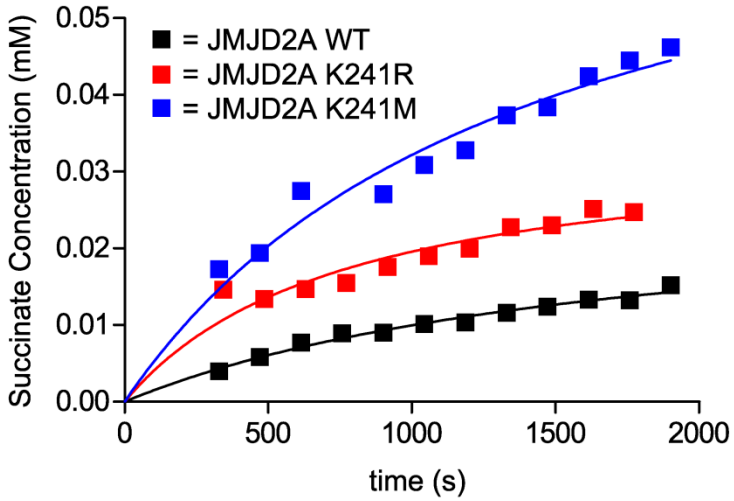

Figure 5.8 Variation in succinate concentrations over time in samples containing wild-type JMJD2A (black), JMJD2A K241R (red) and JMJD2A K241M (blue).

b) Histone Peptide Demethylation

The observation that the two variants are able to catalyse the oxidation of 2-oxoglutarate to succinate indicated that the variants may be able to catalyse demethylation of histone peptides. Experiments containing histone peptides trimethylated at H3K9 (sequence ARKme3STGGK) were analysed using both MALDI-TOF mass spectrometry and NMR in order to probe the extent of demethylation (Figure 5.9).

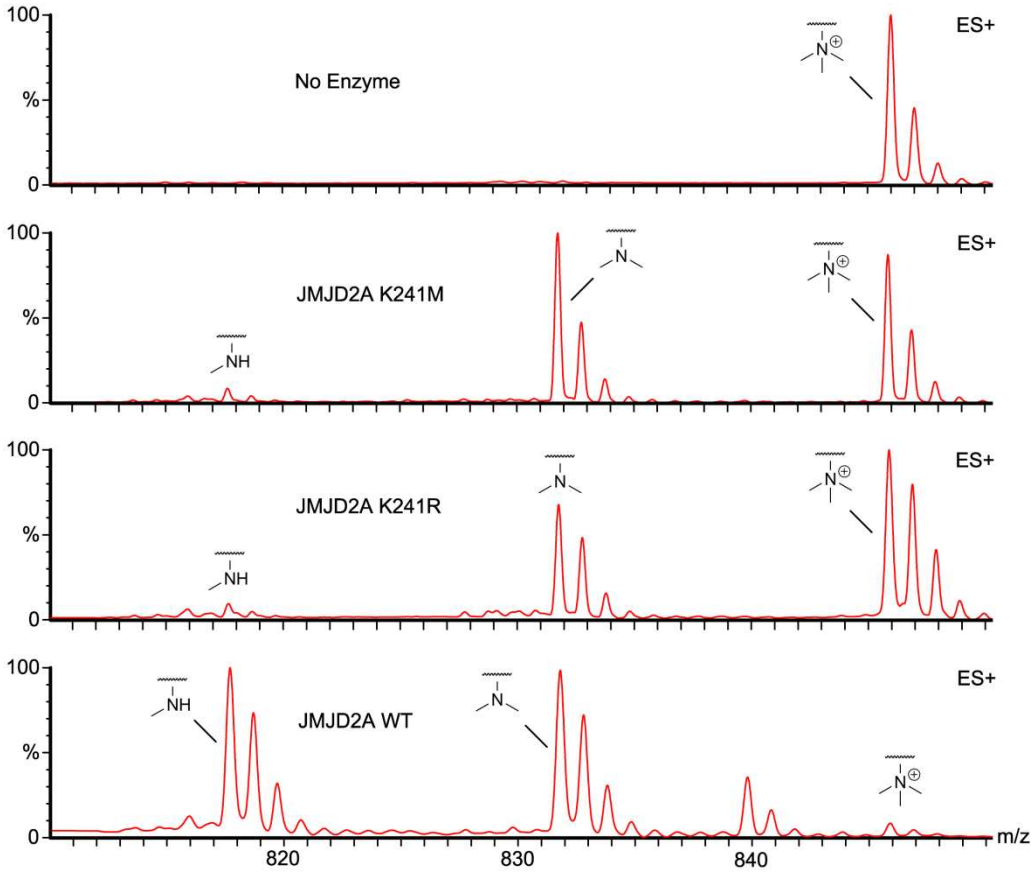

Figure 5.9 MALDI-TOF spectra probing the demethylation of the histone peptide ARKme3STGGK by wild-type JMJD2A and K241 mutants after one hour at 37 °C. The peak at 841 m/z corresponds to the sodium adduct of the monomethylated peptide.

MALDI Analysis of the samples containing wild-type JMJD2A revealed that the substrate peptide had been almost completely demethylated after one hour at 37 °C. Both the dimethylated and monomethylated products were observed at equivalent concentrations in the samples, suggesting that some of the

dimethylated species had been subsequently demethylated to the monomethyl form. Interestingly, demethylation of the trimethylated peptide was observed for both variants by MALDI analysis, although in both cases, demethylation activity appeared to be significantly lower than in the wild-type samples. The major demethylation product in the variant containing samples was the dimethylated peptide (the monomethylated peptide was observed in trace amounts), indicating that the variants possessed low affinities for the dimethylated peptide. Also, only roughly 50 % of the trimethylated peptide appeared to have reacted in the variant containing samples, with the K241M variant appearing to be slightly more active.

The fact that the demethylation activity of the variants was lower than that of the wild-type protein appeared to contradict the corresponding data on succinate formation. Therefore, ^{1}H NMR experiments were carried out in order to compare the propensities of both succinate formation and peptide demethylation in order to confirm the findings from the previous experiments. NMR samples were prepared in an analogous manner to the samples in Section 5.2.1.a, except that in the new samples, the 8-mer trimethylated peptide substrate (sequence ARKme3STGGK) was added to the mixture. The samples were then monitored by ^{1}H NMR, which allowed simultaneous observation of both succinate formation (by observing the singlet resonance at δ_H 2.35 ppm) and peptide demethylation (by observing a singlet resonance at δ_H 2.81 ppm, corresponding to the N^{ε}-dimethyllysine residue). The intensities of these characteristic signals were then normalised and compared. The spectra after 30 minutes are shown in Figure 5.10.

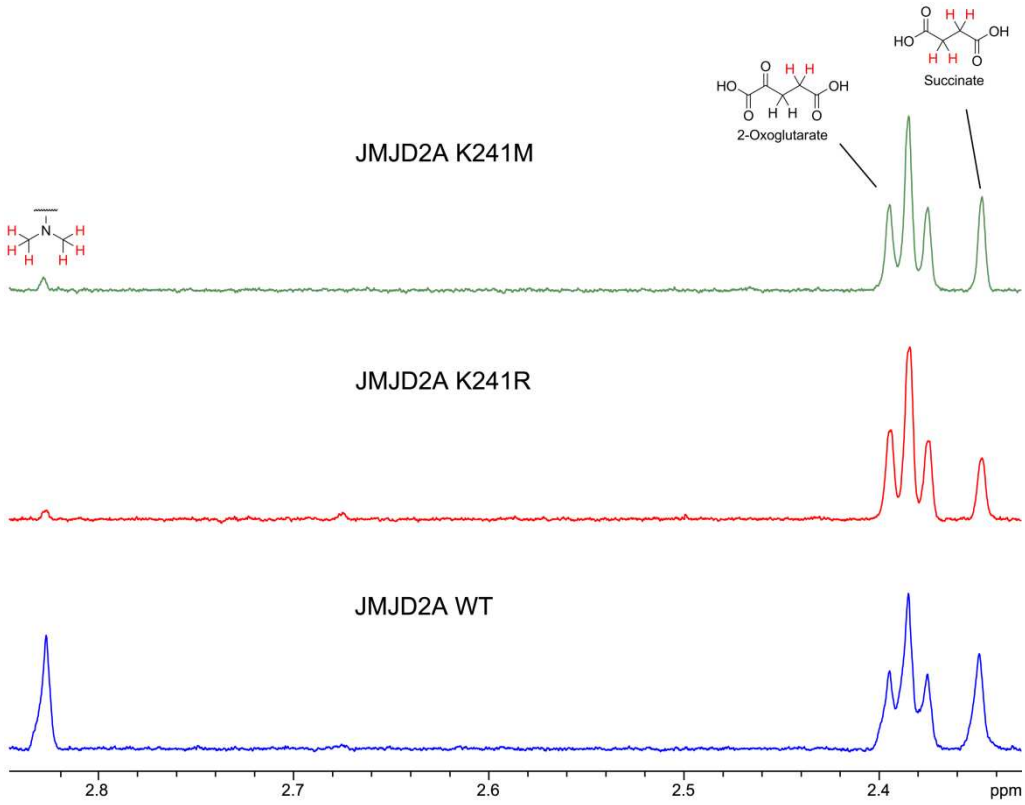

Figure 5.10 ^{1}H NMR spectra (700 MHz) monitoring succinate formation and peptide demethylation by wild-type JMJD2A (bottom), JMJD2A K241R (middle) and JMJD2A K241M (top) in dAFN buffer. Signals corresponding to 2OG, succinate and N^{ε}-dimethyllysine are highlighted.

Demethylation of the peptide substrate was observed in all samples after 30 minutes, reaffirming the demethylation activity observed by MALDI analyses. Also, demethylation appeared to be more efficient in the sample with wild-type protein, which correlated with the MALDI data. However, the coupling ratio (i.e. the degree of peptide demethylation versus overall succinate formation) varied greatly in the samples (Figure 5.11).

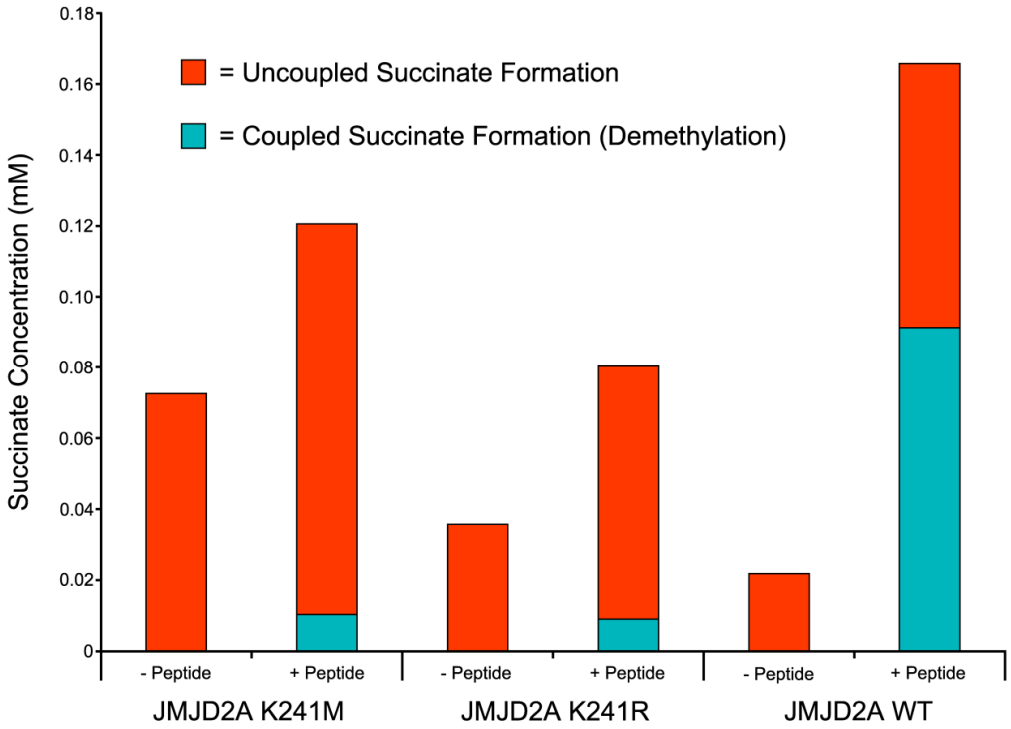

Figure 5.11 Succinate concentrations in samples of wild-type JMJD2A (right), JMJD2A K241R (middle) and JMJD2A K241M (left) with and without peptide substrate after 30 minutes.

All three JMJD2A variants tested (K241R, K241M and the wild-type) catalysed peptide demethylation and 2OG oxidation in the NMR experiments. Although the overall 2OG turnover in the samples with added peptide was greatest in the sample containing the wild-type protein, it was noted that the succinate concentrations in the samples containing the K241 variants after 30 minutes were significantly higher than the concentrations of dimethylated peptide (no subsequent demethylation of the dimethylated peptide was observed). These observations imply that the majority of catalytic cycles facilitated by the variants do not result in peptide demethylation. However, the concentrations of 'uncoupled' succinate formed in the samples containing the peptide (calculated by subtracting the concentrations of the demethylated peptide from the overall succinate concentrations) was greater than the overall succinate concentrations in the corresponding samples omitting peptide. Therefore, it appears that uncoupled 2OG turnover is accelerated in the presence of peptide, suggesting

that the peptide may be able to bind to the protein (thus stimulating formation of the iron (IV) intermediate), but is not efficiently demethylated. This suggests that K241 is involved in orientating the peptide substrate within the active site, without effectively increasing the peptide binding propensity; however, further experimentation is required before the role K241 plays in peptide binding can be verified.

Overall, the NMR and MALDI data have shown that K241R and K241M variants of JMJD2A are capable of catalysing both the conversion of 2OG to succinate and also the demethylation of histone peptides. The rates of variant-catalysed succinate formation were found to be comparable to the wild-type protein; however, the variants appeared to be significantly less active with respect to peptide demethylation. These findings suggest that K241 is unlikely to be involved in an oxygen transport process during catalysis as such a mechanism would be expected to be impeded upon removal of K241 (particularly in the case of a K241M mutation), resulting in a loss of activity. Also, the low demethylation activity relative to succinate formation may indicate that catalytically active binding of the substrate peptide is prohibited in the K241 variants, presumably due to either subtle changes in active site geometry, or the loss of hydrogen bonding with the substrate.

5.3 Conclusions and Future Work

Work in this Chapter has concentrated upon investigating two JMJD2A K241 variants, which has offered new insights into the roles K241 plays during histone demethylation. Structural and activity studies showed (at least with the two variants tested) that substitution of K241 resulted in folded protein, which was able to catalyse both succinate formation and, surprisingly, histone peptide demethylation. These findings argue against a role for K241 in oxygen transport (as previously proposed) and suggest that this residue may be involved in binding the histone substrate, thus mediating demethylation.

Regarding future experiments, it should first be noted that the demethylation activity data presented using the K241R and K241M variant proteins conflict with analogous data with the previously described K241A and K241L variants. Therefore, any future experimentation could initially focus on cloning and expressing these proteins and ascertaining whether any enzymatic activity can be observed. Also, detailed kinetic analyses of variant catalysed demethylation and 2OG turnover would assist in confirming the observations from the time-course experiments, and therefore give a concise appraisal of K241 function. Also, more experimentation is required to conclusively ascertain the affinity of the variant proteins for histone substrates and also to probe the nature of any interactions that exist between the substrate and the mutated active sites. Quantitative analysis of binding affinity may be achieved using isothermal titration calorimetry (ITC); however, experimentation using this method may be impeded by the requirement for large amounts of protein and peptide substrate. Crystal structures of the mutants bound to the substrate might give good indication of the nature of substrate binding in the active site, and therefore confirm whether an alteration in binding mode occurs upon removal of K241. However, the requirement for large protein and peptide quantities during crystallisation screening may also hamper this approach.

In addition to regulating substrate binding, it is also possible that K241 may be important for maintaining enzymatic activity by other mechanisms. For example, increased stability of the zinc site was observed in the wild-type relative to the two mutant proteins, suggesting that K241 may be involved in maintaining the integrity of zinc binding. Crystal structures of the two variants would be useful for investigating this hypothesis, as changes in the zinc site could be identified easily by comparing the structures with that of the wild-type protein. It may also be useful to investigate whether the previously observed ‘v-shaped’ region of electron density is present in the variant structures in order to assist in the assignment of this region of the structure. Additionally, it was noted that the K241M mutant appeared to have a stronger affinity for ferrous iron than both the K241R mutant and the wild-type, indicating that mutating

K241 to a smaller, non-polar residue may lead to stabilised iron binding. This finding should be confirmed by binding studies (possibly by ITC) before any further experimentation; however, it may be interesting to investigate the role of K241 in iron binding by measuring the affinity of iron in a variety of K241 variants.

Chapter 6

Investigating Cleavage of Histone Peptides *in vitro*

6.1 Introduction

The experiments in Chapters 3 and 4 identified a number of novel oxidative reactions catalysed by histone demethylases. In addition to these reactions, the work with FBXl11 using MALDI mass spectrometry also detected another transformation in the samples, i.e. apparent cleavage of the histone peptides. Although it was proposed that this cleavage was most likely facilitated by protease impurities in the enzyme sample, it was considered that demethylases may possess the ability to hydrolyse peptide bonds, possibly by metal dependent oxidative or non-oxidative pathways. There is precedent for oxidative cleavage from work with aminocyclopropanecarboxylate oxidase, which is closely related to the 2OG oxygenases and catalyses fragmentation in an Fe(II), oxygen and ascorbate dependent manner.[185] Also, the cysteine protease Cathepsin L has been implicated in site specific cleavage of histone H3, which is postulated to play some role in chromatin structure regulation.[186, 187] Therefore, if the observed transformation were confirmed as evidence for fragmentation, the biological implication would be very interesting. Further studies were carried out in order to characterise the nature of the transformation and also to identify the enzyme(s) responsible, as described below.

Experiments with PHF8 were performed by Louise Walport. MALDI-MS/MS was carried out by Dr. Holger Kramer.

6.2 Results

6.2.1 Initial Detection of Cleavage

Peptide cleavage was first observed on a N^{ϵ}-diethyllysine containing peptide synthesised for work described in Chapter 3 (sequence PATGGVKet2KPHRY). Incubation of this peptide with the demethylase FBXL11 (a K36 demethylase) was expected to potentially result in oxidative catalysis on the N^{ϵ}-ethyl groups, producing either deethylated or hydroxylated products. Although MALDI analysis of the sample containing both the crude peptide and FBXL11 (as well as 2OG, ascorbate and ferrous iron, see Chapter 3) did not indicate either of these transformations, a new peak in the spectrum at 698 m/z was observed (Figure 6.1). The mass of this peak corresponded to the expected molecular ion of the peptide KPHRY, suggesting that either the substrate peptide or an impurity had been hydrolysed. Although the peptide was too impure to allow conclusive assignment of the hydrolysed species, the relative intensities of the substrate peak and that of the most abundant impurity (the point deletion peptide PATGGVKPHRY) suggested that the substrate was the most likely species being cleaved.

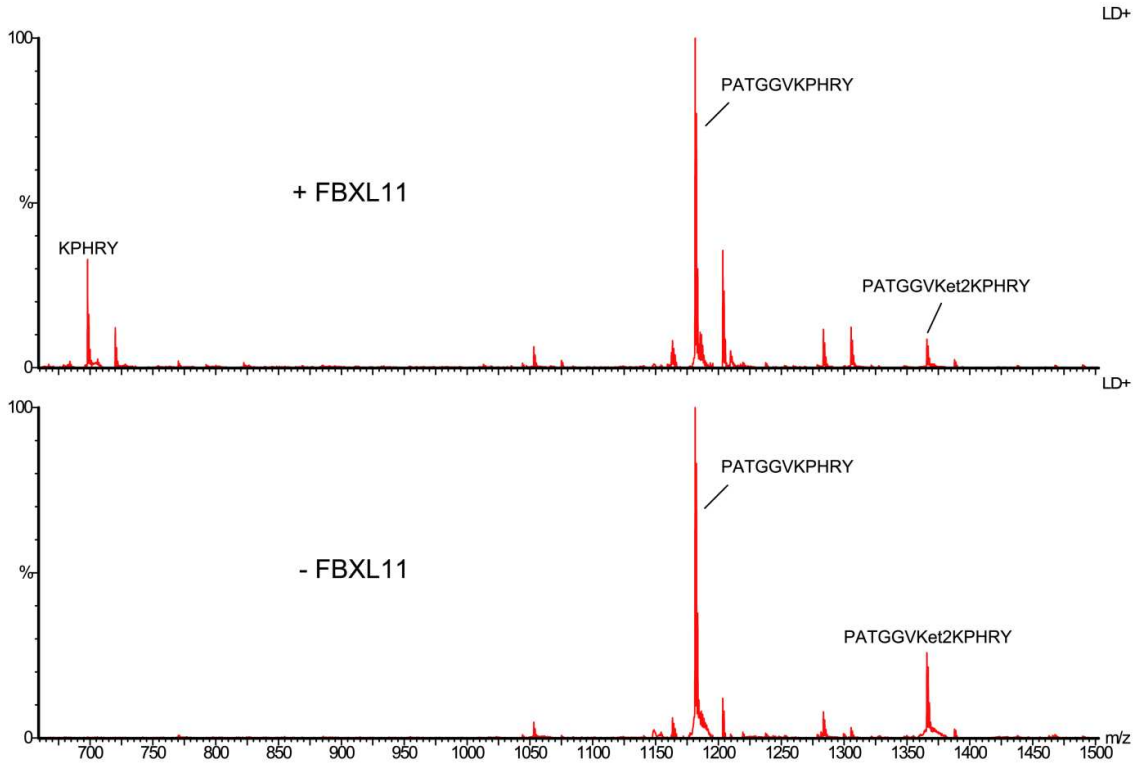

Figure 6.1 MALDI mass spectra of a sample containing FBXL11 (1 µM), PATGGVKet2KPHRY (10 µM), 2OG (50 µM), ascorbate (100 µM) and ferrous iron (10 µM) after 30 minutes at 37 °C. The control experiment without enzyme is shown below.

Experiments using another batch of FBXL11 protein (the same construct, prepared at the Structural Genomics Consortium in Oxford, UK) also indicated formation of the species at 698 m/z. In this sample, however, the overall cleavage appeared to be significantly less (< 10 % overall peptide cleaved after 30 minutes), implying that cleavage activity may be strongly batch dependent.

6.2.2 MS/MS Analysis

In order to confirm that peptide cleavage had occurred in the sample, MS/MS analysis of the species at mass 698 m/z was undertaken. It was hoped that analysing the fragmentation pattern of this species would enable the assignment of its amino acid sequence, and therefore allow its identification. A sample containing the new species was fragmented using a Bruker MALDI-TOF-TOF mass spectrometer, which allowed detection of new peaks corresponding to the peptide fragments (Figure 6.2).

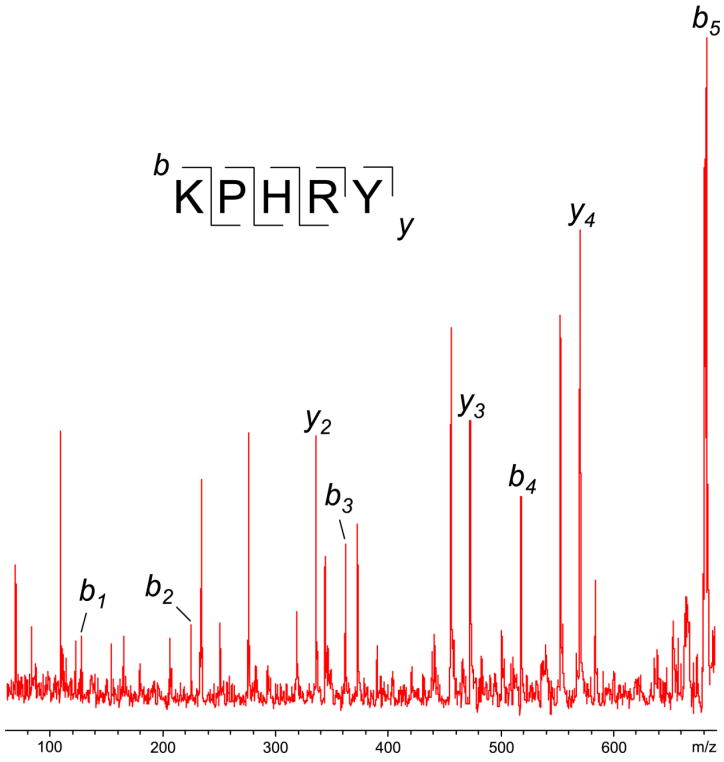

Figure 6.2 MALDI MS/MS spectrum of the species at 697 m/z. Identified fragment ions are highlighted.

Although the MS/MS spectrum revealed many peaks, it was possible to identify all the expected B ions, and also three of the expected Y ions (corresponding to $[PHRY]^+$, $[HRY]^+$ and $[RY]^+$) of the peptide KPHRY. These findings strongly suggest that the peptide is derived from the *C*-terminal portion of the substrate peptide, cleaved immediately after the modified lysine (between K36 and K37). Although the mass spectrometry data did not give any evidence of an oxidative cleavage mechanism (for example by identifying desaturation or hydroxylation of the *C*-terminal fragment), it was noted that the proximity of the cleavage site to the substrate lysine may indicate that hydrolysis is catalysed by FBXL11. It was also intriguing that the *N*-terminal portion of the substrate could not be detected in the MALDI mass spectra, possibly implying that the mechanism of cleavage may result in further degradation of this species.

6.2.3 Cleavage of a N^{ϵ}-Dimethyllysine Peptide

In order to fully characterise the formation of the peptide KPHRY during incubation with FBXL11, it was important to confirm whether the cleavage product was derived from the substrate peptide, and also to probe whether the cleavage reaction is dependent upon the presence of N^{ϵ}-diethyllysine. Therefore, the standard 12-mer N^{ϵ}-dimethyllysine containing peptide (sequence PATGGVKme2KPHRY) was incubated with FBXL11 and analysed over a wide mass region in order to detect any cleavage products. The peptide was synthesised and purified to over 90 % purity (by preparative HPLC), and therefore, it was expected that any observed cleavage products in the reaction mixture would derive from this species. Also, cleavage of the natural substrate (albeit a truncated peptide) may suggest that this reaction has the potential to occur in cells. The MALDI mass spectrum of the reaction after 30 minutes incubation at 37 °C is shown in Figure 6.3.

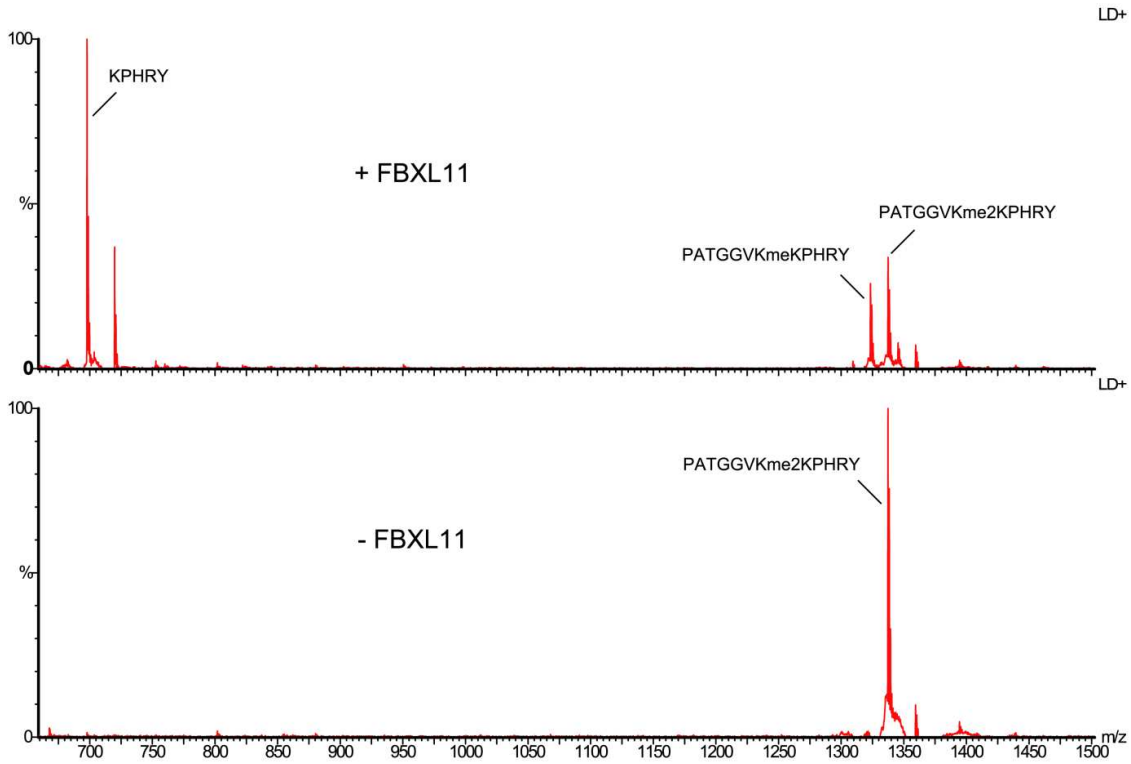

Figure 6.3 MALDI mass spectra of a sample containing FBXL11 (1 µM), PATGGVKme2KPHRY (10 µM), 2OG (50 µM), ascorbate (100 µM) and ferrous iron (10 µM) after 30 minutes at 37 °C. The control experiment without enzyme is shown below.

Cleavage of the dimethyllysine peptide was observed in the MALDI mass spectrum after 30 minutes, indicating that peptide bond hydrolysis is not dependent upon the presence of an N^{ϵ}-ethyl group on the lysine. Over 50 % of the substrate peptide appeared to have been hydrolysed during the reaction period; however, significant demethylation (forming the monomethyl 12-mer peptide) had also occurred. The fact that no reaction was observed on the diethyllysine peptide during the work described in Chapter 3 may imply that the peptide does not bind the enzyme in a catalytically active conformation. This may suggest that the peptides can bind in different modes during demethylation and cleavage, or that the cleavage of this peptide is catalysed by a proteolytic impurity in the enzyme sample. Cleavage was also observed in a sample containing the *N*-terminally biotinylated dimethyllysine peptide Bn-PATGGVKme2KPHRY (*provided by Dr. Akane Kawamura*), suggesting that larger groups on the *N*-terminal do not significantly affect the cleavage reaction. This peptide is known to bind FBXL11 and is used for determining kinetic parameters (of demethylation) using a fluorescence based Alpha-screen activity assay. The fact that the *N*-terminal fragment of this peptide (Bn-PATGGVKme2) is not expected to be a substrate for FBXL11, and also that this fragment is able to bind the donor and acceptor beads used for determining demethylation activity by Alpha-screen (assuming no further degradation), it is possible that the cleavage reaction may result in erroneous kinetic data being collected. Interestingly, Alpha-screen data using the *C*-terminally biotinylated peptide SAPATGGVKme2KPHRYRPGTVAL-Bn (*Dr. Akane Kawamura*) revealed a loss of fluorescence intensity upon incubation with FBXL11. This may suggest that this peptide is also cleaved, resulting in a loss of fluorescence caused by separation of the biotin from the modified lysine.

6.2.4 Dependence on 2OG and ascorbate

The cleavage observed in the samples containing FBXL11 suggested that peptide bond hydrolysis may proceed via an oxidative pathway. In order to investigate this hypothesis, the cleavage reaction was carried out in the absence of the co-substrate 2OG. It was expected that removal of this species from the reaction mixture would

inhibit the formation of the catalytic Fe(IV) intermediate in the enzyme active, which is proposed to facilitate oxidation of the substrate peptide. Therefore, the presence of cleavage in the absence of 2OG should indicate that peptide bond hydrolysis occurs via a non-oxidative mechanism. Interestingly, cleavage of the peptide was not affected upon removal of 2OG, suggesting that an Fe(IV) species is not involved in hydrolysis.

The observation that cleavage is probably not dependent upon oxidation was further endorsed by experiments carried out in the absence of ascorbate. Because ascorbate is known to increase the oxidative activities of many 2OG oxygenases (possibly by providing a reducing environment in the reaction mixture, see Chapter 2), it was proposed that any effect on the cleavage reaction by ascorbate would indicate a redox mechanism. No effect in the extent of cleavage was observed upon the removal of ascorbate, implying that cleavage is independent of ascorbate action.

6.2.5 Dependence on Fe(II)

Although the cleavage of histone peptides did not appear to rely on oxidation catalysed by FBXL11, it was noted that the demethylase may still be able to facilitate cleavage by accelerating a non-oxidative hydrolysis mechanism. In this case, it was expected that cleavage involving binding at the enzyme active site would likely still require a bound metal ion in order to regulate active site geometry and facilitate peptide binding. It is interesting to note at this stage that a number of 2OG oxygenases, including the putative demethylases PHF2 and JARID2,[188, 189] do not possess the ubiquitous histidine-histidine-aspartate/glutamate iron binding site. Although, in some cases, it is postulated that iron binding and subsequent oxidation may occur, the possibility that these enzymes may catalyse non-oxidative reactions should not be discounted. In order to investigate the effect of iron upon peptide hydrolysis, the cleavage reaction (on the peptide PATGGVKme2KPHRY) was attempted in the absence of iron, and the reaction was analysed after 30 minutes (at 37 °C) using MALDI mass spectrometry (Figure 6.4).

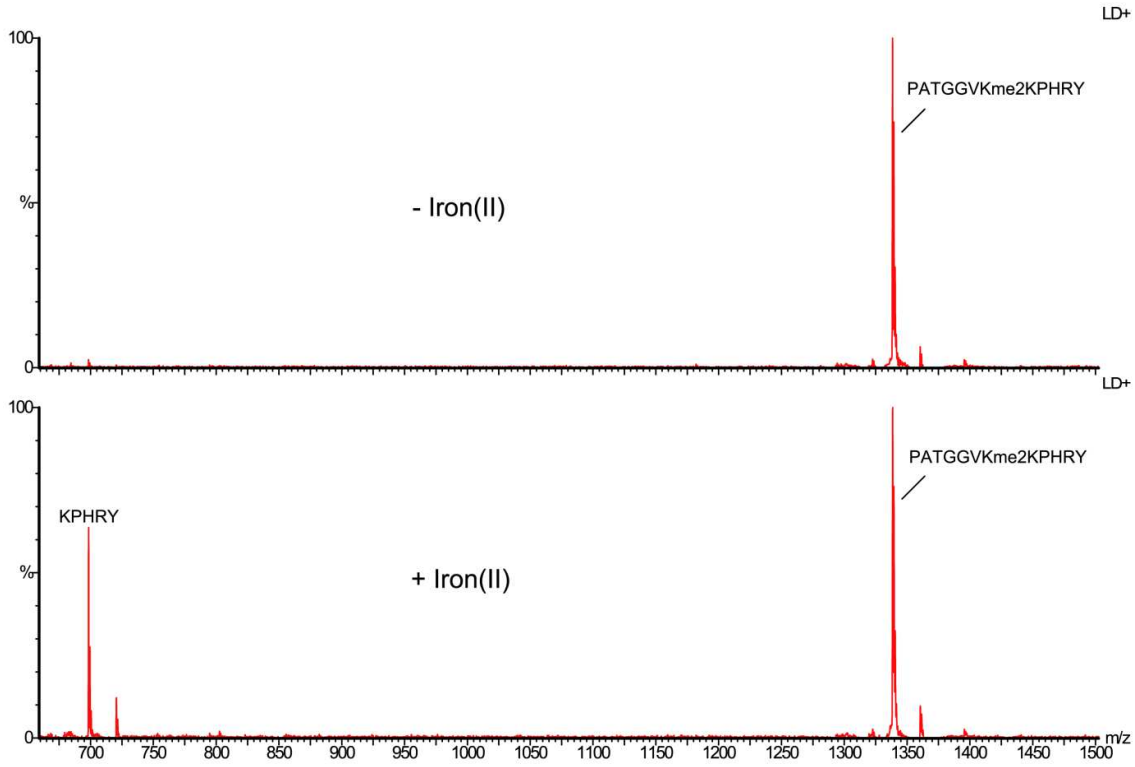

Figure 6.4 MALDI mass spectra of a sample containing FBXL11 (1 µM) and PATGGVKme2KPHRY (10 µM), either in the presence (Below) or absence of 10 µM iron (Above).

Interestingly, only a small degree of cleavage was observed in the sample, suggesting that Fe(II) is important for cleavage activity, albeit in a non-oxidative role. Analysis of the cleavage reaction at different Fe(II) concentrations revealed a dose-response curve (Figure 6.5).

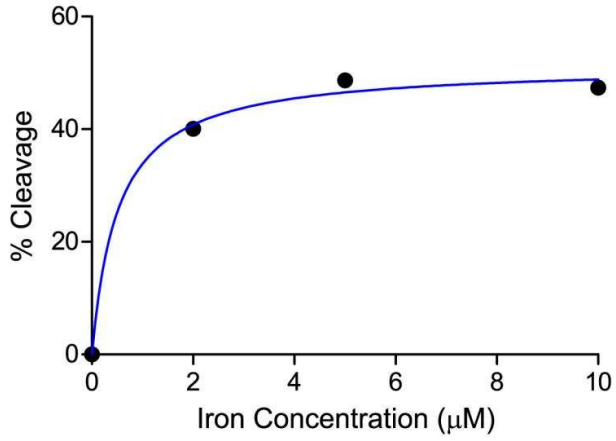

Figure 6.5 Dose-response curve of iron-mediated peptide cleavage.

The fact that cleavage is stimulated by Fe(II) argues against the hypothesis that cleavage is induced by serine or cysteine proteases. However, the genome of *E. coli* (the organism in which the protein was expressed) appears to code for a number of putative manganese-dependent metalloproteases (as indicated in the epd E. Coli protease database, http://www.cardiff.ac.uk/biosi/staffinfo/ehrmann-/tools/proteases.index.html) which may be able to incorporate iron in place of the natural manganese co-factor. In order to investigate whether such proteolysis could be a factor, the reaction mixture was incubated at 37 °C with 10 μM manganese chloride and the percentage of cleavage in the sample was measured after 30 minutes. Comparable levels of cleavage relative to the iron-containing samples were observed, indicating manganese-dependent hydrolysis (Figure 6.6). Potential cleavage by zinc-dependent metalloproteases was discredited by the lack of significant cleavage (above the residual activity observed in the absence of iron, Figure 6.6) upon addition of 10 μM zinc chloride to the sample. Also, addition of EDTA to a sample containing the dimethylated peptide and FBXL11 (100 μM final concentration) revealed no demethylation after 30 minutes at 37 °C, suggesting that cleavage had been inhibited by removal of residual metal in the sample.

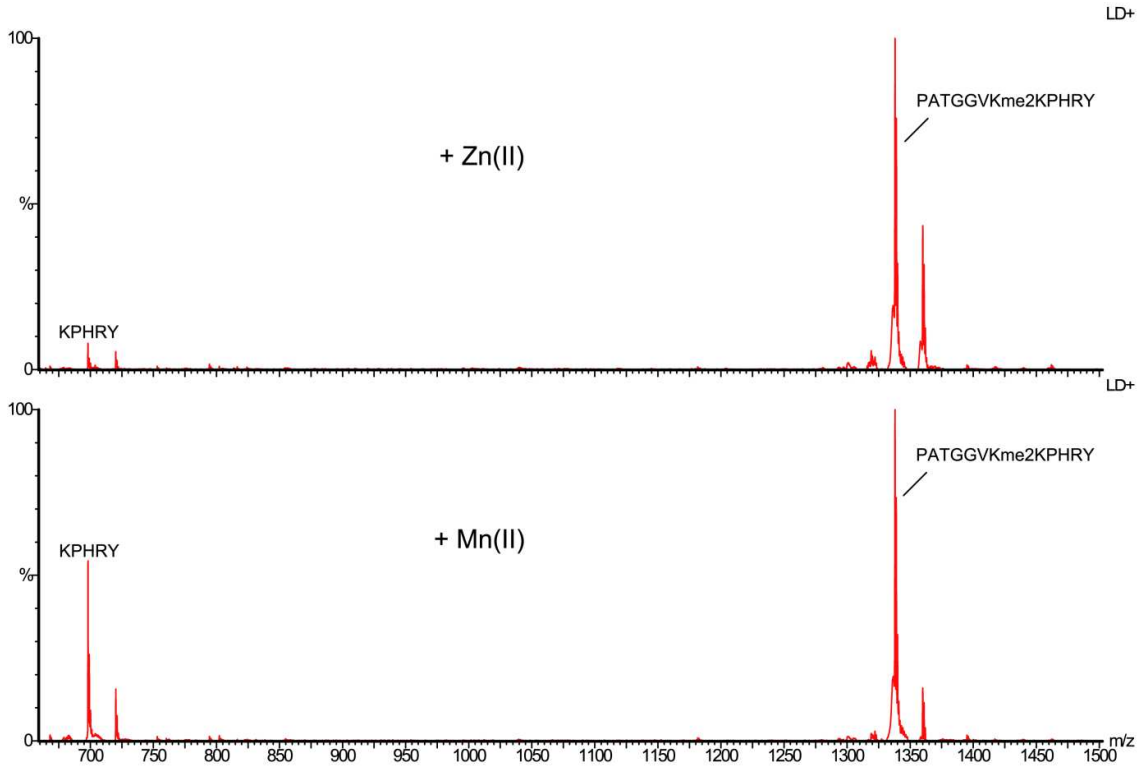

Figure 6.6 MALDI mass spectra of a sample containing FBXL11 (1 µM) and PATGGVKme2KPHRY (10 µM), either in presence of 10 µM manganese (Below) or presence of 10 µM zinc (Above).

6.2.6 Control Experiments with Inhibitors

Having confirmed that cleavage requires iron (or manganese) for reaction, work was then carried out in order to probe whether the reaction could be inhibited. It was hoped that these experiments would help to identify the enzyme responsible for the observed cleavage by analysing the cleavage activity in the presence of known protease and demethylase inhibitors. The cleavage reaction was first incubated with a protease inhibitor mixture, which contains competitive inhibitors for a broad range of serine and cysteine proteases. After 30 minutes (at 37 °C), no inhibition was observed. Additionally, incubation with benzamidine (a known competitive inhibitor of trypsin, Figure 6.7) did not affect the degree of cleavage observed in the sample. These findings suggest that serine/cysteine proteases were not responsible for the observed peptide cleavage, as also indicated by the apparent iron dependence of the reaction.

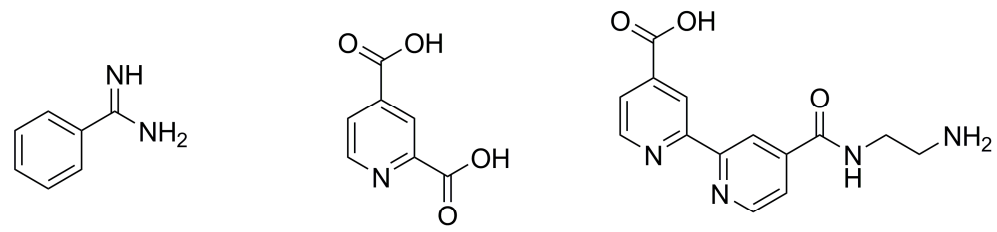

Figure 6.7 Structures of benzamidine (Left), 2,4-PDCA (Middle), and OC248 (Right).

In order to probe the dependence of FBXL11 upon peptide cleavage, the reaction was incubated with two known FBXL11 active site binders. Both 2,4-pyridine dicarboxylic acid (2,4-PDCA) and the bipyridyl compound 4'-[(2-aminoethyl)carbamoyl]-2,2'-bipyridine-4-carboxylic acid (OC248, *provided by Kai-Hsuan Chang*, Figure 6.7) are known 2OG mimetic inhibitors of demethylation (the IC_{50} of 2,4-PDCA is 4 μM using the Alpha-screen activity assay, Dr. Akane Kawamura, personal communication).[190] Therefore, it was expected that, if peptide binding during cleavage is analogous to the binding mode during demethylation, this binding propensity may drop upon addition of the bulky inhibitors, reducing cleavage activity. However, analysis of the sample containing 1 mM 2,4-PDCA did not indicate any loss of demethylation.

As stated above, it is possible that binding of the peptide during the cleavage reaction is different to the binding of the peptide during demethylation. This binding, however, would likely be suitably close to the active site in order to explain the observed iron dependence. Analysis of the FBXL11 crystal structure (PDB ID 2YU1)[170] indicates that it may be possible to accommodate both 2,4-PDCA and the substrate peptide in the active site, although the binding geometry of the substrate in the active site of FBXL11 is not known, and therefore, analysis of the structure is somewhat speculative. These studies suggest that 2,4-PDCA has little effect on the binding efficiency of the peptide in the active site during cleavage, resulting in no observed inhibition. Incubation of the sample with OC248, however, did reveal inhibition of cleavage (Figure 6.8).

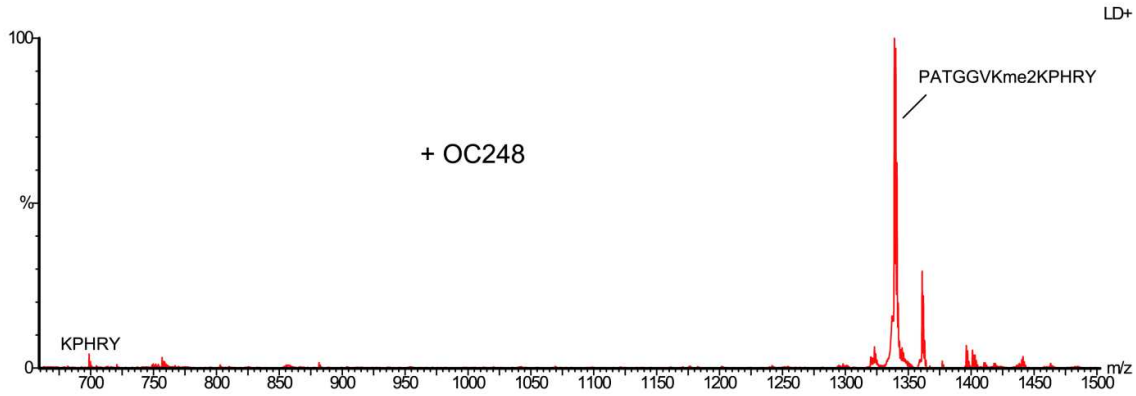

Figure 6.8 MALDI mass spectrum of a sample containing FBXL11 (1 µM) PATGGVKme2KPHRY (10 µM), iron (10 µM) and OC248 (1 mM), after 30 minutes at 37 °C.

Although it is tempting to equate the loss of cleavage activity with the competitive binding of OC248 and peptide in the enzyme active site, it should be noted that OC248 is known to bind ferrous iron (and likely Mn(II)) in solution, thus removing the available metal ions required for catalysis. It is therefore difficult to determine whether the observed inhibition is due to competitive binding. Overall, the experiments with inhibitors have eliminated the possibility that cleavage is facilitated by either serine or cysteine proteases and suggest that FBXL11 may still be considered a potential catalyst of cleavage. However, more experimentation is required in order to confirm this hypothesis.

6.2.7 Probing Peptide Selectivity

a) K36 Peptides

Having identified the dimethyllysine peptide as a substrate for cleavage, samples were prepared containing unmethylated, monomethylated and trimethylated lysine peptide in order to investigate their relative cleavage propensities. Each sample, containing one of the peptides, was incubated for 30 minutes at 37 °C, and the degree of cleavage in each sample was compared to that observed with the dimethyllysine peptide. Interestingly, both the monomethyl and non-methyl peptides appeared to be hydrolysed to a similar

extent as the dimethyl peptide, implying that mono- or dimethylation of the K36 lysine residue has limited effect on the cleavage activity (Figure 6.9). This suggests that both the substrates and products of FBXL11-catalysed demethylation are substrates for cleavage.

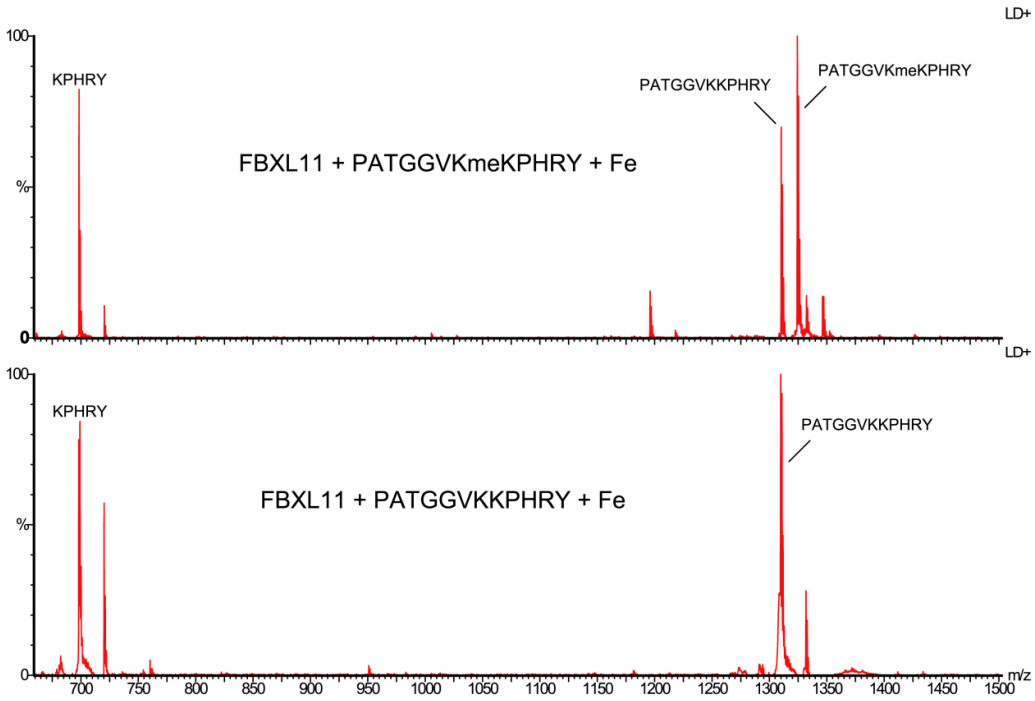

Figure 6.9 MALDI mass spectrum of samples containing FBXL11 (1 µM), iron (10 µM) and either non-methylated (Bottom) or monomethylated (Above) substrate peptide (10 µM).

The sample containing the trimethylated lysine at K36 did show some cleavage, although the overall amount of KPHRY formed was lower than in the other samples (Figure 6.10). The trimethyllysine peptide is not demethylated by FBXL11; however, there is some evidence using an Alpha-screen binding assay (*Akane Kawamura*) that this peptide (biotinylated on the *N*-terminal) can bind weakly to FBXL11. The lack of substantial cleavage of this peptide, therefore, may be due to its weak affinity for FBXL11 (or a protease contaminant).

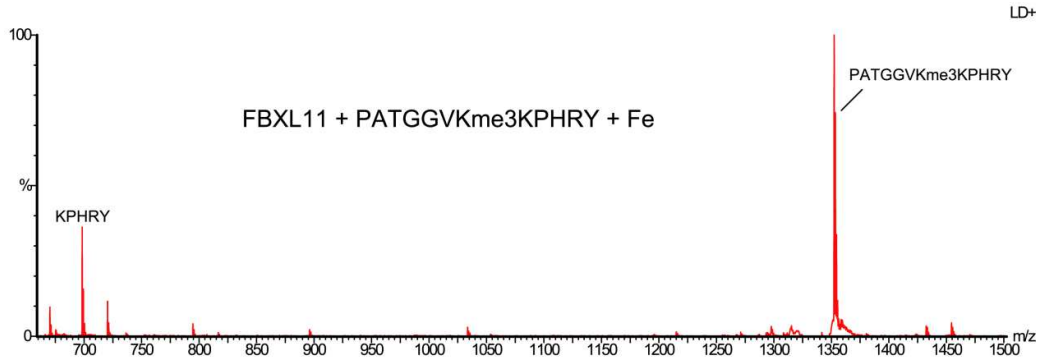

Figure 6.10 MALDI mass spectrum of a sample containing FBXL11 (1 µM), iron (10 µM) and trimethylated substrate peptide (10 µM).

Having confirmed that the substrate peptide can be cleaved with the K36 lysine at all methylation states, cleavage experiments were carried out on the other K36 lysine analogue peptides produced in Chapter 3. It was hoped that probing the substrate selectivity in this manner might indicate that cleavage is FBXL11-catalysed by revealing selectivity for particular lysine modifications. Analysis of the MALDI spectra revealed cleavage of each of the K36 lysine analogue peptides at a comparable degree to the dimethyllysine peptide. However, the enzyme batch used for this study was significantly less active with respect to cleavage for both the analogues and the dimethyllysine peptide, making quantification difficult.

The *N*-terminal fragment from the cleavage reaction was detected in MALDI experiments using the H3 isoform peptide PSTGGVKKPHRYRPG. This peptide (*prepared using a Multipep synthesiser by Dr. Wei Ge*) only differs from the 12-mer peptides described above by three extra residues on the *C*-terminal and an alanine to serine substitution, and therefore, it was expected that this peptide would be a substrate for cleavage. Interestingly, a number of new peaks at lower mass than the substrate peptide were detected in the MALDI mass spectrum after 30 minutes. The majority of these peaks did not appear to correspond to peptide fragment products, potentially indicating that protein hydrolysis occurred during the reaction period (Figure 6.11). However, it was

possible to identify peaks corresponding to both the *C*-terminal fragment (KPHRYRPG, at 1010 m/z) and the *N*-terminal fragment (PSTGGVK, at 646 m/z). The observation of the *N*-terminal peptide in the sample supports the hypothesis that the transformation observed corresponds to peptide hydrolysis after K36, and also implies that the inclusion of serine in place of alanine either encourages peptide ionisation or inhibits degradation of the fragment.

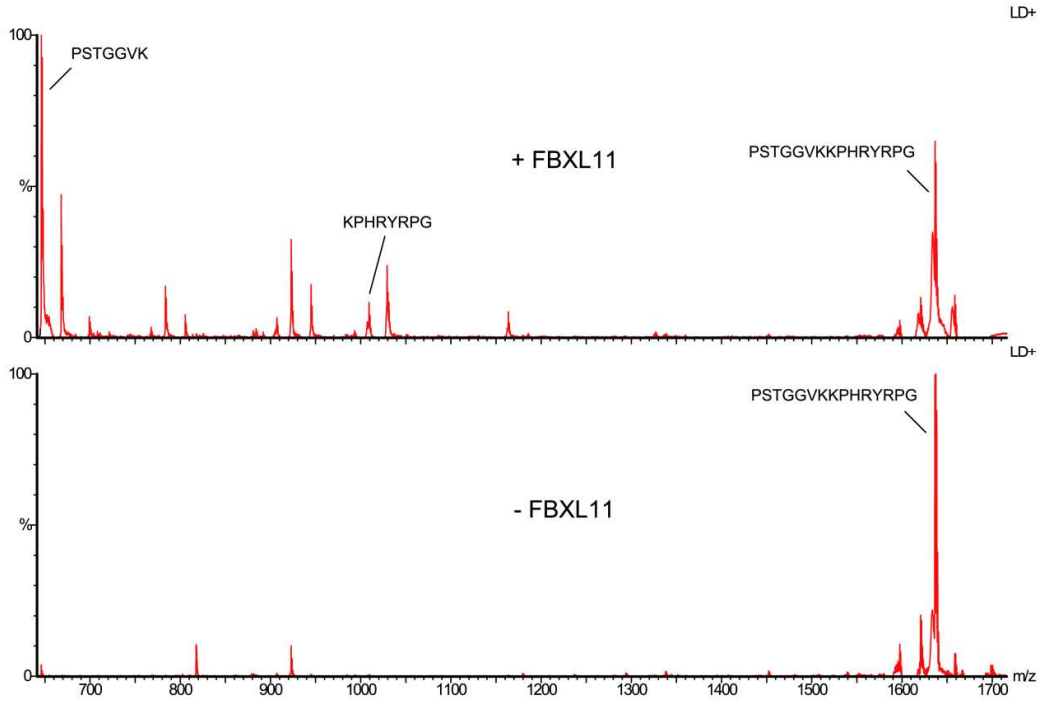

Figure 6.11 MALDI mass spectrum of a sample containing FBXL11 (1 µM), iron (10 µM) and PSTGGVKKPHRYRPG (10 µM) after 30 minutes at 37 °C. The control experiment without enzyme is shown below.

It was also noted that the relative intensities of the *C*-terminal and *N*-terminal fragment peaks appear to fluctuate depending on the substrate (the *N*-terminal fragment peak in the sample described above was significantly larger than the corresponding *C*-terminal peptide). Although this may be explained by the possibility of further peptide hydrolysis after fragmentation, it is also possible that the different peak intensities are due to their variable ionisation propensities under MALDI conditions. This ambiguity regarding the efficiency of ionisation

may complicate the accumulation of quantitative cleavage data (relative to, for example, demethylation) using MALDI analysis.

b) K9 Peptide

In order to probe the selectivity of the K36 peptide, FBXL11 and ferrous iron were incubated with the histone peptide ARTKQTARKme2STGGK (representing dimethylated H3K9). Analysis of the sample revealed some new peaks (at low levels) in the low mass region after 30 minutes reaction, including a relatively large peak at 541 m/z. However, these peaks could not be assigned to any cleavage products of the K9 peptide, implying that either rearrangement of the peptide, or proteolysis was the source of these species in the reaction mixture. Therefore, the MALDI data does not reveal cleavage of the K9 peptide directly after the modified lysine in the peptide sequence.

6.2.8 Investigations with JMJD2A and PHF8

Having shown that peptide cleavage appears to be selective for the K36 peptide sequence, the cleavage reaction was attempted using the K36 demethylase JMJD2A. This protein is capable of demethylating both K9 and K36 histone peptides, and therefore, it was hoped that the availability of two orthogonal substrates with respect to cleavage (the K9 peptide was not expected to be hydrolysed by analogy with the findings with FBXL11) may allow competition experiments to be undertaken. These experiments may indicate whether the extent of K36 cleavage is diminished upon addition of another JMJD2A substrate (and vice versa), and therefore, should indicate whether JMJD2A is catalysing both the demethylation and cleavage reactions. However, analysis of a reaction mixture containing JMJD2A (8 μM), ferrous iron (100 μM) and the dimethylated K36 peptide (sequence PATGGVKme2KPHRY, 10 μM) after 30 minutes at 37 °C revealed no evidence of peptide cleavage. The fact that JMJD2A does not catalyse cleavage of the K36 peptide may suggest that the binding orientation of the peptide required for cleavage may not be possible in the JMJD2A

active site. However, it should be noted that the data are also consistent with the possibility that a protease/peptidase co-purifies with FBXL11 but not with JMJD2A.

Although K36 is not a natural demethylation substrate of the K9 demethylase PHF8, it has been found in our laboratory that the dimethylated 12-mer K36 peptide is capable of binding to the enzyme active site. (Dr. Oliver N. F. King, personal communication). Therefore, a K36 peptide (sequence PATGGVKme2KPHRY) was incubated with PHF8 (2 μM) and ferrous iron (10 μM) in order to investigate whether the enzyme can facilitate cleavage. Interestingly, over 30 % of the peptide was observed to be cleaved after 30 minutes at 37 °C (Figure 6.12).

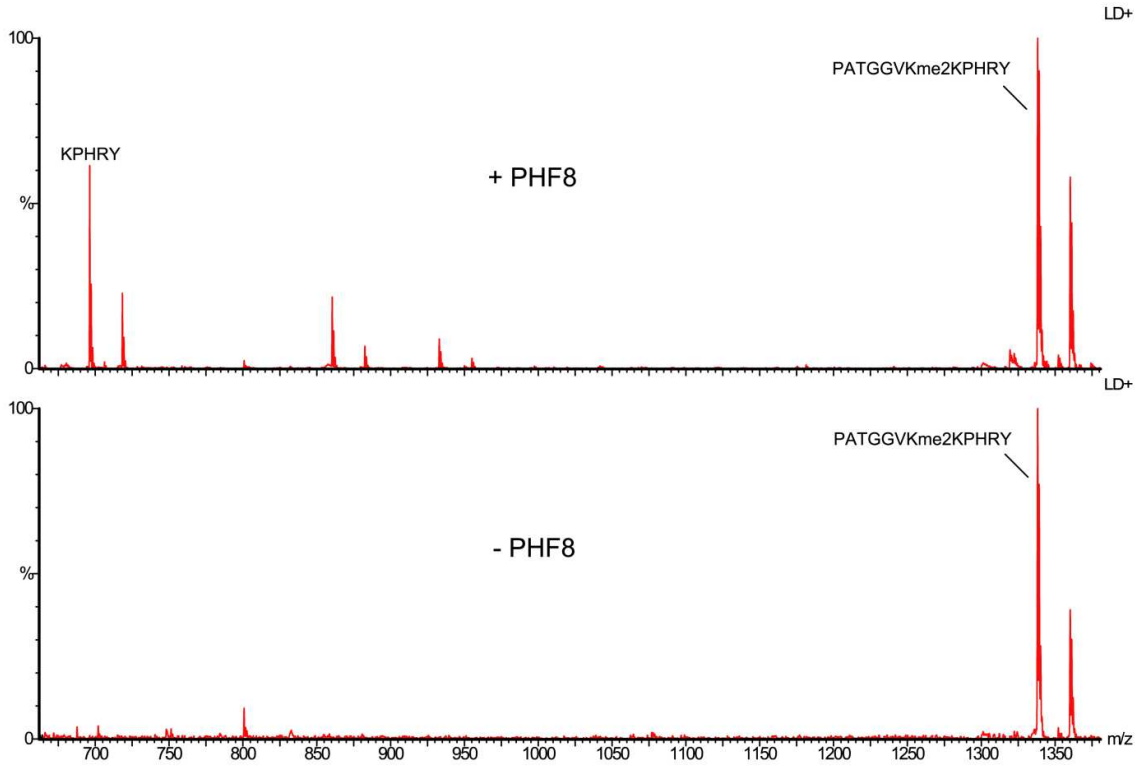

Figure 6.12 MALDI mass spectrum of a sample containing PHF8 (2 μM) PATGGVKme2KPHRY (10 μM) and iron (10 μM) after 30 minute at 37 °C.

The observed cleavage in the PHF8 reaction mixture indicated that the competition experiments described for JMJD2A should be attempted for PHF8. A 1:1 mixture of the dimethylated K36 peptide and the PHF8 substrate peptide ARTKme3QTARKme2STGGK was first prepared, and then PHF8 (2 μM), 2OG (50

μM), ascorbate (100 μM) and ferrous iron (10 μM) were added to the mixture. The reaction mixture was then incubated at 37 °C, and monitored after 20 minutes, 40 minutes, and 60 minutes incubation using MALDI mass spectrometry. The percentage demethylation of the K9 peptide was then plotted as a function of time, and the values attained were compared to those acquired from a sample omitting the K36 peptide. The results suggested that the K36 peptide does not affect the rate of K9 demethylation, suggesting limited (if any) competitive inhibition by this peptide (Figure 6.13)

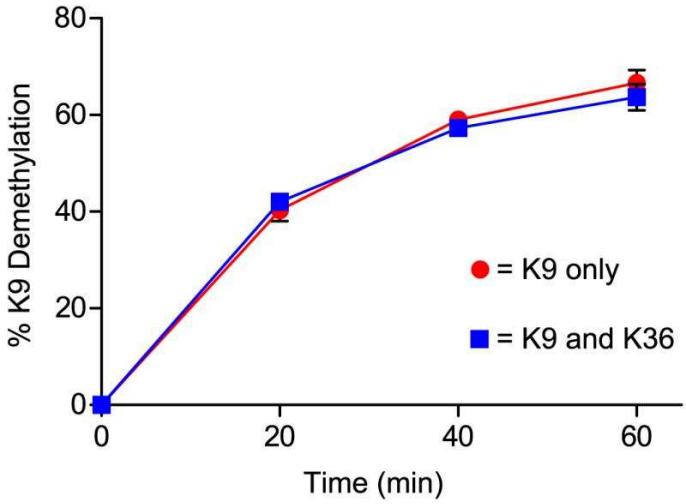

Figure 6.13 Percentage demethylation of ARTKme3QTARKme2STGGK by PHF8 in the presence (Blue) or absence (Red) of PATGGVKme2KPHRY.

Additionally, the percentage of K36 peptide cleavage in the sample was plotted as a function of time, and the acquired rate was compared to that of a sample omitting the K9 peptide. No observable decrease in cleavage propensity was observed (Figure 6.14).

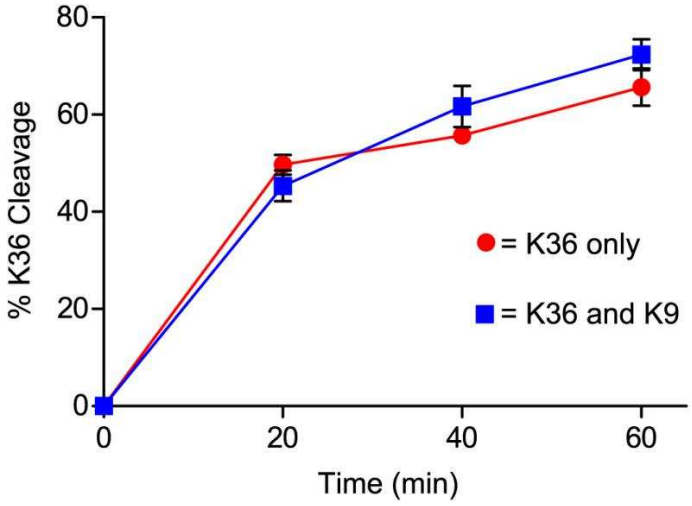

Figure 6.14 Percentage cleavage of PATGGVKme2KPHRY in the presence (Blue) or absence (Red) of ARTKme3QTARKme2STGGK.

Overall, the competition experiments with PHF8 indicate that demethylation of the K9 peptide and cleavage of the K36 peptide are independent processes. This observation implies that either PHF8 (and by extension FBXL11) is capable of facilitating both demethylation and hydrolysis by independent pathways (by presumably allowing binding of two peptides simultaneously at separate sites), or that cleavage is facilitated by impurities in the enzyme samples and is not in fact dependent on the presence of demethylase. As it is hard to envisage the presence of multiple binding sites on both PHF8 and FBXL11 that allow binding of peptides in oxidisable and hydrolysable orientations independently of one another, it seems likely that cleavage cannot be facilitated by these enzymes. Therefore it is probable that cleavage is not demethylase catalysed.

6.3 Conclusions and Future Work

Work in this Chapter has documented the identification and attempted characterisation of histone peptide cleavage in samples containing 2OG demethylases. During this work, the nature of the substrate peptide and the position of hydrolysis were identified using both MALDI-MS and MALDI-MS/MS analyses, which suggested that the cleavage mechanism may be catalysed by the demethylase enzymes. This hypothesis was further

endorsed by the observation that histone peptides methylated at K36 were substrates for cleavage by FBXL11, and also that the cleavage appeared to be dependent upon ferrous iron. However, the fact that cleavage activity in samples appeared to vary depending on the protein batch, and also that other low mass peaks were present in a number of mass spectra (including K9), indicated that protease activity may be present in the samples. Inhibition data using 2,4-PDCA suggested that the inhibition of demethylation had no effect on cleavage activity, implying that the two processes are independent of one another. This conclusion, however, was challenged by the observed decrease in cleavage upon addition of the bipyridyl compound OC248, although the observed loss in activity may be due to the sequestering of iron, or other metals, in solution. Finally, competition experiments with PHF8 indicated that peptide demethylation and cleavage occur at separate sites, strongly implying that cleavage is not catalysed by the demethylases (or at least at the demethylase active sites).

Although the cleavage of histone peptides does not appear to be the result of demethylase catalysis, it is important to acknowledge that such reactions can occur in samples containing the demethylase enzymes. This is of crucial importance when attempting to quantify the extent of peptide demethylation by FBXL11, as cleavage of the substrate peptide will most likely result in a decrease in available substrate in the assay, thus invalidating the kinetic data. It was noted during this work that the extent of cleavage for different batches of enzyme varied significantly, suggesting that subtle changes in expression and purification techniques may have a large effect on the cleavage activity. These findings imply that impurities in the FBXL11 (and PHF8) samples may be minimised by more efficient purification procedures, thus reducing the extent of peptide cleavage. The batches used in this work were generally purified in two stages using affinity chromatography and size-exclusion chromatography (personal communication). However, these batches generally showed a relatively high level of cleavage activity, suggesting that the protease(s) facilitating cleavage were not removed during purification. Interestingly, the least active batch of FBXL11 used was a longer construct than the other batches of protein. This protein (containing amino acids 1-759)

possesses the CXXC and PHD domains in addition to the catalytic JmjC domain, and therefore, it was initially proposed that the extra domains may block peptide cleavage. However, it is possibly more likely that this protein sample, which underwent purification by affinity chromatography, ion-exchange chromatography and size-exclusion chromatography, did not contain significant amounts of protease impurities, presumably due to efficient purification. More recently, attempts at purifying the shorter construct (amino acids 1-517) using affinity and size-exclusion chromatography has resulted in a significant reduction in cleavage activity. This reduction was achieved by improving the efficiency of the affinity chromatography step by including more wash cycles during the purification (work *carried out by Tristan Smart*).

One potential focus for future investigations is to identify the protease/peptidase responsible for the observed cleavage. The observation that cleavage is dependent upon iron (or manganese), and also that cleavage is not inhibited by benzamidine or the protease inhibitor cocktail, implies that the cleavage is catalysed by one or many metalloproteases. However, none of the characterised metalloproteases present in *E. coli* appear to possess the correct selectivity profile to allow cleavage of the K36 peptides. It can be presumed, based on the observation that cleavage can occur next to a variety of modified lysines, that the selectivity of the protease(s) may not be due to subtle interactions in the S1 pocket (i.e. the enzyme binding site for K36). Therefore, it can be assumed that selectivity is induced by other residues in the substrate sequence besides K36, the identity of which may be derived by experiments using modified K36 peptides. In order to identify the protease(s), proteomic analyses may be required on the protein samples in the hope that impurities present can be elucidated from the mass spectra. This may prove difficult, however, as it is likely that only miniscule amounts of protease may be sufficient to allow observable cleavage in the sample. Another area of future investigation may be to ascertain whether samples of other demethylase enzymes may facilitate cleavage. Although work with JMJD2A did not indicate cleavage (at least not cleavage that could be identified by MALDI analyses), it is possible that this sample may be ‘too pure’ to allow observable cleavage. It is therefore possible that the same

proteases may be present in samples containing other demethylases (purified in a less efficient manner), resulting in cleavage of the histone peptides. Having identified the samples containing proteases, further work will be required to improve the expression and purification procedures for these enzymes. After this, the protease impurities will hopefully be eradicated, and therefore, the cleavage observed in the *in vitro* experiments should be minimised.

Chapter 7

Studies on the Mechanism of Histone Lysine Demethylation using Deuterated Lysine Substrates

7.1 Introduction

Work described in Chapters 2 and 3 indicates that demethylation of methylated lysines by histone demethylases most likely proceeds via hydroxylation of the N^{ϵ}-methyl groups. As this process is presumed to involve direct insertion of an oxygen atom into an alkyl C-H bond,[23, 191] it has been proposed that this step in the demethylation mechanism may be slow (and potentially irreversible), implying that hydroxylation may be rate-determining. However, in the absence of experimental evidence, the importance of the hydroxylation step on the reaction rate is presently unclear.

In order to further investigate the mechanism of demethylation catalysed by the 2OG demethylases, work in this Chapter focuses on monitoring the demethylation reaction using deuterated lysine substrates. As the rate of hydroxylation (i.e. C-H bond insertion) is expected to be dependent upon the N^{ϵ}-methyl C-H bond strengths (which are strengthened upon deuteration), it was hoped that these experiments would give insights into the importance of the hydroxylation step upon demethylation by allowing comparison of the protiated and deuterated peptide reaction rates. These findings should help to ascertain whether hydroxylation is a rate-determining process during demethylation and may therefore indicate whether the consensus demethylation mechanism (Scheme 1.1 and Scheme 1.4)[23, 74] should be revised. Experiments were initially focused upon investigating the reactions of a deuterated dimethyllysine containing peptide with JMJD2E, in the expectation that this system would represent a

good model for investigating the effect of deuteration. Studies with FBXL11 and PHF8 were also attempted, as described below.

UV-Vis spectroscopy experiments were carried out by Dr. Elena Sanchez Fernández.

7.2 Results

7.2.1 Synthesis of Deuterated Fmoc-Lys(Me2)-OH

Experiments were initially conducted on JMJD2E using an 8-mer histone peptide, dimethylated at lysine-9 (sequence ARKme2STGGK, see Chapter 2). Synthesis of the deuterated N^{ε}-dimethyllysine was achieved via a similar method to that described in Section 2.2.4a. Firstly, the hydrochloride salt of the N^{α}-Fmoc protected lysine was dissolved in deuterated methanol (CD_3OD). 20 % w/w Deuterated HCHO solution in D_2O (DCDO, 5 eq.) was then added to the solution, followed by $NaBD_3CN$ (2.1 eq.) predissolved in CD_3OD. The reaction was then left stirring for one hour, before the solution was acidified using concentrated DCl solution in D_2O, and the solvent (after reacidification with DCl) was removed *in vacuo*. The product was then extracted from the solid using acetone. Removal of the solvent revealed the product as a white solid, which was deemed suitably pure for direct use in solid phase peptide synthesis (as assessed by ^{1}H NMR analysis).

7.2.2 Synthesis of Deuterated ARKme2STGGK

The deuterated dimethyllysine was incorporated into the histone peptide via the method described in Section 2.2.4b. The peptide was purified via preparative HPLC using mass-directed fraction analysis, and the purity of the combined product fractions was assessed as over 95 % by ^{1}H NMR. The NMR spectrum was identical to that of the protiated dimethyl peptide described in Chapter 2, with the exception of the N^{ε}-methyl ^{1}H signals (which were not observed for the deuterated peptide, Figure 7.1).

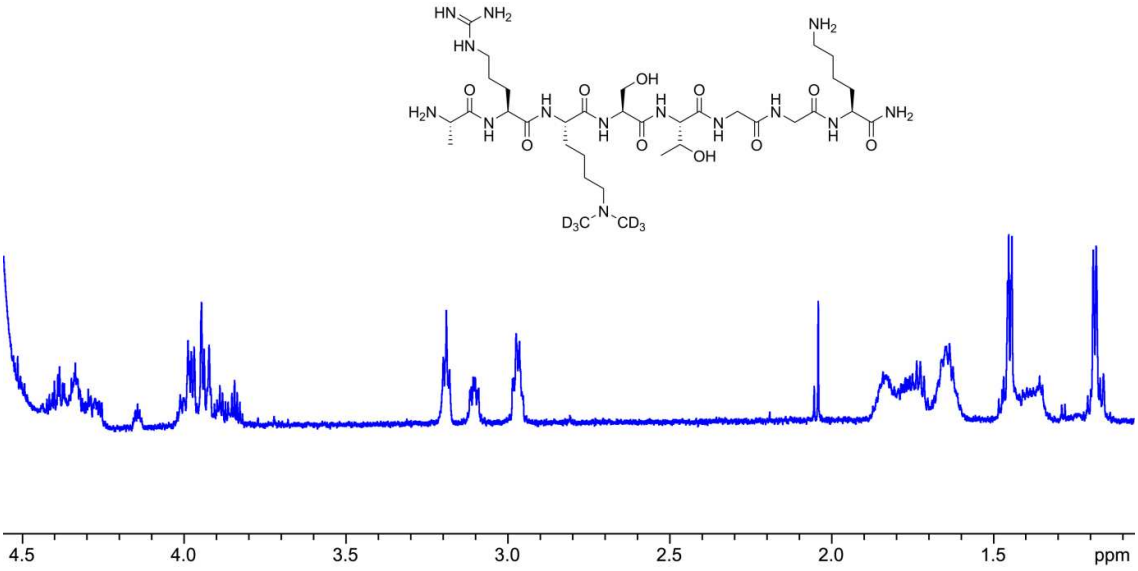

Figure 7.1 ^{1}H NMR spectrum (700 MHz) of deuterated ARKme2STGGK in dAFN buffer.

7.2.3 Experiments with JMJD2E

Experiments with JMJD2E were carried out using MALDI mass spectrometry, ^{1}H NMR spectroscopy and UV-Vis spectroscopy, as described below.

a) MALDI Experiments

Initial analysis of the demethylation reaction using deuterated peptide was undertaken using MALDI mass spectrometry. Time course experiments containing both the protiated and deuterated peptides (at equal concentrations) were run in order to compare the individual demethylation rates. Analysis of the MALDI mass spectra at different time points during the reaction allowed identification of the relative demethylation propensities of each substrate independently, due to their different masses. Before time course experiments could be carried out, it was essential to ensure that the concentrations of the protiated and deuterated peptides were identical in the reaction mixtures. Therefore, a stock solution containing both peptides was first prepared (Figure 7.2).

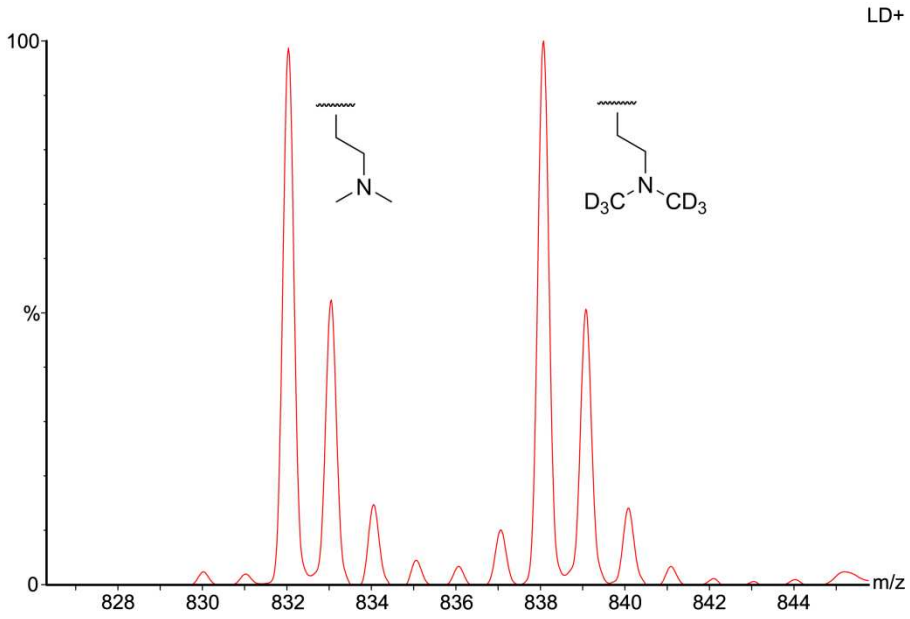

Figure 7.2 MALDI mass spectrum of a stock solution of both protiated and deuterated ARKme2STGGK. The peptides are shown to be at equal concentration (each at 50 μM).

The stock solution of peptide was then incubated (at 5 μM final concentrations of each peptide) with JMJD2E (2 μM), 2OG (50μM), ascorbate (1 mM) and ferrous iron (10 μM), and the reaction was analysed after 1, 2, 3, 5, 10, 15 and 30 minutes respectively (at 25 °C). The mass spectra at each time point for one sample (the experiment was carried out in triplicate) are shown in Figure 7.3.

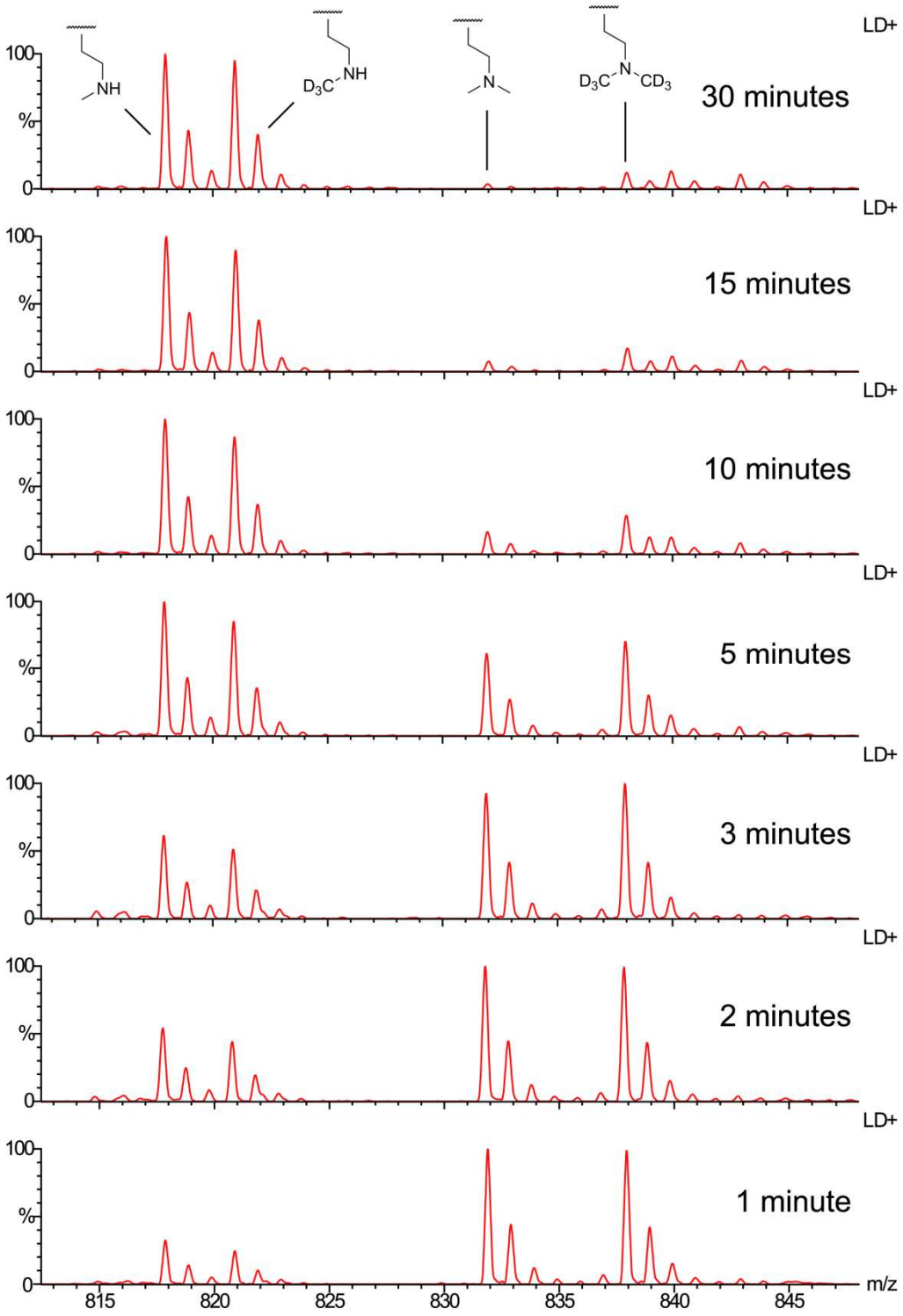

Figure 7.3 MALDI mass spectra of the reaction of a mixture of protiated and deuterated ARKme2STGGK with JMJD2E, 2OG, ascorbate and ferrous iron, after 1 minute, 2 minutes, 3 minutes, 5 minutes, 10 minutes, 15 minutes and 30 minutes respectively.

As expected, the mass spectra revealed the formation of both deuterated and protiated monomethyllysine peptides during the incubation period, confirming

the deuterated peptide as a substrate of JMJD2E. The amount of deuterated monomethyl-peptide produced, however, appeared to be slightly lower than that of the protiated analogue (Figure 7.4), indicating that the protiated dimethyllysine was demethylated more quickly in the samples. This observation implies that a primary isotope effect induces slower demethylation of the deuterated peptide, suggesting that the C-H bond insertion step does have an effect on the overall reaction rate. It was noted, however, that the overall rate decrease observed with the deuterated peptide does not correlate with the substantial strengthening of the C-H bond expected upon deuteration. Assuming that the rate of demethylation is exclusively dependent upon C-H bond insertion (either as a concerted insertion, or via a proton abstraction/radical addition mechanism), the overall reaction rate could be expected to be directly proportional to the strength of the C-H bond. It could be expected that, as the C-D bond should be roughly 5 kJ mol^{-1} stronger than the corresponding C-H bond,[192] the rate of reaction should suffer a significant decrease accordingly. However, the relatively small difference in protiated and deuterated peptide initial demethylation rates in the sample (the kinetic isotope effect was calculated as 1.1, which is significantly smaller than a number of literature values[193, 194]) suggests that other factors must be affecting the demethylation process.

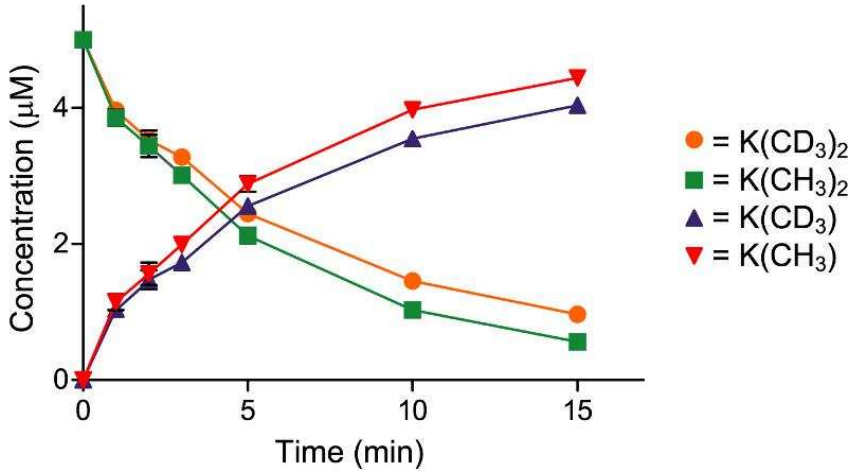

Figure 7.4 Concentrations of protiated and deuterated peptides over time in the sample with JMJD2E (2 μM), as assessed by MALDI mass spectrometry.

b) ^{1}H NMR Studies

Although a small isotope effect on the rate of demethylation was observed by MALDI analyses, these experiments did not give information on the rate of succinate formation. As it can be envisaged that a decrease in the rate of demethylation may induce a greater amount of substrate uncoupled turnover (presumably by allowing the peptide to escape the active site after formation of the Fe(IV) intermediate), it was important to ascertain whether the rate of succinate formation is susceptible to change upon deuteration. The protiated and deuterated peptides were incubated separately with 2OG, ascorbate and ferrous iron, as described in Section 2.2.2, and the reactions were monitored over the initial stages using ^{1}H NMR spectroscopy. Succinate concentrations were then plotted as a function of time in order to determine the relative formation rates (Figure 7.5). Unfortunately, the degree of demethylation could not be assessed in the deuterated peptide sample, as although the formation of monomethylated peptide could in theory be assessed by observation of a ^{1}H-resonance at δ_H 2.96 ppm (corresponding to the ε-lysyl protons adjacent to the monomethylated amine, see Figure 2.2), overlap of signals in this spectral region impeded analysis.

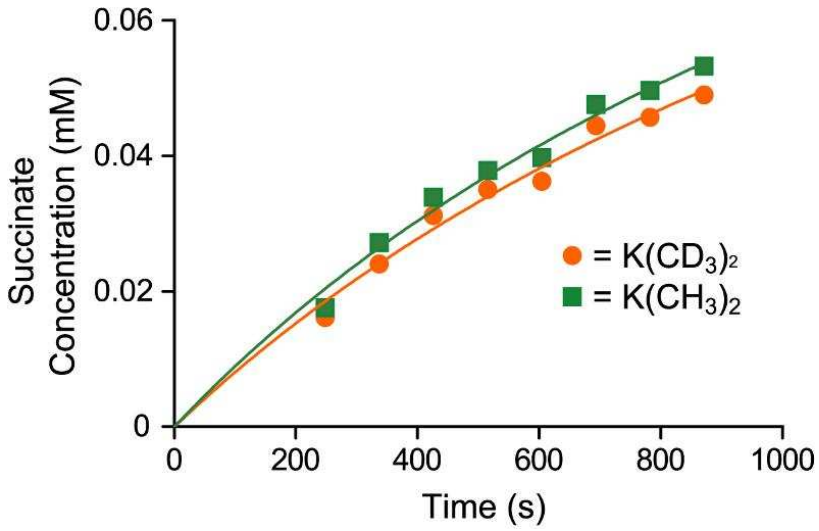

Figure 7.5 Concentrations of succinate over time, as assessed by ^{1}H NMR spectroscopy.

The NMR data revealed that overall formation of succinate was slightly greater in the sample containing the protiated peptide. This implied that succinate formation is intrinsically faster when in the presence of the protiated peptide (although the degree of peptide coupled succinate formation could not be determined in the deuterated sample due to signal overlap). As it is assumed unlikely, based on the consensus mechanism of 2OG oxygenases, that deuteration of the N^{ε}-methyl groups should affect the rate of formation of the Fe(IV) intermediate, it seems probable that the slower C-H bond insertion rate reduces the overall release of succinate from the active site after formation of the Fe(IV). This phenomenon therefore decreases the enzyme turnover rate. As reduction of Fe(IV) can occur by either peptide coupled or peptide uncoupled pathways (which most likely have different reaction rates), this decrease in turnover rate may also be at least partially due to a greater proportion of Fe(IV) species being reduced by the slower pathway. In samples containing peptide, it seems probable that the majority of Fe(IV) is produced in the presence of peptide substrate in the active site, as previous experimentation using UV-Vis spectroscopy has suggested that formation of the Fe(IV) in the absence of peptide is very slow (as judged by monitoring a species absorbing at 320 nm, Dr. Emily Flashman, unpublished data). Therefore, if it is assumed that substrate peptide is usually present in the active site immediately after formation of the Fe(IV), it is probable that the majority of Fe(IV) reduction will result in hydroxylation/demethylation of the peptide (as observed by ^{1}H NMR, see Section 2.2.2). However, if the hydroxylation rate is reduced, such as when the peptide is deuterated, it is possible that some of the peptide may either alter its binding orientation or escape the active site before hydroxylation. This may result in a larger proportion of Fe(IV) being reduced via a peptide uncoupled pathway, potentially leading to a decreased turnover rate (assuming that the rate of uncoupled reduction of the Fe(IV) and subsequent release of succinate from the active site is slower than the combined rate of coupled oxidation and product release). Although this hypothesis may go some way to explaining the observed

decrease in succinate formation in the sample containing deuterated peptide, it is impossible to confirm this proposal without data comparing the degree of coupled and uncoupled reactions under the same conditions.

c) Stopped-Flow UV-Vis Spectroscopy

Previous work investigating the 2OG oxygenases TauD and P4H used UV-Vis spectroscopy, Mössbauer spectroscopy and density functional theory analyses to identify and characterise the Fe(IV) intermediate produced during catalysis.[25, 191, 195-197] Using UV-Vis spectroscopy, the absorbance wavelength of the enzyme-Fe(IV)-succinate-substrate complex was inferred from the observation of a shift in absorbance (from 520 nm to 318 nm) upon addition of molecular oxygen to the reaction mixture. The species at 318 nm was then confirmed as the proposed Fe(IV)=O intermediate by analyses using the other two techniques.

In light of these previous studies, analysis of the JMJD2E-catalysed reaction with deuterated peptide was attempted using stopped-flow UV-Vis spectroscopy. By monitoring the absorbance intensity at ~318 nm (which would likely correspond to the analogous Fe(IV) intermediate in JMJD2E), it was hoped that the formation and degradation rates of the Fe(IV) intermediate could be determined. Comparing these values with those with protiated peptide may then reveal whether deuteration affects the production and stability of the Fe(IV) during catalysis.

The stopped-flow experiments were set up by first preparing two solutions. The first solution was prepared containing JMJD2E, 2OG, ascorbate, Fe(II) and deuterated peptide in deoxygenated HEPES buffer, which resulted in the formation of a purple solution consistent with the presence of the enzyme-Fe(II)-2OG-substrate complex (at 520 nm, by analogy with the data for TauD and P4H). The second solution consisted of oxygenated HEPES buffer. The two mixtures were then injected into the apparatus at 25 °C, and the absorbance of the combined solution was monitored immediately over a period of 0.01 - 1000

seconds after mixing. UV-Vis analysis of the sample revealed the formation and subsequent degradation of a species with an absorbance at 320 nm, which was proposed to correspond to the Fe(IV) intermediate by analogy with the reported data (Figure 7.6).

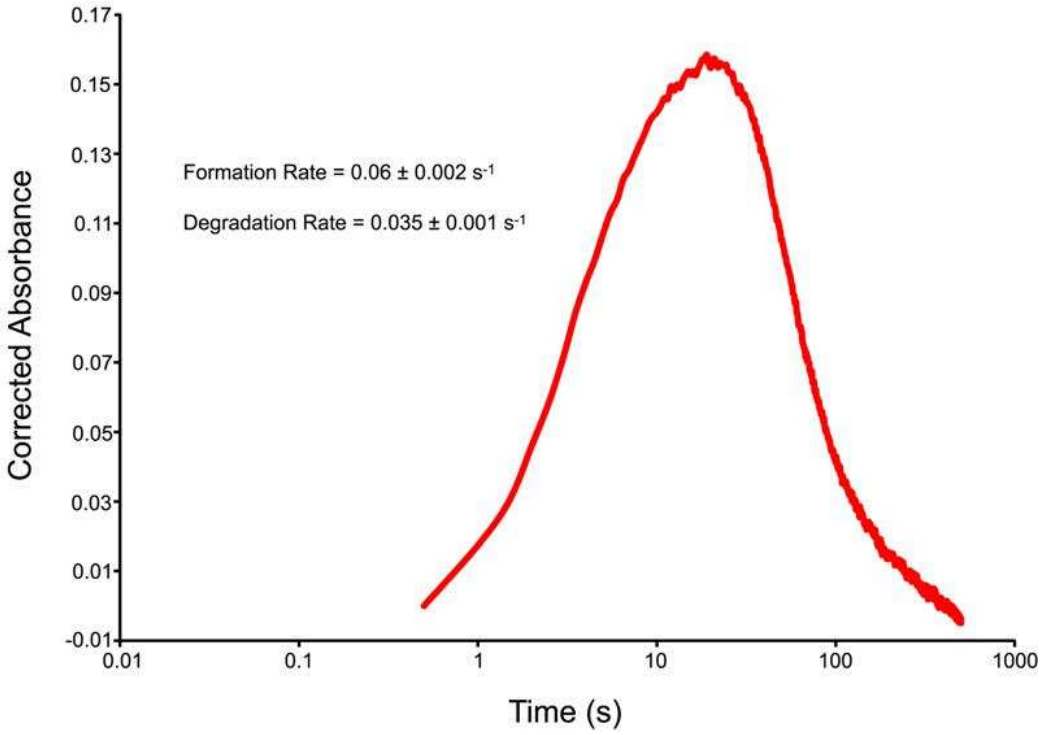

Figure 7.6 UV-Vis absorption spectra (320 nm) for the stopped-flow reaction containing JMJD2E (800 µM), deuterated ARKme2STGGK (800 µM), 2OG (10 mM), ascorbate (5 mM) and Fe(II) (700 µM). Formation rates for the species at 320 nm are shown.

Firstly, it was evident from the UV-Vis data that the maximum concentration of the species at 320 nm (after 19 seconds) appears within the expected timescale of the catalytic cycle (the k_{cat} with protiated peptide was measured at 0.019 s^{-1} by the ^{1}H NMR assay, corresponding to a catalytic cycle period of 53 seconds). Comparison of the formation and degradation rates with those of a sample containing protiated peptide also suggests that the rate of formation of the species at 320 nm was not significantly affected by deuteration of the peptide. The formation rate with deuterated peptide was measured at 0.06 ± 0.002 s^{-1},

which appeared to be slightly higher than the formation rate with protiated peptide ($0.05 \pm 0.006\ s^{-1}$). However, the deviation in the values attained may be a result of inaccurate curve fitting, caused by scattering of the data points (particularly in the protiated sample). The degradation rate in the deuterated sample ($0.035 \pm 0.001\ s^{-1}$) also appeared to be slightly larger than that in the protiated sample ($0.030 \pm 0.004\ s^{-1}$). In this case, however, the difference in rate was smaller than the difference observed between the formation rates. Overall, the UV-Vis data is inconclusive regarding the effect of deuteration, although it appears that any effect induced by changes in the C-H bond strength is probably very small. It is also worth noting that further experimentation should be undertaken (presumably using Mössbauer spectroscopy and density functional theory calculations) in order to confirm that the absorbance at 320 nm corresponds to the Fe(IV) intermediate. Only when the identity of this species is verified can the data from the experiments be fully analysed.

7.2.4 MALDI Analyses with other 2OG Demethylases

Having identified a small deuterium isotope effect during JMJD2E-catalysed demethylation, attention was then focused towards analysing the reactions with FBXL11 and PHF8. For these proteins, the standard 8-mer peptide used with JMJD2E was not sufficient for monitoring reactions, and therefore the deuterated peptides ARKme3QTARKme2STGGK (for studies with PHF8) and PATGGVKme2KPHRY (for studies with FBXL11) were synthesised as described above. Experiments were run using the standard MALDI-TOF demethylation assay (Section 7.2.1) at equal concentrations of protiated and deuterated peptides (5 μM).

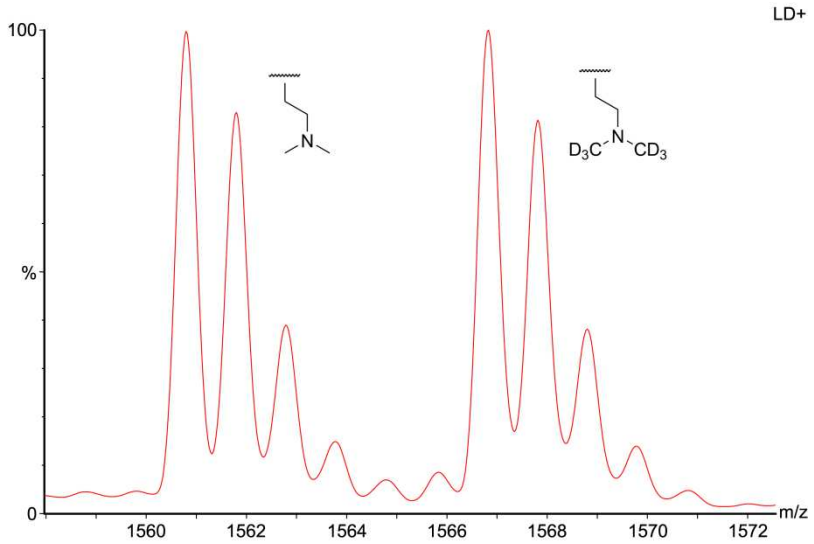

Figure 7.7 MALDI mass spectrum of a stock solution of both protiated and deuterated ARTKme3QTARKme2STGGK. The peptides are shown to be at equal concentrations (each at 50 µM).

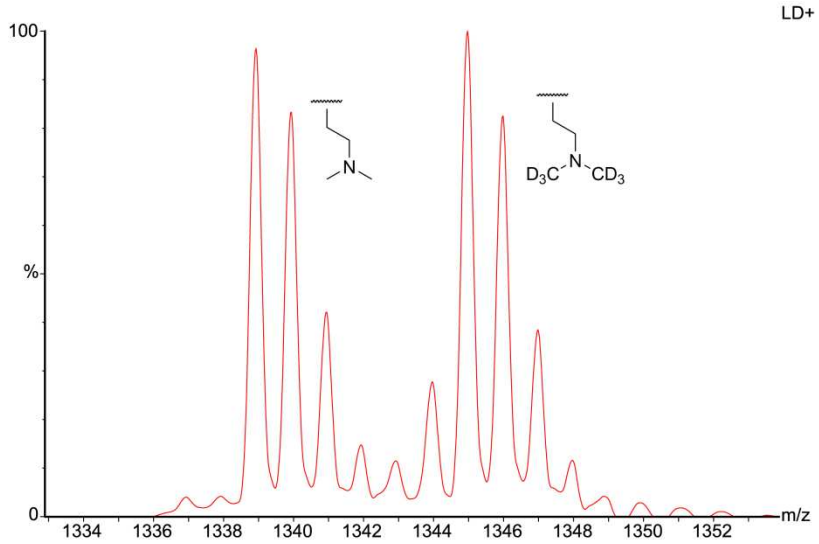

Figure 7.8 MALDI mass spectrum of a stock solution of both protiated and deuterated PATGGVKme2KPHRY. The peptides are shown to be at equal concentrations (each at 50 µM).

a) PHF8

As in the case of JMJD2E-catalysed demethylation, analysis of the reactions with PHF8 revealed a small isotope effect upon demethylation of dimethyllysine (Figure 7.9).

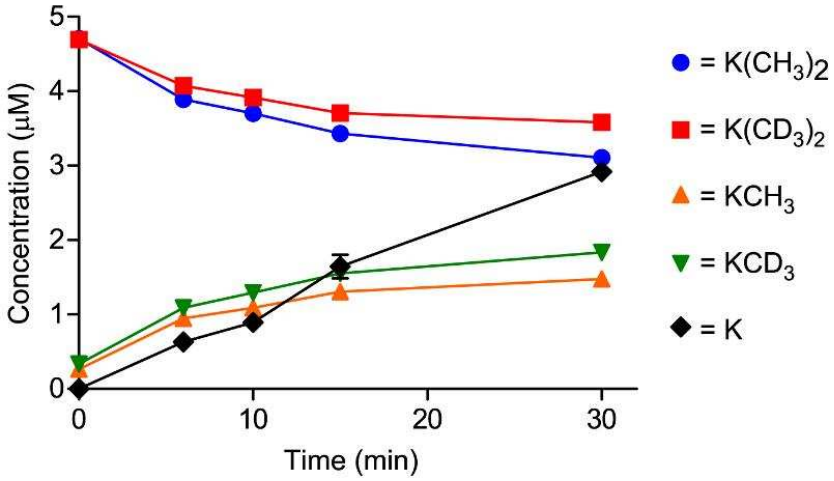

Figure 7.9 Concentrations of protiated and deuterated peptides over time in the sample with PHF8 (2 μM), as assessed by MALDI mass spectrometry.

However, it was also noted that the concentration of protiated monomethyllysine peptide produced via demethylation appeared to be lower than the corresponding deuterated peptide concentration. This observation suggests that subsequent demethylation of the monomethyl peptides to form non-methylated peptide occurs more rapidly on the protiated monomethyl substrate, thus indicating an isotope effect during this process. It is also possible to infer from these data that the isotope effect during monomethylated peptide demethylation is greater than the isotope effect during dimethylated peptide demethylation, as the concentration ratios of the monomethyl peptides are inverted relative to those of the dimethyl peptides. The monomethylated peptide produced in this study is known to be a good substrate for PHF8 (Louise Walport, personal communication) and is observed during time course experiments (of the dimethylated peptide and PHF8) at a relatively constant concentration after ~ 5 minutes. These findings may suggest, therefore, that the rate of monomethylated peptide demethylation is comparable to the demethylation rate of the dimethylated peptide (at least after initial time points). However, the observation of a larger isotope effect during monomethylated peptide demethylation (relative to dimethylated peptide demethylation) implies that another step during the demethylation mechanism of the monomethylated

peptide must be enhanced, possibly peptide binding. Full kinetic data on this peptide is needed to fully verify these hypotheses.

b) FBXL11

Demethylation of the dimethylated K36 peptides was observed in the samples with FBXL11. Interestingly, the mass spectra did not indicate any isotope effect upon demethylation of the dimethylated peptide, although the concentrations of the monomethylated peptide products suggested a small isotope effect during monomethylated peptide demethylation (Figure 7.10). However, it was also noted that the reaction mixture in the absence of enzyme contained impurities at masses coinciding with those of the monomethylated peptides. Therefore, the observed variation in monomethylated peptide concentrations may be due in part to the presence of these impurities.

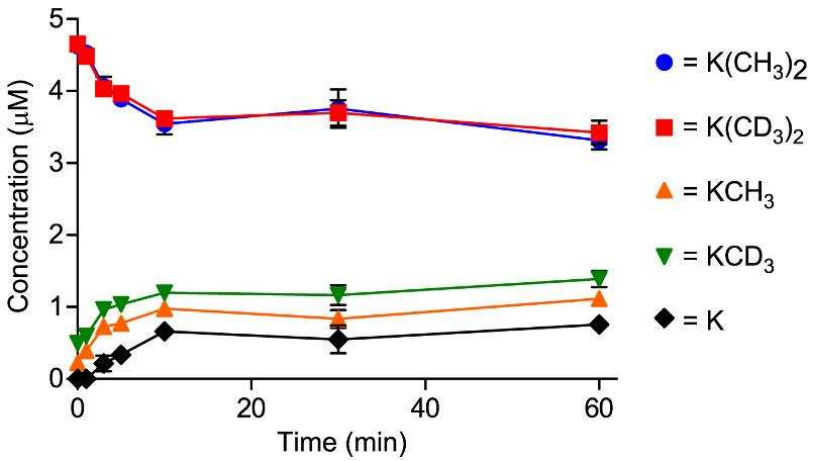

Figure 7.10 Concentrations of protiated and deuterated peptides over time in the sample with FBXL11 (1 μM), as assessed by MALDI mass spectrometry.

7.3 Conclusions and Future Work

Studies with deuterated lysine substrates described in this Chapter outline the first evidence for an isotope effect during 2OG dependent demethylase-catalysed demethylation. These experiments, therefore, reveal that the oxidative step during the demethylation reaction (i.e. the insertion of an oxygen atom into the methyl C-H bond)

contributes to the overall reaction rate (at least with JMJD2E and PHF8), although the relatively small isotope effects observed imply that other processes (such as formation of the Fe(IV) intermediate or release of the products) also contribute. In samples with PHF8 and FBXL11, it was also noted that isotope effects varied between the dimethylated and monomethylated peptides, suggesting variable rates of oxidation for these species. The findings reported here outline the basis for further study on the mechanisms of these enzymes, potentially using other techniques such as Mössbauer, EPR and Raman spectroscopies.

Chapter 8

NMR Studies on the Reactions of Glutathione and Formaldehyde

8.1 Introduction

A conserved feature of histone lysine demethylation is the production of HCHO. HCHO reacts rapidly with nucleophiles, forming adducts with DNA and proteins as well as cross-linking different biomacromolecules and small molecules.[198-205] Although the precise effects such interactions may have on cells and animal physiology are poorly understood, it has been postulated that the ability of HCHO to form such linkages may be the reason for its cytotoxic and mutagenic properties. In order for HCHO produced during histone demethylation to be tolerated, it is proposed that an efficient detoxification process must exist in cell nuclei. The glutathione-dependent HCHO detoxification pathway (Scheme 1.5)[154, 206] is one likely mechanism for HCHO detoxification in nuclei (at least in humans) due to the high concentration of glutathione and nuclear localisation of a class III alcohol dehydrogenase (glutathione-dependent alcohol dehydrogenase 5, ADH5).[207, 208] The first step in the proposed detoxification pathway, i.e. the formation of *S*-hydroxymethylglutathione (HMG), was previously thought to be non-enzymatic. However, recent work with bacterial systems has suggested that this process may be enzyme-catalysed (discussed in Chapter 9).[156]

The roles of glutathione (GSH) as both a redox regulator and an electrophile 'scavenger' have long been established.[209] The presence of a nucleophilic free thiol in its tripeptidic structure enables GSH to react with cellular electrophiles and also, due to the propensity of thiols to oxidise, to act as a reducing agent. With regard to

the reaction of GSH and HCHO, it is interesting to note that in addition to the nucleophilic thiol, GSH also possesses a primary amino group within its structure. The reaction of amines with aldehydes such as HCHO is well documented and can allow for complex macromolecular and cyclic structures to be formed.[210] Therefore, the existence of both thiol and amino groups within GSH offers the possibility of intramolecular cyclisation reactions, which may suggest that other GSH-HCHO derived species may be formed in cells.

8.1.1 Previous Studies

Several studies on the non-enzymatic reaction of GSH and HCHO have been reported.[168, 211, 212] Early work by Naylor *et al.* combined both Nuclear Magnetic Resonance Spectroscopy (NMR) and Fast-Atom-Bombardment Mass Spectrometry to study the GSH HCHO reaction in aqueous solution.[211] This work used ^{13}C-labelled HCHO to accentuate HCHO-derived resonances, allowing the authors to identify adducts in the often complex mixtures by only monitoring the signals from ^{13}C-labelled carbons. By monitoring the reaction over a pH range, the authors were able to identify four novel HCHO-derived ^{13}C-signals (in addition to the well-known ^{13}C-resonances for free hydrated HCHO and HMG) at δ_c 44.0 ppm, δ_c 54.0 ppm, δ_c 61.3 ppm and δ_c 61.9 ppm respectively. The relative intensities of the signals were found to be pH dependent, implying that multiple HCHO-derived species had been formed. Also, it was noted that the intensities of two of the resonances (at δ_c 61.3 ppm and δ_c 61.9 ppm) fluctuated to the same degree, suggesting that the signals were derived from the same adduct. Having proposed the existence of three novel adducts, the authors then attempted to assign the structures using mass spectrometry and both ^{13}C-chemical shift and 2D ^{1}H-^{13}C correlation NMR analyses. Analysis of the ^{13}C-chemical shifts was aided by comparing the observed shifts with those of HCHO-derived adducts with the GSH analogues *S*-methylglutathione, *N*,*S*-diacetylglutathione, cysteine and *N*-acetylcysteine respectively. In the case of *S*-methylglutathione, two separate HCHO-derived ^{13}C-resonances were observed. The first such resonance, at δ_c 70.0 ppm, was found to

appear rapidly in samples above pH 9 and was assigned to the *N*-terminal hemiaminal adduct by analogy to literature data. The second resonance, at 61.3 ppm, was more prevalent in acidic media and was found to be the major HCHO-derived reaction product in all samples below pH 8.5. Given that this resonance shared an identical chemical shift to a previously observed GSH-HCHO adduct resonance, it was assumed that the two corresponding carbons must inhabit near identical chemical environments. It was also assumed that, due to the absence of a ^{13}C-resonance at δ_c 61.9 ppm, the corresponding GSH-HCHO adduct carbon must possess a covalent linkage to the cysteinyl thiol. Further evidence that the thiol was essential to the formation of this resonance, and also that the *N*-terminal amine is capable of reacting with HCHO, was the observation that the reaction of *N*,*S*-diacetylglutathione and HCHO resulted in no detection of novel HCHO-derived signals. It was therefore postulated that the ^{13}C-resonance at δ_c 61.3 ppm was derived from a seven-membered cyclic aminal (Figure 8.1a). Information on the assignment of the GSH-HCHO adduct ^{13}C-resonance at δ_c 54.0 ppm was obtained by monitoring the reaction of HCHO and cysteine, which resulted in the formation of a HCHO-derived ^{13}C-resonance also at δ_c 54.0 ppm. It was therefore concluded that this resonance must correspond to a HCHO-derived CH_2 group in a five-membered ring with linkages to both amino and thiol groups (Figure 8.1b). This assignment was corroborated by the loss of this resonance in the reaction of HCHO and *N*-acetylcysteine, where only a resonance at δ_c 66.6 ppm, corresponding to the hemithioacetal, was observed (Figure 8.1c). Overall, the observations with the GSH analogues resulted in assignments for two of the detected GSH-HCHO adducts, which are shown in Figure 8.1d. Evidence for the cyclic hemiaminal assigned in the monocyclic novel adduct (GF, Figure 8.1d) was obtained by mass spectrometric analysis of the ionisation-induced fragment patterns, which favoured assignment of the six-membered over the analogous five-membered ring system. The hemiaminal in the bicyclic novel adduct (GF_2, Figure 8.1d) was assigned by analogy to GF. The third adduct, although observed at pH 6 by ^{13}C NMR (δ_c 44.0 ppm), was not present in significant quantities in the other reaction mixtures, and therefore the structure of

this species was not assigned.

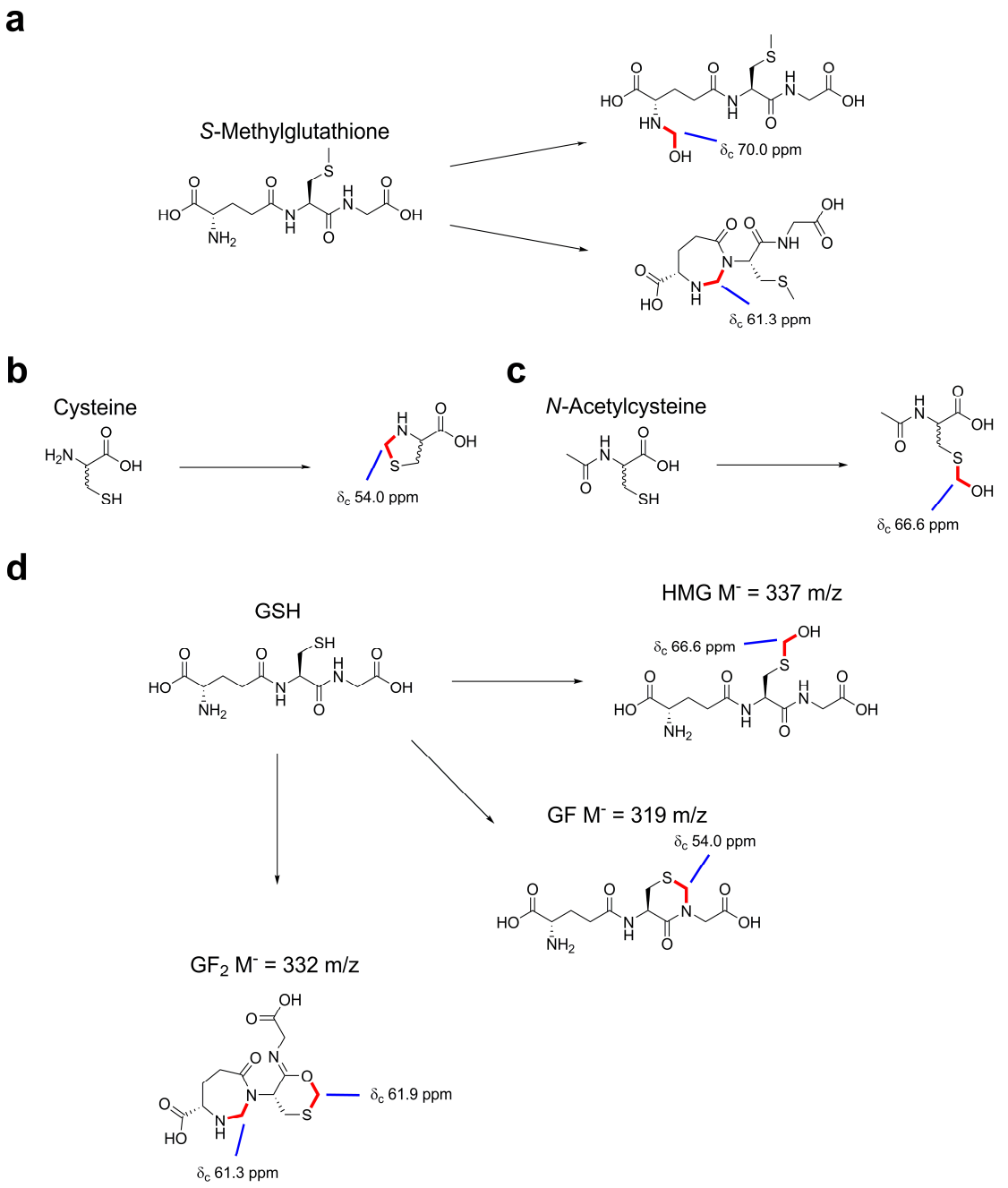

Figure 8.1 Structures of adducts proposed by Naylor *et al.*[211] HCHO-derived CH_2 groups are highlighted in red. a) Adducts from the reaction of *S*-methylglutathione and HCHO. b) Adduct from the reaction of cysteine and HCHO. c) Adduct from the reaction of *N*-acetylcysteine and HCHO. d) Adducts from the reaction of GSH and HCHO. Molecular weights correspond to the ^{13}C-HCHO incorporated adducts.

Recently, work by Bateman *et al.* utilised a combination of NMR and crystallographic approaches to refine the structure of GF_2.[212] During investigations

using X-ray crystallography into the recognition of GSH-derived species by the human enzyme Carbonyl Reductase 1 (CBR1), the authors identified a GSH-HCHO adduct bound to the enzyme active site. This adduct, which contained two HCHO-derived methylene bridges, possessed a novel bicyclic [4.4.1]undecane structure, distinguishing it from the adducts previously assigned. The ^{13}C NMR spectrum of the adduct, however, gave two HCHO-derived resonances at 61.5 ppm and 62.2 ppm respectively, which matched closely to the observed resonances for GF_2. The similarity in the ^{13}C resonances, the fact that a ^{1}H NMR spectrum had not been obtained for GF_2, and also that the new species was formed under comparable conditions to those described for GF_2, led the authors to propose that the new species and GF_2 were the same adduct, and therefore that the structure of GF_2 had been previously misassigned. The structure was revised as (5*R*,10*S*)-5-(carboxymethylcarbamoyl)-7-oxo-3-thia-1,6-diazabicyclo [4.4.1]undecane-10-carboxylic acid ($BiGF_2$, Figure 8.2) based on both the X-ray crystallographic data and on ^{1}H, ^{13}C and 2D COSY spectra of the species in solution.

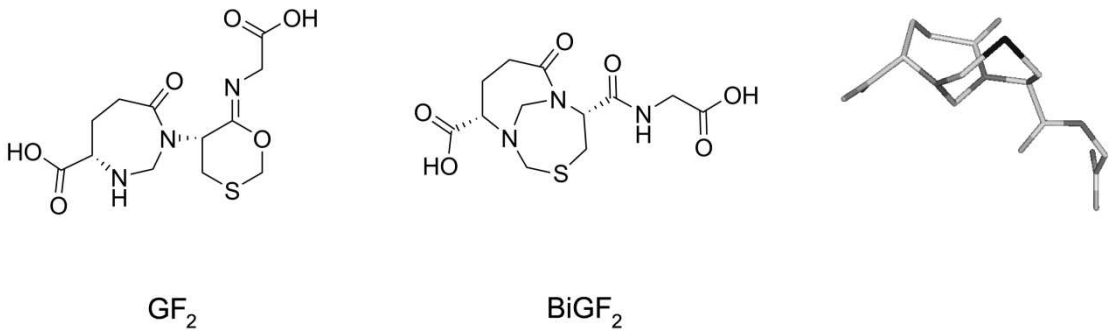

Figure 8.2 (Left) Original NMR-based structural assignment of GF_2, (Centre) Revised structure of the same adduct ($BiGF_2$), based on NMR and X-ray crystallographic data; (Right) Conformation of $BiGF_2$ when bound to human CBR1.[212]

8.1.2 Objectives

The work described in this Chapter uses NMR to investigate the non-enzymatic reaction of GSH and HCHO. Although previous studies have shown that this

reaction has the potential to form many potentially biologically relevant GSH-HCHO adducts, the structures of these species have not been conclusively elucidated. Also, there is presently limited information on each species' relative stability, formation rates and pH-dependency. As shown previously, NMR can act as a useful tool for monitoring such systems due to its ability to identify multiple species simultaneously without the need for separation and purification. Also, NMR allows for the monitoring of the reaction mixture continuously over a reaction period, and thus can facilitate the detection of labile or reversibly formed intermediates/products as well as offering insights into the relative formation rates and stabilities of each species formed. In addition to confirming the structures and ascertaining the relative prevalence of all detected GSH-HCHO adducts in solution, it was hoped that this work should also provide a detailed analysis of the reaction as a whole, and may allow for identification of novel, potentially biologically relevant GSH-HCHO adducts.

Initial NMR work, including initial characterisation of $BiGF_2$ and MGF (Section 8.2.10) and time course experiments, were carried out by Philippa S. Barlow.

8.2 Results

8.2.1 NMR Analyses on HCHO solutions

Work in this section was carried out by Philippa S. Barlow

Given the potent electrophilicity of HCHO, it was envisaged that a number of oligomeric species as well as potential disproportionation products may exist in aqueous solutions of HCHO.[213] Therefore, before analysis of the GSH HCHO reaction could begin, a comprehensive overview of HCHO solutions would be required in order to establish the amount of free HCHO available to react with GSH. A ^{1}H NMR spectrum was recorded of a 160 mM solution of HCHO in D_2O, which was prepared by dissolving paraformaldehyde powder in D_2O at elevated temperatures. The solution was allowed to stand at room temperature for 24 hours to

equilibrate before analysis. The ^{1}H NMR spectrum is shown in Figure 8.3.

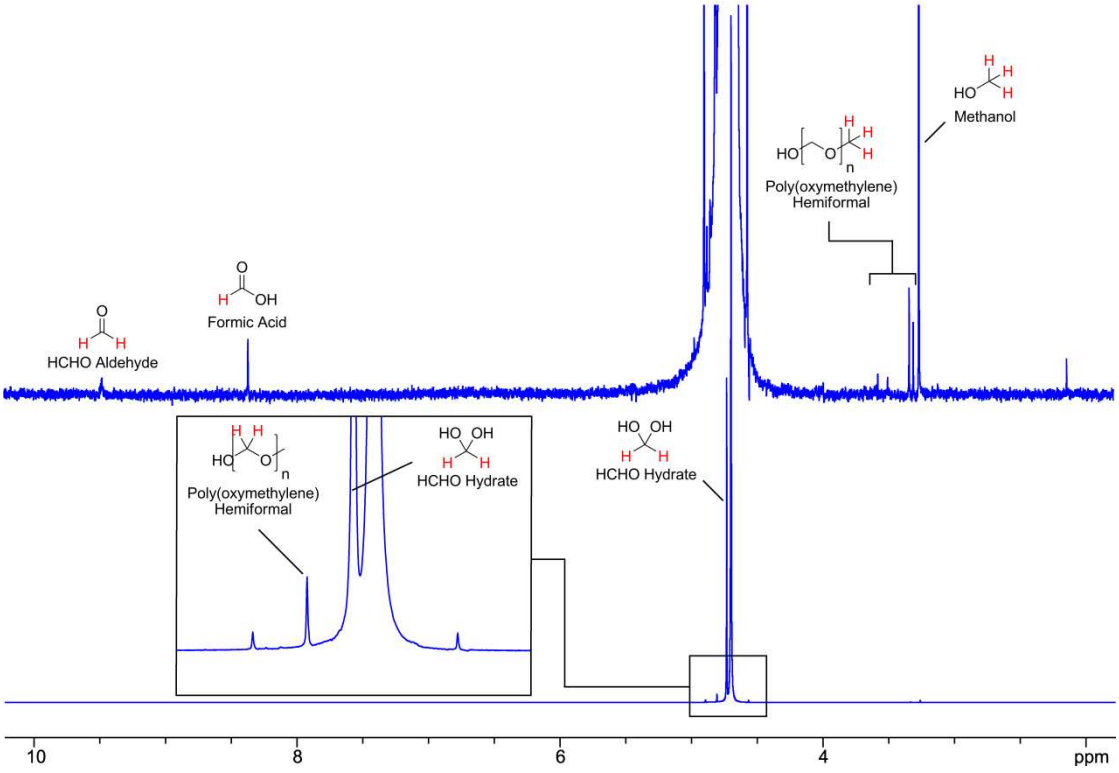

Figure 8.3 (Below) ^{1}H NMR spectrum (700 MHz) of 160 mM HCHO in D_2O. (Above) The spectrum at ×100 zoom.

The dominant species in the solution was hydrated HCHO, which could be identified by its characteristic singlet resonance at δ_H 4.73 ppm. Integration of this resonance indicated that this form of HCHO accounted for over 95 % of all species in the solution. In addition to this resonance, small signals could be observed at both low and high field regions of the ^{1}H NMR spectrum. The resonance at δ_H 9.47 ppm could be attributed to the aldehyde form of HCHO, which appears to exist in significantly lower concentration than the hydrated form in aqueous solution. Although it could be envisaged that the aldehyde form may be more susceptible to nucleophilic attack than the hydrate, and therefore will be more likely to react with GSH, dynamic exchange between the two should allow significant reaction with GSH to occur. The resonance at δ_H 8.37 ppm could be attributed to the carbonyl proton of formic acid, which is a known disproportionation product from the Cannizzaro Reaction (Figure 8.4).[214]

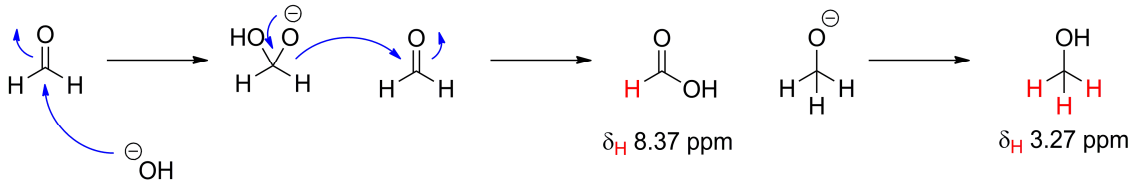

Figure 8.4 Classical reaction mechanism for the base-catalysed Cannizzaro Reaction. Hydride transfer from one HCHO molecule to another results in the formation of formic acid and methanol in equal amounts.

Methanol, the other Cannizzaro product, was detected at δ_H 3.27 ppm. However, the concentration of this species was higher than formic acid, which is probably due to trace methanol present in the commercial source of paraformaldehyde. The assignment of methanol at this resonance was confirmed by repeating the experiments at variable added methanol concentration, which showed a fluctuation in the intensity of this signal depending upon the amount of methanol added (Figure 8.5).

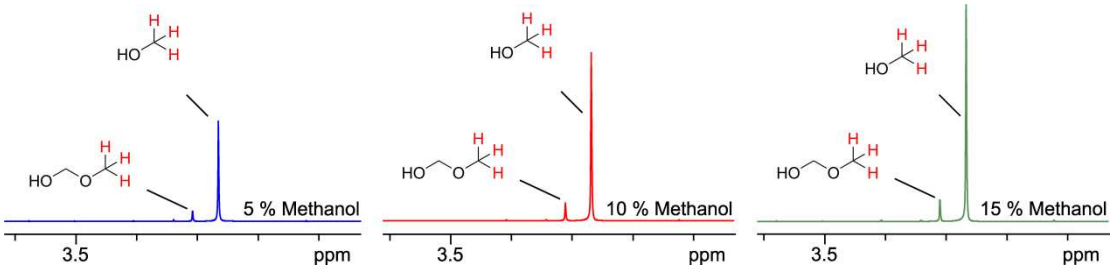

Figure 8.5 ^{1}H NMR spectra (700 MHz) of 160 mM HCHO in D_2O with added methanol. The methanol and hydroxymethylene hemiformal signals increase in intensity upon addition of methanol.

A number of signals were also detected downfield of the methanol resonance, at δ_H 3.30 ppm, δ_H 3.34 ppm, δ_H 3.49 ppm and δ_H 3.59 ppm respectively. These peaks presumably arise from the terminal CH_3 groups of poly(oxymethylene) hemiformals, which can be formed from the reaction of methanol and HCHO (Figure 8.6). It can be assumed that the higher chemical shifts of these signals relative to the methanol resonance are due to the electronegativity of the extra oxygen atoms. The resonances at δ_H 4.81 ppm, δ_H 4.85 ppm and δ_H 4.87 ppm most likely correspond to the internal CH_2 groups of poly(oxymethylene) hemiformals or glycols.

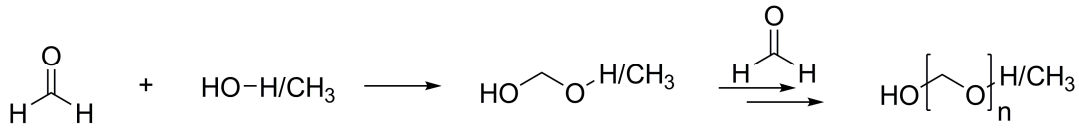

Figure 8.6 Reaction scheme for the formation for poly(oxymethylene) hemiformals and glycols.

The presence of oligomeric structures in aqueous HCHO solutions was also suggested by ^{13}C NMR. Using ^{13}C-labelled HCHO, ^{13}C-resonances for HCHO-derived CH_2 groups were detected in aqueous solution between δ_c 81 ppm and δ_C 90 ppm (Figure 8.7). Under the sample conditions, minimal methanol was observed, suggesting that the CH_2 signals arise from poly(oxymethylene) glycols rather than hemiformals. The lowest ^{13}C-resonance in the above ppm range, at δ_C 81.7 ppm, was assigned to hydrated HCHO. The other signals in the above range could be compartmentalised into two sections based on their chemical shifts, suggesting that the resonances in each region may represent similar CH_2 groups in the oligomeric glycols. The first section contained three distinct signals at δ_C 85.6 ppm, δ_C 86.1 ppm and δ_C 86.4 ppm respectively. These peaks could be assigned to the outer CH_2 groups in the glycols. It could be assumed that the signals in this region with higher chemical shifts arose from CH_2 groups with more oxygen atoms in close proximity, and therefore corresponded to CH_2 groups in the larger oligomers. The second section contained signals at δ_C 89.0 ppm, δ_C 89.5 ppm and δ_C 89.7 ppm respectively, and were assigned to the inner glycol CH_2 groups.

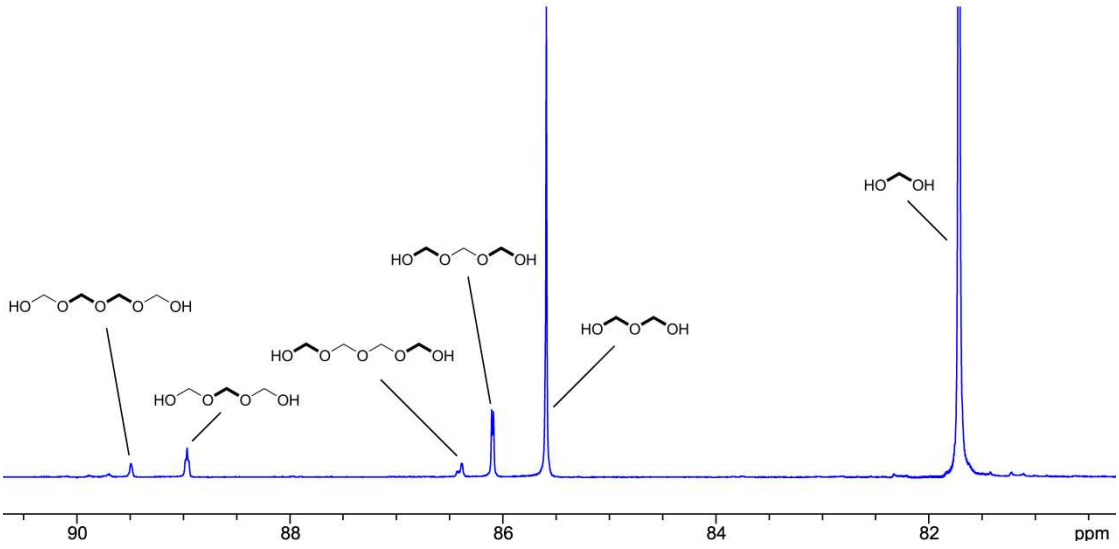

Figure 8.7 ^{13}C NMR spectrum (700 MHz) of 200 mM ^{13}C-HCHO in D_2O. Assignments for each resonance are displayed. Bold bond lines indicate the carbon atoms which correspond to each resonance.

Experiments were then conducted in order to evaluate the degree of oligomerisation and disproportionation under acidic and alkaline conditions. Samples of HCHO in D_2O were prepared at pD 3 and pD 10 using deuterium chloride and sodium deuteroxide to alter the pD. ^{1}H NMR Spectra of these samples revealed that the composition of HCHO-derived species in both samples varied from the neutral solution (Figure 8.8).

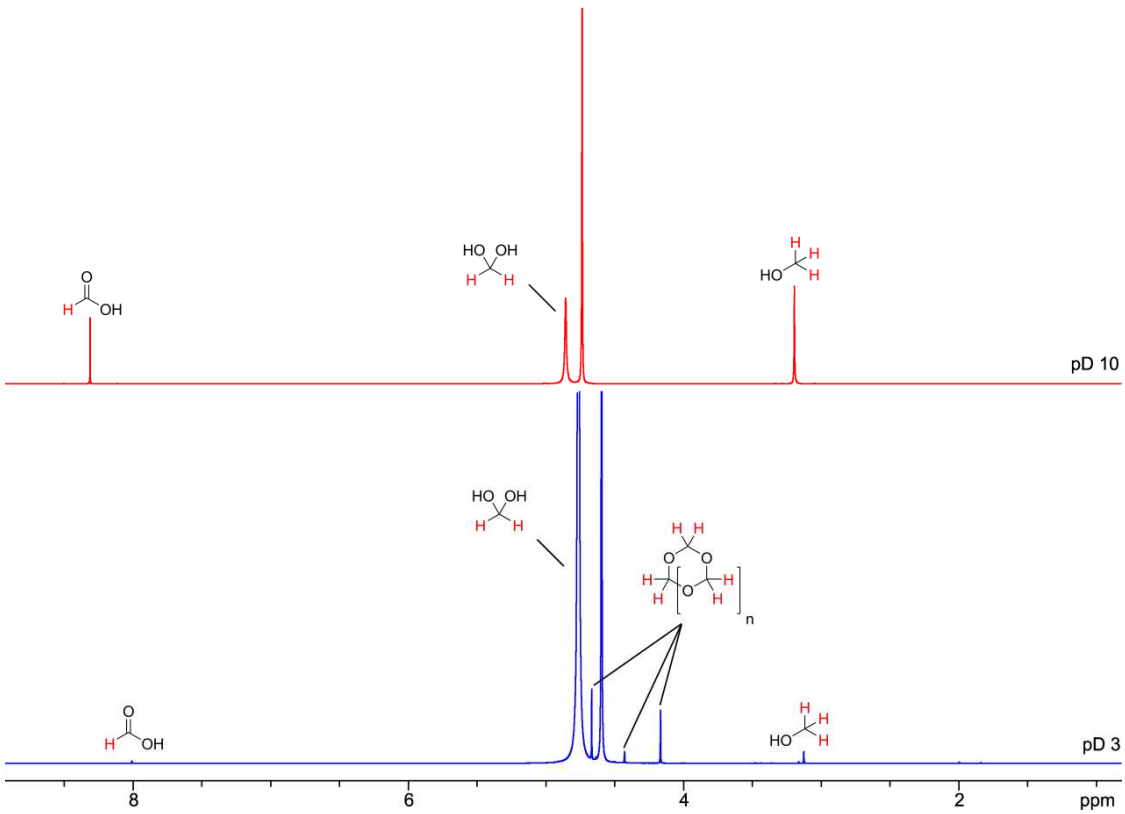

Figure 8.8 ^{1}H NMR spectrum (700 MHz) of 160 mM HCHO in D_2O at pH 3 and pH 10. Assignments for each resonance are displayed.

At pD 3, new signals at δ_H 4.17 ppm, δ_H 4.43 ppm and δ_H 4.67 ppm were observed. It is possible that these new resonances arise from cyclic glycols such as 1,3,5-trioxane, which are proposed to form under acidic conditions. The chemical shifts observed were comparable to literature values for such cyclic species, although the published values were attained under slightly different conditions. The Cannizzaro Reaction products were only present in trace amounts. At pD 10, however, both methanol and formic acid were observed at concentrations comparable to hydrated HCHO. No peaks corresponding to poly(oxymethylene) hemiformals or glycols in the neutral sample, or indeed any of the new peaks present in the acidic sample, could be detected at pD 10. This is presumably because of the requirement for acid catalysis during the formation of such species.

In conclusion, the experiments show that hydrated HCHO is the most abundant form of HCHO present in aqueous mixtures, which should therefore allow such solutions to be used to monitor the reaction of HCHO with GSH. Although the Cannizzaro

Reaction is an important side reaction under alkaline conditions, the slow rate of this reaction relative to the reaction of HCHO with GSH should result in no obvious loss of free HCHO, at least over the initial stages of reaction.

8.2.2 NMR of reduced and oxidised GSH

^{1}H NMR Experiments were carried out in order to clarify the shifts of characteristic resonances corresponding to GSH. It was envisaged that the identification of such resonances would be useful when analysing potentially complex mixtures of GSH-HCHO adducts. It was deemed prudent at this stage to characterise the ^{1}H spectrum of its corresponding disulfide (GSSG) in the expectation that this species may be formed in the reaction samples. Firstly, ^{1}H NMR spectra of 13.3 mM GSH in 50 mM phosphate buffer were run at pD 5.5, pD 6.5, pD 7.5, pD 8.5 and pD 9.5 respectively in order to ascertain the shifts of each resonance across a pD range. The spectra are shown in Figure 8.9.

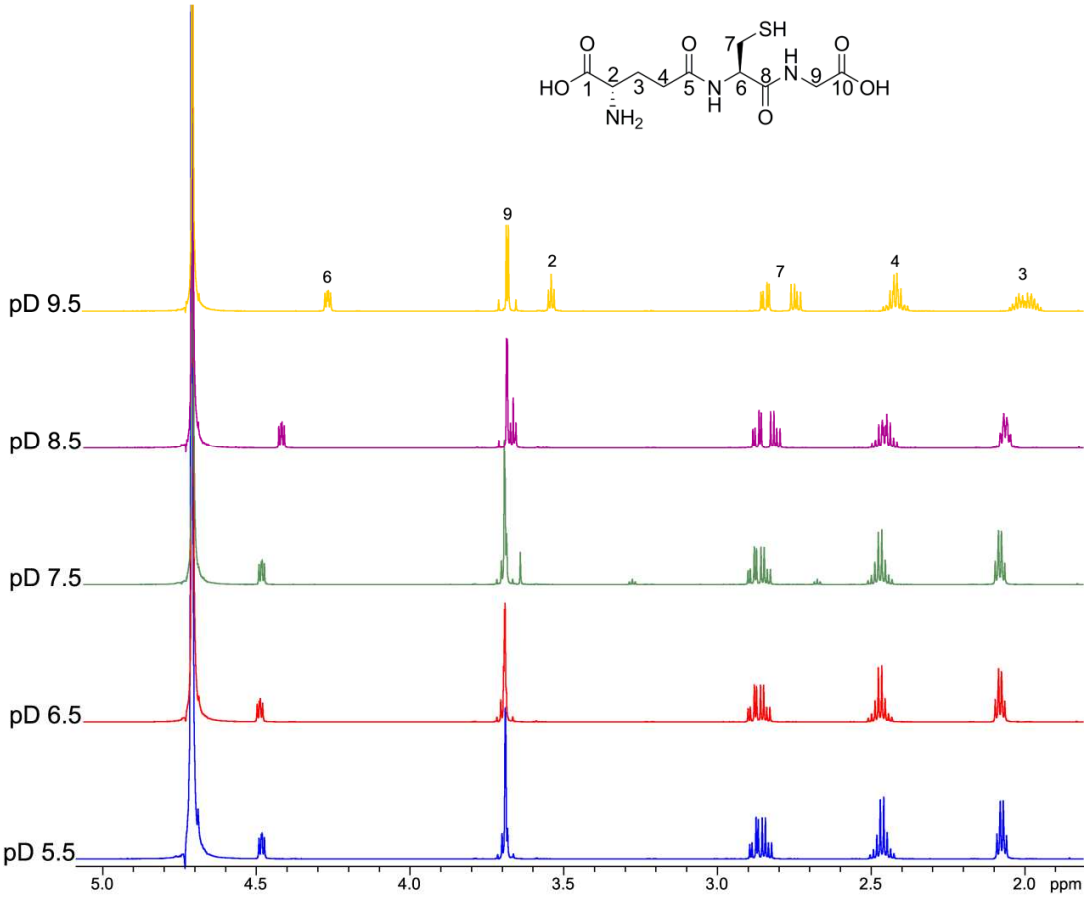

Figure 8.9 ^{1}H NMR spectra (700 MHz) of 13.3 mM GSH in 50 mM phosphate buffer at pD 5.5, pD 6.5, pD 7.5, pD 8.5 and pD 9.5 respectively. ^{1}H NMR assignments are indicated.

As could be expected from the structure of GSH, six distinct ^{1}H resonances could be identified in the spectra, corresponding to the protons attached to the α-glutamate, β-glutamate (two protons), γ-glutamate (two protons), α-cysteine, β-cysteine (two protons) and α-glycine (two protons) carbons. The signals corresponding to the α-glutamyl and α-glycinyl protons possessed the same chemical shift in the samples at pD 5.5, pD 6.5 and pD 7.5, giving only five apparent signals in the spectra. The resonances for the individual protons attached to the β-cysteinyl carbon were observed to diverge at higher pD, which may be due to a restriction of the local conformation upon thiol deprotonation (pKa of the GSH thiol = 9.2). Slight splitting of the β-glutamyl protons was also observed in the sample at pD 9.5. The shifts of both the α-glutamyl, β-glutamyl and α-cysteinyl protons decreased in the samples at pD 8.5 and pD 9.5, which again can be attributed to thiol deprotonation

(predominantly in the case of the α-cysteinyl protons) and also to deprotonation of the positively charged glutamyl amine.

^{1}H NMR Spectra were run on samples of GSSG (13.3 mM) at pD 5.5, pD 7.5 and pD 9.5 (Figure 8.10). Six distinct resonances were observed in the spectra, which corresponded to the analogous proton signals in GSH. All resonances, apart from those corresponding to the α-cysteinyl and β-cysteinyl protons, had near identical chemical shifts to the analogous GSH signals. The α-cysteinyl and β-cysteinyl resonances, however, had markedly different shifts, presumably due to the loss of the free cysteinyl thiol. The β-cysteinyl protons were observed to be diastereotopic, suggesting a loss of free rotation of the cysteinyl side chain. The α-glutamyl and β-glutamyl resonances were observed to shift upfield at pD 9.5 in a manner similar to the analogous GSH signals.

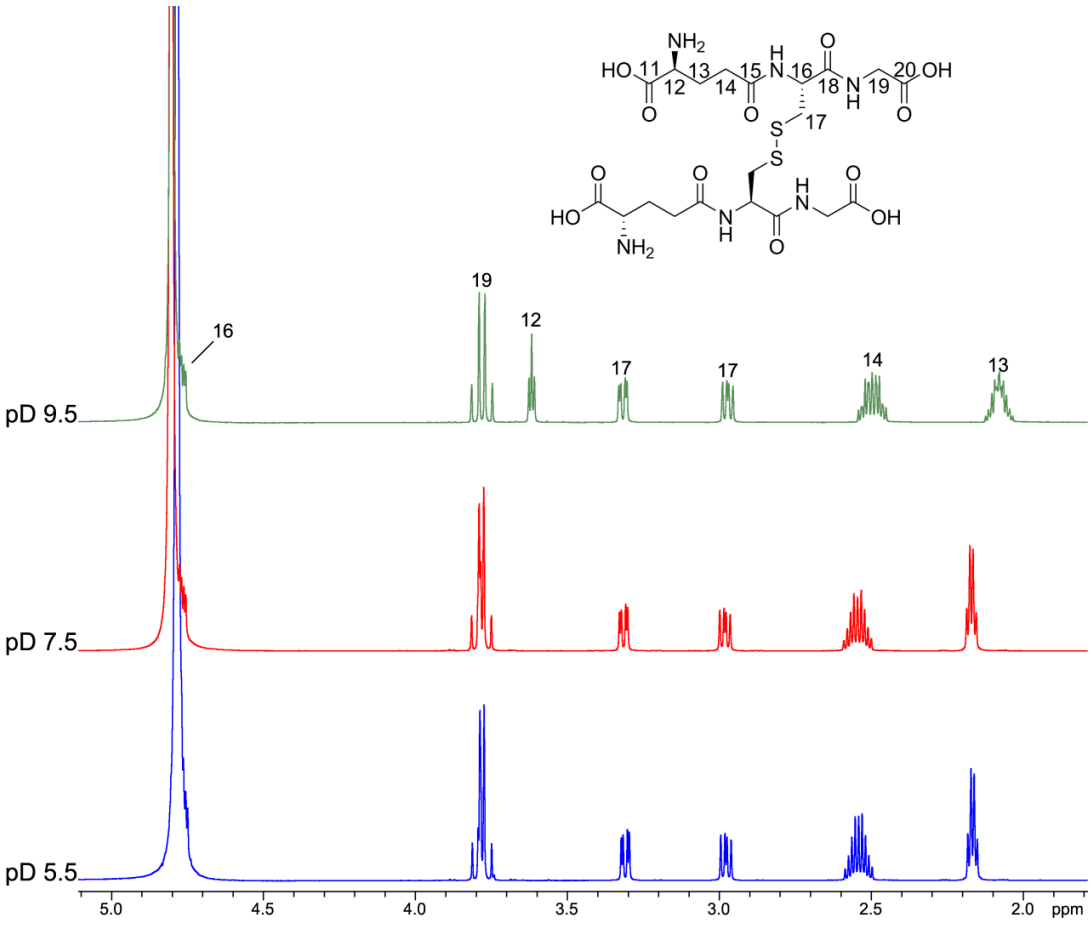

Figure 8.10 ^{1}H NMR spectra (700 MHz) of 13.3 mM GSSG in 50 mM phosphate buffer at pD 7.5 and pD 9.5 respectively. ^{1}H NMR assignments are indicated.

8.2.3 Initial Detection of $BiGF_2$

Initial work on the reaction of GSH and HCHO focused on confirming the formation of $BiGF_2$. Bateman *et al.* reported that $BiGF_2$ could be formed by mixing GSH with an excess of HCHO at pD 8.5. In order to confirm this observation, a sample was prepared under analogous conditions and tested by NMR. A solution of 40 mM stock GSH, buffered to pD 8.5 (phosphate buffer in D_2O), was diluted to 13.3 mM final concentration with a 160 mM stock solution of HCHO in D_2O. This sample was then left for 24 hours at room temperature before being transferred to an NMR tube and analysed directly by ^1H NMR. $BiGF_2$ was identified as the major species in the reaction mixture (Figure 8.11), thus confirming the production of $BiGF_2$ under these conditions.

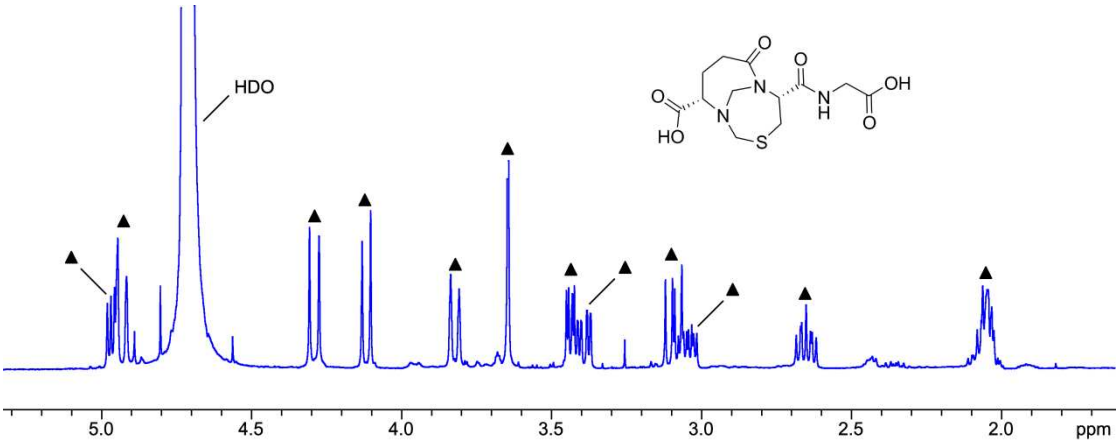

Figure 8.11 ^1H NMR spectrum (500 MHz) for a reaction mixture of GSH and 8 equivalents of HCHO after 24 hours at pD 8.5. Resonances corresponding to $BiGF_2$ are notated with black triangles (*spectrum run by Philippa Barlow*).

8.2.4 The GSH HCHO Reaction at Variable pD

^{13}C NMR experiments by Bateman *et al.* using ^{13}C-labelled HCHO have indicated that $BiGF_2$ is more prevalent in alkaline reaction mixtures. Also, the authors report the presence of another HCHO-derived species at δ_C 44.1 ppm under acidic conditions. The similarity in the chemical shift of this resonance to the unassigned signal observed by Naylor *et al.* (δ_C 44.0 ppm) suggests that these signals probably arise from the same species. However, in the absence of ^1H NMR data it is unclear

whether the identified species is a GSH-HCHO adduct. In order to reassess the prevalence of $BiGF_2$ across a pD range, and also to confirm the formation of the novel species, ^{1}H NMR experiments were carried out after three days on samples containing a four-fold excess of HCHO (non-labelled) at pDs 5.5, 6.5, 7.5, 8.5 and 9.5 respectively. Concentrations of each species were calculated by integrating characteristic resonances for each adduct and then normalising the intensity value relative to the internal standard (3-(trimethylsilyl)-2,2',3,3'-tetradeuteropropionic acid (TSP, δ_H 0.00 ppm). The ^{1}H spectra are shown in Figure 8.12.

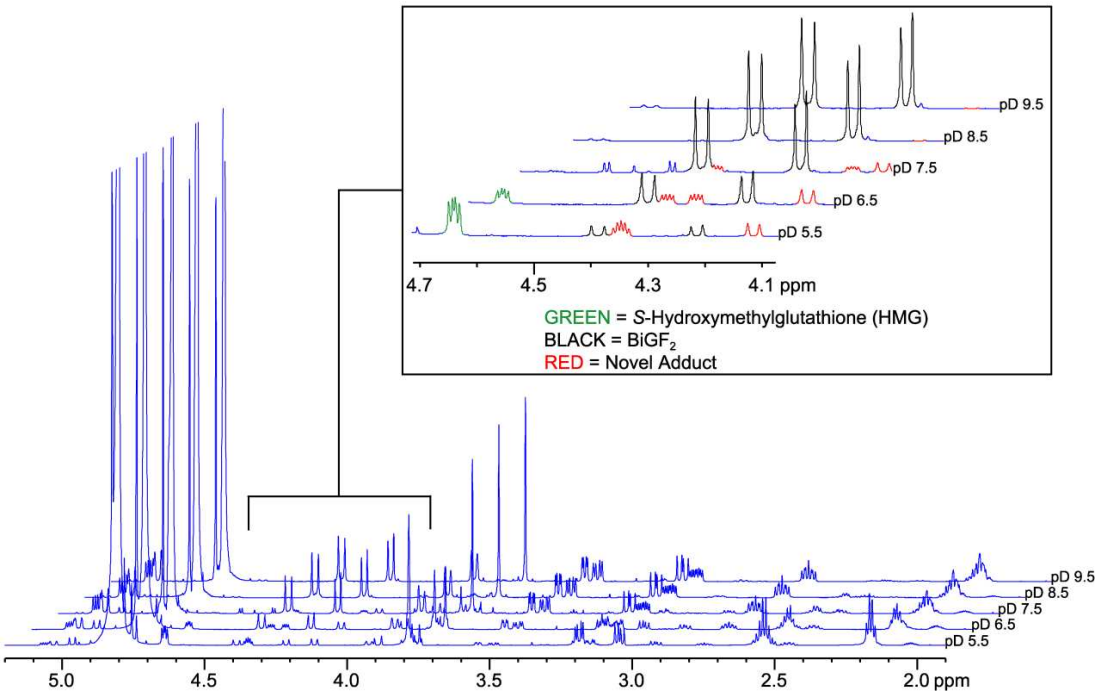

Figure 8.12 ^{1}H NMR spectra (700 MHz) for reaction mixtures of GSH and HCHO (four equivalents) after three days.

Firstly, it was noted that a signal corresponding to unreacted hydrated HCHO was present in all of the samples after three days. Also, it was apparent that all of the GSH added to the samples had reacted during the reaction period, as no signals corresponding to GSH were detected. No evidence for the formation of GSSG was observed in the samples, suggesting that GSH had reacted via the thiol, presumably with HCHO, before oxidation could occur. With regard to the other species in

solution, it was apparent that the composition of each sample was strongly pD dependent. HMG, which could be easily identified by its characteristic α-cysteinyl resonance at δ_H 4.63 ppm, was observed in the samples at pD 5.5 and pD 6.5, reaching a maximum concentration of 7.5 mM (pD 5.5). Although being the most abundant species at pD 5.5, no trace of HMG could be detected in the three more basic samples. $BiGF_2$ was found to be present in all of the samples but its concentration in solution varied greatly over the pD range. At pD 5.5, the concentration of $BiGF_2$ was only 1.5 mM. However, in contrast to HMG, its concentration appeared to increase in a near linear fashion from 1.5 mM at pD 5.5 to 10 mM at pD 7.5. $BiGF_2$ was most prevalent in the sample at pD 9.5, reaching a concentration of 12.7 mM. In addition to HMG and $BiGF_2$, other signals could be detected in the reaction mixtures, implying the presence of at least one other product (highlighted red, Figure 8.12). Analysis of all the samples suggested that the new signal intensities appeared to fluctuate to the same degree across the pD range, implying that the signals corresponded to the same species. It could also be assumed that the novel product had been formed from GSH, as many of the corresponding signals possessed similar chemical shifts to the aliphatic proton resonances in HMG and $BiGF_2$. In order to confirm the existence of a novel GSH-HCHO adduct, a 2D HSQC experiment was run on the sample at pD 5.5 in the expectation that any HCHO-derived signals would be revealed by their ^{13}C chemical shifts. The sample was left for two weeks before analysis by HSQC, which resulted in an increased concentration of the product. The spectrum is shown in Figure 8.13.

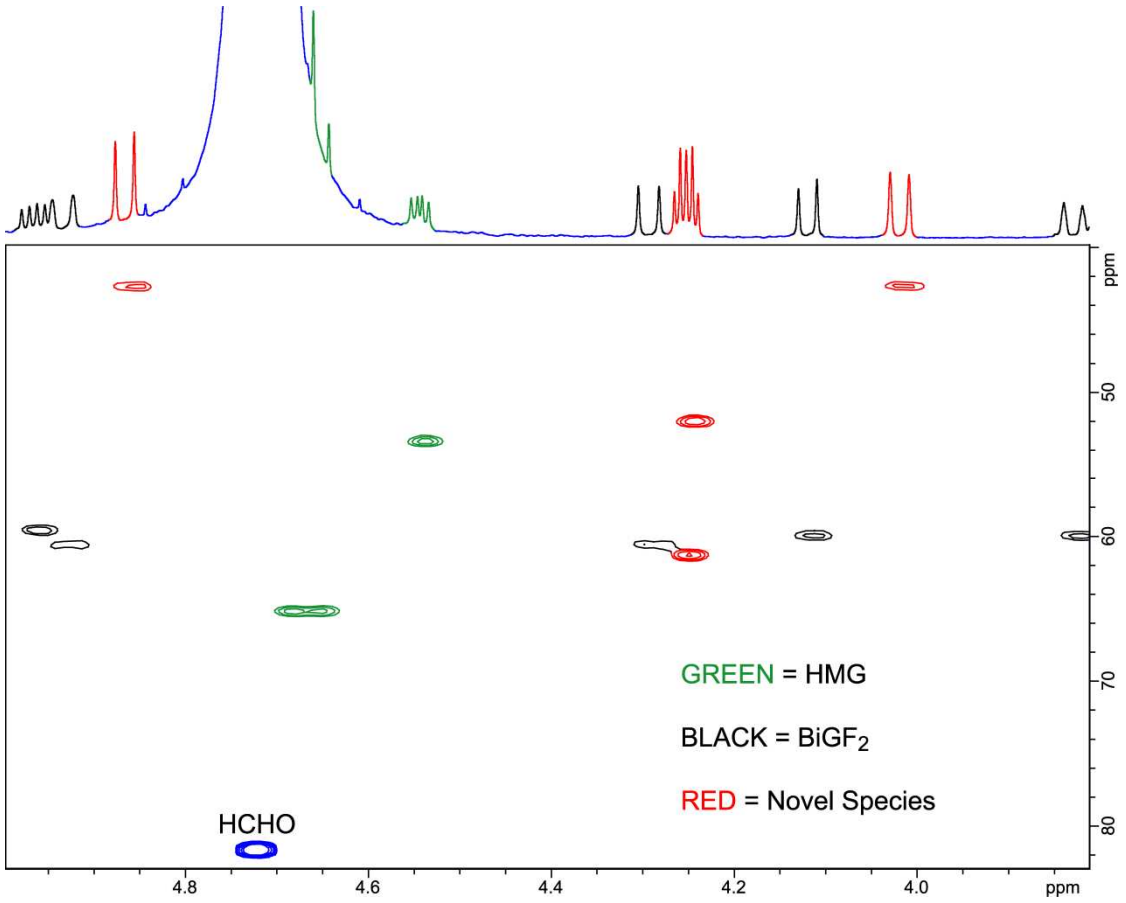

Figure 8.13 2D HSQC spectrum (700 MHz) of a reaction mixture of GSH and HCHO (four equivalents) after two weeks at pD 5.5.

In addition to ^{13}C-resonances corresponding to HCHO, HMG and $BiGF_2$, many new signals could be observed in the HSQC spectrum. Four new cross-peaks with ^{13}C chemical shifts between δ_C 40 ppm and δ_C 90 ppm were observed (two at δ_C 42.8 ppm, one at δ_C 52.0 ppm and one at δ_C 60.8 ppm), and it was assumed that these peaks, based on their ^{13}C shifts, were the most likely signals corresponding to HCHO-derived carbons (highlighted red, Figure 8.13). Of these four peaks, it was noted that the two signals at δ_C 42.8 ppm matched closely to the observed ^{13}C-resonance observed by both Naylor *et al.* and Bateman *et al.* It was thus assumed that the new adduct observed in the samples was in fact the same species that had been previously identified. Interestingly, the two cross-peaks at δ_C 42.8 ppm correlated to two ^{1}H doublet signals with very different chemical shifts (at δ_H 4.16 ppm and δ_H 4.94 ppm). This suggested that the two protons attached to the HCHO-

derived methylene unit had very different local environments, potentially pointing to a sterically restricted local conformation. The two other cross peaks in the aforementioned ^{13}C region (at δ_C 52.0 ppm and δ_C 60.8 ppm) appear to link to the same ^{1}H signal. However, this observation most likely implied that the ^{1}H-resonances corresponding to each ^{13}C-resonance coalesced. It was proposed at this stage that these signals may arise from the α-glutamyl and α-cysteinyl derived carbons in the new adduct.

Having confirmed the formation of the novel adduct, it was possible to monitor its formation across the pD range by calculating its concentrations in the reaction mixtures (Figure 8.14). Interestingly, this product was most abundant at pD 6.5 (4 mM) suggesting that neither strongly acidic nor strongly basic conditions favour its formation and/or stability.

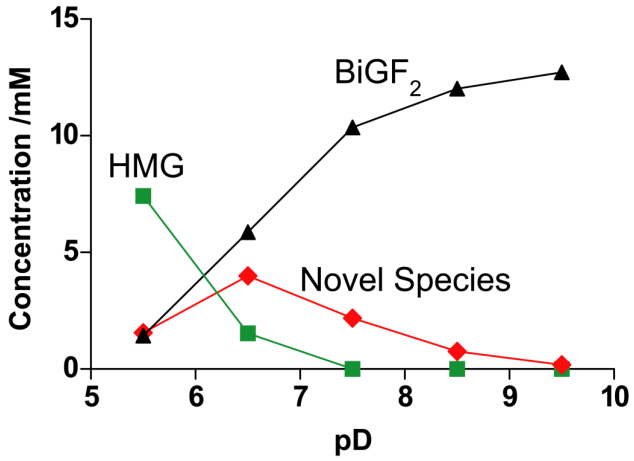

Figure 8.14 Concentrations of HMG, $BiGF_2$ and the novel adduct after three days at different pDs.

8.2.5 Purification of adducts

Given that both $BiGF_2$ and the novel GSH-HCHO adduct could be detected in samples after three days (and indeed after two weeks at pD 5.5), it was hoped that these two species may be sufficiently stable to be isolated and fully characterised. Purification was attempted on a reaction mixture of GSH and four equivalents of HCHO at pD 6.5, which was allowed to react for three days before being quenched

by lyophilisation. The remaining solid was redissolved in H_2O and then injected onto a C18 reverse phase column (Vydac) for HPLC purification, using ESI^- mass spectrometry to detect the separated species.

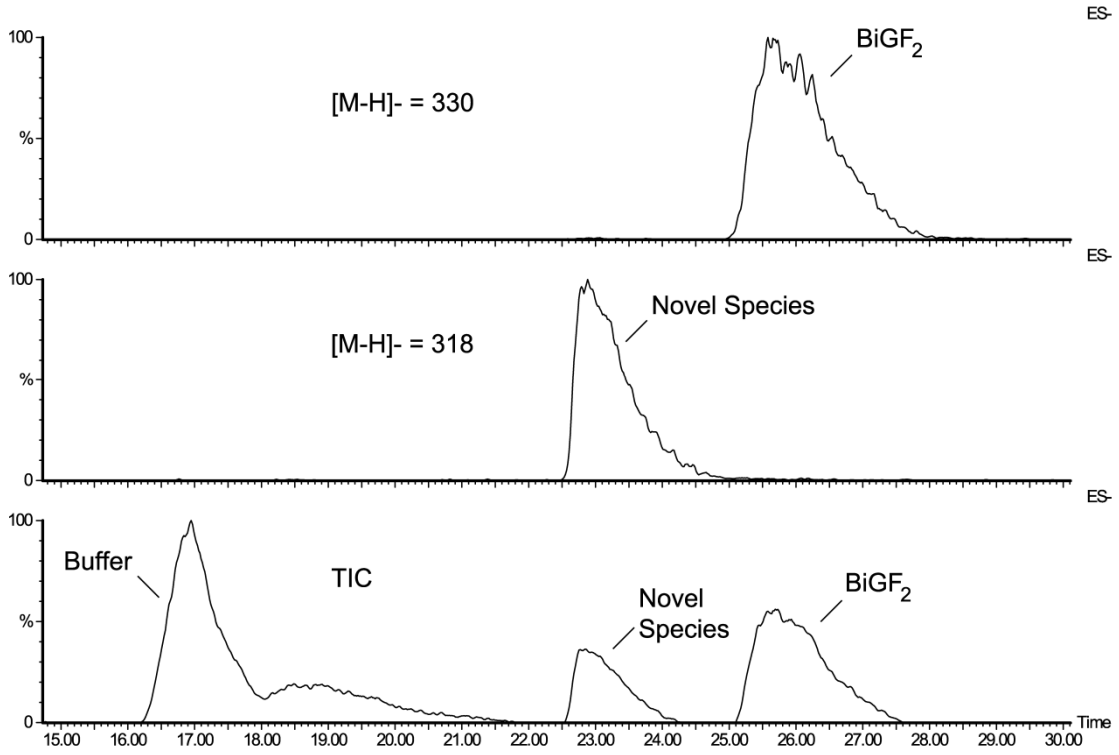

Figure 8.15 LC-MS chromatogram for a reaction mixture containing GSH (13.3 mM) and HCHO (four equivalents) at pD 6.5 after three days.

Four peaks were observed in the chromatogram (Figure 8.15), of which two appeared to correspond to GSH-HCHO adducts. The first of these peaks, which eluted after 22.5 minutes, corresponded to a species with a mass of 319 Da, suggesting a 1:1 GSH-HCHO adduct. The compound which eluted in the second peak (after 25 minutes) had a mass of 331 Da, matching the mass expected for $BiGF_2$. The two peaks were separated and the elution solvent lyophilised to give two white solids. ^1H NMR spectra were collected on samples of the purified species redissolved in D_2O (Figure 8.16), which confirmed the products as the new adduct (the first peak) and $BiGF_2$ (the second peak) respectively.

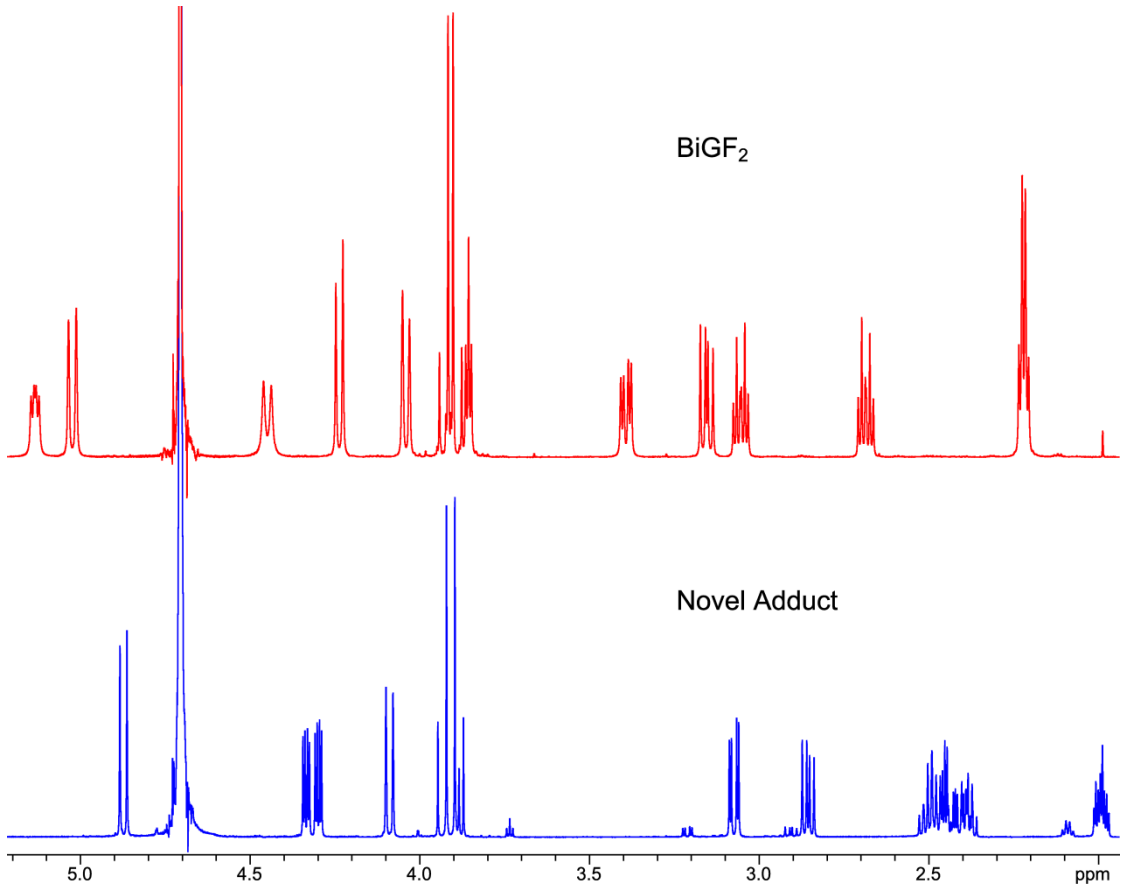

Figure 8.16 ^{1}H NMR spectra (700 MHz) of $BiGF_2$ (Above) and the Novel Adduct (Below) in D_2O.

8.2.6 Characterisation of $BiGF_2$

^{1}H, 2D COSY, 2D HSQC, 2D HMBC and 2D NOESY experiments were conducted on a sample of purified $BiGF_2$ (dissolved in D_2O). It was hoped that the data acquired would fully evaluate the structural reassignment of this adduct by Bateman *et al.*, and therefore clarify its structure in solution. Previously, only ^{1}H, ^{13}C and 2D COSY experiments had been run on samples containing $BiGF_2$, and therefore it was felt that a more comprehensive NMR study should be undertaken to confirm the structural assignments. The 2D HSQC spectrum is shown in Figure 8.17.

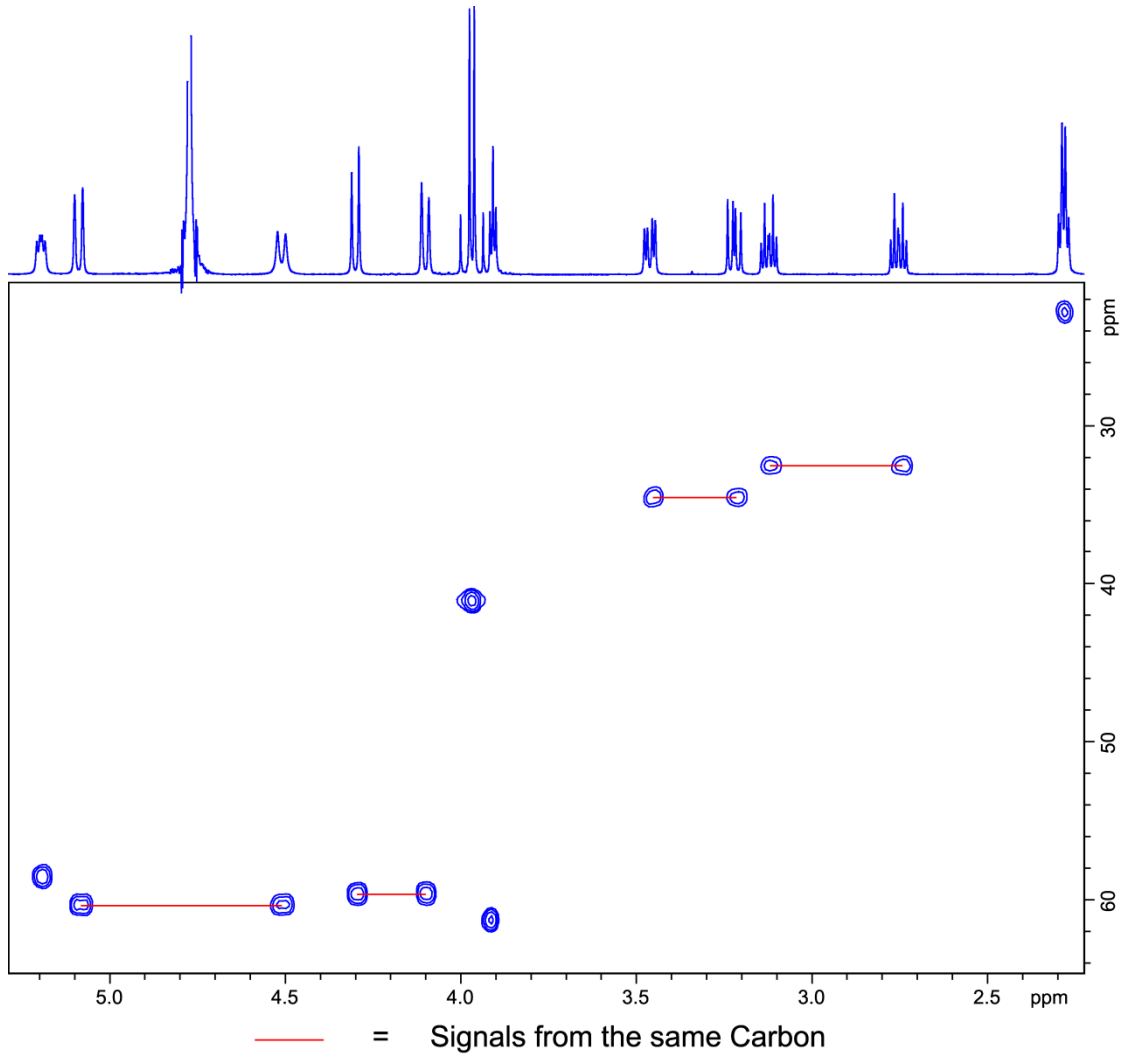

Figure 8.17 2D HSQC spectrum (700 MHz) of $BiGF_2$ in D_2O. Cross-peaks highlighted in red correspond to protons attached to the same carbon.

Although ^{13}C-resonances for $BiGF_2$ had been previously identified,[212] the HSQC spectrum, which correlates each ^{13}C-signal to the resonances of attached protons, offered new insight into the assignment of each ^{13}C-resonance to a carbon in the structure. Firstly, it was apparent that a number of the ^{1}H-signals in the ^{1}H NMR spectrum corresponded to diastereotopic protons attached to the same carbon atom. This observation adds credence to the assigned structure of $BiGF_2$, as it could be expected that this bicyclic structure would lead to protons with restricted conformations. Also, it was possible to assign the ^{13}C-resonance at δ_C 41.2 ppm to the α-glycinyl carbon by direct analogy to the ^{1}H chemical shifts of the attached protons, which could be identified by the similarity of their shifts (δ_H 3.95 ppm and

δ_H 3.99 ppm) to the analogous GSH signals (Figure 8.9).

The 2D COSY spectrum (Figure 8.18) was identical to that run by Bateman *et al.* and allowed for the assignment of the ^{1}H signals of both the glutamyl and cysteinyl protons. It was also possible to assign the ^{13}C-resonances associated with each of these positions by referring to the 2D HSQC data. Assuming no rearrangement of the GSH-derived backbone (a change that was not was proposed by either of the previous assignments), the protons attached to the β-glutamyl-derived carbon could be expected to give cross-peaks to both the α-glutamyl and γ-glutamyl protons. The only resonance to give cross-peaks to two others (excluding geminal pairs) was the resonance at δ_H 2.28 ppm. As no other protons could be expected to give cross-peaks to more than one resonance, except when coupling to geminal partners (highlighted with red lines, Figure 8.19), it was possible to assign the ^{1}H-resonance at δ_H 2.28 ppm, and therefore the ^{13}C-resonance at δ_C 22.9 ppm (Figure 8.18), to this position. The three signals which correlated to the resonance at δ_H 2.28 ppm (at δ_H 2.75 ppm, δ_H 3.12 ppm and δ_H 3.91 ppm respectively) could be assigned by comparing the ^{13}C-signals of their attached carbons. The protons with ^{1}H-signals at δ_H 2.75 ppm and δ_H 3.12 ppm were found to be attached to a carbon with a ^{13}C-resonance at δ_C 32.6 ppm, demonstrating that these signals corresponded to geminal pairs. This observation allowed these signals to be assigned to the γ-glutamyl centre, as the α-glutamyl position was only expected to possess one proton. The ^{1}H-resonance at δ_H 3.91 ppm and the corresponding ^{13}C-resonance at δ_C 61.4 ppm could then be assigned to the α-glutamyl position. The α-cysteinyl and β-cysteinyl centres were assigned by noting COSY correlations between the ^{1}H-signals at δ_H 3.22 ppm and δ_H 3.46 ppm (identified as geminal partners by HSQC) and the ^{1}H-signal at δ_H 5.20 ppm. As no other COSY correlations apart from those already assigned to the glutamyl-derived centres were expected in the molecule, these signals were assigned to the β-cysteinyl and α-cysteinyl protons respectively. HSQC data also allowed assignment of the corresponding ^{13}C-signals (at δ_C 34.7 ppm and δ_C 58.6 ppm respectively).

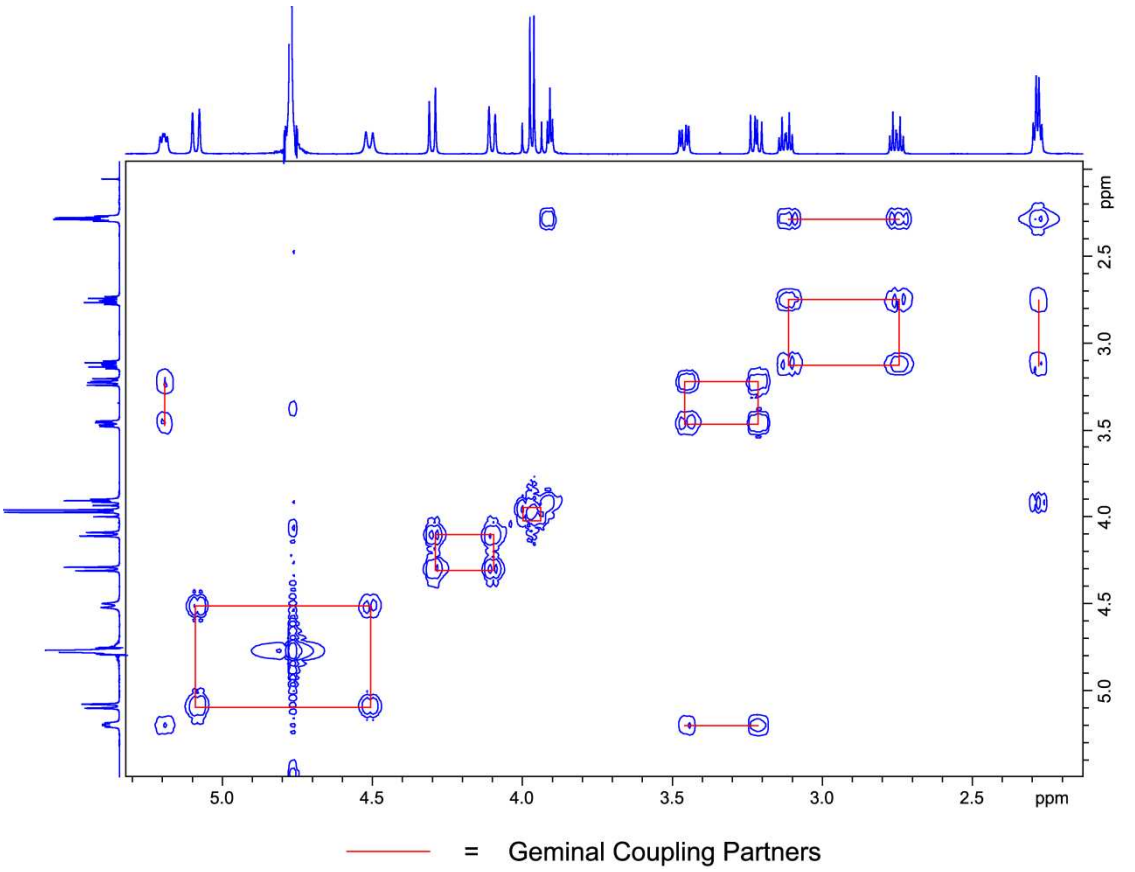

Figure 8.18 2D COSY spectrum (700 MHz) of $BiGF_2$ in D_2O. Cross-peaks highlighted in red correspond to protons attached to the same carbon.

Assignment of the HCHO-derived protons and carbons was achieved by analysis of the 2D HMBC spectrum (Figure 8.19). Although it could be assumed that the ^{1}H-resonances at δ_H 4.10 ppm, δ_H 4.30 ppm, δ_H 4.51 ppm and δ_H 5.09 ppm and the ^{13}C-resonances at δ_C 59.7 ppm and δ_C 60.4 ppm derived from these centres, based on their chemical shifts, it was not possible to conclusively assign each signal to the correct HCHO-derived methylene using the existing data. Therefore it was necessary to identify HMBC correlations between the HCHO-derived protons and the neighbouring carbons in order to assign the signals. Correlations from the ^{1}H resonances at δ_H 4.10 ppm and δ_H 4.30 ppm to both the α-glutamyl and the β-cysteinyl carbons (carbons 22 and 27, Figure 8.19) revealed bonds from the corresponding methylene via both the glutamyl amine and the cysteinyl thiol. This allowed assignment of these ^{1}H-signals to the protons at carbon 31 (δ_C 59.7 ppm, Figure 8.19). The ^{1}H-signal at δ_H 4.51 ppm possessed cross-peaks to both the α-

glutamyl and δ-glutamyl carbons (carbons 22 and 31), which was expected of protons attached to the aminal methylene 32. The correlations from the ^{1}H-resonance at δ_H 5.09 ppm (which corresponds to a proton attached to the same carbon as the resonance at δ_H 4.51 ppm) to the α-cysteinyl carbon and the HCHO-derived hemithioaminal carbon (carbons 26 and 31) confirmed the assignment of the two ^{1}H resonances to this position (δ_C 60.4 ppm). These assignments contradict the assignments by Bateman *et al.*, which proposed that the higher of the two ^{13}C-resonances (δ_C 62.2 ppm) corresponded to the hemithioaminal methylene, based on chemical shift prediction. The HMBC spectrum also facilitated the assignment of the carbonyl carbon ^{13}C-resonances, which had not been visible by HSQC due to the lack of attached protons. By monitoring correlations from the assigned ^{1}H-resonances, it was possible to assign each carbonyl ^{13}C-resonance by referring to the predicted structure. For example, the ^{13}C-resonance at carbon 21 could be elucidated by observing HMBC correlations from the proton at position 22 to a signal at δ_C 175.3 ppm. As it could be expected that the protons at position 22 would only form a strong cross-peak with the carbonyl carbon at position 21, it was possible to assign the resonance to this position. The ^{13}C-resonances for carbons 25, 28 and 30 were also assigned by observing HMBC cross-peaks from the protons at carbons 24, 26 and 29 respectively (Figure 8.19). Correlations between positions 21 and 23, 25 and 26, 25 and 32, and 28 and 29 helped to confirm the carbonyl assignments and validate the proposed structure of $BiGF_2$.

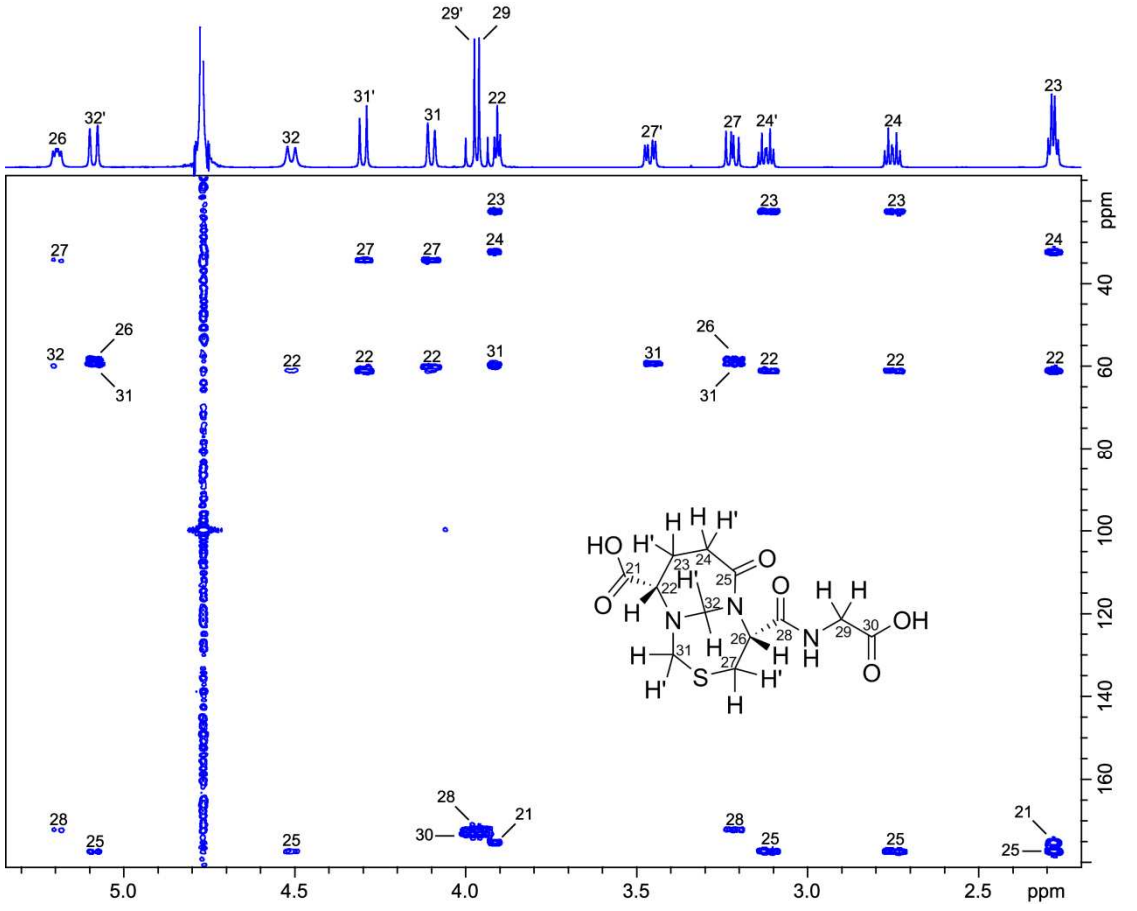

Figure 8.19 2D HMBC spectrum (700 MHz) of $BiGF_2$ in D_2O. Cross-peaks are notated with the carbon number they represent.

Having confirmed the configuration of $BiGF_2$, it was now possible to investigate its solution conformation. A NOESY spectrum of $BiGF_2$ was run in the hope that NOE cross-peaks observed may give information on the proton spatial arrangements. This data should also allow for the assignment of each diastereotopic proton to its respective ^{1}H-resonance. The acquired NOESY spectrum is shown in Figure 8.20.

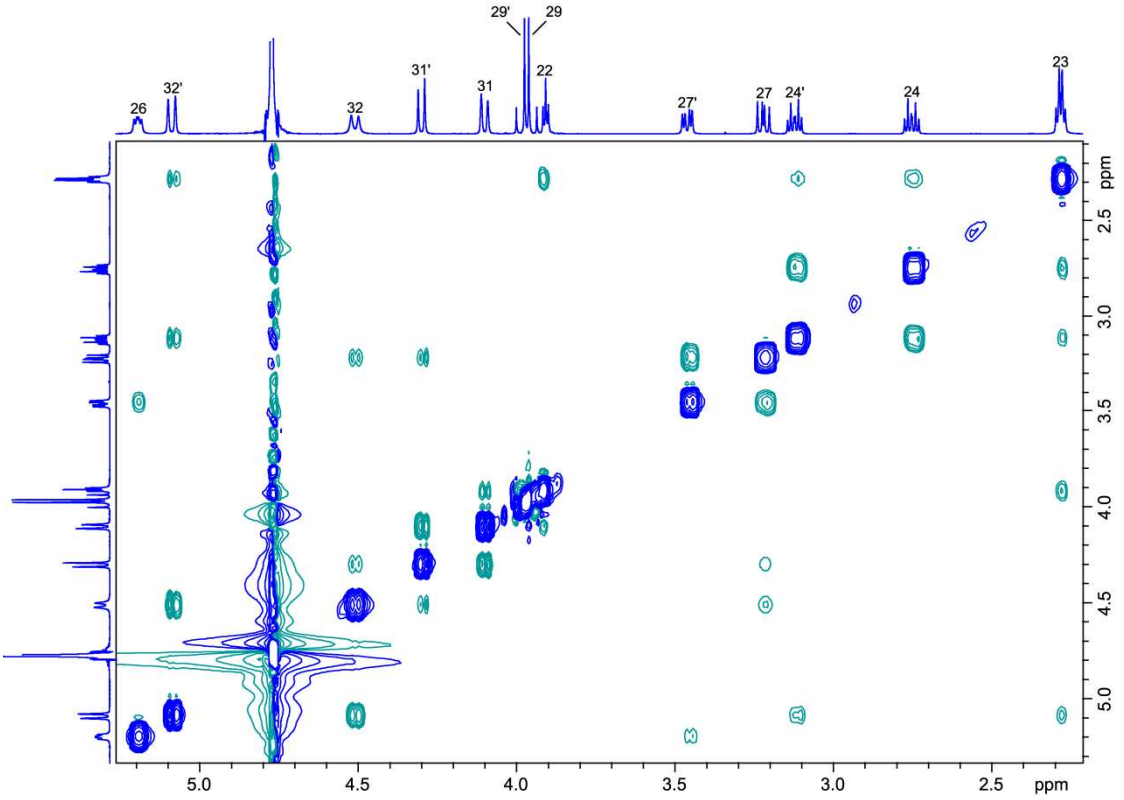

Figure 8.20 2D NOESY spectrum (700 MHz) of $BiGF_2$ in D_2O.

Firstly, it was noted that proton 26 (i.e. the proton attached to carbon 26 in the structure) possessed a positive NOE to one of the protons attached to carbon 27. As NOE correlations arise between protons that are in close proximity, it was therefore proposed that this proton at carbon 27 must be closer to proton 26 than its geminal partner. This suggests that this proton lay *syn* to proton 26. The stereochemistry at carbon 26 was assumed to be analogous to GSH, and therefore the proton at carbon 27 was assigned to the *pro-R* position (proton 27', Figure 8.20). Based on this assignment, it was possible to assign the protons at carbon 32 by identifying an NOE cross-peak between one of these protons (proton 32, δ_H 4.51 ppm) and the other proton at carbon 27 (proton 27, *pro-S*). This proton at carbon 32 could then be assigned to the *pro-R* position. As no NOE cross-peaks could be observed between proton 32 and either proton 26 or proton 27', it was proposed that this proton lies away from these centres, suggesting a solution conformation similar to that observed in the crystal structure (Figure 8.2). Proton 32', which could be assigned to the *pro-S* configuration by analogy to the assignment of proton 32, possessed NOE cross-

peaks to one proton on carbon 23 and also to one proton on carbon 24. As proton 32' was assumed to lie on the same face as proton 32 (i.e. away from proton 26), it was possible to assign this proton's NOE-coupled partners to the *pro-R* (proton 3') and *pro-S* (proton 4') configurations respectively. An NOE correlation was also noted between proton 22 and a proton on carbon 31. This observation allowed the assignment of this proton to the *pro-R* position (proton 11), with the assumption that the stereochemistry of carbon 22 was analogous to that in GSH. The assignment of proton 31' (*pro-S* by analogy with assignment of proton 31) was confirmed by an NOE cross-peak between this proton and proton 32. No NOE correlations from the protons attached to carbon 29 could be observed in the spectrum, and therefore it was not possible to assign each proton at this position to its individual resonance.

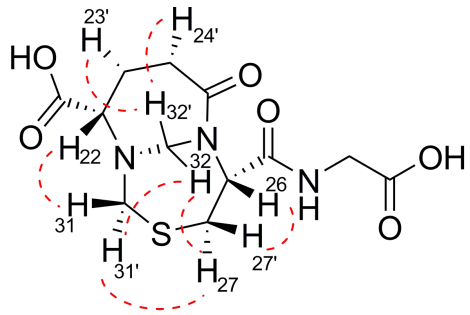

Figure 8.21 Structure of $BiGF_2$ showing important NOE correlations.

In summary, NMR assignment was carried out on a pure sample of $BiGF_2$ for the first time, which allowed assignment of all ^{1}H- and ^{13}C-resonances to protons and carbons in the structure. Full assignments are shown in Figure 8.22.

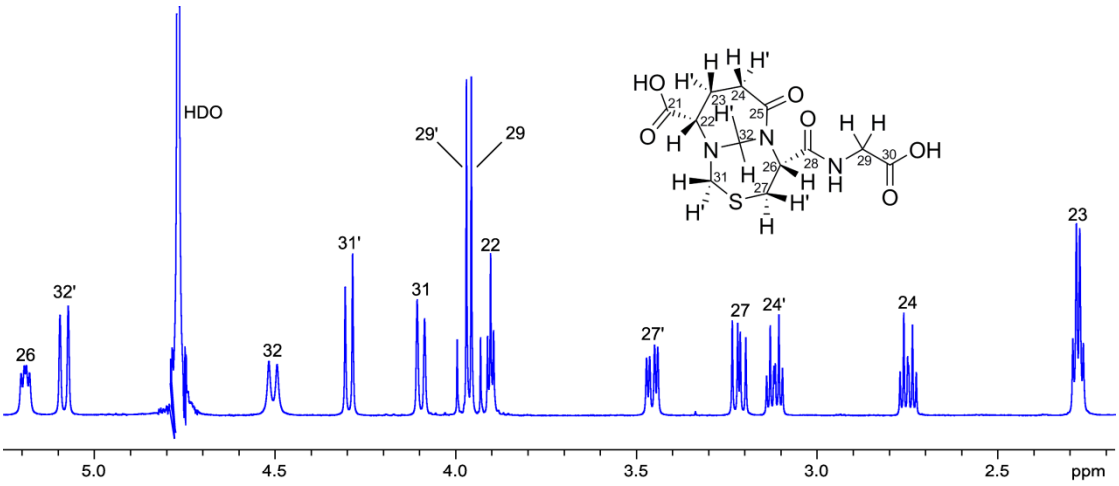

Position	^{13}C/ ppm:	^{1}H/ ppm:	Multiplicity:	Coupling constant/ Hz:	HMBC Correlations (Carbon Atom Number)
21	175.3				
22	61.4	3.91	app t	6.5	21, 23, 24, 31
23	22.9	2.28	app q	6.5	21, 22, 24, 25
24	32.6	2.75	app dt	6.5, 16.5	22, 23, 25
24'		3.12	app dt	6.5, 16.5	22, 23, 25
25	177.4				
26	58.6	5.20	dd	6.5, 10.5	27, 28, 32
27	34.7	3.22	dd	10.5, 15.5	26, 28, 31
27'		3.46	dd	6.5, 15.5	31
28	172.2				
29	41.2	3.95	d	18.0	28, 30
29'		3.99	d	18.0	28, 30
30	173.1				
31	59.7	4.10	d	14.5	22, 27
31'		4.30	d	14.5	22, 27
32	60.4	4.51	d	16.0	22, 25
32'		5.09	d	16.0	25, 26, 31

Figure 8.22 NMR assignments for $BiGF_2$.

The data endorsed the structural configuration proposed by Bateman *et al.*,[212] arguing against the previous assignment,[211] which was based mainly on chemical shift prediction. In addition, the work allowed for correction of the ^{13}C assignments for the HCHO-derived carbons by Bateman *et al.* NOE data suggested a solution conformation similar to the crystal form when bound to CBR1, implying that the bicyclic ring system may possess a large degree of rigidity in solution.

8.2.7 Characterisation of the Novel Adduct

Having assigned the structure of $BiGF_2$, attention was focused towards identifying the structure of the novel adduct. The ^{1}H NMR spectrum of the pure adduct (Figure 8.16) indicated that the structure of this new species differed significantly from the structure of $BiGF_2$, and both NMR and mass spectrometry analysis during

purification suggested that the product possessed only one HCHO-derived methylene unit. Structural characterisation was achieved using 1H, 2D COSY, 2D TOCSY, 2D HSQC, 2D HMBC and 2D NOESY techniques, as detailed below.

The ^{1}H-resonances corresponding to the HCHO-derived CH_2 group had already been established by the 2D HSQC spectrum on the reaction mixture of GSH and HCHO at pD 5.5 (δ_H 4.16 ppm and δ_H 4.94 ppm, Figure 8.13). Identification of other ^{1}H resonances was impeded in this spectrum, however, due to overlapping resonances from the other species in the mixture (HMG and $BiGF_2$). Also, the ^{1}H-resonance at δ_H 4.30 ppm in the ^{1}H NMR spectrum of this reaction mixture appeared to separate to two signals in a ^{1}H NMR spectrum of the pure adduct, thus allowing assignment of the individual ^{13}C-resonances to each of these protons by HSQC. Therefore, a 2D HSQC experiment was run on the purified sample, which is shown in Figure 8.23.

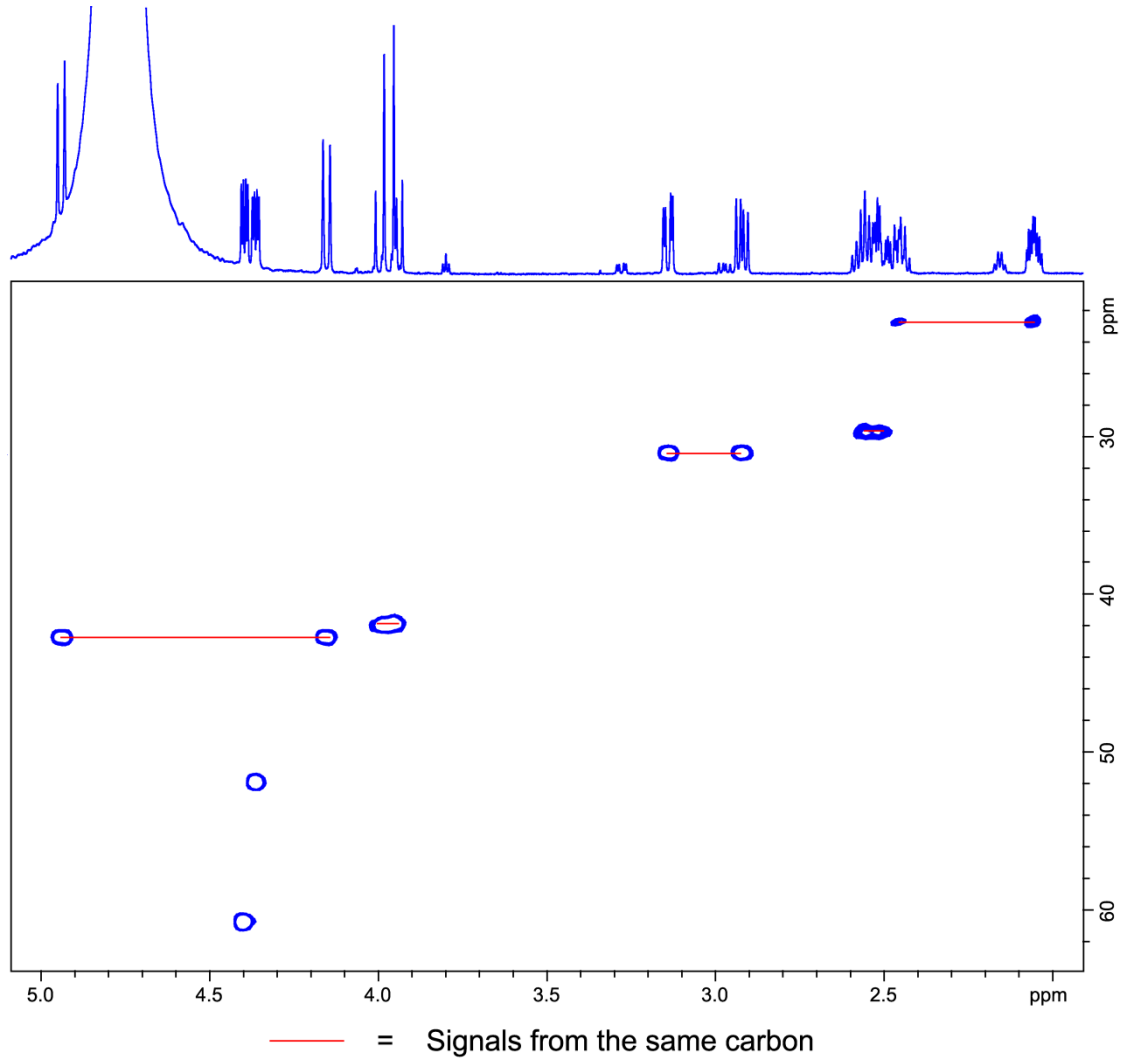

Figure 8.23 2D HSQC spectrum (700 MHz) of the novel adduct in D_2O. Cross-peaks highlighted in red correspond to protons attached to the same carbon.

By analogy with the spectrum for $BiGF_2$, it was possible to predict ^{13}C assignments (and therefore the attached ^{1}H signals) for the GSH-derived carbons. For example, the ^{13}C-resonance at δ_C 22.8 ppm closely resembled the ^{13}C shift for carbon 23 in $BiGF_2$ (δ_C 22.9 ppm), which corresponded to the β-glutamyl carbon in GSH. It was therefore postulated that this resonance in the new adduct corresponded to the β-glutamyl derived carbon. The ^{13}C-resonances for the γ-glutamyl, β-cysteinyl and α-glycinyl derived carbons (at δ_C 29.9 ppm, δ_C 31.1 ppm and δ_C 42.1 ppm respectively) could also be assigned at this stage by analogy with the $BiGF_2$ assignments (at δ_C 32.6 ppm, δ_C 34.7 ppm and δ_C 41.2 ppm respectively).

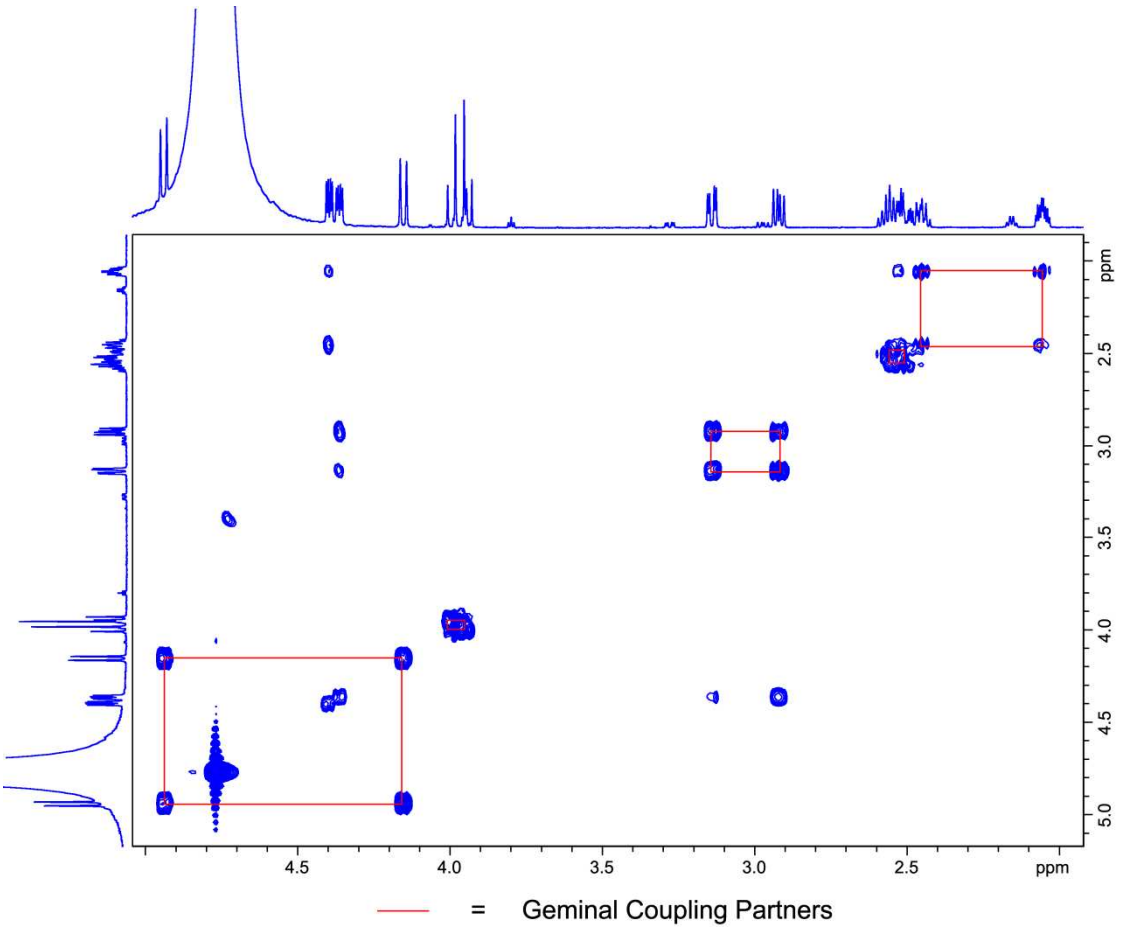

Figure 8.24 2D COSY spectrum (700 MHz) of the novel adduct in D_2O. Cross-peaks highlighted in red correspond to protons attached to the same carbon.

The 2D COSY spectrum (Figure 8.24) allowed verification of the assignments from the HSQC data by displaying one-bond COSY correlations between the assigned protons. It was possible to confirm the ^{1}H and ^{13}C-resonances for the β-glutamyl and γ-glutamyl derived centres by observing correlations between their corresponding protons. A COSY correlation between the protons on the β-glutamyl derived carbons (at δ_H 2.06 ppm and δ_H 2.47 ppm) and the proton resonance at δ_H 4.40 ppm also allowed the assignment of this resonance (and therefore the ^{13}C-resonance at δ_C 60.8 ppm) to the α-glutamyl derived centre. The α-cysteinyl resonances were assigned by observing a correlation between the β-cysteinyl protons (at δ_H 2.93 ppm and δ_H 3.14 ppm) and the ^{1}H-resonance at δ_H 4.37 ppm. These observations confirmed the assignments of the α-glutamyl and α-cysteinyl centres based on the 2D HSQC spectrum of the reaction mixture at pD 5.5 (Figure 8.13). The TOCSY

spectrum (Figure 8.25) further supported the HSQC and COSY based assignments for the glutamyl chain by highlighting correlations between the α-, β- and γ-glutamyl protons. These observations confirmed that formation of the adduct had not resulted in fragmentation of the glutamyl side chain.

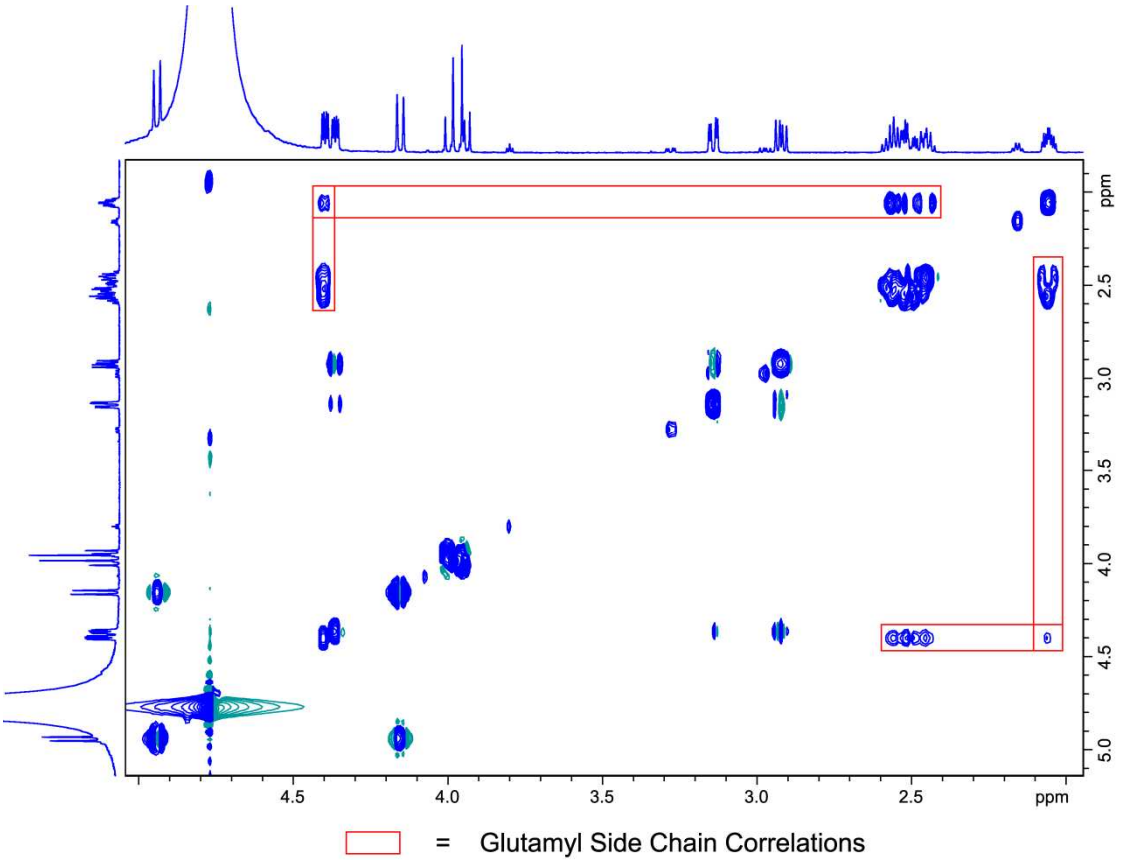

Figure 8.25 2D TOCSY spectrum (700 MHz) of the novel adduct in D_2O. Cross-peaks highlighted in red correspond to correlation between the glutamyl side chain protons.

The most informative data regarding the structural configuration of the new adduct was obtained from the HMBC spectrum (Figure 8.26).

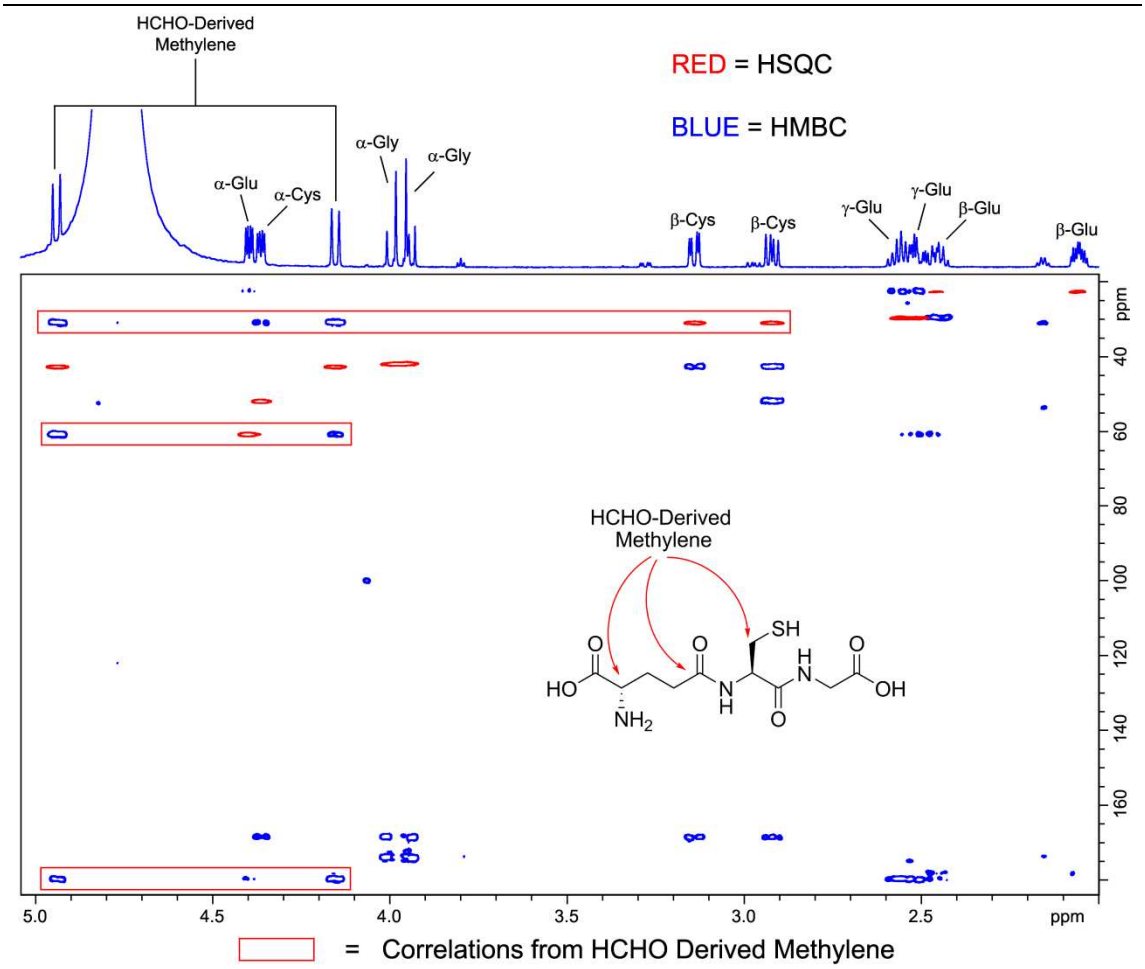

Figure 8.26 Overlaid 2D HSQC (red) and 2D HMBC (blue) NMR spectra (700 MHz) of the novel adduct in D_2O. Correlations highlighted in red correspond to correlations from the HCHO derived methylene protons.

Attention was initially focused upon characterising the connectivity of the HCHO-derived methylene, which was difficult to predict by analogy to the other adducts due to its relatively low ^{13}C-resonance at δ_C 42.8 ppm. HMBC Correlations were observed from the HCHO-derived protons to the carbon resonances at δ_C 31.1 ppm and δ_C 60.8 ppm, which had been assigned to the β-cysteinyl and α-glycinyl derived carbons respectively. These correlations implied that a monocyclic hemithioaminal was present in the structure of the novel adduct, presumably formed from HCHO and both the cysteinyl thiol and the glutamyl amine. However, it was noted that ^{13}C-resonances for hemithioaminal carbons often fall between δ_C 50.0 ppm and δ_C 60.0 ppm, and therefore the relatively low ^{13}C-resonance at δ_C 42.8 ppm suggested that either the HCHO-derived centre was not connected via the thiol and amine, or that

the hemithioaminal species resided in an abnormally shielded local environment. Also, an HMBC correlation was observed between the HCHO-derived methylene and a ^{13}C-resonance at δ_C 178.1 ppm. This resonance was also found to correlate to the γ-glutamyl derived protons, suggesting that this resonance corresponded to the δ-glutamyl derived carbonyl carbon. The observation that the HCHO-derived methylene possessed HMBC correlations to both the β-glutamyl and δ-glutamyl carbons (but not the γ-glutamyl carbon), as well as to the β-cysteinyl carbon, indicated that the novel adduct had undergone a rearrangement of the GSH backbone. The proposed structural configuration is shown in Figure 8.27.

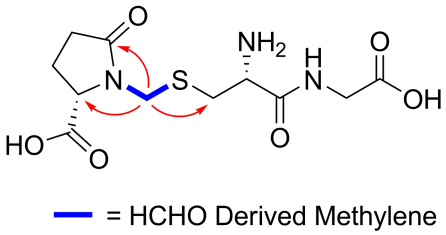

Figure 8.27 Proposed structure of the novel adduct based on HMBC data. Red arrows indicate observed HMBC correlations from the HCHO derived methylene.

The hemithioaminal carbon in the proposed structure was predicted to possess a ^{13}C-resonance at δ_C 45.6 ppm using the ACD/iLab service chemical shift prediction software, which compared favourably with the observed chemical shift at δ_C 42.8 ppm. Further evidence for this structural assignment was obtained from the NOESY spectrum of the adduct (Figure 8.28). Positive NOE's were observed between the hemithioaminal protons and the protons attached to the α-glutamyl and β-cysteinyl derived carbons, indicating that these protons lie in close proximity in the structure. Also, it was possible to detect positive NOE's between the α-glutamyl and β-cysteinyl protons directly. Although the NOE data is insufficient to confirm the rearrangement of the GSH backbone, it strongly supports the assigned hemithioaminal connectivity between the cysteinyl thiol and the glutamyl amine. Interestingly, the downfield HCHO-derived proton (43', Figure 8.28) only exhibited a NOE correlation to one of the β-cysteinyl derived protons, suggesting restricted

rotation of the cysteinyl derived side chain relative to the hemithioaminal. No evidence for cycles encompassing the glycinyl derived moiety was observed in the NOESY spectrum, implying that this part of the molecule remains unaffected after formation of the adduct.

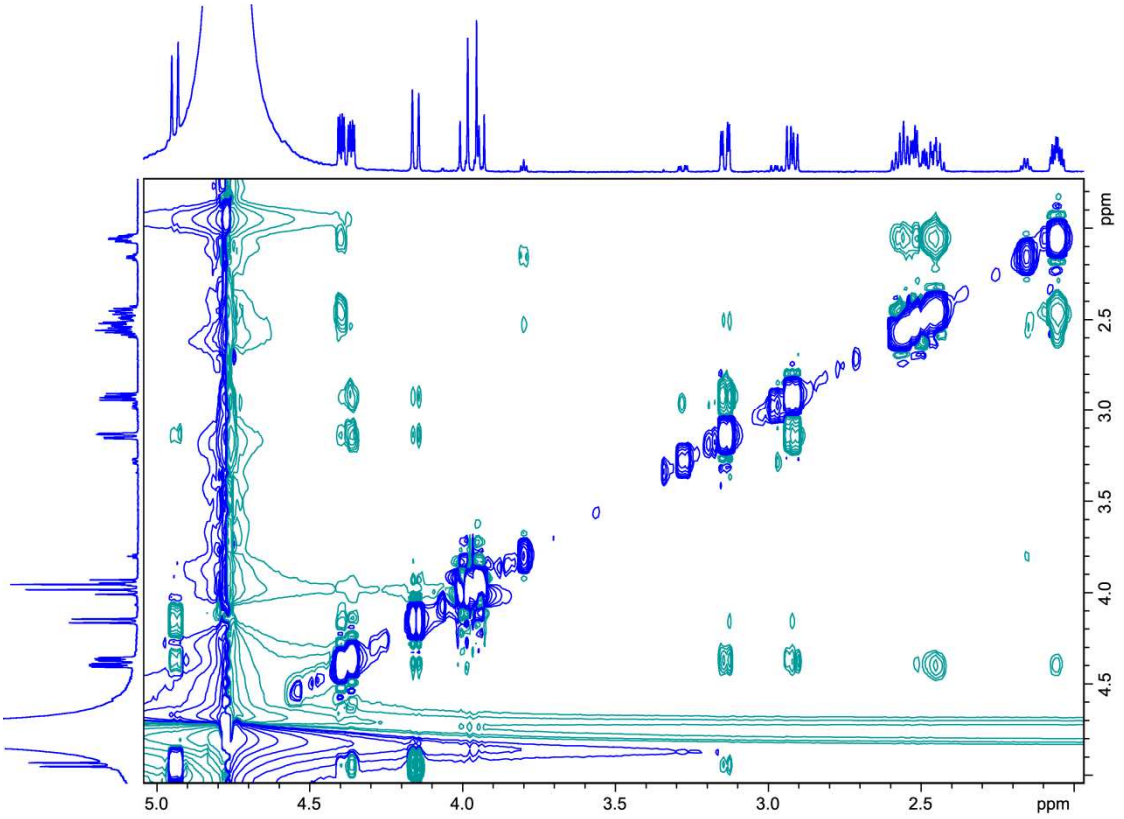

Figure 8.28 2D NOESY spectrum (700 MHz) of the novel adduct in D_2O.

The structural configuration of the novel adduct was also assessed by analysing the ESI mass spectrum obtained during LC/MS purification. Integrating under the corresponding peak in the chromatogram (Figure 8.15), revealed that the novel adduct had undergone fragmentation during ionisation, and therefore, it was possible to investigate the structure by correlating the masses of the fragments to potential fragmentation products. The mass spectrum is shown in Figure 8.29.

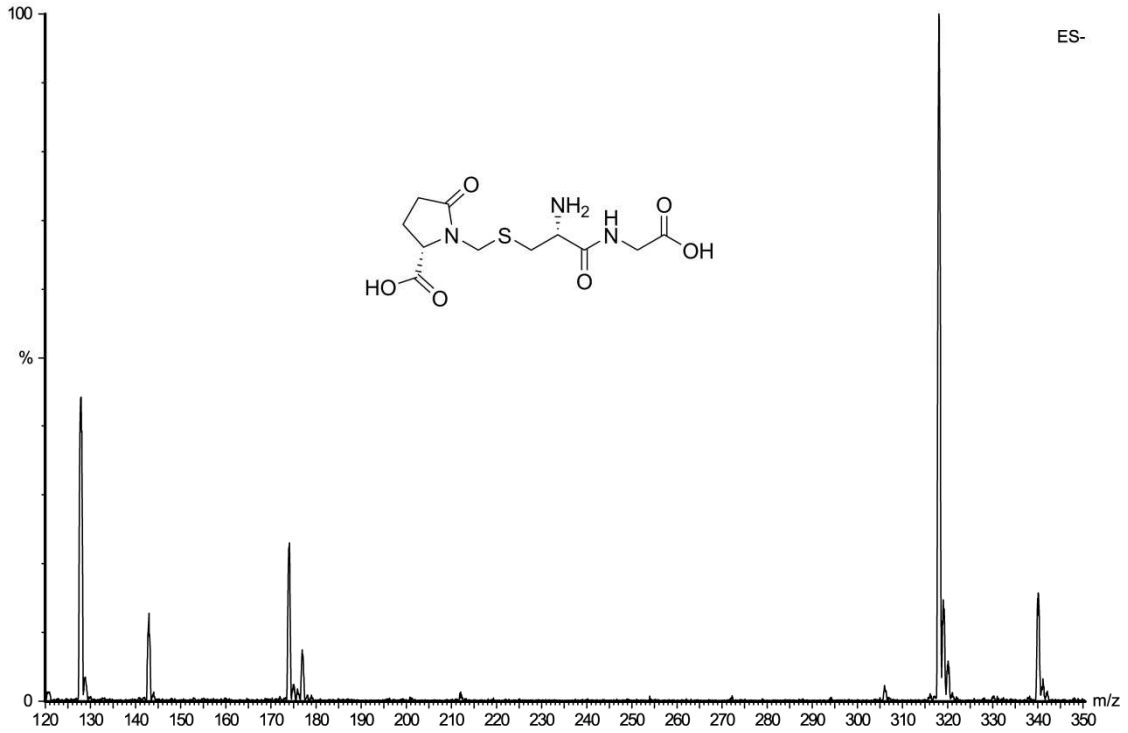

Figure 8.29 ESI mass spectrum of the novel adduct.

The major peak in the mass spectrum was observed at 318 m/z, which corresponds to the molecular ion of the novel adduct. In addition, a peak corresponding to the sodium ion of the intact adduct ($[M+Na-2H]^-$) was also detected at 340 m/z. However, the spectrum also revealed four major fragmentation products at lower m/z values relative to the molecular ion, at 128 m/z, 143 m/z, 174 m/z and 177 m/z respectively. It was noted that the first of these fragment ions (at 128 m/z) appeared to have an identical mass to the expected molecular ion of pyroglutamic acid, which can be formed by breaking the bond between the HCHO-derived methylene and the α-glutamyl amine in the proposed structure of the adduct. It was also noted that the fragment peak at 174 m/z could potentially correspond to pyroglutamic acid attached to a CH_2 group and an SH group. It could be envisaged that such a species could be formed by α,β-elimination at the cysteinyl derived side chain of the adduct, resulting in the release of the observed pyroglutamyl hemithioaminal species and also a dehydroalanyl-glycinyl moiety. This fragmentation pathway was verified by the observation of the peak at 143 m/z, which corresponded to the mass of the

dehydroalanyl containing fragment. The final peak was assigned by noting that its mass (177 m/z) was identical to the dipeptide cysteinylglycine. It was envisaged that this species may be formed by breakdown of the adduct hemithioaminal, presumably to give the unstable pyroglutamyl imine as a side product. The imine could be expected to be unstable under the mass spectrometry conditions, resulting in formation of pyroglutamic acid. It was also envisaged that the hemithioaminal at 174 m/z may also fragment to give pyroglutamic acid. The mass spectrum with peak assignments and a scheme illustrating the proposed fragmentation pathways is shown in Figure 8.30.

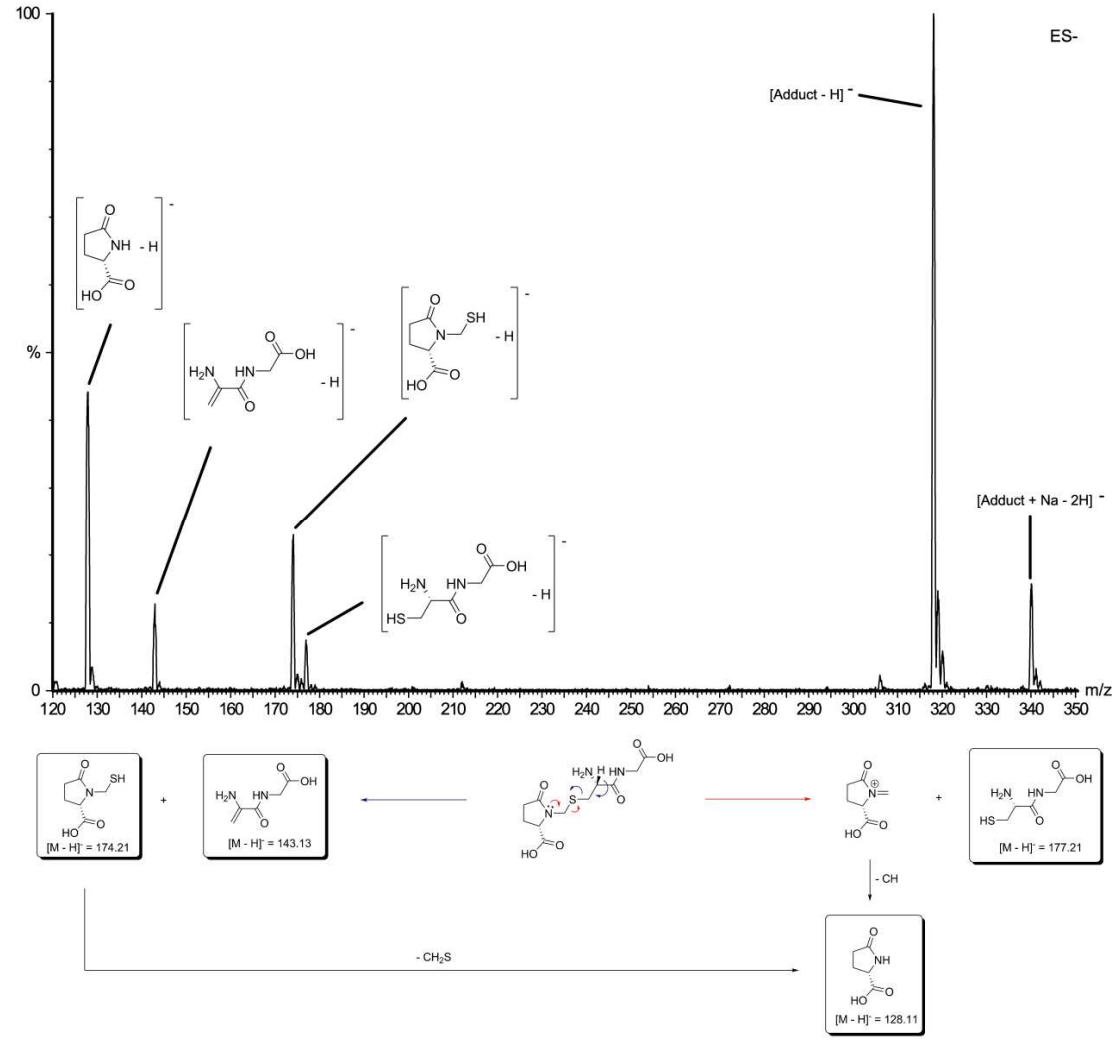

Figure 8.30 ESI mass spectrum of the novel adduct showing assignments for the fragment ions and proposed fragmentation pathways.

Overall, the NMR and mass spectrometric analyses on the purified adduct have allowed structural assignment, which has revealed that the species possesses a markedly different structure relative to GSH and $BiGF_2$. Interestingly, the structure appears to contain a novel five-membered lactam ring, suggesting that formation of the adduct involves a rearrangement of the GSH backbone. Full NMR characterisation of the adduct (hereafter referred to as 'pyroglutamate containing glutathione formaldehyde adduct', PGF) is detailed in Figure 8.31.

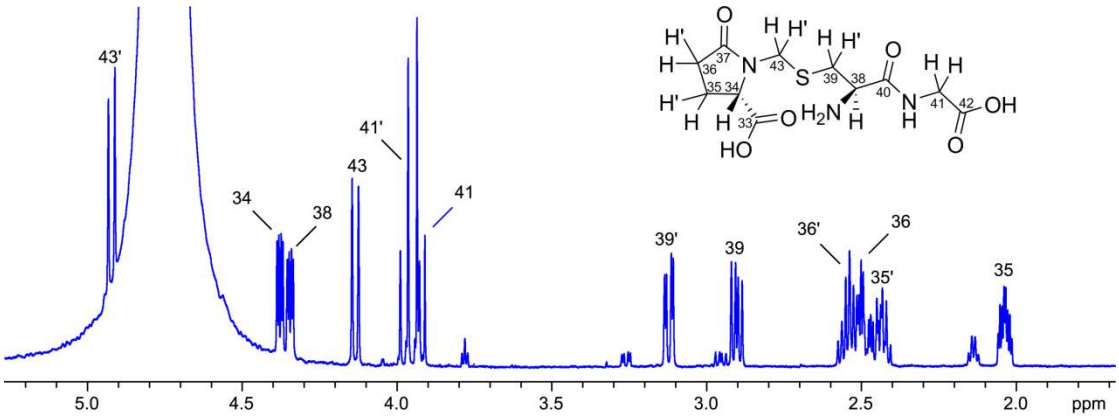

Position:	^{13}C/ ppm:	^{1}H/ ppm:	Multiplicity:	Coupling constant/ Hz:	HMBC Correlations (Carbon Atom Number):
33	178.1				
34	60.8	4.51	dd	4.0, 9.0	33, 35
35	22.8	2.06	m		33, 36
35'		2.47	m		33, 34, 36
36	29.9	2.52	m		34, 35, 37
36'		2.55	m		34, 35, 37
37	179.8				
38	52.0	4.37	dd	4.0, 9.5	39, 40
39	31.1	2.93	dd	9.5, 15.0	38, 40, 43
39'		3.14	dd	4.0, 15.0	40, 43
40	168.5				
41	42.1	3.94	d	17.5	40, 42
41'		4.00	d	17.5	40, 42
42	174.0				
43	42.8	4.16	d	14.5	34, 37, 39
43'		4.94	d	14.5	34, 37, 39

Figure 8.31 NMR assignments for the novel adduct PGF.

8.2.8 Time-course Analysis at Variable pD

Having identified the formation of $BiGF_2$ and the novel adduct PGF in samples after three days, attention was now focused towards analysing mixtures of GSH and HCHO over the initial stages of reaction. Samples containing GSH and a four-fold excess of HCHO were prepared at pDs 5.5, 6.5, 7.5, 8.5 and 9.5 respectively, in an analogous manner to the previous samples. The reactions were then transferred to a 700 MHz NMR spectrometer immediately after mixing and monitored by ^{1}H NMR. In all of the samples, analysis revealed formation of a number of transient species at low levels. It is probable that at least some of these species derive from acyclic hemiaminals, which likely act as intermediates in the formation of other more stable adducts.[215, 216] However, it was also possible to investigate the relative concentrations of HMG, $BiGF_2$ and PGF in the samples. Also these studies revealed formation of a further novel GSH-HCHO adduct, as described below.

a) pDs 5.5 and 6.5

HMG was observed as the major species in all time points during the GSH HCHO reaction at pDs 5.5 and 6.5. In fact, formation of HMG appeared to be completed in both samples before the initial ^{1}H analysis (~ 200 seconds after mixing). At pD 5.5, no trace of $BiGF_2$ or PGF could be detected in the sample over the 105 minute reaction period, implying that formation of these species is very slow under such acidic conditions. However, analysis of the sample at pD 6.5 did indicate the presence of both $BiGF_2$ and PGF at low levels, although HMG remained the predominant adduct in solution during the experiment. These observations may indicate that HMG is an intermediate in the formation of $BiGF_2$ and PGF, possibly via intramolecular rearrangement.

b) pDs 7.5, 8.5 and 9.5

The predominant species at pDs 7.5 and 8.5 over initial time points was HMG; however, in contrast to the two acidic samples (see above), its concentration was observed to decrease in a linear fashion during the analysis period. At pD 9.5, only trace amounts of HMG was observed. Interestingly, $BiGF_2$ concentrations were observed to increase linearly in the three more basic samples, with the highest concentration being recorded at pD 9.5 (8 mM). Conversely, no PGF was observed in these samples, implying that its formation is preferential under more acidic conditions. In addition to these adducts, it was possible to identify a new adduct in the samples (Figure 8.32). This species was found to be prevalent over early time points in the samples at pDs 8.5 and 9.5, after which, its concentration was observed to decrease in a linear fashion (from 3 mM to 1.5 mM at pD 8.5, Figure 8.33). This decrease coincided with the emergence of $BiGF_2$, implying that this new species may be an intermediate in $BiGF_2$ formation. ^{1}H NMR and 2D HSQC analyses indicated that this new adduct possesses

only one HCHO derived methylene unit (with two ^{1}H-resonances at δ_H 3.64 ppm and δ_H 4.12 ppm and a ^{13}C-resonance at δ_C 53.1 ppm), indicating that the species may be derived via a rearrangement of HMG. It was also noted that the ^{13}C-shift of the HCHO derived carbon matched closely to that of 'GF' reported by Naylor *et al.*[211] (Figure 8.1), suggesting that the new species in the samples may be the same adduct.

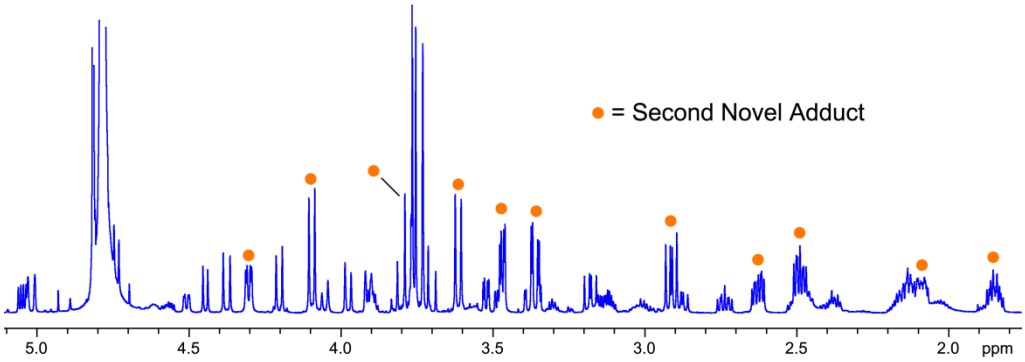

Figure 8.32 ^{1}H NMR spectrum (700 MHz) for a reaction mixture of GSH and four equivalents of HCHO after four minutes at pD 9.5. Resonances corresponding to a second novel adduct are notated with orange circles.

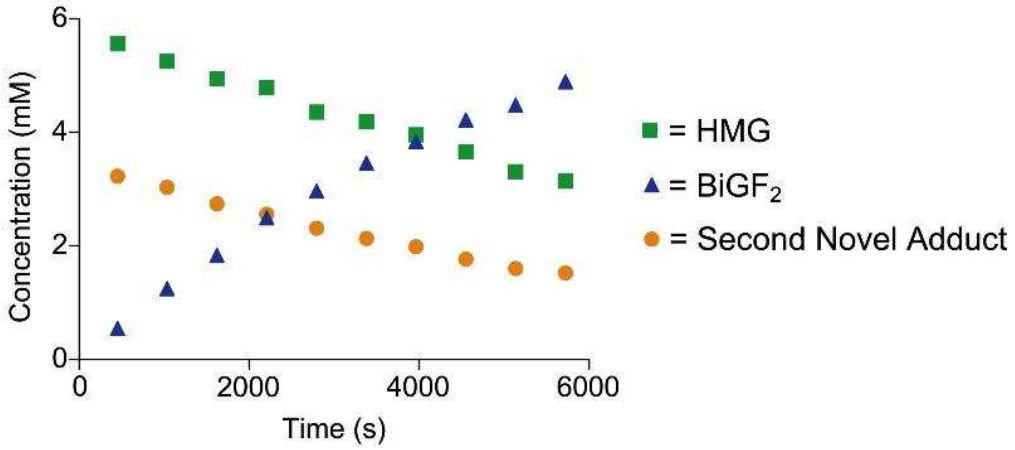

Figure 8.33 Concentrations of HMG, $BiGF_2$ and the second novel adduct over time in a reaction mixture of GSH (13.3 mM) and four equivalents of HCHO at pD 8.5.

8.2.9 Characterisation of the second Novel Adduct

Having identified a new GSH-HCHO adduct, attempts were made to purify and characterise the structure of this species using NMR. Unfortunately, the relative instability of the species did not allow its isolation from the reaction mixtures (using the previously described LC-MS approach), and therefore, structural characterisation by NMR was carried out on the reaction mixtures. In these experiments, it was essential to analyse the samples when the MGF concentration was highest in order to allow good resolution of the relevant signals and also to minimise overlap of resonances with those of other species. ^{1}H and 2D COSY spectra were collected from a sample containing GSH and four equivalents of HCHO at pD 9.5 (as above); however, it was found that the concentration of the new species decreased too quickly in this sample to allow accumulation of 2D HSQC, 2D HMBC and 2D NOESY data. Therefore, these experiments were run on a sample containing only one equivalent of HCHO (at pD 9.5), which facilitated the collection of 2D data due to the prolonged lifetime of the new adduct under the sample conditions. The 2D COSY spectrum is shown in Figure 8.34.

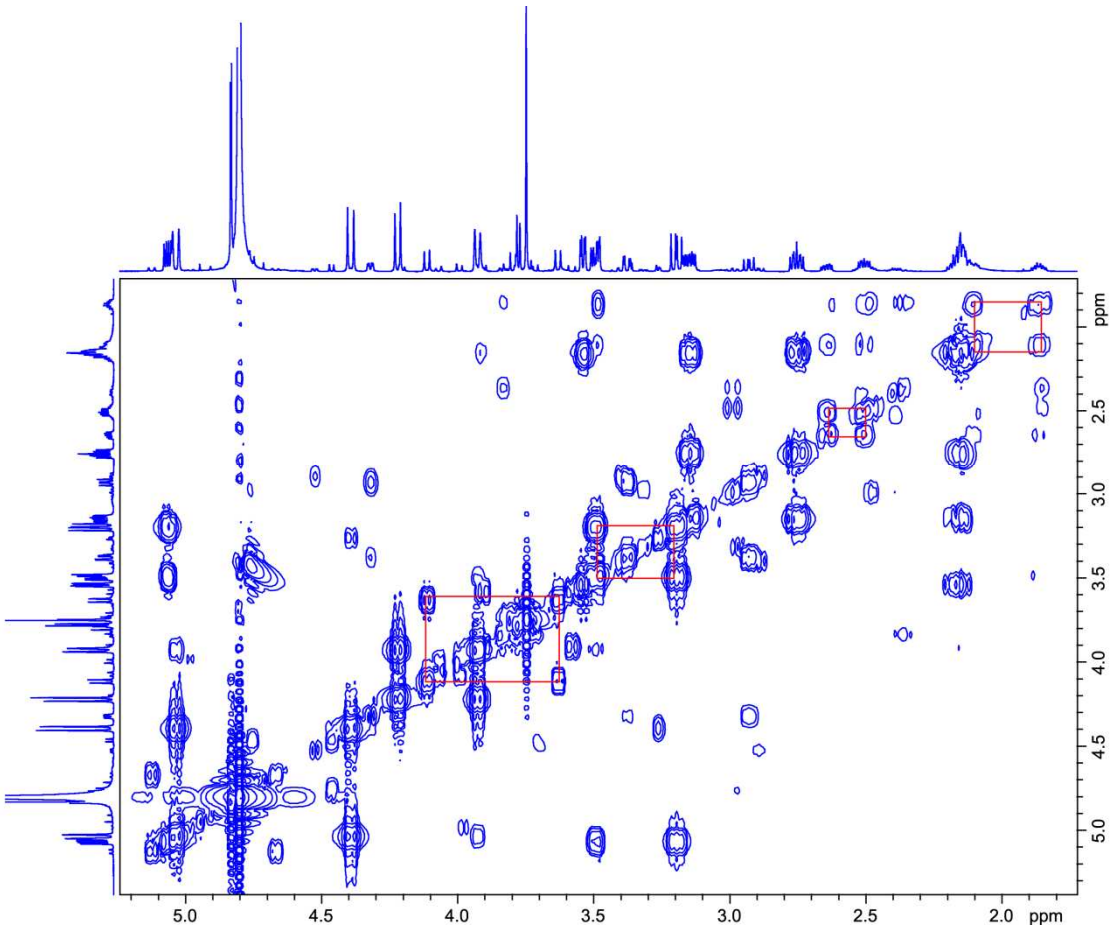

Figure 8.34 2D COSY spectrum (700 MHz) for the reaction of GSH (13.3 mM) and four equivalents of HCHO at pD 9.5 after two hours. Geminal coupling partners corresponding to protons on the second novel adduct are highlighted with red lines.

Firstly, it was noted that the COSY correlations between the proton at δ_H 2.50 ppm with the protons at δ_H 1.87 ppm, δ_H 2.10 ppm and δ_H 2.64 ppm, as well as the correlations between the proton at δ_H 1.87 ppm with the protons at δ_H 2.10 ppm and δ_H 3.49 ppm, implied the presence of an alkyl -$CHCH_2CH_2$- chain, which was assigned to the glutamyl derived chain from GSH. Also, correlations from the proton at δ_H 4.33 ppm to the protons at δ_H 2.93 ppm and δ_H 3.38 ppm suggested that these resonances correspond to a cysteinyl-derived side chain. The assignments were corroborated by the 2D HSQC spectrum of the novel adduct containing mixture, which revealed ^{13}C-resonances similar to those of $BiGF_2$ (Figure 8.35). Also, it was possible to assign a ^{13}C-signal (and the corresponding ^{1}H-resonance) to the α-glycinyl derived position (at δ_H 3.28 ppm and δ_C 43.2 ppm respectively),

although full characterisation at this position was impeded by signal overlap with GSH.

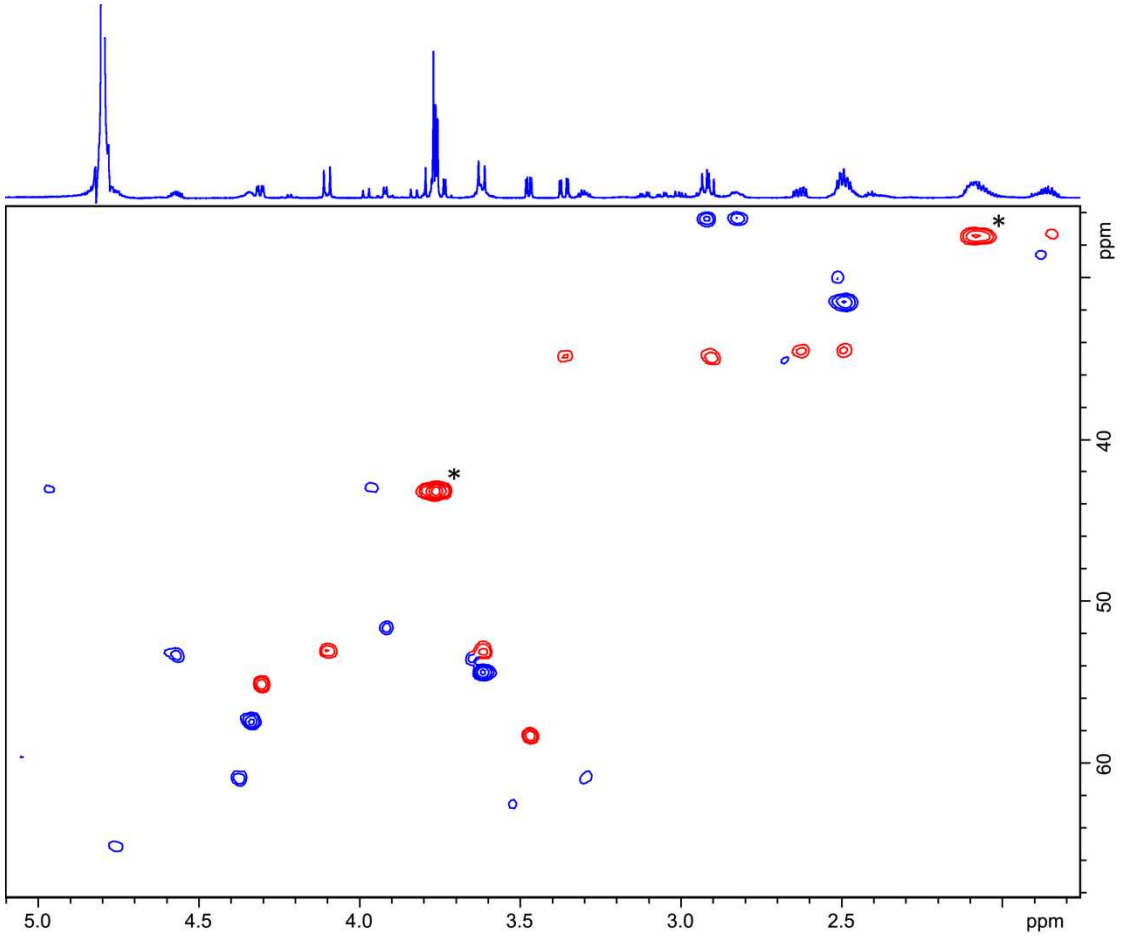

Figure 8.35 2D HSQC spectrum (700 MHz) for the reaction of GSH (13.3 mM) and one equivalent of HCHO at pD 9.5 after 9 hours. Signal corresponding to the second novel adduct are highlighted red. The signals highlighted with an asterisk overlap with resonances from other species.

The 2D HMBC spectrum allowed determination of the new adduct's configuration by highlighting correlations between the HCHO-derived methylene and its neighbouring atoms (Figure 8.36). Specifically, correlations were observed between both the methylene proton resonances (at δ_H 3.64 ppm and δ_H 4.12 ppm respectively) and carbons at δ_C 34.8 ppm and δ_C 58.3 ppm. These ^{13}C-resonances were assigned to the β-cysteinyl and α-glutamyl derived carbons respectively via analogy with the assignment of $BiGF_2$, and therefore, the data implied that the methylene is attached via bonds to the glutamyl amine and cysteinyl thiol. This

assignment was also implied by HMBC correlations between the β-cysteinyl and α-glutamyl protons and the methylene ^{13}C-resonance at δ_C 53.1 ppm.

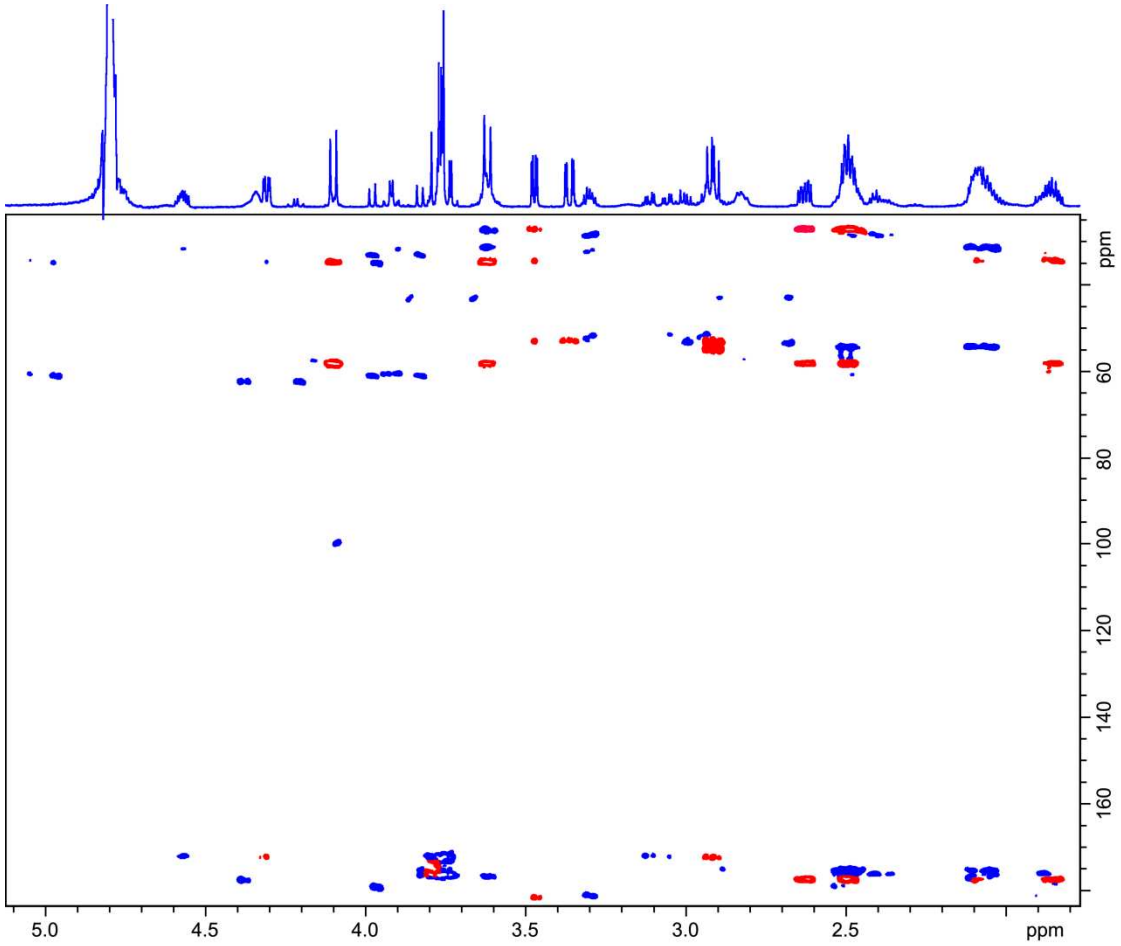

Figure 8.36 2D HMBC spectrum (700 MHz) for the reaction of GSH (13.3 mM) and one equivalent of HCHO at pD 9.5 after 9 hours. Signal corresponding to the second novel adduct are highlighted red.

Overall, the ^1H, 2D COSY, 2D HSQC and 2D HMBC data suggested that the structure of this species contains a novel 10-membered ring (Figure 8.37). This structural assignment differs significantly from that of 'GF' described by Naylor *et al.*, implying either that the new species is an unreported adduct, or that the structure of GF may have been previously misassigned. It is also noted that the cyclodecyl motif (i.e. an HCHO derived methylene bridge connected via the glutamyl amine and cysteinyl thiol) is present within the structure of $BiGF_2$. This observation further implies that the new adduct (hereafter referred to as 'monocyclic glutathione formaldehyde adduct', MGF) is an intermediate of $BiGF_2$ formation.

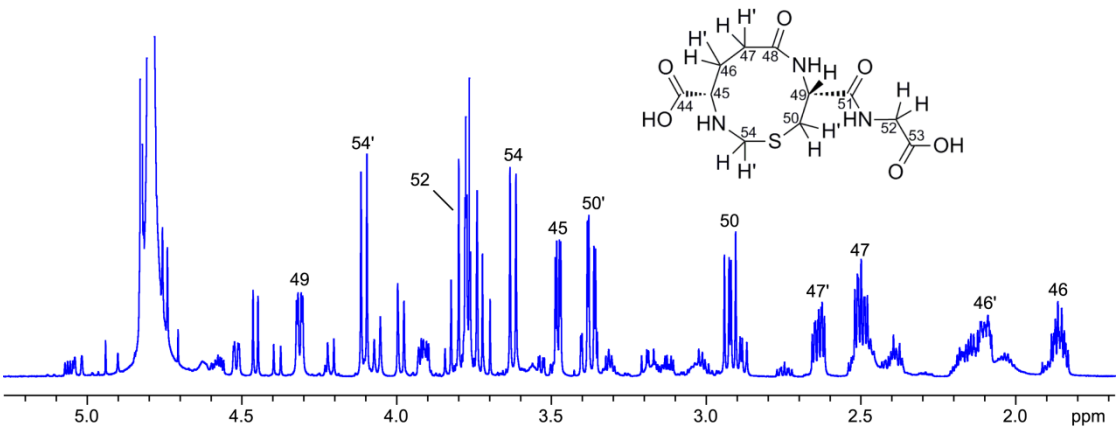

Position:	^{13}C/ ppm:	^{1}H/ ppm:	Multiplicity:	Coupling constant/ Hz:	HMBC Correlations (Carbon Atom Number):
44	181.6				
45	58.3	3.49	dd	3.0, 9.0	44, 46, 47, 54
46	27.3	1.87	m		45, 47, 48
46'		2.10	m		47, 48
47	34.5	2.50	m		45, 46*, 48
47'		2.64	m		45, 46*, 48
48	177.4				
49	55.1	4.33	dd	3.5, 10.5	51
50	34.8	2.93	dd	10.5, 15.0	49, 51, 54
50'		3.38	dd	3.5, 15.0	54
51	172.3				
52	43.2	3.78	m		51, 53*
53	176.4*				
54	53.1	3.64	d	13.5	45, 50
54'		4.12	d	13.5	45, 50

Figure 8.37 NMR assignments for MGF.

8.2.10 The GSH HCHO Reaction at low HCHO Concentration

Having identified and characterised the formation of two novel GSH-HCHO adducts, attention was focused towards monitoring the GSH HCHO reaction at low HCHO concentrations. It was hoped that these experiments would better imitate cellular conditions, and therefore, may give insight into the potential formation propensities of each adduct in cells. Samples containing GSH (13.3 mM final concentration) were mixed with 0.25 equivalent of HCHO at pDs 5.5, 7.5 and 9.5, and the consequent reactions were monitored over an initial 105 minute reaction period, as well as after three days reaction. NMR analysis of the samples at pDs 5.5 and 7.5 identified HMG as the major product over initial time points. However, the major species at pD 9.5 over this period was found to be MGF. MGF was also present over initial time points in the sample at pD 7.5, and was also present in this sample after three days reaction. PGF was present in all three samples over the initial 105 minute reaction period, and was detected at highest concentration (2 mM)

in the sample at pD 7.5 after three days. However, in contrast to the samples containing a four-fold excess of HCHO, $BiGF_2$ was only observed in trace amounts in the samples after three day reaction. These findings imply that, under low HCHO levels, formation of $BiGF_2$ is impaired relative to the formation of the 1:1 GSH-HCHO adducts (HMG, PGF and MGF), suggesting that these species may be more prevalent in cellular contexts.

8.2.11 Reactions of GSH with other Cellular Aldehydes

Experiments were then conducted in order to investigate whether the observed reactions of GSH and HCHO were applicable in samples containing GSH and other cellular aldehydes. GSH (13.3 mM) was incubated with a four-fold excess of acetaldehyde, methylglyoxal and D-glucose (separate samples) at pDs 5.5, 7.5 and 9.5, and the subsequent reactions were monitored over initial stages (105 minutes) and after three days.

a) Reaction of GSH with AcH

AcH is the first metabolite of ethanol metabolism, and therefore, is present in high cellular concentrations after ethanol intoxication.[217] Analysis of the sample containing this aldehyde at pD 5.5 revealed formation of both diastereomers of the HMG homologue (2*S*)-2-amino-5-((2*R*)-1-(carboxymethylamino)-3-(1-hydroxyethylthio)-1-oxopropan-2-ylamino)-5-oxopentanoic acid (HEG) in equal amounts (NMR characterisation of these diastereomers using ^{1}H, 2D COSY, 2D HSQC and 2D HMBC techniques is shown in Figure 8.38). The concentration of these species appeared to be constant throughout the 105 minute analysis, suggesting that equilibrium (assuming no further degradation of HEG to other adducts) had been reached from the first NMR analysis. However, the overall concentration of these species (4 mM of each diastereomer) was significantly less than the observed concentration of HMG in the sample containing HCHO (13 mM) over initial time points. Therefore, it is likely that the position of the GSH-HEG

equilibrium sits further to the free thiol form relative to the analogous GSH-HMG equilibrium under these conditions. At pDs 7.5 and 9.5, HEG was observed in higher concentrations, suggesting that the increased basicity in the samples had resulted in a shift in the equilibrium position. Also, it was apparent that the two diastereomers were in fast exchange, resulting in the detection of broadened signals for the two species. It was also possible to identify a number of new resonances in the ^{1}H NMR spectra at pD 9.5, both over initial time points during the reaction, and also after three days. However, assignment of these signals to adducts in the reaction mixture was not possible due to their relatively low intensities.

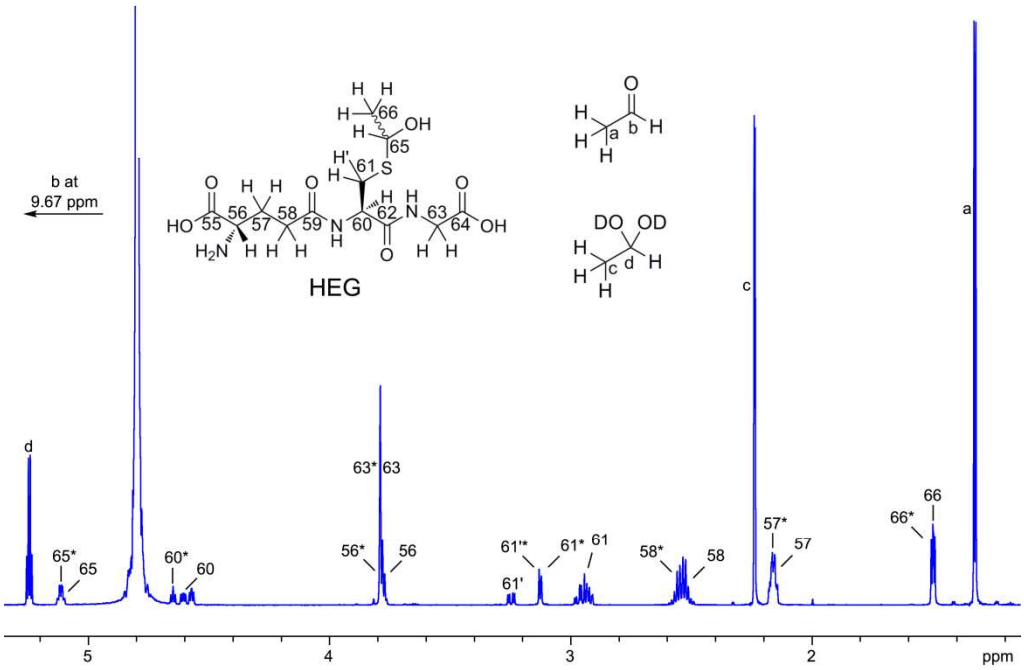

Position	^{13}C/ ppm:	^{1}H/ ppm:	Multiplicity:	Coupling constant/ Hz:	HMBC Correlations (Carbon Atom Number)
55 and 55*	173.3				
56 and 56*	53.6	3.78	m (with 80 and 80*)		55 and/or 55*, 57 and/or 57*, 58 and/or 58*
57 and 57*	25.7	2.16	m		55 and/or 55*, 56 and/or 56*, 58 and/or 58*, 59 and/or 59*
58 and 58*	31.0	2.54	m		56 and/or 56*, 57 and/or 57*, 59 and/or 56*
59	174.5				
59*	174.5				
60	53.2	4.61	dd	5.0, 9.0	61, 62
60*	53.7	4.65	app t	6.5	59*, 61*, 62*
61	30.4	2.97	m		60, 62, 65
61'		3.25	dd	5.0, 14.0	65
61* and 61'*	31.4	3.13	app d	6.5	60*, 62*, 65*
62	172.5				
62*	172.5				
63 and 63*	41.1	3.78	m (with 73 and 73*)		64 and/or 64*
64 and 64*	173.2				
65	73.4	5.11	m (with 82*)		61
65*	74.7	5.11	m (with 82)		61*
66 and 66*	22.9	1.50	m		65, 65*

Figure 8.38 NMR assignments for both diastereomers of HEG. Asterisks indicate signals corresponding to the same diasteremer.

b) Reaction of GSH with Methylglyoxal

The reaction of GSH with methylglyoxal was then investigated. Methylglyoxal (MG) is a reactive cellular aldehyde that has been linked to human diseases including diabetes, hypertension and atherosclerosis, and is also known to react non-enzymatically with GSH to form the HMG homologue (2*S*)-2-amino-5-((2*R*)-1-(carboxymethylamino)-3-(1-hydroxy-2-oxopropylthio)-1-oxopropan-2-ylamino)-5-oxopentanoic acid (MGG).[218, 219] This species is then thought to facilitate MG metabolism by acting as a substrate for the isomerase glyoxalase I, which catalyses the formation of *S*-latoylglutathione via isomerism. This product is then converted to D-lactate and GSH via catalysis by glyoxalase II. The ^{1}H NMR spectrum of MGG has previously been reported under acidic conditions (pH 4.4, unadjusted pH meter reading); however, full NMR characterisation and studies under basic conditions have not been undertaken. Therefore, it was hoped that these studies would reveal the formation of the biologically relevant MGG in basic media. The ^{1}H NMR spectra of all three samples revealed formation of MGG (characterised using ^{1}H, 2D COSY, 2D HSQC and 2D HMBC, as shown in Figure 8.39), although at pDs 7.5 and 9,5, the two diastereomers of MGG appeared to be in fast exchange (i.e. detected as one species with broadened ^{1}H peaks). In fact, formation of MGG appeared to be completed after the first NMR time point (~ 500 s) in all three samples, suggesting that MG reacts quickly with GSH across a pD range. After three days, the sample at pD 9.5 did appear to contain low level signals corresponding to other GSH adducts. Interestingly, it was apparent that trace amounts of $BiGF_2$ and PGF were present in the sample; however, it was concluded that these species were likely formed from HCHO impurities in the commercial source of MG (as observed by NMR). It is also likely, therefore, that trace amounts of HMG were present in the samples over initial time points, although the corresponding resonances were likely hidden by other, more intense, signals.

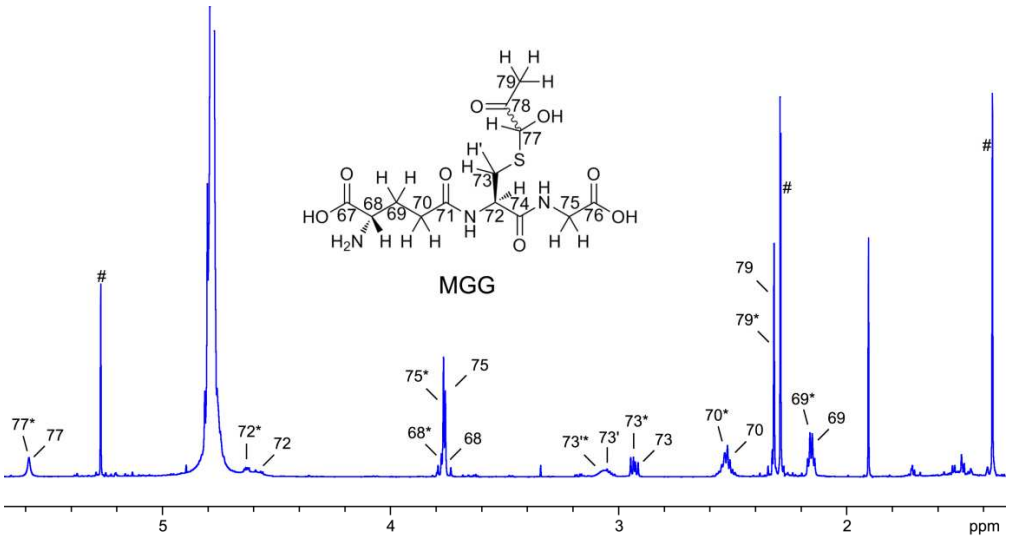

Position	^{13}C/ ppm:	^{1}H/ ppm:	Multiplicity:	Coupling constant/ Hz:	HMBC Correlations (Carbon Atom Number)
67 and 67*	173.9				
68 and 68*	53.9	3.79	m (with 92 and 92*)		67 and/or 67*, 69 and/or 69*, 70 and/or 70*
69 and 69*	26.0	2.17	app q	7.0	67 and/or 67*, 68 and/or 68*, 70 and/or 70*, 71 and/or 71*
70 and 70*	31.3	2.55	m		68 and/or 68*, 69 and/or 69*, 71 and/or 71*
71	174.8				
71*	174.8				
72	53.2	4.60	m		73, 74
72*	53.1	4.65	m		73*
73	29.8	2.95	dd	8.5, 14.0	72, 74, 77
73'		3.08	m (with 90'*)		72, 74, 77
73*	29.8	2.92	dd	8.5, 14.0	72*, 74*, 77*
73'*		3.08	m (with 90')		72*, 74*, 77*
74 and 74*	171.6				
75 and 75*	43.1	3.79	m (with 85 and 85*)		74 and/or 74*, 76 and/or 76*
76 and 76*	176.1				
77 and 77*	78.4	5.60	br s		73 and/or 73*
78 and 78*	205.5				
79 and 79*	25.1	2.34	s		77 and/or 77*

Figure 8.39 NMR assignments for both diastereomers of MGG. Asterisks indicate signals corresponding to the same diasteremer.

c) Reaction of GSH with D-Glucose

Finally, samples containing GSH and D-glucose were monitored in the hope that reaction (presumably via attack of the GSH thiol onto the aldehydic form of glucose) would result in the formation of adducts. However, all three samples (at pDs 5.5, 7.5 and 9.5) did not reveal any signals corresponding to new species, either during the initial 105 minute analysis period, or after three days reaction. It is therefore likely that glusose, which exists predominantly as the pyranose form in aqueous solution, is not sufficiently reactive to form adducts with GSH. This suggests that such reactions in cells, if applicable, likely proceed via enzyme catalysis.

8.2.12 Reaction of γ-Glutamylcysteine with HCHO

Characterisation of the GSH-HCHO adducts indicated that reaction with HCHO occurs at the cysteinyl thiol and glutamyl amine groups of GSH. Formation of adducts, therefore, was not expected to involve the glycinyl moiety present in the GSH structure, suggesting that removal of this group should have no effect upon the reactions with HCHO. In order to test this hypothesis, ^{1}H NMR experiments were carried out monitoring the reactions of γ-glutamyl cysteine (GC, Figure 8.40) with HCHO (at pDs 5.5, 7.5 and 9.5 respectively), in the expectation that adducts analogous to HMG, $BiGF_2$, PGF and MGF would be formed in the reaction mixtures.

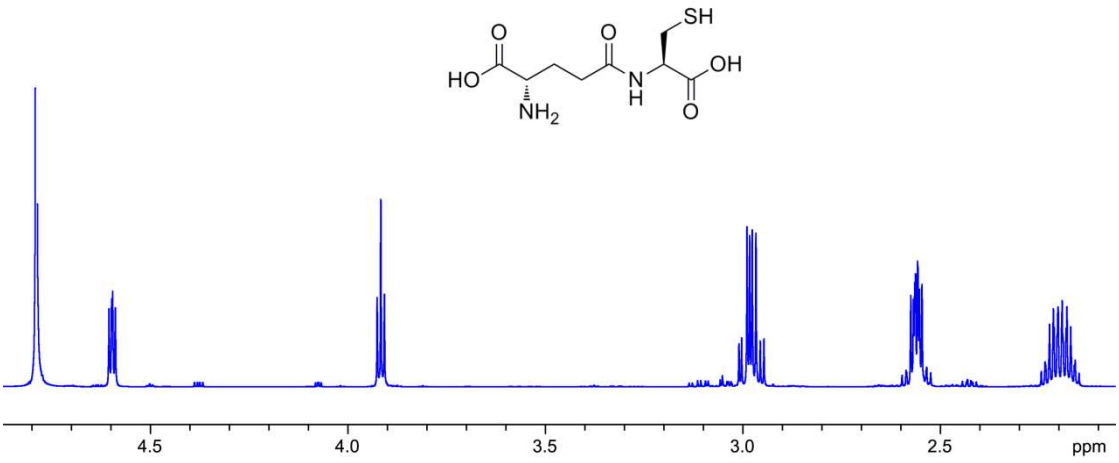

Figure 8.40 ^{1}H NMR spectrum (700 MHz) of γ-glutamylcysteine in D_2O.

As expected, analysis of the samples over an initial 105 minute reaction period revealed formation of all three adducts (named HMGC, $BiGCF_2$, PGCF and MGCF respectively, Figure 8.41 and Figure 8.42).

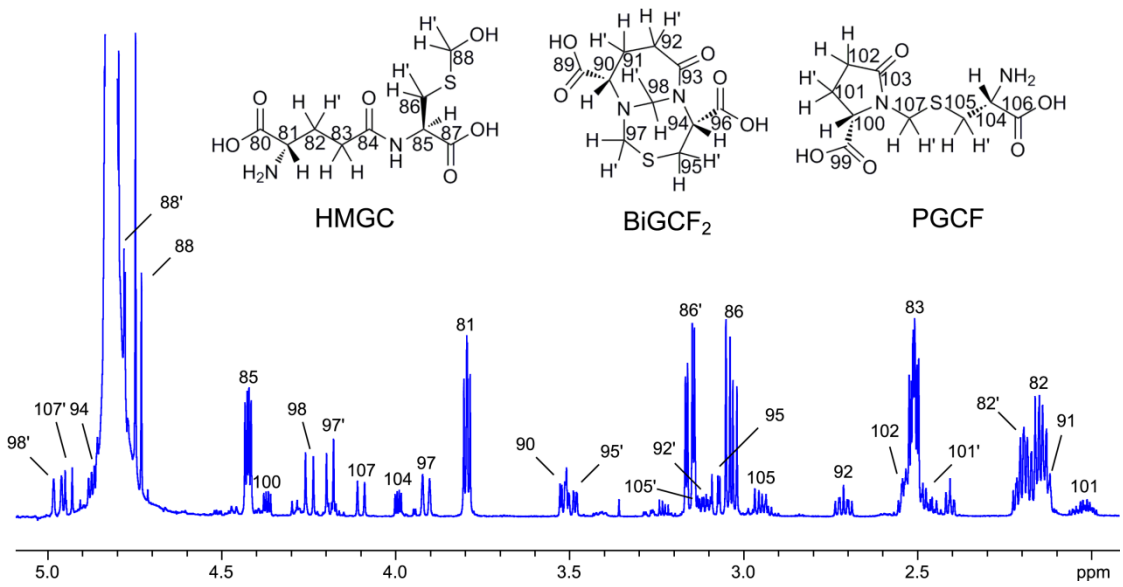

HMGC

Position	^{13}C/ ppm:	^{1}H/ ppm:	Multiplicity:	Coupling constant/ Hz:	HMBC Correlations (Carbon Atom Number)
80	174.1				
81	54.1	3.80	dd	5.5, 7.0	80, 82, 83
82	26.3	2.15	m		81, 83, 84
82'		2.20	m		81, 83, 84
83	31.6	2.51	m		81, 82, 84
84	174.2				
85	54.6	4.43	dd	4.5, 8.0	86, 87
86	33.0	3.04	dd	8.0, 14.0	85, 87, 88
86'		3.16	dd	4.5, 14.0	85, 87, 88
87	176.9				
88	65.1	4.74	d	12.0	86
88'		4.79	d	12.0	86

BiGCF$_2$

Position	^{13}C/ ppm:	^{1}H/ ppm:	Multiplicity:	Coupling constant/ Hz:	HMBC Correlations (Carbon Atom Number)
89	180.0				
90	62.6	3.51	m (with 50')		89, 91
91	23.9	2.15	m		90, 92, 93
92	33.3	2.72	ddd	7.0, 9.5, 17.0	91, 93
92'		3.12	m		91, 93
93	176.4				
94	61.2	4.88	dd	6.0, 12.0	95, 96, 97
95	35.2	3.08	dd	12.0, 15.5	97
95'		3.50	m (with 45)		91, 97
96	177.1				
97	60.0	3.92	d	14.0	95, 98
97'		4.19	d	14.0	90, 95
98	60.6	4.25	d	16.0	90, 93
98'		4.97	d	16.0	

PGCF

Position	^{13}C/ ppm:	^{1}H/ ppm:	Multiplicity:	Coupling constant/ Hz:	HMBC Correlations (Carbon Atom Number)
99					
100	61.2	4.37	dd	4.5, 9.0	
101		2.03	m		
101'		2.47	m		
102	29.9	2.55	m		103
103	179.2				
104	53.3	4.00	dd	4.0, 8.5	
105	31.1	2.96	m		104,107
105'		3.16	m		
106					
107	43.1	4.10	d	14.5	103,105
107'		4.94	d	14.5	103,105

Figure 8.41 NMR assignments for HMGC, BiGCF$_2$ and PGCF.

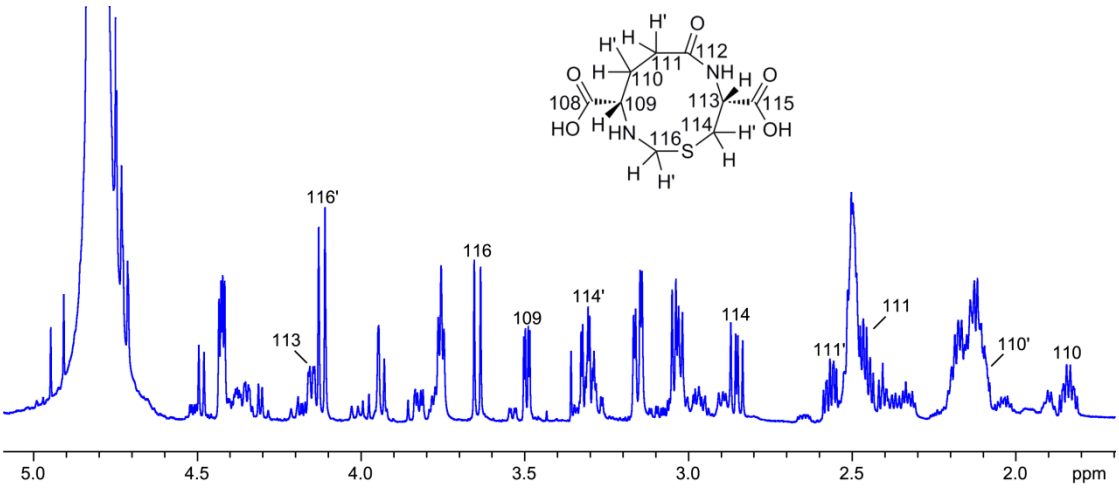

Position	^{13}C/ ppm:	^{1}H/ ppm:	Multiplicity:	Coupling constant/ Hz:
108				
109	58.2	3.49	dd	3.5, 9.5
110	27.3	1.83	m	
110'		2.09	m	
111	34.2	2.45	m	
111'		2.56	m	
112				
113	56.4	4.15	dd	3.5, 10.5
114	36.1	2.85	dd	10.5, 15.0
114'		3.31	dd	3.5, 15.0
115				
116	53.4	3.64	d	13.5
116'		4.11	d	13.5

Figure 8.42 NMR assignments for MGCF.

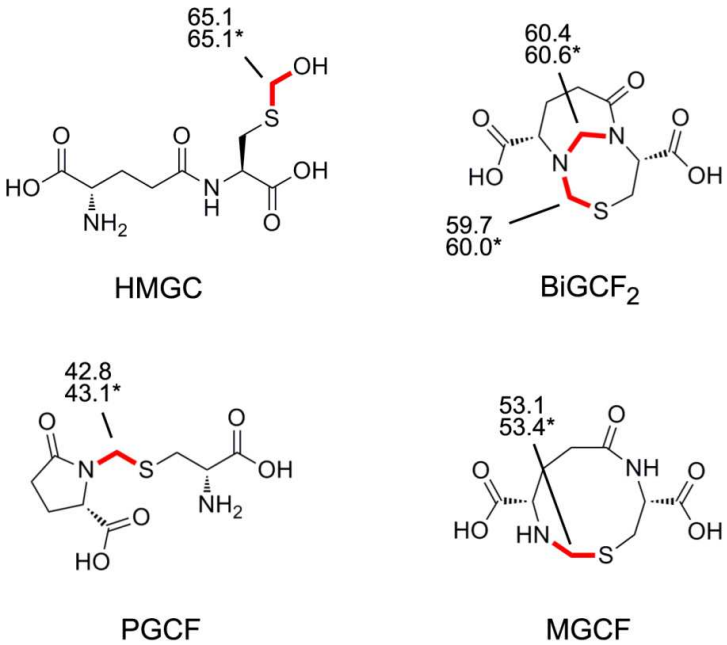

Figure 8.42 Structures of HMGC, $BiGCF_2$, PGCF and MGCF showing their characteristic ^{13}C-resonances for the HCHO derived carbons (asterisked). Equivalent ^{13}C-resonance shifts for the GSH derived adducts are also shown.

At pD 5.5, the predominant species in solution during the initial analysis period and also after three days reaction was the HMG homologue HMGC (*S*-hydroxymethyl-γ-glutamylcysteine). Trace amounts of the PGF homologue (PGCF) were also detected in traces amounts during the initial 105 minutes, suggesting that its formation is faster (albeit only slightly) than the formation of PGF under the same conditions. The $BiGF_2$ analogue, $BiGCF_2$, was present in all three samples and was identified as the major product at pD 9.5 after three days. The production of the MGF homologue MGCF mirrored that of MGF; MGCF was present in the samples at pDs 7.5 and 9.5 during the initial 105 minute analysis period, but could not be detected after three days reaction. Overall, the data from the reactions with GC were near identical to those obtained with GSH, suggesting that their reactions with HCHO are very similar.

8.2.13 Mechanistic Proposals

NMR Studies on samples containing GSH and HCHO have revealed the formation of a number of adducts, four of which (HMG, $BiGF_2$, PGF and MGF) were found to predominate under the applied conditions. The observation that these four adducts are formed at variable rates across a pD range, and also that certain adducts appear to degrade in conjunction with the formation of others, allow some general assumptions on their formation mechanisms to be made. Firstly, it was noted that under acidic conditions (pDs 5.5 and 6.5), the major species in solution is the hemithioacetal HMG over initial stages. This implies that acid-catalysed formation of this species is very fast relative to formation of the other adducts. However, the samples at higher pD (pDs 7.5, 8.5 and 9.5) revealed formation of the hemithioaminal MGF over early time points (MGF was the major species at pDs 8.5 and 9.5), suggesting that the increased nucleophilicity of the glutamyl amine on GSH (induced by deprotonation of the ammonium cation) promotes hemithioaminal formation in the more basic media. However, even under these conditions, it is likely that formation of the hemithioacetal is still fast due to the potent nucleophilicity of the thiol/thiolate. Therefore, these observations may suggest that

HMG is probably an intermediate during formation of MGF, although the mechanism for this cyclisation remains unclear. It is possible that this step proceeds via direct substitution at the hemithioacetal; however, formation of MGF may also occur via an imine intermediate (Scheme 8.1).

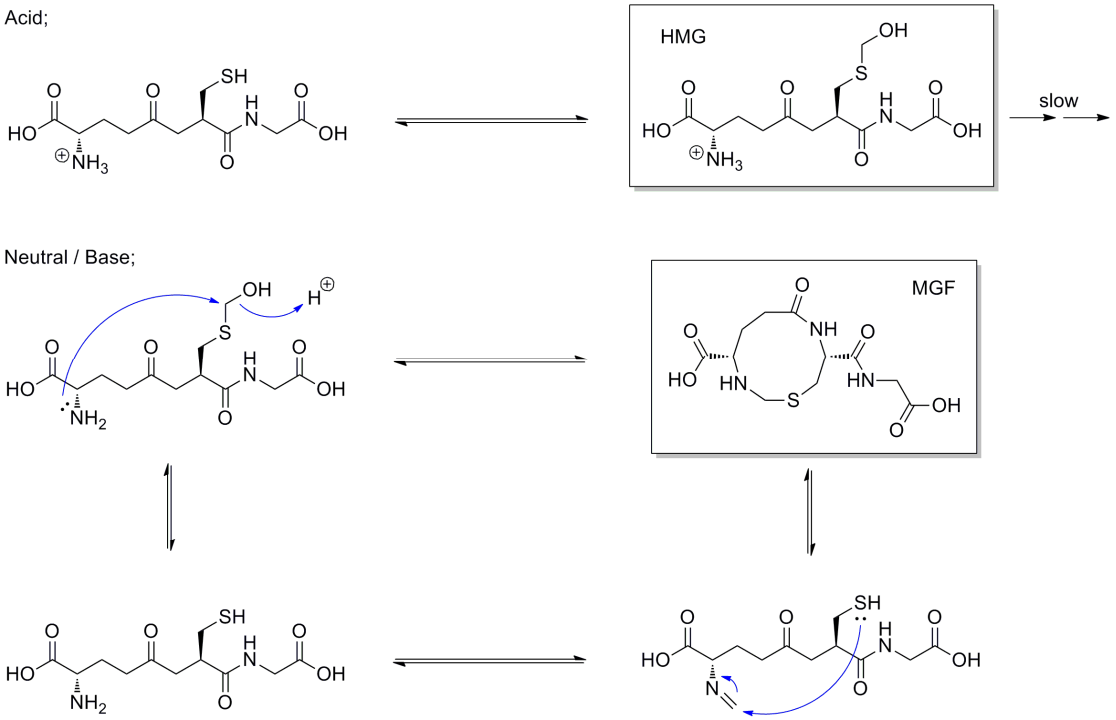

Scheme 8.1 Scheme showing a possible mechanism of MGF formation.

Given the relatively similar structures of MGF and $BiGF_2$, it was noted that MGF may be an intermediate in $BiGF_2$ formation, at least under basic conditions. This transformation would most likely occur via condensation of a second HCHO molecule across the cyclodecyl ring, presumably via an imine intermediate on the glutamyl amine (Scheme 8.2). Although MGF was not observed in the samples at pDs 5.5 and 6.5, the fact that $BiGF_2$ can be formed under such conditions indicates that MGF may be produced as a transient species in acidic media. However, it cannot be ruled out that $BiGF_2$ is formed by other mechanisms.

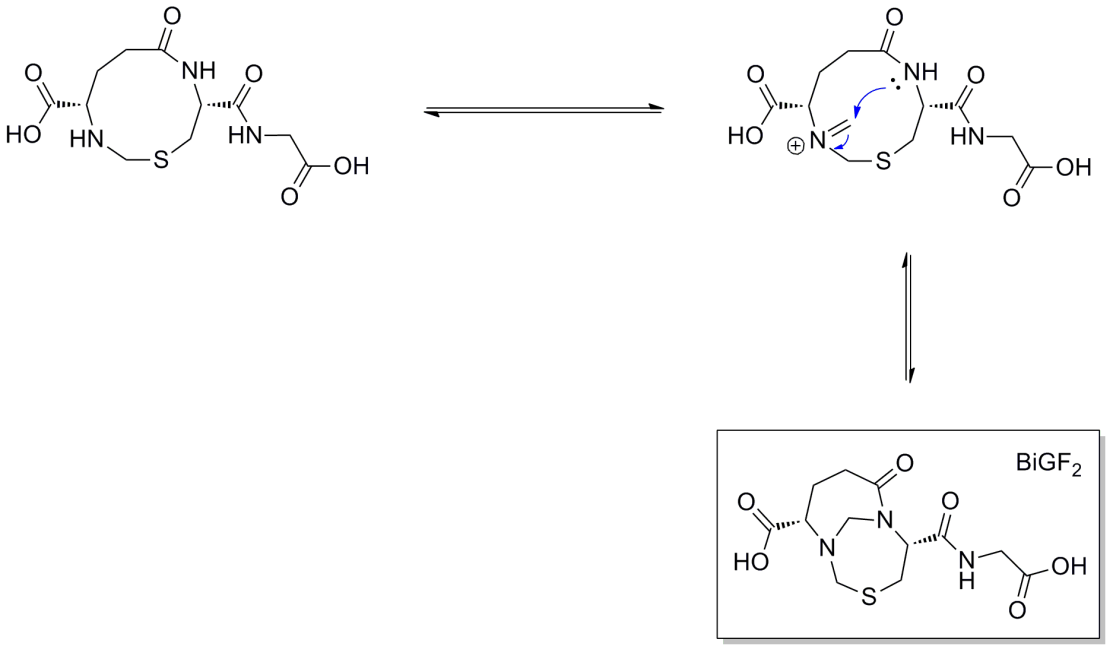

Scheme 8.2 Scheme showing a possible mechanism of $BiGF_2$ formation via the intermediate MGF.

Finally, the formation of PGF appears to be most prevalent in acidic media, suggesting that its formation may be acid-catalysed. It is possible, however, to envisage PGF formation via rearrangement of MGF, which would likely be accelerated under basic conditions. It is proposed that the relative proximity of the amino and the amido functionalities within the cyclodecyl ring of MGF may favour nucleophilic attack at the amide, resulting in formation of the pyroglutamate ring (Scheme 8.3). Although this mechanism would likely rely on a nucleophilic amine (and therefore, it could be expected that PGF formation may be accelerated in base), the lack of significant PGF formation in the more basic samples may be due to competition with $BiGF_2$ formation, which is also favoured in basic media. This hypothesis is supported the observation of increased PGF relative to $BiGF_2$ in the samples with 0.25 equivalents of HCHO.

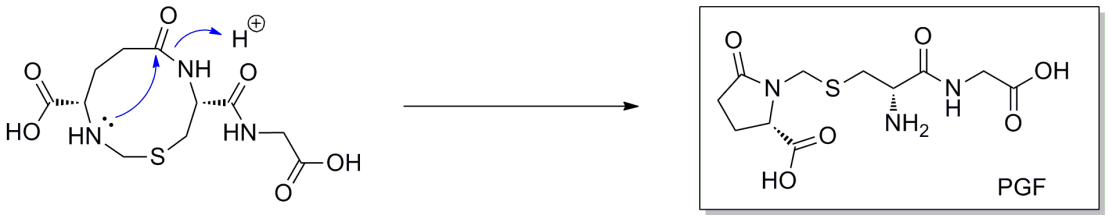

Scheme 8.3 Scheme showing a possible mechanism of PGF formation via the intermediate MGF.

8.3 Conclusions and Future Work

This Chapter describes comprehensive studies investigating the reactions of GSH and HCHO in aqueous solution. During the course of this work, the structures of three GSH-HCHO adducts were characterised, which resulted in the confirmation of one recently revised adduct structure, the revision of another adduct structure (MGF), and the first characterisation of another adduct (PGF). Time course investigations have suggested that two of these species (MGF and PGF) are formed predominantly under low HCHO concentrations (as well as the reported cellular adduct HMG), indicating that these adducts may be formed in cellular environments. Also, experiments with the GSH analogue GC supported the NMR assignments for the GSH-HCHO adducts and indicated that the glycinyl moiety in GSH is not important for adduct formation (at least *in vitro*). Finally, studies with the cellular aldehydes AcH and MG (with GSH) identified the corresponding hemithioacetals as predominating, indicating that cyclic species are not favoured.

The identification of a number of adducts, which can be formed under mild conditions at near neutral pD values, implies that some or all of these products may be produced in cells. Future work may therefore be focused upon identifying the formation of GSH-HCHO adducts within cells, possibly by using cell-based NMR methodology.[168] In particular, it is noted that MGF is produced at a comparable rate to HMG at pD 7.5. Therefore, it is probable that this product may be formed in cells,

especially when the cell conditions are slightly alkaline. Any confirmation of adduct formation in cells might then lead to interesting functional studies with these products.

Chapter 9

Studies on Glutathione-Dependent Formaldehyde-Activating Enzyme (GFA) from *Paracoccus Denitrificans*

9.1 Introduction

Work described in Chapter 8 demonstrated that the reaction of GSH and HCHO results in the formation of multiple species *in vitro*. However, to date, only the well characterised adduct HMG has been identified in cells.[168] Although it is possible that other GSH-HCHO adducts (such as $BiGF_2$, PGF and MGF) may be produced in a cellular environment, it can be postulated, based on the existing evidence, that formation of these species is inhibited. This inhibition may be induced by cells providing a preferential environment for HMG, implying that HMG formation may be enzyme-catalysed.

Glutathione-Dependent Formaldehyde Activating Enzyme (GFA) from *Paracoccus denitrificans* is a zinc-containing enzyme that has been linked to the metabolism of cellular HCHO.[156] GFA is proposed to catalyse the formation of HMG from GSH and HCHO, allowing HCHO to be either used as a carbon source, or to be detoxified by further oxidation.[220-222] Bioinformatic analyses suggest that GFA may be one of a large family of similar enzymes present in many prokaryotes and eukaryotes, implying that its role in cells is conserved throughout many organisms. However, the role of GFA in metabolising cellular HCHO remains somewhat ambiguous. Firstly, studies measuring oxygen uptake (used as a marker for C_1 activation) in *Rhodobacter sphaeroides* (grown on methanol) suggest that GFA plays no role in methanol metabolism.[223] This

observation implies that GFA-mediated formation of HMG may be a minor HMG forming pathway under high methanol concentrations as the non-enzymatic reaction of GSH and HCHO is known to be very fast (see Chapter 8). Also, it is noted that many organisms containing other HCHO metabolism enzymes (such as *E. coli*) do not possess the GFA gene.[156] This may suggest that GFA is not required for HCHO metabolism in these species, although it is also possible that other as-yet uncharacterised 'HCHO-activating' enzymes may facilitate HMG formation in place of GFA.

As described in Chapter 1, the proposed mechanism by which GFA accelerates the formation of HMG involves a migration of catalytic zinc from the active site to another as-yet unspecified position on the protein.[158] This proposed dynamic zinc binding mechanism is unique to GFA and appears to rely upon the formation of a protein-GSH disulfide bond at the 'active site' of the enzyme. However, the sole evidence for the reported mechanism is the observed loss of zinc from GFA upon co-crystallisation with GSH. A crystal structure of the resultant complex revealed no evidence of zinc binding at the active site; however, incubation of the GFA:GSH:Zn complex (one zinc ion remains in the protein in a structural role) with HCHO resulted in reduction of a GFA-GSH disulfide bond and the return of zinc. Although this observation may suggest that the GFA:GSH:Zn complex is an intermediate during HMG formation, the addition of HCHO to the sample may induce breakdown of the GFA:GSH:Zn complex by other mechanisms. It can be reasonably proposed that formation of the disulfide bond between the protein and GSH is formed by a disulfide exchange mechanism (presumably involving GSSG). Although the reducing agent dithiothreitol was added to the sample before crystallisation, the time required for crystallisation to occur (3 - 4 days), coupled with the propensity of GSH to oxidise, may indicate that significant concentrations of GSSG were present in the sample during crystallisation. Therefore, it is possible that formation of the GFA:GSH:Zn complex may be an artefact resulting from the sample conditions, rather than being an important step in the catalytic cycle.

Work described in this Chapter investigates GFA-catalysed HMG formation *in vitro* and also attempts to identify the mechanisms by which catalysis may proceed. These studies were conducted using predominantly NMR and mass spectrometry techniques, as described below.

A pET21b vector containing the GFA gene from Paracoccus denitrificans *(with added TEV cleavage site) was provided by Dr. Nathan R. Rose (originally a gift from Dr. Stefan Becker, Göttingen).* N-*terminally* His_6*-Tagged GFA was also provided by Dr. Nathan R. Rose. Analytical size-exclusion chromatography was carried out by Luc Henry.*

9.2 Results

Initial assays probing GFA activity were carried out using *N*-terminally His_6-Tagged GFA (*prepared previously by Dr. Nathan R. Rose*). However, use of this batch of protein in non-denaturing mass spectrometry experiments indicated that the His-Tagged protein had undergone partial gluconylation at its *N*-terminus, prohibiting interpretation of the mass spectra.[224, 225] Therefore, His-Tag cleaved GFA was prepared as described below, which resulted in non-gluconylated protein suitable for mass spectrometry analysis (Figure 9.6). The majority of experiments described in this Chapter were carried out using His-Tag cleaved GFA, although some experiments were conducted using the His-Tagged protein (where indicated) due to its greater availability at the time of experimentation. The relative activities of the two protein forms are compared in Section 9.2.3c.

9.2.1 Expression and Purification of His-Tag Cleaved GFA

Preparation of His-Tag cleaved GFA was achieved by expressing BL21 (DE3) cells containing a GFA-pET21b vector (*transformed by Dr. Nathan R. Rose*). After growing a pre-culture in ampicillin inoculated 2TY media, the suspended cells were added to larger flasks of the same ampicillin inoculated media and incubated at 37 °C. After reaching OD_{600} 0.9, IPTG was added to the flasks in order to induce protein expression

and the flasks were then left overnight at 18 °C. The cells were separated from the media by centrifugation and the resultant pellets were then combined and stored at -80 °C, before the expressed protein was collected by lysing the cells (resuspended in Ni-column binding buffer) using a sonicator. The resultant soluble matter was purified by injecting the solution onto a Ni-column and washing the column with imidazole containing buffer. The protein was then extracted from the column using a more concentrated imidazole solution. Analysis of the purified protein by SDS-PAGE indicated that the sample was still not sufficiently pure. Therefore, further purification was attempted using size-exclusion chromatography, which provided the protein in over 95 % purity, as assessed by SDS-PAGE analysis (Figure 9.1).

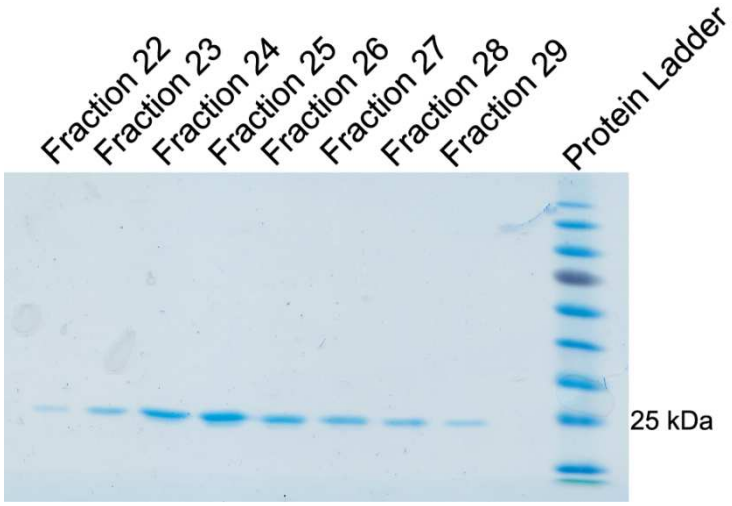

Figure 9.1 SDS-PAGE gel showing fractions containing GFA after size-exclusion chromatography.

Removal of the His-Tag was achieved by treating the protein (in 50 mM tris buffer pH 7.5) with TEV protease. After 12 hours at 4 °C, the cleaved protein was purified by flushing the solution through a Ni-column. His-Tagged impurities remaining in the sample (such as non-cleaved GFA and TEV protease) were trapped on the column, allowing the product to be collected in purified form in the flow-through (Figure 9.2).

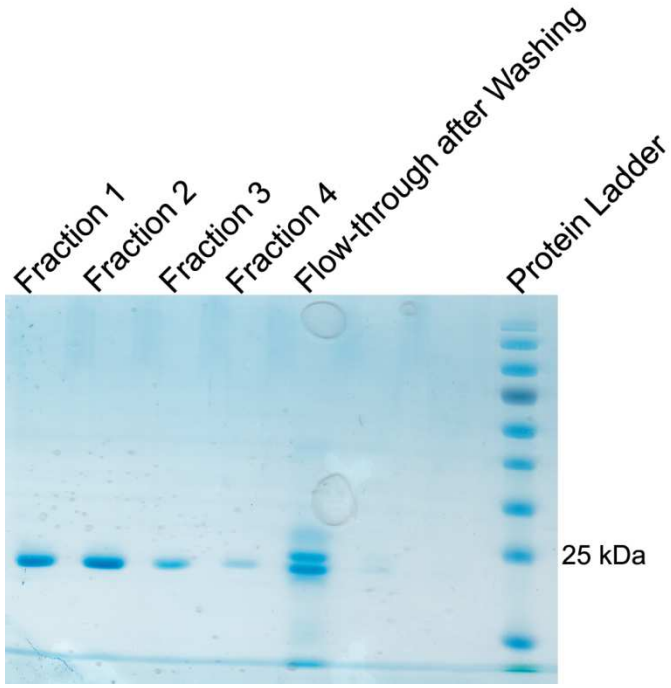

Figure 9.2 SDS-PAGE gel showing fractions containing GFA after TEV-cleavage and Ni-column purification. The His-Tag cleaved protein can be seen to be at slightly lower mass than the residual His-Tagged GFA in the flow-through after column washing.

In total, over 50 mgs of purified His-Tag cleaved GFA was prepared from a 12 litre culture of *E. coli* BL21 (DE3) cells, which was considered sufficient for further experimentation.

9.2.2 Characterisation of GFA

Having prepared a batch of His-Tag cleaved GFA, experiments were carried out using non-denaturing mass spectrometry, size-exclusion chromatography and circular dichroism. It was hoped that these experiments would be able to determine not only that the protein had folded correctly, but also whether the purified GFA contained two zinc ions in its structure. Previous work on GFA had also suggested that the protein exists as a homodimer in solution (at least under the conditions employed), and therefore, it was also hoped that these studies may give insight into the oligomerisation state of GFA under the experimental conditions.

a) Circular Dichroism

The CD spectrum of GFA is shown in Figure 9.3.

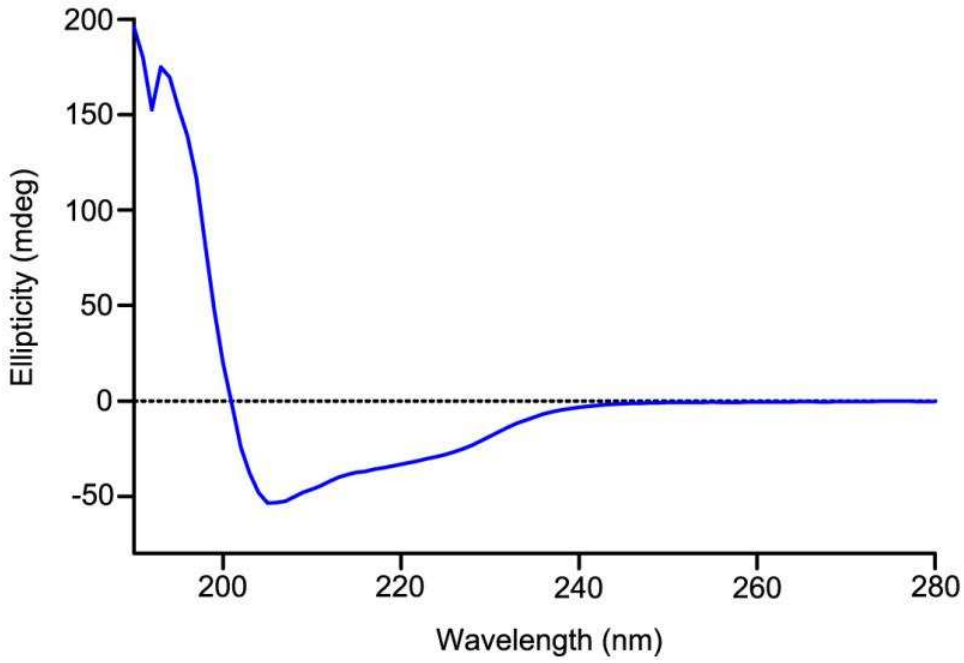

Figure 9.3 CD spectrum of GFA.

CD analyses indicate that the batch of His-Tag cleaved GFA possesses a folded structure (Figure 9.3). Analysis of the spectrum suggested that GFA possesses both α-helical and β-sheet secondary structure elements (by comparison with the spectra of standard samples), which corroborates the structural assignment of the protein by X-ray crystallography. Therefore, this preliminary study indicates that the batch of GFA is folded with at least a similar secondary structure to the previously described protein sample.

b) Size-Exclusion Chromatography

Size-exclusion chromatography allows for the masses of protein species to be determined from their elution times through a gel filtration column. This technique does not result in loss of protein secondary or tertiary structure, and therefore, can be used for the identification of oligomeric species. Previous studies using analytical size-exclusion chromatography have implied that GFA

exists as a homodimer in solution. In order to confirm this finding, the His-Tag cleaved GFA batch was subjected to size-exclusion chromatography experiments using a Superdex S200 column. Firstly, the column was calibrated by monitoring the elution volume of a variety of proteins with known masses and oligomerisation. These experiments then allowed the expected elution volumes for monomeric and homodimeric GFA to be estimated. The size-exclusion chromatograms for the standard protein mixture (used for calibration) and GFA are shown in Figure 9.4.

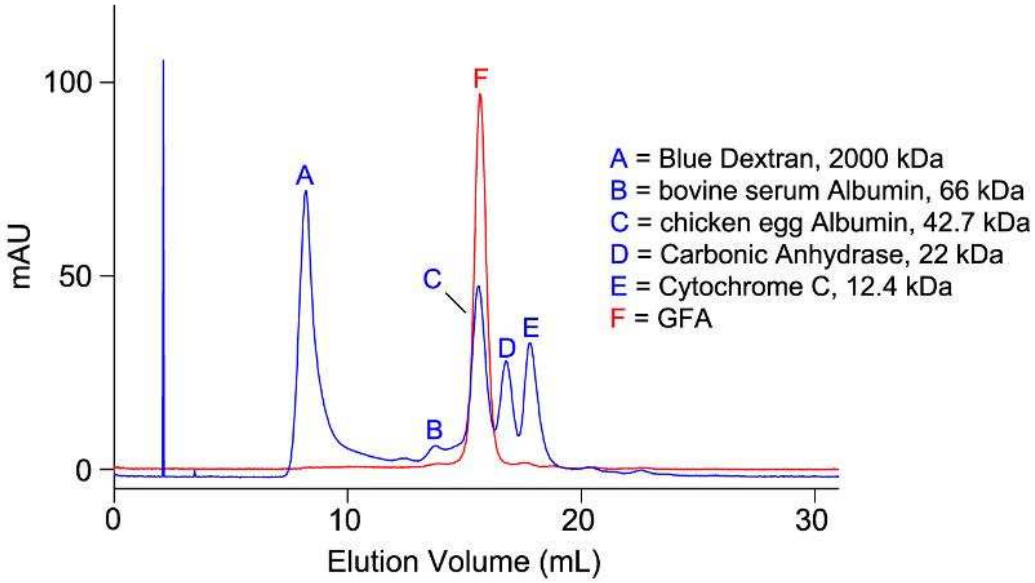

Figure 9.4 Analytical size-exclusion **c**hromatograms (UV detection, A_{280}) for the standard protein mixture (Blue) and His-Tag cleaved GFA (Red).

Analysis of the chromatograms revealed that the majority of GFA in the sample eluted after 15.7 mL. This volume was similar to the elution volume observed for chicken egg albumin (mass 42.7 kDa) in the standard protein sample, suggesting that GFA was present predominantly as a dimer under the experimental conditions. However, the mass corresponding to the GFA peak was calculated as 36 kDa by analogy with the calibration data with standard proteins, which is slightly lower than the expected mass of the homodimer (42.3 kDa). Although this data may suggest the presence of another species in the

mixture, it is likely that the major peak corresponds to the homodimer given the relative similarity of the calculated and expected masses.

c) Non-Denaturing Mass Spectrometry

Analysis of the GFA protein was also attempted using non-denaturing mass spectrometry. It was hoped that this technique would enable the detection of zinc ions in the GFA structure by allowing the protein to remain folded during ionisation and analysis. Although ionisation of the protein samples is achieved using similar electrospray methodology to that adopted during denaturing mass spectrometry (Figure 9.5), the lack of organic solvent or acid used during sample preparation can enable the protein to maintain its folded structure. Also, non-covalent interactions between the protein and metal ions/ligands are often conserved during ionisation, which enables the resultant complex ions to be detected. Therefore, it was hoped that this technique may also be used to investigate the oligomerisation state of GFA, as it could be expected that any interactions between protein molecules may be conserved.

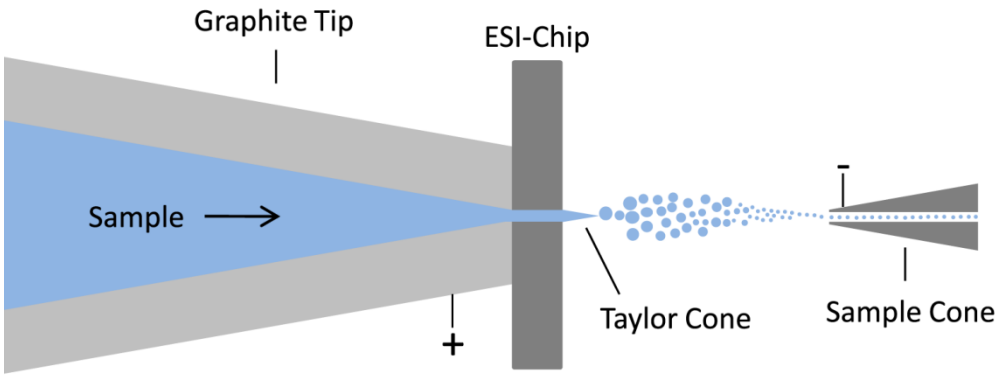

Figure 9.5 Schematic representation of electrospray ionisation in the positive ion mode. The sample is passed through a charged graphite capillary, which separates the species in solution into their separate charge states. Upon passing through the narrow chip, the repulsion of the positively charged species results in the formation of a Taylor cone. This cone thins until the proteins are released in positively charged droplets. Upon evaporation, these droplets result in the formation of charged protein ions. The ions are then pulled through a negatively charged sample cone, focused with a quadrupole, and then passed through a time-of-flight analyser.[226, 227]

In order to attain a non-denaturing mass spectrum of GFA, it was necessary to remove the salt present in the mixture to diminish interference during ionisation. It was also important to transfer the protein into a volatile buffer system in order to facilitate removal of the solvent and buffer by evaporation. Consequently, GFA was desalted using a Bio-Spin 6.0 desalting column (BioRad, UK) and rebuffered into 15 mM ammonium acetate pH 7.5, before the sample was analysed using a Q-TOF mass spectrometer (Micromass, UK) interfaced with a Nanomate (Advion Biosciences, USA). The deconvoluted and non-deconvoluted mass spectra are shown in Figure 9.6.

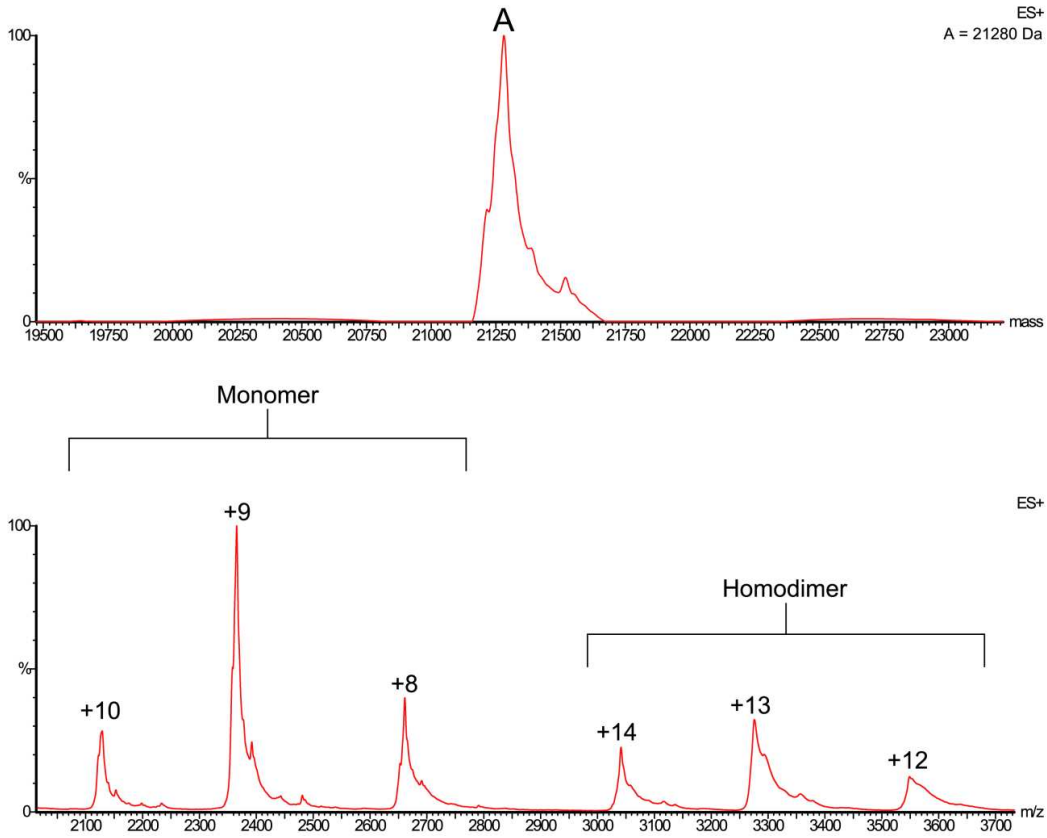

Figure 9.6 Deconvoluted (Above) and non-deconvoluted (Below) non-denaturing mass spectra of His-Tag cleaved GFA.

Interestingly, GFA was detected as both a monomeric species and as a homodimer in the mass spectrum. This observation indicates that the dimeric species observed using size-exclusion chromatography is partially degraded during the mass spectrometry conditions, suggesting that interactions between the two GFA molecules are relatively weak. Deconvolution of the spectrum revealed a monomeric mass of 21280 Da, which matches closely to the mass calculated for the GFA:Zn:Zn complex (21283 Da). It was also possible to observe a small peak in the deconvoluted spectrum at 21518 Da. This peak may correlate to the GFA:GSH:Zn adduct described by X-ray crystallography (21523 Da), indicating that partial oxidative zinc removal may have occurred during protein expression/purification.

9.2.3 NMR Experiments on GFA Activity

Having determined that the batch of His-Tag cleaved GFA is suitably folded, preliminary experiments were concentrated upon assessing enzyme activity. This work primarily involved analysis of exchange sepectroscopy (EXSY) experiments, as described below.

a) EXSY – Background

Previous studies utilised EXSY to determine GFA activity, and therefore, this technique was chosen for initial experiments.[156] EXSY relies upon the transfer of longitudinal magnetisation between two species in dynamic exchange under equilibrium conditions, and can facilitate the acquisition of rate constants for the exchange process by allowing the degree of magnetisation transfer to be quantified.[228] Typically, these experiments utilise a standardised NOESY pulse sequence,[228] which enables exchange between two species to be visualised by displaying cross peaks between by their constituent ^{1}H resonances. EXSY cross-peaks possess the same sign as the parent resonances, and therefore, can be easily distinguished from both NOE (for small molecules) and COSY-type correlations in the EXSY spectra.

Quantitative analysis is possible by two conventional methods.[229] The first method relies upon the dependence of magnetisation transfer on the experiment mixing time τ_m (Figure 9.7).

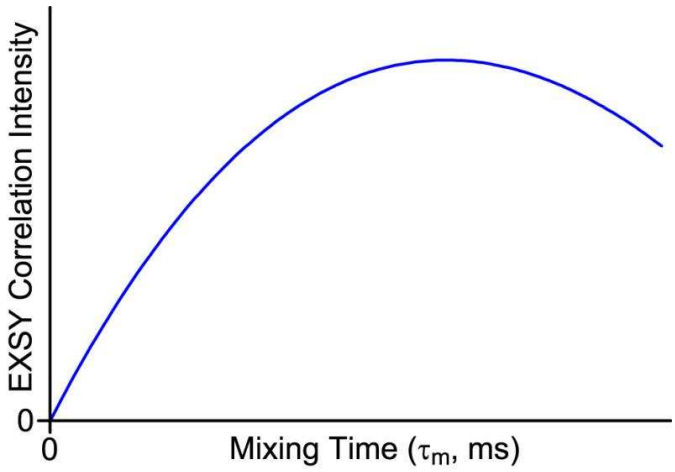

Figure 9.7 Representative plot of EXSY cross-peak intensity versus mixing time (τ_m).

Over small τ_m values, the cross-peak intensity shows a linear dependence on τ_m, and therefore, the slope of the curve in this region correlates directly to the pseudo first order rate constant of the exchange process (Scheme 9.1 and Equation 9.1). However, analysis by this method often requires accumulation of multiple spectra, resulting in significant machine time per experiment (particularly when using 2D EXSY).

$$[A] \underset{k_-}{\overset{k_+}{\rightleftharpoons}} [B]$$

Scheme 9.1 Reaction scheme for a two-site exchange reaction. [A] = the concentration of species A, [B] = the concentration of species B, k_+ = the rate constant for the forward reaction, k_- = the rate constant for the backward reaction.

$$B_{ij}(\tau_m) = \frac{V_{ij}(\tau_m)}{V_{jj}(\tau_m)} \xrightarrow{\tau_m \to 0} k_{ij}\tau_m$$

Equation 9.1 Equation for the determination of rate constants from normalised EXSY correlations in the linear range. $B_{ij}(\tau_m)$ = Normalised EXSY correlation intensity, $V_{ij}(\tau_m)$ = Intensity of EXSY correlation, $V_{jj}(\tau_m)$ = Intensity of diagonal ^{1}H resonance, k_{ij} = rate constant.[229]

Conversely, the second quantification method only requires data from one experiment, although the selected τ_m must be large enough to allow suitably intense signals, but also not too large to become insensitive to the exchange kinetics. Rate constants can then be calculated from the normalised cross-peak intensities by computational analysis.[230]

b) 2D EXSY of the GSH HCHO Reaction

Qualitative investigation of GFA activity was carried out using 2D EXSY. Firstly, exchange between glutathione (GSH) and *S*-hydroxymethylglutathione (HMG) in the absence of enzyme was investigated by analysing a sample containing glutathione (13.3 mM final concentration) and formaldehyde (13.3 mM) in deuterated tris buffer pD 7.5. Attempts at preparing the sample using the reported conditions (phosphate buffer pD 6.0) resulted in protein precipitation, and therefore, optimisation of the sample conditions was required before NMR analysis could be performed. The optimised sample was left to equilibrate for one hour at 25 °C before being transferred to a 2 mm NMR tube and analysed by ^{1}H and 2D EXSY. The ^{1}H spectrum revealed that the major species in solution were GSH and HMG (no significant quantities of MGF, PGF or $BiGF_2$ were observed, see Chapter 8), which suggested that analysis of the exchange between the two species could be facilitated by the EXSY experiment. This hypothesis was confirmed by the observation of cross-peaks between the β-cysteinyl protons of GSH and HMG in the 2D EXSY spectrum (Figure 9.8).

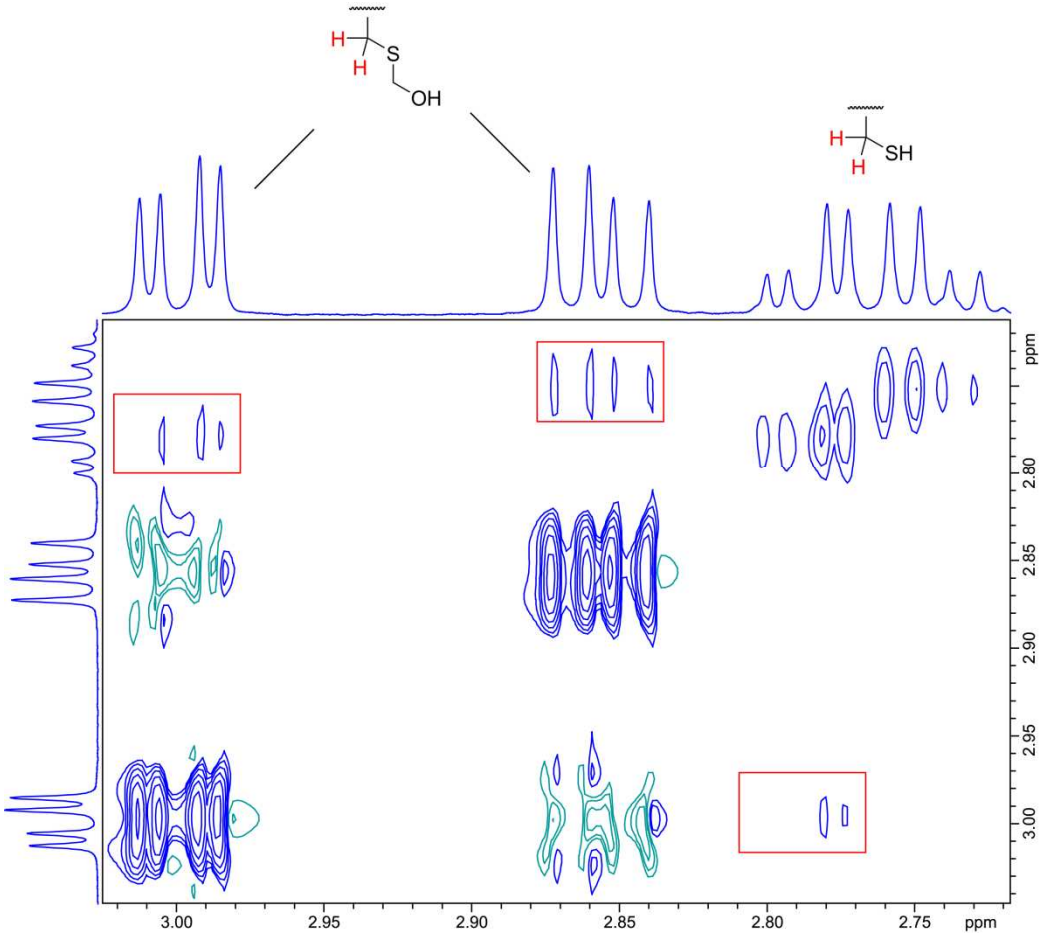

Figure 9.8 2D EXSY spectrum (700 MHz) of a sample containing GSH (13.3 mM) and HCHO (13.3 mM) in deuterated tris buffer pD 7.5. EXSY correlations are displayed in red boxes.

Having observed dynamic exchange in the absence of protein, a separate sample was prepared with added His-Tag cleaved GFA (16 μM final concentration) and analysed by 2D EXSY. The spectrum revealed cross-peaks at greater intensity than those observed in the absence of GFA, implying that the enzyme had catalysed exchange in the reaction mixture (Figure 9.9). A third sample containing His-Tagged GFA also displayed EXSY correlations at greater intensity, confirming the activity of the tagged protein.

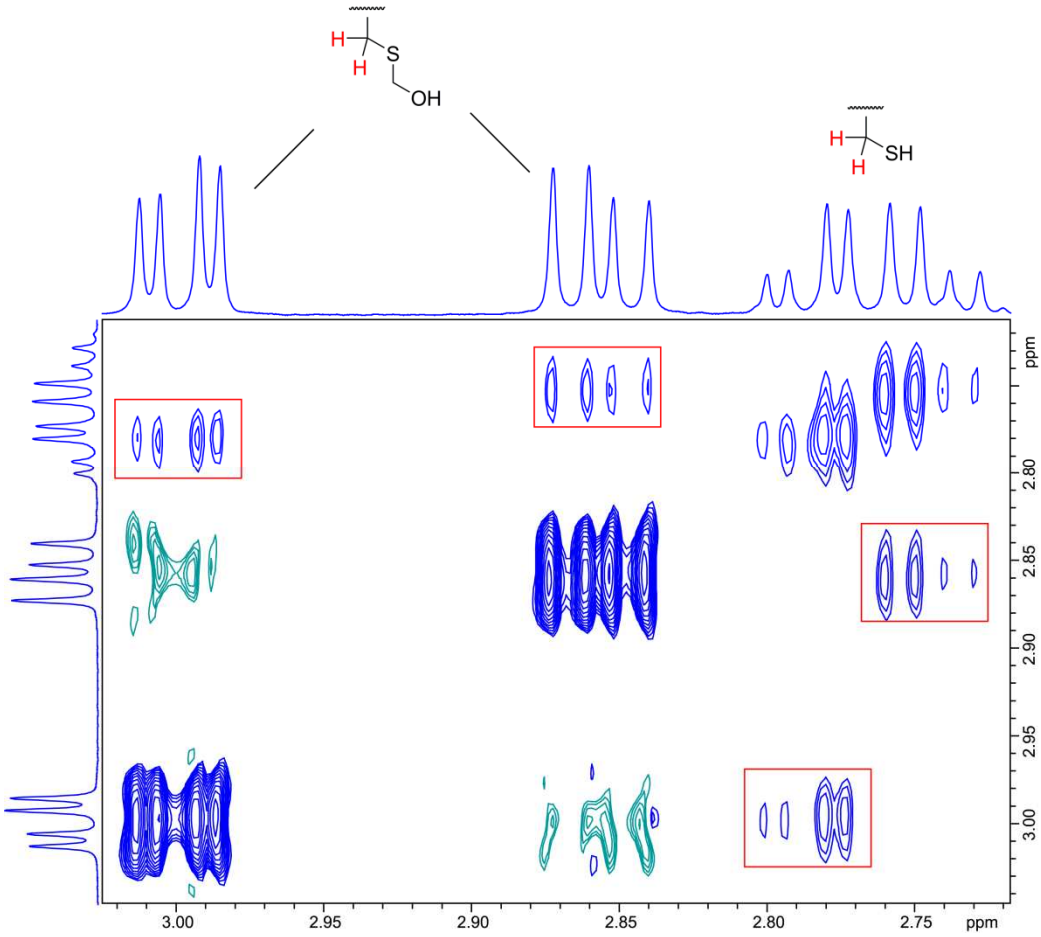

Figure 9.9 2D EXSY spectrum (700 MHz) of a sample containing GSH (13.3 mM), HCHO (13.3 mM) and His-Tag cleaved GFA (16 µM) in deuterated tris buffer pD 7.5. EXSY correlations are displayed in red boxes.

c) 1D EXSY of the GSH HCHO Reaction

Rate constants for the reversible formation of HMG were then determined using 1D EXSY. This technique, which irradiates only the ^{1}H resonance(s) of interest (in this case the HMG β-cysteinyl proton resonance at δ_H 2.97 ppm), facilitates the observation of exchange cross-peaks over a shorter time frame than the corresponding 2D experiment, and therefore allows for faster analysis of the reaction. For these experiments, it was first important to identify a standardised mixing time that would allow the linear rate approach for determining rate constants to be valid as well as providing suitable signal intensities above the background noise. Therefore, 1D EXSY experiments were carried out on a

sample containing GSH, HMG and GFA (His-Tagged) over a variety of mixing times in order to identify a mixing time suitable for future experiments (Figure 9.10). The normalised EXSY correlations from the spectra suggested that analysis of the samples at τ_m = 80 ms would be sufficient for rate constant determination.

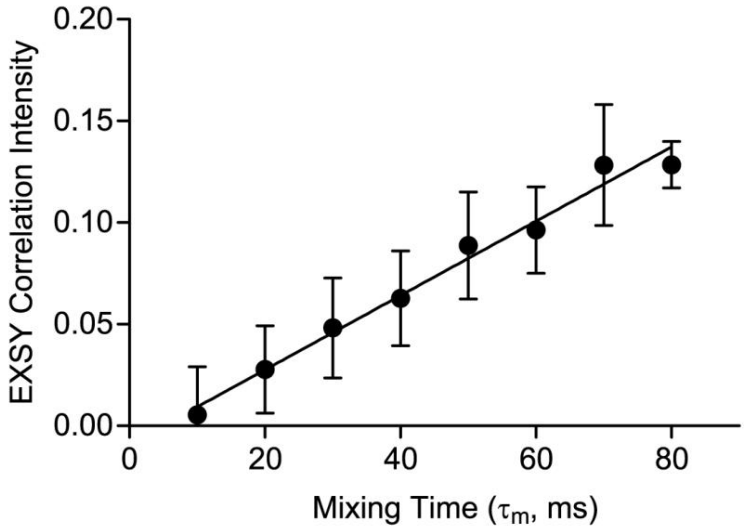

Figure 9.10 Plot of normalised EXSY correlation intensities for a sample containing GSH (13.3 mM), HCHO (13.3 mM) and His-Tagged GFA (18 μM) in deuterated tris buffer pD 7.5 at different mixing times.

The pseudo-first order rate constants for the exchange between GSH and HCHO in the presence and absence of GFA (k_x and k_{-x}, Scheme 9.2) were calculated by determining the normalised EXSY correlation intensities and dividing the empirical value by the mixing time (80 ms). For this work, the ^{1}H resonance at δ_H 2.97 ppm (corresponding to a β-cysteinyl proton on HMG) was selected for irradiation due to the lack of neighbouring signals, thus avoiding irradiation of multiple species. The 1D EXSY spectra (Figure 9.11) revealed correlations at δ_H 2.86 ppm (corresponding to the equivalent β-cysteinyl proton on GSH), and also at δ_H 2.90 ppm (corresponding to the other β-cysteinyl proton on GSH, which is presumably derived from a secondary magnetisation transfer from the proton at δ_H 2.86 ppm). The intensity of the normalised EXSY correlation (at δ_H 2.86 ppm and δ_H 2.90 ppm combined) therefore allowed the rate constant for the backward

reaction (k_{-x}, Scheme 9.2) to be calculated directly; however, the rate constant for the forward reaction (k_{x}, Scheme 9.2) could also determined by noting the concentrations of GSH and HMG at equilibrium (Equation 9.2).

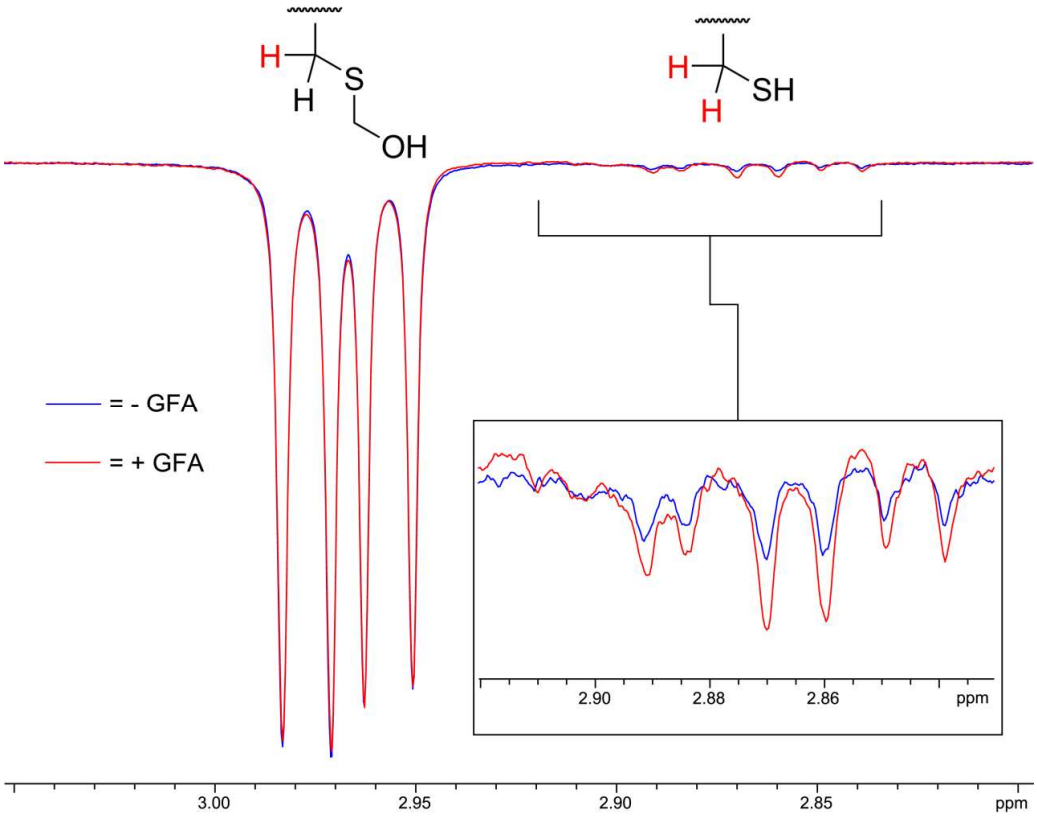

Figure 9.11 1D EXSY spectra (700 MHz) for samples containing GSH (13.3 mM) and HCHO (13.3 mM), either in the presence (Red) or absence (Blue) of His-Tag cleaved GFA (16 µM). The observed signals at δ_H 2.86 ppm and δ_H 2.90 ppm correspond to EXSY correlations.

$$\mathrm{GSH} \underset{k_{-x}}{\overset{k_x}{\rightleftharpoons}} \mathrm{HMG}$$

Scheme 9.2 Reaction scheme for the two-site exchange of GSH and HMG. k_x = the rate constant for HMG formation , k_{-x} = the rate constant for HMG fragmentation.

$$v_x = k_x[GSH] = v_{-x} = k_{-x}[HMG]$$

$$k_x = k_{-x}\frac{[HMG]}{[GSH]}$$

Equation 9.2 Equation showing the correlation between the rate constants k_x and k_{-x} at equilibrium. v_x = rate of the HMG formation, v_{-x} = rate of HMG fragmentation.

Rate constants calculated from the 1D EXSY experiments, as well as the specific activities for both protein batches, are displayed in Table 9.1. The specific activity of the His-Tagged protein (53 units mg^{-1}, where one unit is defined as 1 μmole of HMG converted to GSH per minute at equilibrium) was higher than that of the His-Tag cleaved batch (33 units mg^{-1}), which may indicate that protein activity is lost during TEV cleavage. The specific activity of His-Tag cleaved batch matched closely to that reported for His-Tag cleaved GFA in cell extracts from *Paracoccus denitrificans* (35 units mg^{-1});[156] however, the specific activity reported for the recombinant protein was significantly higher (350 units mg^{-1}), potentially indicating a strong activity dependence upon the sample conditions used.

Table 9.1 Table showing k_x, k_{-x} and specific activity values for His-Tagged GFA and His-Tag cleaved GFA, calculated using 1D EXSY. Specific activities were calculated by subtracting the activity in the absence of enzyme (in μmole min^{-1}) from the activity in the presence of enzyme.

Conditions	k_x (s^{-1})	k_{-x} (s^{-1})	Specific Activity (units mg^{-1})
- GFA	0.67	0.22	
+ His-Tagged GFA	1.78	0.59	53
+ His-Tag cleaved GFA	1.27	0.42	33

The observed acceleration in exchange rates between GSH and HCHO in the presence of GFA prompted investigations with other enzymes. It was hoped that these experiments would confirm that the increase in equilibrium exchange rate constants are due to specific catalysis by GFA, and are not due to changes in the sample conditions upon addition of a generic enzyme. A variety of enzymes

were added to equilibrium mixtures of GSH and HCHO (as described above) and the normalised EXSY correlations (corresponding to k_{-x}) were determined from the 1D EXSY spectra. In contrast to the samples containing GFA, no increases in k_{-x} were observed relative to the samples without enzyme, indicating that these enzymes do not accelerate the equilibrium dynamics (Figure 9.12). It was therefore concluded that GFA is specifically catalysing the exchange reactions at equilibrium, resulting in an increase in the exchange rate constants.

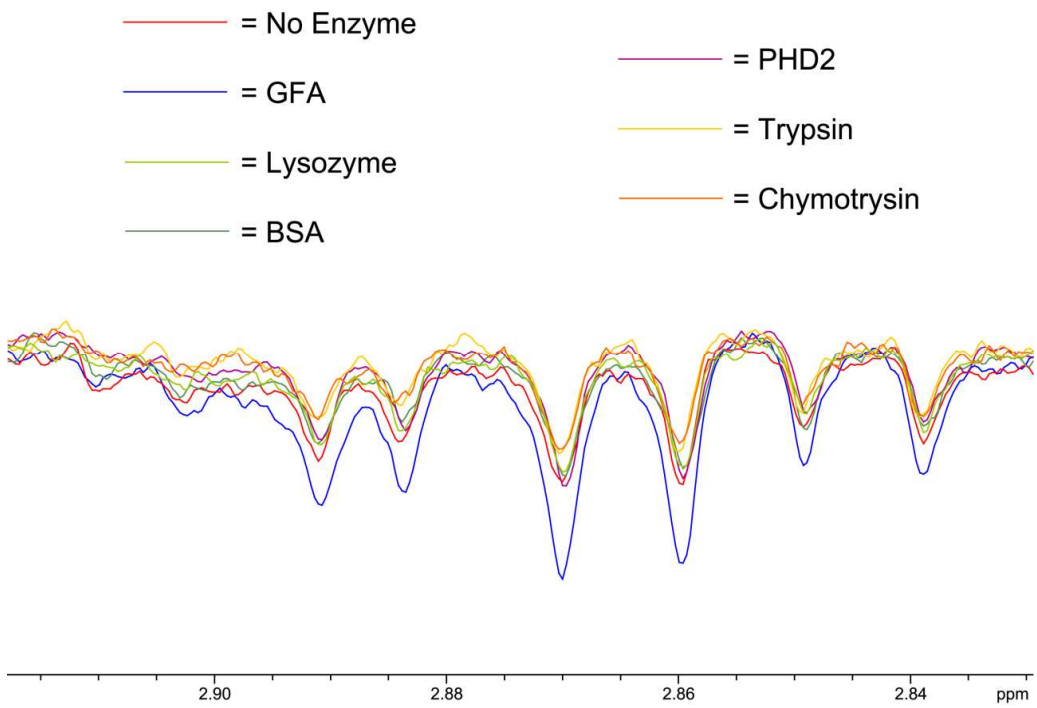

Figure 9.12 1D EXSY spectra (700 MHz) for samples containing GSH (13.3 mM) and HCHO (13.3 mM), in the presence of a variety of enzymes (at 16 µM). The control experiments with GFA (His-Tag cleaved) and without enzyme are shown.

Given that the forward and backward reactions in the sample with GFA could occur by enzymatic and non-enzymatic pathways, analysis of the EXSY data was then focused upon determining the rate constants for each of these processes. The modified rate equation, containing terms for both the enzymatic and non-enzymatic pathways, is given in Equation 9.3.

$$v_x = k_1[GSH][HCHO] + k_2[GSH][HCHO] = v_{-x} = k_{-1}[HMG] + k_{-2}[HMG]$$

$$k_x = k_1[HCHO] + k_2[HCHO] \qquad k_{-x} = k_{-1} + k_{-2}$$

$$k_2 \propto [GFA] \qquad k_{-2} \propto [GFA]$$

Equation 9.3 Rate equations for HMG formation (v_x) and fragmentation (v_{-x}). Constants k_1 and k_{-1} correspond to the non-enzymatic reaction. Constants k_2 and k_{-2} correspond to the enzymatic reaction, and are therefore dependent on the enzyme concentration. These equations assume that HMG formation, both non-enzymatic and enzymatic, is first order with respect to GSH and HCHO respectively. Fragmentation of HMG is also assumed to be first order.

When the enzymatic pathway is not present (i.e. when there is no GFA in the sample), Equation 9.3 may be simplified to contain terms representing the non-enzymatic reaction exclusively (Equation 9.4). Therefore, values for the constants k_1 and k_{-1} could be ascertained.

$$v_{-x} = k_{-1}[GSH][HCHO] = v_{-x} = k_{-1}[HMG]$$

$$k_x = k_1[HCHO]$$

$$k_{-x} = k_{-1}$$

Equation 9.4 Simplified rate equations for the forward (v_x) and backward reactions (v_{-x}) in the absence of GFA.

Having identified values for k_1 and k_{-1} from the control experiment, it was possible to determine values for k_2 and k_{-2} in samples containing enzyme by subtracting the values for k_1 and k_{-1} from the terms for k_x and k_{-x} respectively (Table 9.2).

Table 9.2 Table showing calculated values for k_1, k_{-1}, k_2 and k_{-2} respectively.

	k_1 (mM^{-1} s^{-1})	k_{-1} (s^{-1})	k_2 (mM^{-1} s^{-1})	k_{-2} (s^{-1})
-GFA	0.20	0.22		
His-Tagged GFA			0.34	0.37
His-Tag Cleaved GFA			0.18	0.20

Further evidence for specific catalysis by GFA was acquired from 1D EXSY experiments conducted at varying pD. These studies enabled values for k_{-x} in the absence and in the presence of GFA (His-Tagged) to be calculated across a pD range, thus allowing the pD dependence upon the overall rate to be determined. The EXSY spectra were collected for samples at pD 6.0, 6.5, 7.0, 7.5, 8.0, 8.5 and 9.0, and the corresponding k_{-x} values were plotted as a function of pD (Figure 9.13).

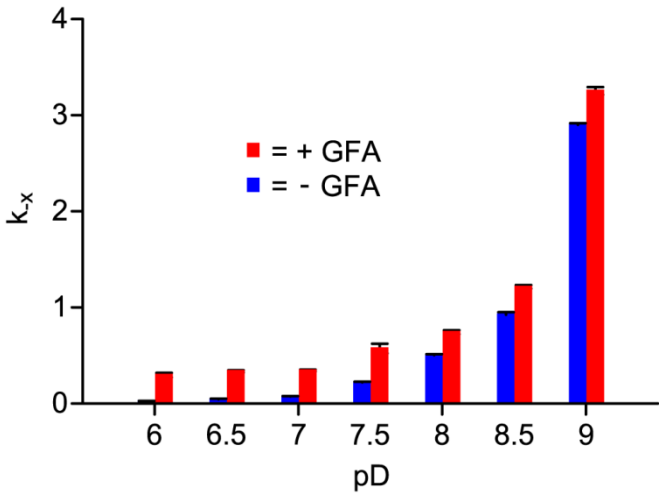

Figure 9.13 Plot of the rate constants for HMG fragmentation in the presence and absence of GFA, at different pDs.

The data revealed that the overall rate constant (k_{-x}) increased at higher pD, both in the absence and in the presence of GFA. However, the ratio between k_{-x} in the presence of GFA and k_{-x} in the absence of GFA suggested that the enzymatic pathway was less affected upon acidification of the reaction mixture (Figure 9.14). These observations imply that GFA may act as a general base catalyst during the exchange reaction.

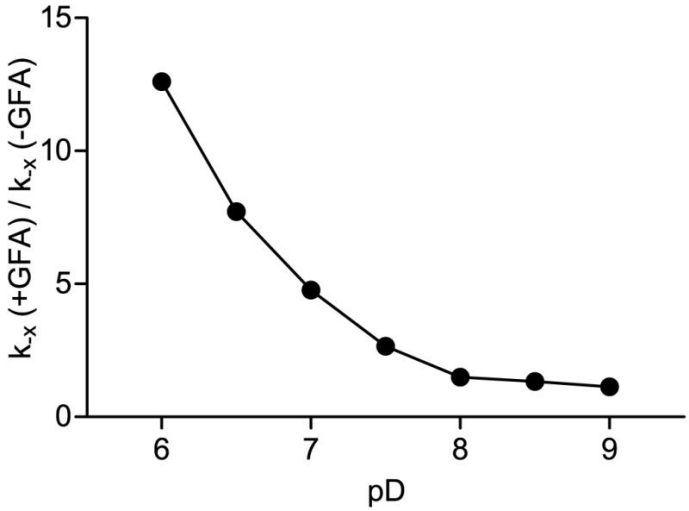

Figure 9.14 Plot of k_{-x} in the presence of GFA, divided by k_{-x} in the absence of GFA, at different pDs.

Having identified an increase in equilibrium rate constants upon addition of GFA, ^{1}H NMR experiments monitoring GSH and HMG concentration over the course of reaction were attempted in order to detect a change in the initial reaction rates. Samples of GSH and HCHO (13.3 mM final concentrations) were prepared either in the presence or absence of His-Tag cleaved GFA (as described above). The samples were transferred to the NMR spectrometer immediately after mixing, and were then monitored over the initial hour of reaction by ^{1}H NMR. The relative populations of GSH and HMG in the samples were then plotted as a function of time (Figure 9.15).

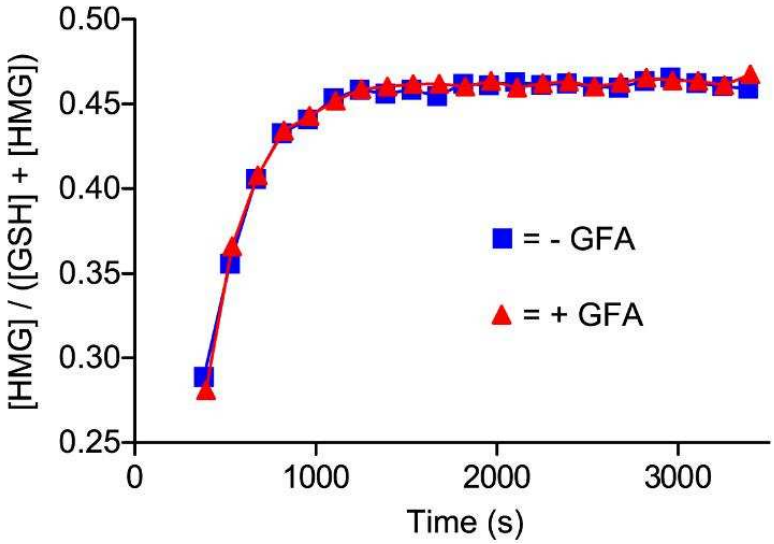

Figure 9.15 Time dependence on the populations of HMG in the presence and absence of GFA.

Interestingly, no difference in the populations of GSH and HMG were detected in the samples, indicating that GFA does not affect the rate at which the reaction mixture reaches equilibrium (the initial rates for both samples was roughly 0.3 mM min^{-1}). This observation is counter-intuitive, as it could be expected that the increase in k_x and k_{-x} values upon addition of GFA would decrease the reaction time required for the sample to reach its equilibrium position. However, it should be noted at this stage that the full rate equation for the reaction of GSH and HCHO is more complex than the simplified two-site exchange rate equations described in Equations 9.2 and 9.3 (as employed for previous studies with GFA). Principally, these equations do not consider the fast equilibrium (the rate of hydration of HCHO was measured at 9.8 s^{-1} at pH 4)[231] between the hydrated and aldehydic forms of HCHO in solution, which is strongly biased towards the hydrate (the equilibrium constant for the aldehydic and hydrated HCHO equilibrium was measured at 4.5×10^{-4} at pH 4).[231-233] As the hydrate is likely to be slower to react directly with GSH, it can be expected that the initial rate of HMG formation is strongly dependent upon the concentration of aldehydic HCHO in solution. As the concentration of aldehydic HCHO is very low, the rate-determining factor for the reaction as a whole is likely to be the

position of the hydrated/aldehydic HCHO equilibrium. Therefore, variations in the rate constants for the exchange between GSH and HMG may not affect the initial rate (Scheme 9.3 and Equation 9.5).

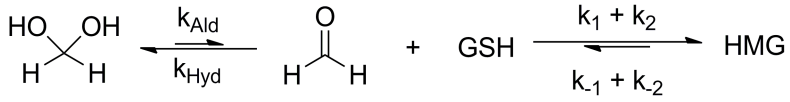

Scheme 9.3 Reaction scheme showing the pre-equilibrium between the hydrated and carbonyl forms of HCHO in aqueous solution. The rate of HMG formation is limited by the low concentration of aldehydic HCHO in aqueous solution. k_{Hyd} = the rate constant for conversion of aldehydic HCHO to hydrated HCHO (large in water), k_{Ald} = the rate constant for the conversion of hydrated HCHO to aldehydic HCHO (small in water). The rate constants k_1, k_2, k_{-1} and k_{-2} are defined in Equation 9.3.

$$[HCHO] = [Hyd] + [Ald]$$

Hydrated HCHO is significantly less reactive than aldehydic HCHO

$$\therefore\ v_x = (k_1 + k_2)[GSH][Ald]$$

$$\frac{[Ald]}{[Hyd]} = \frac{k_{Ald}}{k_{Hyd}} = \mathrm{K_{HCHO}} = \text{ small}$$

$$(4.5 \times 10^{-4} \text{ at pH } 4, 295 \text{ K})(\text{Sutton and Downes } 1972)$$

$$\therefore [Ald] \text{ is small}$$

Equation 9.5 Modified rate equation for the equilibrium of GSH and HMG in aqueous solution. The rate is dependent upon the position of the hydrated/aldehydic HCHO equilibrium (K_{HCHO}). In water, K_{HCHO} is small, and therefore, the availability of aldehydic HCHO is rate limiting.

Overall, the 1D EXSY experiments have indicated that GFA is able to catalyse both the formation of HMG from GSH and HCHO and its subsequent fragmentation, thus increasing the exchange rates of the GSH/HMG equilibrium. However, in aqueous solutions, the rate determining factor may be the availability of aldehydic HCHO, and thus, GFA has limited effects on the

overall rate of HMG formation. These findings may suggest that, in cellular contexts, GFA may be able to facilitate the detoxification of aldehydic HCHO by catalysing HMG formation, although it would seem likely that in most situations, the concentration of the aldehyde would be very small relative to the hydrated form. Therefore, these experiments indicate that any role GFA plays during HCHO detoxification may be confined to localities/situations where the aldehydic HCHO concentrations are high.

9.2.4 Probing GSH Binding

The observation that HMG formation can be catalysed by GFA indicated that GSH, either by direct addition or via reduction of the disulfide, is able to bind GFA in its active site. X-ray crystallography studies have suggested that this binding occurs via removal of the catalytic zinc ion, resulting in the formation of a disulfide bond between GSH and an active site thiol. Initial experiments focused upon investigating the interaction between GSH and GFA were attempted using non-denaturing mass spectrometry and NMR based techniques, as described below.

a) NMR Binding Studies

Firstly, the binding of GSH to GFA was investigated using two complimentary NMR techniques, saturation transfer difference (STD) NMR spectroscopy[234] and water ligand observation with gradient (waterLOGSY) NMR spectroscopy.[235] Both of these experiments rely upon the transfer of magnetisation from an irradiated species to probe the binding propensities of molecules in solution, usually to an enzyme.[236] For STD, proton resonances on the protein are irradiated, which results in partial transfer of magnetisation to protons attached to bound ligands.[237] Therefore, comparison of the ligand ^{1}H-resonance intensities in the irradiated STD spectrum with those in a spectrum without protein irradiation allows for the degree of binding to be visualised. WaterLOGSY NMR also relies upon magnetisation transfer; however, in this case, the solvent water protons, rather than those on the enzyme, are irradiated.

Consequently, direct magnetisation transfer between the water and ligand via an internal NOE results in ligand signal intensities with an opposite sign to the irradiated water peak, due to the fast tumbling (molecular correlation time) of small molecules in solution. However, upon binding of the ligand to the macromolecular protein, the tumbling rate decreases, resulting in partial inversion of the signal sign. Therefore, measuring the waterLOGSY resonance intensities at different ligand concentrations allows a dose-response curve for ligand-protein binding to be acquired.[235]

For STD NMR experimentation, a sample containing GSH (13.3 mM) and GFA (36 µM) in tris buffer pD 7.5 was prepared and analysed over 12 hours using a 700 MHz NMR spectrometer. The STD spectrum is shown in Figure 9.16.

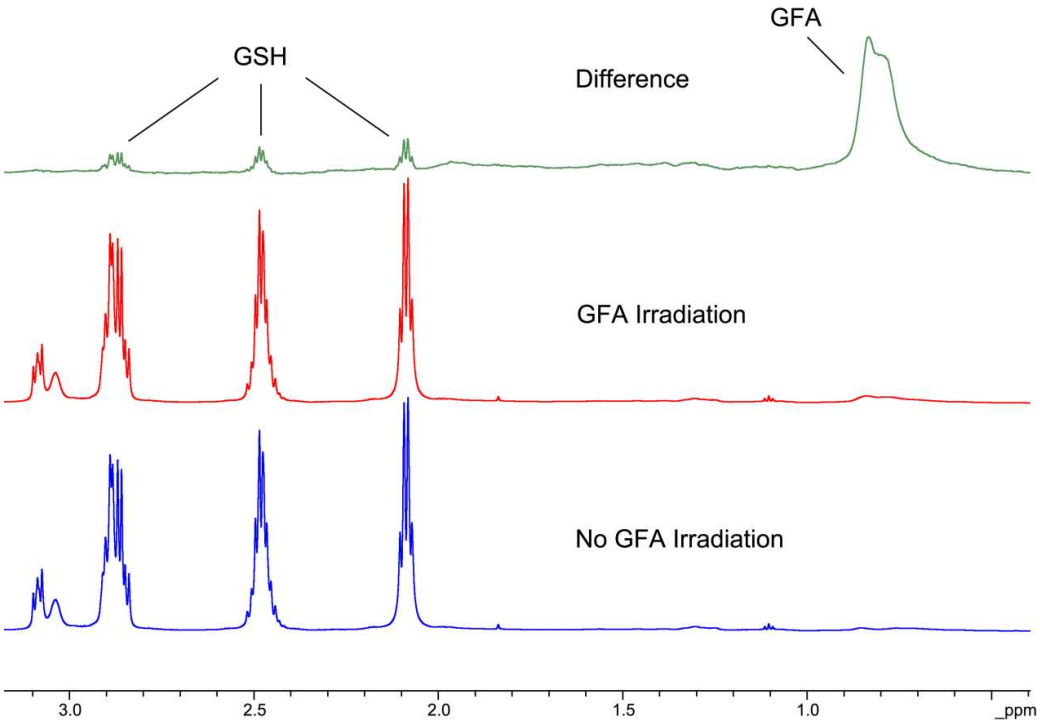

Figure 9.16 STD NMR spectra (700 MHz) of a sample containing GSH (13.3 mM) and His-tagged GFA (36 µM).

The spectrum revealed increased ^{1}H-resonance intensities for the GSH protons during GFA irradiation, indicating GSH binding. However, the large excess of

GSH in the sample relative to GFA may result in substantial non-specific binding with GFA. Therefore, the experiment was repeated with lower GSH concentration (500 µM) in the hope that binding may still be apparent under such conditions. Although the intensity of the GSH proton signals were significantly decreased in this STD spectrum, it was still possible to identify GSH binding. Therefore, this spectrum appeared to corroborate the findings from the previous STD spectra (Figure 9.17), i.e. that GSH binds to GFA.

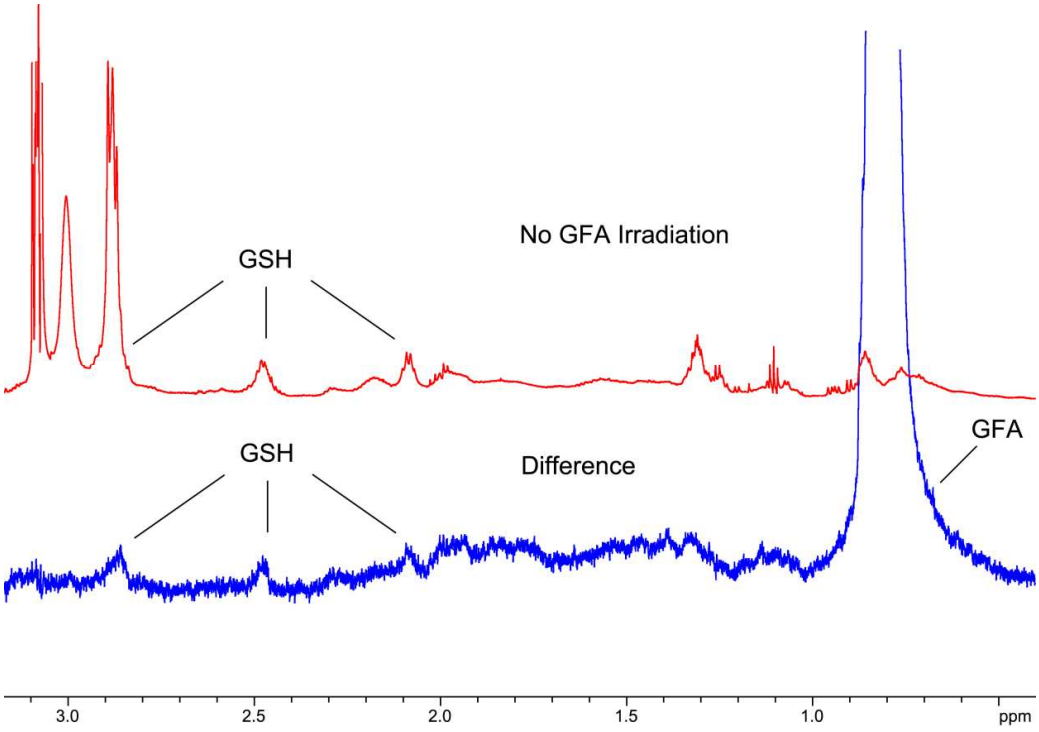

Figure 9.17 STD NMR spectra (700 MHz) of a sample containing GSH (500 µM) and His-tagged GFA (36 µM).

WaterLOGSY experiments were then carried out on samples containing His-Tag cleaved GFA (16 µM) and GSH at variable concentrations, which were subjected to experimentation using a 700 MHz NMR spectrometer. In the absence of protein, the waterLOGSY signal intensities for GSH appeared to increase (i.e. increase in negative intensity relative to the irradiated water resonance) in a linear fashion upon increasing GSH concentration. However, the intensities of the signals in the presence of enzyme were positive over small

GSH concentrations, indicating binding with GFA. Subtracting the intensities of the resonances in the presence of GFA from those in the absence of GFA produced a dose-response curve for GSH, which revealed a K_D of approximately 500 µM (Figure 9.18).

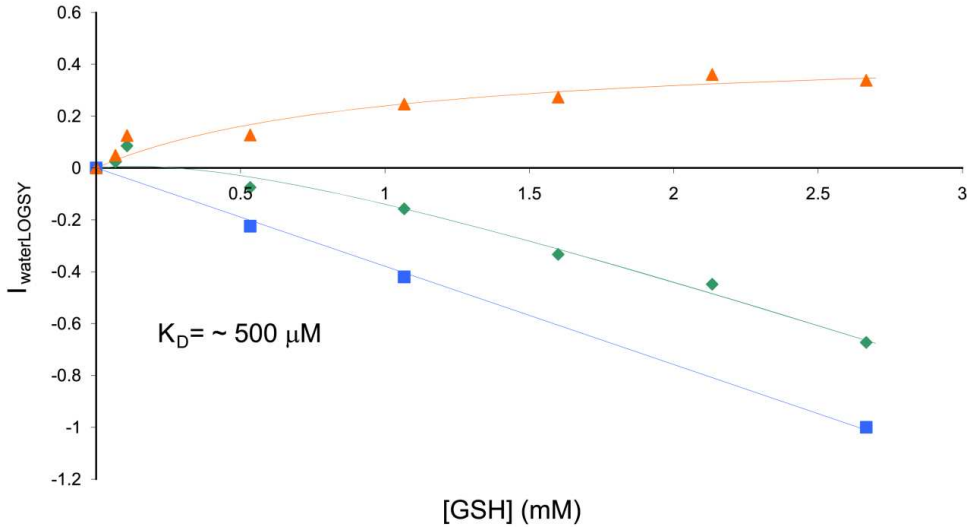

Figure 9.18 Plot of waterLOGSY intensities (for the β-glutamyl protons of GSH) versus GSH concentration. Blue = absence of GFA, Green = presence of GFA, Orange = difference. *Calculation of K_D was carried out by Ivanhoe Leung, using Origin software*.

However, it should be noted that analysis of binding by both STD and waterLOGSY is somewhat inconclusive due to the requirement for fast exchange between enzyme-bound and solution states of the ligand. This exchange is necessary to facilitate the transfer of magnetisation to the bulk ligand in solution, and consequently, the signals for a ligand with slow exchange kinetics (i.e. solution containing a strong protein binder) will not be accentuated. Therefore, it is difficult to predict the binding affinity of GSH to GFA using solely these experiments.[238]

b) Non-denaturing Mass Spectrometry

Having provided evidence for GSH binding to GFA by STD and waterLOGSY NMR, experiments were then carried out using non-denaturing mass spectrometry in order to investigate whether binding of GSH results in removal of zinc from the enzyme. His-Tag cleaved GFA (50 μM final concentration in 15 mM ammonium acetate buffer pH 7.5) was mixed with four equivalents of GSH, and the sample was analysed using a Q-TOF mass spectrometer (Figure 9.19).

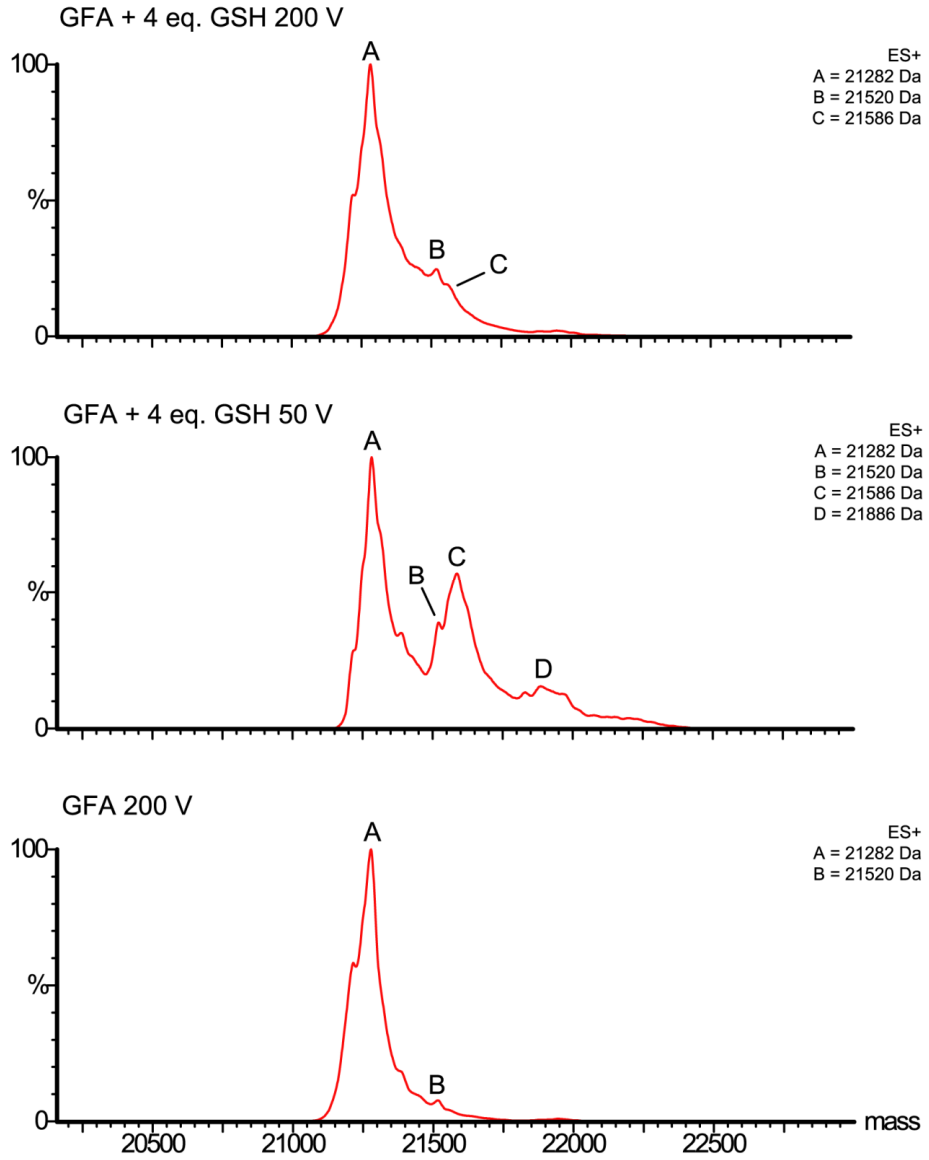

Figure 9.19 Deconvoluted mass spectra of GFA in the presence of GSH (four equivalents), under non-denaturing conditions.

Analysis of the sample at a cone voltage of 50 V revealed the emergence of two new peaks at 21586 and 21886 Da in the mass spectrum. These peaks are close to the expected masses of a GFA:GSH:Zn:Zn complex (21589 Da) and a GFA:GSH:GSH:Zn:Zn complex (21896 Da) respectively, and therefore, it was postulated that GSH was able to bind GFA at more than one position under the sample conditions. The intensities of the new peaks appeared to be lower when the sample was analysed at a sample cone voltage of 200 V, indicating that binding is relatively weak (i.e. non-covalent). Although a peak at 21520 Da could be observed in the spectra at 50 V and 200 V sample cone voltages, the presence of this peak in the control experiment (without added GSH) suggested that this species was not formed during the addition of GSH to the sample. Therefore, it appeared that addition of GSH to GFA does not induce removal of a zinc ion from the enzyme, at least under the conditions of the MS analyses.

Although the mass spectra indicated that zinc remains bound to the enzyme after addition of GSH, it was noted that the proposed reaction mechanism for HMG formation assumes that the catalytic zinc moves from the active site to another zinc binding site during the reaction (although no evidence for this second site is reported by X-ray crystallography). Therefore, it is possible that the lack of zinc removal observed in the mass spectra is due to zinc migration to another binding site. In order to probe this possibility, two samples were prepared containing one and five equivalents of zinc chloride respectively in the hope that the mass spectra of these mixtures would reveal additional binding sites for zinc. The mass spectrum of the first sample (one equivalent of zinc, Figure 9.20) revealed only one significant peak at a sample cone voltage of 200 V (at 21290 Da), which corresponded to the mass of GFA:Zn:Zn complex (expected mass of 21283 Da). In fact, the presence of added zinc in the mixture resulted in better resolution of this species relative to the sample without added zinc, indicating that partial removal of zinc from the enzyme (possibly as a consequence of the ionisation conditions) had been recovered via zinc addition. The lack of a peak

corresponding to the GFA:Zn:Zn:Zn complex, however, suggested that any additional zinc binding to GFA is relatively weak.

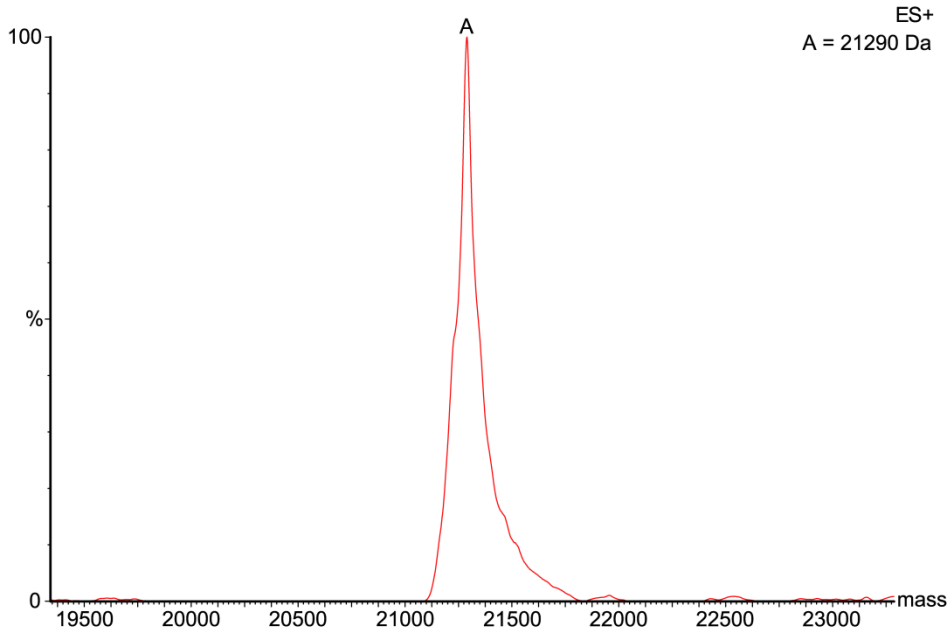

Figure 9.20 Deconvoluted mass spectrum of GFA in the presence of $ZnCl_2$ (one equivalent), under non-denaturing conditions (sample cone voltage = 200 V).

The addition of one equivalent of zinc to the sample containing GFA and four equivalents of GSH revealed identical peaks to the equivalent spectrum without zinc addition, implying that the presence of extra zinc in the sample does not affect binding of GSH to the enzyme (Figure 9.21).

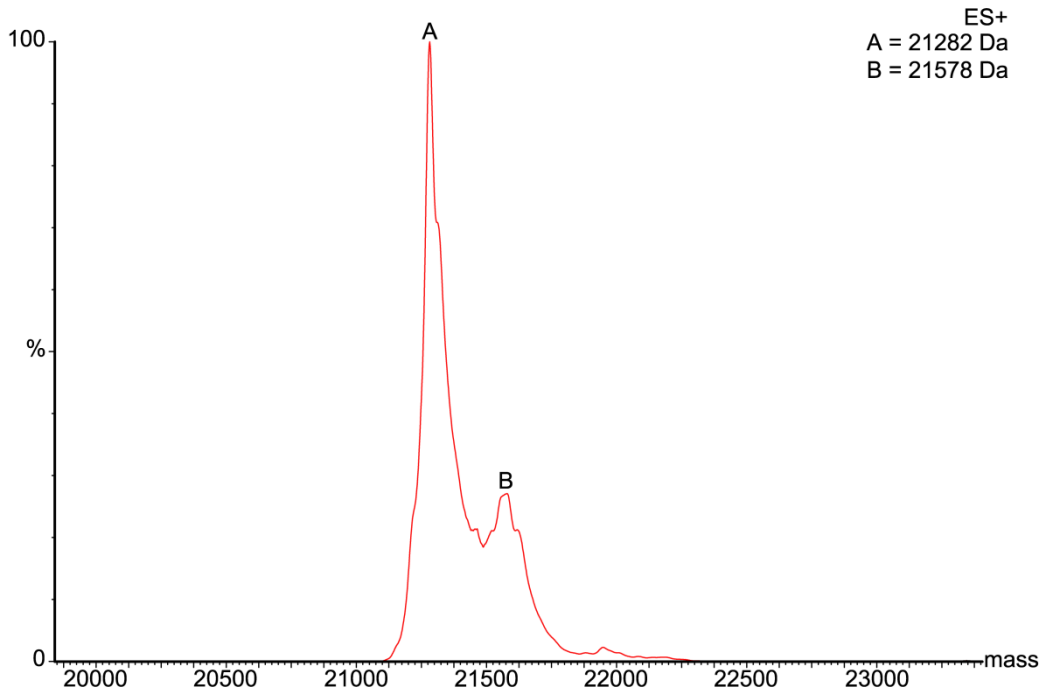

Figure 9.21 Deconvoluted mass spectrum of GFA in the presence of $ZnCl_2$ (one equivalent) and GSH (four equivalents), under non-denaturing conditions (sample cone voltage = 200 V).

Finally, the major peak in the sample containing five equivalents of added zinc (no GSH, Figure 9.22) possessed a mass of 21346 Da, which matched closely the expected mass of the GFA:Zn:Zn:Zn complex (21348 Da, assuming no deprotonation). This suggests at, under high zinc concentrations, another zinc ion can be accommodated within the GFA structure. However, it is unclear whether this observed binding indicates another catalytically important zinc binding site, or whether the binding of the extra zinc is non-specific.

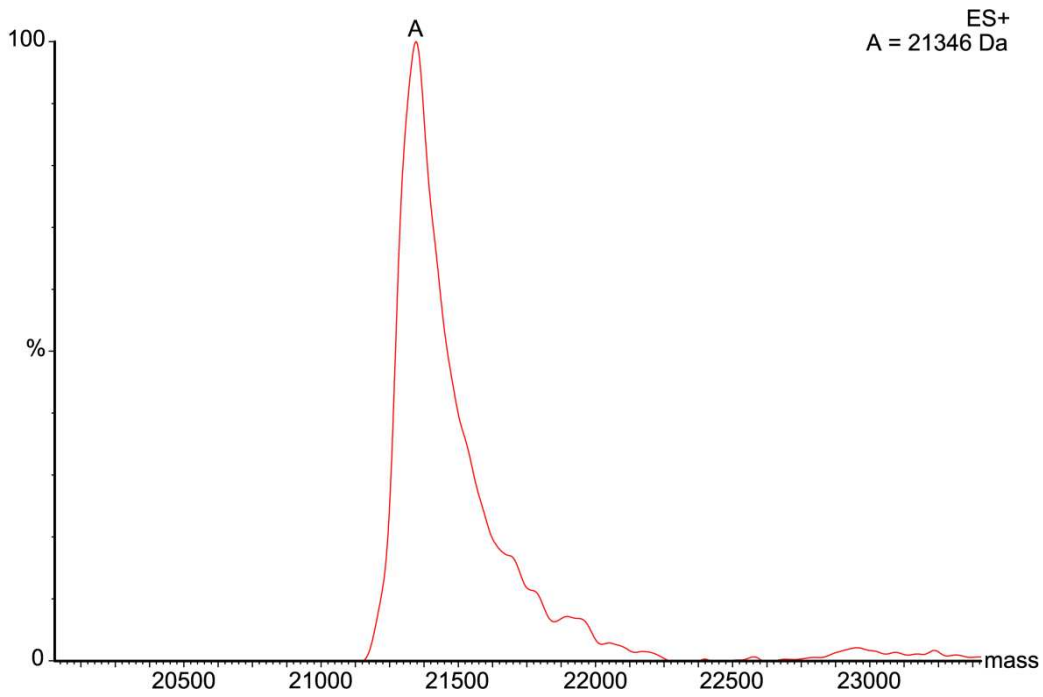

Figure 9.22 Deconvoluted mass spectrum of GFA in the presence of $ZnCl_2$ (five equivalents), under non-denaturing conditions (sample cone voltage = 200 V).

9.2.5 Probing the role of GSSG

Having confirmed that GSH can bind to GFA, experiments then focused upon identifying the role (if any) that the oxidised form of GSH, GSSG, adopts during catalysis. The previously proposed mechanism for GFA-catalysed HMG formation suggests that GSSG binding within the active site of the enzyme facilitates removal of the catalytic zinc, presumably via disulfide exchange with C55. Therefore, EXSY and binding experiments, it was hoped, would help to indicate whether GSSG is able to bind to, and also to accelerate the reactions of, GFA, thus revealing evidence for GSSG dependence.

a) EXSY Experiments on the GFA GSSG reaction

As GSSG is proposed to facilitate zinc removal (and therefore is likely a rate determining factor during GFA-catalysed HMG formation), it was proposed that the addition of GSSG to the reaction mixture containing GSH, HCHO and GFA would likely increase the exchange kinetics of the reaction at equilibrium.

Therefore, samples containing GSSG (13.3 mM), GSH (13.3 mM) and HCHO (13.3 mM) were incubated either in the presence or absence of GFA (16 µM), and the rate constants for HMG fragmentation (k_{-x}) were calculated using EXSY. Interestingly, no change in the rate constant was observed relative to the rate constant in the samples omitting GSSG (Section 9.2.3), suggesting that GSSG plays no role during HMG fragmentation. Also, a sample containing only GSSG (13.3 mM) and HCHO (one equivalent) was incubated with GFA (16 µM) in the expectation that disulfide exchange with the enzyme may facilitate release of GSH, thus allowing the GSH HCHO reaction to proceed. However, no evidence for GSH or HMG formation was observed after one hour at 25 °C, indicating that GSSG is not reduced by GFA.

b) Binding of GFA and GSSG

i) NMR

The binding propensity of GSSG to GFA was initially investigated using NMR. Firstly, an STD NMR spectrum was acquired on a sample containing GSSG (13.3 mM) and GFA (36 µM) using analogous methodology to that used for a sample containing GSH (Section 9.2.4a). Interestingly, the STD data implied binding of GSSG to GFA by revealing an accentuation of ^{1}H-resonance intensities for GSSG after protein irradiation. However, it was noted that non-specific binding of GSSG to the protein surface may also result in STD signals (as acknowledged in the case with GSH), and therefore, the experiment was repeated at lower GSSG concentration (500 µM). In this case, no ^{1}H-resonances corresponding to GSSG were evident in the difference spectrum, suggesting that binding of GSSG to GFA is weaker than GSH binding. These findings were corroborated by analysis using waterLOGSY NMR, which did not reveal any change in ^{1}H-signal intensities upon addition of GFA.

ii) Non-Denaturing Mass Spectrometry

The non-denaturing mass spectrum of a sample containing His-Tag cleaved GFA (50 μM) and four equivalents of GSSG revealed the formation of a peak at 21904 Da at low levels (with a sample cone voltage of 50V, Figure 9.23). This peak was assigned to a GFA:GSSG:Zn:Zn complex (expected mass 21875 Da, assuming no deprotonation), suggesting that GSSG is able to bind GFA (at least possibly in a non-specific manner), albeit weakly relative to GSH. Two other low level peaks in the mass spectrum at 50 V (at 21532 Da and 21678 Da) were assigned to a GFA:GSH:Zn complex and a GFA:GSH:Zn:Zn complex respectively. Therefore, it was apparent that reduction of GSSG to form GSH had occurred in the sample. This observation was not detected using EXSY experiments with GSSG (see above), however, which implied that reduction of GSSG was induced under the sample or mass spectrometry conditions. Also, the relative intensity of the peak at 21532 Da (representing the GFA:GSH:Zn complex) was not significantly greater than that in samples containing no added GSSG. Therefore, it was concluded that this species likely existed in solution before addition of GSSG. Finally, analysis of the sample at a cone voltage of 200 V resulted in the peaks at 21678 Da and 21904 Da decreasing in intensity, implying that these complexes are unstable under such conditions.

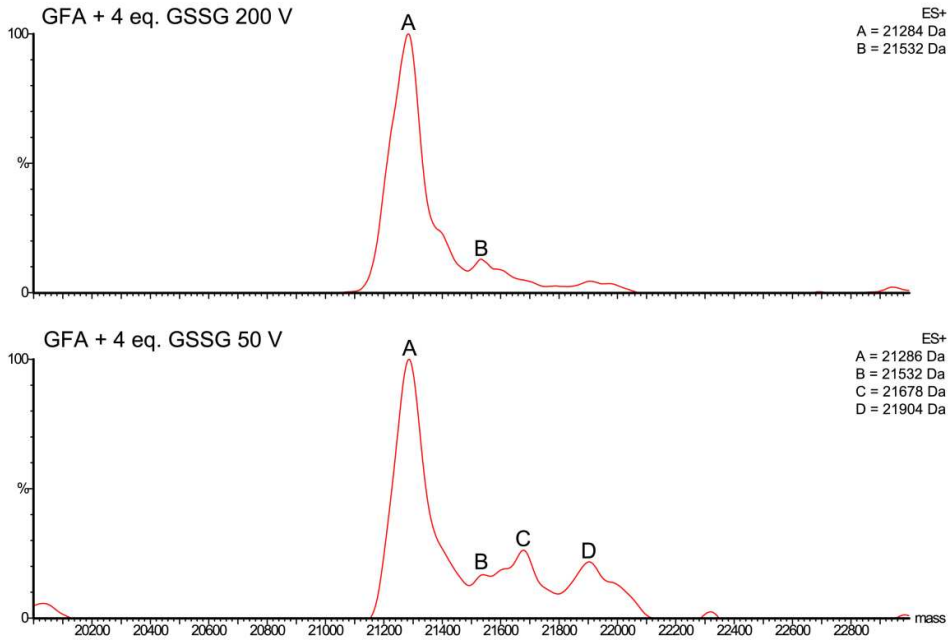

Figure 9.23 Deconvoluted mass spectra of GFA in the presence of GSSG (four equivalents), under non-denaturing conditions.

Overall, the NMR and mass spectrometry experiments indicate that GFA is unlikely to require GSSG for catalysis. This hypothesis is supported by the lack of increased reaction activities in the EXSY experiments upon addition of GSSG, and also by the observation that GFA is unable to catalyse formation of GSH from GSSG, at least under the NMR sample conditions. Also, no significant formation of the GFA:GSH:Zn complex (if any) was observed upon addition of GSSG using non-denaturing mass spectrometry, which implies that this species is not formed in high concentrations by disulfide exchange.

9.2.6 Probing Substrate Selectivity

In addition to the observed GFA-mediated acceleration of equilibrium dynamics for HMG formation and fragmentation, it was proposed that this enzyme may also catalyse similar reactions with other substrates. Therefore, experiments were carried out in order to investigate the specificity of GFA for GSH and HCHO, as described below.

a) GSH Analogues

Firstly, the selectivity of GFA for binding GSH was investigated by running waterLOGSY NMR experiments with a number of GSH analogues. For these studies, a constant concentration of substrate (533 µM) was selected, and the waterLOGSY signal intensities for the substrates were compared in the absence and presence of His-Tag cleaved GFA (16 µM). The results from these experiments are summarised in Table 9.3.

Table 9.3 Table showing the structures of the tested GSH analogues, and their respective binding propensities for GFA (as observed using waterLOGSY NMR).

Substrate Name	Substrate Structure	Evidence of GFA Binding
S-Methylglutathione	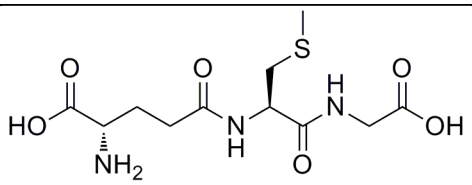	No
γ-Glutamylserinylglycine	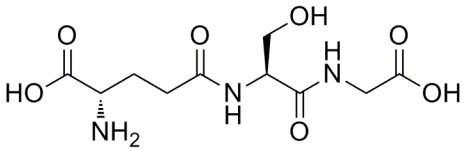	No
γ-Glutamyl-D-cysteinylglycine	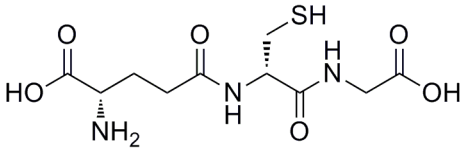	No
γ-Glutamylcysteine	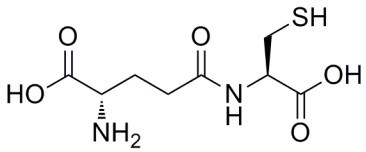	No
Cysteinylglycine	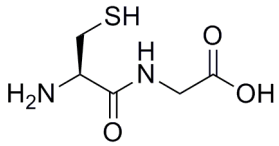	No
Cysteine	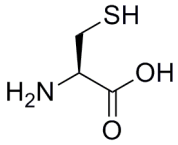	No
N-Acetylcysteine	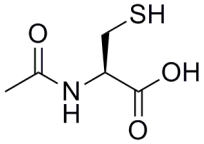	No
Cysteamine	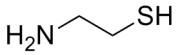	No
N-Acetylcysteamine	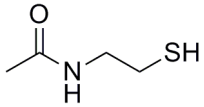	No

The observation that none of the tested GSH analogues bind GFA (at least by waterLOGSY analysis) implied that these species were unlikely to be substrates. In order to test this hypothesis, the thiol containing compounds (except cysteine and cysteamine, due to competing hemithioaminal formation reactions in solution) were incubated with one equivalent of HCHO (13.3 mM) and the reactions between the substrate and its hemithioacetal product were monitored at

equilibrium using 1D EXSY. In all cases, no acceleration of the hemithioacetal fragmentation (and therefore formation) was detected in the samples, suggesting that these reactions are not catalysed by GFA.

b) HCHO Analogues

NMR experiments were then carried out using GSH and other aldehydes. Samples were prepared containing GSH (13.3 mM) and the aldehydes acetaldehyde, propionaldehyde, caproaldehyde and 2,4-dihydroxybenzaldehyde (13.3 mM), and the reactions were monitored over initial stages (using ^{1}H NMR) and by 1D EXSY at equilibrium. The samples with the aliphatic aldehydes were buffered at pD 6.0, using 50 mM BisTris buffer, in order to allow detection of both *R* and *S* diastereomers of the hemithioacetals (at pD 7.5, the diastereomers were observed to be in fast exchange). With the exception of the sample containing 2,4-dihydroxybenzaldehyde (which did not react with GSH either in the absence or presence of GFA), all the other aldehydes were observed to reach equilibrium by the first NMR analysis.[232] These findings indicate that the dynamicity of the hemithioacetal/GSH exchange is sufficiently fast to allow rapid equilibration in the samples. This increased exchange was also inferred from the increased EXSY correlation relative to the samples with HCHO. In the case of acetaldehyde, the value for k_{-1} was calculated at 15 s^{-1}, which roughly equates to 75 times the value of k_{-1} in samples containing HCHO. Also, it was evident that the rate of exchange between GSH and the corresponding hemithioacetals was accelerated in samples containing GFA and the aliphatic aldehydes (Table 9.4). It was also possible to observe a slight preference for accelerating the fragmentation of one of the diastereomers in each sample, although overlap of the signals for the hemithioacetals and GSH impeded conclusive quantitative analysis.

Table 9.4 Table showing the structures of the tested aldehydes, and their respective activities with GFA.

Aldehyde Name	Aldehyde Structure	Evidence for GFA Catalysis
Acetaldehyde		Yes
Propionaldehyde	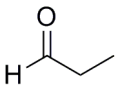	Yes
Caproaldehyde	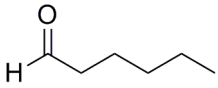	Yes
2,4-Dihydroxybenzaldehyde	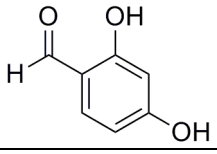	No

Finally, experiments were carried out investigating the reactivity of GFA with other substrates. Specifically, it was proposed that GFA may be able to facilitate the breakdown of HCHO derived hemithioaminals, hemiaminals, aminals and/or 1,3-dithianes (cf. hemithioacetal fragmentation of HMG), potentially enabling repair of protein and/or DNA cross-links. Preliminary studies were therefore attempted to probe the reactions of GSH and a series of small molecules containing such functionalities (Figure 9.24). No reactions were observed in the samples by ^{1}H NMR analysis, suggesting that GFA does not catalyse such reactions (at least on the small molecules tested). Also, no reactions were observed between GSH and the HCHO analogues dichloromethane, acetone and acetonitrile, implying that GFA is unable to promote nucleophilic attack on these species.

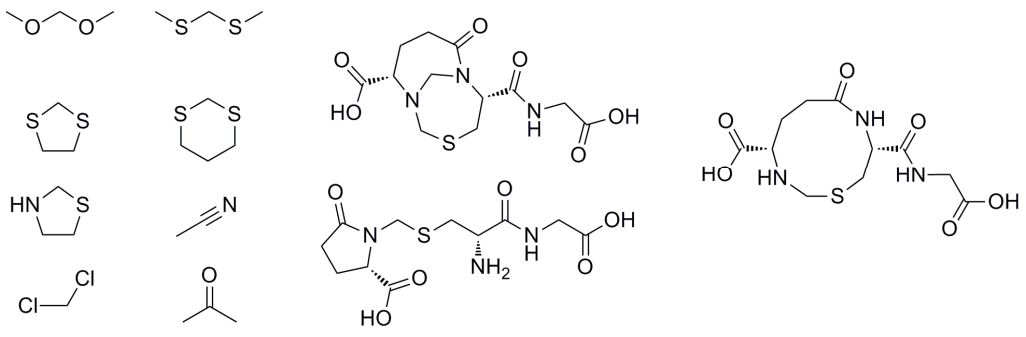

Figure 9.24 Structures of non-aldehydic HCHO analogues tested for activity with GFA.

Finally, it was hypothesised that GFA may catalyse the demethylation of *S*-methylglutathione, forming glutathione and (presumably) methanol as products. However, incubation of *S*-methylglutathione with GFA did not indicate any reaction.

9.3 Conclusions and Future Work

This Chapter describes experiments investigating a proposed GSH HCHO activating enzyme (GFA), which have revealed new insights into the activity and mechanism of GFA. Specifically, 1D and 2D EXSY experiments have indicated GFA catalysis of both HMG formation and fragmentation at equilibrium, corroborating previously reported data. EXSY analysis across a pD range has also suggested that GFA acts as a general catalyst during both the forward and backward reactions. Despite these findings, time course experiments using ^{1}H NMR did not reveal any acceleration of HMG formation over initial stages of reaction, indicating that the availability of aldehydic HCHO may be limiting in aqueous solution. Binding experiments using NMR and mass spectrometry techniques indicate that GSH binds to GFA in a specific manner. However, binding of GSSG, which is proposed to be essential for GFA catalysis, was observed to be weaker than binding of GSH and does not appear to result in significant ejection of zinc from the protein. No reaction of GSSG with GFA was observed by NMR, nor was the rate of HMG formation accelerated upon addition of GSSG, thus suggesting that GSSG is not essential for GFA activity. Experiments with GSH analogues suggest that GFA is selective for GSH; however, GFA was observed to increase the dynamicity of the reactions between GSH and three other aliphatic aldehydes. These findings may indicate that GFA is able to catalyse reactions between GSH and a number of cellular aldehydes/electrophiles, thus implying that GFA is involved in the metabolism of aldehydes other than HCHO *in vivo*.

Although these studies give good evidence against the proposed redox zinc mechanism, further experimentation is required (such as X-ray crystallography, protein NMR and site-specific mutagenesis studies) in order to confirm the stability of zinc binding. Also,

the fact that GFA may be able to catalyse a multitude of reactions with GSH indicates that further analyses on GFA specificity should be undertaken. Regarding the role of GFA in cells, investigations on the human homologue, CENP-V, have suggested that this protein is essential for cell stability. However, studies with the homologue from *Rhodobacter sphaeroides* have discredited a role in HCHO metabolism, and therefore, the manner in which this protein maintains cell homeostasis is currently unknown. Any future analysis of cellular function might be better studied on CENP-V; however, initial characterisation of this protein *in vitro* would likely be necessary before detailed cellular work could be carried out. Finally, it is noted that, given the reaction of GSH and HCHO is known to produce a number of products under varying conditions, it is possible that the function of GFA may vary depending upon the cellular environment. It is likely that cell nuclei possess efficient mechanisms for removing HCHO derived cross-links, which may be formed more readily when GSH concentrations are lowered, or when the cell environment is basic. Therefore, it is possible that GFA is involved in either promoting the formation of HMG under such disfavourable conditions, or in repairing HCHO induced damage to cellular macromolecules. Both of these hypotheses warrant further investigation.

Chapter 10

Materials and Methods

10.1 Microbiological Techniques

All techniques were carried out under sterilised conditions. Before use, all instruments and pipettes were sterilised in TouchClave® II autoclave (LTE Scientific) at 121 °C for 20 min or by γ-irradiation.

10.1.1 Plasmids

The JMJD2A variants (Chapter 5) were expressed from constructs encoding residues 1-359, cloned into pNIC28-Bsa4. GFA (Chapter 9) was expressed from a construct encoding residues 1-196, cloned into pET16b (*provided by Dr. Stefan Becker*). The plasmids were transformed into a phage-resistant derivative of *E. Coli* BL21 (DE3) carrying the pRARE2 plasmid (supplying tRNA for rare codons).

10.1.2 Incubations

Bacterial plate cultures were grown at 37 °C overnight in a Hereus® TypB 6030 incubator (Thermo Fisher Scientific). Cultures were incubated in a New Brunswick Scientific G25 environmental shaker at 200 rpm.

10.1.3 2TY Growth Medium

2TY growth medium was prepared as described in Table 10.1. All media was sterilised using an autoclave prior to growth.

Table 10.1 Table showing composition of 2TY growth medium.

Component	Concentration (g/L)
Tryptone	16
Yeast Extract	10
Sodium Chloride	5

10.1.4 Starter Cultures

Starter cultures were grown in 5 mL (in 50 mL Falcon tubes) or 100 mL (in 500 mL Duran® flasks, Schott UK) of 2TY medium (containing the appropriate antibiotics), inoculated from a single colony on an agar plate or from a glycerol freeze, at 37 °C overnight.

10.1.5 Large-Scale Growths

Large-scale growths were grown in 600 mL of 2TY medium (in 2000 mL PYREX® narrow-mouth graduated Erlenmeyer flasks), which was supplemented with either 50 µg/mL kanamycin (for cultures of the JMJD2A variants) or 50 µg/mL ampicillin (for cultures of GFA). After preincubation at 37 °C for 30 min, the flasks we inoculated with 5 mL of the bacterial starter culture and grown at 37 °C until they reached the appropriate OD_{600} (optical densities were read in 1 mL cuvettes against a reference sample of the growth media using a Novaspec® II spectrophotometer (Pharmacia). Then, the incubation temperature was reduced to 18 °C and each flask was induced with isopropyl-β-D-1-thiogalactopyranoside (IPTG, 500 µM final concentration). The flasks were then incubated overnight at 18 °C, after which, the cells were isolated by centrifugation and frozen in sealable plastic bag at -80 °C.

10.1.6 Protein Extraction

After thawing, the cells were resuspended in lysis buffer containing DNAse I (0.2 mg, Table 10.3) and subjected to sonication at 0 °C (5 × 45 sec with 2 min breaks, using a Vibra Cell VCX 500 sonicator with a 13 mm probe). After lysis, the lysate was centrifuged (23000 rpm for 20 min) and the supernatant was filtered through a 0.2 µm

sterile filter (Millipore) before being loaded onto a 5 mL HisTrap FF^{TM} nickel affinity column (Section 10.2.3).

10.2 Protein Preparation and Purification

10.2.1 TEV Cleavage

Before treatment with TEV protease, GFA was buffer-exchanged into 4 mL of 50 mM tris buffer pH 7.5 (at roughly 1 mM) using Amicon® Ultra centrifugal filters. Then, 5 µL of 10 units µL^{-1} AcTEV® (Invitrogen) was added to the protein sample, and the mixture was left at 4 °C for 12 hours. The TEV protease and remaining His-Tagged impurities were removed by loading the sample onto a HisTrap FF^{TM} nickel affinity column. The column was then washed with wash buffer (Table 10.2) by syringe, and the resultant flow-through was collected, buffer-exchanged into 50 mM tris buffer pH 7.5, and concentrated to 5 mg ml^{-1}. The column was then washed of His-Tagged protein by flushing with affinity chromatography elution buffer (Table 10.4).

Table 10.2 Table showing composition of wash buffer used during purification after TEV cleavage.

Component	Concentration
HEPES	50 mM
Sodium Chloride	500 mM
Imidazole	60 mM

10.2.2 General Fast Protein Chromatography (FPLC) Protocol

FPLC for the purification of proteins was carried out at 4 °C using Äkta^{TM} FPLC systems (GE Healthcare). Samples were loaded from measuring cylinders using the FPLC pump, and elution of the proteins was monitored by UV absorbance at 280 nm, using a UPC-900 monitor. Sample fractions were collected using a Frac-920 fraction collector and the purity of the proteins in each fraction was determined using SDS-PAGE analysis. All buffers used during purification were prepared in Milli-Q water and

filtered through a 0.2 µm filter before use. All columns were cleaned after use according to the manufacturers' instructions.

10.2.3 Affinity Chromatography

Affinity chromatography of the recombinant proteins was achieved using a HisTrap FF™ nickel affinity column. Before use, the column was pre-charged with 3 column volumes (CV) of $NiSO_4$, washed with 5 CVs of water and then primed with 3 CVs of loading buffer. The filtered lysate was then loaded onto the column at 1 mL/min using the FPLC pump. The protein was then eluted in a gradient of 0 - 100 % elution buffer (Table 10.4). Fractions from the purification were collected in 2.5 mL vials, and the protein-containing fractions were combined, concentrated and buffer-exchanged using Amicon® Ultra centrifugal filters.

Table 10.3 Table showing composition of lysis/affinity chromatography loading buffer.

Component	Concentration
HEPES	50 mM
Sodium Chloride	500 mM
Imidazole	20 mM
Glycerol	5 %

Table 10.4 Table showing composition of affinity chromatography elution buffer.

Component	Concentration
HEPES	50 mM
Sodium Chloride	500 mM
Imidazole	520 mM
Glycerol	5 %

10.2.4 Size-Exclusion Chromatography

After affinity chromatography, samples of GFA were further purified by preparative size-exclusion chromatography using a 300 mL Superdex™ 75 column (GE Healthcare). After equilibration with 1 CV of 50 mM tris buffer pH 7.5, the column was loaded with the protein (also in 50 mM tris buffer pH 7.5) at 3 mL/min using a Superloop™ (GE Healthcare). Purification was achieved by elution with 1 CV of 50

mM tris buffer pH 7.5, after which, the protein-containing fractions were combined and concentrated.

10.2.5 SDS-PAGE Analysis

SDS-PAGE gels were set from liquid stocks of SDS-PAGE separating and stacking/loading solutions (Tables 10.5 and 10.6 respectively), which were poured into glass templates (separating gel first, followed by stacking/loading gel) and allowed to solidify. Protein samples (5 µL) were mixed with 5 µL of loading buffer and denatured by heating for 2 min at 110 °C. After loading the protein onto the gel, separation was induced by exerting a constant potential of 200 V, using a Bio-Rad Mini Protean II system. The gel was then stained in Coomassie® Brilliant Blue (Imperial Chemical Industries) for 30 min.

Table 10.5 Table showing composition of SDS-PAGE separating gel.

Component	Amount
Milli-Q water	3.14 mL
Tris.HCl (pH 8.8) 1.5 M	2.5 mL
Acrylamide 30 %	4.16 mL
SDS 1- %	100 µL
Ammonium persulfate 100 mg/mL	100 µL
TEMED	8 µL

Table 10.6 Table showing composition of SDS-PAGE stacking/loading gel.

Component	Amount
Milli-Q water	3.14 mL
Tris.HCl (pH 6.8) 0.5 M	1.25 mL
Acrylamide 30 %	0.5 mL
SDS 1- %	50 µL
Ammonium persulfate 100 mg/mL	50 µL
TEMED	5 µL

10.2.6 Protein Concentration Determination

Protein concentrations were determined by measuring A_{280} in each sample using an ND-1000 Nanodrop spectrophotometer (Thermo Scientific). Extinction coefficients were calculated using an internet-based protein calculator (http://arraygenetics.com).

10.3 Synthesis of Lysine Analogues

10.3.1 Generalities

Reactions were carried out in dry round-bottomed flasks with magnetic stirring in a fume-hood. Thin layer chromatography (TLC) was performed using Merck aluminium foil backed plates precoated with Kieselgel 60 F254. Visualisation of species on the plates was achieved using UV fluorescence (254 nm) or by staining with potassium permanganate stain. NMR experiments were recorded on either a Bruker AVANCE AV400 or a Bruker AVII500 spectrometer. NMR spectra were referenced to the solvent peak using the Bruker internal referencing procedure (edlock). Coupling constants (*J*) are reported to the nearest 0.5 Hz. The following abbreviations are used to describe multiplicities; s = singlet, d = doublet, t = triplet, m = multiplet, dd = double doublet, br s = broad singlet, app t = apparent triplet. High-resolution mass spectra were recorded on Micromass GCT spectrometers. Infrared spectra were recorded as solids using a Bruker Tensor 27 instrument. Absorptions are given in wavenumbers (cm^{-1}). Only peaks of interest are reported. Melting points were carried out using Griffin apparatus and were uncorrected. $[\alpha]_D$ values were collected using a Bellingham and Stanley ADP220 polarimeter. Characterisation of the lysine analogues is reported from samples at over 80 % purity, although partial deprotection of the Fmoc group was detected in some cases during workup. Removal of residual solvent and acetaldehyde from the reaction mixtures was impeded in some cases, despite extensive drying under high vacuum; however, NMR characterisation was not impeded. Numbering for the aromatic carbon atoms is shown in Figure 10.1.

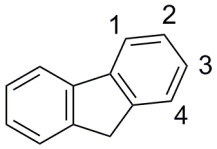

Figure 10.1 Numbering for the Fmoc carbons.

Fmoc-Lys(Boc)-OH and Fmoc-Lys(formyl)-OH were purchased from Bachem. Fmoc-Lys(Me,Boc)-OH was purchased from GM Biochem (Shanghai) Ltd. All other reagents were purchased from Aldrich. All solvents were purchased from either Aldrich or Rathburn Chemicals.

10.3.2 Characterisation of Lysine Analogues

a) Fmoc-Lys($^{13}CH_3)_2$)-OH

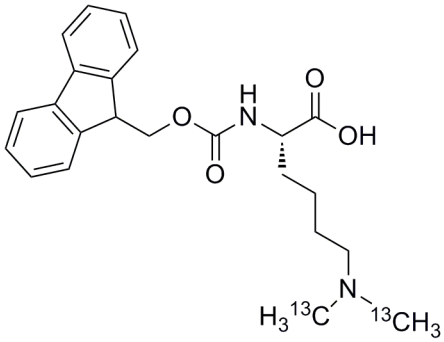

Synthesis was achieved via an optimised literature procedure.[169] Fmoc-Lys(Boc)-OH (2.06 g, 4.39 mmol) was dissolved in 20 mL formic acid and stirred for 3 hours. The solvent was then removed *in vacuo*. Trituration in diethyl ether yielded Fmoc-Lys-OH formate salt as a white solid (1.81 g, 4.37 mmol, 99 %). A sample of this material was then used in crude form in the next step. 20 % aqueous ^{13}C-HCHO (1 mL, 6 eq.) was added to a stirred solution of Fmoc-Lys-OH formate salt (560 mg, 1.35 mmol) in methanol at room temperature. The reaction mixture was then cooled to 0 °C in an ice bath. $NaBH_3CN$ (179 mg, 2.1 eq.) was dissolved in 2 mL of methanol and added dropwise to the reaction over 10 min. After warming to room temperature, the mixture was then stirred for 2 hours. After reaction completion, glacial acetic acid was added dropwise until the solution was neutralised and the solvent was removed *in vacuo*. The product was then redissolved in dry acetone. Filtration of the solution followed by removal of the solvent *in vacuo* yielded the product as a white solid (460 mg, 88 %), which was deemed sufficiently pure for SPPS. Comparison of crude ^{1}H NMR and IR spectra with those of an authentic sample of non-labelled Fmoc-Lys(Me_2)-OH (GL Biochem (Shanghai) Ltd.) revealed resonances consistent with formation of the product. HRMS (ESI+) m/z calcd for $C_{21}{}^{13}C_2H_{29}N_2O_4$ $(M+H)^+$: 399.2189. Found 399.2195. The ^{1}H NMR spectrum of the ^{13}C-labelled

peptide (after incorporation of the product) possessed identical resonances to the non-labelled peptide (except those from the N^{ε}-methyl groups), thus confirming formation of the correct species.

b) Fmoc-Lys(MeEt)-OH

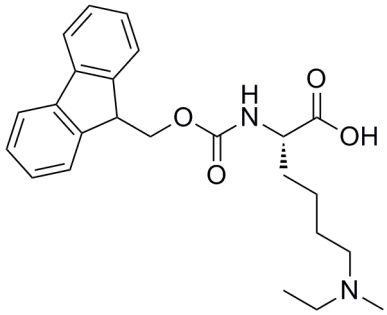

Fmoc-Lys(Me,Boc)-OH (1.00 g, 2.13 mmol) was dissolved in trifluoroacetic acid (10 mL) containing triisopropylsilane (0.48 mL, 1.1 eq.) and the solution was left stirring at room temperature for 1 hour. The solvent was then removed *in vacuo* and the resulting product was then redissolved in 20 mL of ethanol. Acetaldehyde (70 µL, 5 eq.) and $NaBH_3CN$ (147 mg, 1.1 eq.) were added and the mixture was left for 3 hours at room temperature. Then, 1 drop of concentrated HCl was added and the solvent was removed *in vacuo*. The product was extracted into dry acetone and the remaining precipitate was removed by filtration. Removal of solvent after reacidification with HCl *in vacuo* and subsequent trituration in diethyl ether afforded the product as a white solid (430 mg, 49 %). mp 84 °C; $[\alpha]^{25}_{D}$ +20 (c = 0.01 g mL^{-1}, MeOH); IR ν_{max} 1676, 1449, 1203; ^{1}H NMR (400 MHz, DMSO-d_6) δ(ppm) 1.12 (t, *J* = 7.0 Hz, 3H, $NCH_2C\underline{\underline{H}}_3$), 1.24-1.36 (m, 2H, γ-lys), 1.47-1.78 (m, 4H, β-lys, δ-lys), 2.52 (s, 3H, $NC\underline{H}_3$), 2.71-2.82 (m, 2H, ε-lys), 2.82-2.92 (m, 2H, $NC\underline{\underline{H}}_2CH_3$), 3.85 (m 1H, α-lys), 4.18-4.29 (m, 3H, $OC\underline{\underline{H}}_2CH$, $OCH_2C\underline{\underline{H}}$), 7.17 (d, *J* = 7.5 Hz, 1H, $N\underline{\underline{H}}CHCOOH$), 7.34 (t, *J* = 7.5 Hz, 2H, 2×Fmoc$C_2\underline{H}$), 7.41 (t, *J* = 7.5 Hz, 2H, 2×Fmoc$C_3\underline{H}$), 7.68-7.74 (m, 2H, 2×Fmoc$C_1\underline{H}$), 7.88 (d, *J* = 7.5 Hz, 2H, 2×Fmoc$C_4\underline{H}$); ^{13}C NMR (101 MHz, DMSO-d_6) δ(ppm) 9.8 ($NCH_2\underline{\underline{C}}H_3$), 23.2 (γ-lys), 24.2 (δ-lys), 31.4 (β-lys), 39.7 ($N\underline{\underline{C}}H_3$), 46.9 ($OCH_2\underline{\underline{C}}H$), 50.2 ($N\underline{\underline{C}}H_2CH_3$), 54.7 (α-Lys), 54.8 (ε-lys), 65.8 ($O\underline{\underline{C}}H_2CH$), 120.6 (Fmoc$\underline{C}_4H$), 125.6 (Fmoc$\underline{C}_1H$), 127.4 (Fmoc$\underline{C}_2H$), 128.0 (Fmoc$\underline{C}_3H$), 141.6 (Ar$\underline{C}$), 144.7 (Ar$\underline{C}$), 156.7 (NH$\underline{C}$OO), 175.5 ($\underline{C}$OOH), HMBC correlation observed between the $NC\underline{\underline{H}}_2CH_3$ protons and the ε-lysyl

carbon; HRMS (ESI+) m/z calcd for $C_{24}H_{31}N_2O_4$ $(M+H)^+$: 411.2278. Found 411.2275.

c) Fmoc-Lys(Et_2)-OH hydrochloride

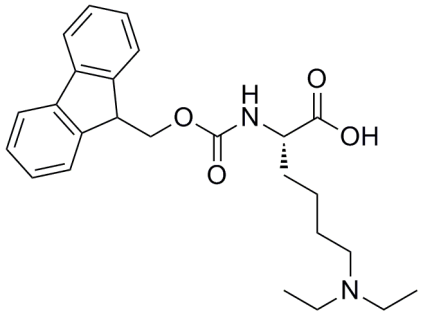

Fmoc-Lys-OH.HCl (500 mg, 1.23 mmol) and acetaldehyde (0.14 mL, 5 eq.) were mixed in 20 mL of ethanol, before $NaBH_3CN$ (163 mg, 2.1 eq.) was added portion-wise. The reaction was then left for 2 hours, after which, 1 drop of concentrated HCl was added to the mixture and the solvent was removed *in vacuo*. The product was extracted into dry acetone and the remaining precipitate was removed by filtration. Removal of solvent after reacidification with HCl *in vacuo* and subsequent trituration in diethyl ether afforded the product (as a hydrochloride) as a white solid (470 mg, 83 %). mp 106 °C; $[\alpha]^{25}_D$ +30 (c = 0.01 g mL^{-1}, MeOH); IR ν_{max} 1709, 1448; ^{1}H NMR (400 MHz, DMSO-d_6) δ(ppm) 1.19 (t, *J* = 7.0 Hz, 6H, $NCH_2C\underline{H_3}$), 1.30-1.40 (m, 2H, γ-lys), 1.54-1.81 (m, 4H, β-lys, δ-lys), 2.91-3.00 (m, 2H, ε-lys), 3.00-3.12 (m, 4H, $NC\underline{H_2}CH_3$), 3.94 (m, 1H, α-lys), 4.18-4.32 (m, 3H, $OC\underline{H_2}CH$, $OCH_2C\underline{H}$), 7.33 (t, *J* = 7.5 Hz, 2H, 2×Fmoc$C_2\underline{H}$), 7.42 (t, *J* = 7.5 Hz, 2H, 2×Fmoc$C_3\underline{H}$), 7.66 (d, *J* = 8.0 Hz, 1H, $N\underline{H}CHCOOH$), 7.73 (dd, J_1 = 3.0 Hz, J_2 = 7.5 Hz, 2H, 2×Fmoc$C_1\underline{H}$), 7.90 (d, *J* = 7.5 Hz, 2H, 2×Fmoc$C_4\underline{H}$), 10.22 (br s, 1H, $CH_2N\underline{H}(CH_2CH_3)_2$); ^{13}C NMR (101 MHz, DMSO-d_6) δ(ppm) 8.7 ($N(CH_2\underline{C}H_3)_2$), 22.7 (δ-lys), 23.2 (γ-lys), 30.8 (β-lys), 46.2 ($N(\underline{C}H_2CH_3)_2$), 46.9 ($OCH_2\underline{C}H$), 50.5 (ε-lys), 54.2 (α-Lys), 65.9 ($O\underline{C}H_2CH$), 120.4 (Fmoc$\underline{C}_4H$), 125.7 (Fmoc$\underline{C}_1H$), 127.4 (Fmoc$\underline{C}_2H$), 127.9 (Fmoc$\underline{C}_3H$), 141.6 (Ar$\underline{C}$), 144.7 (Ar$\underline{C}$), 157.1 (NH$\underline{C}$OO), 175.1 ($\underline{C}$OOH), HMBC correlation observed between the $N(C\underline{H_2}CH_3)$ protons and the ε-lysyl carbon; HRMS (ESI+) m/z calcd for $C_{25}H_{33}N_2O_4$ $(M+H)^+$: 425.2435. Found 425.2436.

d) Fmoc-Lys(iPr)-OH hydrochloride

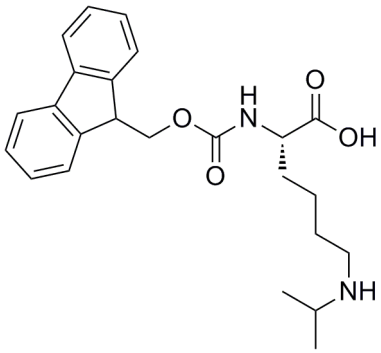

Fmoc-Lys-OH.HCl (1.00 g, 2.46 mmol) was dissolved in 20 mL of ethanol, before 1 mL of acetone was added. $NaBH_3CN$ (170 mg, 2.2 eq.) was then added portion-wise to the mixture and the reaction was left at room temperature. After 2 hours, 1 drop of concentrated HCl was added to the mixture and the solvent was removed *in vacuo*. The product was then extracted into dry acetone and the remaining precipitate was removed by filtration. Removal of solvent after reacidification with HCl *in vacuo* and subsequent trituration in diethyl ether afforded the product (as a hydrochloride) as a white solid (900 mg, 82 %). mp 95 °C; $[\alpha]^{25}_D$ +34 (c = 0.01 g mL^{-1}, MeOH); IR ν_{max} 1693, 1449, 1208; ^{1}H NMR (400 MHz, DMSO-d_6) δ(ppm) 1.22 (d, *J* = 6.5 Hz, 6H, NCH(C*H*$_3$)$_2$), 1.31-1.44 (m, 2H, γ-lys), 1.54-1.78 (m, 4H, β-lys, δ-lys), 2.77-2.88 (m, 2H, ε-lys), 3.23 (m, 1H, NC*H*(CH$_3$)$_2$), 3.94 (m, 1H, α-lys), 4.18-4.32 (m, 3H, OC*H*$_2$CH, OCH$_2$C*H*), 7.33 (t, *J* = 7.5 Hz, 2H, 2×FmocC$_2$H), 7.42 (t, *J* = 7.5 Hz, 2H, 2×FmocC$_3$H), 7.67 (d, *J* = 8.0 Hz, 1H, N*H*CHCOOH), 7.73 (dd, J_1 = 3.0 Hz, J_2 = 7.5 Hz, 2H, 2×FmocC$_1$H), 7.89 (d, *J* = 7.5 Hz, 2H, 2×FmocC$_4$H), 8.79 (br s, 2H, CH$_2$N*H*CH(CH$_3$)$_2$); ^{13}C NMR (101 MHz, DMSO-d_6) δ(ppm) 18.9 (NCH(*C*H$_3$)$_2$), 23.1 (γ-lys), 25.5 (δ-lys), 30.6 (β-lys), 43.8 (ε-lys), 46.9 (OCH$_2$*C*H), 49.6 (N*C*H(CH$_3$)$_2$), 53.9 (α-lys), 65.9 (O*C*H$_2$CH), 120.4 (FmocC$_4$H), 125.6 (FmocC$_1$H), 127.3 (FmocC$_2$H), 128.0 (FmocC$_3$H), 141.6 (ArC), 144.7 (ArC), 157.1 (NHCOO), 175.1 (COOH), HMBC correlation observed between the NC*H*(CH$_3$)$_2$ protons and the ε-lysyl carbon; HRMS (ESI+) m/z calcd for $C_{24}H_{31}N_2O_4$ $(M+H)^+$: 411.2278. Found 411.2272.

e) Fmoc-Lys(MeiPr)-OH

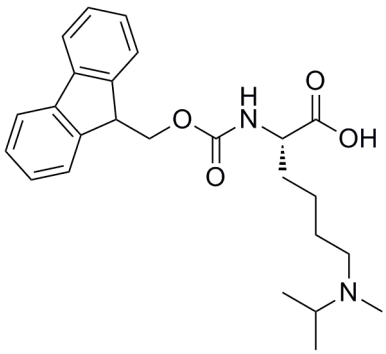

Fmoc-Lys(Me,Boc)-OH (1.00 mg, 2.13 mmol) was dissolved in trifluoroacetic acid (10 mL) containing triisopropylsilane (0.48 mL, 1.1 eq.) and the solution was left stirring at room temperature for 1 hour. The solvent was then removed *in vacuo* and the resulting product was then redissolved in 20 mL of ethanol. Acetaldehyde (0.07 mL, 5 eq.) and $NaBH_3CN$ (147 mg, 1.1 eq.) were added and the mixture was left for 3 hours at room temperature. Then, 1 drop of concentrated HCl was added and the solvent was removed *in vacuo*. The product was extracted into dry acetone and the remaining precipitate was removed by filtration. Removal of solvent after reacidification with HCl *in vacuo* and subsequent trituration in diethyl ether afforded the product as a white solid (609 mg, 67 %). mp 90 °C; $[\alpha]^{25}_{D}$ +22 (c = 0.01 g mL^{-1}, MeOH); IR ν_{max} 1681, 1602, 1206; ^{1}H NMR (400 MHz, DMSO-d_6) δ(ppm) 1.10 (d, *J* = 7.5 Hz, 6H, NCH(C*H*$_3$)$_2$), 1.24-1.32 (m, 2H, γ-lys), 1.49-1.80 (m, 4H, β-lys, δ-lys), 2.41 (s, 3H, NCH$_3$), 2.64-2.77 (m, 2H, ε-lys), 3.23 (m, 1H, NC*H*(CH$_3$)$_2$), 3.75 (m 1H, α-lys), 4.17-4.33 (m, 3H, OC*H*$_2$CH, OCH$_2$C*H*), 6.87 (d, *J* = 7.5 Hz, 1H, N*H*CHCOOH), 7.33 (t, *J* = 7.5 Hz, 2H, 2×FmocC$_2$H), 7.41 (t, *J* = 7.5 Hz, 2H, 2×FmocC$_3$H), 7.65-7.72 (m, 2H, 2×FmocC$_1$H), 7.88 (d, *J* = 7.5 Hz, 2H, 2×FmocC$_4$H); ^{13}C NMR (101 MHz, DMSO-d_6) δ(ppm) 16.7 (NCH(*C*H$_3$)$_2$), 23.2 (γ-lys), 24.8 (δ-lys), 31.4 (β-lys), 35.8 (N*C*H$_3$), 47.0 (OCH$_2$*C*H), 52.4 (ε-lys), 54.8 (N*C*H(CH$_3$)$_2$), 55.4 (α-Lys), 65.6 (O*C*H$_2$CH), 120.3 (Fmoc*C*$_4$H), 125.6 (Fmoc*C*$_1$H), 127.3 (Fmoc*C*$_2$H), 127.7 (Fmoc*C*$_3$H), 141.6 (Ar*C*), 144.8 (Ar*C*), 156.5 (NH*C*OO), 175.9 (*C*OOH), HMBC correlation observed between the NC*H*(CH$_3$)$_2$ protons and the ε-lysyl carbon; HRMS (ESI+) m/z calcd for $C_{24}H_{31}N_2O_4$ $(M+H)^+$: 425.2435. Found 425.2432.

f) Fmoc-Orn(Me_2)-OH hydrochloride

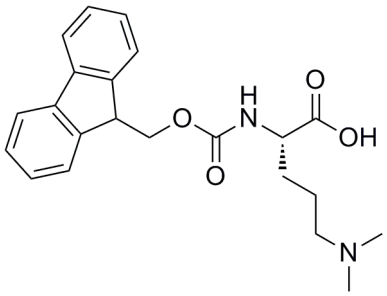

0.5 mL of aqueous HCHO (37 % in H_2O, 6 eq.) was added to a ethanolic solution of Fmoc-Orn-OH.HCl (500 mg, 1.28 mmol). $NaBH_3CN$ (170 mg, 2.2 eq.) was then added portion-wise to the mixture and the reaction was left at room temperature for 1 hour. After this time, 1 drop of concentrated HCl was added and the solvent was removed *in vacuo*. Removal of solvent after reacidification with HCl *in vacuo* and subsequent trituration in diethyl ether afforded the product as the hydrochloride salt (as a yellow-white solid,150 mg, 28 %). mp 145 °C; $[\alpha]^{25}_D$ +30 (c = 0.01 g mL^{-1}, MeOH); IR ν_{max} 1699, 1524, 1448, 1202; ^{1}H NMR (400 MHz, DMSO-d_6) δ(ppm) 1.50-1.80 (m, 4H, C*H*$_2$$CH_2CH_2N$, CH_2C*H*$_2$$CH_2N$), 2.71 (d, *J* = 4.5 Hz, 6H, N(CH_3)$_2$), 2.95-3.06 (m, 2H, CH_2CH_2C*H*$_2$N), 3.97 (m, 1H, NHC*H*COOH), 4.18-4.36 (m, 3H, OC*H*$_2$CH, OCH_2C*H*), 7.34 (t, *J* = 7.5 Hz, 2H, 2×FmocC_2H), 7.42 (t, *J* = 7.5 Hz, 2H, 2×FmocC_3H), 7.68-7.76 (m, 3H, 2×FmocC_1H, N*H*CHCOOH), 7.90 (d, *J* = 7.5 Hz, 2H, 2× FmocC_4H), 10.20 (m, 1H, CH_2N*H*(CH_3)$_2$); ^{13}C NMR (101 MHz, DMSO-d_6) δ(ppm) 21.1 (CH_2*C*H_2CH_2N), 28.2 (*C*$H_2CH_2CH_2N$), 42.3 (N(*C*H_3)$_2$), 46.7 (OCH_2*C*H), 53.6 (NH*C*HCOOH), 56.4 (CH_2CH_2*C*H_2N), 65.9 (O*C*H_2CH), 120.4 (FmocC_4H), 125.6 (FmocC_1H), 127.4 (FmocC_2H), 127.9 (FmocC_3H), 141.6 (Ar*C*), 144.7 (Ar*C*), 157.1 (NH*C*OO), 175.1 (*C*OOH), HMBC correlation observed between the N(CH_3)$_2$ protons and the CH_2CH_2*C*H_2N carbon; HRMS (ESI+) m/z calcd for $C_{22}H_{27}N_2O_4$ $(M+H)^+$: 383.1965. Found 3863.1959.

g) Fmoc-Orn(Et_2)-OH hydrochloride

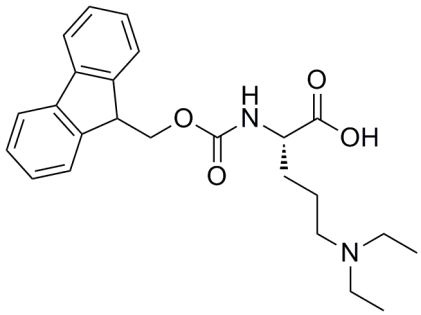

Fmoc-Orn-OH.HCl (500 mg, 1.28 mmol) was dissolved in 20 mL of ethanol, before acetaldehyde (0.36 mL, 5 eq.) was added to the solution. $NaBH_3CN$ (170 mg, 2.2 eq.) was then added portion-wise to the mixture and the reaction was left at room temperature for 3 hours. 1 drop of concentrated HCl was added and the solvent was removed *in vacuo*. The product was then extracted into dry acetone and the remaining precipitate was removed by filtration. Removal of solvent after reacidification in HCl *in vacuo* and subsequent trituration in diethyl ether afforded the product (as the hydrochloride) as a white solid (450 mg, 79 %). mp 180 °C; $[\alpha]^{25}_D$ +43 (c = 0.01 g mL^{-1}, MeOH); IR ν_{max} 1744,1714, 1518, 1444; ^{1}H NMR (400 MHz, DMSO-d_6) δ(ppm) 1.19 (t, *J* = 7.5 Hz, 6H, $N(CH_2C\underline{H_3})_2$), 1.59-1.84 (m, 4H, $C\underline{H_2}CH_2CH_2N$, $CH_2C\underline{H_2}CH_2N$), 2.91-3.10 (m, 6H, $CH_2CH_2C\underline{H_2}N$, $N(C\underline{H_2}CH_3)_2$), 3.99 (m, 1H, NHC*H*COOH), 4.18-4.36 (m, 3H, $OC\underline{H_2}CH$, $OCH_2C\underline{H}$), 7.33 (t, *J* = 7.5 Hz, 2H, 2×FmocC_2H), 7.42 (t, *J* = 7.5 Hz, 2H, 2× FmocC_3H), 7.73 (app t, *J* = 7.5 Hz, 3H, 2× FmocC_1H, N*H*CHCOOH), 7.89 (d, *J* = 7.5 Hz, 2H, 2× FmocC_4H), 10.38-10.50 (br s, 1H, $CH_2N\underline{H}(CH_2CH_3)_2$); ^{13}C NMR (101 MHz, DMSO-d_6) δ(ppm) 8.5 ($N(CH_2\underline{C}H_3)_2$), 20.1 ($CH_2\underline{C}H_2CH_2N$), 28.2 ($\underline{C}H_2CH_2CH_2N$), 46.3 ($N(\underline{C}H_2CH_3)_2$), 46.8 ($OCH_2\underline{C}H$), 50.1 ($CH_2CH_2\underline{C}H_2N$), 53.4 (NH*C*HCOOH), 65.9 ($O\underline{C}H_2CH$), 120.4 (Fmoc$\underline{C}_4$H), 125.5 (Fmoc$\underline{C}_1$H), 127.4 (Fmoc$\underline{C}_2$H), 127.8 (Fmoc$\underline{C}_3$H), 141.6 (Ar*C*), 144.7 (Ar*C*), 157.1 (NH*C*OO), 175.1 (*C*OOH), HMBC correlation observed between the $N(C\underline{H_2}CH_3)_2$ protons and the $CH_2CH_2\underline{C}H_2N$ carbon; HRMS (ESI+) m/z calcd for $C_{24}H_{31}N_2O_4$ $(M+H)^+$: 411.2278. Found 411.2276.

h) Fmoc-Lys(CD_3)$_2$)-OH hydrochloride

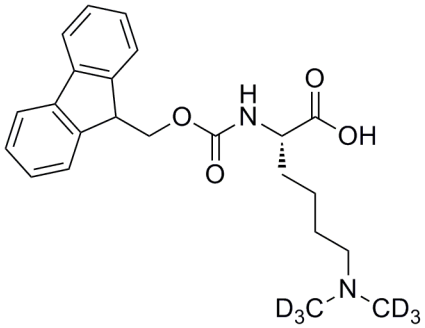

Fmoc-Lys-OH.HCl (500 mg, 1.23 mmol) was dissolved in 10 mL of deuterated MeOH, before 0.5 mL of 20 % deuterated HCHO (HCHO-d_2, 3.2 eq.) was added. $NaBD_3CN$ (171 mg, 2.1 eq.) was then added portion-wise to the mixture and the reaction was left at room temperature. After 2 hours, 1 drop of concentrated HCl was added to the mixture and the solvent was removed *in vacuo*. The product was then extracted into dry acetone and the remaining precipitate was removed by filtration. Removal of solvent *in vacuo* and subsequent trituration in diethyl ether afforded the product as a white solid (466 mg, 86 %), which was deemed suitable for SPPS. Comparison of crude ^{1}H NMR and IR spectra with those of an authentic sample of non-labelled Fmoc-Lys(Me_2)-OH (GL Biochem (Shanghai) Ltd.) revealed resonances consistent with formation of the product. HRMS (ESI+) m/z calcd for $C_{23}H_{23}D_6N_2O_4$ $(M+H)^+$: 399.2189. Found 399.2195. The ^{1}H NMR spectrum of the ^{13}C-labelled peptide (after incorporation of the product) possessed identical resonances to the non-labelled peptide (except those from the N^{ε}-methyl groups), thus confirming formation of the correct species.

10.4 Peptide Synthesis

Solid phase peptide synthesis (SPPS) was carried out using automated peptide synthesisers (CS336S and CS336X synthesisers, CS Bio). Peptides were synthesised in a sequential manner from their *C*-termini, using standard Fmoc-based SPPS protocol. 4-(2',4'-Dimethoxyphenyl-Fmoc-aminomethyl)-phenoxyacetamido-norleucyl-MBHA resin (100-200 mesh) was reacted with N^{α}-Fmoc protected amino acids, which were preactivated with diisopropylcarbodiimide and hydroxybenzotriazole (incubation for 30 min) before addition to the resin. After incubation with shaking for 3 hours, the solution phase reactants were drained from the reaction vessel and the resin was treated with a

solution of 20 % piperidine in DMF to remove the N^{α}-Fmoc group. Then, the next activated amino acid was added. After the final amino acid was attached (and the *N*-terminal Fmoc group had been removed by piperidine treatment), the resin was washed and stored in a dessicator overnight. The peptide was then cleaved from the resin by treatment with 4 mL of cleavage mix (97.5 % TFA, 2.5 % triisopropylsilane) for 3 hours (the side protecting groups were also cleaved during cleavage mix treatment). After cleavage, the peptide was precipitated from the cleavage mix with diethyl ether and the resultant solid was redissolved in H_2O. Removal of solvent by lyophilisation resulted in the isolation of the crude peptide as a solid.

All amino acids used were purchased from either CS Bio or Novabiochem. Typically, amino acids were added in large excess (10 eq.) to ensure efficient coupling. However, addition of valuable amino acids (such as methylated lysines and arginines) occurred at lower excesses (3-5 eq.) for cost efficiency reasons. Piperidine was purchased from Merck Chemicals. Diisopropylcarbodiimide and trifluoroacetic acid were purchased from Aldrich. Hydroxybenzotriazole was purchased from AGTC Bioproducts. Solvents (DMF, dichloromethane, dimethylsulfoxide) were purchased from Rathburn Chemicals, Aldrich and Merck Chemicals respectively.

10.5 HPLC Purification of Peptides and GSH-HCHO Adducts

Purification of peptides after synthesis was achieved on multiple HPLC systems. Predominantly, purification was carried out on an Agilent technologies 1200 series HPLC system attached to an Agilent Technologies 6120 quadrupole mass spectrometer for mass-directed fraction collection. Samples were purified through a SunFire™ Prep column (C18, 5 µm, 150 mm length, 10 mm internal diameter). Samples were eluted by a gradient of acetonitrile in H_2O (typical gradient on the Agilent system was 5 % to 30 % acetonitrile over 15 min). The elution solvents also contained 0.1 % trifluoroacetic acid to improve resolution. After collection of fractions containing the purified peptides, the solvent was removed by lyophilisation. All peptides used for NMR studies were over 95 % pure. Purification of $BiGF_2$ and PGF (Chapter 8) was achieved on a 1525µ HPLC system (Waters Corporation) attached to a Quattro Micro™ API mass

spectrometer (Micromass), using a Grace/Vydac 218TP C18 column (C18, 10-15 µm, 250 mm length, 22 mm internal diameter).

10.6 Enzyme Assays

10.6.1 MALDI-TOF Demethylation Assay

Samples were mixed in either eppendorf tubes or 96-well plates to a final volume of 20 µL. Firstly, two pre-solutions were prepared; substrate mix – containing substrate peptide (10 µM) and 2OG (50 µM), and enzyme mix – containing enzyme (1-8 µM), ascorbate (100 µM) and ferrous iron (10 µM). The two solutions were then mixed and the samples were transferred to a 37 °C incubator and left for 30 minutes – 1 hour before quenching with 20 µL of methanol. The samples were then spotted directly onto MALDI plates (see Section 10.7.1). Time course experiments by MALDI (Chapters 3 and 4) were carried out at 25 °C in order to facilitate quenching of the samples under comparable conditions. All reagents were prepared in 50 mM HEPES buffer pH 7.5, except the ferrous iron, which was prepared as a stock solution (100 mM) in 20 mM aqueous HCl. This stock was then diluted in water. Experiments with PHF8 were conducted in 100 mM HEPES 500 mM NaCl buffer solution pH 7.5.

10.6.2 FDH Demethylation Assay

A sample containing a 2OG demethylase (2 µM), FDH (0.1 unit), NAD^+ (500 µM), ascorbate (100 µM), peptide substrate (10 µM) and ferrous iron (10 µM) was incubated at 37 °C and were monitored by fluorescence every 30 seconds (355 nm excitation, 460 nm emission) using an EnVision™ 2104 Multilabel Reader (Perkin Elmer). Samples were prepared in 50 mM HEPES buffer pH 7.5, except ferrous iron, which was prepared as described in Section 10.5.1. All kinetic analyses were carried out in triplicate.

10.6.3 Zinc Ejection Assay

10 µL of 10 µM stock JMJD2A (wild type or K241 variants) in 50 mM HEPES buffer pH 7.5 were added to 85 µL of the same buffer in a Greiner µ Assay 384 well plate. Then, 5 µL of 500 µM Ebselen in DMSO was added and the mixture was monitored at

30°C by fluorescence every 40 seconds (485 nm excitation, 520 nm emission) using a Novostar Plate Reader (BMG Labtech).

10.7 NMR Experiments

All NMR experiments (except those described in Section 10.2.2) were conducted on a Bruker Avance AVIII 700 MHz spectrometer with an inverse TCI cryoprobe optimised for ^{1}H observation, and installed with TOPSPIN 2 software. All samples were prepared in eppendorf tubes before being transferred to 2 mm NMR tubes (Wilgenberg) for analysis. The solvent deuterium signal was used as the internal lock signal. The spectrometer conditions were optimised before each experiment and spectra were processed using automated routines. All spectra were acquired at 25 °C, except the waterLOGSY analyses, which were conducted at 7 °C.

10.7.1 ^{1}H NMR Time-Courses

Time course experiments were run according to automated routines. The samples were first prepared as two solutions (see preparation of MALDI demethylation assay samples, Section 10.5.1) and then were mixed in eppendorf tubes. Immediately after mixing, the samples were transferred to 2 mm Bruker MATCH NMR tubes (75 µL capacity) for NMR analysis. The total lag time between mixing and the first NMR analysis was 300-800 sec. The duration of individual ^{1}H NMR experiments varied for each experiment (between 89 and 350 sec). In some cases, water suppression was achieved either via presaturation at the water resonance, or by excitation sculpting using a sinc pulse. All kinetic analyses were carried out in triplicate.

10.7.2 1D HSQC Method

The 1D HSQC method used to detect ^{13}C-HCHO release (Chapter 2) was adapted from a standard 2D HSQC sequence. For these experiments, the t_1 period and ^{13}C-decoupling were removed during data acquisition, and the $1/2J_{CH}$ delays were optimised for $^{1}J_{CH}$ of 145 Hz. Each 1D experiment accumulated 8 transients corresponding to 39 seconds of total acquisition time.

10.7.3 EXSY Methods

EXSY experiments utilised 1D and 2D NOESY pulse sequences using selective refocusing with Gaussian and CHIRP pulses. For the 2D studies, experiments were run accumulating 32 transients with a τ_m of 400 ms. 1D experiments accumulated 64 transients with a τ_m of 80 ms (selected after an initial screen).

10.7.4 STD NMR Method

STD experiments were run according to a standard sequence, in which selective saturation of the protein was achieved by a train of Gaussian shaped pulses (50 ms). A sinc pulse was employed for water suppression. The on-resonance was selected at 565.92 Hz and the off-resonance was 35000 Hz. The saturation time and relaxation delay were 10 s and 18 s respectively.

10.7.5 WaterLOGSY NMR Method

WaterLOGSY NMR was carried out using a standard sequence with a 16 ms square pulse. The relaxation delay was 2 s and the mixing time was 1 s. A 2 ms sinc pulse was used for water suppression. Each experiment accumulated 64 transients at 280 K.

10.8 Mass Spectrometry Experiments

10.8.1 MALDI-TOF Mass Spectrometry

MS analysis of peptide assays was carried out using a MALDI Micro MX™ mass spectrometer (Waters Corporation). Samples were prepared by mixing 1 µL of peptide sample (in H_2O or in assay buffer) with 1 µL of α-cyano-4-hydroxycinnamic acid (CHCA) matrix (LaserBioLabs), and then spotting the mixture on a 12 × 8 target plate (Waters Corporation). The sample was then left to dry before analysis in the positive ion reflectron mode with flight tube and reflectron voltages of 12000 V and 5200 V respectively. Data was processed using MassLynx 4.0 software.

10.8.2 Non-Denaturing Mass Spectrometry

Protein mass spectra under non-denaturing conditions were recorded using a Q-TOF mass spectrometer (Q-TOF micro, Waters Corporation) attached to a Nanomate

(Advion Biosciences) with a chip voltage of 1700 V. Samples were prepared in 364 well plates and placed in the Nanomate, from where aliquots were injected into the MS at a delivery pressure of 0.25 psi. Processing of the spectra was carried out using MassLynx 4.0 software.

10.9 Circular Dichroism

0.5 mL of 0.5 mg/ml protein in buffer (50 mM HEPES pH 7.5 for the JMJD2A variants, 50 mM tris pH 7.5 for GFA) was injected into a 1 mm path length cuvette. The cuvette was then placed into a chirascan circular dichroism spectrometer (Applied Photophysics) and scanned every 0.5 nm in the range of 180-300 nm. Each experiment was repeated three times and the results were averaged. The path length was set to 10 and a bandwidth of 1 nm was used.

Chapter 11

References

1. Hausinger, R. P., Fe(II)/(alpha)-Ketoglutarate-Dependent Hydroxylases and Related Enzymes. *Critical Reviews in Biochemistry and Molecular Biology* **2004,** 39, 21-68.

2. Clifton, I. J.; McDonough, M. A.; Ehrismann, D.; Kershaw, N. J.; Granatino, N.; Schofield, C. J., Structural studies on 2-oxoglutarate oxygenases and related double-stranded [beta]-helix fold proteins. *Journal of Inorganic Biochemistry* **2006,** 100, 644-669.

3. Costas, M.; Mehn, M. P.; Jensen, L.; Que, L., Dioxygen Activation at Mononuclear Nonheme Iron Active Sites; Enzymes, Models, and Intermediates. *Chemical Reviews* **2004,** 104, 939-986.

4. Schofield, C. J.; Zhang, Z., Structural and mechanistic studies on 2-oxoglutarate-dependent oxygenases and related enzymes. *Current Opinion in Structural Biology* **1999,** 9, 722-731.

5. Loenarz, C.; Schofield, C. J., Expanding chemical biology of 2-oxoglutarate oxygenases. *Nature Chemical Biology* **2008,** 4, 152-156.

6. Flashman, E.; Schofield, C. J., The most versatile of all reactive intermediates? *Nature Chemical Biology* **2007,** 3, 86-87.

7. Blasiak, L. C.; Vaillancourt, F. H.; Walsh, C. T.; Drennan, C. L., Crystal structure of the non-haem iron halogenase SyrB2 in syringomycin biosynthesis. *Nature* **2006,** 440, 368-371.

8. Watanabe, M.; Sumida, N.; Murakami, S.; Anzai, H.; Thompson, C. J.; Tateno, Y.; Murakami, T., A phosphonate-induced gene which promotes penicillium-mediated bioconversion of *cis*-propenylphosphonic acid to fosfomycin. *Applied and Environment Microbiology* **1999,** 65, 1036-1044.

9. Clifton, I. J.; Doan, L. X.; Sleeman, M. C.; Topf, M.; Suzuki, H.; Wilmouth, R. C.; Schofield, C. J., Crystal structure of carbapenem synthase (CarC). *Journal of Biological Chemistry* **2003,** 278, 20843-20850.

10. Zhang, Z.; Ren, J.; Stammers, D. K.; Baldwin, J. E.; Harlos, K.; Schofield, C. J., Structural origins of the selectivity trifunctional oxygenase clavaminic acid synthase. *Nature Structural Biology* **2000,** 7, 127-133.

11. Baldwin, J. E.; Adlington, R. M.; Coates, J. B.; Crabbe, M. J. C.; Crouch, N. P.; Keeping, J. W.; Knight, G. C.; Schofield, C. J.; Ting, H.-H.; Vallejo, C. A.;

Throniley, M.; Abraham, E. P., Purification and initial characterisation of an enzyme with deacetoxycephalosporin C synthetase and hydroxylase activities. *Biochemical Journal* **1987,** 245, 831-841.

12. McDonough, M. A.; Schofield, C. J., Cellular oxygen sensing: Crystal structure of hypoxia-inducible factor prolyl hydroxylase (PHD2). *Proceedings of the National Academy of Sciences of the United States of America* **2006,** 103, 9814-9819.

13. Couture, J. F.; Collazo, E.; Ortiz-Tello, P. A.; Brunzelle, J. S.; Trievel, R. C., Specificity and mechanism of JMJD2A, a trimethyllysine-specific histone demethylase. *Nature Structural and Molecular Biology* **2007,** 14, (8), 689-695.

14. Krebs, C.; Galonic Fujimori, D.; Walsh, C. T.; Jr, B. J. M., Non-heme Fe(IV)-oxo intermediates. *Accounts of Chemical Research* **2007,** 40, 484-492.

15. Jaakkola, P.; Mole, D. R.; Tian, Y. M.; Wilson, M. I.; Gielbert, J.; Gaskell, S. J.; von Kriegsheim, A.; Hebestreit, H. F.; Mukherji, M.; Schofield, C. J.; Maxwell, P. H.; Pugh, C. W.; Ratcliffe, P. J., Targetting of HIF-α to the von Hippel-Lindau ubitquitylation complex by O_2-regulated prolyl hydroxylation. *Science & Justice* **2001,** 292, 468-472.

16. Loenarz, C.; Mecinovic, J.; Chowdhury, R.; McNeill, L. A.; Flashman, E.; Schofield, C. J., Evidence for a Stereoelectronic Effect in Human Oxygen Sensing. *Angewandte Chemie International Edition* **2009,** 48, 1784-1787.

17. Ozer, A.; Bruick, R. K., Non-heme dioxygenases: cellular sensors and regulators jelly rolled into one? *Nature Chemical Biology* **2007,** 3, 144-153.

18. Murad, S.; Grove, D.; Lindberg, K. A.; Reynolds, G.; Sivarajah, A.; Pinnell, S. R., Regulation of collagen synthesis by ascorbic acid. *Biochemistry* **1981,** 78, (5), 2879-2882.

19. Smith, T. G.; Talbot, N. P., Prolyl Hydroxylases and Therapeutics. *Antioxidants & Redox Signaling* **2010,** 12, (4), 431-433.

20. Kuttan, R.; Parrott, D. P.; Kaplan, S. R.; Fullar, G. C., Effect of ascorbic acid on prolyl hydroxylase activity, collagen hydroxylation and collagen synthesis in human synovial cells in culture. *Research Communications in Chemical Pathology and Pharmacology* **1979,** 26, (2), 337-345.

21. Myllyla, R.; Majamaa, K.; Gunzler, V. A.; Hanauske-Abel, H. M.; Kivirikko, K. I., Ascorbate Is Consumed Stoichiometrically in the Uncoupled Reactions Catalyzed by Prolyl 4-Hydroxylase and Lysyl Hydroxylase. *Journal of Biological Chemistry* **1984,** 259, (9), 5403-5405.

22. Chowdhury, R.; McDonough, M. A.; Mecinovic, J.; Loenarz, C.; Flashman, E.; Hewitson, K. S.; Domene, C.; Schofield, C. J., Structural basis for binding of hypoxia-inducible factor to the oxygen-sensing prolyl hydroxylases. *Structure* **2009,** 17, 981-989.

23. Hanauske-Abel, H. M.; Gunzler, V. A., A stereochemical concept for the catalytic mechanism of prolylhydroxylase. Applicability to classification and design of inhibitors. *Journal of Theoretical Biology* **1982,** 94, 421-455.

24. Flashman, E.; Hoffart, L. M.; Hamed, R. B.; Bollinger Jr, J. M.; Krebs, C.; Schofield, C. J., Evidence for the slow reaction of hypoxia-inducible factor prolyl hydroxylase 2 with xygen. *FEBS (Federation of European Biochemical Societies) Journal* **2010,** 277, 4089-4099.

25. Hoffart, L. M.; Barr, E. W.; Guyer, R. B.; Bollinger Jr, J. M.; Krebs, C., Direct spectroscopic detection of a C-H-cleaving high-spin Fe(IV) complex ina prolyl-4-hydroxylase. *Proceedings of the National Academy of Sciences of the United States of America* **2006,** 103, (40), 14738-14743.

26. Di Lullo, G. A.; Sweeney, S. M.; Korkko, J.; Ala-Kokko, L.; San Antonio, J. D., Mapping the Ligand-binding Sites and Disease-associated Mutations on the Most Abundant Protein in the Human, Type 1 Collagen. *Journal of Biological Chemistry* **2002,** 277, 4223-4231.

27. Myllyharju, J.; Kivirikko, K. I., Collagens, modifying enzymes and their mutations in humans, flies and worms. *Trends in Genetics* **2004,** 20, 33-43.

28. Jenkins, C. L.; Raines, R. T., Insights on the conformational stability of collagen. *Natural Product Reports* **2002,** 19, 49-59.

29. Turpeenniemi-Hujanen, T. M.; Puistola, U.; Kivirikko, K. I., Isolation of lysyl hydroxylase, an enzyme of collagen synthesis, from chick embryos as a homogeneous protein. *Biochemical Journal* **1980,** 189, 247-253.

30. Kivirikko, K. I.; Ryhanen, L.; Anttinen, H.; Bornstein, P.; Prockop, D. J., Further Hydroxylation of Lysyl Residues in Collagen by Procollagen Lysyl Hydroxylase *in vitro*. *Biochemistry* **1973,** 12, (24), 4966-4971.

31. Ruotsalainen, H.; Sipila, L.; Vapola, M.; Sormunen, R.; Salo, A. M.; Uitto, L.; Mercer, D. K.; Robins, S. P.; Risteli, M.; Aszodi, A.; Fassler, R.; Myllyla, R., Glycosylation catalyzed by lysyl hydroxylase 3 is essential for basement membranes. *Journal of Cell Science* **2006,** 119, (4), 625-635.

32. Bruick, R. K.; McKnight, S. L., A Conserved family of Prolyl-4-Hydroxylases That Modify HIF. *Science* **2001,** 294, 1337-1340.

33. Epstein, A. C. R.; Gleadle, J. M.; McNeill, L. A.; Hewitson, K. S.; O'Rourke, J.; Mole, D. R.; Mukherji, M.; Metzen, E.; Wilson, M. I.; Dhanda, A.; Tian, Y. M.; Masson, N.; Hamilton, D. L.; Jaakkola, P.; Barstead, R.; Hodgken, J.; Maxwell, P. H.; Pugh, C. W.; Schofield, C. J.; Ratcliffe, P. J., C. elegans EGL-9 and Mammalian Homologs Define a Family of Dioxygenases that Regulate HIF by Prolyl Hydroxylation. *Cell & Tissue Research* **2001,** 107, 43-54.

34. Maxwell, P. H.; Wiesener, M. S.; Chang, G. W.; Clifford, S. C.; Vaux, E. C.; Cockman, M. E.; Wykoff, C. C.; Pugh, C. W.; Maher, E. R.; Ratcliffe, P. J., The Tumour Suppressor Protein VHL Targets Hypoxia Inducible Factors for Oxygen Dependent Proteolysis. *Nature* **1999,** 399, (6733), 271-275.

35. Ivan, M.; Kondo, K.; Yang, H.; Kim, W.; Valiando, J.; Ohh, M.; Salic, A.; Asara, J. M.; Lane, W. S.; Kaelin Jr, W. G., HIF-α Targetted for VHL-mediated Destruction by Proline Hydroxylation: Implications for O_2 Sensing. *Science* **2001,** 292, (5516), 464-468.

36. Yu, F.; White, S. B.; Zhao, Q.; Lee, F. S., HIF-1α Binding to VHL is Regulated by Stimulus-Sensitive Proline Hydroxylation. *Proceedings of the National Academy of Sciences of the United States of America* **2001,** 98, (19), 9630-9635.

37. Semenza, G. L., Oxygen Dependent Regulation of Mitochondrial Respiration by Hypoxia-Inducible Factor 1. *Biochemical Journal* **2007,** 405, (1), 1-9.

38. Lando, D.; Peet, D. J.; Whelan, D. A.; Gorman, J. J.; Whitelaw, M. L., Asparagine Hydroxylation of the HIF Transactivation Domain. *Science* **2002,** 295, (5556), 858-861.

39. Sang, N.; Fang, J.; Srinivas, V.; Leshchinsky, I.; Caro, J., Carboxyl Terminal Transactivation Activity of Hypoxia-Inducible Factor 1-alpha is Governed by a von Hippel-Lindau Protain Independent, Hydroxylation Regulated Association with p300/CBP. *Molecular and Cellular Biology* **2002,** 22, (9), 2984-2992.

40. Hewitson, K. S.; McNeill, L. A.; Riordan, M. V.; Tian, Y. M.; Bullock, A. N.; Welford, R. W.; Elkins, J. M.; Oldham, N. J.; Bhattacharya, S.; Gleadle, J. M.; Ratcliffe, P. J.; Pugh, C. W.; Schofield, C. J., Hypoxia Inducible Factor (HIF) Asparagine Hydroxylase is Identical to Factor Inhibiting HIF (FIH) and is Related to the Cupin Structural Family. *Journal of Biological Chemistry* **2002,** 277, (29), 26351-26355.

41. Cockman, M. E.; lancaster, D. E.; Stolze, I. P.; Hewitson, K. S.; McDonough, M. A.; Coleman, M. L.; Coles, C. H.; Yu, X.; Hay, R. T.; Lay, S. C.; Pugh, C. W.; Oldham, N. J.; Masson, N.; Schofield, C. J.; Ratcliffe, P. J., Posttranslational Hydroxylation of Ankyrin Repeats in IkB proteins by the Hypoxia-Inducible Factor (HIF) Asparaginyl Hydroxylase, Factor Inhibiting HIF (FIH). *Proceedings of the National Academy of Sciences of the United States of America* **2006,** 103, (40), 14767-14772.

42. Coleman, M. L.; McDonough, M. A.; Hewitson, K. S.; Coles, C. H.; Mecinovic, J.; Edelmann, M.; M., C. K.; Cockman, M. E.; Lancaster, D. E.; Kessler, B. M.; Oldham, N. J.; Ratcliffe, P. J.; Schofield, C. J., Asparaginyl Hydroxylation of the Notch Ankyrin Repeat Domain by Factor Inhibiting Hypoxia-Inducible Factor. *Journal of Biological Chemistry* **2007,** 282, (33), 24027-24038.

43. Vaz, F. M.; Wanders, R. J. A., Carnitine biosynthesis in mammals. *Biochemical Journal* **2002,** 361, 417-429.

44. Hulse, J. L.; Ellis, S. R.; henderson, L. M., Carnitine biosynthesis. β-Hydroxylation of trimethyllysine by an a-ketoglutarate-dependent mitochondrial dioxygenase. *Journal of Biological Chemistry* **1978,** 253, 1654-1659.

45. Englard, S.; Blanchard, J. S.; Madelfort, C. F., γ-Butyrobetaine hydroxylase: stereochemical course of the hydroxylation reaction. *Biochemistry* **1985,** 24, 1110-1116.

46. Leung, I. K. H.; Krojer, T. J.; Kochan, G. T.; Henry, L.; von Delft, F.; Claridge, T. D. W.; Oppermann, U.; McDonough, M. A.; Schofield, C. J., Structural and Mechanistic Studies on g-Butyrobetaine Hydroxylase. *Chemistry & Biology* **2010,** 17, 1316-1324.

47. Schofield, C. J.; McDonough, M. A., Structural and mechanistic studies on the peroxisomal oxygenase phytanoyl-CoA 2-hydroxylase. *Biochemical Society Transactions* **2007,** 35, (5), 870-875.

48. Webby, C. J.; Wolf, A.; Gromak, N.; Dreger, M.; Kramer, H.; Kessler, B. M.; Nielsen, M. L.; Schmitz, C.; Butler, D. S.; Yates 3rd., J. R.; Delahunty, C. M.; Lengeling, A.; Mann, M.; Proudfoot, N. J.; Schofield, C. J.; Bottger, A., Jmjd6 catalyses lysyl hydroxylation of U2AF65, a protein associated with RNA splicing. *Science* **2009,** 325, (5936), 90-93.

49. Mantri, M.; Krojer, T.; Bagg, E. A.; Webby, C. J.; Butler, D. S.; Kochan, G.; Kavanagh, K. L.; Oppermann, U.; McDonough, M. A.; Schofield, C. J., Crystal Structure of the 2-Oxoglutarate- and Fe(II)-Dependent Lysyl Hydroxylase JMJD6. *Journal of Molecular Biology* **2010,** 401, (2), 211-222.

50. Boeckel, J.-N.; Guarani, V.; Koyanagi, M.; Roexe, T.; Lengeling, A.; Schermuly, R. T.; Gellert, P.; Braun, T.; Zeiher, A.; Dimmeler, S., Jumonji domain-containing protein 6 (Jmjd6) is required for angiogenic sprouting and regulates splicing of VEGF-receptor 1. *Proceedings of the National Academy of Sciences of the United States of America* **2011,** 108, (8), 3276-3281.

51. Chang, B.; Chen, Y.; Zhao, Y.-F.; Bruick, R. K., JMJD6 is a histone arginine demethylase. *Science* **2007,** 318, (5849), 444-447.

52. Mantri, M.; Loik, N. D.; Hamed, R. B.; Claridge, T. D. W.; McCullagh, J. S. O.; Schofield, C. J., The 2-Oxoglutarate-Dependent Oxygenase JMJD6 Catalyses Oxidation of Lysine Residues to give 5S-Hydroxylysine Residues. *ChemBioChem* **2011,** 12, (4), 531-534.

53. Sedgwick, B.; Bates, P. A.; Paik, J.; Jacobs, S. C.; Lindahl, T., Repair of alkylated DNA: Recent Advances *DNA Repair* **2007,** 6, 429-442.

54. Trewick, S. C.; Henshaw, T. F.; Hausinger, R. P.; Lindahl, T.; Sedgewick, B., Oxidative demethylation by *Escherichia coli* AlkB directly reverts DNA base damage. *Nature* **2007,** 419, 174-178.

55. Yi, C.; Jia, G.; Hou, G.; dai, Q.; Zhang, W.; Zheng, G.; Jian, X.; Yang, C.-G.; Cui, Q.; He, C., Iron-catalysed oxidation intermediates captured in a DNA repair dioxygenase. *Nature Letters* **2010,** 468, 330-333.

56. Delaney, J. C.; Essigmann, J. M., Mutagenesis, genotoxicity, and repair of 1-methyladenine, 3-alkylcytosines, 1-methylguanine, and 2-methylthymine in

alkB *Escherichia coli*. *Proceedings of the National Academy of Sciences of the United States of America* **2004,** 101, 14051-14056.

57. Frick, L. E.; Delaney, J. C.; Wong, C.; Drennan, C.; Essigmann, J. M., Alleviation of 1,N6-ethanoadenine genotoxicity by the *Escherichia coli* adaptive response protein AlkB. *Proceedings of the National Academy of Sciences of the United States of America* **2007,** 104, 755-760.

58. Delaney, J. C.; Smeester, L.; Wong, C.; Frick, L. E.; Taghizadeh, K.; Wishnok, J. S.; Drennan, C.; Samson, L. D.; Essigmann, J. M., AlkB reverses etheno DNA lesions caused by lipid osidation *in vitro* and *in vivo*. *Nature Structural and Molecular Biology* **2005,** 12, 855-860.

59. Ringvoll, J.; Nordstrand, L. M.; Vagbo, C. B.; Talstad, V.; Reite, K.; Aas, P. A.; Lauritzen, K. H.; Liabakk, N. B.; Bjork, A.; Doughty, R. W.; Falnes, P. O.; Krokan, H. E.; Klungland, A., Repair deficient mice reveal mABH2 as the primary oxidative demethylase for repairing 1meA and 3meC lesions in DNA. *EMBO Journal* **2006,** 25, 2189-2198.

60. Born, E. V. D.; Vagbo, C. B.; Songe-Moller, L.; Leihnel, V.; Lien, G. F.; Leszczynska, G.; Malkiewicz, A.; Krokan, H. E.; Kirpekar, F.; Klungland, A.; Falnes, P. O., ALKBH8-mediated formation of a novel diastereomeric pair of wobble nucleosides in mammalian tRNA. *Nature Communications* **2011,** 2, Article Number 172.

61. Gerken, T.; Girard, C. A.; Tung, Y.-C. L.; Webby, C. J.; Saudek, V.; Hewitson, K. S.; Rorsman, G.; Robins, P.; Prieur, X.; Coll, A. P.; Ma, M.; Jovanovic, Z.; Farooqi, I. S.; Sedgewick, B.; Barroso, I.; Lindahl, T.; Ponting, C. P.; Ashcroft, F. M.; O'Rahilly, S.; Schofield, C. J., The Obesity-Associated FTO Gene Encodes a 2-Oxoglutarate-Dependent Nucleic Acid Demethylase. *Science* **2007,** 318, 1469-1472.

62. Frayling, T. M.; Timpson, N. J.; Weedon, M. N.; Zeggini, E.; Freathy, R. M.; Lindgren, C. M.; Perry, J. R. B.; Elliot, K. S.; Lango, H.; Rayner, N. W.; Shields, B.; Harries, L. W.; Barrett, J. C.; Ellard, S.; Groves, C. J.; Knight, B.; Patch, A.-M.; Ness, A. R.; Ebrahim, S.; Lawlor, D. A.; Ring, S. M.; Ben-Shlomo, Y.; Jarvelin, M.-R.; Sovio, U.; Bennett, A. J.; Melzer, D.; Ferrucci, L.; Loos, R. J. F.; Barroso, I.; Wareham, N. J.; Karpe, F.; Owen, K. R.; Cardon, L. R.; Walker, M.; Hitman, G. A.; Palmer, C. N. A.; Doney, S. F.; Morris, A. D.; Smith, G. D.; Consortium, T. W. T. C. C.; Hattersley, A. T.; McCarthy, M. I., A Common Variant in the FTO Gene is Associated with Body Mass Index and Predisposes to Childhood and Adult Obesity. *Science* **2007,** 316, 889-894.

63. Jia, G.; Yang, C.-G.; Yang, S.; Jian, X.; Yi, C.; Zhou, Z.; He, C., Oxidative demethylation of 3-methylthymine and 3-methyluracil in single-stranded DNA and RNA by mouse and human FTO. *FEBS Letters* **2008,** 582, 3313-3319.

64. Tahiliani, M.; Koh, K. P.; Shen, Y.; Pastor, W. A.; Bandukwala, H.; Brudno, Y.; Agarwal, S.; Iyer, L. M.; Liu, D. R.; aravind, L.; Rao, A., Conversion of 5-Methylcytosine to 5-Hydroxymethylcytosine in Mammalian DNA by MLL Partner TET1. *Science* **2009,** 324, 930-935.

65. Thalhammer, A.; Mecinovic, J.; Loenarz, C.; Tumber, A.; Rose, N. R.; Heightman, T. D.; Schofield, C. J., Inhibition of the histone demethylase JMJD2E by 3-substituted pyridine 2,4-dicarboxylates. *Organic & Biomolecular Chemistry* **2011,** 9, 127-135.

66. Thalhammer, A.; Hansen, A. S.; El-Sagheer, A. H.; Brown, T.; Schofield, C. J., Hydroxylation of methylated CpG dinucleotides reverses stabilisation of DNA duplexes by cytosine 5-methylation. *Chemical Communications* **2011,** 47, 5325-5327.

67. Chen, Z.; Zang, J.; Whetstine, J.; Hong, X.; Davrazou, F.; Kutateladze, T. G.; Simpson, M.; Mao, Q.; Pan, C. H.; Dai, S.; Hagman, J.; Hansen, K.; Shi, Y.; Zhang, G., Structural insights into histone demethylation by JMJD2 family members. *Cell* **2006,** 125, (4), 691-702.

68. Cloos, P. A.; Christensen, J.; Agger, K.; maiolica, A.; Rappsilber, J.; Antal, T.; Hansen, K. H.; Haelin, K., The putative oncogene GASC1 demethylates tri- and dimethylated lysine 9 on histone H3. *Nature* **2006,** 442, (7100), 307-311.

69. Fodor, B. D.; Kubicek, S.; Yonezawa, M.; O'Sullivan, R. J.; Sengupta, R.; Perez-Burgos, L.; Opravil, S.; Mechtler, K.; Schotta, G.; Jenuwein, T., Jmjd2b antagonizes H3K9 trimethylation at pericentric heterochromatin in mammalian cells. *Genes & Development* **2006,** 20, (12), 1557-1562.

70. Klose, R. J.; Yamane, K.; Bae, Y.; Zhang, D.; Erdjument-Bromage, H.; Tempst, P.; Wong, J.; Zhang, Y., The transcriptional repressor JHDM3A demethylates trimethyl histone H3 lysine 9 and lysine 36. *Nature* **2006,** 442, (7100), 312-316.

71. Whetstine, J. R.; Nottke, A.; Lan, F.; Huarte, M.; Smolikov, S.; Chen, Z.; Spooner, E.; Li, E.; Zhang, G.; Colaiacovo, M.; Shi, Y., Reversal of lysine trimethylation by the JMJD2 family of histone demethylases. *Cell* **2006,** 125, (3), 467-481.

72. Wissmann, M.; Yin, N.; Muller, J. M.; Greschik, H.; Fodor, B. D.; Jenuwein, T.; Vogler, C.; Schneider, R.; Gunther, T.; Buettner, R.; Metzger, E.; Schule, R., Cooperative demethylation by JMJD2C and LSD1 promotes androgen receptor-dependent gene expression. *Nature Cell Biology* **2007,** 353, (3), 347-353.

73. He, J.; Kallin, E. M.; Tsukada, Y.; Zhang, Y., The H3K36 demethylase Jhdm1b/Kdm2b regulates cell proliferation and senescence through p15(Ink4b). *Nature Structural and Molecular Biology* **2008,** 15, (11), 1169-1175.

74. Tsukada, Y.; Fang, J.; Erdjument-Bromage, H.; Warren, M. E.; Borchers, C. H.; Tempst, P.; Zhang, Y., Histone Demethylation by A Family of JmjC Domain-containing Proteins. *Nature* **2006,** 439, 811-816.

75. Yamane, K.; Toumazou, C.; Tsukada, Y.; Erdjument-Bromage, H.; Tempst, P.; Wong, J.; Zhang, Y., JHDM2A, a JmjC-Containing H3K9 Demethylase, FacilitatesTranscription Activation by Androgen Receptor. *Cell* **2006,** 125, (3), 483-495.

76. Agger, K.; Christensen, J.; Cloos, P. A.; Helin, K., The emerging functions of histone demethylases. *Current Opinion in Genetics & Development* **2008,** 18, (2), 159-168.

77. Christensen, J.; Agger, K.; Cloos, P. A.; Pasini, D.; Rose, S.; Sennels, L.; Rappsilber, J.; Hansen, K. H.; Salcini, A. E.; Helin, K., RBP2 belongs to a family of demethylases, specific for tri- and di-methylated lysine 4 on histone 3. *Cell* **2007,** 128, (6), 1063-1076.

78. Agger, K.; Cloos, P. A.; Christensen, J.; Pasini, D.; Rose, S.; Rappsilber, J.; Issaeva, I.; Canaani, E.; Salcini, A. E.; Helin, K., UTX and JMJD3 are histone H3K27 demethylases involved in HOX gene regulation and development. *Nature* **2007,** 449, (7163), 731-734.

79. Kouzarides, T., SnapShot: Histone-Modifying Enzymes. *Cell* **2007,** 128, (4), 802.e1-802.e2.

80. Waddington, C. H., The epigenotype. *Endeavor* **1942,** 1, 18-20.

81. Russo, V. E.; Martienssen, R. A.; Riggs, A. D., Epigenetic Mechanisms of Gene Regulation. *Cold Spring Harbour Laboratory Press* **1996**.

82. Bird, A., Perceptions of Epigenetics. *Nature* **2007,** 447, (7143), 396-398.

83. Berger, S.; Kouzarides, T.; Shiekhattar, R.; Shilatifard, A., An operational definition of epigenetics. *Genes & Development* **2009,** 23, (7), 781-783.

84. Crick, F., Ideas on Protein Synthesis. **1956**.

85. Davey, C. A.; Sargent, D. F.; Luger, K.; Maeder, A. W.; Richmond, T. J., Solvent mediated interactions inthe structure of the nucleosome core particle at 1.9 Å resolution. *Journal of Molecular Biology* **2002,** 319, (5), 1097-1113.

86. Ramakrishnan, V.; Finch, J. T.; Graziano, V.; Lee, P. L.; Sweet, R. M., Crystal structure of globular domain of histone H5 and its implications for nucleosome binding. *Nature* **1993,** 362, 219-223.

87. Turner, B. M., Histone acetylation and an epigenetic code. *Bioessays* **2000,** 22, 836-845.

88. Mitra, D.; Parnell, E. J.; Landon, J. W.; Yu, Y.; Stillman, D. J., SWI/SNF binding to the HO promotor requires histone acetylation and stimulates TATA-binding protein recruitment. *Molecular and Cellular Biology* **2006,** 26, (11), 4095-4110.

89. Allis, C. D.; Jenuwein, T.; Reinberg, D.; Caparros, M.-L., Epigenetics. *Cold Spring Harbor Press* **2007**.

90. Hebbes, T. R.; Thorne, A. W.; Crane-Robinson, C., A direct link between core histone acetylation and transcriptionally active chromatin. *EMBO Journal* **1988,** 7, 1395-1402.

91. Fischle, W.; Tseng, B. S.; Dormann, H. L.; Ueberheide, B. M.; Garcia, B. A.; Shabanowitz, J.; Hunt, D. F.; Funabiki, H.; Allis, C. D., Regulation of HP1-chromatin binding by histone H3 methylation and phosphorylation. *Nature* **2005,** 438, (7071), 1116-1122.

92. Hochstrasser, M., Ubiquitin-dependent protein degradation. *Annual Review of Genetics* **1996,** 30, 405-439.

93. Cao, R.; Tsukada, Y.; Zhang, Y., Role of Bmi-1 and Ring1A in H2A ubiquitylation and Hox gene silencing. *Molecular Cell* **2005,** 20, 845-854.

94. Bergink, S.; Salomons, F. A.; Hoogstraten, D.; Groothuis, T. A.; de Waard, H.; Wu, J.; Yuan, L.; Cutterio, E.; Houtmuller, A. B.; Neefjes, J.; Hoeijmakers, J. H. J.; Vermeulen, W.; Dantuma, N. P., DNA damage triggers nucleotide excision repair-dependent monoubiquitylation of histone H2A. *Genes & Development* **2006,** 20, 1343-1352.

95. Osley, M. A., Regulation of histone H2A and H2B ubiquitylation. *Briefings in Functional Genomics and Proteomics* **2006,** 5, 179-189.

96. Wyce, A.; Xiao, T.; Whelan, K. A.; Kosman, C.; Walter, W.; Eick, D.; Hughes, T. R.; Krogan, N. J.; Strahl, B. D.; Berger, S. L., H2B ubiquitylation acts as a barrier to Ctk1 nucleosomal recruitmant prior to removal by Ubp8 within a SAGA-related complex. *Molecular Cell* **2007,** 27, 275-288.

97. Sanchez, C.; Sanchez, I.; Demmer, J. A.; Rodriguez, P.; Strouboulis, J.; Vidal, M., Proteomics analysis of Ring1B/Rnf2 interactors identifies a novel complex with the Fbxl10/Jhdm1B histone demethylase ans the Bcl6 interacting corepressor. *Molecular Cell Proteomics* **2007,** 6, 820-834.

98. Shiio, Y.; Eisenmann, R. N., Histone sumoylation is associated with transcriptional repression. *Proceedings of the National Academy of Sciences of the United States of America* **2003,** 100, 13225-13230.

99. Nathan, D.; Ingvarsdottir, K.; Sterner, D. E.; Bylebyl, G. R.; Dokmanovic, M.; Dorsey, J. A.; Whelan, K. A.; Krsmanovic, M.; Lane, W. S.; Meluh, P. B.; Johnson, E. S.; Berger, S. L., Histone sumoylation is a negative regulator in *Saccharomyces cerevisiae* and shows dynamic interplay with positive-acting histone modifications. *Genes & Development* **2006,** 20, 966-976.

100. Stanley, J. S.; Griffin, J. B.; Zempleni, J., Biotinylation of histones in human cells. Effects of cell proliferation. *European Journal of Biochemistry* **2001,** 268, (20), 5424-5429.

101. Hassan, Y. I.; Zempleni, J., A novel, enigmatic histone modification: biotinylation of histones by holocarboxylase synthetase. *Nutrition Reviews* **2008,** 66, (12), 721-725.

102. Hymes, J.; Fleischhauer, K.; Wolf, B., Biotinylation of histones by human serum biotinidase: assessment of biotinyl-transferase activity in sera from normal individuals and children with biotinidase deficiency. *Biochemical and Molecular Medicine* **1995,** 56, 76-83.

103. Hymes, J.; Wolf, B., Human biotinidase isn't just for recycling biotin. *Journal of Nutrition* **1999,** 129, 485S-9S.

104. Ballard, T. D.; Wolff, J.; Griffin, J. B.; Stenley, J. S.; Calcar, S. V.; Zempleni, J., Biotinidase catalyzes debiotinylation of histones. *European Journal of Nutrition* **2002,** 41, 78-84.

105. Zempleni, J., Uptake, localization and noncarboxylase roles of biotin. *Annual Review of Nutrition* **2005,** 25, 175-196.

106. Peters, D. M.; Griffin, J. B.; Stanley, J. S.; Beck, M. M.; Zempleni, J., Exposure to UV light causes increased biotinylation on histones in Jurkat cells. *American Journal of Physiology Cell Physiology* **2002,** 283, 878-884.

107. Kothapalli, N.; Zempleni, J., Double strand breaks of DNA decrease biotinylation of lysine 12 in histone H4 in JAr cells. *FASEB (Federation of American Societies for Experimental Biology) Journal* **2004,** 18, 103-104.

108. Cuthbert, G. L.; Daujat, S.; Snowden, A. W.; Erdjument-Bromage, H.; Hagiwara, T.; Yamada, M.; Schneider, R.; Gregory, P. D.; Tempst, P.; Bannister, A. J.; Kouzarides, T., Histone Deimination Antagonizes Arginine Methylation. *Cell* **2004,** 118, (5), 545-553.

109. Nakashima, K.; Hagiwara, T.; Yamada, M., Nuclear localization of peptidylarginine deiminase V and histone deimination in granulocytes. *Journal of Biological Chemistry* **2003,** 277, (51), 49562-49568.

110. Iberg, A. N.; Espejo, A.; Cheng, D.; Kim, D.; Michaud-Levesque, J.; Richard, S.; Bedford, M. T., Arginine methylation of the histone h3 tail impedes effector binding. *Journal of Biological Chemistry* **2008,** 283, 3006-3010.

111. Denis, H.; Deplus, R.; Putmans, P.; Yamada, M.; Metivier, R.; Fuks, F., Functional Connection between Deimination and Deacetylation of Histones. *Molecular and Cellular Biology* **2009,** 29, (18), 4982-4993.

112. Nelson, C. J.; Santos-Rosa, H.; Kouzarides, T., Proline isomerization of histone H3 regulates lysine methylation and gene expression. *Cell* **2006,** 126, (5), 905-916.

113. Lin, W. J.; Gary, J. D.; Yang, M. C.; Clarke, S.; Herschmann, H. R., The mammalian immediate-earl TIS21 protein and the leukemia-associated BTG1 protein interact with a protein-arginine N-methyltransferase. *Journal of Biological Chemistry* **1996,** 271, 15034-15044.

114. Frankel, A.; Clarke, S., PRMT3 is a distinct member of the protein arginine N-methyltransferase family. Conferral of substrate specificity by a zinc-finger domain. *Journal of Biological Chemistry* **2000,** 275, 32974-32982.

115. Frankel, A.; Yadav, N.; Lee, J.; Branscombe, T. L.; Clarke, S.; Bedford, M. T., The novel human protein arginine N-methyltransferase PRMT6 is a nuclear enzyme displaying unique substrate specificity. *Journal of Biological Chemistry* **2002,** 277, 3537-3543.

116. Lee, J.; Sayegh, J.; Daniel, J.; Clarke, S.; Bedford, M. T., PRMT8, a new membrane-bound tissue-specific member of the protein arginine methyltransferase family. *Journal of Biological Chemistry* **2005,** 280, 32890-32896.

117. Zhang, X.; Cheng, X., Structure of the Predominant Protein Arginine Methyltransferase PRMT1 and Analysis of Its Binding to Substrate Peptides. *Structure* **2003,** 11, 509-520.

118. Gonsalvez, G. B.; Tian, L.; Ospina, J. K.; Boisvert, F. M.; Lamond, A. I.; Matera, A. G., Two distinct arginine methyltransferases are required for biogenesis of Sm-class ribonucleoprotins. *Journal of Cell Biology* **2007,** 178, 733-740.

119. Qi, C.; Chang, J.; Zhu, Y.; Yeldandi, A. V.; Rao, S. M.; Zhu, Y. J., Identification of protein arginine methyltransferase 2 as a coactivator for estrogen receptor alpha. *Journal of Biological Chemistry* **2002,** 277, (32), 28624-28630.

120. Pal, S.; Vishwanath, S. N.; Erdjument-Bromage, H.; Tempst, P.; Sif, S., Human SWI/SNF-Associated PRMT5 Methylates Histone H3 Arginine 8 and Negatively Regulates Expression of ST7 and NM23 Tumor Suppressor Genes. *Molecular and Cellular Biology* **2004,** 24, (21), 9630-9645.

121. Zhang, Y.; Reinberg, D., Transcription regulation by histone methylation: interplay between different covalent modifications of the core histone tails. *Genes & Development* **2001,** 15, 2343-2360.

122. Waldmann, T.; Izzo, A.; Kamieniarz, K.; Richter, F.; Vogler, C.; Sarg, B.; Lindner, H.; Young, N. L.; Mittler, G.; Garcia, B. A.; Schneider, R., Methylation of H2AR29 is a novel repressive PRMT6 target. *Epigenetics & Chromatin* **2011,** 4, (11), 1-10.

123. Flanagan, J. F.; Mi, L. Z.; Chruszcz, M.; Cymborowski, M.; Clines, K. L.; Kim, Y.; Minor, W.; Rastinejad, F.; Khorasanizadeh, S., Double chromodomains cooperate to recognize the methylated histone H3 tail. *Nature* **2005,** 438, (7071), 1181-1185.

124. Kirmizis, A.; Santos-Rosa, H.; Penkett, C. J.; Singer, M. A.; Vermeulen, M.; Mann, M.; Bahler, J.; Green, R. D.; Kouzarides, T., Arginine methylation at H3R2 controls deposition of H3K4 trimethylation. *Nature Letters* **2007,** 449, 928-934.

125. Li, X.; Hu, X.; Patel, B.; Zhou, Z.; Liang, S.; Ybarra, R.; Qiu, Y.; Felsenfeld, G.; Bungert, J.; Huang, S., H4R3 methylation facilitates β-globin transcription by regulating histone acetyltransferase binding and H3 acetylation. *Blood* **2010,** 115, (10), 2028-2037.

126. Zhao, Q.; G., R.; Tan, Y. T.; Li, H.; Moritz, R. L.; Simpson, R. J.; Cerruti, L.; Curtis, D. J.; Patel, D. J.; Allis, C. D.; Cunningham, J. M.; Jane, S. M., PRMT5-mediated methylation of histone H4R3 recruits DNMT3A, coupling histone and

DNA methylation in gene silencing. *Nature Structural and Molecular Biology* **2009,** 16, (3), 304-311.

127. Guo, H.-B.; Guo, H., Mechanism of histone methylation catalyzed by protein lysine methyltransferase SET7/9 ad origin of product specificity. *Proceedings of the National Academy of Sciences of the United States of America* **2007,** 104, (21), 8797-8802.

128. Wysocka, J.; Swigut, T.; Xiao, H.; Milne, T. A.; Kwon, S. Y.; Landry, J.; Kauer, M.; Tackett, A. J.; Chait, B. T.; Badenhorst, P.; Wu, C.; Allis, C. D., A PHD finger of NURF couples histone H3 lysine 4 trimethylation with chromatin remodelling. *Nature* **2006,** 442, (7098), 86-90.

129. Hung, T.; Binda, O.; Champagne, K. S.; Kuo, A. J.; Johnson, K.; Change, H. Y.; Simon, M. D.; Kutateladze, T. G.; Gozani, O., ING4 mediates crosstalk between histone H3 K4 trimethylation and H3 acetylation to attenuate cellular transformation. *Molecular Cell* **2009,** 33, (2), 248-256.

130. Taverna, S. D.; Ilin, S.; Rogers, R. S.; Tanny, J. C.; Lavender, H.; Li, H.; Baker, L.; Boyle, J.; Balair, L. P.; Chait, B. T.; Patel, D. J.; Aitchison, J. D.; Tackett, A. J.; Allis, C. D., Yng1 PHD finger binding to H3 trimethylated at K4 promotes NuA3 HAT activity at K14 of H3 and transcription at a subset of targeted ORFs. *Molecular Cell* **2006,** 24, (5), 785-796.

131. Shi, X.; Hong, T.; Walter, K. L.; Wewalt, M.; Michishita, E.; Hung, T.; Carney, D.; Pena, P.; Lan, F.; Kaadige, M. R.; Lacoste, N.; Cayrou, C.; Davrazou, F.; Saha, A.; Cairns, B. R.; Aver, D. E.; Kutateladze, T. G.; Shi, Y.; Cote, J.; Chua, K. F.; Gozani, O., ING2 PHD domain links histone H3 lysine 4 methylation to active gene repression. *Nature* **2006,** 442, (7098), 96-99.

132. Bergmann, J. H.; Rodriguez, M. G.; Martins, N. M. C.; Kimura, H.; Kelly, D. A.; Masumoto, H.; Larionov, V.; Jansen, L. E. T.; Earnshaw, W. C., Epigenetic engineering shows H3K4me2 is required for HJURP targeting and CENP-A assembly on a synthetic human kinetochore. *EMBO Journal* **2011,** 30, 328-340.

133. Shi, Y.; Lan, F.; Matson, C.; Mulligan, P.; Whetstine, J. R.; Cole, P. A.; Casero, R. A.; Shi, Y., Histone demethylation mediated by the nuclear amine oxidase homolog LSD1. *Cell* **2004,** 119, (7), 941-953.

134. Metzger, E.; Wissmann, M.; Yin, N.; Muller, J. M.; Schneider, R.; Peters, A. H. F. M.; Gunther, T.; Buettner, R.; Schule, R., LSD1 demethylates repressive histone marks to promote androgen-receptor-dependent transcription. *Nature* **2005,** 437, (7057), 436-439.

135. Karytinos, A.; Formeris, F.; Profumo, A.; Ciossani, G.; Battaglioli, E.; Binda, C.; Mattevi, A., A Novel Mammalian Flavin-dependent Histone Demethylase. *Journal of Biological Chemistry* **2009,** 284, (26), 17775-17782.

136. Ballas, N.; Battaglioli, E.; Atouf, F.; Andres, M. E.; Chenoweth, J.; Anderson, M. E.; Burger, C.; Moniwa, M.; Davie, J. R.; Bowers, W. J.; Federoff, H. J.;

Rose, D. W.; Rosenfeld, M. G.; Brehm, P.; Mandel, G., Regulation of neuronal traits by a novel transcriptional complex. *Neuron* **2001,** 31, (3), 353-365.

137. Wang, J.; Hevi, S.; Kurash, J. K.; Lei, H.; Gay, F.; Bajko, J.; Su, H.; Sun, W.; Chang, H.; Xu, G.; Gaudet, F.; Li, E.; Chen, T., The lysine demethylase LSD1 (KDM1) is required for maintenance of global DNA methylation. *Nature Genetics* **2009,** 41, (1), 125-129.

138. Hillringhaus, L.; Yue, W. W.; Rose, N. R.; Ng, S. S.; Gileadi, C.; Loenarz, C.; Bello, S.; Bray, J. E.; Schofield, C. J.; Oppermann, U., Structural and evolutionary basis for the dual substrate electivity of the human KDM4 histone demethylase family. *Journal of Biological Chemistry* **2011,** 286, 41616-41625.

139. Ng, S. S.; Kavanagh, K. L.; McDonough, M. A.; Butler, D.; Pilka, E. S.; Lienard, B. M.; Bray, J. E.; Savitsky, P.; Gileadi, C.; Von Delft, F.; Rose, N. R.; Offer, J.; Scheinost, J. C.; Borowski, T.; Sundstrom, M.; Schofield, C. J.; Oppermann, U., Crystal structures of histone demethylase JMJD2A reveal basis for substrate specificity. *Nature* **2007,** 448, 87-91.

140. Horton, J. R.; Upadhyay, A. K.; Qi, H. H.; Zhang, X.; Shi, Y.; Cheng, X., Enzymatic and structural insights for substrate specificity of a family of jumonji histone lysine demethylases. *Nature Structural and Molecular Biology* **2010,** 17, 38-43.

141. Ageing, A. D. o. H. a., Formaldehyde in clothing and other textiles. **2007**.

142. www.health-report.co.uk, Formaldehyde Fact Sheet. **1999**.

143. Bosetti, C.; McLaughlin, C.; Tarone, R. E.; Pira, E.; LaVecchia, C., Formaldehyde and cancer risk: a quantitative review of cohort studies through 2006. *Annals of Oncology* **2008,** 19, (1), 29-43.

144. Yu, P. H.; Deng, Y. L., Endogenous formaldehyde as a potential factor of vulnerability of atherosclerosis: involvement of semicarbazide amine-oxidase-mediated methylamine turnover. *Atherosclerosis* **1998,** 140, (2), 142-147.

145. Bannister, A. J.; Schneider, R.; Kouzarides, T., Histone Methylation: Dynamic or Static? *Cell* **2002,** 109, 801-806.

146. Trezl, L.; Lehel, H.; Jaszay, Z. M.; Szarvas, T.; Petnehazy, I.; Szende, B.; Bocsi, J.; Takats, Z.; Vakay, K.; Toke, L., Antagonistic reactions of arginine and lysine against formaldehyde and their relation to cell proliferation, apoptosis, folate cycle and photosynthesis. *Molecular and Cellular Biochemistry* **2003,** 244, 167-176.

147. Hernandez, M.; Sole, M.; Boada, M.; Unzeta, M., Soluble semicarbazide sensitive amine oxidase (SSAO) catalysis induces apoptosis in vascular smotth muscle cells. *Biochimica et Biophysica Acta* **2006,** 1763, (2), 164-173.

148. Nudelman, A.; Levovich, I.; Cutts, S. M.; Phillips, D. R.; Rephaeli, A., The Role of Intracellularly Released Formaldehyde and Butyric Acid in the Anticancer

Activity of Acyloxyalkyl Esters. *Journal of Medicinal Chemistry* **2005,** 48, 1042-1054.

149. Lovschall, H.; Eiskjaer, M.; Arenholt-Bindslev, D., Formaldehyde cytotoxicity in three human cell types assessed in three different assays. *Toxicology In Vitro* **2002,** 16, (1), 63-69.

150. Olsen, J. H.; Jensen, S. P.; Hink, M.; Faurbo, K.; Breum, N. O.; Jensen, O. M., Occupational formaldehyde exposure and increased nasal cancer risk in man. *International Journal of Cancer* **1984,** 34, (639-644).

151. Gustavsson, P.; Jokobsson, R.; Johansson, H.; Lewin, F.; Norell, S.; Rutkvist, L.-E., Occupational exposures and squamous cell carcinoma of the oral cavity, pharynx, larynx, and oesophagus: a case-control study in Sweden. *Occupational and Environmental Medicine* **1998,** 55, 393-400.

152. Shaham, J.; Bomstein, Y.; Meltzer, A.; Kaufman, Z.; Palma, E.; Ribak, J., DNA-protein crosslinks, a biomarker of exposure to formaldehyde - *in vitro* and *in vivo* studies. *Carcinogenesis* **1996,** 17, (1), 121-125.

153. Merk, O.; Speit, G., Significance of Formaldehyde-Induced DNA-Protein Crosslinks for Mutagenesis. *Environmental and Molecular Mutagenesis* **1998,** 32, (3), 260-268.

154. Harms, N.; Ras, J.; Reijnders, W. N. M.; van Spanning, R. J. M., *S*-Formylglutathione Hydrolase of *Paracoccus denitrificans* is Homologous to Human Esterase D: a Universal Pathway for Formaldehyde Detoxification? *Journal of Bacteriology* **1996,** 178, (21), 6296-6299.

155. Adinolfi, A.; Adinolfi, M.; Hopkinson, D. A., Immunological and biochemical characterization of the human alcohol dehydrogenase X-ADH isozyme. *Annals of Human Genetics* **2007,** 48, (1), 1-10.

156. Goenrich, M.; Bartoschek, S.; Hagemeier, C. H.; Griesinger, C.; Vorholt, J. A., A Glutathione-dependent Formaldehyde-activating Enzyme (Gfa) from *Paracoccus denitrificans* Detected and Purified via Two-dimensional Proton Exchange NMR Spectroscopy. *Journal of Biological Chemistry* **2002,** 277, (5), 3069-3072.

157. Tadeu, A. M. B.; Ribeiro, S.; Johnston, J.; Goldberg, I.; Gerloff, D.; Earnshaw, W. C., CENP-V is required for centromere organization, chromosome alignment and cytokinesis. *EMBO Journal* **2008,** 27, 2510-2522.

158. Neculai, A. M.; Neculai, D.; Griesinger, C.; Vorholt, J. A., A Dynamic Zinc Redox Switch. *Journal of Biological Chemistry* **2005,** 280, (4), 2826-2330.

159. Kalasz, H., Biological Role of Formaldehyde, and Cycles Related to Methylation, Demethylation, and Formaldehyde Production. *Mini Reviews in Medicinal Chemistry* **2003,** 3, 175-192.

160. Kallen, R. G.; Jencks, W. P., The Mechanism of the Condensation of Formaldehyde with Tetrahydrofolic Acid. *Journal of Biological Chemistry* **1966,** 241, (24), 5851-5863.

161. Loenen, W. A., S-adenosylmethionine: jack of all trades and master of everything? *Biochemical Society Transactions* **2006,** 34, (2), 330-333.

162. Kristensen, J. B. L.; Nielsen, A. L.; Jorgensen, L.; Kristensen, L. H.; Helgstrand, C.; Juknaite, L.; Kristensen, J. L.; Kastrup, J. S.; Clausen, R. P.; Olsen, L.; Gajhede, M., Enzyme kinetic studies of histone demethylases KDM4C and KDM6A: Towards understanding selectivity of inhibitors targeting oncogenic histone demethylases. *FEBS Letters* **2011,** 585, 1951-1956.

163. Kawamura, A.; Tumber, A.; Rose, N. R.; King, O. N. F.; Daniel, M.; Oppermann, U.; Heightman, T. D.; Schofield, C. J., Development of homogeneous luminescence assays for histone demethylase catalysis and binding. *Analytical Biochemistry* **2010,** 404, 86-93.

164. Loenarz, C.; Ge, W.; Coleman, M. L.; Rose, N. R.; Cooper, C. D. O.; Klose, R. J.; Ratcliffe, P. J.; Schofield, C. J., *PHF8*, a gene associated with cleft lip/palate and mental retardation, encodes for an N^{ε}-dimethyl lysine demethylase. *Human Molecular Genetics* **2009,** 19, (2), 217-222.

165. Sakurai, M.; Rose, N. R.; Schultz, L.; Quinn, A.; Jadhav, A.; Ng, S. S.; Oppermann, U.; Schofield, C. J.; Simeonov, A., A Miniaturized Screen for Inhibitors of Jumonji Histone Demethylases. *Molecular Biosystems* **2009,** 6, (2), 357-364.

166. Koehntop, K. D.; Marimanikkuppam, S.; Ryle, M. J.; Hausinger, R. P.; Que, L., Self-hydroxylation of taurine/a-ketoglutarate dioxygenase: evidence for more than one oxygen activation mechanism. *Journal of Biological Inorganic Chemistry* **2006,** 11, 63-72.

167. Sardi, E.; Tyihak, E., Simple Determination of Formaldehyde in Dimedone Adduct Form in Biological Samples by High Performance Liquid Chromatography. *Biomedical Chromatography* **1994,** 8, 313-314.

168. Mason, R. P.; Sanders, J. K. M., .; Crawford, A.; K., H. B., Formaldehyde metabolism by *Escherichia coli*. Detection by *in vivo* carbon-13 NMR spectroscopy of S-(hydroxymethyl)glutathione as a transient intracellular intermediate. *Biochemistry* **1986,** 25, (16), 4504-4507.

169. Huang, Z.-P.; Du, J.-T.; Zhao, Y.-F.; Li, Y.-M., Synthesis of Site-Specifically Dimethylated and Trimethylated Peptides Derived from Histone H3 N-Terminal Tail. *International Journal of Peptide Research and Therapeutics* **2006,** 12, (2), 187-193.

170. Han, Z.; Liu, P.; Gu, L.; Hong, L.; Chen, S.; Chai, J., Structural Basis for Histone Demethylation by JHDM1. *Frontier Science* **2007,** 1, 52-61.

171. Feng, W.; Yonezawa, M.; Jung, Y.; Jenuwein, T.; Grummt, I., PHF8 activates transcription of rRNA genes through H3K4me3 binding and H3K9me1/2 demethylation. *Nature Structural and Molecular Biology* **2010,** 17, 445-450.

172. Bedford, M. T.; Clarke, S. G., Protein Arginine Methylation in Mammals: Who, What, and Why. *Molecular Cell* **2009,** 33, 1-13.

173. Bedford, M. T.; Richard, S., Arginine Methylation: An Emerging Regulator of Protein Function. *Molecular Cell* **2005,** 18, 263-272.

174. Balint, B. L.; Gabor, P.; Nagy, L., Genome-wide localization of histone 4 arginine 3 methylation in a differentiation primed myeloid leukemia cell line. *Immunobiology* **2005,** 210, (2-4), 141-152.

175. Michaud-Levesque, J.; Richard, S., Thrombospondin-1 Is a Transcriptional Repression Target of PRMT6. *Journal of Biological Chemistry* **2009,** 284, (32), 21338-21346.

176. Kowenz-Leutz, E.; Pless, O.; Dittmar, G.; Knoblich, M.; Leutz, A., Crosstalk between C/ETPb phosphorylation, arginine methylation, and SWI/SNF/Mediator implies an indexing transcription factor code. *EMBO Journal* **2010,** 29, 1105-1115.

177. Goulet, I.; Gauvin, G.; Boisvenue, S.; Cote, J., Alternative splicing yield protein arginine methyltransferase 1 isoforms with distinct activity, substrate specificity, and subcellular localization. *Journal of Biological Chemistry* **2007,** 282, 33009-33021.

178. Lee, J.; Bedford, M. T., PABP1 identified as an arginine methyltransferase substrate using high-density protein arrays. *EMBO Reports* **2002,** 3, 268-273.

179. Nishioka, K.; Reinberg, D., Methods and tips for the purification of human histone methyltransferases. *Methods* **2003,** 31, 49-58.

180. Lacroix, M.; Messaoudi, S. E.; Rodier, G.; Le Cam, A.; Sardet, C.; Fabbrizio, E., The histone-binding protein COPR5 is required for nuclear functions of the protein arginine methyltransferase PRMT5. *EMBO Reports* **2008,** 9, 452-458.

181. Meyer, R.; Wolf, S. S.; Obendorf, M., PRMT2, a member of the protein arginine methyltransferase family, is a coactivator of the androgen receptor. *Journal of Steroid Biochemistry and Molecular Biology* **2007,** 107, 1-14.

182. Wang, Y.; Wysocka, J.; Savegh, J.; Lee, Y. H.; Perlin, J. R.; Leonelli, L.; Sonbuchner, L. S.; McDonald, C. H.; Cook, R. G.; Roeder, R. G.; Clarke, S.; Stallcup, M. R.; Allis, C. D.; Coonrod, S. A., Human PAD4 regulates histone arginine methylation levels via demethylimination. *Science* **2004,** 306, (5694), 279-283.

183. Cloos, P. A.; Christensen, J.; Agger, K.; Helin, K., Erasing the methyl histone mark: histone demethylases at the center of cellular differentiation and disease. *Genes & Development* **2008,** 22, (9), 1115-1140.

184. Sekernik, R.; Rose, N. R.; Thalhammer, A.; Seden, P. T.; Mecinovic, J.; Schofield, C. J., Inhibition of the histone demethylase JMJD2A by ejection of structural Zn(II). *Chemical Communications* **2009**, 6376-6378.

185. Zhang, Z.; Schofield, C. J.; Baldwin, J. E.; Thomas, P.; John, P., Expression, purification and characterization of 1-aminocyclopropane-1-carboxylate oxidase from tomato in *Escherichia coli*. *Biochemical Journal* **1995,** 307, (1), 77-85.

186. Adams-Cioaba, M. A.; Krupa, J. C.; Xu, C.; Mort, J. S.; Min, J., Structural basis for the recognition and cleavage of histone H3 by Cathepsin L. *Nature Communications* **2011,** 2, Article Number 197.

187. Duncan, E. M.; Muratore-Schroeder, T. L.; Cook, R. G.; Garcia, B. A.; Shabanowitz, J.; Hunt, D. F., Cathepsin L Proteolytically Processes Histone H3 During Mouse Embryonic Stem Cell Differentiation. *Cell* **2008,** 135, (2), 284-294.

188. Horton, J. R.; Upadhyay, A. K.; Hashimoto, H.; Zhang, X.; Cheng, X., Structural basis for human PHF2 Jumonji domain interaction with metal ions. *Journal of Molecular Biology* **2011,** 406, (1), 1-8.

189. Li, G.; Margueron, R.; Ku, M.; Chambon, P.; Bernstein, B. E.; Reinberg, D., Jarid2 and PRC2, partners in regulating gene expression. *Genes & Development* **2010,** 24, 368-380.

190. Chang, K.-H.; King, O. N. F.; Tumber, A.; Woon, E. C. Y.; Heightman, T. D.; McDonough, M. A.; Schofield, C. J.; Rose, N. R., Inhibition of Histone Demethylases by 4-Carboxy-2,2'-Bipyridyl Compounds. *ChemMedChem* **2011,** 6, 759-764.

191. Price, J. C.; Barr, E. W.; Tiraputi, J.; Bollinger Jr, J. M.; Krebs, C., The First Direct Characterization of a High-Valent Iron Intermediate in the Reaction of an a-Ketoglutarate-Dependent Dioxygenase: A High-Spin Fe(IV) Complex in Taurine/a-Ketoglutarate Dioxygenase (TauD) from *Escherichia coli*. *Biochemistry* **2003,** 42, 7497-7508.

192. Hornbach, J. M., Organic Chemistry.

193. Lewis, E. S.; Robinson, J. K., The Influence of Tunneling on the Relation between Tritium and Deuterium Isotope Effects. The Exchange of 2-Nitropropane-2-t. *Journal of the American Chemical Society* **1968,** 90, 4337-4344.

194. Roecker, L.; Meyer, T. J., Hydride Transfer in the Oxidation of Alcohols by [(bpy)2(py)Ru(0)]2'. A kH/kD Kinetic Isotope Effect of 50. *Journal of the American Chemical Society* **1987,** 109, 746-754.

195. Grzyska, P. K.; Hausinger, R. P.; Proshlyakov, D. A., Metal and substrate binding to an Fe(II) dioxygenase resolved by UV spectroscopy with global regression analysis. *Analytical Biochemistry* **2010,** 399, 64-71.

196. Ryle, M. J.; Padmakumar, R.; Hausinger, R. P., Stopped-Flow Kinetic Analysis of *Escherichia coli* Taurine/a-Ketoglutarate Dioxygenase: Interactions with a-Ketoglutarate, Taurine and Oxygen. *Biochemistry* **1999,** 38, 15278-15286.

197. Grzyska, P. K.; Ryle, M. J.; Monterosso, G. R.; Liu, J.; Ballou, D. P.; Hausinger, R. P., Steady-State and Transient Kinetic Analyses of taurine/a-Ketoglutarate Dioxygenase: Effects of Oxygen Concentration, Alternative Sulfonates, and Active-Site variants on the Fe^{IV}-oxo Intermediate. *Biochemistry* **2005,** 44, 3845-3855.

198. Metz, B.; Kersten, G. F. A.; de Jong, A.; Meiring, H.; ten Hove, J.; Hennink, W. E.; Crommelin, D. J. A.; Jiskoot, W., Identification of formaldehyde-induced modifications in proteins:reactions with diphtheria toxin.

199. McGhee, J. D.; Von Hippel, P. H., Formaldehyde as a probe of DNA structure. I. Reaction with exocyclic amino groups of DNA bases. *Biochemistry* **1975,** 14, (6), 1281-1296.

200. McGhee, J. D.; Von Hippel, P. H., Formaldehyde as a probe of DNA structure. II. Reaction with endocyclic imino groups of DNA bases. *Biochemistry* **1975,** 14, (6), 1297-1303.

201. Chaw, Y. F. M.; Crane, L. E.; Lange, P.; Shapiro, R., Isolation and identification of cross-links from formaldehyde-treated nucleic acids. *Biochemistry* **1980,** 19, (24), 5525-5531.

202. Metz, B.; Kersten, G. F. A.; Hoogerhout, P.; Brugghe, H. F.; Timmermans, H. A. M.; De Jong, A.; Meiring, H.; Ten Hove, J.; Hennink, W. E.; Crommelin, D. J. A.; Jiskoot, W., Identification of Formaldehyde-induced Modifications in Proteins. *Journal of Biological Chemistry* **2004,** 279, (8), 6235-6243.

203. Speit, G.; Schütz, P.; Merk, O., Induction and repair of formaldehyde-induced DNA-protein crosslinks in repair-deficient human cell lines. *Mutagenesis* **2000,** 15, (1), 85-90.

204. Lu, K.; Ye, W.; Zhou, L.; Collins, L. B.; Chen, X.; Gold, A.; Ball, L. M.; Swenberg, J. A., Structural Characterization of Formaldehyde-induced Cross-links Between Amino Acids and Deoxynucleosides and Their Oligomers. *Journal of the American Chemical Society* **2010,** 132, (10), 3388-3399.

205. Lu, K.; Boysen, G.; Gao, L.; Collins, L. B.; Swenberg, J. A., Formaldehyde-induced histone modifications *in vitro*. *Chemical Research in Toxicology* **2008,** 21, (8), 1586-1593.

206. Gonzalez, C.; Proudfoot, M.; Brown, G.; Korniyenko, Y.; Maori, H.; Savchenko, A.; Yakunin, A., Molecular basis for formaldehyde detoxification. Characterization of two S-formylglutathione hydrolases from Escherichia coli, FrmB and YeiG. *Journal of Biological Chemistry* **2006,** 281, 14514-14522.

207. Bellomo, G.; Vairetti, M.; Stivala, L.; Mirabelli, F.; Richelmi, P.; Orrenius, S., Demonstration of nuclear compartmentalization of glutathione in hepatocytes.

Proceedings of the National Academy of Sciences of the United States of America **1992,** 89, (10), 4412-4416.

208. Galter, D.; Carmine, A.; Buervenich, S.; Duester, G.; Olson, L., Distribution of class I, III and IV alcohol dehydrogenase mRNAs in the adult rat, mouse and human brain. *FEBS Journal* **2003,** 270, (6), 1316-1326.

209. Meister, A.; Anderson, M. E., Glutathione. *Annual Review of Biochemistry* **1983,** 52, 711-760.

210. Sprung, M. M., A summary of the reactions of aldehydes with amines. *Chemical Reviews* **1940,** 26, (3), 297-338.

211. Naylor, S.; Mason, R. P.; Sanders, J. K. M.; Williams, D. H.; Moneti, G., Formaldehyde adducts of glutathione. *Biochemical Journal* **1988,** 249, 573-579.

212. Bateman, R.; Rauh, D.; Shokat, K. M., Glutathione traps formaldehyde by formation of a bicyclo[4.4.1]undecane adduct. *Organic & Biomolecular Chemistry* **2007,** 5, 3363-3367.

213. Hahnenstein, I.; Albert, M.; Hasse, H.; Kreiter, C. G.; Maurer, G., NMR Spectroscopic and Densimetric Study of reaction Kinetics of Formaldehyde Polymer Formation in Water, Deuterium Oxide, and Methanol. *Industrial and Engineering Chemistry Research* **1995,** 34, 440-460.

214. Cannizzaro, S., Ueber den der Benzoësäure entsprechenden Alkohol. *Justus Liebigs Annalen der Chemie* **1853,** 88, (1), 129-130.

215. Cordes, E. H.; Jencks, W. P., On the Mechanism of Schiff Base Formation and Hydrolysis. *Journal of the American Chemical Society* **1962,** 84, (5), 832-837.

216. Kallen, R. G.; Jencks, W. P., Equilibria for the Reaction of Amines with Formaldehyde and Protons in Aqueous Solution. *Journal of Biological Chemistry* **1966,** 241, (24), 5864-5878.

217. Lands, W. E. M., A Review of Alcohol Clearance in Humans. *Alcohol* **1998,** 15, (2), 147-160.

218. Kalapos, M. P., Methylglyoxal in living organisms Chemistry, biochemistry, toxicology and biological implications. *Toxicology Letters* **1999,** 110, 145-175.

219. Desai, K. M.; Chang, T.; Wang, H.; Banigesh, A.; Dhar, A.; Liu, J.; Untereiner, A.; Wu, L., Oxidative stress and aging: Is methylglyoxal the hidden enemy? *Canadian Journal of Physiology and Pharmacology* **2010,** 88, 273-284.

220. de Vries, G. E.; Harms, N.; Maurer, G., Methanol metabolism in Paracoccus denitrificans II. Regulation of methanol dehydrogenase induction. *Antonie Van Leeuwenhoek* **1985,** 51, 555.

221. Harms, N.; De Vries, G. E.; Maurer, G.; Stouthamer, A. H., Methanol metabolism in *Paracoccus denitrificans*. Isolation and characterization of

mutants with defects in utilization. *Antonie Van Leeuwenhoek* **1985,** 51, 550-551.

222. Harms, N.; Van Spanning, R. J. M., C1 metabolism in *Paracoccus denitrificans*: genetics of *Paracoccus denitrificans*. *Journal of Bioenergetics and Biomembranes* **1991,** 23, (2), 187-210.

223. Wilson, S. M.; Gleisten, M. P.; Donohue, T. J., Identification of proteins involved in formaldehyde metabolism by *Rhodobacter sphaeroides*. *Microbiology* **2008,** 154, (1), 296-305.

224. Geoghegan, K. F.; Dixon, H. B. F.; Rosner, P. J.; Hoth, L. R.; Lanzetti, A. J.; NBorzilleri, K. A.; Stroh, J. G., Spontaneous a-N-6-Phosphogluconoylation of a "His Tag" in *Escherichia coli*: The cause of Extra Mass of 258 or 178 Da in Fusion Proteins. *Analytical Biochemistry* **1999,** 267, (1), 169-184.

225. Yan, Z.; Caldwell, G. W.; McDonell, P. A., Identification of a Gluconic Acid Derivative Attached to the N-Terminus of Histidine-Tagged Protein Expressed in Bacteria. *Biochemical and Biophysical Research Communications* **1999,** 262, (3), 793-800.

226. Sharon, M.; Robinson, C. V., The Role of Mass Spectrometry in Structure Elucidation of Dynamic Protein Complexes. *Annual Review of Biochemistry* **2007,** 76, 167-193.

227. Kebarle, P. A., A Brief Overview of the Present Status of the Mechanisms Involved in Electrospray Mass Spectrometry. *Journal of Mass Spectrometry* **2000,** 35, 804-817.

228. Jeener, J.; Meier, B. H.; Bachmann, P.; Ernst, R. R., Investigation of exchange processes by 2-dimensional NMR-spectroscopy. *Journal of Chemical Physics* **1979,** 71, (11), 4546-4553.

229. Carmichael, D.; Ricard, L.; Seeboth, N.; Brown, J. M.; Claridge, T. D. W.; Odell, B., Synthesis, structure and dynamics of methyoxynapthalene-substituted phospha-ruthenocenes and -ferrocenes. *Dalton Transactions* **2005**, 2173-2181.

230. Abel, E. W.; Coston, T. P. J.; Orrell, K. G.; Sik, V.; Stephenson, D., Two-dimensional NMR exchange spectroscopy. Quantitative treatment of multisite exchanging systems. *Journal of Magnetic Resonance* **1986,** 70, (1), 34-53.

231. Sutton, H. C.; Downes, T. M., Rate of Hydration of Formaldehyde in Aqueous Solution. *Journal of the Chemical Society, Chemical Communications* **1972,** 1, 1-2.

232. Gruen, L. C.; McTigue, P. T., Hydration Equilibria of Aliphatic Aldehydes in H_2O and D_2O. *Journal of the Chemical Society* **1963**, 5217-5223.

233. Bell, R. P.; Evans, P. G., Kinetics of the Dehydration of Methylene Glycol in Aqueous Solution. *Proceedings of the Royal Society of London Series A* **1966,** 291, 297-323.

234. Mayer, M.; Meyer, B., A Fast and Sensitive Method to Characterise Ligand Binding by Saturation Transfer Difference NMR Spectra. *Angewandte Chemie International Edition* **1999,** 9, 2946-2949.

235. Dalvit, C.; Fogliatto, G.; Stewart, A.; Veronesi, M.; Stockman, B., WaterLOGSY as a method for primary NMR screening: Practical aspects and range of apllicability. *Journal of Biomolecular NMR* **2001,** 21, 349-359.

236. Fielding, L., NMR methods for the determination of protein-ligand dissociation constants. *Progress in Nuclear Magnetic Resonance Spectroscopy* **2007,** 51, 219-242.

237. Mayer, M.; Meyer, B., Characterization of Ligand Binding by Saturation Transfer Difference NMR Spectroscopy. *Angewandte Chemie International Edition* **1999,** 38, (12), 1784-1788.

238. Meyer, B.; Peters, T., NMR Spectroscopy Techniques for Screening and Identifying Ligand Binding to Protein Receptors. *Angewandte Chemie International Edition* **2003,** 42, (864-890).